ANALYSIS OF THE STRUCTURAL BEHAVIOUR OF GROUTED PILE/SLEEVE CONNECTIONS FOR OFFSHORE STRUCTURES.

G.A.CHILVERS, B.Sc.

Thesis submitted to The City University for the Degree of Doctor of Philosophy in the Department of Civil Engineering.

February, 1984

TABLE OF CONTENTS

LIST OF TABLES

LIST OF ILLUSTRATIONS

ACKNOWLEDGEMENTS

The author wishes to express thanks to Professor J.E.Gibson for providing facilities to carry out this research in the Department of Civil Engineering at The City University, London, and to Dr.L.F.Boswell for his advice and encouragement in the supervision of this project.

From Wimpey Laboratories, thanks are due to Dr.C.J.Billington for making available many of the results obtained at Wimpey Laboratories, and Dr.K.Ward for his comments and expert guidance.

Thanks are also due to the under-mentioned:-

Dr.C.D'Mello for providing results from the City University Test Programme.

Mr.A.Jones for arranging the necessary laboratory facilities to carry out the steel/grout joint tests.

Mr.R.Counsell for his assistance with the joint tests, and to many other technicians who contributed to the project.

Mr.Seaman of Barking Shot Blast Co. Ltd., who kindly agreed to shot-blast the steel plates free-of-charge before each bond test.

Wimpey Laboratories Ltd. for providing grouting materials.

Mr.R.Lawrence for his advice on computer facilities.

The Science and Engineering Research Council for providing maintenance and support grants.

DECLARATION

I grant powers of discretion to the University Librarian to allow this thesis to be copied in whole or in part without further reference to me. This permission covers only single copies made for study purposes, subject to normal conditions of acknowledgement.

ABSTRACT

Existing experimental results are studied to determine the factors (including those not previously identified) affecting the strength of grouted connections. The current bond strength formula is evaluated and its limitations noted. Previous analytical work is examined and strengths and weaknesses investigated.

A nonlinear finite element analysis is developed using a friction-gap element to model the steel/grout bond. This includes a dilation effect when slip occurs and successfully simulates the behaviour of plain pipe connections up to ultimate load.

An elastic-plastic,work-hardening,cracking and crushing constitutive model is developed to represent the behaviour of grout material. This is used for a detailed finite element analysis of the load-slip behaviour of individual shear keys of various shapes.

The friction-gap element is adapted to give a representation of the shear keys using data derived from the detailed shear key analysis. A confinement factor is used to give higher ultimate shear key loads when the bond opening is small. This accounts for the observed fact that higher key loads are achieved with increased sleeve and pile dimensions due to greater confinement of the grout.

Load-slip behaviour and strains up to ultimate load for shear keyed connections are successfully simulated using the friction-gap element. Bond stress distributions show that high normal bond stress concentrations are necessary to balance the bending moments in the grout annulus. Various extreme geometries are analysed and their failure modes determined. The effects of connection length,stiffeners,alternative loading arrangements, scale and shear key geometry are also fully investigated.

Results are used to produce a new bond strength formula which takes into account most factors affecting bond strength and is able to give good results over the full range of geometries.

Experimental tests have been conducted to determine the coefficient of friction between shot-blasted steel and grout for use in the numerical analyses.

KEY TO SYMBOLS

a , α	Material constant for grout, see eqn. (6.11)
β	Material constant for grout, see eqn. (6.12), or shear key load ratio.
γ, γ	Stiffness parameter, see eqn. (8.12a), or displacement measurement in the bond tests.
γ_{oct}	Octahedral shear strain.
δ_u	Slip
δ_{um}	Mean slip
δ_{sh}	Radial shrinkage on the sleeve bond
δ'	Mean radial bond opening parameter
δ_s , δ_p	Mean radial sleeve and pile bond openings respectively
$\epsilon, \epsilon_z, \epsilon_\theta$	Strain, Axial strain and Hoop strain respectively
ϵ_{oct}	Octahedral normal strain
$\bar{\epsilon}_\theta$	Mean hoop strain
$d\epsilon_{ij}$	Increment of strain
$d\epsilon^e_{ij}$	Increment of elastic strain
$d\epsilon^p_{ij}$	Increment of plastic strain
η	Factor for restoring stability to the iterative process when divergence occurs.
θ	Stiffness parameter, see eqn.(8.12b), or orientation of the bond element to the Z-axis, or crack angle in the grout.
K'	Statistical constant, see eqn.(2.11)
$d\lambda$	Elasto-plastic parameter, see eqn.(6.21)
μ	Coefficient of friction between steel (shot-blasted) and grout.
ν	Poisson's Ratio
σ_e	Effective stress for grout material = $\sqrt{f}$
σ_i	i = 1 to 3, Principal stresses
σ_n	Normal bond stress
$\bar{\sigma}_n$	Mean normal bond stress
σ_{no}	Normal bond stress due to dilation u_4
σ_θ	Circumferential (or hoop) stress
$\bar{\sigma}_\theta$	Mean hoop stress

$\{\sigma(r)\}$	Bond stresses at position r in the friction-gap element
σ_{oct}	Octahedral normal stress
σ_{key}	Mean stress on a shear key in the axial direction
σ_m	Constant, defining shear key strength, see eqn.(8.3a)
σ	Stress or standard deviation
$\bar{\sigma}_z$	Mean axial stress
σ_{sk}	Normal bond stress generated by shear keys
τ	Shear bond stress or grout yield criterion, see eqn.(6.10)
τ_{oct}	Octahedral shear stress
τ_{sk}	Maximum bond stress due to shear keys
τ_o, τ_u	Constants describing the grout material, see eqns. (6.7) and (6.9)
$\phi_{kl;j}$	Elasto-plastic parameters, see eqn. (6.22)
ψ	Constant, see Appendix A
ω	" " " "

A, B, C, D, E, F, G, a, b, c, C'	Various constants
A	Bond surface area for one element
A_s	Total plan area of the shear keys
A_p	Total grouted surface area of the pile
A_{stiff}	Total cross-sectional area of the stiffeners
A_o, A_u	Constants describing the grout material, see eqns.(6.6) and (6.8)
[B]	Matrix relating strains or relative displacements to the displacements.
c	$\cos\theta$
C_L	l/d_p parameter
C_{31}	Factor to adjust bond strength to the 31-day strength
C_s	Surface roughness parameter
c	Adhesion on the steel/grout bond (N/mm^2)
CONF	Confinement factor = $u_a/\Delta n$
[D]	Matrix giving stresses in terms of relative displacements or strains.
d, D	Outside diameter
E	Young's Modulus

f_{bu}	Ultimate bond strength
f_{buc}	Characteristic bond strength
$\bar{f}_{bu}$	Mean ultimate bond strength
f_{cu} , f_c'	Uniaxial ultimate compressive strength of a 76mm cube
f_c	Uniaxial compressive yield stress
f_t', f_t	Tensile ultimate and yield stresses respectively
f_{bc}' , f_{bc}	Ultimate and yield stresses respectively under biaxial compression.
f, $f(\sigma_{ij})$	Grout material failure surface, see eqn.(6.10)
F_s	Normalised bond stress
F_{BU}	Normalised ultimate bond strength
F_{BUM}	Normalised ultimate bond strength for grout cured for M days.
F_{BUC}	Characteristic normalised ultimate bond strength
F	Uniformly distributed radial force per unit length in the axial direction.
$\{F^e\}$	Vector of nodal applied loads
FAC1, FAC2	Factors for reducing k_n, k_t when the bond slips or opens respectively.
G	A scalar function to define plastic grout strains, see eqn.(6.14)
H	Work-hardening rate for the grout, see eqn.(6.23)
H'	See eqn.(6.24)
h	Shear key height (or upstand)
h_{eff}	Effective shear key height
IPEL	Grout material status (elastic, plastic, cracked or crushed)
I_1 , I_1^ϵ	First invariants of stress and strain respectively
J_2 , J_2^ϵ	Second invariants of deviatoric stress and strain
K, K', K'', K''' etc.	Constants
K	Stiffness Factor, see eqn.(2.3)
K_m	Stiffness Factor adjusted to allow for longitudinal stiffeners
k_n	Normal bond stiffness factor (N/mm^3)
k_t	Tangential bond stiffness factor (N/mm^3)
[K]	Tangential stiffness matrix
k_{sc}	Tangential shear key stiffness (N/mm^3)

l, l	Grouted length, or length of one bond element
n	Constant defining rate of increase of u_a, see eqn.(5.36)
Δn	Relative bond opening
N	Load increment count
N_i	Shape functions (i=1 to 3 for quadratic shape functions)
NUMCR	Code for crack status
p	Pressure
P_i	Force in Y-direction on node i
ΔP	Axial load increment
P	Axial load applied to the grouted connection, or vertical load used in the bond tests.
Q	Internal nodal forces
R	Cylinder radius, or the ratio used to find the grout stresses to reach the failure surface, f.
R_{ob}	Out-of-balance, (or residual) loads.
r	Local coordinate for friction-gap element, or cylinder radius.
[R]	Transformation matrix used to rotate the cracked grout [D] matrix into the global orientation.
R_i	Nodal force perpendicular to $\underline{r}$ on node i for a friction - gap element.
S_i	Nodal force parallel to $\underline{r}$ on node i for a friction-gap element.
S	$\sin\theta$
s	Shear key spacing
SF	Ostroot's stiffness factor, see eqn.(3.10)
T	Horizontal shear load in the bond tests
t	Cylinder thickness
Δt	Relative bond slip
u	Displacement
Δu	Displacement increment
u_i	Displacement of node i in the Y-direction.
u_a	Surface roughness bond dilation.
u_m	Maximum bond dilation.
$\{\Delta u^e\}$	Vector of nodal relative displacements on a bond element.
$\{u^e\}$	Vector of nodal displacements for a bond element.

$\{u(r)\}$	Nodal displacements at position r in a bond element.
$\{\Delta u(r)\}$	Relative nodal displacements at position r in a bond element.
$\delta\{u^e\}$	Virtual displacement vector.
V	Axial shear key force per unit circumference (N/mm)
V_R	Radial shear key force per unit circumference (N/mm)
v_i	Displacement of node i in the Z-direction.
V_i	Force on node i in the Z-direction.
Y_i, Z_i	Coordinates of node i in the global Y, Z axes.

Subscripts

χ_s	Sleeve or Steel
χ_p	Pile or Principal direction
χ_g	Grout
χ_t	Tangential, or time t

CHAPTER 1

INTRODUCTION

1.1 The use of Grouted Connections in the Construction of Steel Offshore Platforms

In recent years demand for oil has led to the development of offshore oilfields in ever increasing water depths. Many technical problems have had to be overcome in order to achieve this, and one of these involves the structural use of grouted connections. A popular form of construction for fixed offshore platforms is the piled steel jacket. Steel tubular piles are driven (or placed into predrilled holes) through the legs of the structure or through tubular sleeves attached to the lower part of the structure. The annulus between the pile and jacket leg or sleeve is then filled with cement grout.

In shallow water conditions it is normal for a single pile to be placed through each leg of the structure. The pile often extends to the top of the leg so that the deck structure can be welded directly to it. The jacket resists the effects of wave loading, stabilizes the piles and stiffens the complete structure. The grout transmits lateral forces between the piles and jacket and protects against corrosion, but is not normally required to transmit vertical loads from the deck superstructure to the piles. Bond stresses at the steel/grout interfaces are low and debonding is unlikely to cause any problems.

For more recent developments in the deeper waters of the North Sea, the piles do not extend to the surface and are either grouped in clusters around the main legs of the structure, as shown in Figure 1.1, or in some cases are evenly distributed around the base of the structure.

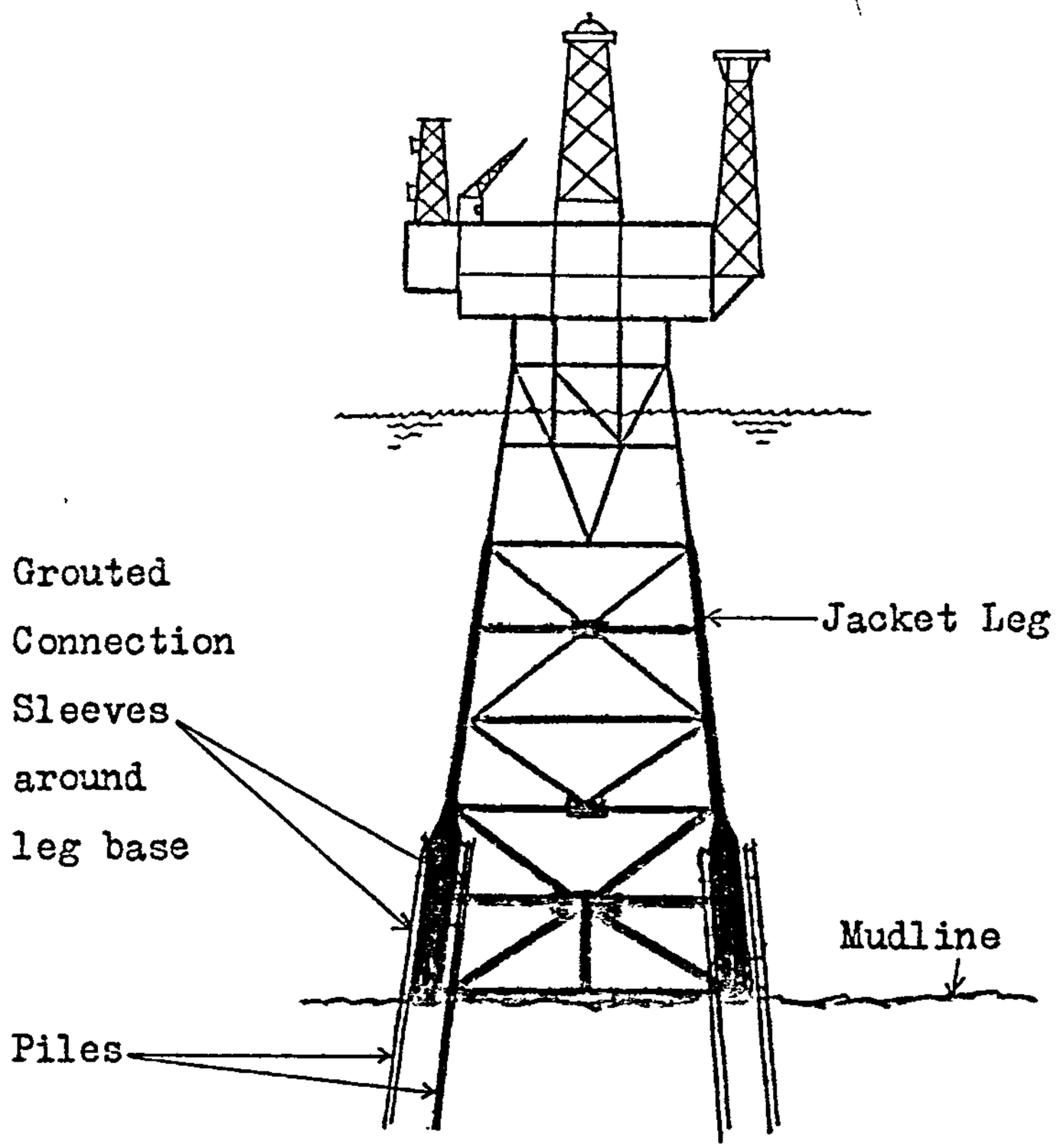

(a) Location

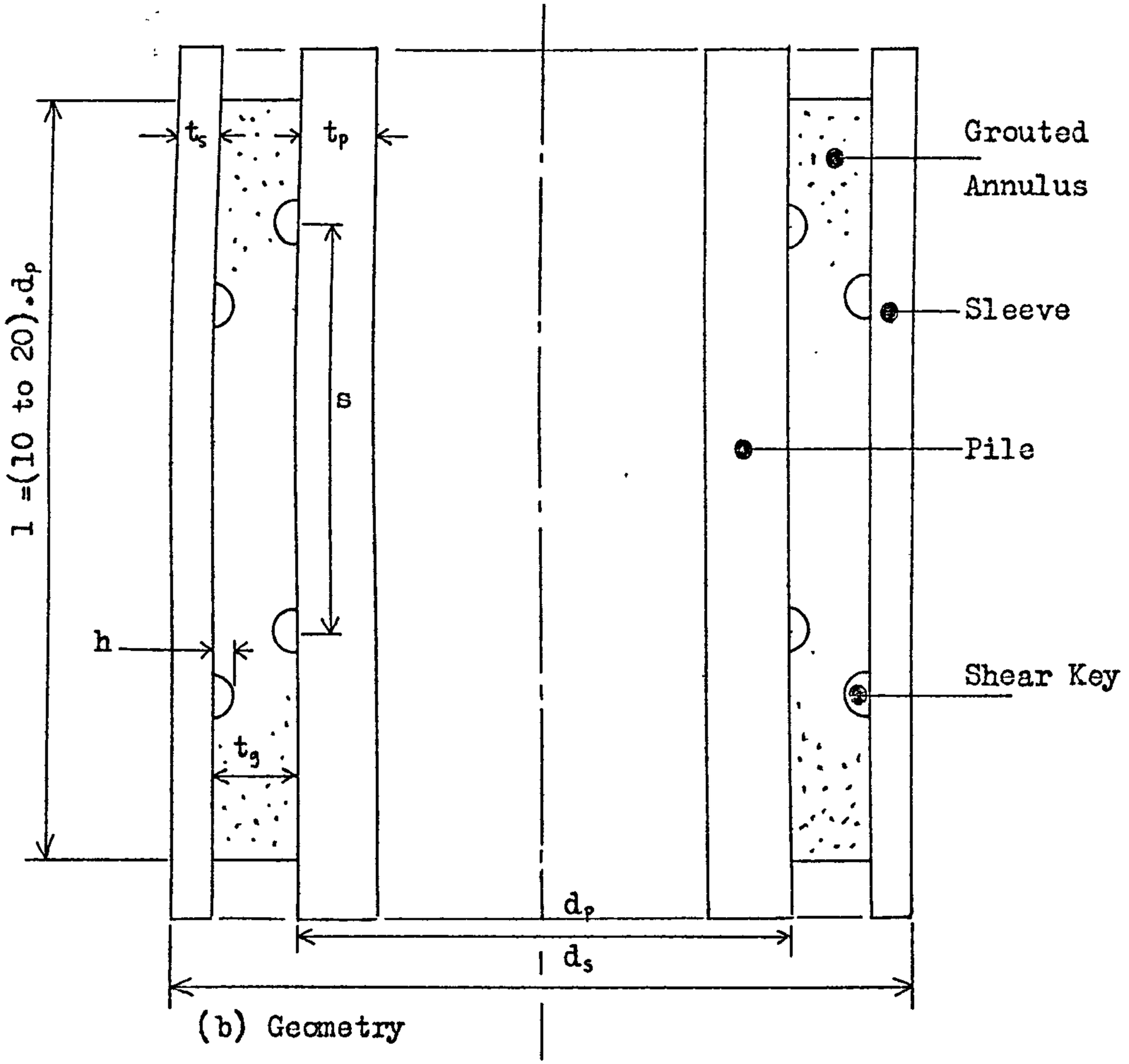

(b) Geometry

FIGURE 1.1 THE USE OF GROUTED PILE/SLEEVE CONNECTIONS ON OFFSHORE PLATFORMS.

The grouting forms the only structural connection between the jacket and its foundations. The grout must, therefore, transmit all the forces arising from the dead weight of the jacket, deck and superstructure, and from the environmental loading. In addition, as the capacity of offshore construction plant for handling and driving piles has increased, a trend towards foundations consisting of smaller numbers of larger diameter, less radially stiff connections has made it necessary to investigate the factors affecting the strength of grouted connections.

The results of tests on large diameter plain pipe connections showed inadequate strength for northern North Sea conditions and as a result mechanical shear keys were introduced. These consist of weld beads or welded bars, forming rings around the circumference of the inner surface of the sleeve and outer surface of the pile, which key into the grout and greatly increase the bond strength.

The dimensions of grouted connections can be very great, for example: 2 metres diameter by 40 metres long. The shear connectors are typically around 10 mm high and spaced 300 mm apart. The axial design load may be as much as 6000 tonnes, and with a safety factor of six, the actual capacity may be much larger still.

Grouted connections can also be used for nodal and tubular strengthening and for applying additional bracing to jacket structures without the need for underwater welding. Grouting has an additional advantage here in being able to accommodate geometrical imperfections between the new and existing structural components.

1.2 Previous Experimental Test Programmes

Programmes of experimental work have been carried out at Wimpey Laboratories to verify the designs of grouted connections for a number of North Sea platforms. These include work for B.P., Burmah Oil, Chevron Petroleum, Union Oil, Lafarge and others (1,2,3,4,5,6,7). These tests were useful in establishing the parameters which affect the bond strength and provide a great deal of experimental data on the static, axially loaded situation. The results did not cover all aspects of the problem, however, and could not enable rationally based design recommendations to be formulated covering the likely range of practical parameters. A detailed programme of research, (funded by the Department of Energy (8)) was therefore formulated and carried out at Wimpey Laboratories. This included many static tests covering a wide range of geometries. Also included were tests to study the effect of long term cyclic loading (fatigue) and short term cyclic loading (relative movements of tubulars during grouting and curing). Tests on construction and durability of a section of grouted leg recovered from B.P.'s West Sole field have also been carried out. The results of these recovery tests are very favourable. A similar testing programme, but on a smaller scale, has been carried out in Norway by DnV (9).

More recently the range of tubular geometries used has expanded with the advent of grouted connections used to repair and strengthen jacket structures. This has resulted in further research programmes at Wimpey Laboratories to investigate extreme geometries, and split-sleeves which can be assembled around an existing pile or brace (10).

Further tests on connections with extreme geometries, and various types of shear key are being carried out at The City University, London. These tests, which are extensively strain-gauged, should enable comparisons to be

made with theoretical methods of analysis such as those developed later in this thesis.

1.3 Bond Strength Formulae

Design formulae, which can predict the strength of a grouted connection, have resulted from work funded by the Department of Energy. These are based only on the experimental results available and do not include any theoretical reasoning. Although useful for most design purposes, the latest formulae are proving less accurate for the extreme geometries needed in grouted repair work. Also, effects such as the length of connection, scale, surface roughness and sleeve stiffeners are not necessarily represented very well. For these reasons, it would be useful to develop a theoretical analysis of the behaviour of grouted connections which can be used to produce a more rational strength formula.

1.4 The Scope of this Research Project

The following chapters develop a finite element analysis to simulate the performance of an axially loaded grouted connection up its ultimate capacity. In order to reproduce the experimentally observed behaviour, special properties have to be introduced into the steel/grout bond elements. These properties are then used to develop a new bond strength formula which can account for all the factors known to affect this strength. Thus, the bond strengths of connections with more extreme geometries can be predicted with confidence.

Experimental testing of the steel/grout bond is used to verify the friction properties used in the analysis.

A detailed non-linear finite element analysis around the shear keys is also made, which enables the effects of shear key shape, size and spacing to be investigated.

CHAPTER 2

APPRAISAL OF EXPERIMENTAL BOND STRENGTH FORMULAE

2.1 Early Design Guidance

The findings from work carried out at Wimpey Laboratories led to a number of improvements in the design formulae for grouted connections, Billington, Lewis and Tebbett (11,12). Previously, the only guidance available on design was from the American Petroleum Institute (13). This gives a limiting design bond stress of 0.183 N/mm^2 for use in the absence of design data, where the bond stress is defined to be the total axial load on the grouted connection divided by the total surface area of the pile/grout interface.

The factor of safety inherent in this design value is not stated, but a factor of six is widely considered to be reasonable. A study of partial safety factors (12), to allow for variations in material properties, loading and the uncertain nature of offshore construction conditions demonstrates the validity of this safety factor.

This would imply an ultimate bond strength of 1.105 N/mm^2 , (as this is six times the API design strength). Test results for plain pipe connections show that bond strengths fall below this value on larger diameter connections with a grout cube strength of 50 N/mm^2. Some connections even give a factor of safety of less than 1.5 compared with the recommended value of six. The API recommendations do not allow for the effects of grout strength or radial stiffness of the connection and this would contribute to lower factors of safety. These API recommendations had been based on data derived from tests on small diameter

radially stiff plain connections.

2.2 Effect of Surface Roughness

Various grout mixes were used in order to enhance the strength of plain pipe connections. Portland cement, expansive portland cement, epoxy resin and high alumina cement have been used as the basis for the grout material. Also, various surface treatments, such as shot-blasted, epoxy coated, epoxy with sand coating, new steel with mill varnish removed, and rusted steel have been used to improve bond (1). As a result of these tests, it was found that smoother surfaces gave lower bond strengths. The effect of the epoxy coating on the pile was to reduce the bond strength by 80%. Similar results were obtained when the surface roughness was reduced by grinding the steel surface, clearly demonstrating that the bond must be frictional rather than chemical.adhesion.

2.3 Influence of Grout Cube Strength

It was also found that irrespective of grout type, the bond strength, f_{bu}, can be expressed as:

$$f_{bu} = A \sqrt{f_{cu}} \qquad (2.1)$$

where f_{cu} is the grout cube strength, and A is a constant dependent upon surface roughness and geometry. Figure 2.1 shows the effects of grout cube strength and surface roughness on bond strength.

Long term weakening due to grout shrinkage was also shown to be significant. A 31-day specimen was 42% weaker than a similar 3-day specimen, even though the former's cube strength was 61% greater.

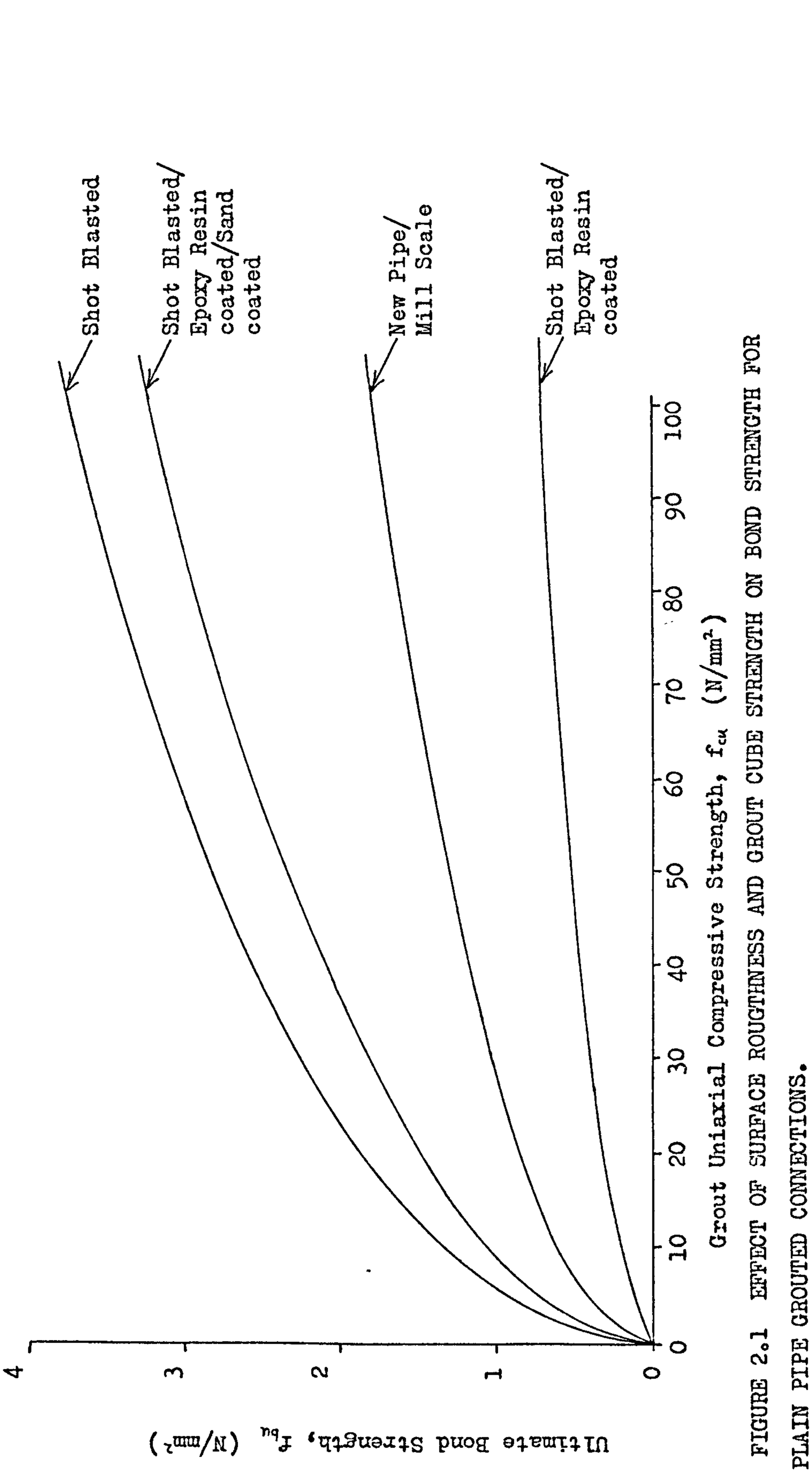

FIGURE 2.1 EFFECT OF SURFACE ROUGTHNESS AND GROUT CUBE STRENGTH ON BOND STRENGTH FOR PLAIN PIPE GROUTED CONNECTIONS.

2.4 Significance of Radial Stiffness

The results of tests in which the connection geometry was varied showed the radial stiffness to be another important factor. According to Billington and Lewis (11), the radial stiffness of the pile or sleeve which may be expressed in terms of a uniformly distributed radial force, F, and radial deflection, u, is proportional to Young's Modulas, E, and the ratio of tubular thickness to diameter (t/d).

$$\text{i.e.} \quad F/u \simeq E.(t/d) \qquad (2.2)$$

If the radial stiffness of the complete connection is considered, various stiffness factors proportional to the radial stiffness of pile, sleeve and grout cylinders can be derived. This led to the creation of a stiffness factor, K, given by:-

$$K = \frac{E_g}{E_s} \cdot (t/d)_g + \left[(d/t)_s + (d/t)_p\right]^{-1} \qquad (2.3)$$

where subscripts g, s and p refer to grout, sleeve and pile respectively. It was found that a plot of K against ultimate bond stress, normalised with respect to a grout compressive strength of 50 N/mm^2 using the parabolic relationship of equation (2.1), gave a possible straight line, as shown in Figure 2.2.

$$\text{i.e.} \quad f_{bu} = B.K.\sqrt{f_{cu}} \qquad (2.4)$$

where B is a constant dependent on surface roughness, ℓ/d_p, and h/s for the case when shear keys are used. There is a substantial amount of scatter in these results and a curve is suggested in Figure 2.2 which is a better fit to the data. A curve seems to be more rational than the straight line as there must be an upper limit on the bond strength however large K may be.

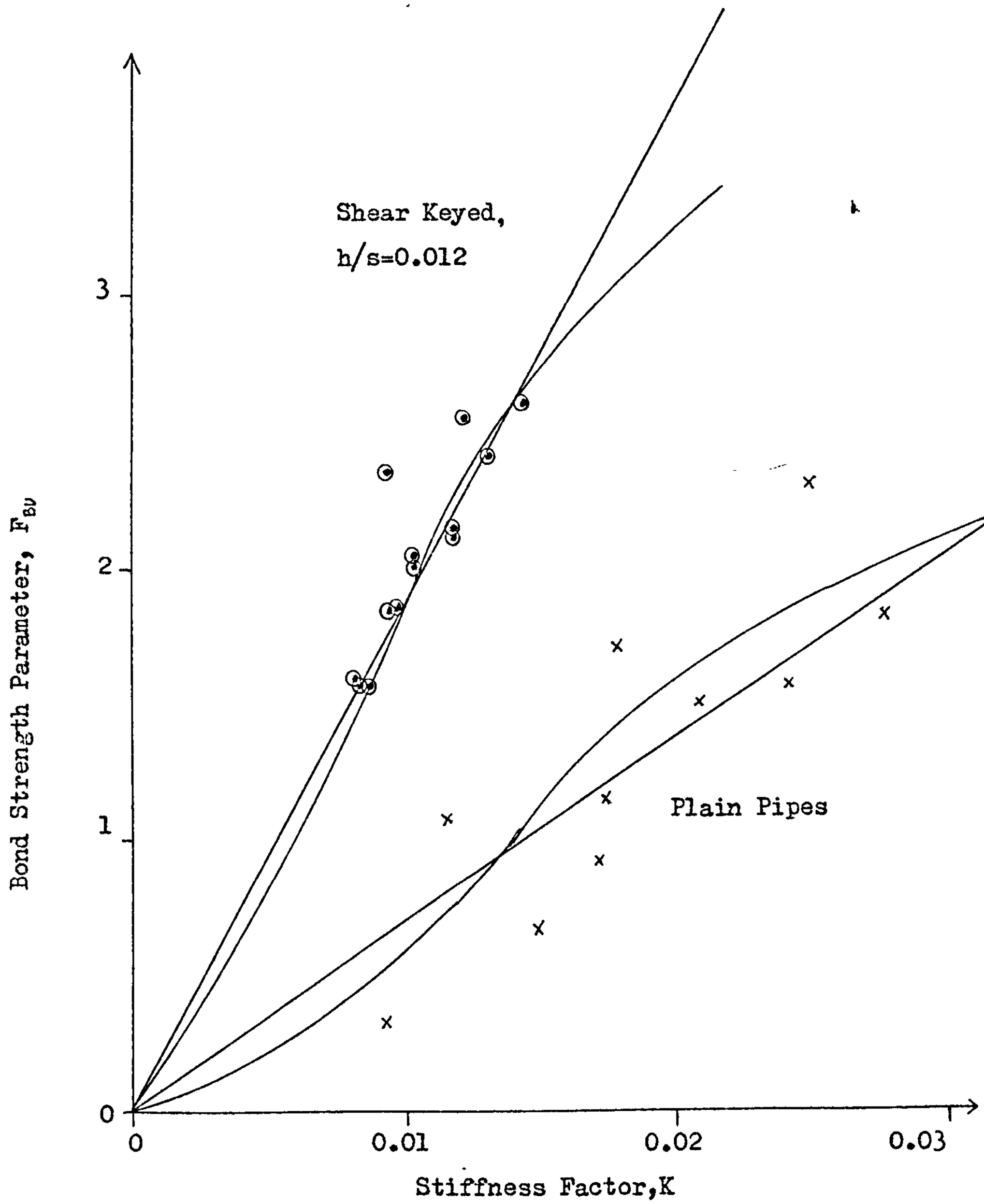

FIGURE 2.2 POSSIBLE RELATIONSHIPS BETWEEN BOND STRENGTH AND STIFFNESS FACTOR,K.

The relationship between f_{bu} and F can be considered in simple terms as follows. Equation (2.5) shows how these two quantities are related, where $F/d = \sigma_n$, the normal bond stress, and $f_{bu} \propto \sigma_n$, due to friction.

Therefore: $f_{bu} \propto F/d$ (2.5)

Substituting equation (2.5) into equation (2.2) gives:-

$$f_{bu} \propto E.(t/d^2).u \qquad (2.6)$$

Another formula where (t/d^2) is the main stiffness parameter is developed in Chapter 8.

2.5 Effect of ℓ/d on Bond Strength

A variety of tests have been carried out to investigate the effect of varying ℓ/d_p (1,4,8). Most tests use an ℓ/d_p of 1 or 2 whereas a full-scale connection may have an ℓ/d_p of up to 20. There is a gradual weakening of bond strength with increase of length, and this can be expected as the longer connection carries a higher load, and so is more highly stressed at the loaded end. For low ℓ/dp there is also a weakening effect, which can be attributed to the influences of end restraints. The value of ℓ/d_p for which maximum bond strength occurs seems to vary with geometry. This makes sense, because for stiffer connections, end restraints will obviously have less effect. Figure 2.3 shows two sets of results, both with shear keys. The A-series has an abnormally thick sleeve and pile to prevent buckling, and so the end effects only influence $\ell/d_p < 2$. The more typical O-series has thinner tubulars and is stiffened by longitudinal stiffeners, which do not affect the hoop stiffness. Hence the effects of end restraints now extend to $\ell/d_p = 3.5$.

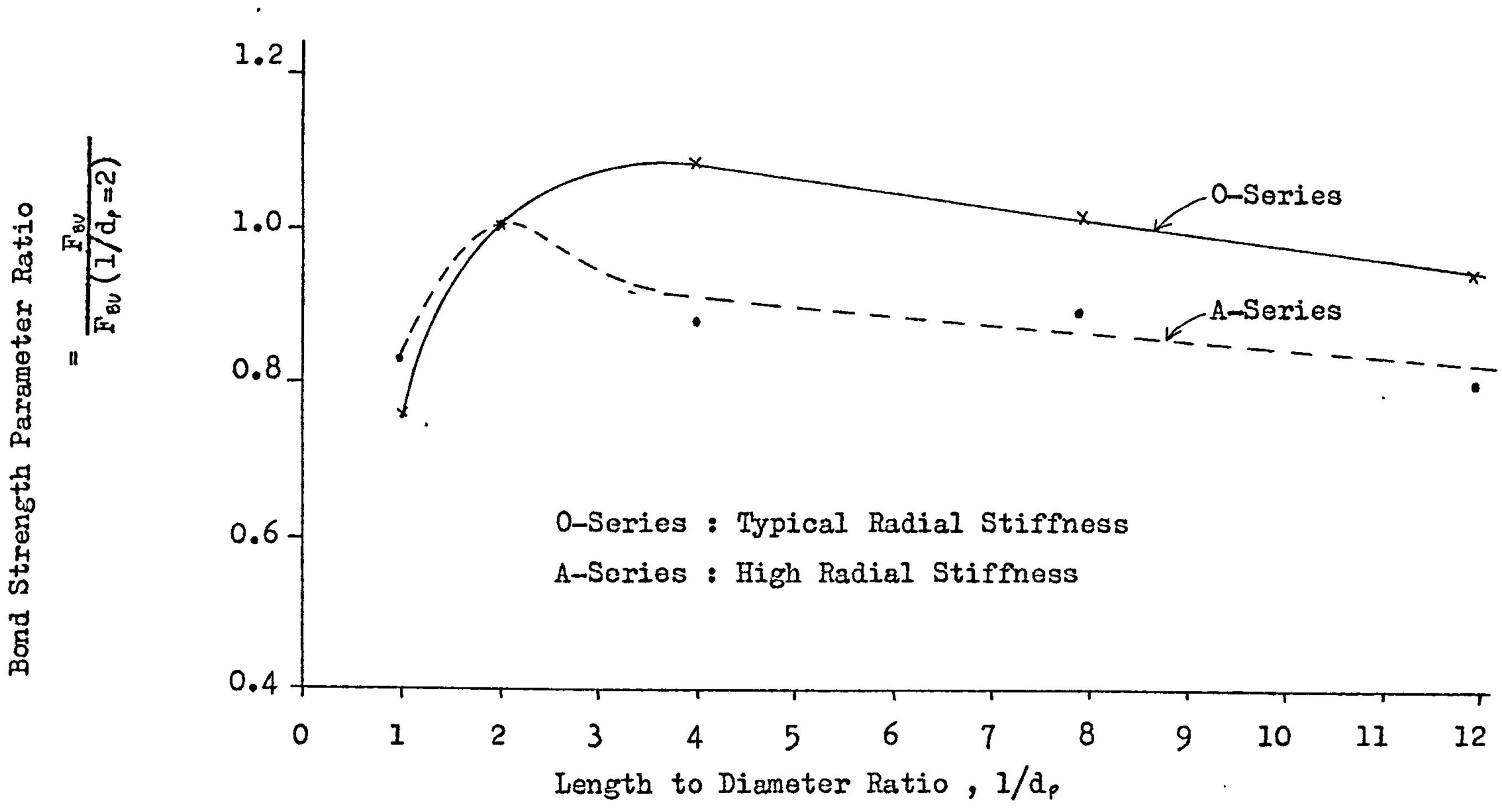

FIGURE 2.3 EFFECT OF LENGTH TO DIAMETER RATIO ON BOND STRENGTH.

2.6 Effect of Shear Keys

Tests were carried out on connections with shear keys and these showed that the parabolic relationship between bond strength and grout compressive strength is applicable. Also, the strength appeared to obey the following formula:-

$$f_{bu} = C.K.(h/s).\sqrt{f_{cu}} \qquad (2.7)$$

where h and s are the shear key height and spacing respectively (see Figure 1.1), and C is a constant dependent on ℓ/d. Effects of surface roughness or grout shrinkage do not appear to be significant when shear keys are used and ultimate bond strengths are substantially greater than for plain pipe connections.

Later tests included four pairs of specimens with differing h, including h = 0 (i.e. plain pipes), but with other geometric ratios kept constant. The results demonstrated two important facts:

(a) A linear relationship is seen to exist between F_{BU} and h/d_p.

(b) The line intercepts the F_{BU} axis at the plain pipe strength. This indicates that contributions to the bond strength from plain pipe bond (i.e. frictional), and from the weld bead shear connectors are additive.

Three pairs of specimens with different d_p/s values, but with other geometric parameters held constant, were also tested. The ℓ/d_p ratio used for these tests was set at 1.0 in order to allow testing of connections with closely spaced shear connectors within the load capacities of the steel tubulars. As the ℓ/d_p ratio was 2.0 for the h/d_p tests, a direct comparison with the d_p/s results was not possible, but a linear relationship between F_{BU} and d_p/s was indicated.

2.7 Interim Design Code

Since the presence of shear keys greatly enhances the bond strength, the Department of Energy revised its Guidance Notes (14). These notes recommended the use of shear keys and provided a conservative design approach which, in the absence of test data to justify higher values, gave the ultimate bond strength as follows:-

$$f_{bu} = \frac{A_s f_{cu}}{A_p} \qquad (2.8)$$

where A_s is the total plan area of the shear keys within the grouted length, A_p is the total surface area of the pile within the grouted length, and f_{cu} is the grout cube strength. The diameter/thickness ratios of the sleeve and pile had to be not greater than 120 and 30 respectively, and the shear key pitch, s, not less than 300 mm. These restrictions reflected the extent of available test data at that time.

2.8 Non-Dimensional Bond Strength Parameter

Having established a parabolic relationship between bond strength and grout compressive strength, both with and without shear connectors, Wimpey Laboratories decided to normalise test results to a common grout strength in order to be able to investigate the effects of other parameters. A non-dimensional ultimate bond strength parameter, F_{BU}, may be defined as follows:-

$$F_{BU} = \frac{f_{bu}}{1.105}\sqrt{\frac{50}{f_{cu}}} \qquad (2.9)$$

where f_{bu} and f_{cu} are measured in N/mm^2, and 1.105 N/mm^2 is six times the APIRP2A recommended design bond stress for extreme conditions (15). Thus, F_{BU} equals 1.0 when the bond strength equals the API ultimate bond strength with a safety factor of six if the grout cube strength is $50N/mm^2$. Further test results are expressed in terms of F_{BU} to eliminate the effect

of grout cube strength variations.

2.9 Current Bond Strength Formula

By combining the above results, the following formula was determined:-

$$F_{BU} = KC_L(AC_S + B\frac{h}{s}) \qquad (2.10)$$

where A and B are constants to be determined from test results. C_L is an ℓ/d_p parameter, equal to 1.0 when $\ell/d_p = 2$, and C_S is the surface roughness parameter. By plotting F_{BU}/KC_L against h/s for all results, a straight line should be obtained, from which A and B can be determined. This was carried out by Wimpey Laboratories, plotting many results including those of plain pipes for which $h/s = 0$. Figure 2.4 shows a plot of the results. A least squares analysis for a mean linear relationship provided an intercept at $h/s = 0$ of 76, and a gradient of 9468, taking $C_S = 1.0$ for the test surface condition (shot-blasted). This equation gives a mean result, but leaves considerable scatter about the mean line, which must be accounted for in design. To do this, the concept of characteristic strength is used, which is defined to be the strength below which not more than 5% of the results of an infinite number of tests would fall. This can be calculated from:-

$$f_{buc} = \overline{f}_{bu} - K'\sigma \qquad (2.11)$$

where f_{buc} is the characteristic strength, $\overline{f}_{bu}$ is the mean ultimate bond strength, σ is the standard deviation, and K' is a constant dependent on population size, see Baker (16). For the large population of results available (in excess of 400), $K' = 1.645$. Results indicate a characteristic strength which is 75% of the mean strength, both with and without shear connectors. So the characteristic ultimate bond strength parameter can be given by:-

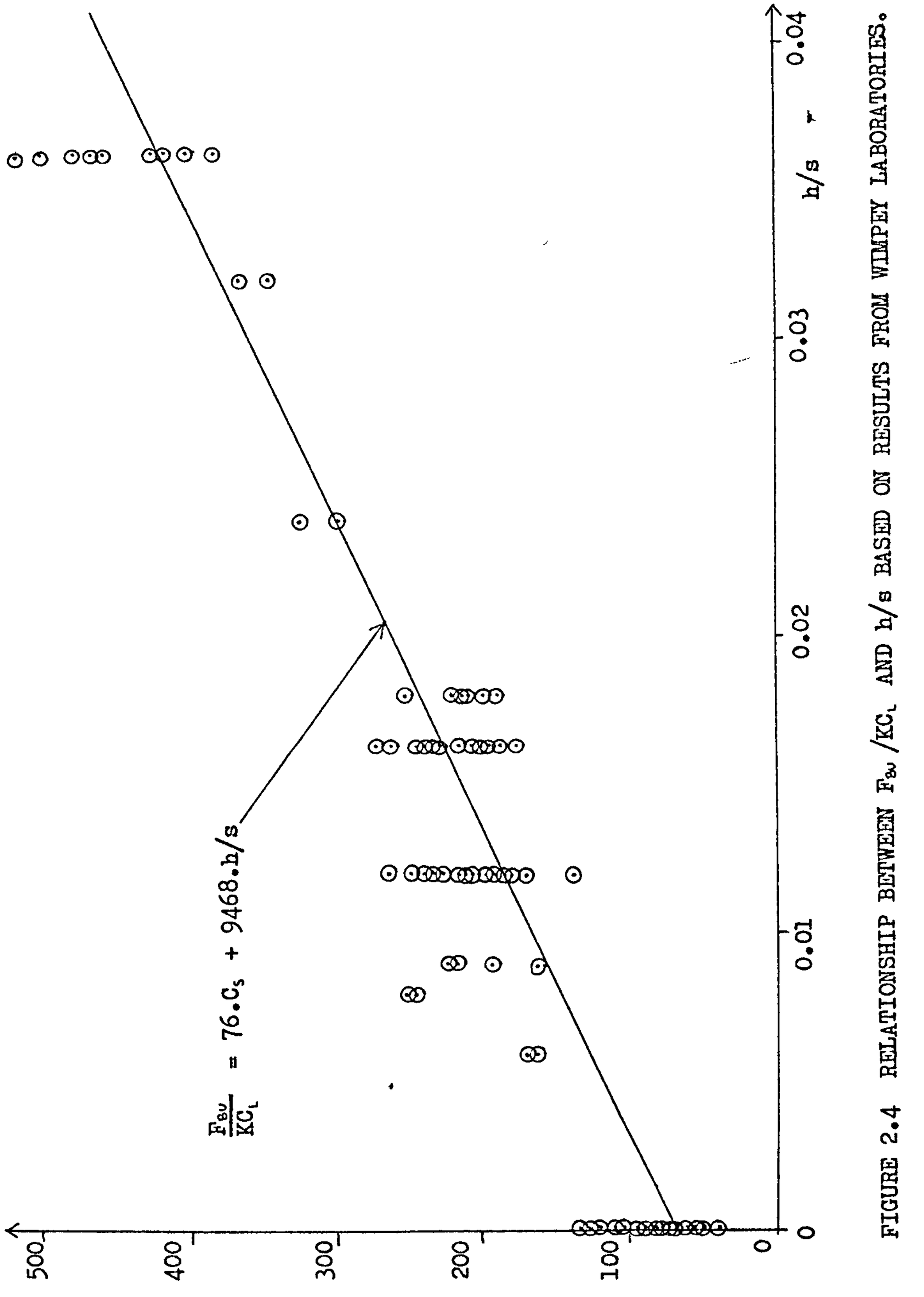

FIGURE 2.4 RELATIONSHIP BETWEEN F_{sv}/KC_L AND h/s BASED ON RESULTS FROM WIMPEY LABORATORIES.

$$F_{Buc} = KC_L(57C_S + 7100\,\frac{h}{s}) \qquad (2.12a)$$

and the characteristic ultimate bond strength is given by:-

$$f_{buc} = KC_L(9C_S + 1100\,\frac{h}{s})\sqrt{f_{cu}} \qquad (2.12b)$$

If plain pipes alone are considered, the standard deviation is larger, and the sample size smaller. The larger deviation is considered to be due to variability in surface roughness and effects of grout shrinkage. Age and curing arrangements for the grout may also be important. Allowance can be made by varying the parameter C_s, and Table 2.1 gives suggested values. It would have been interesting to see how much this correction factor reduced the standard deviation of the plain pipe results since the effects of shrinkage could still be a problem for the long term tests.

Recommended values for the ℓ/d_p factor C_L, based on what little experimental data is available, are given in Table 2.2. Model tests have only been conducted with $\ell/d_p \leqslant 12$. The limitation is due to the requirement of the higher loads associated with greater lengths. Since practical values may require $\ell/d_p = 25$, extrapolation is necessary. The need to extrapolate emphasises the advantages of developing an analytical approach to the problem which can be extended over any extremes of strength and geometry.

It is interesting to compare the design formulae for a given geometry in order to show the progress made towards more efficient design. Figure 2.5 shows such a comparison and is based on the design for the B.P. Magnus Field (7). Full details of the latest design formula are published by CIRIA (17).

Surface Condition		C_s
Connections with shear keys.		1.0
Plain pipes	Shot-blasted or lightly rusted.	0.8
	With mill scale.	0.6
	Painted or epoxy coated.	0.3

TABLE 2.1 VALUES FOR THE SURFACE CONDITION PARAMETER

$\ell/d_p \geq$	C_L
1	0.8
2	1.0
4	0.9
8	0.8
12	0.7
20	0.6

TABLE 2.2 VALUES FOR THE LENGTH TO DIAMETER RATIO FACTOR

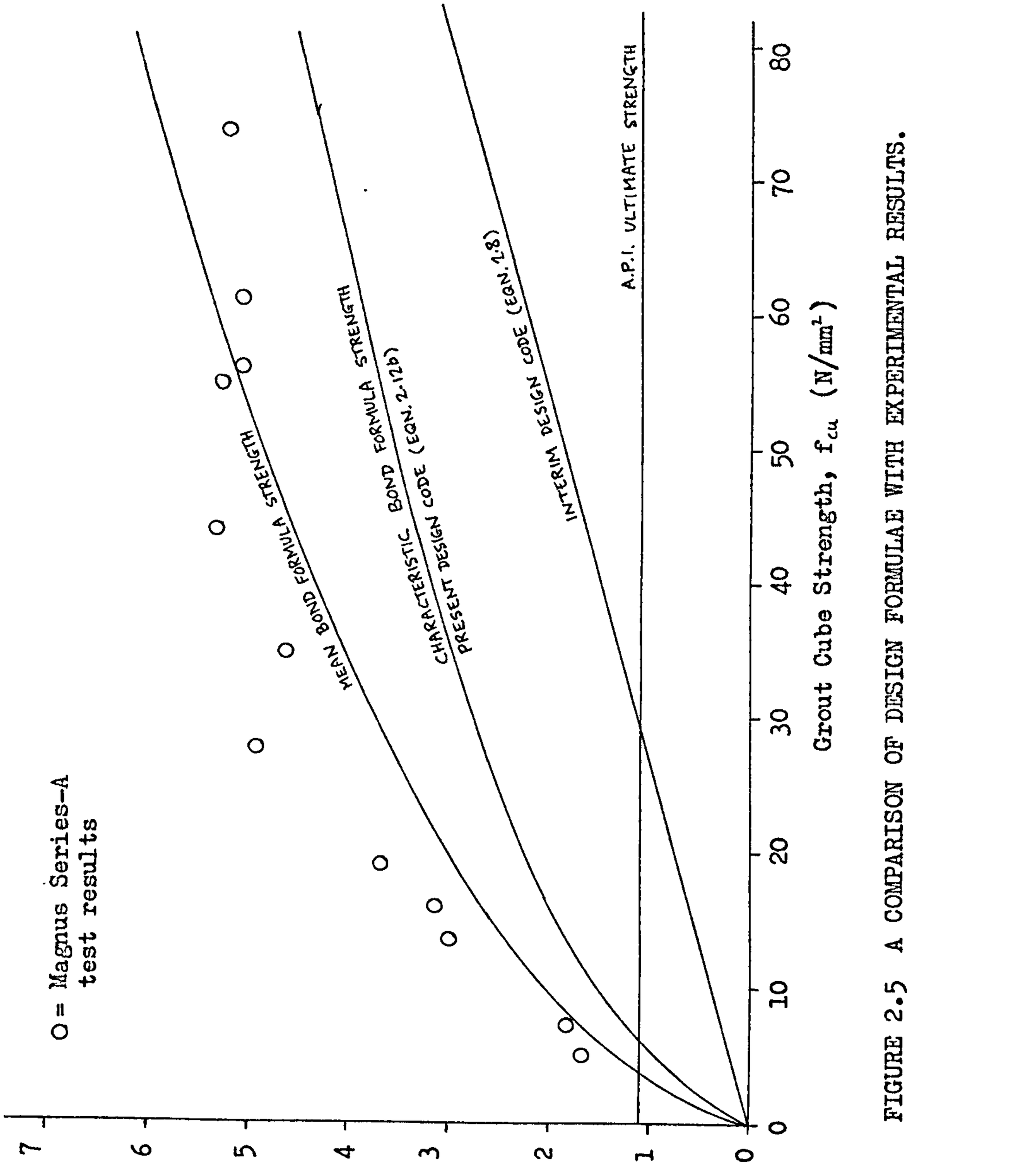

FIGURE 2.5 A COMPARISON OF DESIGN FORMULAE WITH EXPERIMENTAL RESULTS.

2.10 Method of Loading

Specimens are generally loaded with the pile in tension and the sleeve in compression, Figure 2.6. Poisson effects resulting from this loading arrangement cause the pile to shrink and sleeve to expand, separating the sleeve and pile from the grout, thus giving a conservative loading condition. The real structure will be loaded with both pile and sleeve in compression (some tests have been made with this arrangement), or with pile and sleeve both in tension. Results indicate that differences in bond strength due to a change in loading arrangement can be quite substantial in some cases. The tension-compression loading is however always the weakest, as would be expected.

Another point is that in the laboratory tests, the loads are normally applied at the end of the connection, whereas in reality the load is transferred from leg to sleeve along the length of the sleeve by means of shear plates and diaphragms. A condition which must be less severe than end loading. An exception to this was the testing for the B.P. Magnus Field (7), where the structure from leg to sleeve was also modelled. Series-A tests were end-loaded and gave a strength of $F_{BU} = 4.79$, but Series-G tests were loaded via the leg structure and gave a strength of $F_{BU} = 7.18$. This is a 50% strength increase. The only differences between the tests, apart from the leg structure, being the addition of pile stiffening on series-G, and loading with pile and sleeve both in compression, while the pile in series-A was loaded in tension. Considering that the pile is much stiffer than the sleeve, these differences should not greatly affect the bond strength. The distributed transfer of load from leg to sleeve must therefore considerably enhance the bond strength.

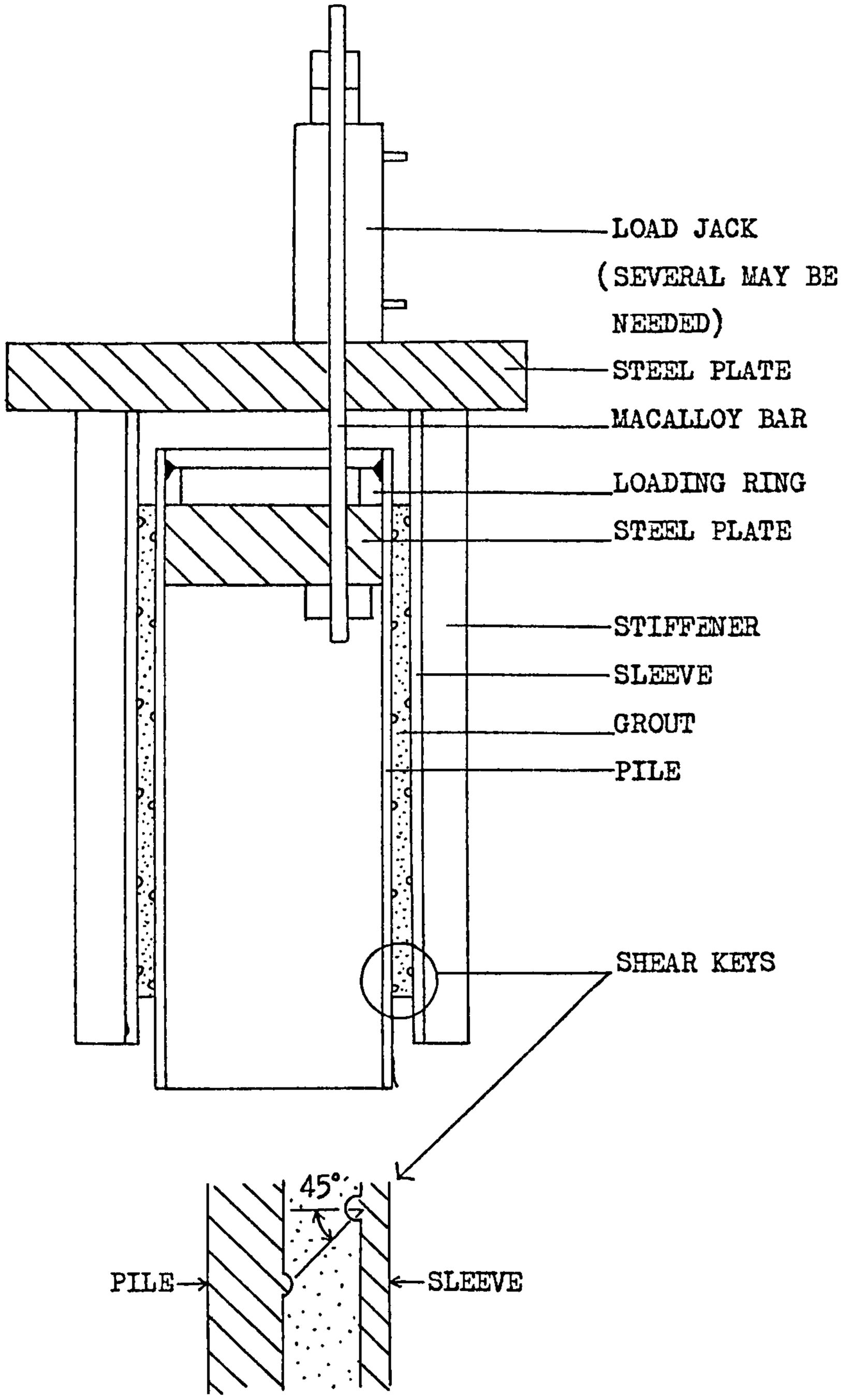

FIGURE 2.6 TYPICAL LOADING ARRANGEMENT WITH THE PILE IN TENSION AND SLEEVE IN COMPRESSION.

These tests which included the leg structure were made specifically to investigate the effects of shear and bending loads on the connection. The results proved the connections to be well able to resist the combined axial, shear and bending loads, at a safety factor of greater than 4 without failing (only a factor of 3 was required). It seems possible, therefore, that the substantial increase in axial load capacity resulting from the leg-sleeve load transfer system could be used to reduce the overall length of the connection.

2.11 Longitudinal Stiffeners

Longitudinal stiffeners are often welded onto the sleeve to prevent the sleeve buckling or yielding. These are necessary since the factor of safety for the steel components is generally less than for the grouted bond, reflecting the lower level of uncertainty with steel construction. The stiffeners reduce the level of stress in the sleeve without greatly affecting the hoop stiffness. In the bond strength formula, the value of $(d/t)_s$ is reduced by subtracting the total thickness of stiffeners and welds from the sleeve circumference. This has the effect of slightly increasing K, to give K_m, and provides a slightly higher bond strength prediction. Experimental results seem to confirm this effect, which can be expected, since the lower axial stress in the sleeve will also result in lower Poisson effects, even though the circumferential stiffness is unchanged.

2.12 Effect of Curing Period

The effect of cube strength variation has already been allowed for in F_{BU}, but age of grout is also important, producing an additional variation

as shown by Figure 2.7. From these results, the factors given in Table 2.3 were produced to standardise F_{BU} for 31-day grout. These factors are equally applicable with or without shear keys.

Then: $$F_{BU31} = F_{BU}/C_{31} \qquad (2.13)$$

No allowance for age is made in the current bond strength formula, and neither has there been any allowance for age effect made when comparing laboratory test results of different ages in the past.

As different grout mixes perform differently, these age factors are only applicable for the standard Oilwell B cement mixed with seawater in the correct proportions, cured at 8°C, and kept moist. Any variation in these conditions will affect the rate of gain of strength, making the factor C_{31} no longer correct. For example, if high alumina cement grout is used, and tested at an early date, F_{BU} will be low. This is because this mix has a rapid initial rate of gain of strength, but a lag in the development of stiffness. The type of grout mix for which the above factors apply is given in Table 2.4.

The main reason for long term weakening may be shrinkage of the grout. However, the specimen may not actually get weaker, but F_{BU} reduces because f_{cu} continues to rise with time. If the grout is allowed to dry out, shrinkage will be much more significant, causing a large reduction in bond strength for plain-pipe connections.

2.13 Scale Effects

It is suggested in various reports of experimental data (11,4), that reduced scale models give the same bond strengths as full scale models. Quarter scale specimens have been tested with various grout types and at various ages. In these tests the length to pile diameter ratio (ℓ/d_p) was

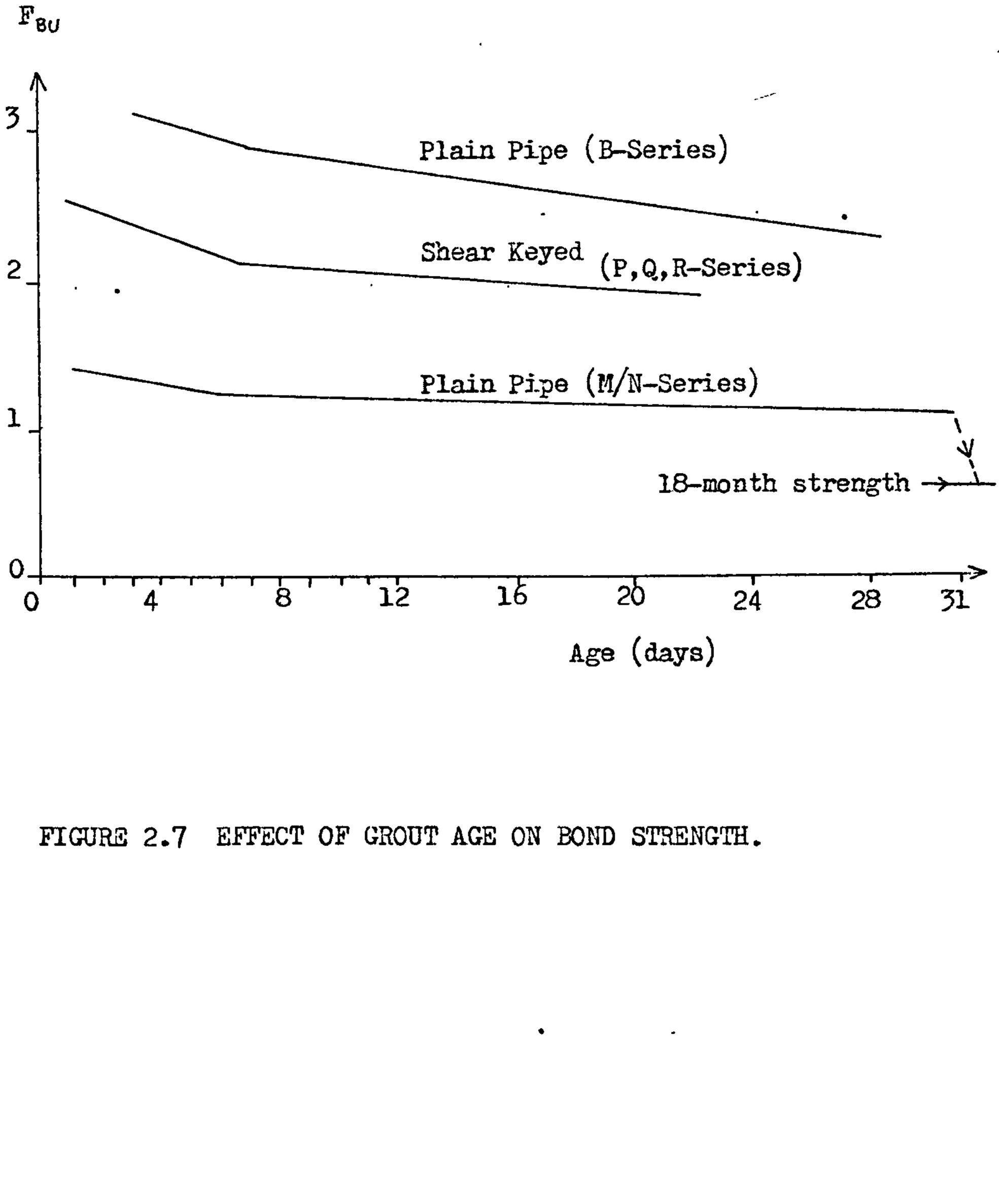

FIGURE 2.7 EFFECT OF GROUT AGE ON BOND STRENGTH.

Age of Grout (days)	C_{31}
31	1.00
28	1.03
22	1.04
9	1.18
7	1.22
6	1.24
3	1.29
2	1.34
1	1.46

TABLE 2.3. FACTOR TO ADJUST ALL BOND STRENGTHS TO AN AGE OF 31-DAYS.

Ingredient	Quantity
Oilwell'B'Cement	100 kg
Seawater	35 litres
Calcium Chloride	1 kg
Cormix SP1G	1 kg

TABLE 2.4. RECOMMENDED GROUT MIX.

equal to two. The full scale specimens referred to in the reports were all of the same grout type (Oilwell B), but tested at various ages and with ℓ/d_p=1. A 20% reduction of bond strength was made to the $\ell/d_p = 2$ results to make them equivalent to the $\ell/d_p = 1$ results. The amount of the reduction was obtained from the findings of previous work to determine the effects of ℓ/d, (see Table 2.2). This resulted in a general agreement of the bond strengths for the two scales. However, the mean quarter scale result for Oilwell B cement grout alone is $F_{BU} = 1.88$. The full scale mean result is $F_{BU} = 1.30$, which is a 31% reduction on the $\ell/d_p = 2$ result. Only this comparison, where grout types and curing conditions are identical, is reasonable. Other grouts, especially the Halliburton grout, give a lower F_{BU}.

If the results are adjusted to a 31-day result using the factors given in Table 2.3, then $F_{BU31} = 1.50$ for quarter scale, and $F_{BU31} = 0.98$ for full scale, which is 35% weaker than quarter scale. This difference cannot be explained by ℓ/d_p alone and it is suggested that scale effects exist. A further investigation of scale is made in Chapter 8.

2.14 Failure Mechanism

Figure 2.8 shows a typical plot of normalised bond stress against slip between sleeve and pile for a connection with shear keys. The gradient of the curve changes at $F_s \simeq 0.4$, when the friction bond breaks and the shear keys begin to take up load. Gradually, stresses build up around the shear connectors, tensile cracks occur in the grout, and the grout begins to crush around the shear connectors. Eventually, there is no further resistance to slip, but most tests show a large post-ultimate strength, even after substantial slips have occurred.

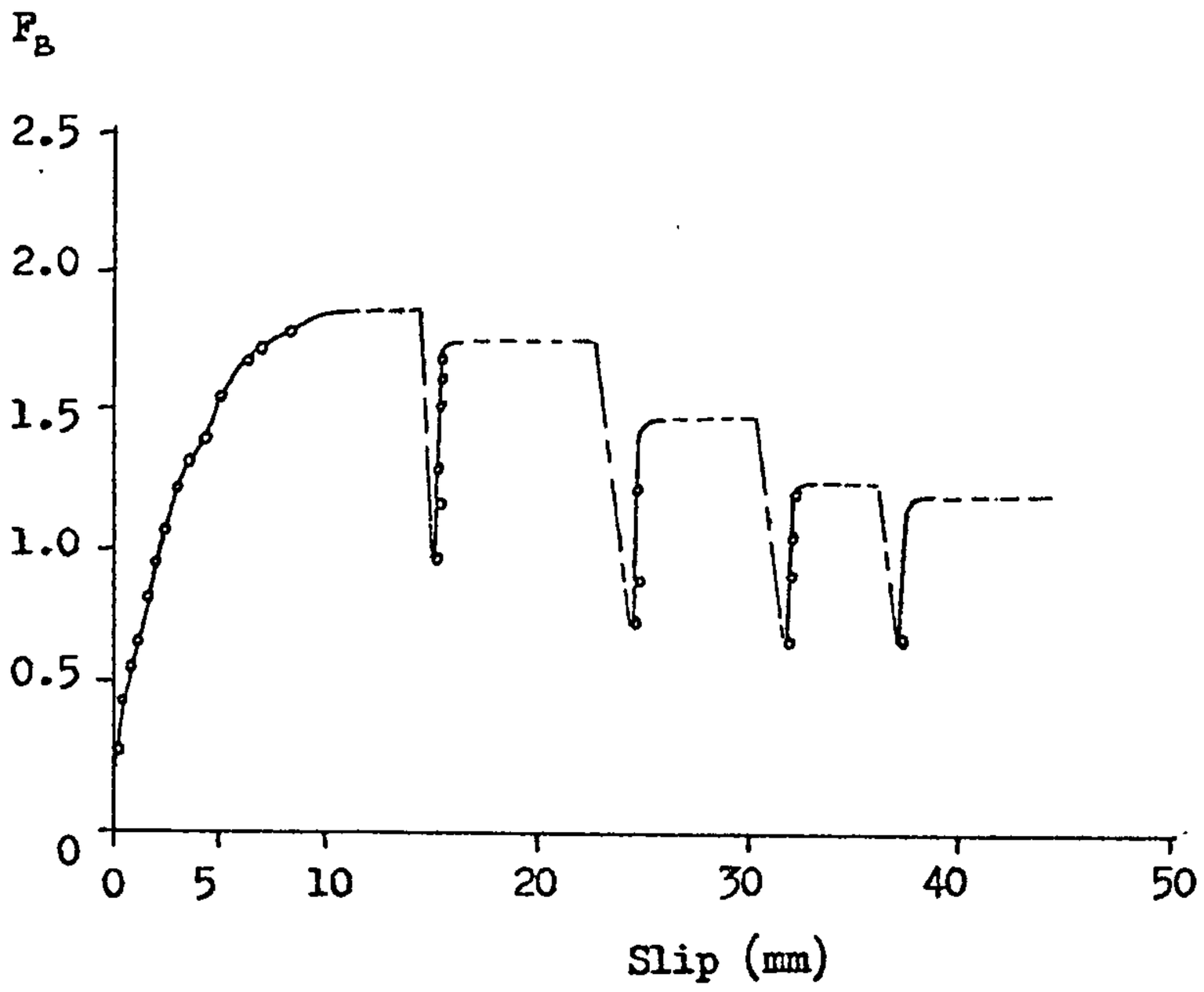

FIGURE 2.8 TYPICAL TEST RESULT OF NORMALISED BOND STRESS AGAINST SLIP FOR A QUARTER-SCALE CONNECTION WITH SHEAR KEYS.

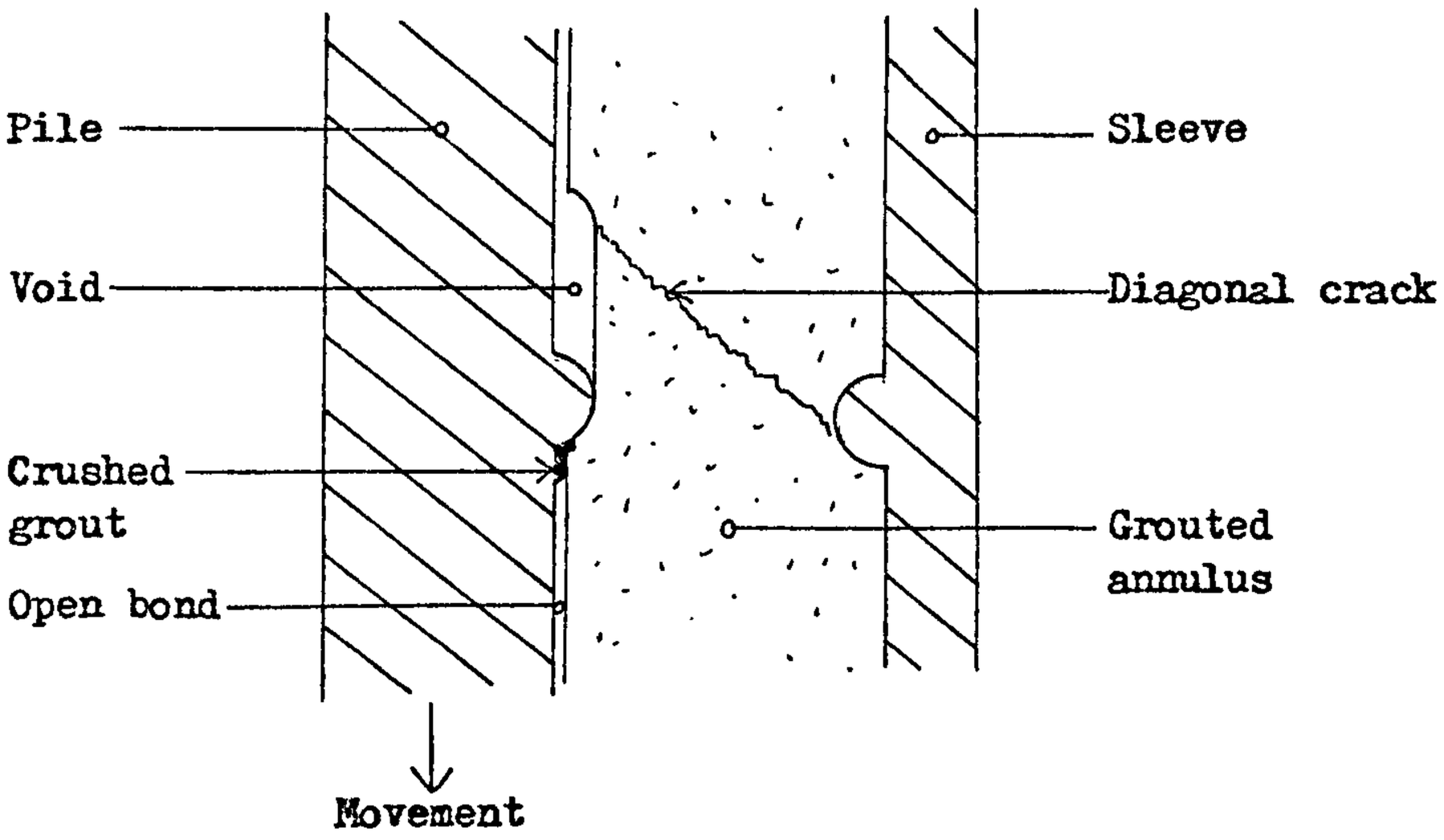

FIGURE 2.9 TYPICAL FAILURE MODE AROUND A SHEAR KEY.

On unloading and reloading, there may or may not be a drop in ultimate load. Presumably, as the load is reapplied, there may be a chance for the stresses to alter the physical state of the bond, resulting in a post-ultimate capacity either increased or decreased, depending on the movement of fractured grout on the grout/steel interface. Additionally, if there is a degree of lack of roundness in the tubulars, this will give extra strength until the action of slip overcomes such geometric imperfections.

Slip is generally greater on the pile/grout interface, since the bond area is smaller, and hence the stresses are larger. When weld beads are used for shear connectors, a void is left behind the bead, with some expansion of the annulus occurring to accommodate the crushed grout. Diagonal cracks have a tendency to propagate from the shear keys on the plane of maximum tensile stress which result from the high shear stresses. A typical failure is shown in Figure 2.9. The cracks are concentrated around the shear keys where the stress applied to the grout is predominately a large shear stress in the plane of the bond. The crack plane will be approximately 45°to the bond plane. The cracks always spread from the weld bead positions and are more numerous towards the ends of the connection. This is understandable as the stresses are generally higher near the connection ends, where the loads are applied and end effects occur.

In order to give the weakest possible orientation of shear keys in the laboratory tests, the inner shear key is positioned on a line 45°to the horizontal from outer shear key (see Figure 2.6), so that cracks propagating from each key will meet. In actual offshore installations the relation between pile and sleeve shear keys cannot be controlled.

2.15 Deflections

Deflection, or more accurately slip, has been mentioned for its importance in the serviceability limit state (12). Referring to Figure 2.8, it can be seen that ultimate load is achieved after about 10mm slip. As this is a quarter-scale test, it is argued that the actual slip would be 40mm. The basis for this argument is an investigation in which the mean values of slip at ultimate load, δ_{um}, have been noted for each test series, and the ratio d_p/δ_{um} is then calculated. This ratio has a fairly constant value of 40, so that $\delta_u = d_p/40$. Evaluating the test results, however, there appears to be a large variability in δ_u for all scales and it is not always clear how to determine δ_u as the strength may continue to rise very slowly with δ. Also, δ may be different for alternative grout types and age of curing.

The value of δ_u may in fact be 10-15mm for all scales, as the grout/steel bond is precisely the same in these cases. The shot-blasting is not scaled down, nor can the grout bonds be reduced. Only the overall structural dimensions can be scaled and these do not affect the mechanism of bond failure or shear key crushing.

2.16 Summary and Conclusions

The current bond strength formula has identified the most important factors affecting the ultimate bond strength. Its application is, however, limited since formula overestimates bond strengths of connections with high radial stiffness. Such connections with extreme geometries are now used for grouted repair work. This has also become apparent where piles have been grouted into rock which effectively has an infinite radial sleeve stiffness.

For this case the current formula predicts an infinite ultimate failure load. Since this is physically impossible ,there must be an upper limit to the bond strength.

There is also experimental evidence that larger scale test specimens have a lower bond strength. This fact is not accounted for by the present formula.

The following chapters will seek to understand and remove these anomalies by the development and application of an improved bond strength formula.

CHAPTER 3

REVIEW OF EXISTING ANALYTICAL WORK

3.1 Introduction

Only a very limited amount of analysis has been carried out since the study of grouted connections is only a recent problem. The American Petroleum Institute has funded a programme to develop an analytical model and this work, which has been carried out by Paslay Incorporated (18) is now reviewed.

3.2 Paslay Analytical Model

3.2.1 Behaviour of the Connection

The analysis is designed to simulate a grouted connection loaded axially in compression, transferring load from the pile at one end to the sleeve at the other end. Three mechanisms are used to transfer the load across the steel/grout interface. These mechanisms are:-

1. Adhesion of the grout to the sleeve or pile.

   When the connection is fabricated an adhesion of the grout to the steel occurs which can transfer shear and tensile stresses across the steel/grout interface. So long as this bond is intact the axial strains at the interface are equal for the grout and the steel. The bond will break when stresses on the interface exceed the adhesive strength, and this mechanism is no longer active in load transfer.

2. Load transfer may occur through Coulomb friction when the adhesive bond has broken. That is, $\tau \leq \mu \sigma_n$, where τ is the shear stress on the bond, σ_n is the normal compressive stress across the boundary

and μ is the coefficient of friction. Relative slip may occur on the interface for the condition $\tau=\mu\sigma_n$. No tensile stress may be carried across the boundary once the adhesive bond is broken.

3. Even though the adhesive bond is broken at the location of a shear key the shear key can also transfer load to the grout. The concentrated loads at the shear keys are based on experimental values which give both axial and radial components. These loads are defined as a function of slip and effective key height (actual height less radial separation).

Although all three of the above mechanisms are included in the analysis, the adhesive bond is not really necessary. Once this bond breaks, (the adhesive strength is low anyway), it plays no further role in the bond strength of the connection.

Material behaviour of the grout is assumed to be elastic-perfectly plastic in the analysis, where the yield point is determined from the cube strength of the grout as follows:-

$$\text{Yield Point} = f_{cu}/\sqrt{3} \qquad (3.1)$$

3.2.2 The Generic Element

The grouted connection is divided into a series of axial sections, or elements. Each element has a shear key on one end of the pile and the other end of the sleeve. Hence, the element lengths must equal the shear key spacing. The shear keys on the sleeve are always in line with the pile shear keys, rather than being staggered as in the laboratory tested connections. Figure 3.1 shows an exploded view of a typical element, including all forces and displacements essential to the analysis.

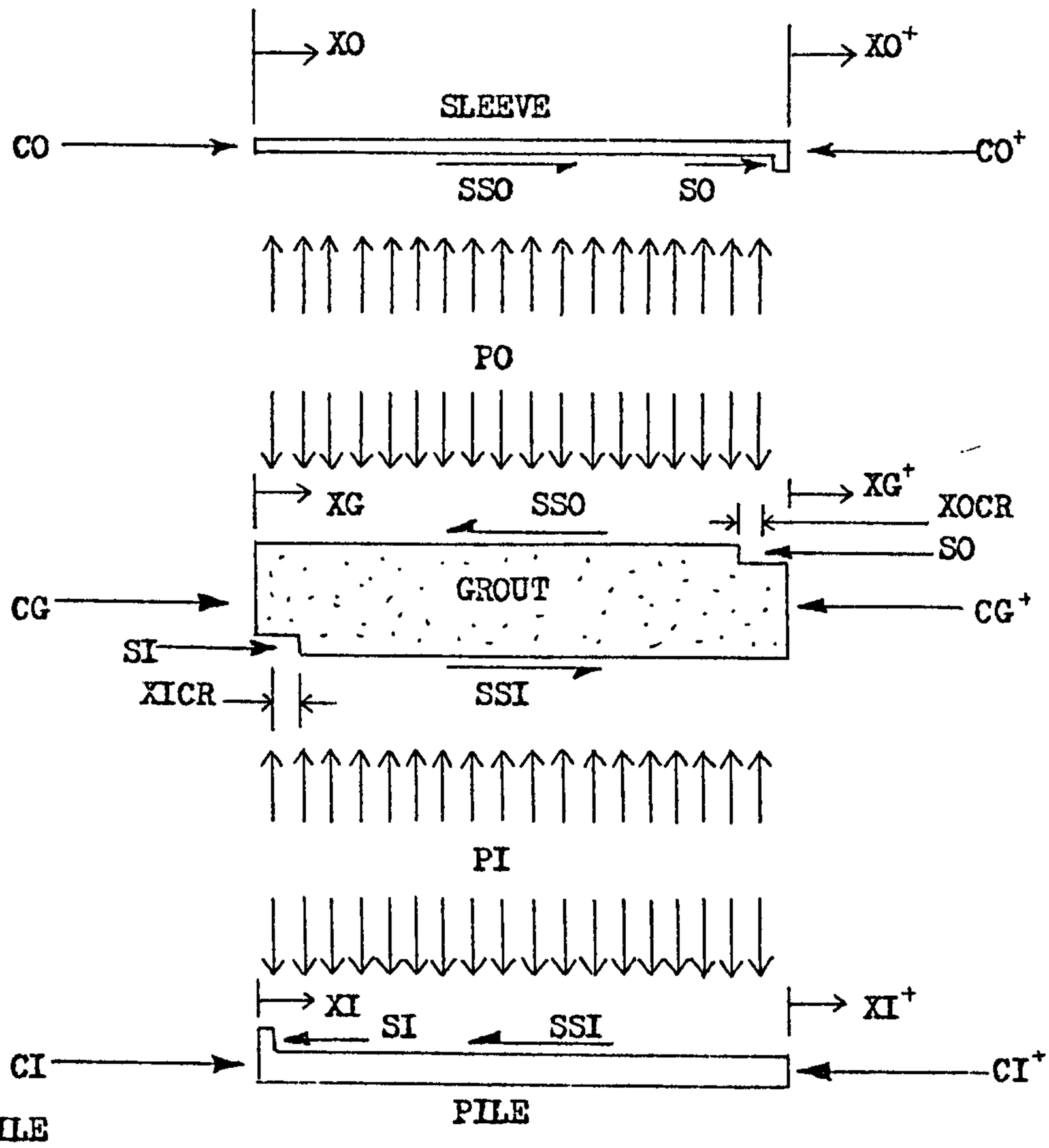

FIGURE 3.1 GENERIC ELEMENT OF THE PASLAY MODEL, SHOWING ALL THE FORCES AND DISPLACEMENTS DESCRIBED IN SECTION 3.2.2.

These are represented symbolically as follows:-

CG : Axial compressive force on grout, left end

CI : Axial compressive force on pile, left end

CO : Axial compressive force on sleeve, left end

PI : Average pressure between grout and pile

PO : Average pressure between grout and sleeve

SI : Axial component of force on pile shear key, left end

SO : Axial component of force on sleeve shear key, right end

SSI : Shear stress between grout and pile

SSO : Shear stress between grout and sleeve

XG : Axial displacement of grout, left end

XI : Axial displacement of pile, left end

XICR : Axial crush at pile shear key, left end

XO : Axial displacement of sleeve, left end

XOCR : Axial crush at sleeve shear key, right end

ξ^+: Value of ξ at right end

The grout-to-grout forces, CG, are restricted to be compressive because of the observation of cracks in the grout from the sleeve to pile at shear key locations in the failed specimens. In fact, the analysis can be simplified by ignoring these grout forces since they are negligible anyway.

The element assumes a constant level of bond stress between shear keys but this may lead to large errors. The finite-element analysis (see Chapter 7) has shown that large variations of the bond stresses occur over this length. Also, the analysis does not allow for the effects of stiffeners attached to the sleeve, which is the case for

most experimental tests. These would reduce the level of axial stress in the sleeve.

3.2.3 Governing Equations

Twenty four simultaneous equations are written for each element, which can be solved to find the forces and displacements. Some equations vary according to whether any bonds are broken, keys crushing or grout yielding. The equations are based on the following conditions:-

Axial force equilibrium

Elastic stress-strain formulae

Shear key force - crush length

Coulomb friction

Von-Mises yield condition for the grout

Since many of the above equations are nonlinear, an incremental approach is used to obtain a solution. A linear solution is obtained for each small increment of load and the incremental equations are modified as the bond states change. Also, the load increment size is adjusted automatically, thus enabling one state to just change on each load step.

There appears to be a source of error in the bond stress equations. If the adhesion is broken, it is stated that:-

$$\tau = \mu \sigma_n, \qquad (3.2a)$$

but this should be:-

$$\tau \leq \mu \sigma_n \qquad (3.2b)$$

The bond stress will often be less than $\mu \sigma_n$, but as the analysis does not include a shear stiffness, there is no means of determining the true value of τ.

Another shortcoming in the analysis is the lack of consideration of surface roughness. If the pile was loaded in tension and the sleeve in compression, the normal bondstresses would be reduced to zero by Poisson effects. If there were no shear keys, this would result in zero strength apart from the adhesive strength. Actual results (1) show bond strength to vary widely according to the geometry of the connection and so friction bond stresses must still exist. This is possible if the interface between grout and steel is considered as a rough surface, so that dilation will take place on the bond when slip occurs.

3.2.4 Shear Key Loads

Simple experiments were carried out in order to determine a load-slip relationship for the shear keys. Figure 3.2 illustrates the analogy between the actual shear key crushing and the experimental model used by Paslay. Due to its symmetry, the punch resembles two shear keys back-to-back in which the centreline corresponds to a friction-less wall separating the two. The fact that there is grout only below the punch does not hamper the analogy, because the free surface remains largely unaffected during crushing. The resistance to motion is provided by the underlying grout.

The figure shows that a square shape punch was used when the actual shape of the key is in fact hemispherical. The hemispherical shape will produce a larger lateral load as the key pushes into the grout and this will reduce the degree of confinement of the grout under the key. As a result, the actual stress at which the grout crushes will be lower and the experimental results obtained with the square punch will give crushing loads which are too high. Also, the level of confinement of the grout

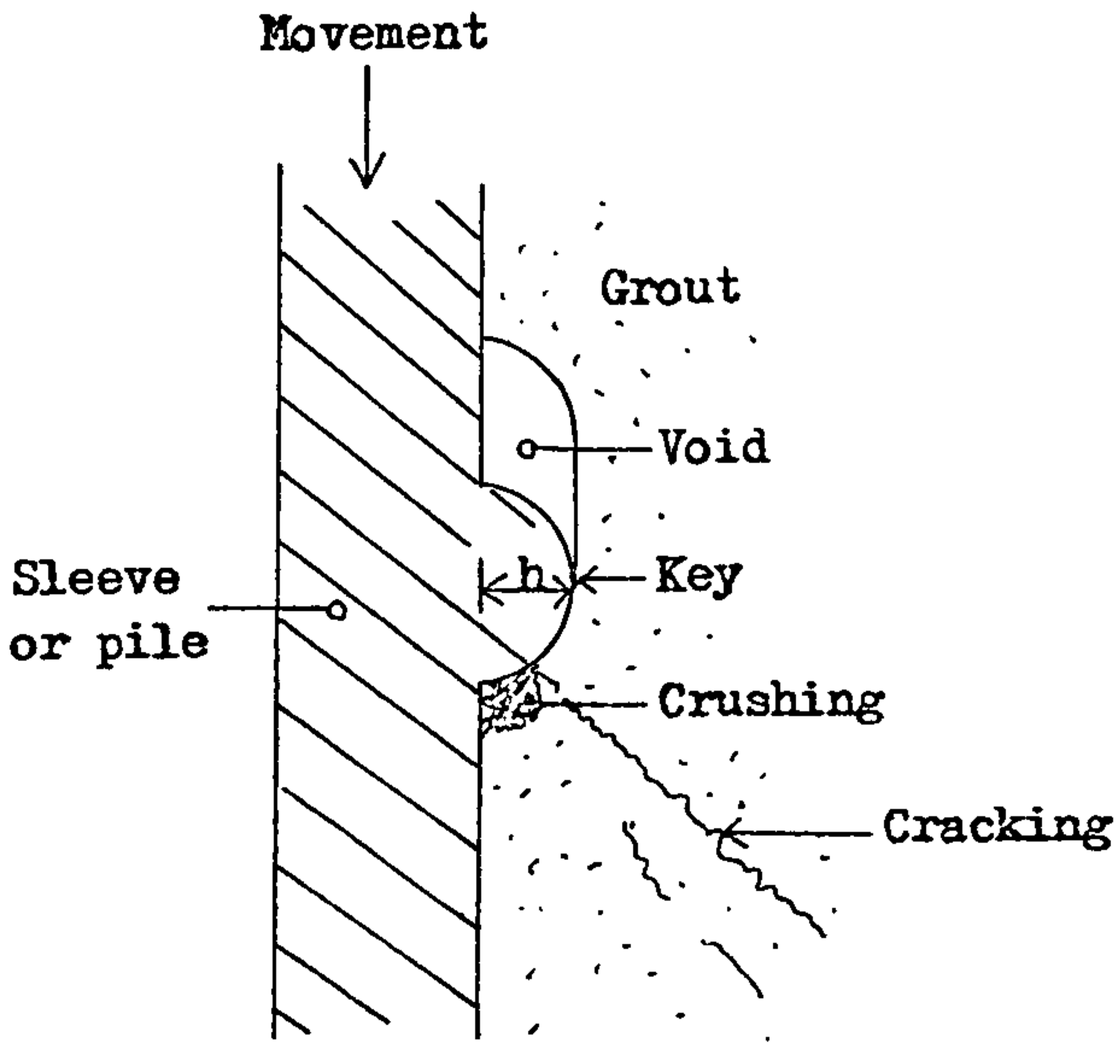

(a)Actual shear key crushing

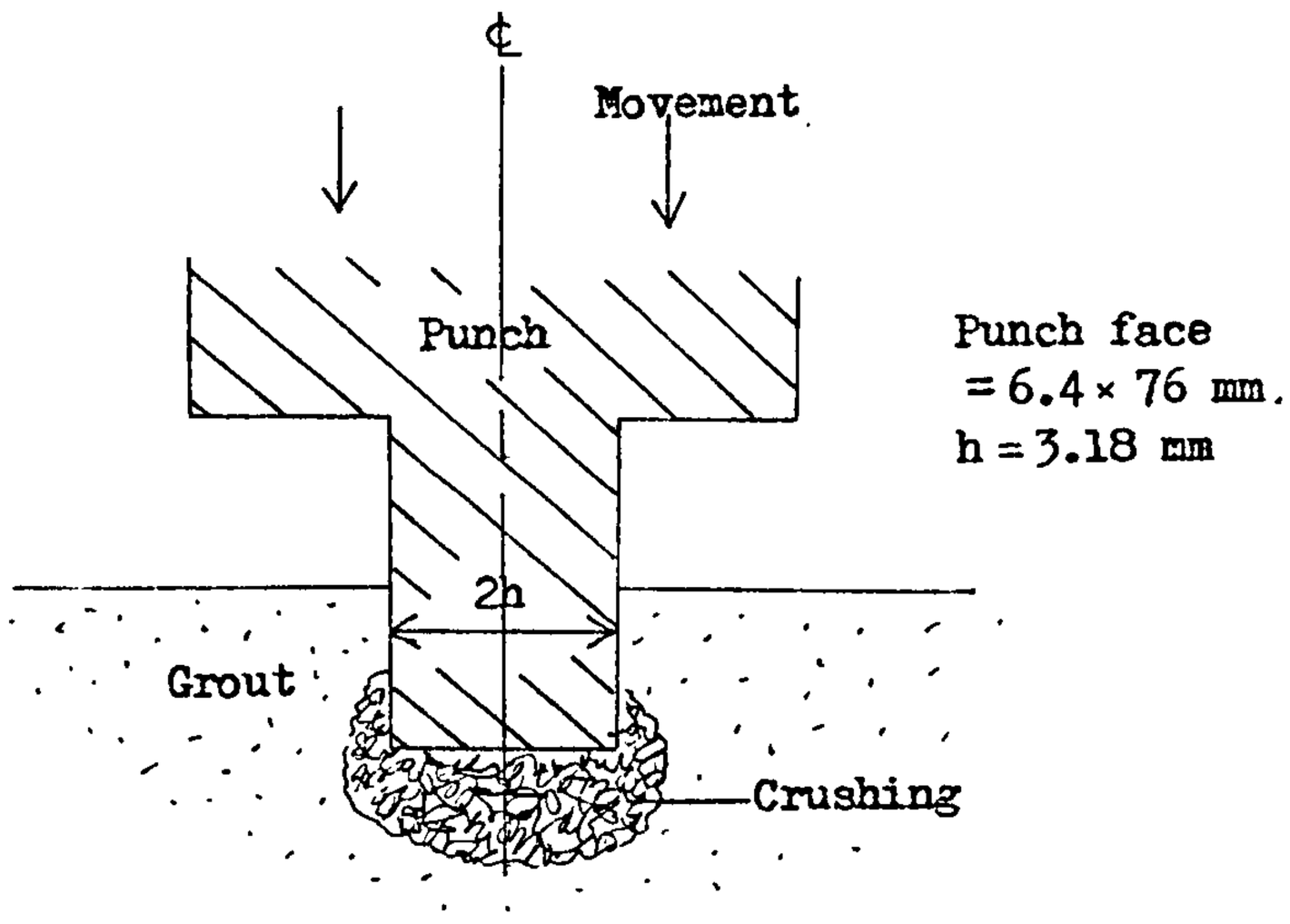

The grout is restrained by being cast in a steel trough 76 mm wide, 38 mm deep and 305 mm long.

(b)Experimental punch crushing

FIGURE 3.2 ANALOGY BETWEEN ACTUAL SHEAR KEY AND THE EXPERIMENTAL ARRANGEMENT USED BY PASLAY.

provided by the steel trough, does not necessarily reflect the level of confinement provided by a given grouted connection geometry.

Cement mixed with an equal weight of sand was used as the grout in the Paslay experiments. This is not typical of North Sea practice, however, in which sand is not used. Also, the specimens were cured at 27° Centigrade, whereas the North Sea temperature is only 8° Centigrade. This may affect the grout properties.

Figure 3.3 shows typical load-deflection curves obtained from these tests. Initially it was thought that one trough of grout could accommodate several tests, but it was discovered that end effects and interaction between indentations lowered the ultimate force the grout can withstand. The lateral force on the grout is very great and was demonstrated in one experiment where it caused the weld at the end of the grout confining trough to break, thus relieving the pressure under the punch. These effects emphasise the importance of the pile and sleeve in confining the grout to enhance the overall strength capacity.

Results from the tests indicated that the maximum punch pressure is approximately five to six times the cube strength of the grout.

$$\text{i.e.} \qquad \sigma_{key} = (5 \text{ or } 6) \times f_{cu} \qquad (3.3)$$

It was also seen that the punch indentation is accommodated through compaction of the grout, rather than by plastic flow, and that the compacted region has roughly the same dimensions as the indentation.

Paslay also made the observation that the ultimate strength of a grouted connection can be estimated as follows:-

$$f_{bu} = 6 \times f_{cu} \times A_s/A_p \qquad (3.4)$$

Therefore:

$$\sigma_{key} = 6 \times f_{cu} \qquad (3.5)$$

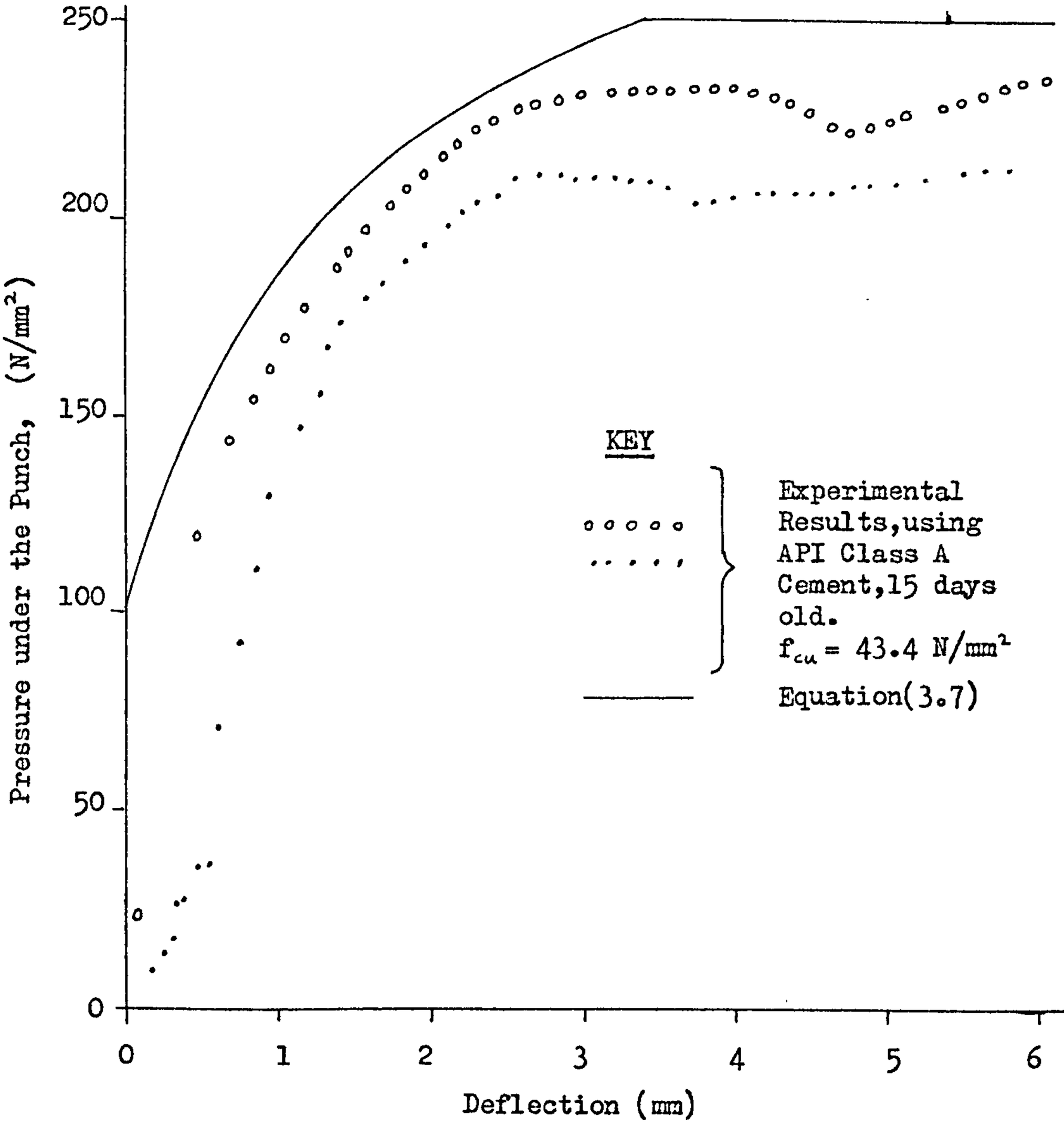

FIGURE 3.3 TYPICAL PUNCH INDENTATION TEST RESULTS, WITH EQUATION (3.7) PLOTTED FOR COMPARISON.

This is six times stronger than the interim Department of Energy design code given by equation (2.8), and may reflect the greater strengths obtained by loading in tension and using square shear keys. Paslay noted that the value of the constant in equation (3.5) compared well with the results of the punch tests, concluding that equation (3.3) was realistic.

On checking equation (3.5) against the Wimpey results, it was found that:-

$$\sigma_{key} = (2.7 \text{ to } 7.1) \times f_{cu} \qquad (3.6)$$

and some of the results are tabulated in Table 5.3. There is a large variation in the 'constant' factor, which can be attributed to the age of grout, hoop stiffnesses of the sleeve and pile, and shear key height and spacing. No allowance is made in equation (3.4) for a contribution to the bond strength from bond friction, but later analysis in Chapter 7 shows the bond to be open at high loads, and so it is reasonable to assume all the load is taken by the shear keys.

In the Paslay analysis, the following shear key force-crushing displacement function is used to give the axial key force per unit circumference, V, as:-

$$V = \left\{ 2.5 + 3 \times \sqrt{\frac{\text{Crushing displacement}}{h}} \right\} \times h \times f_{cu} \qquad (3.7)$$

for crushing displacement $\leqslant$ h.

The punch test results formed the basis for the above equation, which gives a maximum key stress of:-

$$\sigma_{key} = 5.5 . f_{cu} \qquad (3.8)$$

when the crushing displacement is $\geqslant$ h. Figure 3.3 shows a reasonably close fit with the experimental data.

Equation(3.7) implies that larger keys will require a larger crush displacement to reach ultimate load. After the examination of the Wimpey results (8), for varying h, it was found that the total slip at ultimate load certainly does not vary with h, but is approximately constant.

Paslay assumes the radial key force per unit circumference, V_R, to be half of V. He justifies this by showing that the maximum possible value of V_R equals V, but that the radial flexibility of the tubulars probably reduce V_R . This seems to be rather simplified as a large range of radial flexibilities are possible. Also, the radial force component must depend on the shape of the shear key used, since the surface of the shear key interacts with the grout which is trying to slip past the shear key. V_R may have an important effect as it tends to open the bond, reducing surface friction, and at the same time reducting the penetration of the shear key into the grout. The detailed analysis in Chapter 7 determines values for V_R, according to the shape of the keys used.

3.2.5 Programme Results

A programme is included in the report which can carry out the previously described analysis. Computer analyses have been conducted for the connection geometries which were also experimentally examined by the Chicago Bridge and Iron Company and by Wimpey Laboratories. Thus it was possible to establish the accuracy of Paslay's method. For the Wimpey tests, the pile is in tension and the sleeve in compression. The load is applied from only one end. In order to accommodate this loading arrangement in the analysis, certain changes were apparently made to the boundary conditions. Typical property values used were:-

$E_g = 1.24 \times 10^4$ N/mm^2, $\nu_g = 0.2$, $\mu = 0.2$ and $f_{cu} = 54$ N/mm^2.

The value for Poisson's Ratio seems low, as values of 0.25 to 0.30 are typical (19). The friction coefficient is also low since the joint tests reported in Chapter 9 show $\mu = 3.0$. The adhesive bond strengths are equal to zero as these are not important when shear keys are used. Figure 3.4 shows the shear key layout for the P9/10 tests, and the representation by the Paslay Model. It can be seen that the positions of the shear keys may lead to some discrepancies, particularly at the extreme ends of the connection where the shear keys do not have enough grout cover to generate the shear key forces given by the programme.

The predicted load-slip curve for the P9/10 tests, together with the experimental results, are shown in Figure 3.5. It can be seen that the Paslay model substantially overestimates the bond strength and this was found to be the case with other geometries too. If according to the lower factors in equation (3.6), the maximum shear key loads were substantially reduced, then the results are improved. Alternatively, if in the Wimpey tests square shear keys had been used, the load achieved with the sleeve in tension, then possibly the results would have been closer to the Paslay prediction.

3.2.6 Evaluation of Trends

Parameters affecting the bond strength were varied independently to establish the trends the Paslay model would give. Using published values of Young's Modulus for a given cube strength (11), it was possible to investigate the effect of f_{cu}. This gave:-

$$f_{bu} \propto (f_{cu})^n \quad , \text{ where } n = 0.92 \qquad (3.9)$$

Experimentally it has been found that $n = 0.5$, thus suggesting that the

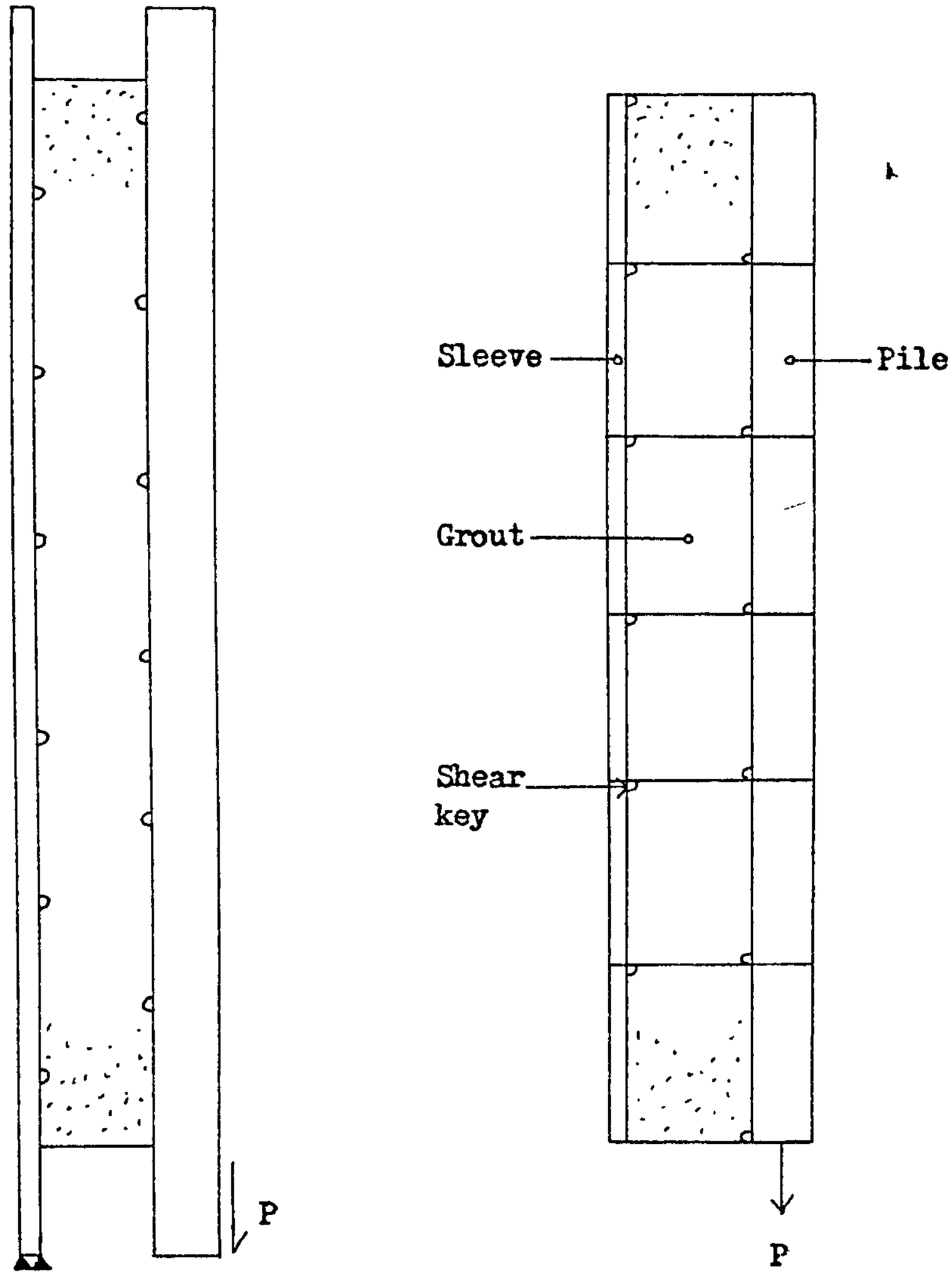

(a)Actual test

(b)Paslay model

FIGURE 3.4 COMPARISON BETWEEN THE ACTUAL TEST GEOMETRY AND THE PASLAY MODEL.

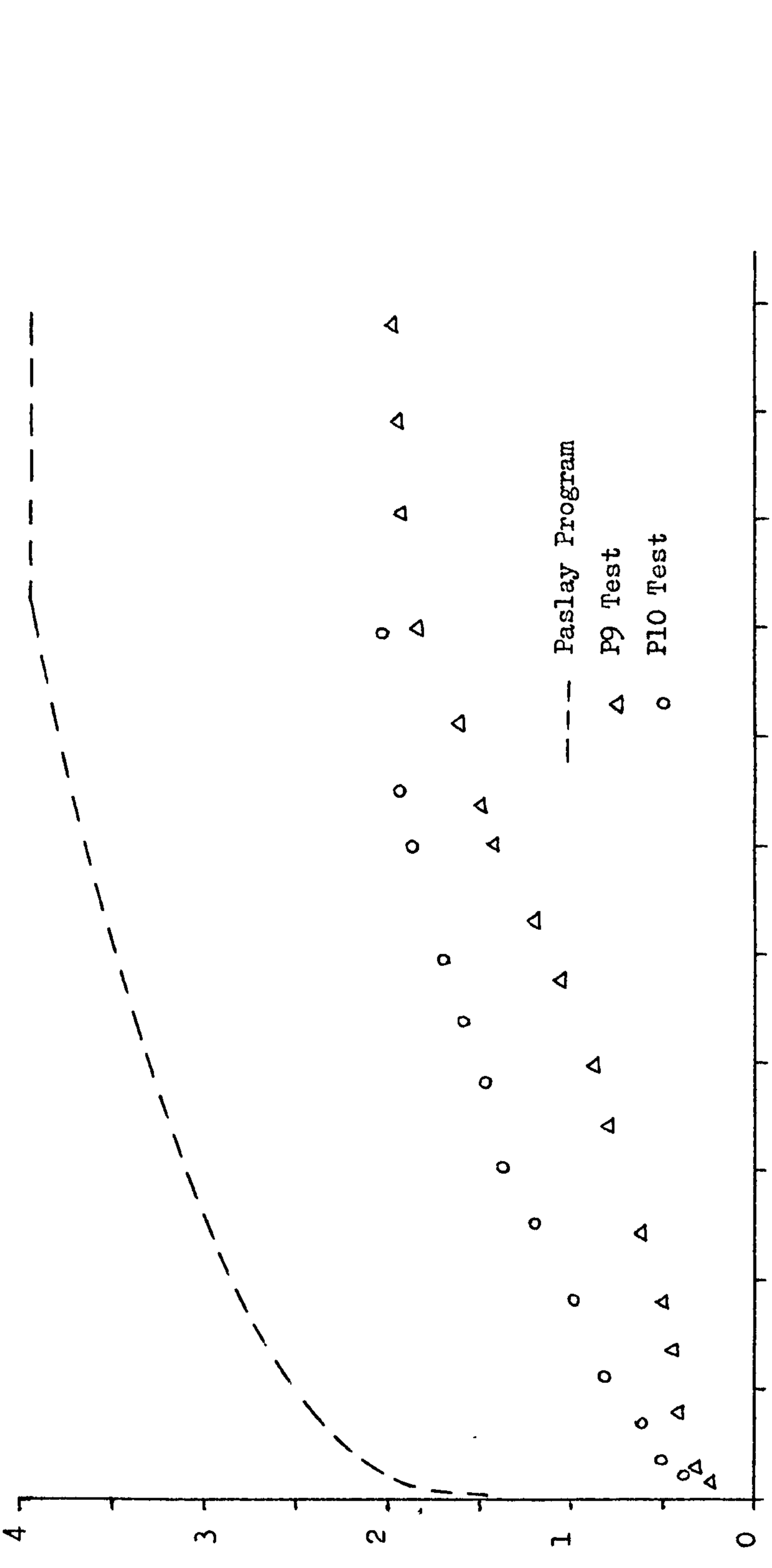

FIGURE 3.5. LOAD-SLIP CURVE FOR THE P9/10 TESTS COMPARED TO PASLAY'S PROGRAM RESULTS.

shear key force, which has been made proportional to f_{cu} in equation(3.7), should be proportional to the square root of cube strength instead.

Varying the length of the connection by changing the number of elements, shows a reduction in bond strength with increasing length, which is approximately equal to the experimental trend. The reduction in bond strength for $l/d_p<2$ is not apparent as the analysis does not include the bending effects caused by end restraints.

The effects of hoop stiffness were investigated by varying the sleeve and pile thickness in turn. A plot of predicted bond strength against K, the hoop stiffness factor, is given in Figure 3.6. The strength predictions from the standard bond strength formula, a new formula described in Chapter 8, and the finite element analysis results, are also plotted. The new formula, Paslay's results, and the finite element results all seem to indicate an upper limit on bond strength with increasing K, unlike the standard formula which continues to show a strength rise. Table 3.1 gives the numerical results for this graph.

Figure 3.7a shows the effect of pile or sleeve thickness on bond strength in a more direct way. The solid curve corresponds to sleeve shear key crushing while the broken lines correspond to pile shear key crushing. Figure 3.7a shows the Paslay predictions. It can be seen that varying the sleeve thickness above 5mm makes little difference to the bond strength. This was also fqund to be the case for the finite element results, given in Figure 3.7c. The finite element analysis shows that large increases in sleeve thickness have little effect on bond strength, as the pile bond always opens anyway. As a result, the pile key forces are much larger than the sleeve key forces which are helped by bond friction on the sleeve, and crushing occurs around the

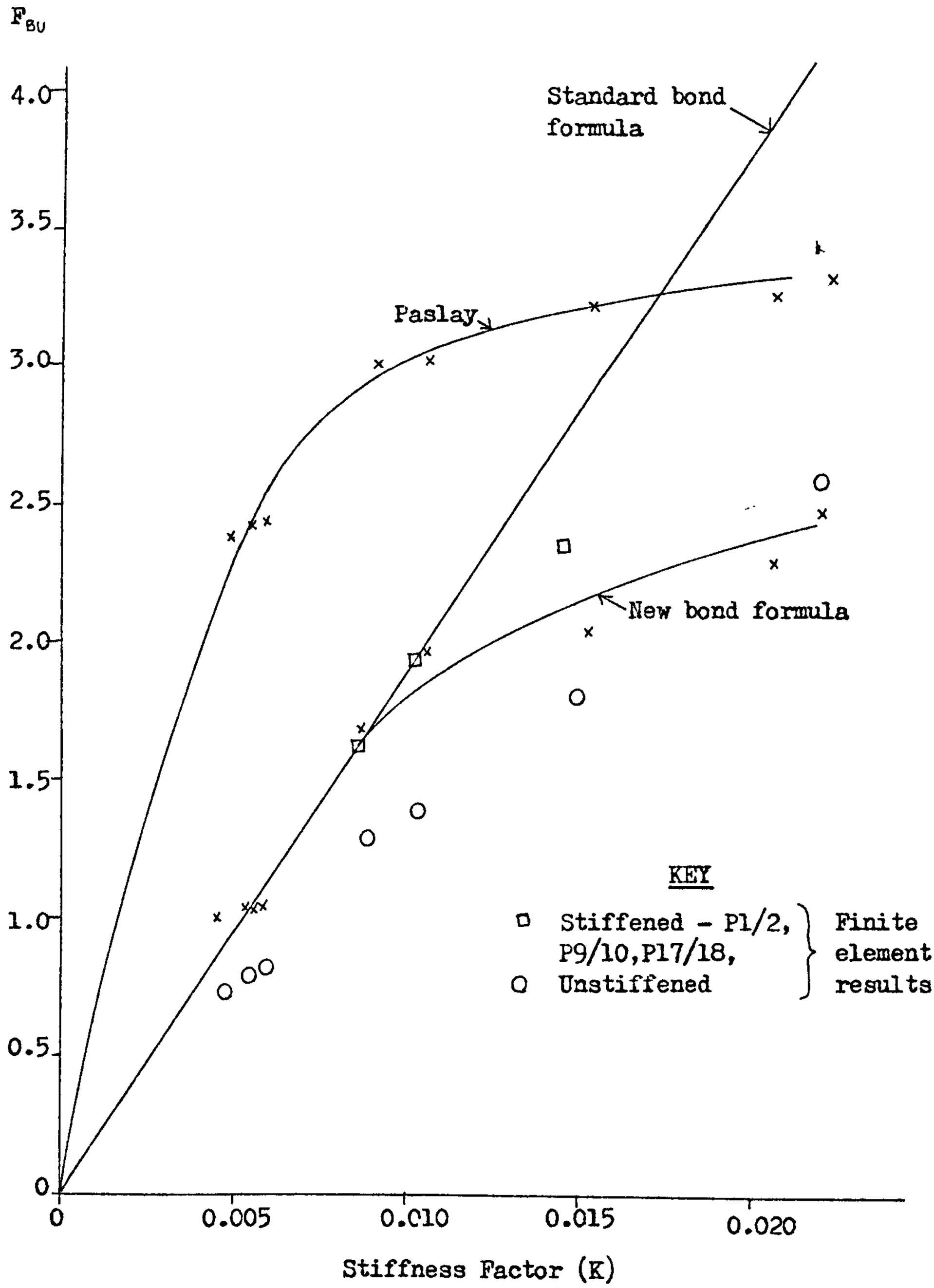

FIGURE 3.6 BOND STRENGTH AGAINST STIFFNESS FACTOR PREDICTED BY VARIOUS FORMULAE AND ANALYSES. DETAILS ARE GIVEN IN TABLE 3.1.

Sleeve Thickness mm	Pile Thickness mm	K	θ mm^{-1}	$\gamma \times 10^4$ mm	F_{su} Prediction			
					Paslay	New Formula	Existing Formula	Finite Element
5.08	2.54	0.00467	0.4945	4.0244	2.40	1.02	0.89	0.76 p
12.70	2.54	0.00550	0.45092	3.1353	2.43	1.06	1.04	0.80 p
25.40	2.54	0.00588	0.42696	2.83918	2.47	1.09	1.12	0.83 p
5.08	15.88	0.00891	0.16377	1.89103	3.02	1.71	1.69	1.30 s
12.70	15.88	0.01522	0.12020	1.00190	3.25	2.07	2.88	1.83 p
25.40	15.88	0.02056	0.09623	0.705782	3.28	2.32	3.90	2.10 p
5.08	63.50	0.01059	0.11654	1.58755	3.02	1.96	2.01	1.40 s
12.70	63.50	0.02217	0.07297	0.69842	3.36	2.52	4.21	2.63 p
25.40	63.50	0.03705	0.04900	0.4023	3.42	3.03	7.03	2.88 p

p = Pile keys crush, s = Sleeve keys crush.

TABLE 3.1. PREDICTED EFFECT OF PILE/SLEEVE THICKNESS ON BOND STRENGTH.

All dimensions, other than thicknesses, are as for the P9/10 tests. No stiffeners are used in these analyses. The Paslay results are obtained from pages 77/78 of the Final Report (18).

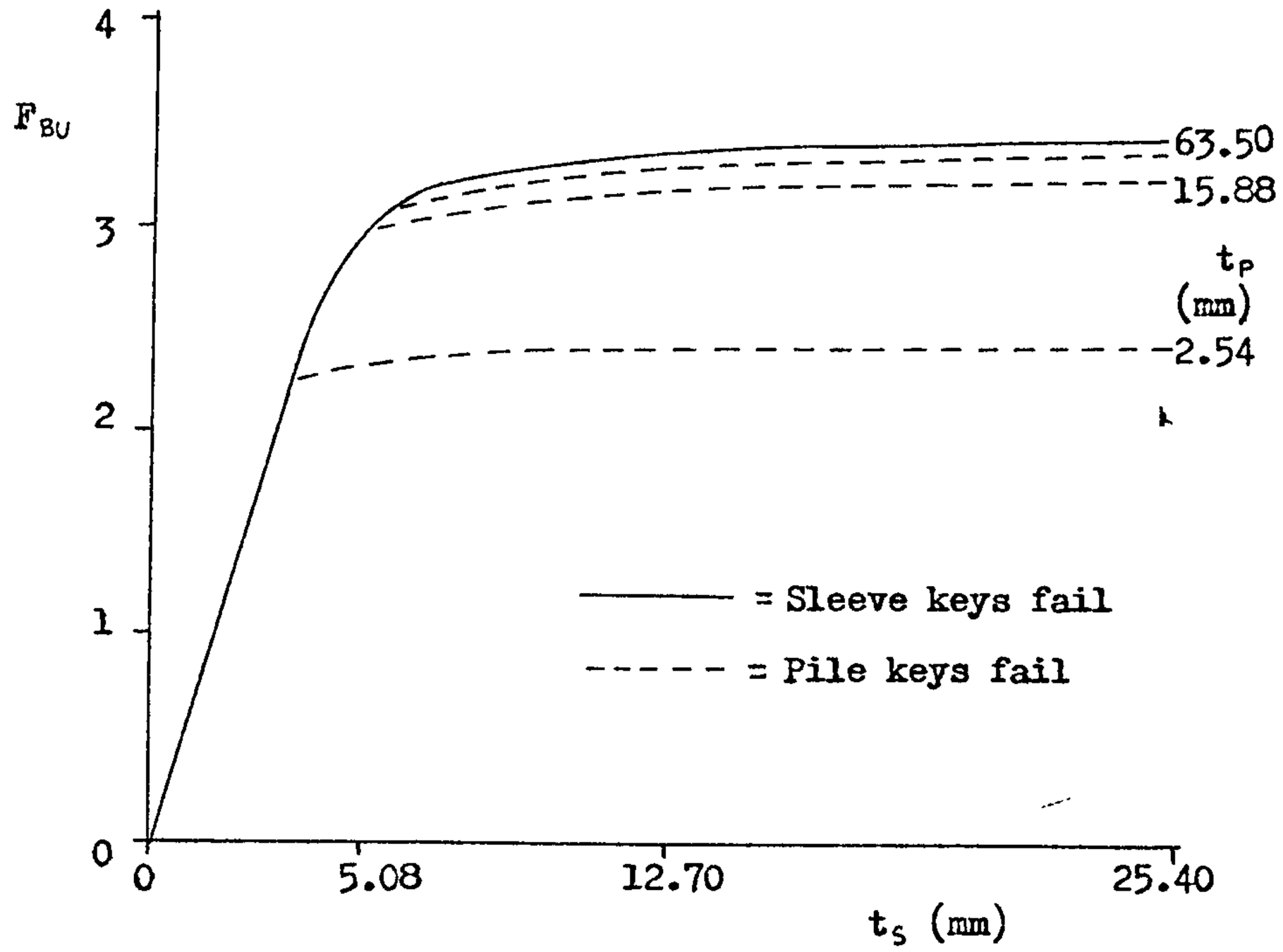

(a)Paslay Predictions

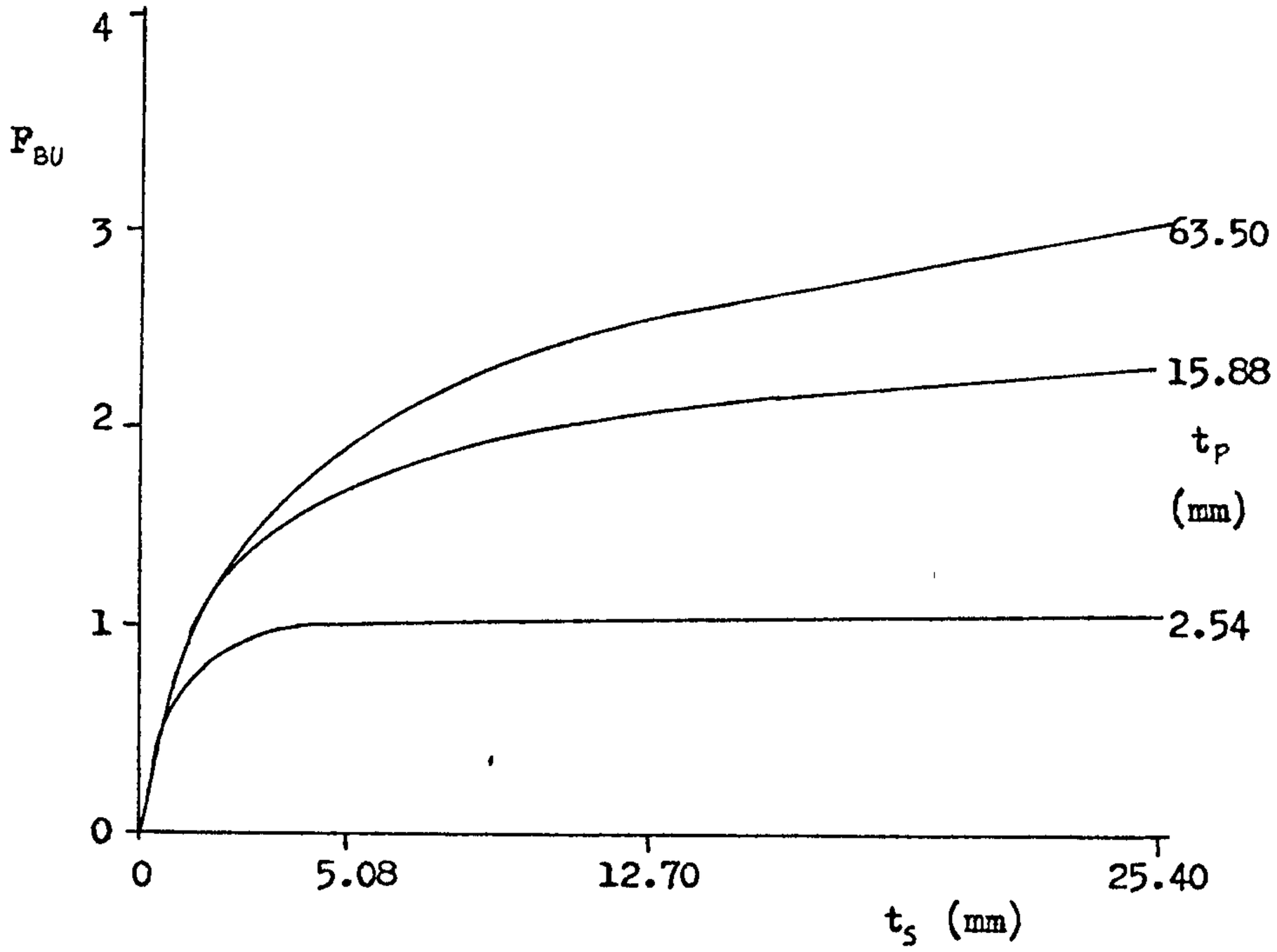

(b)New Bond Strength Formula Predictions

FIGURE 3.7 PREDICTED EFFECT OF PILE OR SLEEVE THICKNESS ON BOND STRENGTH. OTHER DIMENSIONS ARE AS FOR THE P9/10 TESTS.

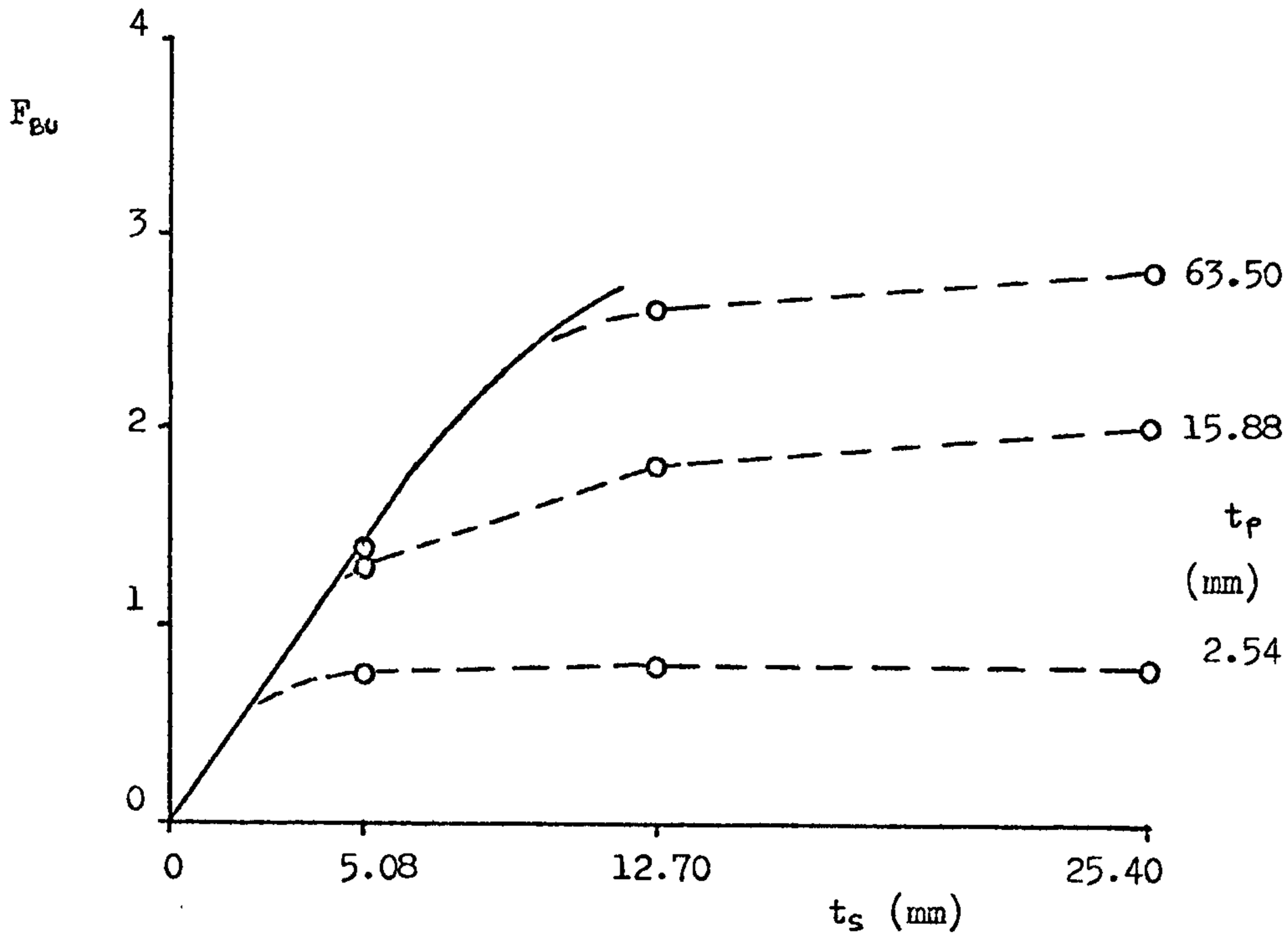

——— = Sleeve keys fail

— — — = Pile keys fail

(c) Finite Element Predictions

FIGURE 3.7 continued.

pile keys. However, when the sleeve thickness is very low, the sleeve bond opens before the pile bond. This results in higher key forces on the sleeve and failure then takes place around the sleeve keys.

When longitudinal stiffeners are used on the sleeve (not in Paslay's analysis), the Poisson effects in the sleeve are reduced, and failure is nearly always on the pile keys.

Figure 3.7b shows the predictions from the new bond formula in Chapter 8 for comparison.

Another interesting trend results from varying the shear key upstand, h. Paslay shows the bond strength to be proportional to h for $h \leq 5.08$mm on the basic P9/10 geometry. For $h > 5.08$mm, i.e. $h/s > 0.03$, no further strength is gained because the yield point of the grout is reached. Actual test results at Wimpey Laboratories have shown a linear increase in f_{bu} with h up to $h/s = 0.06$, but the strength increase with h is less than predicted by Paslay. If Paslay's results gave a lower strength increase with h, then the yield point could be reached at $h/s = 0.06$, which is the case for the experimental results. This seems encouraging since the strength increase with h can easily be corrected by modifying the shear-key load formula. This approach has already been suggested.

3.3 Other Reports

3.3.1 R. Van Lee Report

Another analysis of grouted connections, limited to plain pipes only, has been carried out by R. Van Lee at Massachusetts Institute of Technology (20). The important details of the report are now reviewed.

Three models were produced. The first one considered axial stresses and displacements only. These were equated by means of linear elastic

stress-strain relations for each material, and a linear bond stress-slip relation which is to be described later. The stress-strain and equilibrium equation results are combined in a fourth order differential equation which is solved by a computer programme in a similar manner to the Paslay analysis.

The second model was similar to the first, but included the addition of radial and hoop stresses. Both of these models are applicable only in the linear-elastic range.

The third model was a nonlinear finite element analysis, which enables the bond stress-slip relation to be nonlinear. Also, bending effects were included in this analysis, which accounted for the effects of end restraints on radial displacements.

Figure 3.8 shows the bond stress-slip relation used in all three models. The unloading section can only be applied in the finite element analysis and the numerical values are based upon overall bond stress-slip results from a plain pipe test at one third scale. This does not account for local variations in bond stress. Also, the maximum value of bond stress is fixed and no account of the effect of normal bond stress on the shear bond stress is made. This is an important omission since the normal bond stress varies according to the hoop stiffness of the sleeve and pile.

The results of all three models are in reasonable agreement with the experimental results, but this is not surprising as the data for k_t and τ_m came from the same experiment. The bond shear stress is a simple function of slip and so it must be fairly constant over the whole length of the connection, as the elastic displacements within each cylinder can only vary gradually. Had a Coulomb friction law been

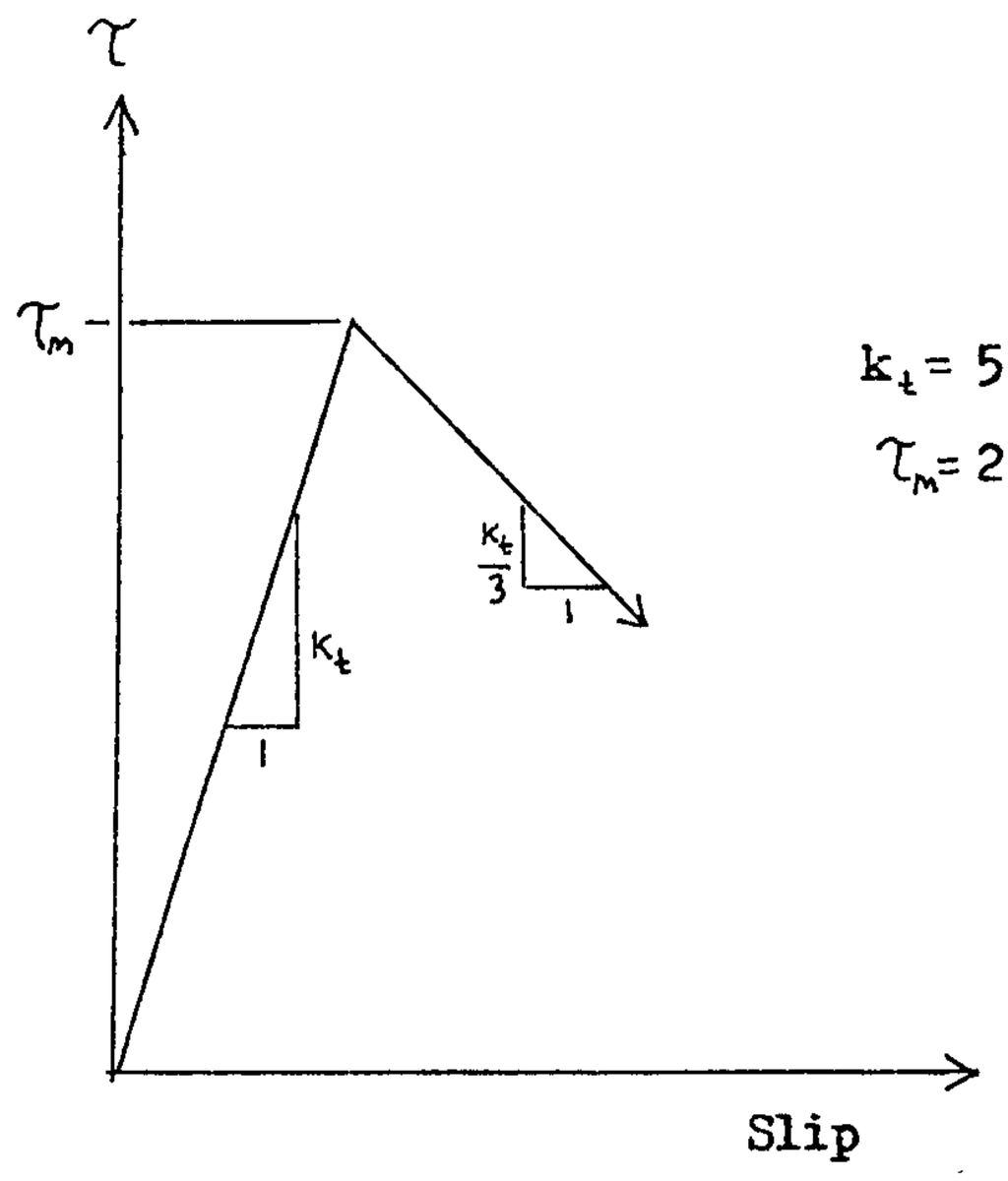

$k_t = 5.7\ N/mm^3$

$\tau_m = 2.76\ N/mm^2$

FIGURE 3.8 BOND STRESS-SLIP RELATION USED BY VAN LEE.

used, the bond stresses may have been more variable, particularly at the ends of the connection. In fact, the report suggests that by increasing the bond stiffness, the shear stress distribution becomes more nonlinear with peaks at the ends of the connection. A high bond stiffness may be more realistic as the shot-blasted steel surfaces are very rough.

Finally, an interesting fact is given in Van Lee's literature survey. A paper by G.W. Ostroot (21) defines another stiffness factor based on empirical correlation. In dimensionless form, this correlation gives

$$\text{stiffness factor, SF} = \left(\frac{d_s^2}{t_g}\right) \times \left(\frac{1}{t_s} + \frac{1}{t_p}\right) \qquad (3.10)$$

where bond strength, $f_{bu} \propto 1/SF$.

This is an interesting alternative to the stiffness factor, K, in the standard bond strength formula, and to the factor, γ, in the new bond formula proposed in Chapter 8.

3.3.2 Brown and Root Report

In a report from Brown and Root (22), an attempt is made using thin shell theory, to find the key nondimensional parameters affecting the strength of a grouted connection. Many assumptions and simplifications are necessary regarding the interactions on the steel/grout bond and as the bond behaviour is of key importance it is unlikely that the resulting parameters will give more than a rough guide. Shear keys are not considered. Six nondimensional parameters are produced, including some which are used in the formula for K, but it is difficult to see how these six parameters could be brought together into a single bond strength equation.

The parameters are:

$P/E.t.R$, δ_w/ℓ , R/t , ℓ/R , ν and μ

where: P = axial load δ_u = slip

R = cylinder radius t = cylinder thickness

ℓ = connection length μ = friction coefficient

E, ν = elastic properties

There are three sets of the above parameters which describe the sleeve, grout and pile.

3.3.3 Wimpey Laboratories Analysis

One other interesting study worth mentioning is a linear elastic finite element analysis of a grouted connection with shear keys which has been reported by Wimpey Laboratories (23). The steel and grout are coupled only at the shear key locations, with no other load transfer on the bond. This is a simple form of analysis in which no slip is possible. It provides an indication of the load transfer along the connection. The most interesting results concern the radial displacements on the interfaces. Figure 3.9 shows the results for the sleeve/grout bond, which is similar to the characteristics shown for the pile/grout bond. It can be seen that there are alternate areas of separation and contact of the steel from the grout between each shear key. This effect emphasises the error in the Paslay model, where a constant normal bond stress is used over the whole length between keys.

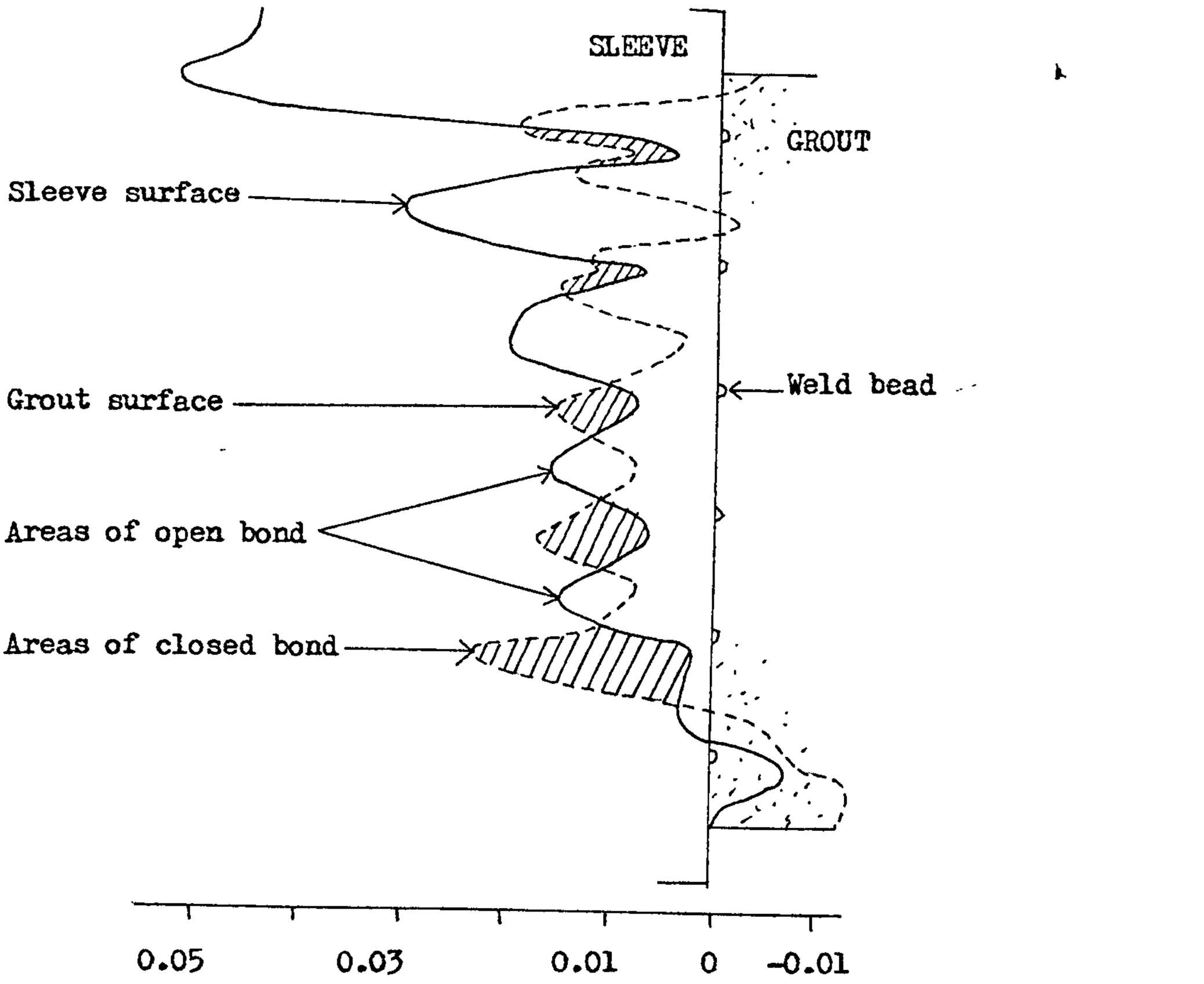

FIGURE 3.9 RADIAL DISPLACEMENT ON THE SLEEVE/GROUT INTERFACE UNDER COMPRESSION LOADING, GIVEN BY LINEAR FINITE ELEMENT ANALYSIS. THE BOND IS COUPLED AT THE SHEAR KEYS.

CHAPTER 4

THE FINITE ELEMENT ANALYSIS

4.1 Solution Procedure

Non-linear finite element analysis is well established and programmes such as NONSAP (25) are readily accessible. The procedures involved are described in papers by Bathe, Ozdemir, Wilson and Zienkiewicz (24,25,26). This material has been taken as the basis of the finite element programme which has been developed for the work reported in this thesis.

Only a brief introduction to the standard methods employed is therefore required since the techniques are well documented elsewhere. Later chapters describe in detail the finite element development and implementation which have been carried by the author to enable the technique to be used for the analysis of grouted connections.

Specified load increments are applied to the grouted connection and the resulting displacement response is calculated until the applied load becomes so large that the analysis becomes invalid. This breakdown is normally due to the stiffness of the connection becoming too low to sustain further load and so it represents the ultimate load capacity of the connection. This state is normally indicated by an inability to reach equilibrium in a specified number of iterations.

The solution procedure used is the Modified Newton Raphson Method, in which the global stiffness matrix is updated for each new load increment but not for individual iterations (Figure 4.1). This is more efficient than the standard Newton Raphson process, where much computational effort is spent on updating the stiffness matrix for every

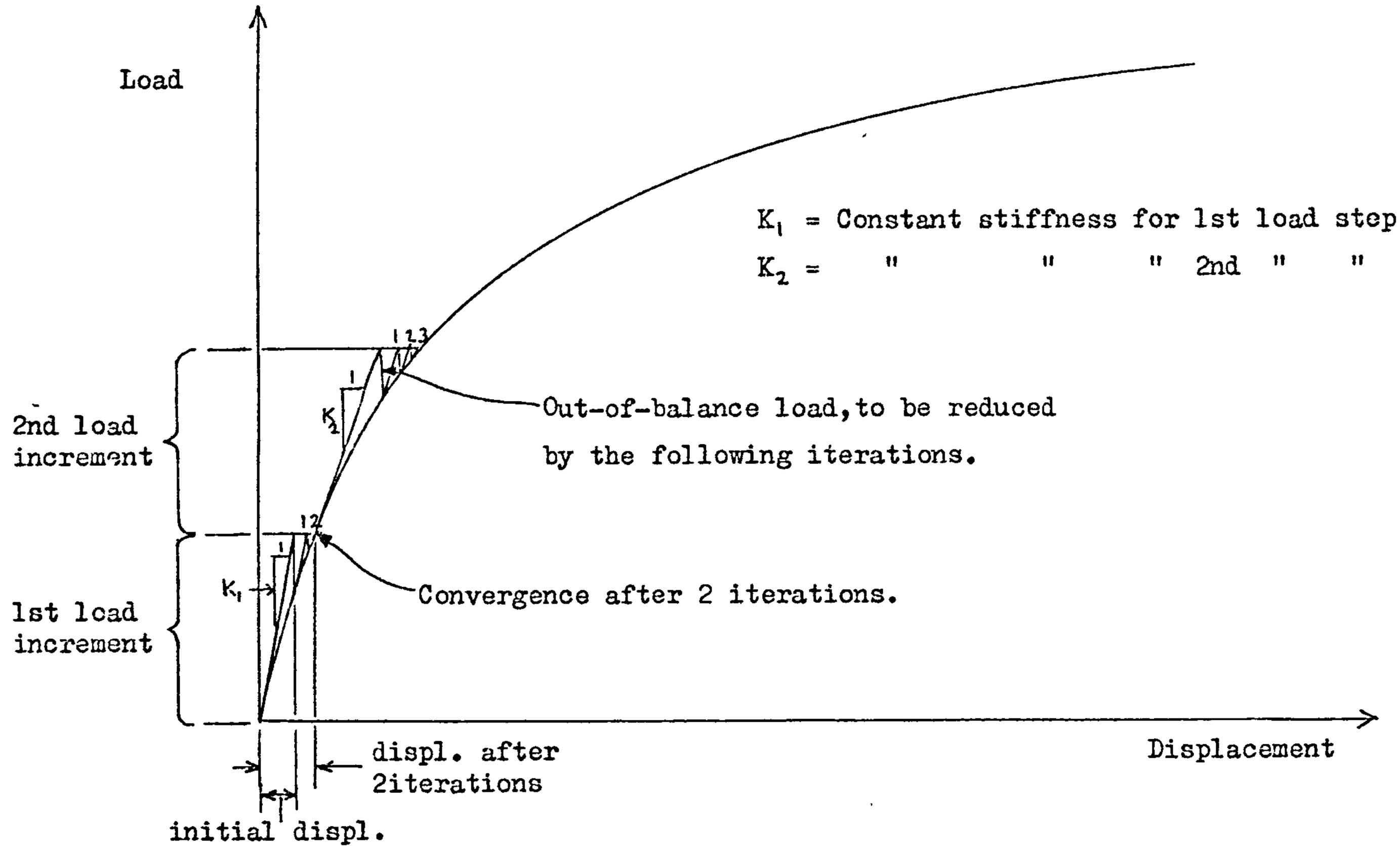

FIGURE 4.1 MODIFIED NEWTON-RAPHSON METHOD.

iteration. At the other extreme, it is possible to not update the stiffness matrix at all. This would require an ever increasing number of iterations to reach convergence as more bonds open or slip and lose stiffness. The displacements would also tend to be underestimated and so it is preferable to update the stiffness matrix for each new load increment.

The size of the load increments need to be made gradually smaller as the load increases and the connection becomes less stiff. If the load increment is too large the stiffness may deteriorate to such an extent that no number of iterations will converge. Alternatively, the ultimate load capacity may even be exceeded, in which case the analysis will become unstable.

Also, it is important to keep the load increments as small as possible when the nonlinear grout material becomes plastic, cracks or crushes. The strain increments are predetermined as a function of the stresses at the end of the last load step. This is acceptable in the elastic state, but if the grout moves into the plastic state during the current load step, the rate of strain should increase in one direction due to the existence of plastic flow. This cannot occur because the strain increments are predetermined for the whole structure and so the resulting stress increments, which are related to the strain increments, will also be inaccurate.

The total stresses and strains at the end of the load step will include the above errors and as the strains calculated for the next load step are a function of these stresses, the errors will accumulate with each load increment. These strain errors are only large when a state change is initiated, such as elastic to plastic, or the formation of a

new crack, which has a large effect on the succeeding strains. Errors are minimised by restricting the size of these strain increments when state changes are likely to occur. This is achieved by the use of small load increments when the total load becomes large enough to make state changes probable.

4.2 Iteration Process

The iterative process proceeds in the following way. Before the application of a new load increment vector $\{\Delta P\}$, the global tangential stiffness matrix $[K_t]$, is calculated from the stresses and strains at the end of the last load increment. Then, the displacement increment vector $\{\Delta u\}$, can be estimated as follows:

$$\{\Delta u\} = \{\Delta P\}[K_t]^{-1} \qquad (4.1)$$

and the displacement vector is updated to give

$$\{u\}_t = \{u\}_{t-1} + \{\Delta u\} \ . \qquad (4.2)$$

For the solid continuum elements, it is now necessary to use numerical integration techniques to determine the strains and the nodal forces. Weight coefficients of the Gaussian Quadrature Formula (26) are used with $n = 2$, i.e. four Gauss Points in the case of rectangular isoparametric elements. For each Gauss Point, the quadratic interpolation functions and their derivatives are formulated. The Jacobean matrix and its determinate are then found and from these the strain matrix $[B]$, can be determined. The strains can be calculated as follows:

$$\{\epsilon\} = [B]\{u\} \ . \qquad (4.3)$$

The stresses $\{\sigma\}$, are then determined using linear-elastic stress-strain relations, or in the case of the grout material, using the

relations defined in Chapter 6. The internal force vector $\{Q\}$, is then given by

$$\{Q\} = [B]^T \{\sigma\}. \qquad (4.4)$$

In the case of the friction-gap elements, there are no strain calculations and the internal force vector is calculated in the same way as that in Chapter 5.

The out-of-balance, or residual loads $\{R_{oB}\}$, are then given by

$$\{R_{oB}\} = \{P\} + \{\Delta P\} - \{Q\}. \qquad (4.5)$$

In order to satisfy the equilibrium conditions, $\{R_{oB}\}$ must be reduced to zero and this requires a further displacement increment $\{\Delta u_1\}$, which results from the first iteration and is calculated as follows:

$$\{\Delta u_1\} = \{R_{oB}\}[K_t]^{-1}. \qquad (4.6)$$

The total displacement increment is then

$$\{u_1\} = \{\Delta u\} + \{\Delta u_1\}.$$

The residual force vector is then recalculated and if necessary more iterations are carried out until convergence criteria are met.

4.3 Convergence Criteria

Convergence is satisfied if the ratio of the Euclidean Norms of the incremental displacements to the total displacements is less than a specified tolerance. That is, for convergence after the i th iteration

$$\frac{\sum(\Delta u_i)^2}{\sum(u_{i-1} + \Delta u_i)^2} \leq \text{Specified Tolerance} \qquad (4.7)$$

where typically, tolerance = 0.0001 in order to achieve convergence in a reasonable number of iterations.

For the analysis of grouted connections, as the slip on the steel/grout interfaces increase, the displacement increments become larger.

This enables the convergence criteria to be satisfied by less accurate results since the denominator of equation (4.7) is increased by the large rate of slip. Also, whilst the shear stiffness of the bonds are kept constant, the results will always underestimate the slip and bond stress required for equilibrium. This is particularly so when ultimate failure is on only the sleeve or the pile bond, which is normally the case. When this happens, convergence is very good on the unfailed bond, where slip is small, but the slip on the failed bond may be significantly underestimated and give the impression that the ultimate load of the connection is somewhat higher than it would be with good convergence. Therefore, rather than using a more exacting convergence tolerance, which would greatly increase the number of iterations needed, the ultimate load is assumed to be reached when the slip on one bond reaches 5 mm. Ultimate load is taken to be when the grout is crushing under all shear keys on one bond when shear keys are included.

To some extent, the number of iterations can be reduced by reducing the bond stiffness when slipping or opening of the bond occurs.

If equation (4.7) is not satisfied at the end of the iteration, $\{R_{os}\}$ is again calculated and a further iteration carried out. It may be necessary to check for divergence before the next iteration. Divergence is an indication that the iteration process is becoming unstable, which can happen in highly nonlinear situations and is defined as follows:

$$\frac{\sum(R_{os})^2}{\sum(\Delta P)^2} > 1.1 \quad \text{for divergence.} \qquad (4.8)$$

Divergence does not necessarily lead to problems in the first few iterations, but if it persists, then corrective action or termination of the analysis will be needed. This condition often occurs at the ultimate

load of a structure.

A method by Crisfield (38), has been added to the programme to correct divergence when it is not too large. It is during iterations to update the displacement vector. This has been done in equation (4.9) below, where $\eta_i = 1.0$.

$$\{u_{i+1}\} = \{u_i\} + \eta_i \{\Delta u_i\} \qquad (4.9)$$

However, when this leads to divergence, as defined by equation (4.8), a smaller fraction of the displacement increment can often restore stability. This fraction is calculated as follows:

$$\eta_i = 0.8 \times \frac{\sum(\Delta P)^2}{\sum(R_{oB})^2} \quad . \qquad (4.10)$$

The analysis is terminated if this fraction is less than 0.1, otherwise the new displacements are re-calculated using the reduced value of η_i and hopefully stability will be restored. This process works well when the applied load increments ΔP may be a little large for the analysis, causing considerable nonlinear changes in one load step. Figure 4.2 shows this process as a flow-chart.

It is possible to use the nodal loads rather than the displacements in the convergence criteria, but as local sudden changes in stresses can occur, for example, due to grout cracking, it is considered that the displacement criteria is more practical. .

Figure 4.3 outlines the whole solution procedure used for solving the grouted connection problems.

4.4 Modelling the Grouted Connection

Two axisymmetric finite element models have been proposed. In the first model it is intended to represent the complete grouted connection.

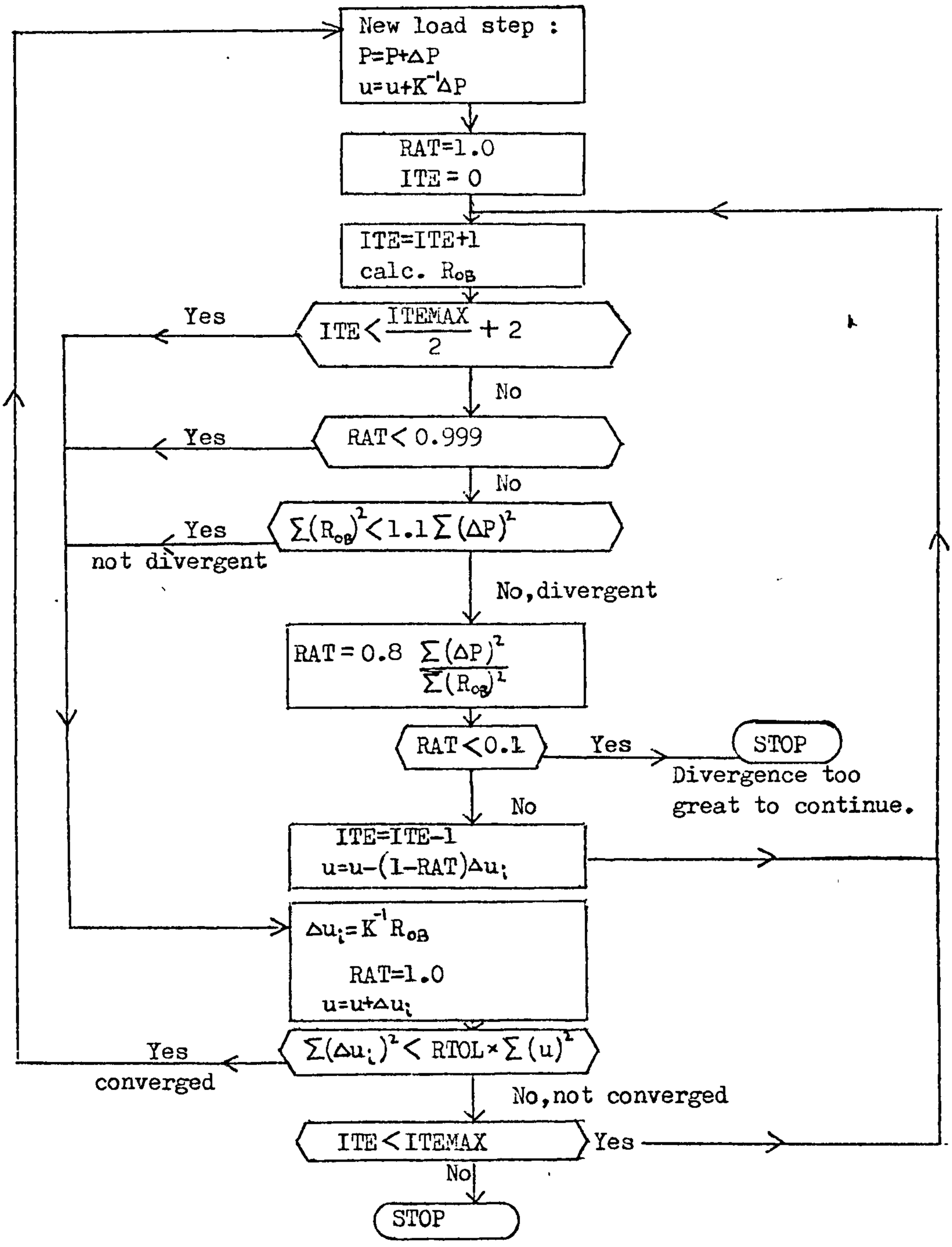

FIGURE 4.2 ITERATION PROCESS,INCLUDING REDUCED DISPLACEMENT INCREMENTS WHEN DIVERGENCE OCCURS.

RAT = η
ITE = i= iteration count
ITEMAX = max. allowed no. of iterations
RTOL= convergence tolerance
K = global stiffness matrix

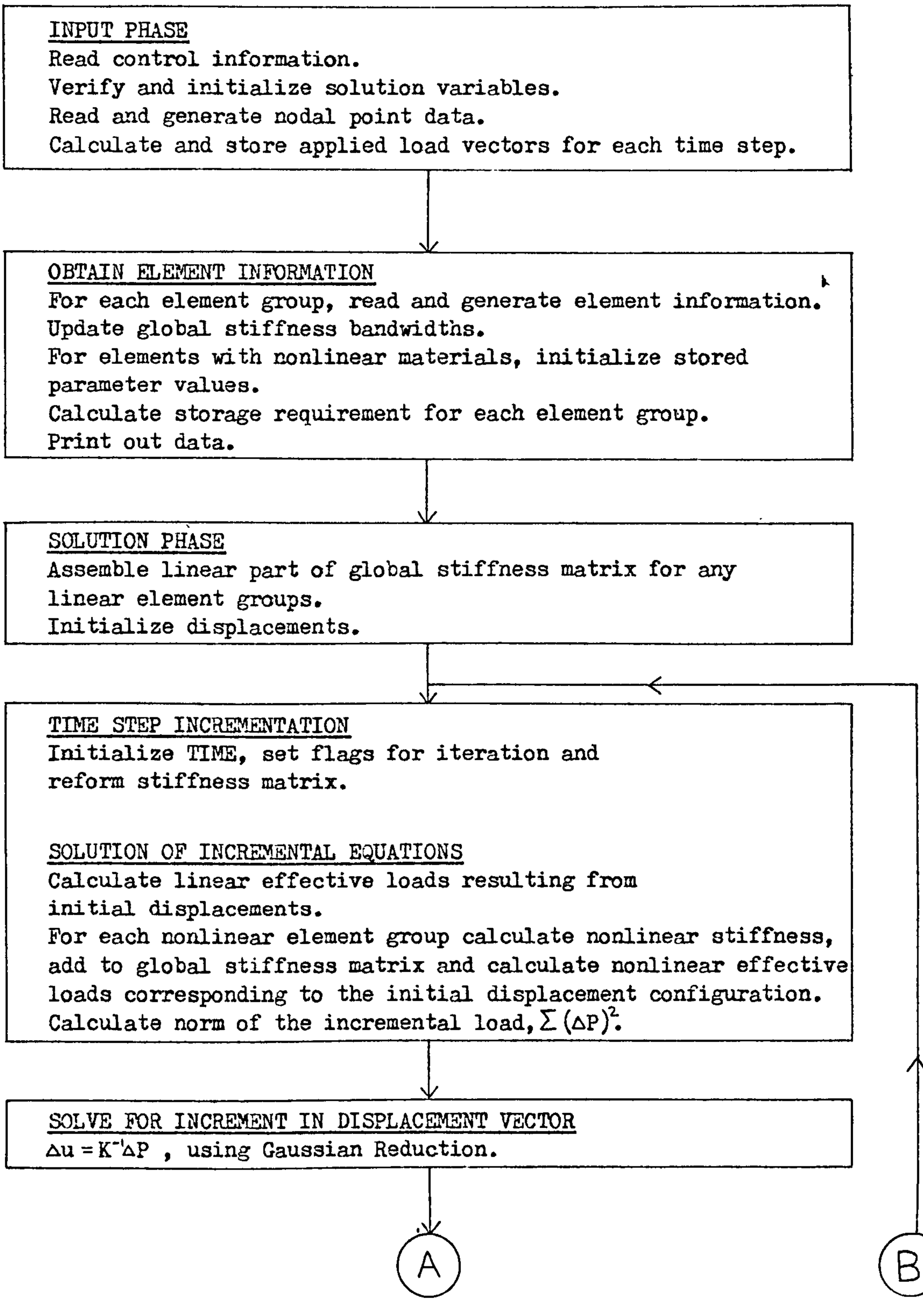

FIGURE 4.3 FLOW-CHART OUTLINING THE STEP-BY-STEP SOLUTION PROCEDURE.

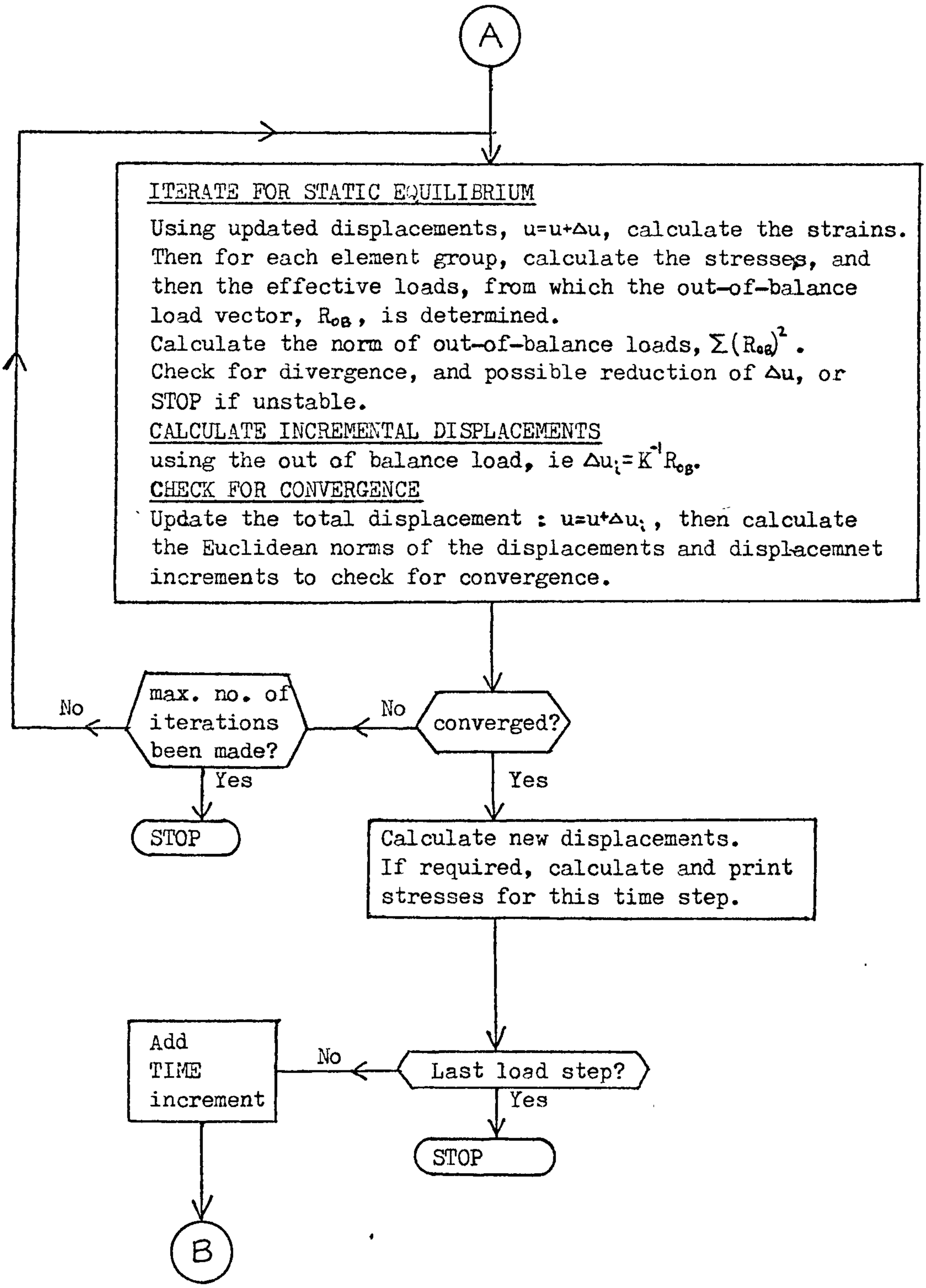

FIGURE 4.3 Contd.

The second model enables a detailed examination of the nonlinear behaviour around a shear key. The detailed shear key analysis incorporates one shear key on each of the sleeve and pile in a short length of grouted connection. A large number of elements are used so that the progressive cracking and crushing behaviour around the shear keys can be observed as the loads on the shear keys steadily increase. The results of this analysis enable the overall load-slip behaviour of the shear key to be determined. These results are used in the model of the complete grouted connection where the load-slip behaviour of the shear keys is incorporated into the friction-gap elements on the steel/grout interface at the shear key locations. Thus, the need for a high density of elements around the shear keys is avoided. The number of degrees of freedom are reduced by using larger elements and so it is possible to analyse much longer connections with many shear keys. Later analysis shows that nonlinear grout behaviour is only associated with the shear keys and not with plain pipe connections, and so as the shear key effects are included in the friction-gap elements, it is possible to use linear-elastic grout in this analysis. The elements are in any case too large to accurately reflect the nonlinear behaviour; grout failure would spread in large steps as the Gauss Points are so widely spread.

Figures 4.4 and 4.5 show the finite element meshes for the whole connection and the detailed key analysis, respectively. A range of additional boundary restraints were used on the detailed analysis in order to prevent the connection failing prematurely in such a short bond length. This feature is described in Chapter 7.

In the complete connection analysis three rows of elements having the same length were used between each shear key. The use of fewer rows would

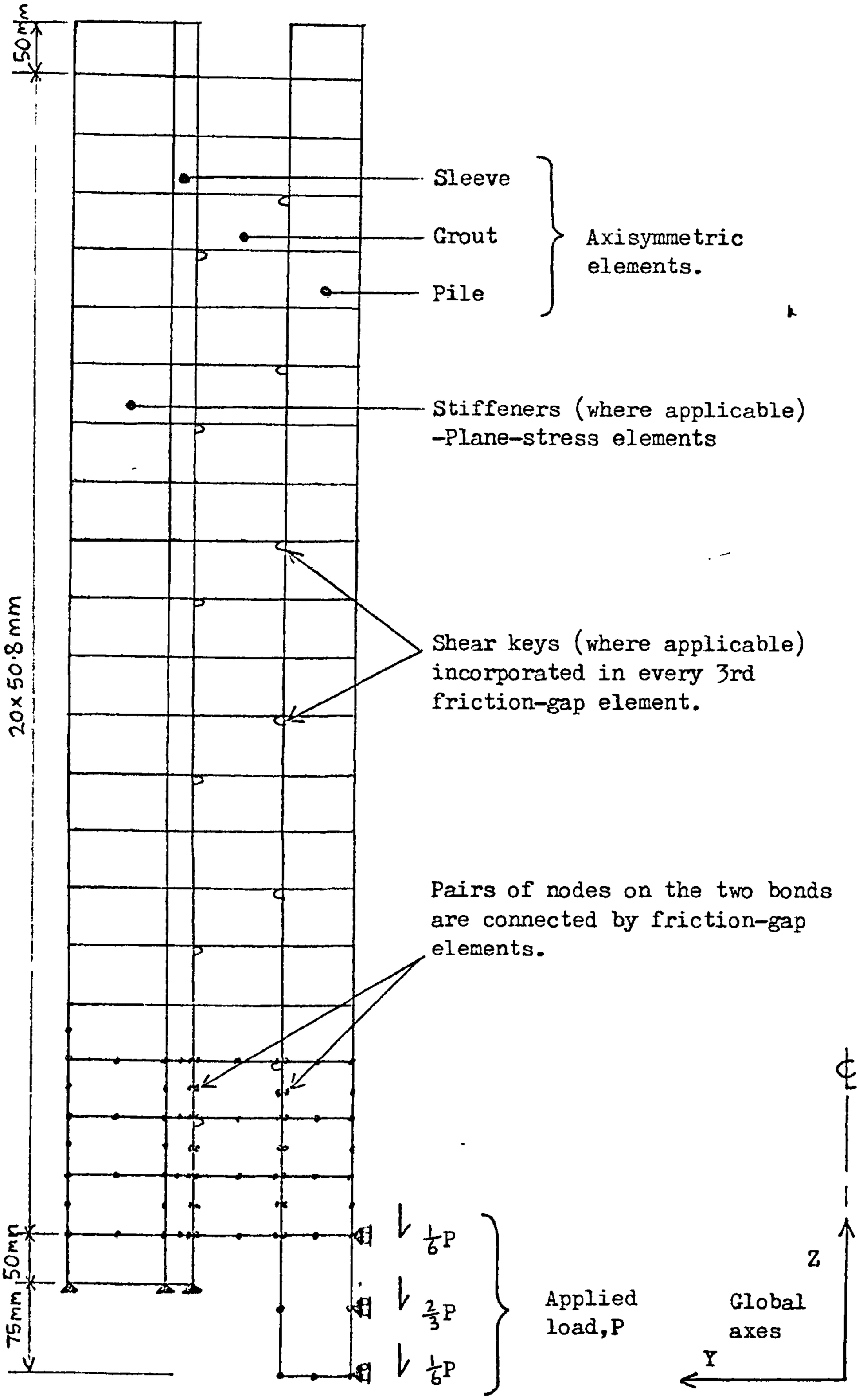

FIGURE 4.4 FINITE ELEMENT MESH FOR A WHOLE LENGTH GROUTED CONNECTION, SIMULATING THE P9/10 LABORATORY TESTS.

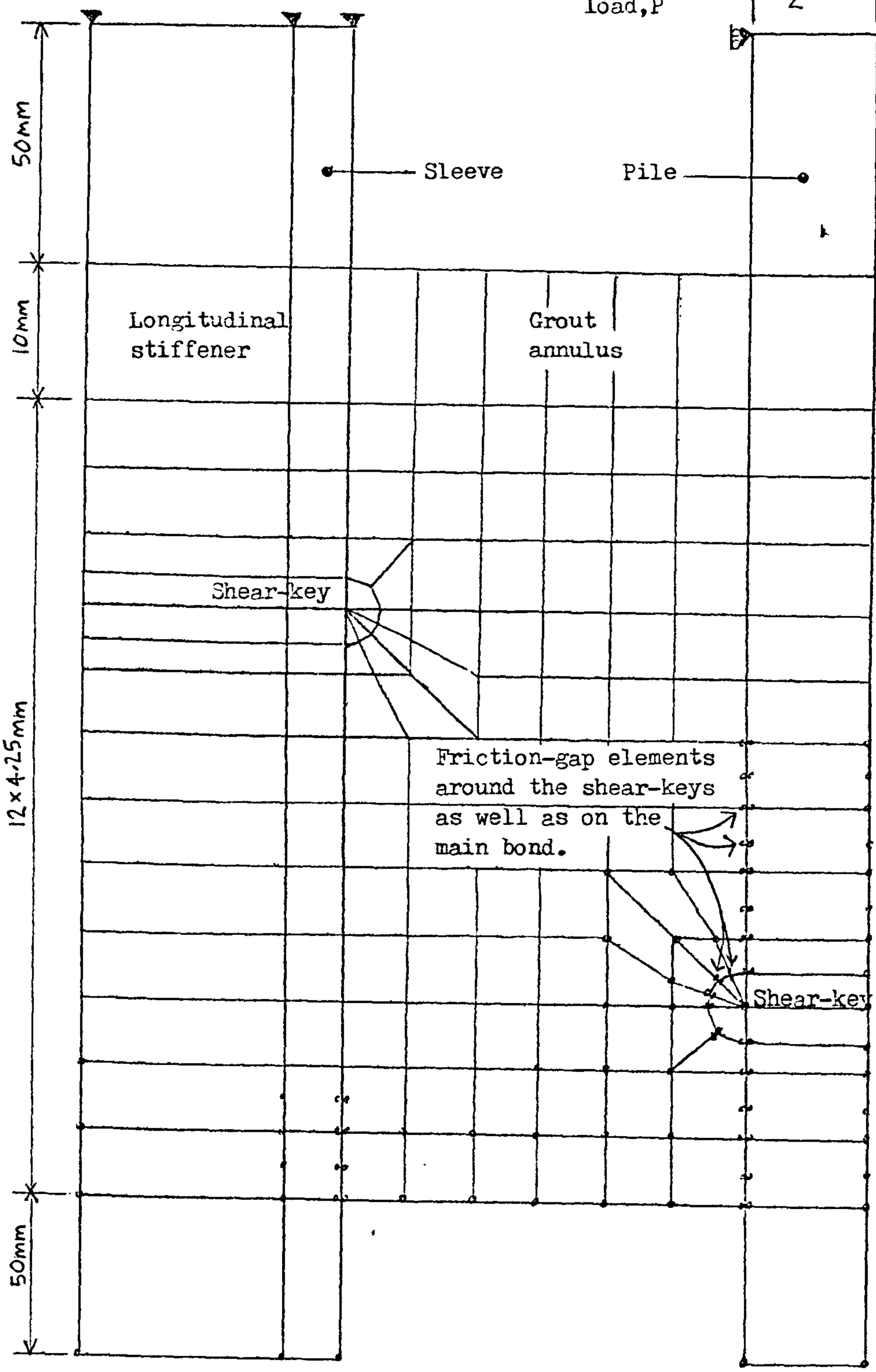

FIGURE 4.5 FINITE ELEMENT MESH FOR THE DETAILED SHEAR-KEY ANALYSIS, BASED ON A SHORT LENGTH OF THE P9/10 TEST GEOMETRY.

not be able to accurately reflect the changes in stress between shear keys. For plain pipe connections, longer elements have been tried but these gave errors due to not being able to show the large rate of change of bond stress at the connection ends.

4.5 Element Types

For both finite element meshes, the sleeve, pile and grout are represented by eight or six noded solid, isoparametric, axisymmetric elements. The isoparametric element has been proved to be very effective in linear analysis (26) and it has been shown, both in NONSAP (24) and elsewhere, that general nonlinear continuum mechanics formulations can also be efficiently implemented using such elements. Eight-noded elements are used on the whole grouted connection model since the elements are large and so considerable variations in strain are likely across their dimensions. The elements are much smaller for the detailed shear key analysis and, therefore, fewer nodes are used.

The steel/grout bond is a major source of nonlinearity and is modelled by a specially developed friction-gap element. This element simulates both the bond behaviour and where specified, the effects of shear connectors. A full description of this element is given in Chapter 5.

The laboratory test specimens normally have longitudinal stiffeners which have at least a small effect on the ultimate bond strength. It was considered necessary to simulate the stiffeners in some way. Individual stiffeners cannot be represented in axisymmetric analysis and so an approximation is made by attaching plane-stress elements to the outside of the sleeve. Their thickness is set equal to the sum of

all the stiffener thicknesses, divided by 2π , (as the analysis is carried out per radian). This should produce the correct stiffnesses, but the forces from the stiffener elements will be uniformly distributed around the circumference, rather than at localised stiffener positions. This is an acceptable approximation since there are normally six or twelve stiffeners evenly distributed around the sleeve.

4.6 Constitutive Laws

The steel and grout are both treated as linear elastic for the whole connection analysis. In the case of the detailed shear key analysis the constitutive law for the grout must include cracking and crushing modes. Also, in order to simulate the gradual build up of microcracking prior to ultimate failure, an elasto-plastic strain-hardening function is used. This function has to consider a three-dimensional stress state to include the radial confining action of the steel tubulars on the grout, which enhances the load capacity of the grout. The constitutive law used is based on that developed by Chen (40) for concrete, and is described in detail in Chapter 6.

4.7 Stress and Strain Definitions

Stresses and strains are generally defined in terms of the initial geometric configuration and geometric nonlinearities are not calculated, except for the nonlinear grout. This is because the only significant displacements are due to slip on the steel/grout bonds and these displacements will not affect the stiffnesses of the cylinders. In the case of the grout large shear strains and cracking and crushing can occur. The strains, therefore, of individual elements are not small and

geometric effects must be considered. The material law used enables the stresses and strains to be defined by the Total Lagrangian formulation, that is, relative to the initial configuration. The stresses and strains in the nonlinear grout are therefore 2nd Piola-Kirchoff stresses and Green-Lagrange strains. The stresses are converted into the true Cauchy stresses for output purposes, using the definitions and formulae given by Malvern (27).

CHAPTER 5

THE FRICTION-GAP ELEMENT WITH DILATION EFFECTS

5.1 Background

The configurations for many finite element analysis problems in structural engineering and mechanics include the interface between dissimilar materials. If, throughout the loading history, perfect bond is maintained, then the presence of an interface offers no difficulties; the interface merely serves as a boundary between neighbouring rows or columns of elements with dissimilar properties. If at some point in the loading history, however, the bond breaks down and there is relative movement between the two adjacent surfaces, such as in the case of the grouted connection problem, then special analysis procedures are necessary.

There are many examples of problems in which material interfaces play a prominent role. For example, soil-structure interaction, bonding in reinforced concrete and reinforced earth, jointing in rock, brick-mortar bonding in masonry, machine-part interfaces such as gears and rollers, and nuclear reactor fuel element assemblies.

The physical behaviour of an interface separating two continua involves tangential slip initiation when the tangential component of bond stress exceeds the shear strength of the discontinuity. The subsequent slip proceeds according to some sliding friction law. Bond separation may also occur if the normal component of bond stress exceeds the tensile strength of the discontinuity. Slip, separation and recontact may all occur during a given stress-time history.

The interface problem is complex and inherently nonlinear. Several investigators (28,29), with an objective of representing the joint behaviour in rocks with a finite element model have developed so-called "slip or joint elements" and have achieved moderate success in simulating the gross behaviour of some physical problems. In using these slip elements for simulating interfaces or joints with thicknesses small in comparison to other typical element dimensions, however, serious difficulties are encountered. A pseudothickness for the element must be assumed and in order to maintain normal-displacement compatibility across the interface a large stiffness in this direction must be assumed, which in addition to creating an ill-conditioned stiffness matrix causes difficulty in simulating actual interface debonding.

A more accurate approach which is taken by other investigators (30, 31,32,33,34) assumes an interface discontinuity to be represented by a sequence of node-pairs, one on each side of the interface. The inter-connection between node-pairs can be controlled by bond stiffness factors, such as is the case for the bond element developed in this thesis for the grouted connection or by modifying the global stiffness equations of the elements neighbouring the interface. The latter approach eliminates the need for constructing a slip-element and so avoids the difficulties due to pseudothickness and fictitious material properties or joint stiff-nesses. In the current friction-gap element which has been developed for the grout/steel interface, the use of joint stiffnesses has proved to be satisfactory because the bonds in general show a tendency to open. The large values of normal stiffness needed for closed bonds are, therefore, not used and the associated numerical difficulties are avoided.

5.2 Element Formulation

The element can include either two or three node-pairs, depending on the application and number of nodes on the adjacent continuum elements. Three node-pairs are more suitable for analysing whole grouted connections with larger elements, but the simpler two node-pair version is useful for detailed analysis around individual shear keys. As the two node-pair version is a simple variant of the three node-pair version, only the latter need be described in detail.

Figure 5.1 shows the geometric arrangement and the local node numbering of the element's six nodes used to connect the sleeve and grout. Normally the angle θ is zero , so that the element axis coincides with the direction of the global Z-axis and the centreline of the grouted connection.

The following definitions can now be made:-

$$\text{Global displacement vector} = \begin{Bmatrix} u_1 & u_2 & \cdots & u_6 \\ v_1 & v_2 & \cdots & v_6 \end{Bmatrix}$$

$$\text{Element coordinates} = \begin{Bmatrix} Y_1 & Y_3 & Y_5 \\ Z_1 & Z_3 & Z_5 \end{Bmatrix} \qquad (Y_2 = Y_1,\ Z_2 = Z_1 \text{ etc.})$$

Then:

$$DZ = Z_5 - Z_1 \tag{5.1a}$$

$$DY = Y_5 - Y_1 \tag{5.1b}$$

$$\text{Element length, } \ell = \sqrt{DZ^2 + DY^2} \tag{5.2}$$

$$\text{Cos}\,\theta = DZ/\ell \quad , \quad \text{Sin}\,\theta = DY/\ell \tag{5.3}$$

The three sets of relative displacements normal and tangential to the bond surface, Δn and Δt respectively, are calculated as follows:-

$$\Delta t_1 = -(v_1 - v_2)\text{Cos}\,\theta - (u_1 - u_2)\text{Sin}\,\theta \tag{5.4a}$$

$$\Delta t_2 = -(v_3 - v_4)\text{Cos}\,\theta - (u_3 - u_4)\text{Sin}\,\theta \tag{5.4b}$$

$$\Delta t_3 = -(v_5 - v_6)\text{Cos}\,\theta - (u_5 - u_6)\text{Sin}\,\theta \tag{5.4c}$$

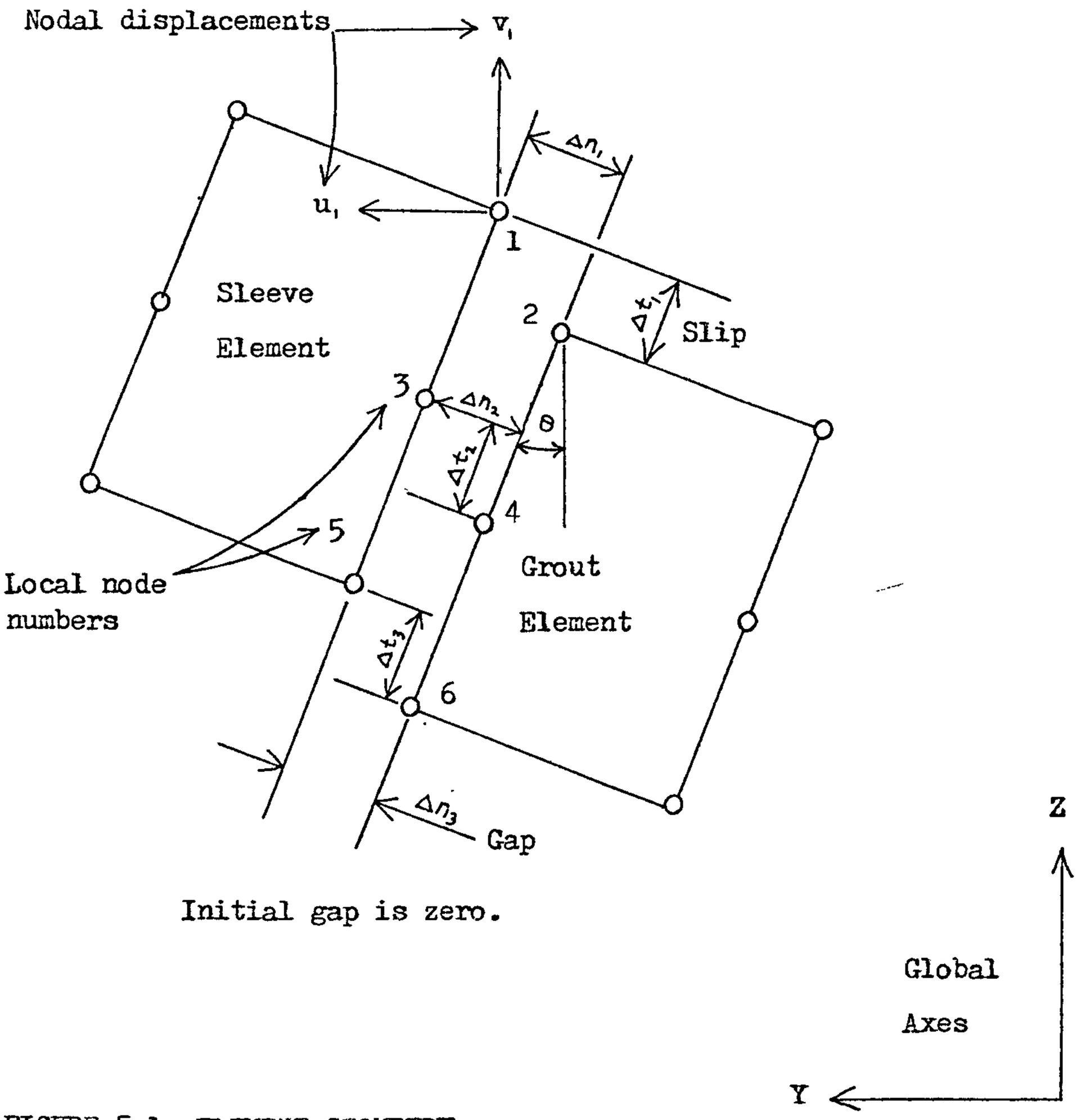

Initial gap is zero.

FIGURE 5.1 ELEMENT GEOMETRY.

$$\frac{dl}{dr} = \frac{l}{2}$$

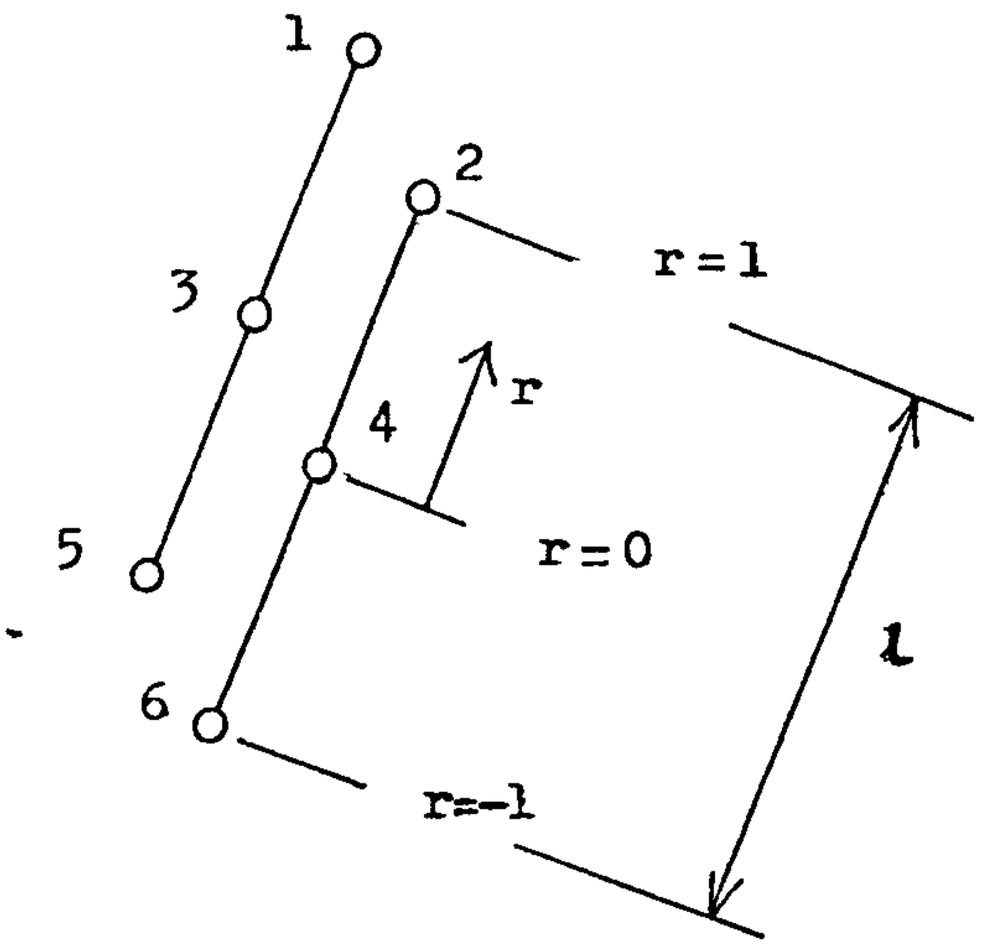

FIGURE 5.2 DEFINITION OF LOCAL COORDINATE SYSTEM.

$$\Delta n_1 = (v_1 - v_2)\mathrm{Sin}\theta - (u_1 - u_2)\mathrm{Cos}\theta \qquad (5.4d)$$

$$\Delta n_2 = (v_3 - v_4)\mathrm{Sin}\theta - (u_3 - u_4)\mathrm{Cos}\theta \qquad (5.4e)$$

$$\Delta n_3 = (v_5 - v_6)\mathrm{Sin}\theta - (u_5 - u_6)\mathrm{Cos}\theta \qquad (5.4f)$$

The stress-relative displacement relations are required in place of the more familiar stress-strain relations. By introducing normal and tangential stiffness factors, k_n and k_t, the normal bond stress and shear bond stress, are defined as:-

$$\sigma_{ni} = k_{ni}\,\Delta n_i \qquad (5.5)$$

$$\tau_i = k_{ti}\,\Delta t_i \qquad (5.6)$$

for i = 1, 3 with any one of the three node-pairs.

The shear bond stress is frictional and is, therefore, bounded by the limit:

$$|\tau_i| \leq c - \mu\sigma_{ni} \qquad (5.7)$$

where c is the adhesion and μ is the coefficient of friction. A negative stress represents compression.

Also, as the tensile strength of the bond is lost when slipping commences, no tension is allowed across the bond, so:-

$$\sigma_{ni} \leq 0 \qquad (5.8)$$

The adhesive strength c, in equation (5.7), is generally small in comparison to the very large friction strength (see Section 9.1), and in any case reduces to zero once slip is initiated. Since the post-slip initiation process is of most importance for ultimate strength analysis, it is therefore reasonable to use zero adhesive strength in the equation.

In terms of matrices, equation (5.4) can be expressed as:-

$$\{\Delta u^e\} = [B]\ \{u^e\} \qquad (5.9)$$

where:
$$\{\Delta u^e\}^T = \{\Delta n_1 \quad \Delta t_1 \quad \Delta n_2 \quad \Delta t_2 \quad \Delta n_3 \quad \Delta t_3\}$$

$$\{u^e\}^T = \{u_1 \quad v_1 \quad u_2 \quad v_2 \quad \ldots\ldots \quad u_6 \quad v_6\}$$

$$[B] = \left[\begin{array}{cccc|cccc|cccc} -c & s & c & -s & & & & & & & & \\ -s & -c & s & c & & & 0 & & & & 0 & \\ \hline & & & & -c & s & c & -s & & & & \\ & & 0 & & & & & & & & 0 & \\ & & & & -s & -c & s & c & & & & \\ \hline & & & & & & & & -c & s & c & -s \\ & & 0 & & & & 0 & & & & & \\ & & & & & & & & -s & -c & s & c \end{array}\right]$$

and: $c = \cos\theta$, $s = \sin\theta$

A local coordinate r, is used to define position along the element, (Figure 5.2). Shape functions, expressed in terms of r, can then be used to define the bond stresses and displacements along the element.

With three node pairs, the shape functions are quadratic, as described below, but when there are only two node-pairs, linear shape functions have to be used. The three quadratic shape functions are:-

$$N_1 = \tfrac{1}{2}(r^2-r)$$

$$N_2 = (1-r^2) \qquad (5.11)$$

$$N_3 = \tfrac{1}{2}(r^2+r)$$

Then: $$\{u(r)\} = [N]\{u^e\} \qquad (5.12)$$

where: $\{u(r)\}^T = \{u(r) \quad v(r)\}$ = Displacement at position r.

$$[N] = \left[\begin{array}{cc|cc|cc} N_1 & 0 & N_2 & 0 & N_3 & 0 \\ \hline 0 & N_1 & 0 & N_2 & 0 & N_3 \end{array}\right] \qquad (5.13)$$

Similarly: $$\{\Delta u(r)\} = [N]\{\Delta u^e\}$$

Therefore: $$\{\Delta u(r)\} = [N][B]\{u^e\} \qquad (5.14)$$

5.3 Equilibrium Equations

Applying the principal of Virtual Work for nodal applied loads $\{F^e\}$ and virtual displacements $\delta\{u^e\}$:-

$$\int_{-1}^{1} \delta\{\Delta u(r)\}^T \{\sigma(r)\} .2\pi R dr = \delta\{u^e\}^T \{F^e\} \qquad (5.15)$$

where: R = radius of the bond surface

$$\{\sigma(r)\}^T = \{\sigma_n(r) \quad \tau(r)\}$$

and $\{\sigma(r)\}^T . 2\pi R dr$ is the bond force.

Equations (5.14) and (5.15) combine to give:-

$$\int_{-1}^{1} \delta\{u^e\}^T [B]^T [N]^T \{\sigma(r)\} . \, 2\pi R dr = \delta\{u^e\}^T \{F^e\} \qquad (5.16)$$

Nodal stresses are defined by the [D] matrix as follows:-

$$\{\sigma^e\} = [D]\{\Delta u^e\} = [D][B]\{u^e\} \qquad (5.17)$$

Therefore: $$\{\sigma(r)\} = [N][D][B]\{u^e\} \qquad (5.18)$$

$$[D] = \begin{bmatrix} k_{n1} & & & & & \\ & k_{t1} & & 0 & & \\ & & k_{n2} & & & \\ & & & k_{t2} & & \\ & 0 & & & k_{n3} & \\ & & & & & k_{t3} \end{bmatrix} \qquad (5.19)$$

k_n and k_t are joint stiffnesses in N/mm^3, that is stiffness per unit bond area. The values of k_n and k_t can be reduced if slipping or opening of the bond occurs by setting the values of FAC1 and FAC2 greater than unity in the following:-

On slipping, $k_t \longrightarrow k_t/FAC1$

On bond $k_t \longrightarrow k_t/FAC2$

opening, $k_n \longrightarrow k_n/FAC2$

In reality the stiffness factors should be reduced to zero for an open bond, but in order to maintain good stability and control of the displacements, it is better not to reduce the stiffness too much. This is particularly important where increased friction may stop the slipping, or stress redistribution may reclose a bond. Exact stiffness factors are not required so long as the bond stresses are correctly calculated.

The iterative solution process will converge to the correct solution.

A further comment worth mentioning is that no cross-coupling is allowed in the [D] matrix. If the k terms are updated independently for each node pair, then any cross-coupling would result in the stiffness matrix losing its symmetry. This restricts the complexity of the stress-relative displacement functions that can be used.

5.4 Stiffness Matrix

Substituting equation (5.18) into equation (5.16) gives:-

$$\int_{-1}^{1} [B]^T [N]^T [N][D][B].2\pi R dr.\{u^e\} = \{F^e\} \qquad (5.20)$$

which can be expressed as:-

$$[K]\{u^e\} = \{F^e\}$$

where the stiffness matrix is given by:-

$$[K] = \int_{-1}^{1} [B]^T [N]^T [N][D][B].2\pi R dr \qquad (5.21)$$

On expanding and integrating:-

$$\int_{-1}^{1} [N]^T [N] dr = \frac{1}{15} \begin{bmatrix} 4 & 0 & 2 & 0 & -1 & 0 \\ 0 & 4 & 0 & 2 & 0 & -1 \\ 2 & 0 & 16 & 0 & 2 & 0 \\ 0 & 2 & 0 & 16 & 0 & 2 \\ -1 & 0 & 2 & 0 & 4 & 0 \\ 0 & -1 & 0 & 2 & 0 & 4 \end{bmatrix} \qquad (5.22)$$

Let A = Bond Area = $2\pi R\ell$ (5.23)

Then expanding equation (5.21) gives:-

$$[K] = \frac{A}{30} \times \tag{5.24}$$

$$\left[\begin{array}{cccc|cccc|cccc}
4k_{n1} & 0 & -4k_{n1} & 0 & 2k_{n2} & 0 & -2k_{n2} & 0 & -k_{n3} & 0 & k_{n3} & 0 \\
0 & 4k_{t1} & 0 & -4k_{t1} & 0 & 2k_{t2} & 0 & -2k_{t2} & 0 & -k_{t3} & 0 & k_{t3} \\
-4k_{n1} & 0 & 4k_{n1} & 0 & -2k_{n2} & 0 & 2k_{n2} & 0 & k_{n3} & 0 & -k_{n3} & 0 \\
0 & -4k_{t1} & 0 & 4k_{t1} & 0 & -2k_{t2} & 0 & 2k_{t2} & 0 & k_{t3} & 0 & -k_{t3} \\
\hline
2k_{n1} & 0 & -2k_{n1} & 0 & 16k_{n2} & 0 & -16k_{n2} & 0 & 2k_{n3} & 0 & -2k_{n3} & 0 \\
0 & 2k_{t1} & 0 & -2k_{t1} & 0 & 16k_{t2} & 0 & -16k_{t2} & 0 & 2k_{t3} & 0 & -2k_{t3} \\
-2k_{n1} & 0 & 2k_{n1} & 0 & -16k_{n2} & 0 & 16k_{n2} & 0 & -2k_{n3} & 0 & 2k_{n3} & 0 \\
0 & -2k_{t1} & 0 & 2k_{t1} & 0 & -16k_{t2} & 0 & 16k_{t2} & 0 & -2k_{t3} & 0 & 2k_{t3} \\
\hline
-k_{n1} & 0 & k_{n1} & 0 & 2k_{n2} & 0 & -2k_{n2} & 0 & 4k_{n3} & 0 & -4k_{n3} & 0 \\
0 & -k_{t1} & 0 & k_{t1} & 0 & 2k_{t2} & 0 & -2k_{t2} & 0 & 4k_{t3} & 0 & -4k_{t3} \\
k_{n1} & 0 & -k_{n1} & 0 & -2k_{n2} & 0 & 2k_{n2} & 0 & -4k_{n3} & 0 & 4k_{n3} & 0 \\
0 & k_{t1} & 0 & -k_{t1} & 0 & -2k_{t2} & 0 & 2k_{t2} & 0 & -4k_{t3} & 0 & 4k_{t3}
\end{array}\right]$$

Symmetry is lost if $k_{n1} \neq k_{n2} \neq k_{n3}$ or $k_{t1} \neq k_{t2} \neq k_{t3}$, so the following solution has been used.

Consider $k_{n1} = k_{n2} = k_{n3} = k_n$ and that the displacement u at all three node pairs are equal. The three pairs of nodal loads can be given by:-

$$\begin{aligned} Q_{11} &= K_{11} \cdot u \\ Q_{22} &= K_{22} \cdot u \\ Q_{33} &= K_{33} \cdot u \end{aligned} \tag{5.25}$$

and the stiffness coefficients of equation (5.24) simplify to:-

$$\begin{aligned} K_{11} = K_{33} &= k_n \frac{A}{30}(4+2-1) = \frac{Ak_n}{6} \\ K_{22} &= k_n \frac{A}{30}(2+16+2) = \frac{2Ak_n}{3} \end{aligned} \tag{5.26}$$

As k_{n1}, k_{n2}, k_{n3} may differ, an approximate solution is to use:-

$$K_{11}^{n} = \frac{Ak_{n1}}{6}$$

$$K_{22}^{n} = \frac{2Ak_{n2}}{3} \qquad (5.27)$$

$$K_{33}^{n} = \frac{Ak_{n3}}{6}$$

Shear stiffness coefficients are similar, but using k_t instead of k_n.

This enables differing values of k_n and k_t to be used on individual node pairs, but the effects of displacements on other node pairs cannot be accounted for in the final stiffness matrix which is given below:-

$$[K] = \qquad (5.28)$$

$$\left[\begin{array}{cccc|cccc|cccc}
K_{11}^{n} & 0 & -K_{11}^{n} & 0 & & & & & & & & \\
0 & K_{11}^{t} & 0 & -K_{11}^{t} & & & & & & & & \\
-K_{11}^{n} & 0 & K_{11}^{n} & 0 & & 0 & & & & 0 & & \\
0 & -K_{11}^{t} & 0 & K_{11}^{t} & & & & & & & & \\
\hline
 & & & & K_{22}^{n} & 0 & -K_{22}^{n} & 0 & & & & \\
 & 0 & & & 0 & K_{22}^{t} & 0 & -K_{22}^{t} & & 0 & & \\
 & & & & -K_{22}^{n} & 0 & K_{22}^{n} & 0 & & & & \\
 & & & & 0 & -K_{22}^{t} & 0 & K_{22}^{t} & & & & \\
\hline
 & & & & & & & & K_{33}^{n} & 0 & -K_{33}^{n} & 0 \\
 & 0 & & & & 0 & & & 0 & K_{33}^{t} & 0 & -K_{33}^{t} \\
 & & & & & & & & -K_{33}^{n} & 0 & K_{33}^{n} & 0 \\
 & & & & & & & & 0 & -K_{33}^{t} & 0 & K_{33}^{t}
\end{array}\right]$$

This symmetric K - matrix is exact for the case of an even loading on all three node pairs and so any errors will tend to zero as the element size (i.e. length, ℓ) tends to zero.

If $\cos\theta \neq 1$, then the K-matrix must be rotated to the global orientation as follows:

$$K_{rr_i} = K^n_{ii} \cdot \cos^2\theta + K^t_{ii} \cdot \sin^2\theta$$

$$K_{zz_i} = K^t_{ii} \cdot \cos^2\theta + K^n_{ii} \cdot \sin^2\theta \qquad \text{for } i = 1 \text{ to } 3 \qquad (5.29)$$

(K_{zz_i}: Global; K^t_{ii}, K^n_{ii}: Local)

It is in fact possible to use the correct stiffness matrix, equation (5.24), if k_n and k_t are not reduced when slipping or opening of the bond occurs (i.e. FAC1 = FAC2 = 1). This may be practical where fixing k_n and k_t does not greatly affect the number of iterations needed for convergence, or limit the slip on the failure bond. The bond stresses vary quadratically along the length of the friction-gap element since they are proportional to the displacements. Using the correct isoparametric stiffness formulation would enhance this variation. Since the adjoining continuum elements only have a linear stress variation along their length, (being proportional to the internal strains), the forces between these different element types may not converge so easily with the correct stiffness matrix. The stiffness matrix of equation (5.28) is preferred therefore.

Alternatively, the problem of unsymmetrical matrices can be solved by not having bond element stiffnesses at all, but modifying the global stiffness matrix instead (34), this has been mentioned in Section 5.1.

5.5 Nodal Forces

Nodal forces are defined in the global and local element axes by Figure 5.3. The force vectors are:

Global force vector $\{Q_g\}^T = \{P_1 \;\; V_1 \;\; P_2 \;\; V_2 \;\; \ldots \;\; P_6 \;\; V_6\}$

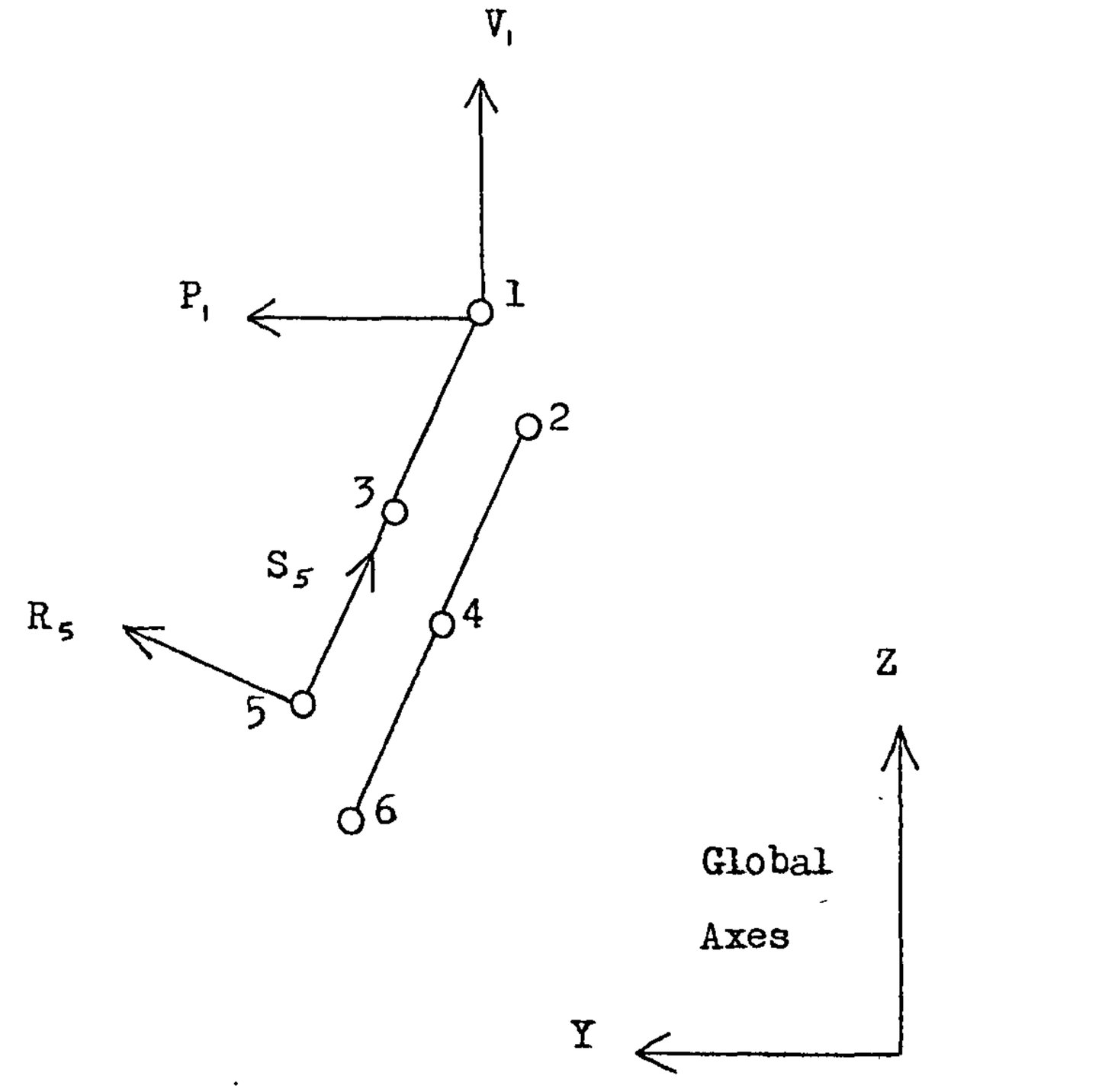

FIGURE 5.3 DEFINITION OF NODAL FORCES.

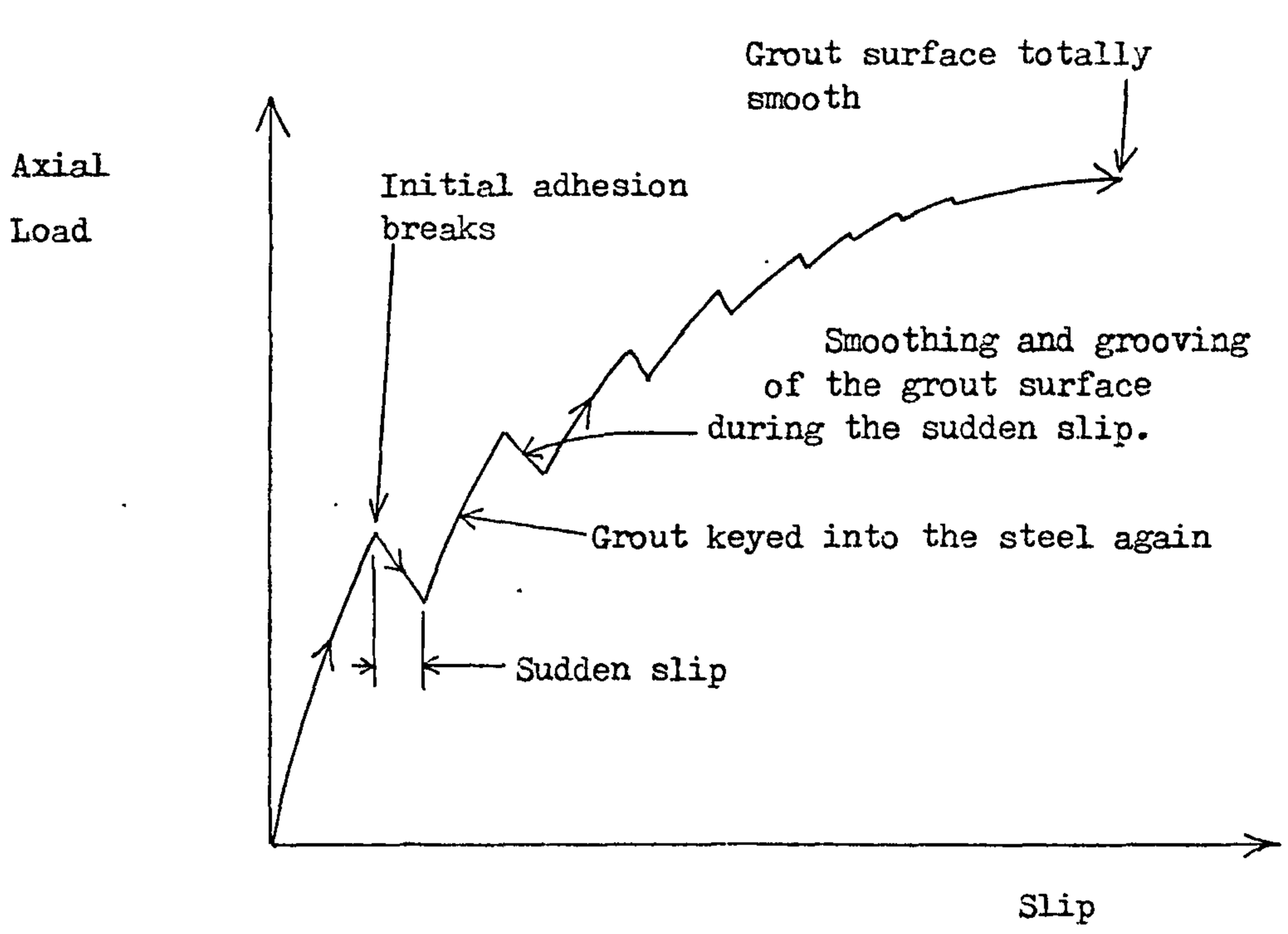

FIGURE 5.4 TYPICAL LOAD-SLIP BEHAVIOUR RELATED TO THE BOND FAILURE MECHANISM.

where P = force in the global Y-direction,

and V = " " " " Z- " .

Local force vector $\{Q\}^T = \{R_1\ S_1\ R_2\ S_2 \ldots . R_6\ S_6\}$

Consider nodal force R_i at node i.

Let the relative displacement increment at point i = 1, and zero elsewhere.

i.e. $\delta\{\Delta u_i^e\} = 1$, $\delta\{\Delta u(r)\} = N_i(r)\times 1$, $\delta\{\Delta u_j^e\} = 0$, $j \neq i$

By the Principal of Virtual Work,

$$R_i \times 1 = \int_{-1}^{1} [N]^T . \{\sigma_n(r)\} . 2\pi R dr \times 1 \qquad (5.30)$$

$$\therefore R_i = \int_{-1}^{1} [N]^T [N] \{\sigma_n^e\} . 2\pi R dr \qquad (5.31)$$

Substituting the values for $\int_{-1}^{1} [N]^T [N] dr$, given by equation (5.22), into equation (5.31), gives:-

$$R_1 = -R_2 = \left[\frac{4}{15}\sigma_{n1} + \frac{2}{15}\sigma_{n2} - \frac{1}{15}\sigma_{n3}\right]\frac{A}{2} \qquad (5.32a)$$

$$R_3 = -R_4 = \left[\frac{2}{15}\sigma_{n1} + \frac{16}{15}\sigma_{n2} + \frac{2}{15}\sigma_{n3}\right]\frac{A}{2} \qquad (5.32b)$$

$$R_5 = -R_6 = \left[-\frac{1}{15}\sigma_{n1} + \frac{2}{15}\sigma_{n2} + \frac{4}{15}\sigma_{n3}\right]\frac{A}{2} \qquad (5.32c)$$

where A = bond area = $2\pi R\ell$

Replacing R by S and σ_n by τ gives the corresponding shear forces.

Global forces are then given by:-

$$P_i = -R_i\cos\theta - S_i\sin\theta \qquad (5.33a)$$

$$V_i = R_i\sin\theta - S_i\cos\theta \qquad (5.33b)$$

5.6 Surface Roughness of the Bond

The friction-gap element in the form so far described, was applied to the analysis of a typical plain-pipe grouted connection with the sleeve loaded in compression and pile in tension. The mesh given in

Figure 4.4 was used, but without shear keys and the analysis immediately failed, giving a zero strength prediction. This was because the Poisson effects in the sleeve and pile caused them to radially expand and contract respectively. As a result, all bonds opened, making load transfer across the interface impossible. The actual test specimens did have strength and so a closer examination was needed to investigate its origin.

There are two possible causes (or a combination of both) for this strength: (a) Adhesive bond strength, or (b) Surface roughness. If adhesion is the cause then all plain pipe connections will have the same adhesive bond strength. In fact there is a large variation in bond strengths, depending on the hoop stiffnesses of the connection tubulars and so the adhesive strength cannot be a significant factor.

The surface roughness concept on the other hand, seems to be much more realistic since the steel tubulars are normally shot-blasted, giving them a rough finish. This has been done since early tests for the Forties field (1), which showed surface roughness to be an important factor. These tests showed that epoxy coated pipes, or smoothed steel pipes, are about 80% weaker than shot-blasted pipes.

The failure mechanism on the steel/grout bond surface has to be visualised and defined for application to the friction-gap element. This mechanism is only imaginary as the actual failure process cannot be observed until the specimen is cut open after testing, but the following information has come from the results of experiments.

(a) Hoop Strains

The Forties field tests included a strain-gauged plain pipe specimen. On this test, substantial circumferential strains remained after

unloading, from which the radial sleeve expansion and pile contraction have been calculated and presented in Table 5.1. The pile bond dilation appears to be less than on the sleeve, but this is not necessarily so, as the restraining action of the pile, which is twice as thick as the sleeve, will be much greater.

In order to investigate this effect, a thin-shell analysis which is described in Appendix A, was carried out. Final slip failure normally takes place on the pile/grout bond and so the dilation effect may only take place on this bond. In Appendix A, various values of dilation u_m, are tried on the pile bond alone and on both bonds, in order to find out what values of u_m will give the radial displacements in Table 5.1. The results of this analysis, given in Table 5.2, indicate that if equal dilation occurs on both bonds, then $u_m = 0.065$ mm gives a very close match to the experimental radial displacements. If dilation only occurs on the pile bond, then u_m needs to be approximately doubled to 0.135 mm in order to give the same radial displacements.

It can be seen from Table 5.2 that the normal bond stress on the sleeve is substantially less than on the pile when dilation is limited to the pile. As the bond stress is limited by the size of σ_n, this may result in slipping commencing on the sleeve bond as well. Therefore, although the main slip failure will be on the pile bond, a small slip causing some dilation is still likely on the sleeve bond. The probable value for u_m is therefore between the two values obtained above and the mean value gives $u_m = 0.10$ mm.

There is in fact a possible source of error in this reasoning. The mean radial displacements have been used, but there were in fact

	Mean circumferential strain x 10^{-6}	Pipe radius	Radial expansion/ contraction
Sleeve	150	343 mm	0.0514 mm
Pile	90	279 mm	0.0252 mm

TABLE 5.1. MEAN CIRCUMFERENTIAL STRAINS AND RADIAL DISPLACEMENTS IN A FAILED PLAIN-PIPE SPECIMEN AFTER COMPLETELY REMOVING THE AXIAL LOAD.

Dilation	Radial Displacements			Normal Bond Stresses		
u_m mm	u_g mm	u_s mm	u_p mm	σ_{ns} N/mm^2	σ_{np} N/mm^2	$\bar{\sigma}_n$ N/mm^2
<u>For Dilation on BOTH Bonds:</u>						
0.06	0.0115	0.0487	0.0232	1.14	1.27	1.20
<u>0.065</u>	0.0124	<u>0.0528</u>	<u>0.0251</u>	1.23	1.37	<u>1.30</u>
0.07	0.0134	0.0569	0.0271	1.33	1.48	1.40
<u>For Dilation on PILE Bond ONLY:</u>						
0.10	0.0562	0.0383.	0.0209	0.89	1.14	1.02
<u>0.135</u>	0.0758	<u>0.0517</u>	<u>0.0283</u>	1.21	1.54	<u>1.38</u>
0.15	0.0843	0.0575	0.0314	1.34	1.72	1.53

TABLE 5.2. PREDICTED RADIAL DISPLACEMENTS FOR A GIVEN BOND DILATION, USING THIN SHELL ANALYSIS.

variations along the length of the connection. These may have been due to large axial stresses being retained in the cylinders as a result of the frictional bond stresses acting to prevent the release of these stresses on unloading. This would result in Poisson effects contributing to the radial displacements and so the true value of u_m should be less. It is concluded, therefore, that $u_m < 0.1$ mm.

The permanent radial expansion can be easily explained as follows. Initially the grout is moulded onto the steel surface, but as soon as slipping begins, the surfaces must be forced apart so that the grout can traverse the protrusions of the shot-blasted steel surface. This separation will remain after the connection is unloaded, as it is impossible to return the grout surface to its original form and position.

Similar tests were made on several Thistle field specimens which included shear keys (2). In these cases, the sleeve outer diameter was 1549 mm and the residual strain about 3×10^{-4}, which gives a radial displacement of 0.23 mm. This is much larger than the Forties specimen and must be due to the effects of the shear keys, which would also tend to force the sleeve outwards. It is, therefore, not possible to directly measure the surface roughness dilation effect when shear keys are used.

(b) Prestressing

At Imperial College, London, experiments have been made to increase the strength of plain pipe grouted connections by prestressing the sleeve and pile. This can be achieved by several means, including filling the annulus between sleeve and pile with pressurised grout. The end result is a normal bond stress increased by about 4 N/mm^2 of prestress and this has the useful effect of increasing the bond strength fourfold.

As the bond strength is mainly frictional, it can be roughly assumed that the ultimate bond strength is proportional to the normal bond stress.

ie $\sigma_n = a.F_{BU}$ where a = constant,

and σ_n = mean normal bond stress without prestress.

For the case of prestress:-

$$(\sigma_n + 4) = a.4.F_{BU}$$

Therefore: $\sigma_n + 4 = 4.\sigma_n$

$\sigma_n = 4/3 = 1.33$ N/mm^2 , gives the unprestressed mean normal bond stress.

Compared with the strain-gauged Forties field test reported in section (a) above, the Imperial College test uses a smaller diameter, (sleeve O.D. = 244 mm), and so the radial stiffness of the tubulars will be greater in this test. This will result in greater confinement of the grout and so σ_n will also be greater. As the axial load is applied for this calculation , Poisson effects will exist, resulting in a reduction in σ_n.

On balance, therefore, the above effects will make σ_n much the same for both the loaded Imperial College test and the post-ultimate unloaded Forties field test. It is therefore possible to compare the value of σ_n obtained here with the values given in Table 5.2 for the Forties field geometry. This shows that for σ_n=1.33 N/mm^2, the values of u_m are exactly in agreement with those obtained from the Forties field test results and so the same conclusions on u_m can be reached.

(c) Load-Slip Curves

Figure 5.4 shows the typical load-slip behaviour for a plain-pipe grouted connection which can be explained as follows.

On reaching the load peak there is often a loud crack as the adhesion breaks. The peaks on the steel shot-blasted surface come out of the troughs in the corresponding grout surface and the steel slides freely. In doing so, the grout surface is partially smoothed and grooves are cut in the direction of slip. The load will fall, causing the bond to close and partially interlock again.

On the next round of load increase, the bond resistance may increase, because the partially smoothed grout will result in a greater area of contact between steel and grout. This cyclical process of loading and slipping can be repeated until the grout surface is completely smooth. Once this happens, no further physical changes to the interface can take place and the ultimate load capacity is reached.

Each time the interlock reforms after unloading, the dilation u_a will have increased slightly, until it reaches its final value u_m, when the bond is completely smooth. This process is described in three phases by means of magnified diagrams of the bond surface, (Figure 5.5).

As the grout becomes totally smoothed, but the steel remains rough, the maximum dilation u_m, must approach half of the shot-blasted upstand. For a typical shot-blasted steel roughness of 0.08 mm, therefore, the value of u_m will be 0.04 mm.

5.7 Dilation Function

The importance of dilation on an interface has been noticed by other investigators, both with respect to rock mechanics and more recently, reinforced concrete (35,36,37). For this particular problem, the dilation u_a, must be expressed as some function of slip Δt. The rate of increase of u_a with slip must decrease in proportion to the roughness of

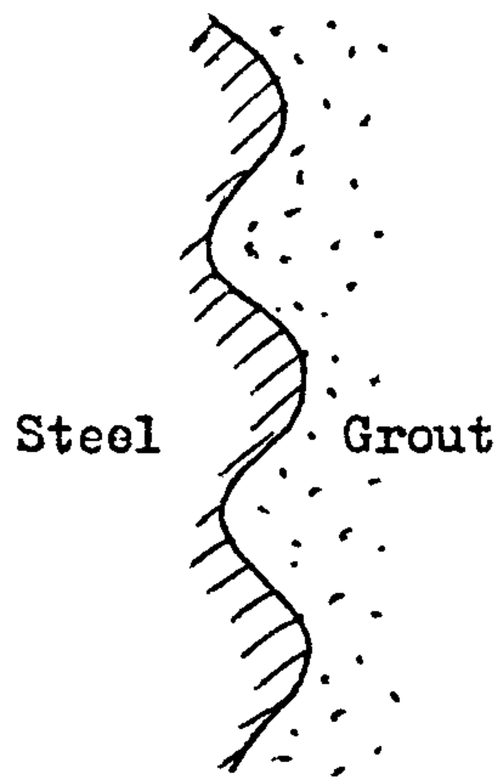

(a)Initial Stage

$u_a = 0$

Perfect contact.
Both surfaces
equally rough.
No slip.

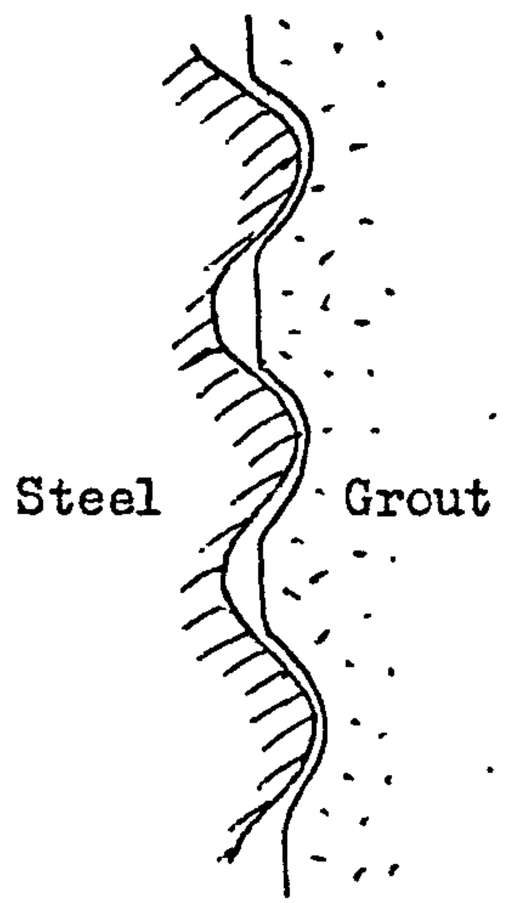

(b)Intermediate Stage

$0 < u_a < u_m$

Some slipping has
cut grooves and
partially smoothed
the grout surface.

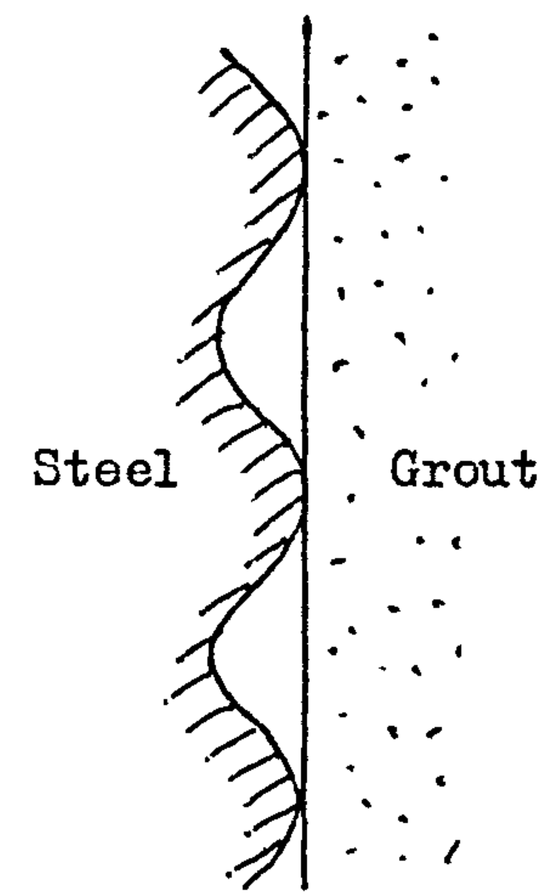

(c)Ultimate Stage

$u_a = u_m$

Grout surface completely
smooth,as found on
failed experimental
specimens.

FIGURE 5.5 POSSIBLE CAUSE OF THE BOND DILATION EFFECT.

the grout at that instant, as the potential to smooth the surface is proportional to the existing roughness.

$$\text{Roughness} = (u_m - u_a)$$

Therefore:
$$\frac{\partial u_a}{\partial \Delta t} = \frac{1}{n}(u_m - u_a) \qquad (5.34)$$

where: n = constant

On integration w.r.t. Δt, this gives:-

$$u_a = u_m - e^{-\Delta t/n}$$

Therefore:
$$u_a = u_m\left(1 - \frac{1}{u_m e^{\Delta t/n}}\right) \qquad (5.35)$$

A reasonable amount of roughness is needed even as slipping commences to give adequate initial strength. The formula is modified to give $u_a = u_m/2$ initially.

Hence:
$$u_a = u_m\left(1 - \frac{1}{2e^{\Delta t/n}}\right) \qquad (5.36)$$

in which n can be chosen to give u_a approaching u_m after a reasonable amount of slip.

The condition n = 1 gives $u_a = 0.997.u_m$ after $\Delta t = 5$ mm slip, which gives the most realistic results. Doubling n will double the slip needed for a given value of u_a.

The hoop stiffnesses of the sleeve and pile restrains the bond dilation and results in an additional normal bond stress σ_{no}, which is given by:-

$$\sigma_{no} = -k_n u_a \,, \qquad (5.37)$$

Therefore:
$$\sigma_n = k_n(\Delta n - u_a) \qquad (5.38)$$

5.8 Shear Connectors

A shear connector causes large stress discontinuities in the sleeve or pile, where a large load is transferred by means of the weld bead

keying into the grout. This can be represented on one end of a friction-gap element simply by adding additional stiffness k_{sc}, to the existing bond shear stiffness k_t, at the node pair representing the shear key. From a typical load-slip curve for a shear-keyed grouted connection, (Figure 5.6) it can be judged that the overall shear key stiffness is less than for the surface bond. This is not surprising considering that the surface bond acts on a much greater area, (although the ultimate strength is of course much greater for the shear key).

The slope of the curve shows approximately double stiffness, as the slip is occurring on both the sleeve and pile bonds. Results from the P-series tests in the Department of Energy Programme (8), where h=2.03mm, s=169mm, (h/s=0.012), show the value of k_{sc} to be fairly constant, in the range 25 - 35 N/mm^3. However, this value is based on the overall behaviour which includes friction bond effects. It is likely that the frictional bond stress will gradually reduce as the keys tend to push the surfaces apart. Therefore, allowing for this weakening effect, the true value of k_{sc} may be larger.

It has already been mentioned in Chapter 4, that a detailed finite element analysis has been made around a pair of shear keys. Friction-gap elements were used around the shear keys, with zero dilation, as well as on the main steel/grout bonds. This enabled the grout to slide around the keys and force open the bond in a realistic manner. The results were very encouraging, as they indicated a value for k_{sc} of 37 N/mm^3, which appears to be realistic and is therefore the value used. It should also be noted that by varying the radial restraint on the sleeve, the value of k_{sc} was unchanged, although the stress level at which crushing and cracking commenced was affected. This indicates that k_{sc} is unaffected

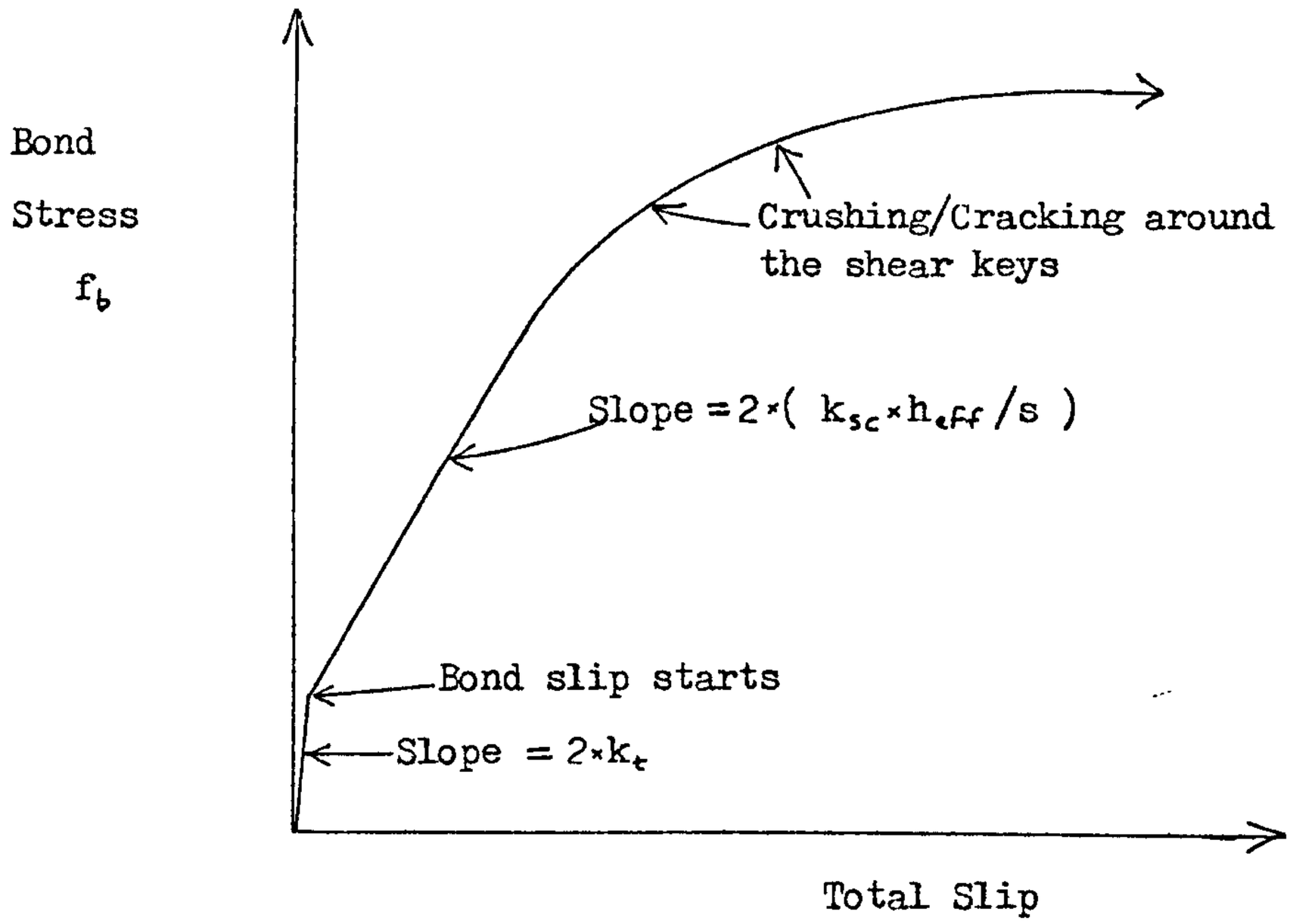

FIGURE 5.6 TYPICAL LOAD-SLIP CURVE FOR A CONNECTION WITH SHEAR KEYS.

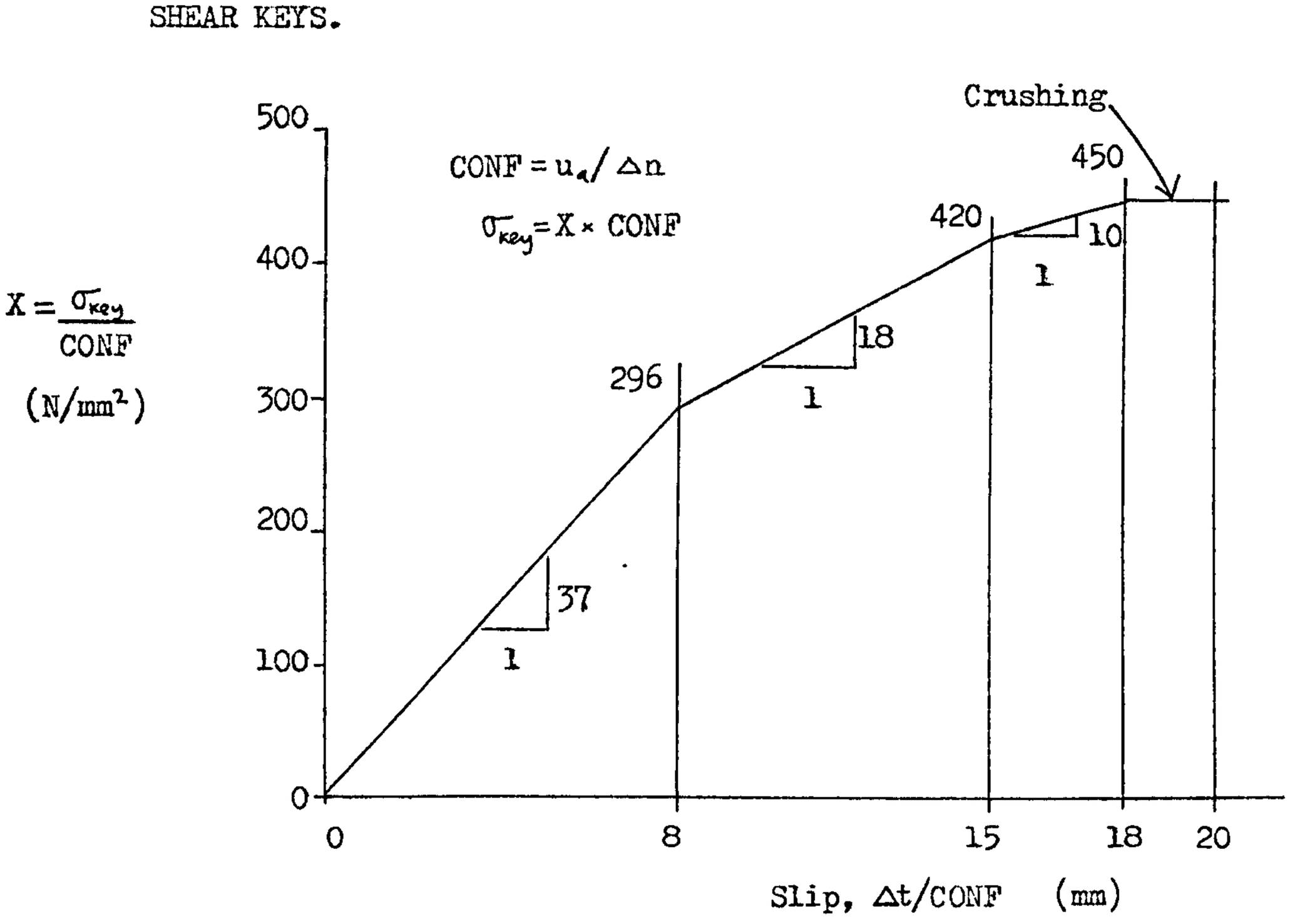

FIGURE 5.7 SHEAR KEY STRESS-SLIP CURVE.

by the radial stiffness of the tubulars, but that the ultimate load will vary according to the level of confinement of the grout, (see Section 7.1 for detailed results).

The shear key force per unit circumference V, is calculated as follows:-

$$V = \sigma_{key} \times h_{eff} \qquad (5.39)$$

where: σ_{key} = stress under the shear key as a function of slip, Δt, and bond opening, Δn.

h_{eff} = $h-\Delta n$ = key height in contact with grout.

The stress under the shear key σ_{key}, is defined by the shear key stress-slip curve, given in Figure 5.7. The gradient gives the tangential shear key stiffness k_{sc}, which starts off at 37 N/mm^3 for low loads, but ultimately reduces to zero as the grout crushes. The term $u_a/\Delta n$ = CONF is used to account for the effects of variable grout confinement. When the bond opening Δn, is small, the confinement is large, and a high σ_{key} is possible. This is reflected in the formula by dividing the slip by CONF before applying to the stress-slip curve and then multiplying the corresponding stress by CONF to give the true key stress. The higher the confinement pressure, the greater the load the grout can sustain; this is a characteristic property of concrete and grout materials and is discussed further in Chapter 6.

A study of the key pressures at ultimate load obtained from the experimental results shows how more radially stiff connections have a higher σ_{key}/f_{cu} factor at ultimate load. Table 5.3 shows the results of this study, where σ_{key}/f_{cu} is calculated as follows:-

$$\sigma_{key}/f_{cu} = \frac{f_{bu}.r_p^2.(1/d_p).4.\pi}{f_{cu}.(\text{no. key pairs}).h.r_p.2.\pi}$$

TEST	K_m	h/s	σ_{key}/f_{cu}
P1/2	0.0146	0.012	4.75
P3/4	0.0106	"	3.62
P5/6	0.0093	"	2.70
P8	0.0131	"	4.25
P9/10	0.0100	"	3.32
P11/12	0.0088	"	2.68
P13/14	0.0120	"	3.85
P15/16	0.0095	"	3.18
P17/18	0.0085	"	2.78
P19/20	0.0121	"	3.84
Q1/2	0.0105	"	5.31
Q3/4	"	0.024	4.46
Q5/6	"	0.032	3.44
R1/2	"	0.006	7.11
R3/4	"	0.018	3.76
R5/6	0.0095	0.012	4.75
R7/8	0.0125	"	5.21
R9/10	0.0105	"	3.69

TABLE 5.3. EFFECT OF K_m AND h/s ON THE ULTIMATE SHEAR KEY STRESS, σ_{key}.

σ_{key} gives the pressure on the shear keys assuming the entire load to be evenly distributed over all the keys and gives an estimate of the overall performance. The above equation neglects any frictional bond, which would make σ_{key} smaller, but at ultimate load the frictional bond stress is likely to be very small anyway. Table 5.3 also gives the stiffness factor K_m, for each test, which gives a measure of hoop stiffness and from this it can be seen that σ_{key}/f_{cu} is less for smaller K_m. Also, for the Q and R series, it can be seen that σ_{key} reduces with increasing h/s. This may be due to the higher bending stresses and larger bond openings associated with larger h/s and is discussed further in Section 7.3.

Since the experimental results have shown the ultimate bond strength to be proportional to the square root of grout cube strength, it is probable that $\sigma_{key}^{max} = 450 \times CONF$, should be replaced by $\sigma_{key}^{max} = a\sqrt{f_{cu}}.CONF$, where a = constant. Therefore, when analysing a connection with cube strength other than 50 N/mm^2, the ultimate shear key stress should be

$$\sigma_{key}^{max} = 450\sqrt{\frac{f_{cu}}{50}}.CONF \qquad (5.40)$$

The penetration of the shear keys into the grout reduces as the bond tends to open, hence further reducing the load capacity. This is accounted for in the shear key force, equation (5.39), by h_{eff} , which also reduces as the bond gap opens. A significant part of this reduction in h_{eff} can be attributed to the radial component of shear key force V_R. The value of V_R is expressed as a constant ratio of the axial key force, V.

i.e. $\qquad V_R = \beta.V \qquad$ where β = constant $\qquad (5.41)$

The value of β will depend on the shear key shape and is examined in more detail in Section 7.1. For hemispherical shape weld beads, the value of β has been found to be 0.5 according to the detailed finite element

analysis and interestingly, Paslay also chose $\beta = 0.5$.

It should be noted that the axial shear key load creates a small bending moment which is not included in the friction-gap element shear-key representation. The load V is applied at the node on the bond surface, but should be eccentric to this surface as the shear key is embedded in the grout, (Figure 5.8). Although it is possible to rectify this error, it was found that when sleeve stiffeners are used and the pile is of typical thickness, the resulting bending stresses are too low to justify any correction. Even so, when exceptionally large shear keys are used, the moment arm will be greater and so errors could possibly occur.

5.9 Typical Parameter Values

The following values have been found to give good results generally, for all grouted connection problems analysed with the finite element method.

$u_m = 0.04$ mm* For shot-blasted steel tubulars.

$k_t = 5$ N/mm^3 In reality this factor should be much larger prior to slip, but for the purposes of the analysis this value has always proved reliable.

$k_n = 50$ N/mm^3 In theory, increasing k_n increases σ_n and the bond strength, but in practice, above 50 N/mm^3, there is very little strength increase. This is because the limited sleeve and pile stiffnesses cannot resist very large σ_n and so there is no advantage in using larger k_n.

$\mu = 3.0$ This is the friction coefficient between shot-blasted steel and grout, which was determined experimentally (see Section 9.1).

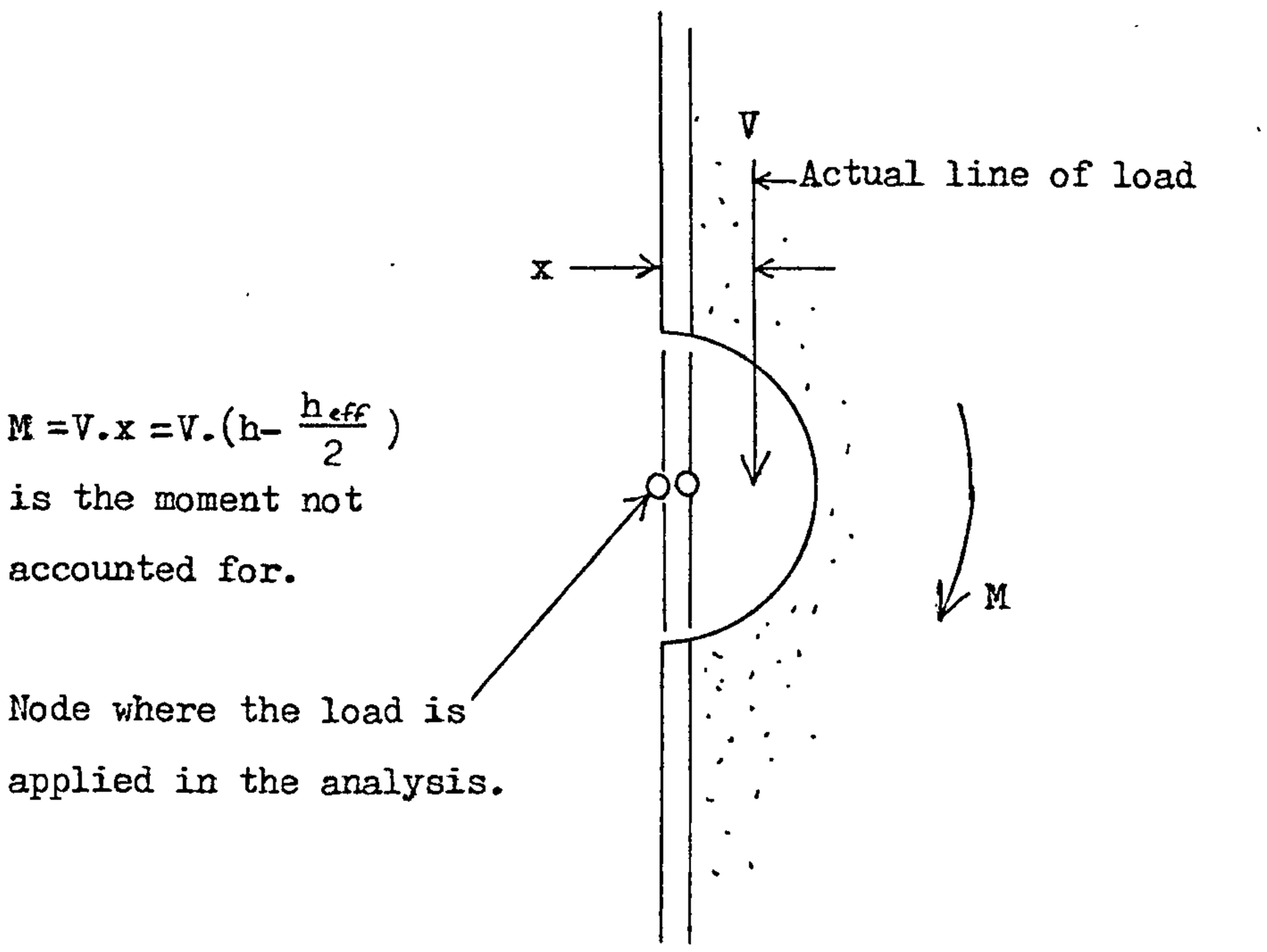

$M = V.x = V.(h - \frac{h_{eff}}{2})$ is the moment not accounted for.

Node where the load is applied in the analysis.

FIGURE 5.8 LOADING ERROR RESULTING FROM THE SIMPLIFIED SHEAR KEY REPRESENTATION.

* The value of u_m may be reduced by shrinkage of the grout, which can significantly weaken the plain pipe bond strengths. As the grout shrinks the pile/grout bond will become compressed, but the sleeve/grout bond will open. This results in failure occurring on the sleeve bond. To account for this effect, the radial shrinkage on the sleeve bond δ_{sh}, must be estimated. Then the value of u_m for the sleeve bond is reduced by δ_{sh}. Also, the slip needed to reach the reduced u_m will be less and so n is reduced from 1.0 to 0.1. This will agree with the experimental results, where it is found that maximum load is achieved at a very small slip when shrinkage has occurred, (such as the B-series tests mentioned in Section 9.2).

5.10 Flow Chart for the Element Subroutine

The processes described in the previous sections are brought together and carried out in logical order by the friction-gap element subroutine, which is described by the flow chart of Figure 5.9. The subroutine listing which is designed for use with the NONSAP programme is given in Appendix C.

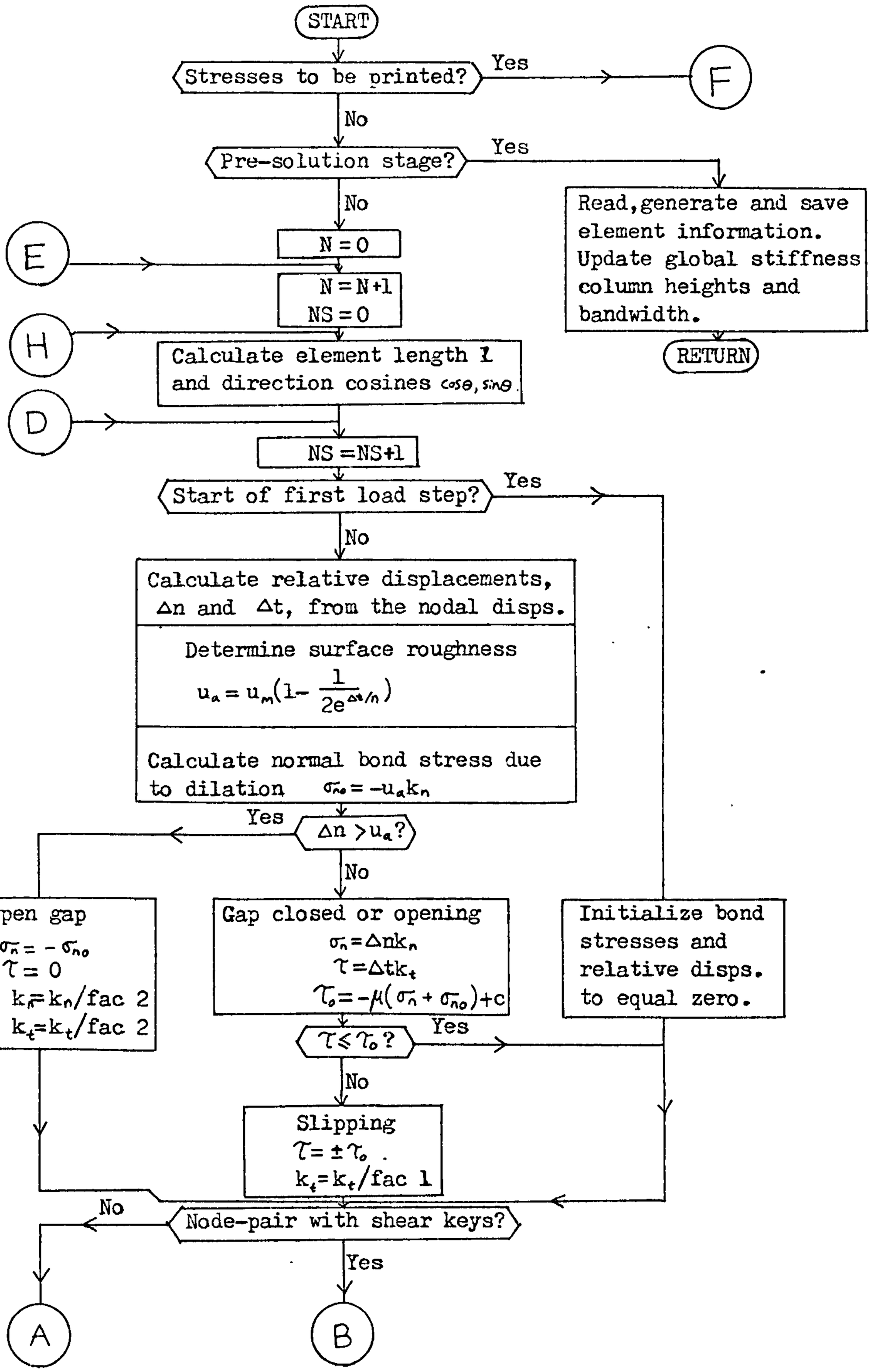

FIGURE 5.9 FLOW-CHART OF THE PROCEDURES CARRIED OUT FOR THE FRICTION-GAP ELEMENT WITHIN THE PROGRAM NONSAP.

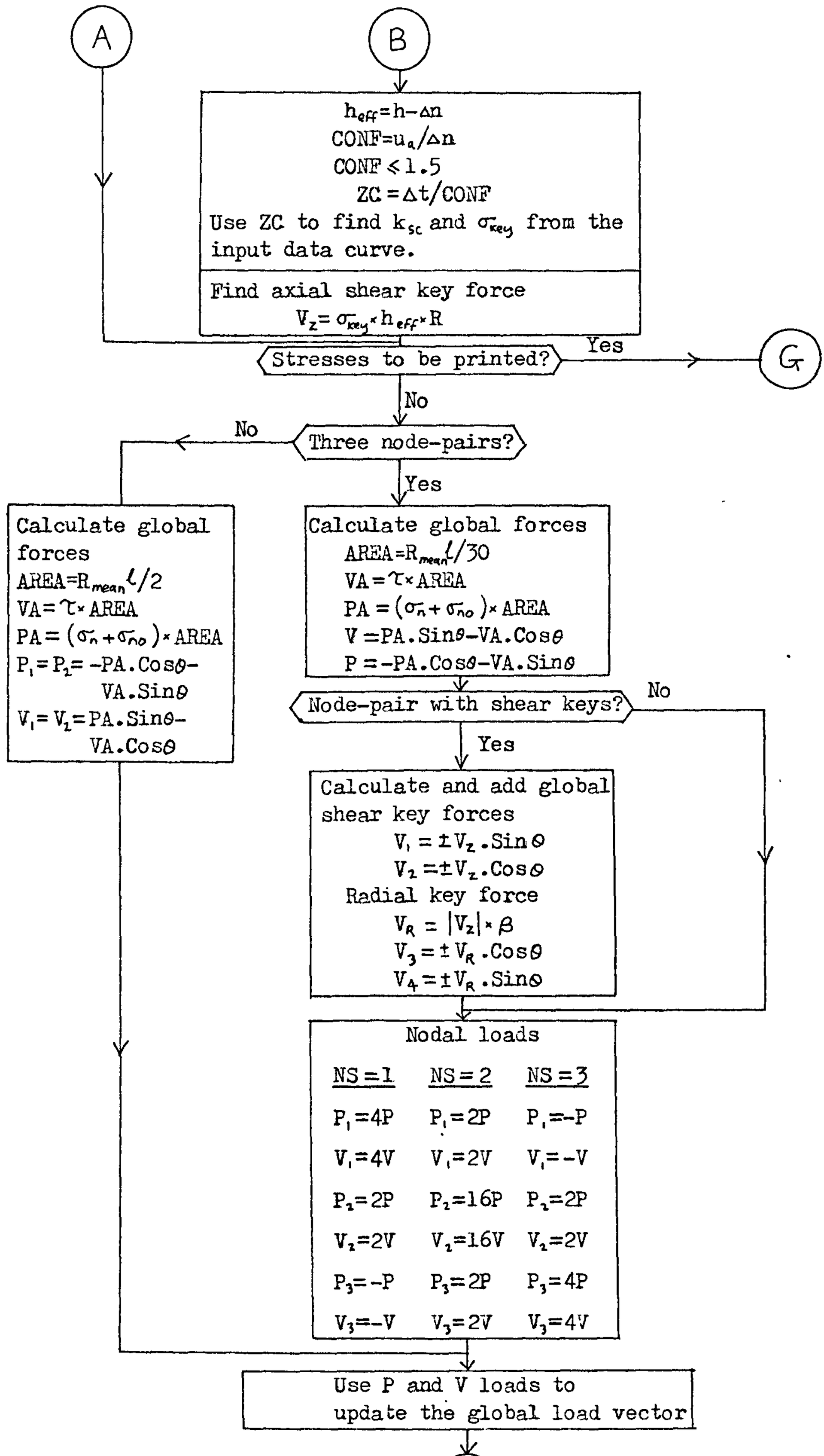

FIGURE 5.9 Continued

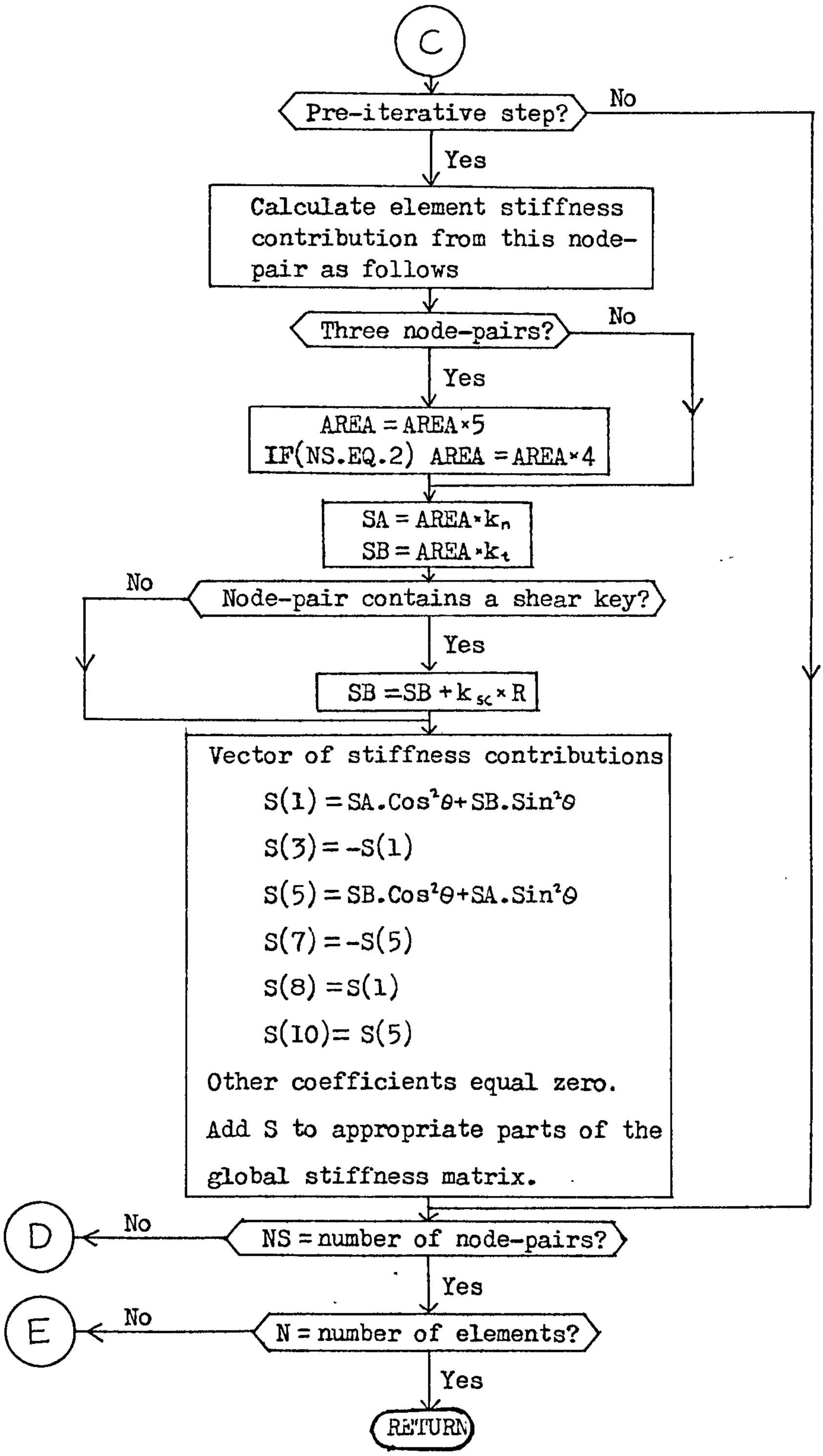

FIGURE 5.9 Continued

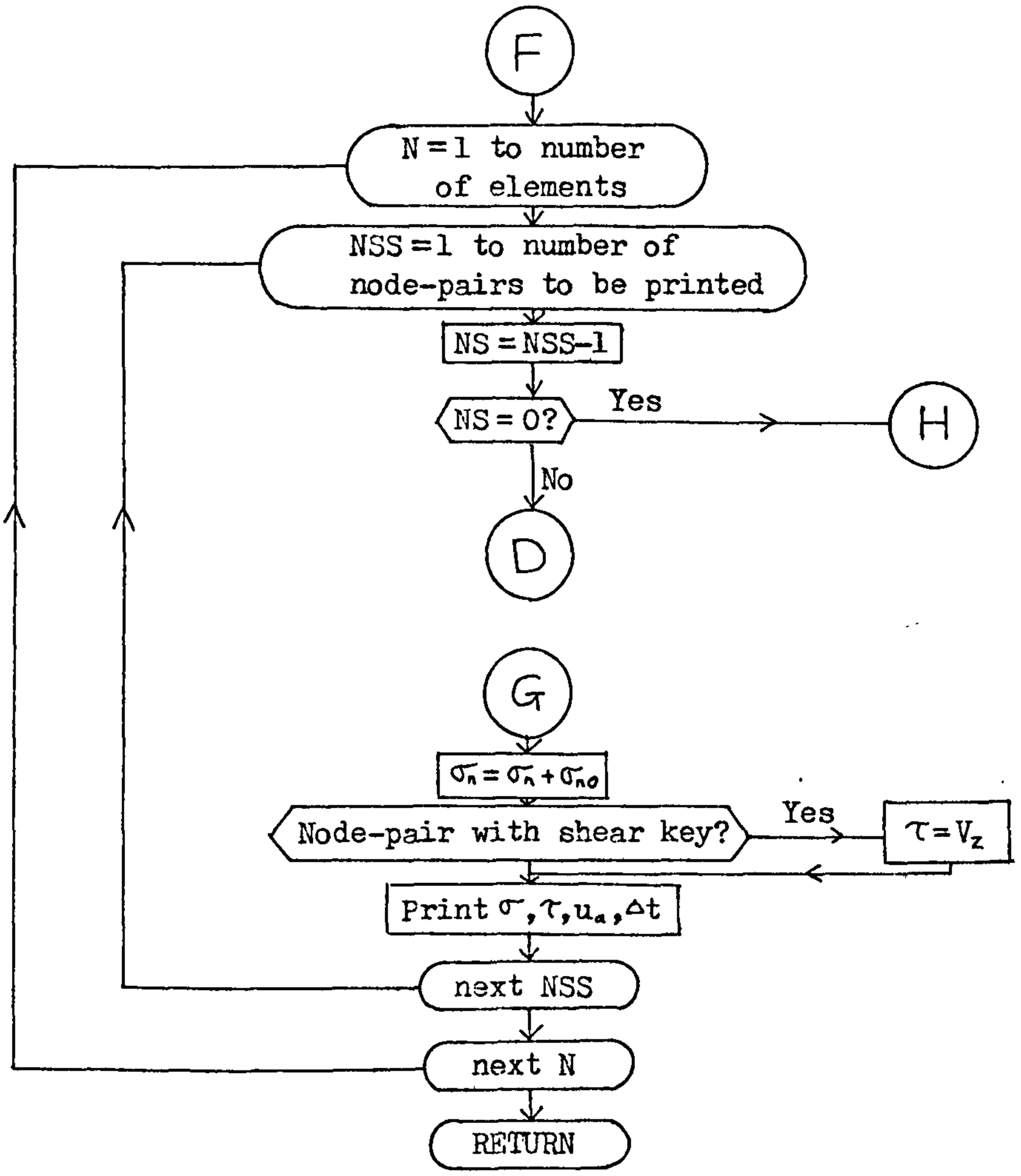

FIGURE 5.9 Continued

CHAPTER 6

CONSTITUTIVE LAW FOR THE MATERIAL BEHAVIOUR OF GROUT

6.1 Pysical Properties of Grout

The grout used in offshore construction is essentially a mixture of cement and water, as used in concrete, but without any sand or aggregate. For the purpose of the analyses conducted and reported in this thesis it is assumed that the behaviour of the two materials will be similar, with perhaps the exception of one detail. That is, when concrete cracks, substantial shear stresses can still be carried across the plane of that crack due to the roughness of the crack and interlock of the aggregate. In the case of grout, the crack surfaces are smooth and so no shear stiffness is transferred across the crack planes. It is extremely difficult to obtain experimental or analytical information about the nonlinear properties of grout. This is in complete contrast to the enormous amount of published work on concrete.

Kotsovos (39) attributes the nonlinear behaviour of concrete to be caused by the internal fracture processes occurring under increasing stress. As the stresses increase, microcracks extend and propagate in the direction of maximum principal compressive stress, thus reducing the high tensile stress concentrations which exist near crack tips and causing void formation within the body of the material, (Figure 6.1).

The reduction of high tensile stress concentrations tends to reduce the volume of the concrete (or grout), but on the other hand, the formation of voids will increase the volume. The combined effect tends to reduce volume at relatively low stress levels, but towards ultimate

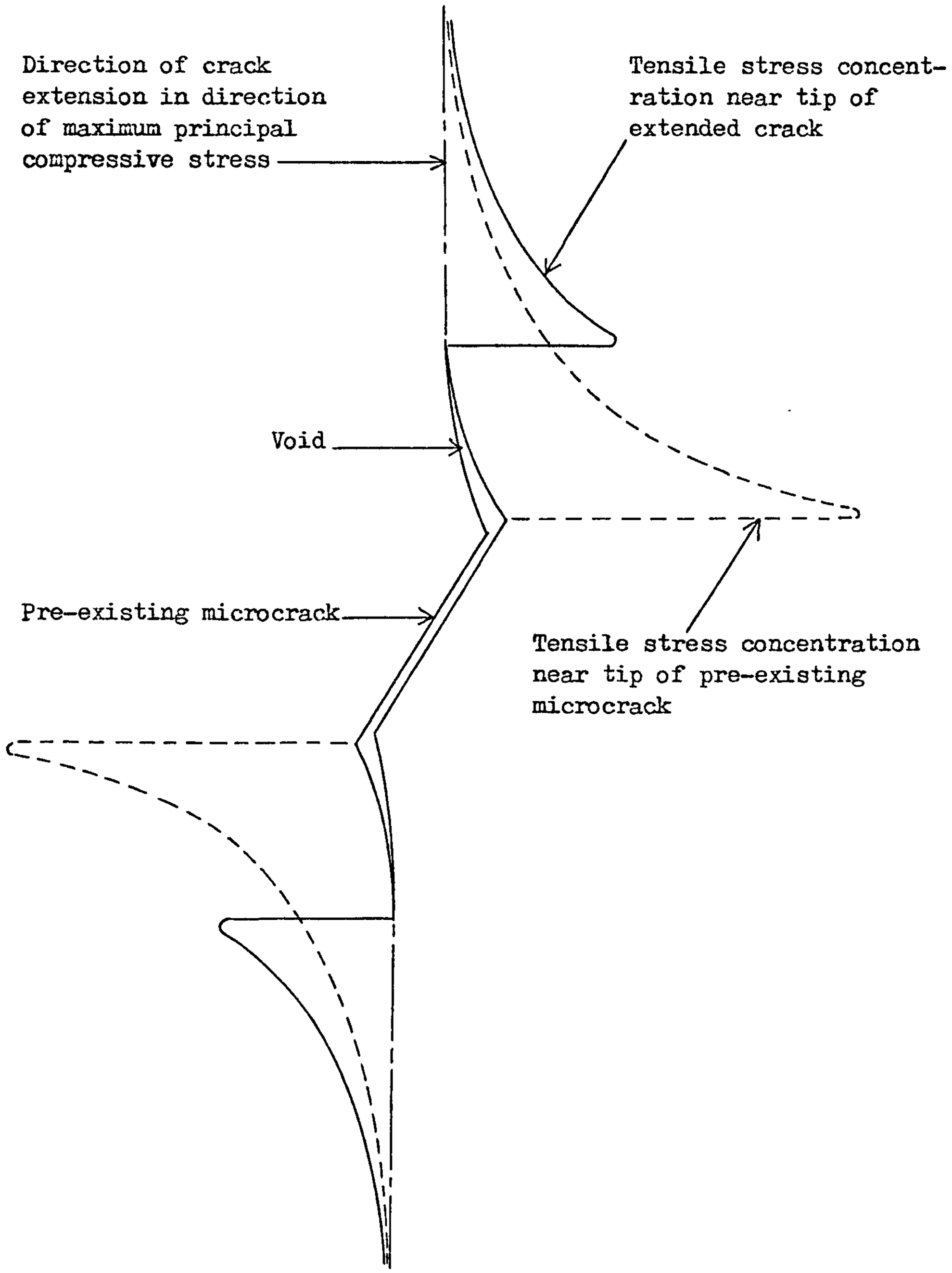

FIGURE 6.1 SCHEMATIC REPRESENTATION OF STRESS REDISTRIBUTION AND VOID FORMATION CAUSED BY CRACK EXTENSION.

stress, void formation predominates, increasing the material volume. The stress-strain behaviour of concrete has been summarised by Chen (40, 41), and is illustrated in Figure 6.2.

The stress-strain curve, as shown in Figure 6.2a, does not become nonlinear until the stress reaches about 60% of the ultimate load. Above this load, internal microcracking commences, which causes permanent deformation, similar to the permanent plastic deformation which occurs in metals. Beyond the ultimate load, the strain-softening characteristics are not well defined. In the case of the grout, which is fully confined by the steel tubulars, the stress may simply reach a plateau at ultimate load, as the grout material cannot be displaced to allow any load reduction. Unloading and reloading in the plastic range follows the initial elastic gradient which results in a permanent deformation when unloaded. The return to the elastic modulus occurs when the stresses are below their peak, hence being unable to induce further microcracks. As the microcracking is responsible for the plastic strains, the material must return to an elastic state until the stresses reach a new peak enabling cracks to spread. The tensile strength is invariably about one tenth of the compressive strength for uniaxial or biaxial tensile loading. The brittleness of the tensile failure does not necessarily mean that the behaviour is linear up to fracture. A characteristic of a tensile type of failure in concrete is that the failure itself is abrupt with the development of one major crack and this pattern has been observed in grout as well. In the case of a compressive type of failure, several major cracks develop in concrete, but grout has been observed to pulverise to a fine powder. This must enable the grout to become mobilised at ultimate load, allowing it to relieve the stress concentrations.

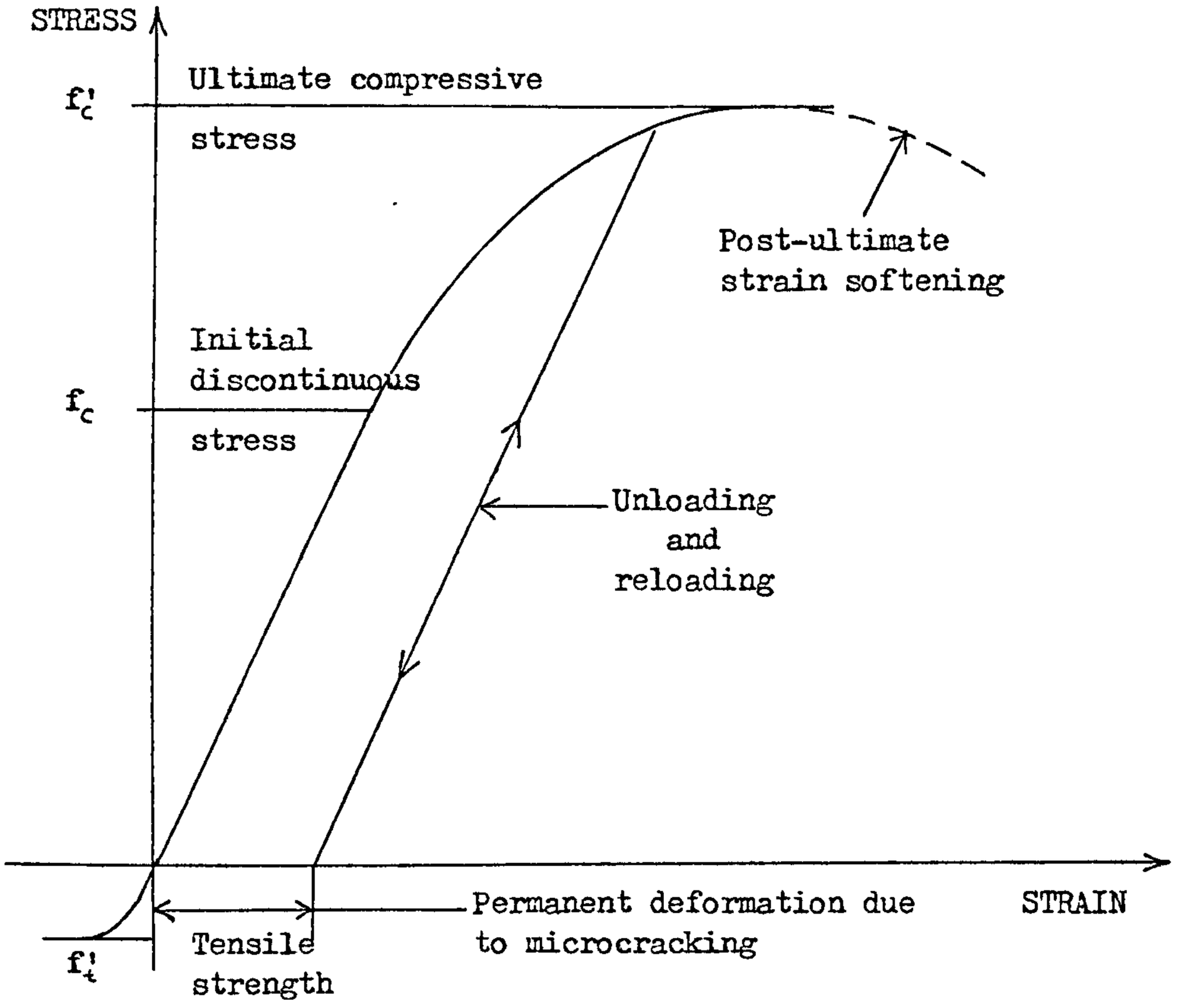

(a)Uniaxial Tension and Compression.

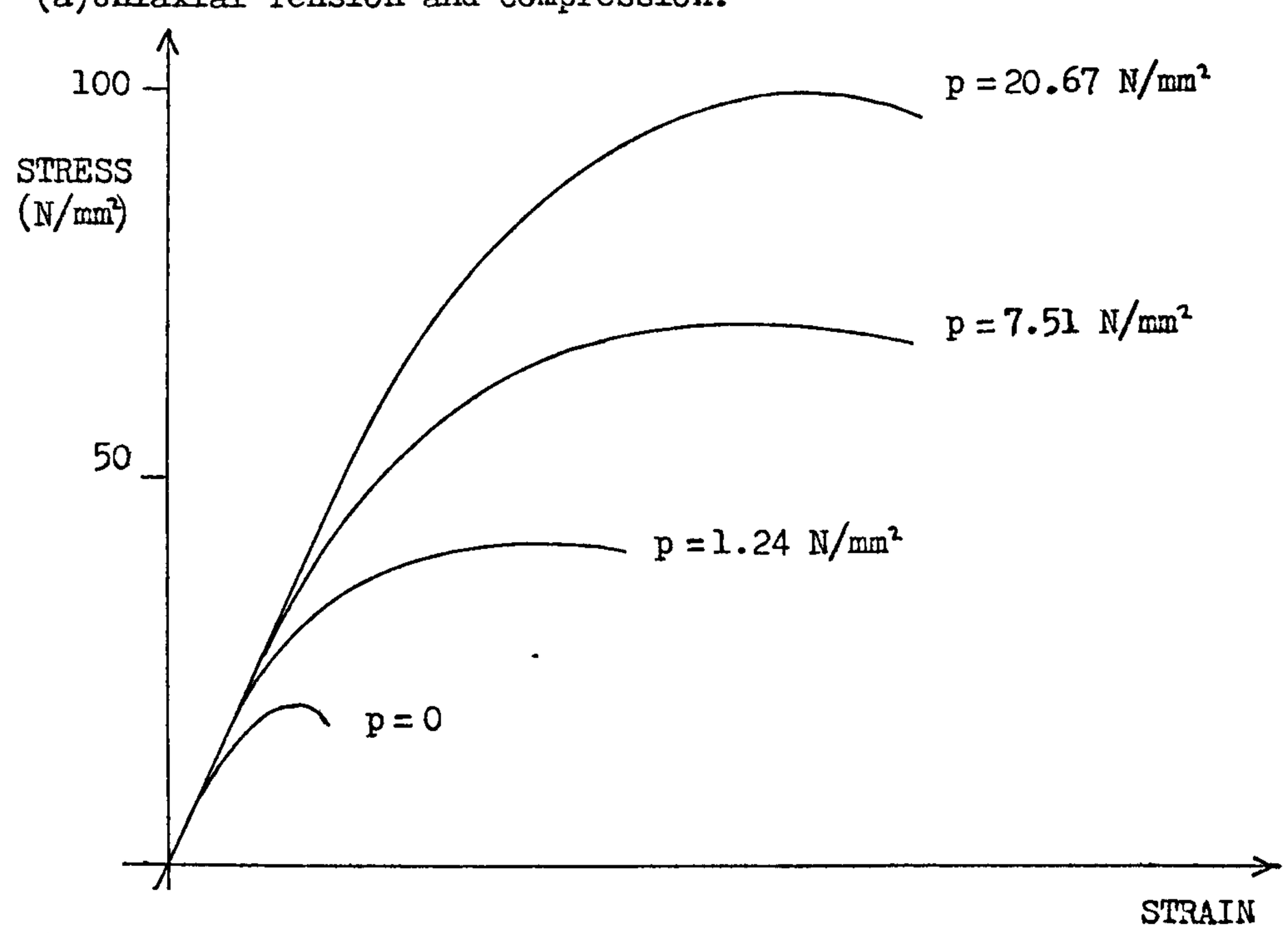

(b)Compression and lateral pressure,p.

FIGURE 6.2 TYPICAL STRESS-STRAIN CURVE FOR CONCRETE.

The true nature of concrete behaviour under triaxial compression is difficult to determine since it develops considerable strength and is difficult to load experimentally. Figure 6.2b shows how the strength increases under an increasing confinement pressure. Hydrostatic pressure is seen largely to increase both maximum stress and maximum strain during compression and the unstable strain softening portion gradually vanishes for increasing pressures. Since the grout is confined by the sleeve and pile, the hydrostatic pressure may rise and lead to an enhanced crushing strength under the shear keys. Therefore, it is important to include these properties in the constitutive model for the grout.

6.2 Choice of Constitutive Model

Most constitutive models for concrete (and grout) materials are two-dimensional, (plane stress). This makes them unsuitable to represent the three-dimensional nature of the grouted connection, where axial, radial and circumferential stresses are all of importance. Also, not all models include the volume increase near to peak stress, or the strengthening caused by hydrostatic stress.

A number of researchers (39,42,43,44) have found from experimental results that approximately unique relationships exist between octahedral normal stress (σ_{oct}) and strain (ϵ_{oct}), defined as

$$\sigma_{oct} = I_1/3 \qquad (6.1)$$

$$\epsilon_{oct} = I_1^{\epsilon}/3$$

where

$$I_1 = \sigma_{mm} \qquad (6.2)$$

$$I_1^{\epsilon} = \epsilon_{mm}$$

are the first invariants of stress (I_1) and strain (I_1^{ϵ}).

A second unique relationship exists between the octahedral shear stress (τ_{oct}) and strain (γ_{oct}), given by

$$\tau_{oct} = \sqrt{2J_2/3}$$
$$2\gamma_{oct} = \sqrt{8J_2^{\epsilon}/3} \qquad (6.3)$$

where
$$J_2 = \tfrac{1}{2}\sigma_{ij}\sigma_{ij} - I_1^2/6$$
$$J_2^{\epsilon} = \tfrac{1}{2}\epsilon_{ij}\epsilon_{ij} - I_1^{\epsilon 2}/6 \qquad (6.4)$$

are the second invariants of deviatoric stress (J_2) and strain (J_2^{ϵ}).

Under triaxial compression, concrete can flow like a ductile material on the yield or failure surface before reaching its crushing strains. This fact has been used by Chen (40,45) to develop an elastic-plastic strain-hardening and fracture model for concrete. The yield and failure surfaces are functions of the first and second stress invariants, as previously described. To construct the stress-strain relation in the plastic range, normality of the plastic deformation rate vector to the yield surface is used, (i.e. the flow rule). The dependence of the yield function on the mean normal stress and the concept of flow rule lead, in general, to a plastic volume increase under pressure. This dilatency near failure is a feature of concrete and other rock type materials and the grout is assumed to be no exception and to behave in the same way.

Chen's concrete model appears to take account of all the nonlinear features of the material in three-dimensions, and has been developed for use in finite element analysis (46). Input data includes the initial elastic material constants, which are known for the grout and compressive and tensile ultimate strengths of the material. These strength values govern the shape and size of the ultimate load surface. The available data should enable a good representation of the grout behaviour to be achieved, which is an advantage over some other material models that

require far more experimentally determined quantities.

6.3 Chen's Elastic-Plastic Strain-Hardening Model

6.3.1 Loading Surface

The failure surface is defined in stress space such that once the stress state reaches this surface the material will either crack or crush. The initial yield surface is reached elastically and if unloading takes place within this surface, no permanent deformation occurs. If the grout is stressed beyond this initial yield surface, a new yield surface will be developed and microcracks will propagate in the grout resulting in irrecoverable deformation upon unloading. Unloading and reloading of the grout will not result in further permanent deformation until the new yield surface, called the loading surface, is reached.

The failure surface is represented by two different functions for the compression region and the tension or tension-compression regions. These functions depend upon the first invariant of stress (I_1) and the second invariant of deviatoric stress (J_2), defined in equations (6.2, 6.4). The failure functions are given by

$$f_u(\sigma_{ij}) = J_2 - \frac{I_1^2}{12} \pm \frac{I_1^2}{12} + \frac{A_u I_1}{3} = \tau_u^2 \qquad (6.5)$$

where the third term is positive for the compression region and negative for the tension or tension-compression regions. The initial yield function is similar to equation (6.5), but A_u and τ_u are replaced by A_o and τ_o. A_o, A_u, τ_o and τ_u are all constants, which are calculated from the material strength values as follows:

$$A_o = \frac{f_{bc}^2 - f_c^2}{2f_{bc} - f_c} \qquad (6.6a)$$

$$A_u = \frac{f_{bc}'^2 - f_c'^2}{2f_{bc}' - f_c'} \tag{6.6b}$$

$$\tau_o^2 = \frac{f_c f_{bc} (2f_c - f_{bu})}{3(2f_{bc} - f_c)} \tag{6.7a}$$

$$\tau_u^2 = \frac{f_c' f_{bc}' (2f_c' - f_{bc}')}{3(2f_{bc}' - f_c')} \tag{6.7b}$$

for the compression region and for the tension or tension-compression regions, the constants are

$$A_o = (f_c - f_t)/2 \tag{6.8a}$$

$$A_u = (f_c' - f_t')/2 \tag{6.8b}$$

$$\tau_o^2 = f_c . f_t/6 \tag{6.9a}$$

$$\tau_u^2 = f_c' . f_t'/6 \tag{6.9b}$$

In the above equations, f_c', f_t' and f_{bc}' denote the ultimate strength of the grout under uniaxial compression, uniaxial tension and equal biaxial compression, respectively, while f_c, f_t, and f_{bc}, denote the initial yield strength of the grout under the corresponding loading.

The subsequent loading surfaces are bounded by the initial yield and failure surfaces and their shapes are similar in form. The kinematics of the loading surface are such that the loading surface translates along the $\sigma_1 = \sigma_2 = \sigma_3$ axis and simultaneously expands in an isotropic manner. In other words, the loading function is a combination of kinematic hardening and isotropic hardening models used frequently in the theory of plasticity. The function can be expressed as

$$f(\sigma_{ij}) = \frac{J_2 - \frac{I_1^2}{12} \pm \frac{I_1^2}{12} + \frac{\beta}{3} I_1}{1 - \frac{\alpha}{3} I_1} = \tau^2 \tag{6.10}$$

where the positive-negative term is positive for the compression region and negative for the tension or tension-compression regions. In order that the function should match the initial yield function when $\tau = \tau_o$,

or the failure function when $\tau = \tau_u$, the values of α and β are given by

$$\alpha = \frac{A_u - A_o}{\tau_u^2 - \tau_o^2} \tag{6.11}$$

$$\beta = \frac{A_o \tau_u^2 - A_u \tau_o^2}{\tau_u^2 - \tau_o^2} \tag{6.12}$$

Equation (6.10) gives the loading surfaces, (Figure 6.3a), when plotted in octahedral shear and normal stress space. It can be seen that a high hydrostatic stress, represented by σ_{oct}, makes failure more unlikely, unless the shear stresses, represented by τ_{oct}, are increased. This agrees well with the observed behaviour of concrete.

Figure 6.3b shows a plot of the initial and ultimate yield surfaces, based on the properties used for grout. Also shown is a plot of the line

$$\tau_{oct}/\sqrt{2} + \sigma_{oct} = 0$$

This line is important since it separates the region where the tension-compression yield surface is most critical from the region where the compression yield surface is most critical. This line therefore gives the criteria for choosing the appropriate yield surface, thus:

For tension region:

$$\sigma_{oct} > 0 \tag{6.13a}$$

For tension-compression region:

$$\tau_{oct}/\sqrt{2} + \sigma_{oct} \geq 0 \tag{6.13b}$$

For compression region:

$$\tau_{oct}/\sqrt{2} + \sigma_{oct} < 0 \tag{6.13c}$$

and
$$\sigma_{oct} < 0 \tag{6.13d}$$

In the loading function, equation (6.10), the term $(\beta/3)I_1$ represents the fact that tensile strength is much less than compressive strength. The quantity $(\alpha/3)I_1$ represents the kinematic translation of the subsequent loading surfaces. The denominator of equation (6.10) should

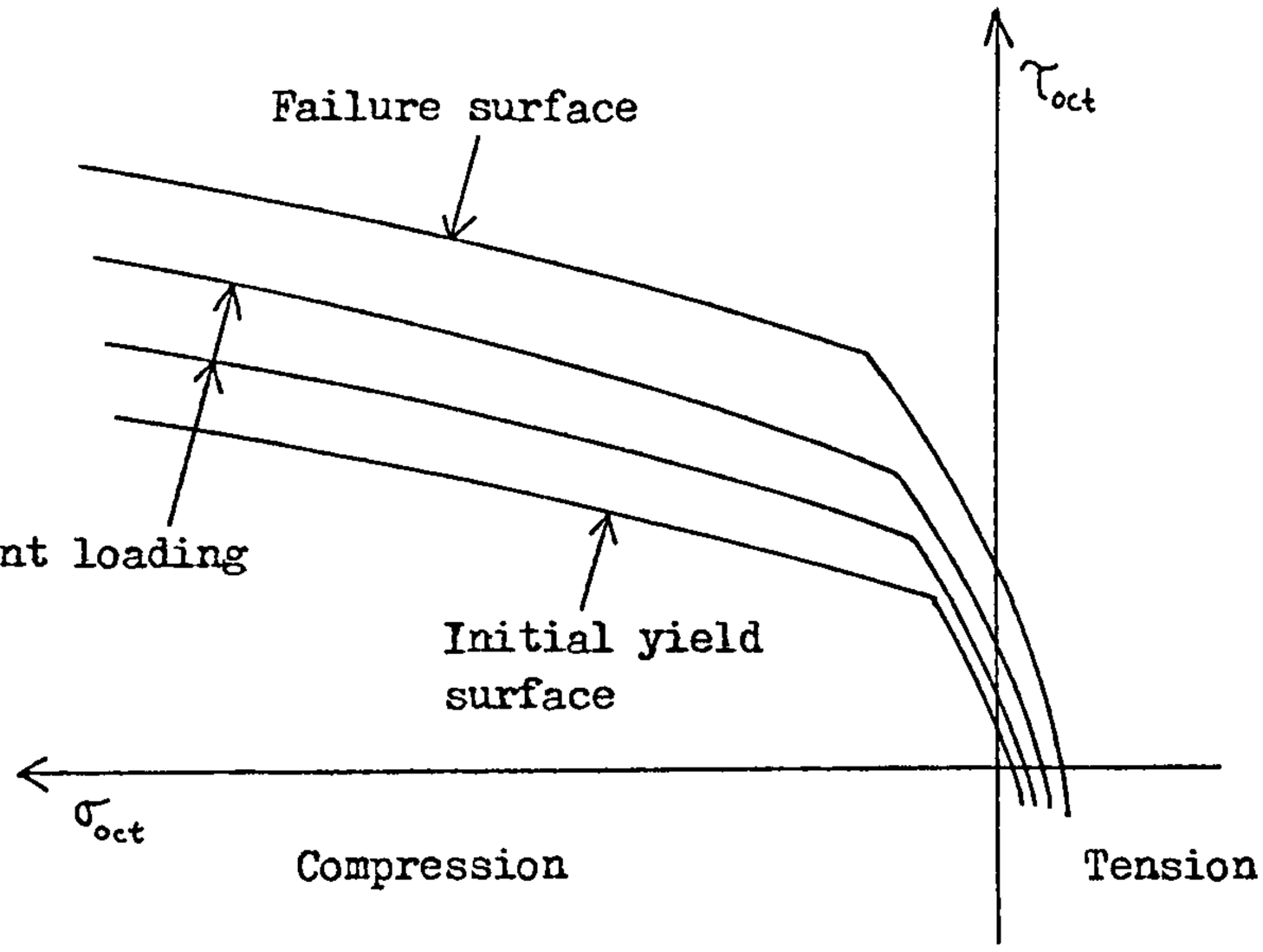

FIGURE 6.3a INITIAL, SUBSEQUENT AND FAILURE SURFACES IN OCTAHEDRAL STRESS SPACE.

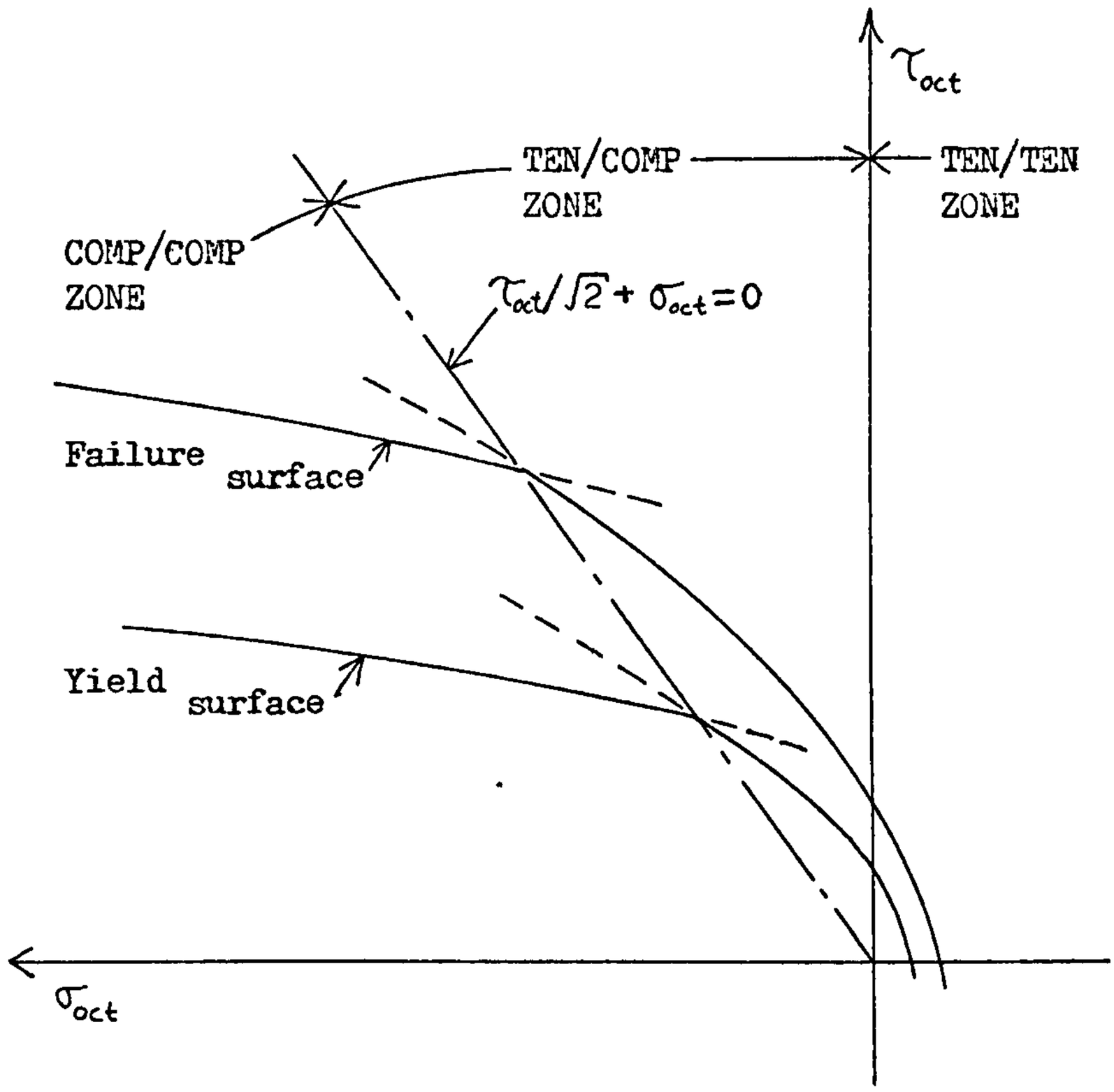

FIGURE 6.3b INITIAL YIELD AND FAILURE SURFACES, TOGETHER WITH THE DIVIDING LINE BETWEEN TENSION/COMPRESSION AND COMPRESSION/COMPRESSION ZONES.

always be positive. This condition was found to be necessary in the analysis after large tensile stresses had caused the yield function to go negative, when in fact, the failure surface should have been reached. This was due to the denominator of equation (6.10) becoming negative and thereby giving the false impression that the material had returned to the elastic state.

6.3.2 Stress-Strain Relations

Denoting the general loading function by $f(\sigma_{ij})$, the normality of the incremental plastic strain $(d\epsilon^p_{ij})$, to $f(\sigma_{ij})$ requires that

$$d\epsilon^p_{ij} = G \frac{\partial f}{\partial \sigma_{ij}} df \qquad (6.14)$$

where G is a scalar function depending upon the current state of stress and strain and the stress history. The elastic stress-strain relation gives

$$d\sigma_{kL} = D_{kLij}\, d\epsilon^e_{ij} = D_{kLij}\,(d\epsilon_{ij} - d\epsilon^p_{ij}) \,. \qquad (6.15)$$

Substituting equation (6.14) into equation (6.15) gives

$$d\sigma_{kL} = D_{kLij}\,(d\epsilon_{ij} - G \frac{\partial f}{\partial \sigma_{ij}} df) \,. \qquad (6.16)$$

Using the relation

$$df = \frac{\partial f}{\partial \sigma_{mn}} d\sigma_{mn} \qquad (6.17)$$

and substituting from equation (6.16) gives

$$df = \frac{\partial f}{\partial \sigma_{mn}} D_{mnij}\,(d\epsilon_{ij} - G \frac{\partial f}{\partial \sigma_{ij}} df) \,.$$

and collecting terms gives

$$df(1 + \frac{\partial f}{\partial \sigma_{mn}} D_{mnij}\, G \frac{\partial f}{\partial \sigma_{ij}}) = \frac{\partial f}{\partial \sigma_{mn}} D_{mnij}\, d\epsilon_{ij}$$

Therefore

$$df = \frac{\frac{\partial f}{\partial \sigma_{mn}} D_{mnij}}{1 + \frac{\partial f}{\partial \sigma_{mn}} D_{mnij} G \frac{\partial f}{\partial \sigma_{ij}}} d\epsilon_{ij} \tag{6.18}$$

Substituting equation (6.18) into equation (6.16) gives

$$d\sigma_{KL} = \left[D_{KLij} - \frac{D_{KLij} \frac{\partial f}{\partial \sigma_{ij}} \frac{\partial f}{\partial \sigma_{mn}} D_{mnij}}{\frac{1}{G} + \frac{\partial f}{\partial \sigma_{mn}} D_{mnij} \frac{\partial f}{\partial \sigma_{ij}}} \right] d\epsilon_{ij} \tag{6.19}$$

i.e. $$d\sigma_{KL} = \left[D_{KLij} - d\lambda \phi_{KLij} \right] d\epsilon_{ij} \tag{6.20}$$

where $$\frac{1}{d\lambda} = H \sqrt{\frac{\partial f}{\partial \sigma_{pq}} \frac{\partial f}{\partial \sigma_{pq}}} + \frac{\partial f}{\partial \sigma_{mn}} D_{mnij} \frac{\partial f}{\partial \sigma_{ij}} \tag{6.21}$$

and $$\phi_{KLij} = D_{KLij} \frac{\partial f}{\partial \sigma_{ij}} \frac{\partial f}{\partial \sigma_{mn}} D_{mnij} \tag{6.22}$$

$$H = \frac{df}{\sqrt{d\epsilon^p_{rs} \, d\epsilon^p_{sr}}} = \text{the work hardening rate} \tag{6.23}$$

Equation (6.20) gives the basic form of the isotropic, plastic, strain hardening, incremental stress-strain relations from which the matrix constitutive relations are formed. These have been quoted elsewhere by Chen (46), for the three-dimensional, plane strain and plane stress states as well as the axisymmetric state used here.

The strain-hardening rate (H) must be determined from experimental results. This is found by plotting $\sqrt{f}$ against ϵ^p for a given set of results. This data may include uniaxial, biaxial, or even triaxial results in order to get the best multiaxial representation. The plastic strain term (ϵ^p) can be determined by subtracting the elastic strain components from the total strains.

Then $$\epsilon^p = \sqrt{\epsilon_1^{p^2} + \epsilon_2^{p^2} + \epsilon_3^{p^2}}$$

The gradient of the $\sqrt{f}$ against ϵ^p curve will be

$$H' = \frac{\partial \sqrt{f}}{\partial \epsilon^p} = \frac{\partial \sigma_e}{\partial \epsilon^p} \tag{6.24}$$

where $\sigma_e = \sqrt{f}$ = effective stress.

But $H = df/d\epsilon^p$ and as $\sigma_e^2 = f$,

$$\frac{\partial f}{\partial \sigma_e} = 2\sigma_e$$

Therefore $$H = \frac{\partial f}{\partial \sigma_e}\frac{\partial \sigma_e}{\partial \epsilon^p} = 2\sigma_e \frac{\partial \sigma_e}{\partial \epsilon^p}$$

i.e. $$H = 2\sigma_e H' \qquad (6.25)$$

Equation (6.25) enables H to be specified for any stress state. The curve of σ_e against ϵ^p has been found to be fairly constant for different three-dimensional stress combinations and the curve in the compression region can be simply scaled down for the tension region curve. Since nonlinear stress-strain data are not available for the grout material, the same data will be used as for concrete. This should give a reasonable first approximation of the grout behaviour and errors should not be large, as the nonlinearities due to cracking and crushing are far more significant than the plastic strains.

6.4 Post-Ultimate Behaviour

6.4.1 Effects of Crushing or Cracking

The grout around the shear connectors is likely to suffer high stress concentrations at critical points and small areas of cracking or crushing will occur long before the ultimate load is reached. It is necessary to include the post-ultimate behaviour of the grout therefore, if these effects are to be successfully simulated.

Chen has included the theory of post-ultimate behaviour in some of his work (47,48). In Chen's work crushing indicates the complete rupture and disintegration of the material under compression type of stress states. After crushing, the current stresses reduce suddenly to zero and

the concrete is assumed to lose its resistance completely against further deformation. In the analysis now to be proposed, the grout is assumed to pulverise, but the stresses are held constant, rather than being reduced to zero, as the crushed grout is confined by the surrounding steel and grout and so it cannot release its stresses.

Cracking is used to indicate a failure of the material across the plane of maximum principal tensile stress. Once a crack has formed, the tensile stress across the crack reduces suddenly to zero and the stiffness of the material normal to the crack direction becomes zero. Material parallel to the crack is assumed to carry stress, however, according to the biaxial or uniaxial conditions prevailing in that direction. Up to three cracks can form perpendicular to each other, in the planes of the principal stresses. Obviously, if all three cracks occur, then the stresses and stiffness will all be reduced to zero. In Chen's work only two crack planes are allowed; the possibility of radial cracks caused by tensile circumferential stresses being ignored. He also assumes the behaviour of the sliced material between cracks to be linear-elastic. In the analysis to be used, the material between cracks follows the same elastic-plastic constitutive laws as the uncracked material. Around the shear keys, it is sometimes found that after cracking the material will enter the compression zone, the crack may or may not close, but the remaining material often becomes plastic under compression and may later crush. Therefore, it is important to not simply treat the partially cracked material as elastic.

Cracking or crushing failure criteria are largely governed by the failure surface described earlier. When the failure surface is reached,

crushing occurs if in the compression zone and cracking is initiated on the plane of maximum principal stress if in the tension or tension-compression region. Also, if any of the principal stresses exceed τ_u in the tension region, then a crack is formed.

As the failure surface is a function of stress, all failures are governed by the current stress levels. Chen has also recognised the importance of strain in governing failure and has used experimental results to form appropriate strain-based failure criteria, in addition to the stress-based criteria. In the case of grout, experimental work is lacking in this field and so the failure criteria have been based on stress alone.

6.4.2 Cracked Material

The basic stress-strain relations may be expressed as follows:

$$\{\sigma\}_p = [D]_p \{\epsilon\}_p \tag{6.26}$$

where the p suffix signifies the principal stress orientation. In expanded form this gives

$$\begin{Bmatrix} \sigma_1 \\ \sigma_2 \\ \tau_{YZ} \\ \sigma_3 \end{Bmatrix}_p = \begin{bmatrix} A1 & B1 & 0 & B1 \\ B1 & A1 & 0 & B1 \\ 0 & 0 & C1 & 0 \\ B1 & B1 & 0 & A1 \end{bmatrix}_p \begin{Bmatrix} \epsilon_1 \\ \epsilon_2 \\ \gamma_{YZ} \\ \epsilon_3 \end{Bmatrix}_p \tag{6.27}$$

where σ_3 = circumferential principal stress, and

σ_1, σ_2 = principal stresses in the Y-Z plane at an angle θ to the Y-axis.

When the material is elastic and uncracked, the constants A1, B1 and C1 are given by

$$A1 = \frac{E}{1+\nu}\left(1 + \frac{\nu}{1-2\nu}\right)$$

$$B1 = \frac{E}{(1+\nu)}\frac{\nu}{(1-2\nu)} \qquad (6.28)$$

$$C1 = \frac{E}{2(1+\nu)}$$

If one crack has occurred, then a biaxial stress state exists and the constants A1 and B1 become

$$A1 \quad \frac{E}{1-\nu^2}$$

$$B1 \quad \frac{E\nu}{1-\nu} \qquad (6.29)$$

Then, if say σ_1 is the stress to be reduced to zero by cracking, the terms in row 1 and column 1 of the $[D]_p$ matrix are reduced by some specified factor, say 100, to make them approximately zero in relation to the other terms. Alternatively, if σ_2 was cracked, then the terms in row 2 and column 2 would be reduced. C1 is also reduced if the cracks are due to σ_1 or σ_2, but not if there is only a circumferential crack due to σ_3, as this does not affect the shear stress and stiffness.

If two cracks have occurred, then A1 and B1 represent a uniaxial situation and become

$$A1 = E$$

$$B1 = \nu \qquad (6.30)$$

Before making the above modifications to the $[D]_p$ matrix for cracking, it will need modifying to the plastic $[D]_p$ matrix if the present loading surface is exceeded.

6.4.3 Rotation to the Global Direction

Having calculated the form of the $[D]_p$ matrix in the principal stress (or crack plane) orientation, it is necessary to rotate this matrix back

to the global direction. This will enable the contribution to the global stiffness matrix to be calculated. The transformation matrix $[R]$, used for this purpose is defined below

$$[R] = \begin{bmatrix} c^2 & s^2 & sc & 0 \\ s^2 & c^2 & -sc & 0 \\ -2sc & 2sc & c^2-s^2 & 0 \\ 0 & 0 & 0 & 1 \end{bmatrix} \qquad (6.31)$$

where $c = \cos\theta$, and $s = \sin\theta$.

$$[R]^{-1} = \begin{bmatrix} c^2 & s^2 & -sc & 0 \\ s^2 & c^2 & sc & 0 \\ 2sc & -2sc & c^2-s^2 & 0 \\ 0 & 0 & 0 & 1 \end{bmatrix} \qquad (6.32)$$

Then
$$\{\epsilon\}_p = [R]\{\epsilon\}_x \qquad (6.33)$$

$$\{\epsilon\}_x = [R]^{-1}\{\epsilon\}_p \qquad (6.34)$$

where the x suffix signifies the global orientation. By the property of invariance of internal strain energy

$$\{\epsilon\}_p^T\{\sigma\}_p = \{\epsilon\}_x^T\{\sigma\}_x \qquad (6.35)$$

Substituting equation (6.33) into equation (6.35) gives

$$\{\epsilon\}_x^T[R]^T\{\sigma\}_p = \{\epsilon\}_x^T\{\sigma\}_x$$

therefore
$$\{\sigma\}_x = [R]^T\{\sigma\}_p \qquad (6.36)$$

and similarly
$$\{\sigma\}_p = [R^{-1}]^T\{\sigma\}_x \qquad (6.37)$$

Substituting equation (6.33) into equation (6.26) gives

$$\{\sigma\}_p = [D]_p[R]\{\epsilon\}_x \qquad (6.38)$$

Substituting equation (6.37) into equation (6.38) and multiplying by $[R]^T$ gives

$$\{\sigma\}_x = [R]^T[D]_p[R]\{\epsilon\}_x \qquad (6.39)$$

and hence,
$$[D]_x = [R]^T[D]_p[R] \qquad (6.40)$$

Equation (6.40) gives the required incremental stiffness relation in the

global orientation.

When one of the principal stresses is reduced to zero by cracking, the global stresses are recalculated using equation (6.36).

6.4.4 Crack Status

A record of the crack status is needed in order to know which stresses and stiffnesses are to be reduced. A record of crack angle is also needed since this remains constant from one load step to the next, unless the crack closes. Eight possible crack states are recorded by NUMCR for each Gauss Point of every element using the code given in Table 6.1. When a new increment of stress and strain has been added, it is necessary to recheck the crack status, as cracks may open or close. Figure 6.4 shows how NUMCRK calculates the new crack status for the current stresses. Alternatively, if it is known that another crack should open because the ultimate loading surface has been reached or one of the principal stresses has exceeded the tensile strength, then the new crack status is calculated using the procedure given in Figure 6.5.

NUMCR	0	1	2	3	4	5	6	7
Stresses reduced to zero	No cracks	σ_1	σ_2	σ_1 σ_2	σ_3	σ_3 σ_1	σ_3 σ_2	Fully cracked

TABLE 6.1 CODE USED TO INDICATE CRACK STATUS.

6.5 Computer Algorithm

An outline of the numerical algorithm is given to show how the constitutive relations are incorporated into the finite element method.

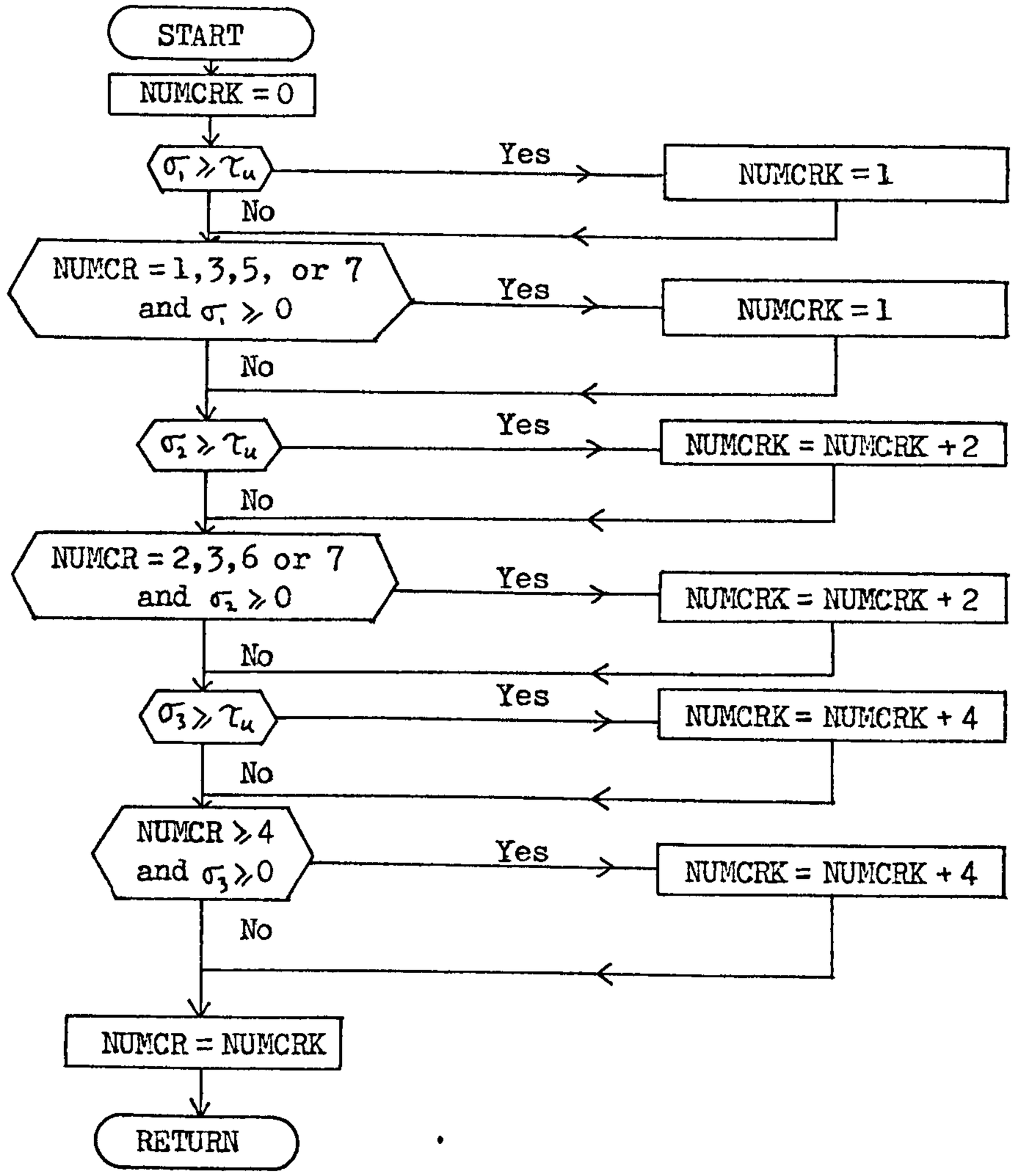

FIGURE 6.4 DETERMINATION OF THE NEW CRACK STATUS WHEN $f<\tau^1$. NUMCR GIVES THE PREVIOUS CRACK STATUS, AND NUMCRK THE NEW CRACK STATUS.

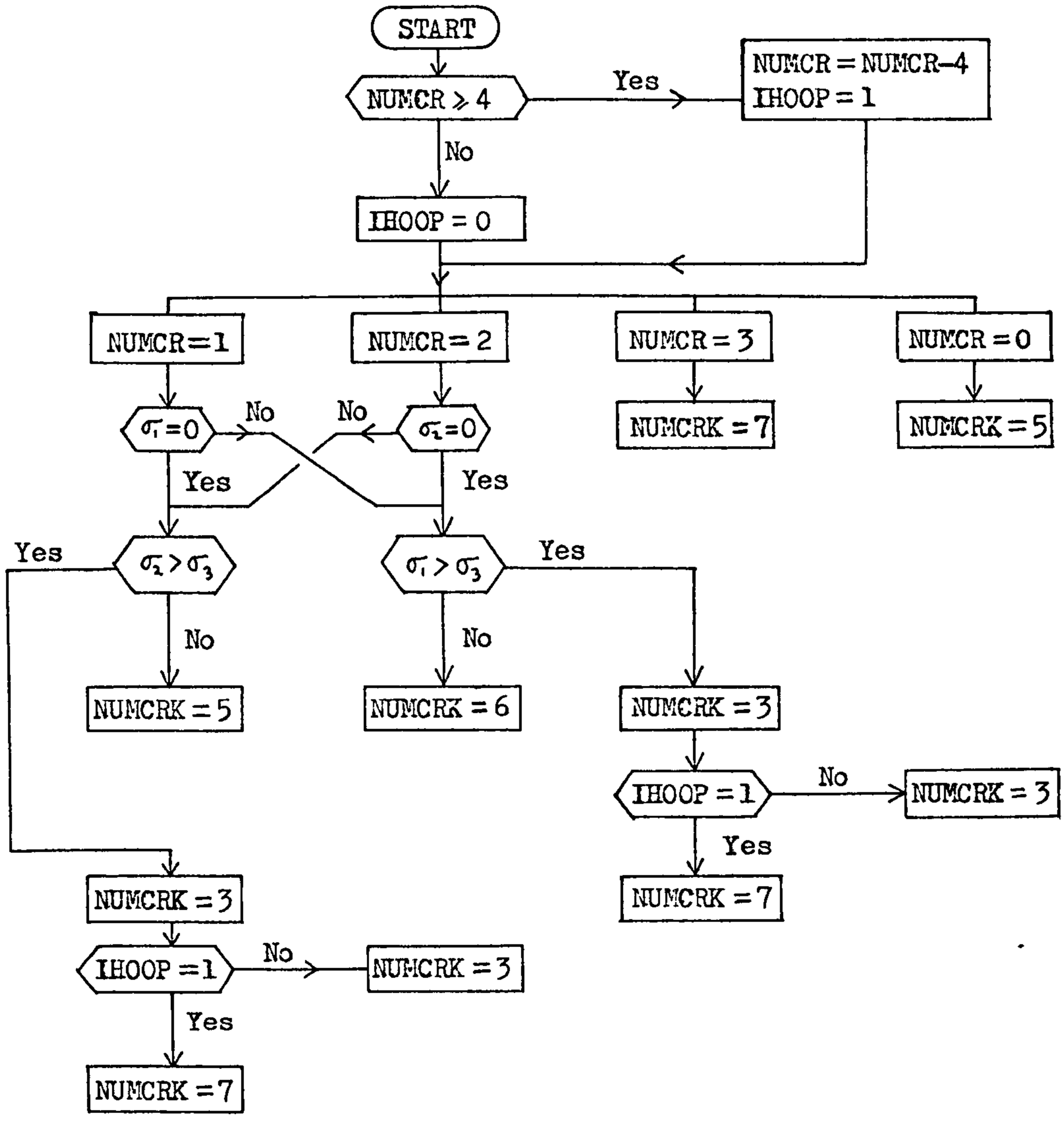

FIGURE 6.5 DETERMINATION OF NEW CRACK STATUS WHEN $f > \tau_u^2$, REQUIRING AN ADDITIONAL CRACK.

IPEL is a flag used to record the status of the grout at the end of the previous load increment. Table 6.2 indicates the four possible states.

IPEL	1	2	3	4
Grout state	Elastic	Plastic	Cracked	Crushed

TABLE 6.2 CODE USED TO INDICATE THE PHYSICAL STATE OF THE GROUT.

The algorithm is divided up into a number of stages which are given below:-

1. Let (N - 1) and N be the previous and current load increments respectively. The corresponding strain components are denoted by ϵ_{ij}^{N-1} and ϵ_{ij}^{N} and at the beginning of the Nth load increment, the incremental strains are calculated as

$$d\epsilon_{ij} = \epsilon_{ij}^{N} - \epsilon_{ij}^{N-1} \qquad (6.41)$$

2.(a) If IPEL = 1, it is assumed that the behaviour is still elastic and the trial stress increments are calculated from the elastic stress-strain law

$$\{d\sigma\} = [D]_e \{d\epsilon\} \qquad (6.42)$$

where $[D]_e$ is the elastic stress-strain matrix.

(b) If IPEL = 2, move to step (4b), and preset the ratio R = 0, as there is no elastic component of stress.

(c) If IPEL = 3, then $\{d\epsilon\}$ is subdivided into ten subincrements and the cracked $[D]_c$ matrix is calculated. The stress increments can then be found and further cracks formed if necessary on succeeding subincrements.

(d) If IPEL = 4, the stresses are held constant and the $[D]_e$ matrix is factored down by a suitable constant to make it effectively zero.

3. Calculate the total stresses

$$\sigma_{ij} = \sigma_{ij}^{N} + d\sigma_{ij} \qquad (6.43)$$

4. Check the current total stresses to determine whether the element has yielded.

(a) If $f(\sigma_{ij}) - \tau^2 \leq 0$, the element is under elastic loading. In this case, the elastic material matrix is used during the stiffness assemblage stage, and the incremental stresses calculated in equation (6.43) are correct.

(b) If $f(\sigma_{ij}) - \tau^2 > 0$, the element is under plastic loading. Set IPEL = 2. In this case, the elastic portion of the stress increment is found by finding the stress needed to just meet the loading surface, as follows

$$f(\sigma_{ij}^{N} + R.d\sigma_{ij}) - \tau^2 = 0 \qquad (6.44)$$

By substituting $\sigma_{ij}^{N} + R.d\sigma_{ij}$ for the stress in the loading function and setting this equal to τ^2, a quadratic equation in R is formed. This is solved as follows, to find R which is the fraction of the stress increment in the elastic state.

$$R = \frac{-B \pm \sqrt{B^2 - AC}}{A} \qquad (6.45)$$

where

$$A = (d\sigma_{ij}.d\sigma_{ij}/2 - d\sigma_{mm}^2/6) + n.d\sigma_{mm}^2 \qquad (6.46)$$

$$B = (\sigma_{ij}^{N}.d\sigma_{ij}/2 - \sigma_{mm}^{N}d\sigma_{nn}/6) + n.\sigma_{mm}^{N}d\sigma_{nn} + \frac{d\sigma_{mm}}{6}(\beta + \alpha\tau^2)$$

$$C = (\sigma_{ij}^{N}.\sigma_{ij}^{N}/2 - \sigma_{nn}^{N^2}/6) + n.\sigma_{mm}^{N^2} + \frac{\sigma_{mm}^{N}}{3}(\beta + \alpha\tau^2) - \tau^2$$

n = 0 in the compression region, and

n = -1/3 in the tension or tension-compression regions.

Thus, the remaining portion of the incremental strain is

$$d\bar{\epsilon}_{ij} = (1 - R)d\epsilon_{ij} \qquad (6.47)$$

To achieve better numerical accuracy, the plastic strain components ($d\bar{\epsilon}_{ij}$) are further divided into small subincrements and the elastic-plastic stress-strain matrix is formed according to equation (6.20) for each subincrement. Subsequently, the incremental stresses ($d\sigma_{ij}$) are calculated.

5. At the end of the stress calculation stage, the stresses and strains in an element are updated to give

$$\sigma_{ij}^{N+1} = \sigma_{ij}^{N} + d\sigma_{ij} \qquad (6.48)$$

$$\epsilon_{ij}^{N+1} = \epsilon_{ij}^{N} + d\epsilon_{ij}$$

These updated stresses and strains are then stored, along with IPEL, τ, NUMCR and if cracked, the crack angle, ready for the start of the next load increment.

6. Return to step (1) for the next load increment.

Figure 6.6 is a flow diagram of the above procedure.

6.6 Material Parameter Values

Only three basic material parameters need to be input into the computational procedure and these are the initial elastic Young's Modulus and Poisson's Ratio, and the uniaxial compressive strength. The compressive strength (f_c') is obtained from the cube strength results. A typical value is $f_c' = 50$ N/mm^2 and will be the standard value used throughout these tests.

Young's Modulus and Poisson's Ratio have been measured in the elastic range for this particular grout type. The reported results (19) show the moduli to increase with cube strength and so suitable values corresponding

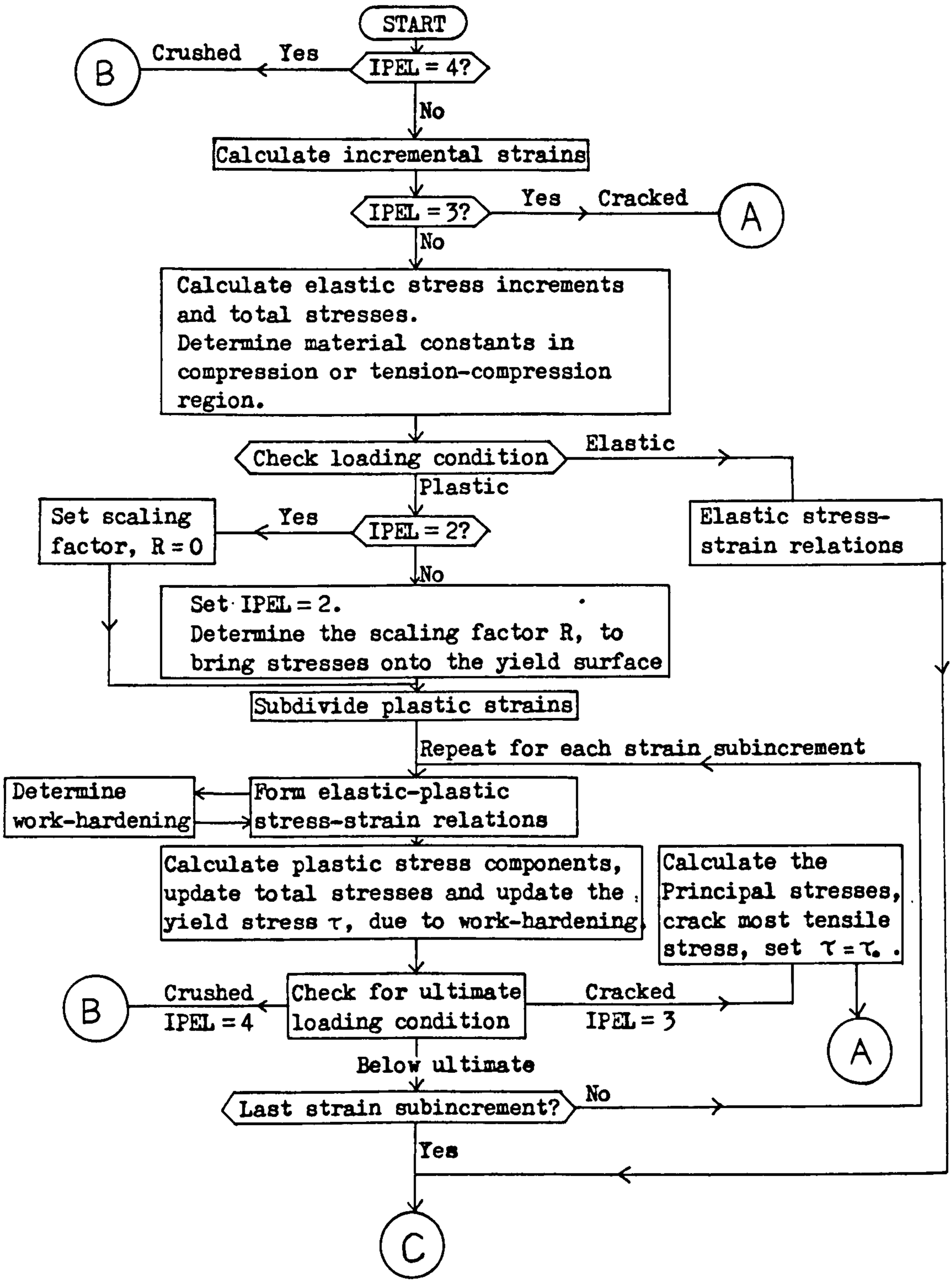

FIGURE 6.6 FLOW DIAGRAM FOR THE COMPUTER PROGRAMME USED TO INCREMENTALLY CALCULATE THE STRESSES AND STRESS-STRAIN RELATIONS OF GROUT FOR GIVEN INCREMENTAL STRAINS.

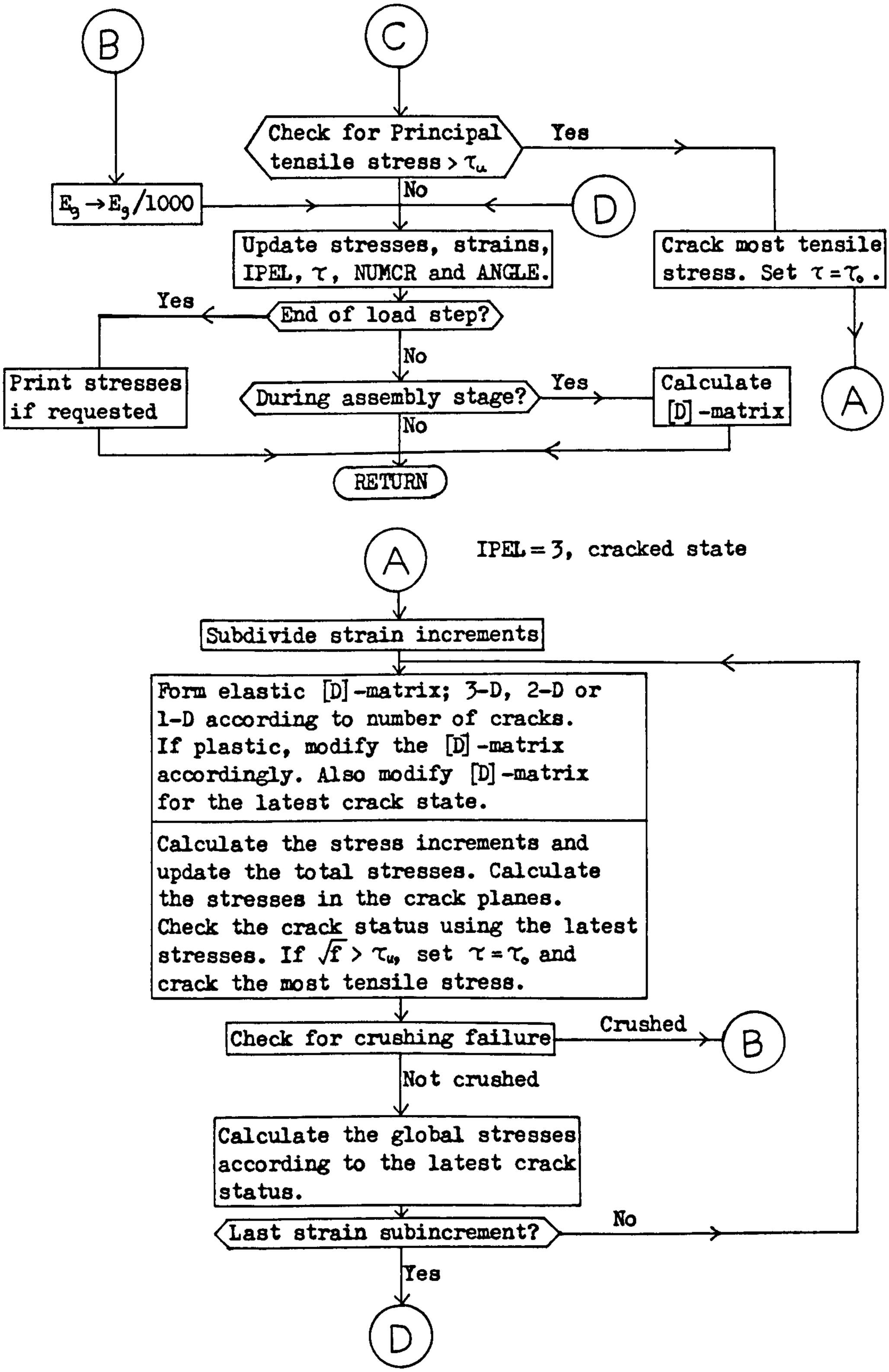

Figure 6.6 continued.

to $f_c' = 50$ N/mm^2 have been chosen. These are $E_g = 1.2 \times 10^4$ N/mm^2 and $\nu_g = 0.25$.

Tensile and biaxial compressive strengths are assumed to be a constant factor of f_c', (Table 6.3). These factors relate to concrete properties but should be similar for grout. The yield strengths are all taken to be 60% of their ultimate values.

The relationship between equivalent stress and plastic strain, which is needed for the calculation of the work-hardening modulus, is input as a series of coordinates, the values of which are given in Figure 6.7 for the compression region. If in the tension or tension-compression regions the equivalent stress is much smaller than that in the compression region, then the equivalent stress is multiplied by $\tau_o^{COMP} / \tau_o^{TEN}$ in order to make it compatible.

Quantity	Relation	Value (N/mm^2)
f_c'		50.0
f_{bc}'	1.16 f_c'	58.0
f_t'	0.09 f_c'	4.5
f_c	0.60 f_c'	30.0
f_{bc}	0.60 f_{bc}'	34.8
f_t	0.60 f_t'	2.7

Quantity	Value	
	Ten/Comp	Comp/Comp
τ_o	3.67 N/mm^2	14.88 N/mm^2
τ_u	6.12 "	24.80 "
A_o	13.65 "	7.85 "
A_u	22.75 "	13.09 "
α	0.3794 mm^3/N	0.0133 mm^3/N
β	8.54 N/mm^2	4.9025 N/mm^2

TABLE 6.3 MATERIAL CONSTANTS DERIVED FROM THE CUBE CRUSHING STRENGTH (f_c') OF THE GROUT.

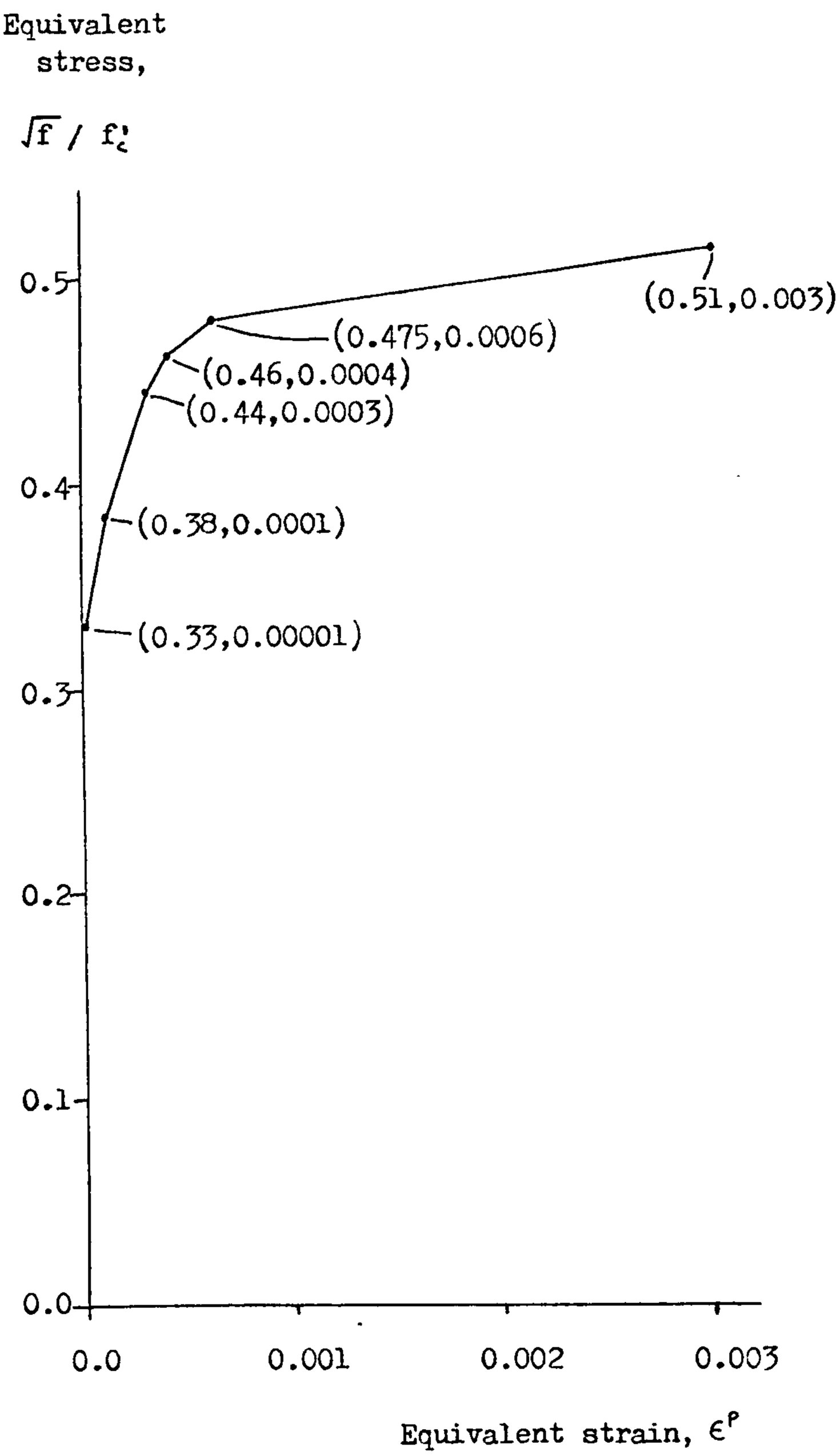

FIGURE 6.7 COORDINATES FOR THE EQUIVALENT STRESS-STRAIN CURVE.

CHAPTER 7

RESULTS OF THE FINITE ELEMENT ANALYSES

7.1 Detailed Shear Key Analysis

7.1.1 The Finite Element Model

The basic finite element mesh used to study the behaviour around a single pair of shear keys was given in Figure 4.5 and the arrangement of elements around the pile key (the sleeve key is similar) is shown in more detail in Figure 7.1. The lower side of the pile key is represented by a coarser element arrangement as the grout/key interface will open up on this side, leading to zero bond stresses. Therefore, no friction-gap elements are needed on the lower face. On the top face, however, the key bears against the grout causing high compressive stresses. In order to obtain a reasonably accurate representation of the key/grout interaction, four two-node-pair friction-gap elements are used to model the upper side of the shear key. Four three-node triangular constant strain elements are used for the top sector of the shear key. These elements can only provide an approximation of the large rates of change of stress in this area, but have nevertheless proved useful in the following analysis.

The friction-gap elements are given the following properties as the weld beads which form the shear keys are smooth.

$k_n = 50\ N/mm^3$ $\qquad$ $k_t = 5\ N/mm^3$

$\mu = 0.4$ $\qquad$ $u_m = 0$

For the friction-gap elements on the main sleeve/grout and pile/grout interfaces, the properties are

$k_n = 50\ N/mm^3$ $\qquad$ $k_t = 5\ N/mm^3$

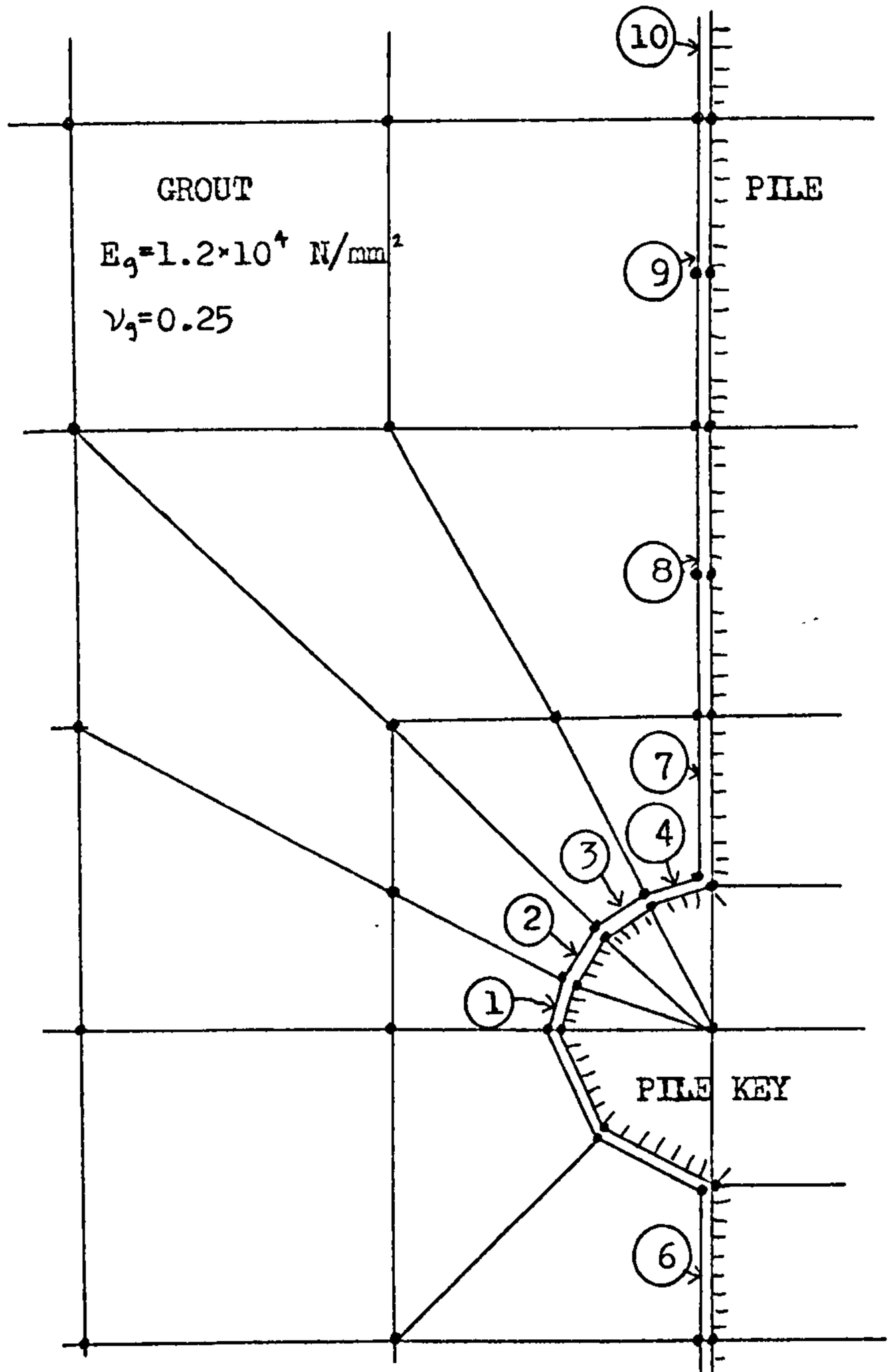

Friction-Gap Element Properties		
Element Nos.	μ	u_m(mm)
1 to 4	0.4	0.0
5,6,10	3.0	0.05
7 to 9	3.0	0.05
	OR 0.2	0.10
	OR 0.2	0.24

KEY

(6) = Friction-Gap element no.

FIGURE 7.1 FINITE ELEMENT ARRANGEMENT AND BOND PROPERTIES AROUND THE PILE SHEAR KEY.

$\mu = 3.0$ $u_m = 0.04$ mm

$n = 1.0$ FAC1 = FAC2 = 1

The grout material around the shear keys is simulated using the Chen model described in Chapter 6. The sleeve is fixed at one end and a tensile load applied to the pile at the same end (Figure 4.5).

Typical results, showing the propagation of cracks from the sleeve shear key, are given in Figure 7.2. In this case, $u_m = 0.1$ mm for friction-gap elements 7 to 9 above the pile key, which provides additional dilation and prevents the initiation of cracks from the pile. The failure load was very low, about 12 kN/radian on the sleeve shear key, with a total pile load of 37 kN/radian. Failure is caused by the diagonal crack bridging the gap between the two shear keys, which then opens allowing the pile to slip free. In a more realistic length of grouted connection this failure would not happen so easily since there would be a greater area of bond friction to resist the crack opening. It is worth noting that shear keys near the end of a grouted connection may have little value as they will fail in this way. Figure 7.3a shows the failure mechanism and Figure 7.3b shows additional restraints applied radially to the sleeve and axially to the grout top in order to resist early failure. This also prevents slip on the sleeve/grout bond and so only the pile key can now be considered.

Figure 7.4 gives the results of this analysis, showing the build up of the effective stress (σ_e), as defined in Chapter 6, during strain-hardening. The grout eventually crushes above the shear key. This effectively limits the ultimate key load to 24.5 kN/radian, which would appear to be low. Experimentally, tests P9/10 had the same radial geometry and key sizes as used for this analysis and so can be used to

Load Step 18

V = 12 kN/rad

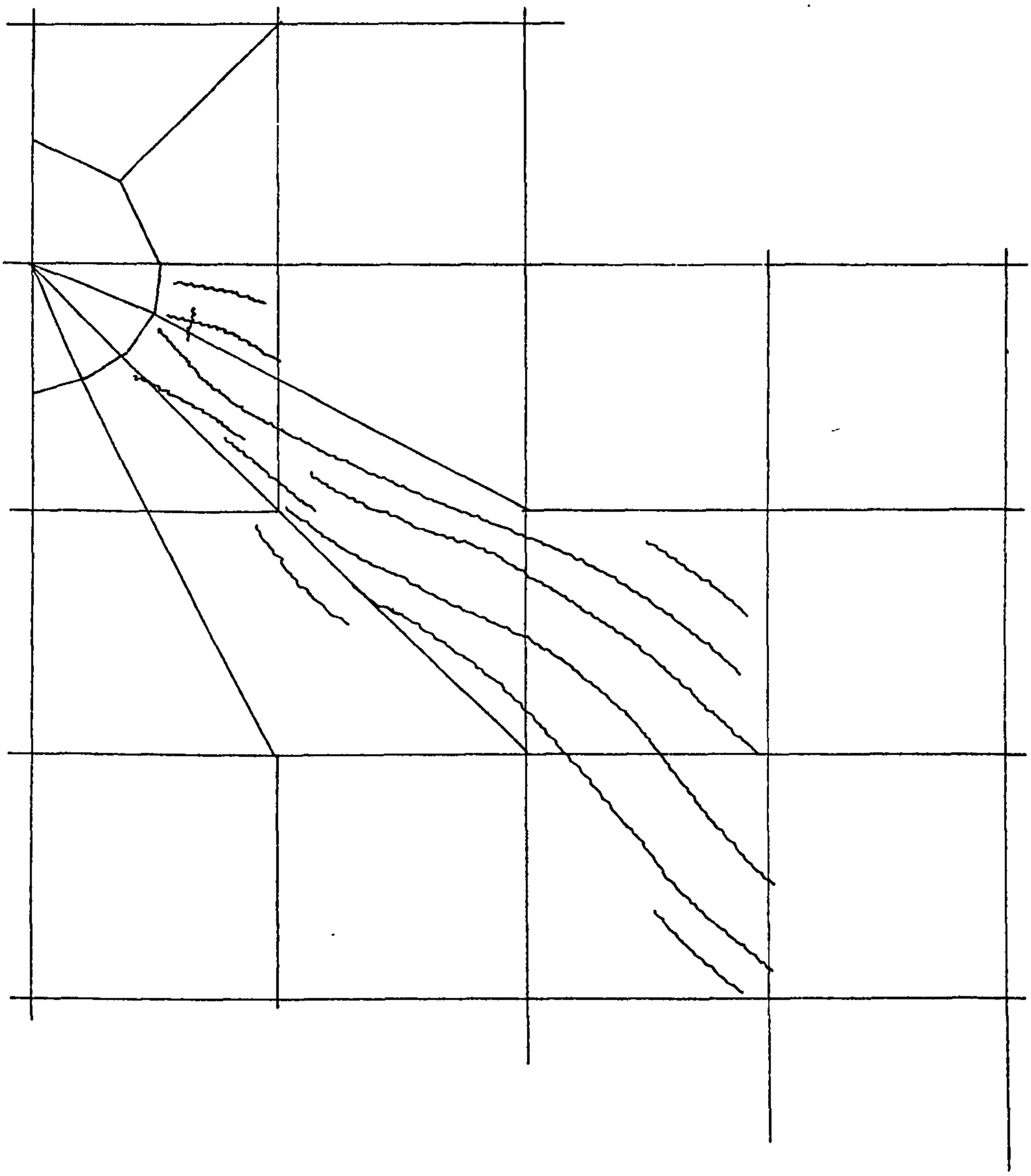

FIGURE 7.2 CRACK PATTERN PRODUCED AROUND THE SLEEVE KEY.

u_m = 0.1 mm ABOVE THE PILE KEY.

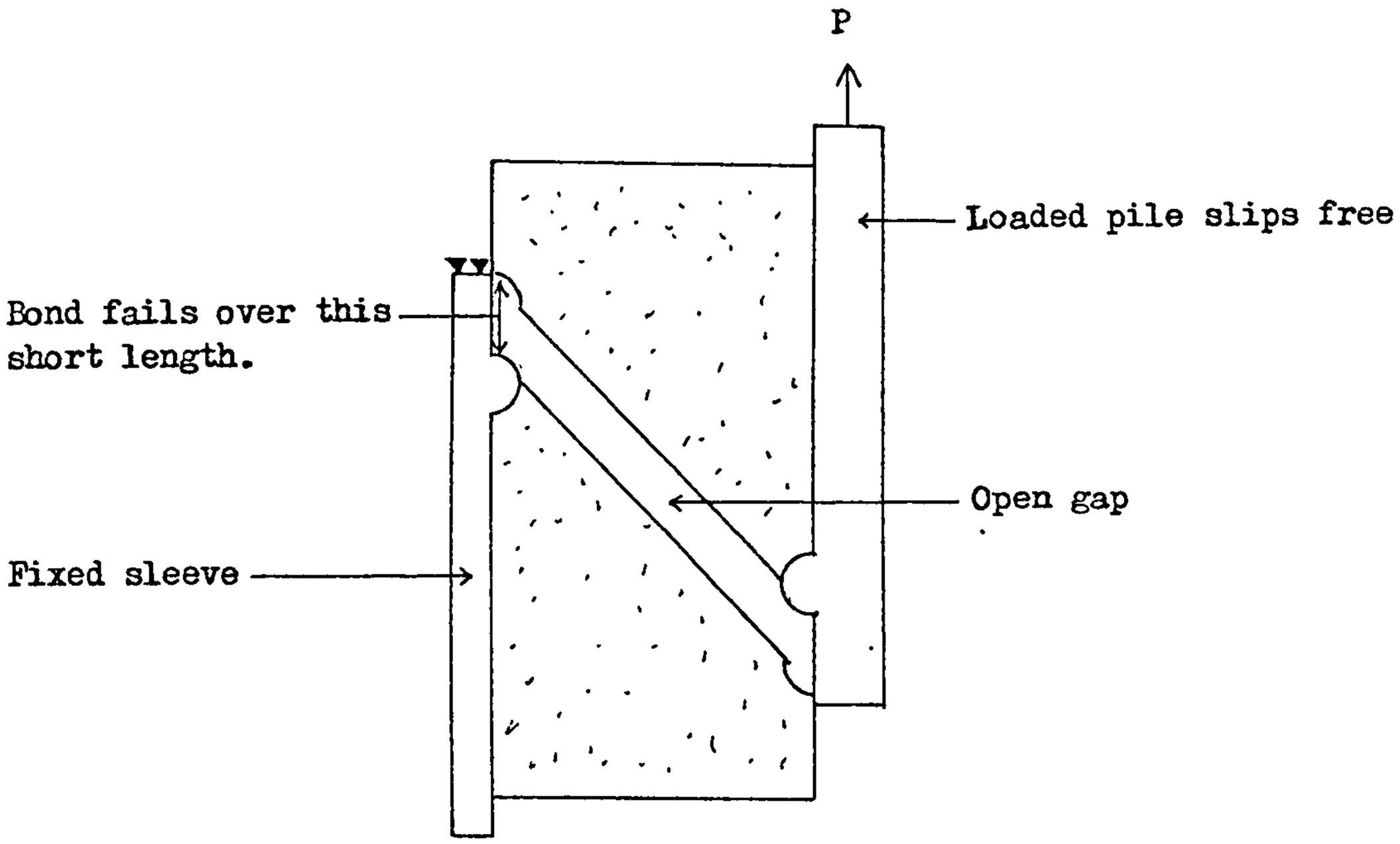

FIGURE 7.3a BASIC FAILURE MECHANISM WHEN SHEAR KEYS ARE CLOSE TO THE END OF THE CONNECTION.

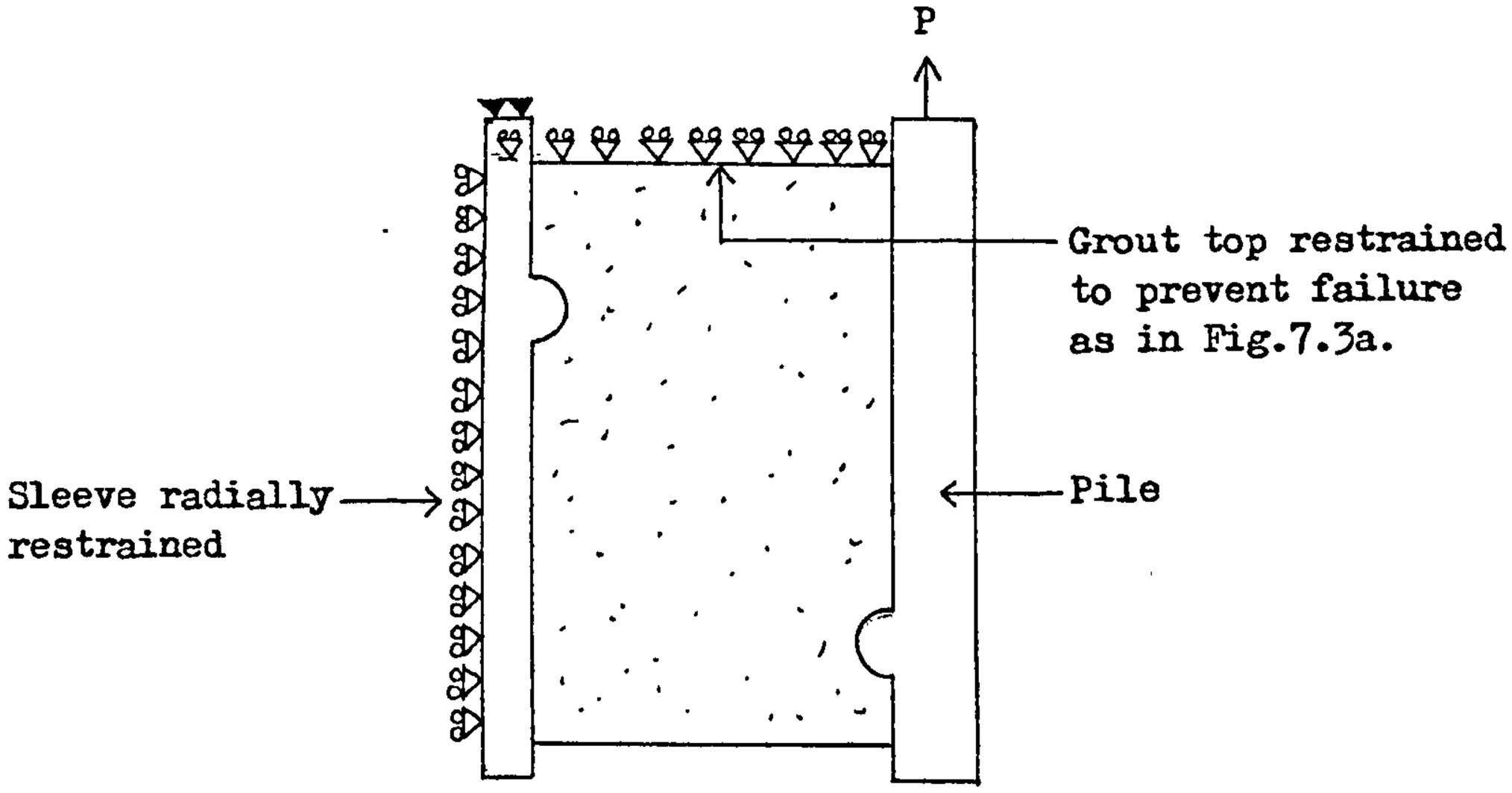

FIGURE 7.3b ADDITIONAL RESTRAINTS USED TO PREVENT FAILURE BEING CAUSED BY THE SHORT LENGTH OF GROUT. SLIP IS CONFINED TO THE PILE/GROUT BOND.

Load step 42

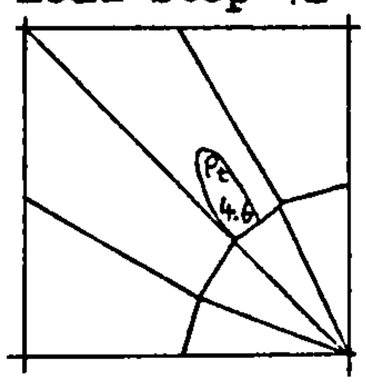

Load step 48

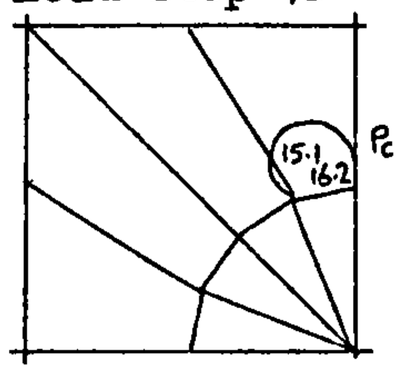

Load step 54

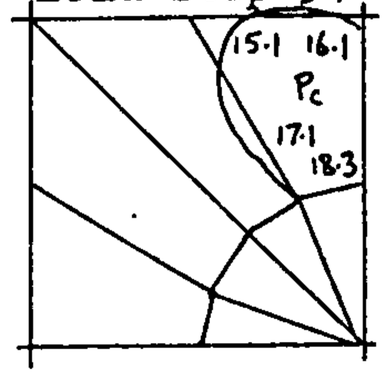

Load step 60

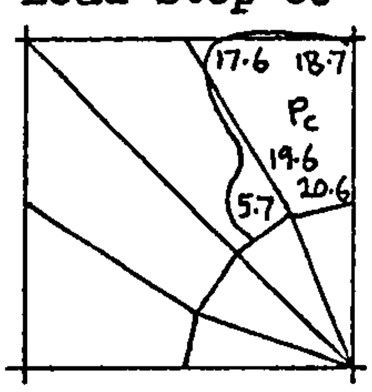

Load step 66

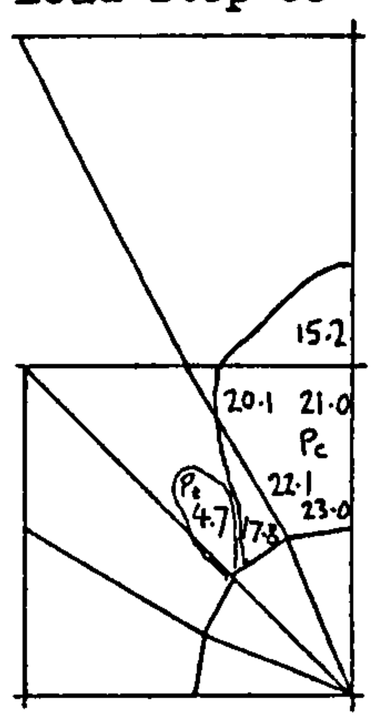

Load step 72

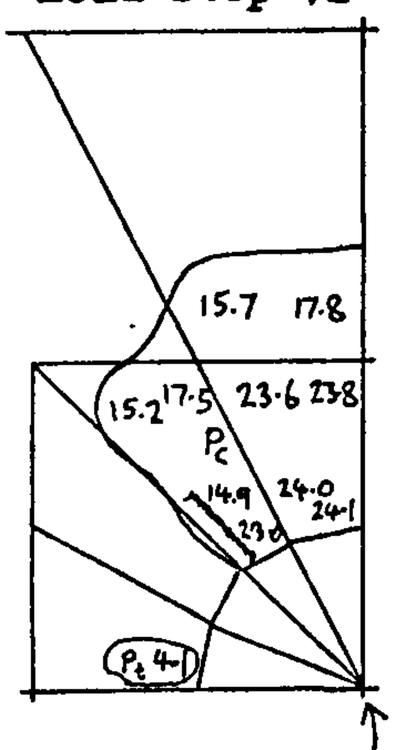

As the key limits slip, tensile stresses build up and cause cracking.

Load step 78 V = 24.5 kN/rad

slip = 1.27 mm V_R = 12.4 kN/rad

KEY

Numbers give the Effective Stress, $\sigma_e = \sqrt{f}$, at the Gauss Points.

P_t = ten/comp zone } Grout in
P_c = comp zone } plastic state

//// Crushed

—— Cracks

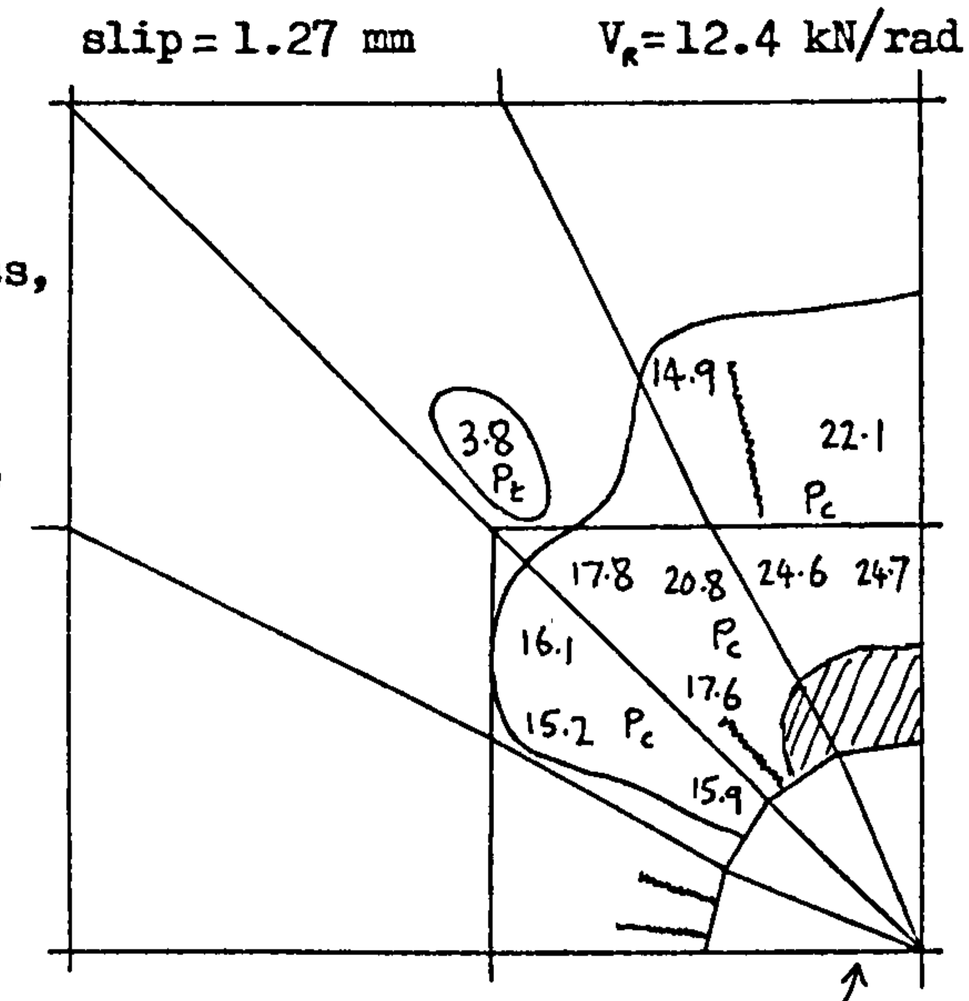

As crushing begins, the compressive zone spreads around the key.

FIGURE 7.4 BUILD UP OF STRESSES AROUND THE PILE KEY WHEN THE SLEEVE AND GROUT TOP ARE RESTRAINED. u_m = 0.05 mm ON THE MAIN BOND SURFACES.

compare the key loads. These tests gave a load per shear key of 90 kN/ radian, but this includes any bond friction occurring between the keys. Even if half the load is taken by bond friction, this would leave 45 kN/ radian as a maximum key load, which is nearly double the load achieved in the analysis. A possible reason for this discrepancy is the short length of the connection analysed. It is known that for connections with an $\ell/d_p < 2$, the strength is significantly reduced and as the analysis used an ℓ/d_p of only 0.12, this could fully explain the weakening. Another possibility relates to what happens when the grout begins to crush. Specimens cut open and examined after failure have shown that the crushed grout, which is a fine powder, flows into the gap between the grout and the pile, (as the bond will have opened). This results in increased confinement of the grout above the shear key and so a higher stress will be required in the grout before further crushing takes place. Hence, the ultimate key load will be significantly higher than that needed for the initial crush.

This kind of phenomena has also been observed in experimental and analytical work on pull-out strengths of form-fit anchors in concrete (49). The form-fit anchor is subject to a local compressive failure at a relatively low load where the form bears against the concrete, just like a shear connector. This represents the ultimate load in the finite element analysis, but because the failed concrete remains partly confined, the anchor can still take substantially greater loads by means of frictional bond, acting in the same way as an expansion anchor fastening.

To simulate the effect of the crushed grout filling the gap on the bond surface, in the case of the shear keys, the value of u_m can be increased on the compressed side of the shear keys. Specimens examined after failure showed this layer of crushed grout to be about 0.2 mm thick

and so a value of $u_m = 0.24$ mm is used. Here, u_m includes the standard roughness of 0.04 mm. This increased roughness is applied to friction-gap elements 7 to 9 in Figure 7.1. The coefficient of friction is reduced to 0.2 on these elements to prevent the high normal bond stresses allowing excessive shear bond stresses.

The results of this analysis (Figure 7.5) give a maximum key load increased to 28.2 kN/radian. Figure 7.6 shows the principal stresses and their directions above the pile key at ultimate load for both $u_m = 0.05$ mm and 0.24 mm above the pile key. From this figure, it can be seen that increasing u_m increases the radial grout stress, which in turn allows a greater axial stress before crushing occurs. It is also noted that just above the key, the radial stress suddenly reduces because the grout is slipping around the shear key. This significantly limits the grout confinement above the shear key and must limit the ultimate load. It is possible that if the shear keys were roughened, there may be less movement, resulting in greater strength. It may also be possible to increase the grout confinement by increasing the surface roughness of the tubulars either side of the shear keys, which would increase the dilation effect when slip occurs.

7.1.2 Loads on the Shear Keys

The loads on a shear key are calculated from the bond stresses given by the friction-gap elements around the key. Figure 7.7 shows the stresses applied to the shear key and from this the axial key load V, can be calculated as follows:

Load step 18

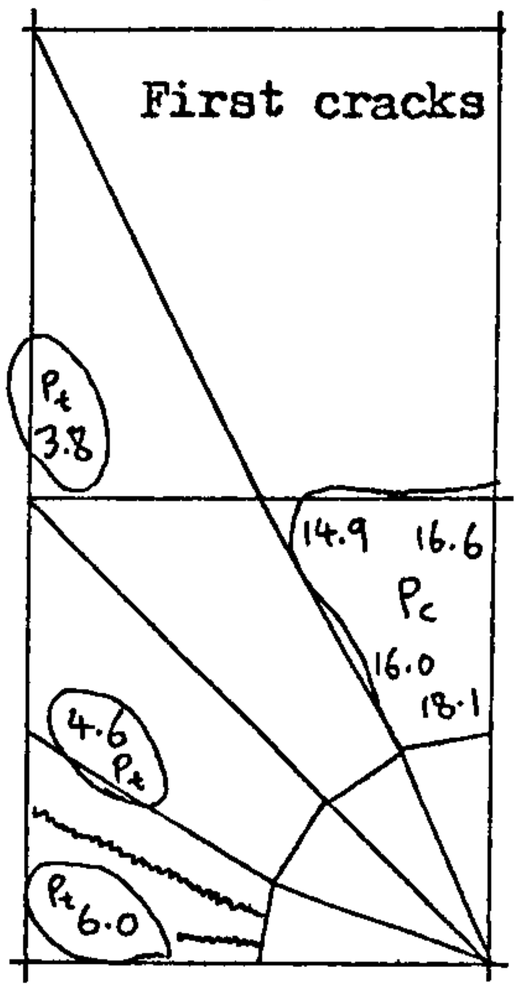

Load step 42

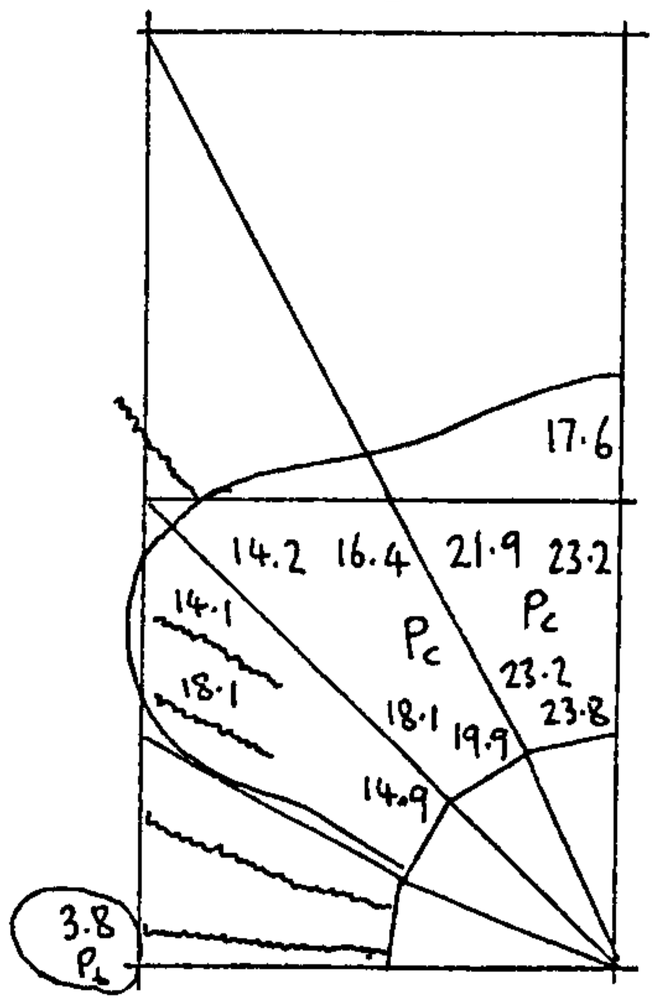

Load step 48

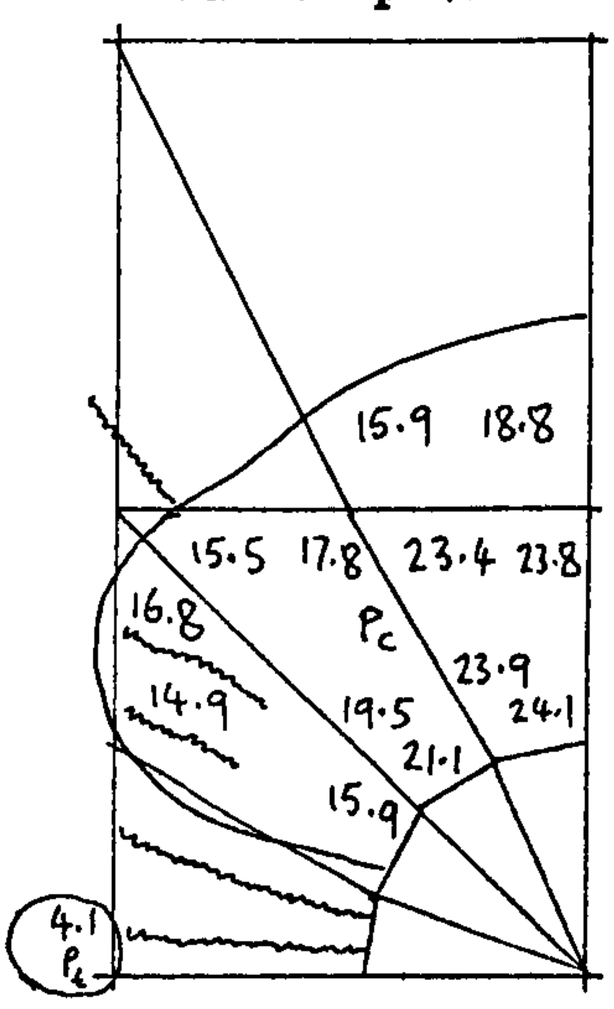

Load step 54

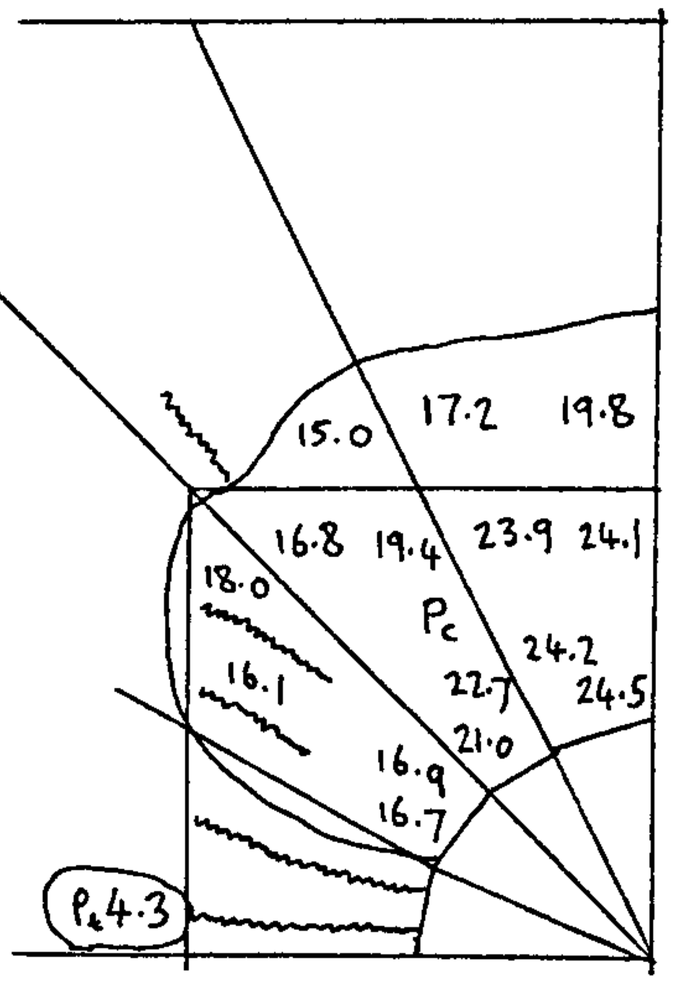

Load step 60

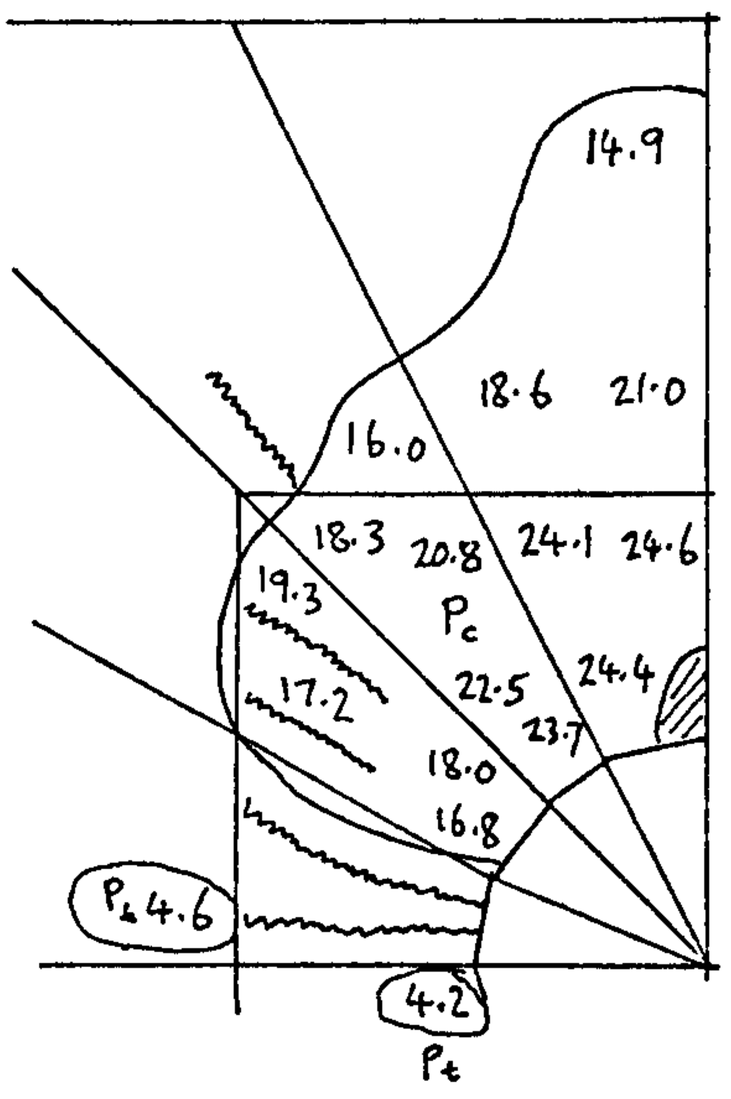

Load step 66

V = 28.2 kN/rad

V_R = 13.4 kN/rad

Slip = 0.48 mm

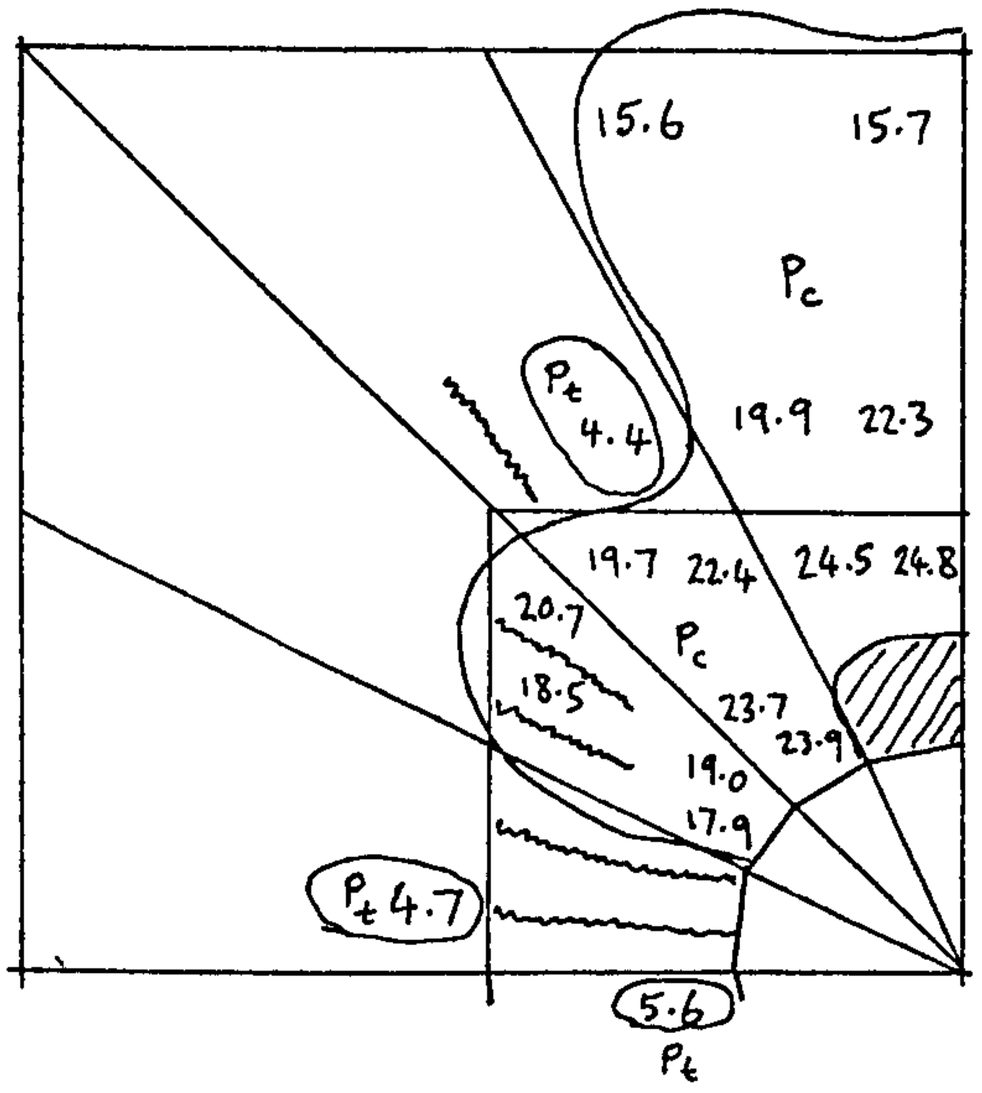

FIGURE 7.5 EFFECTIVE STRESSES (σ_e) AROUND THE PILE KEY WHEN u_m = 0.24 mm ABOVE THE KEY.

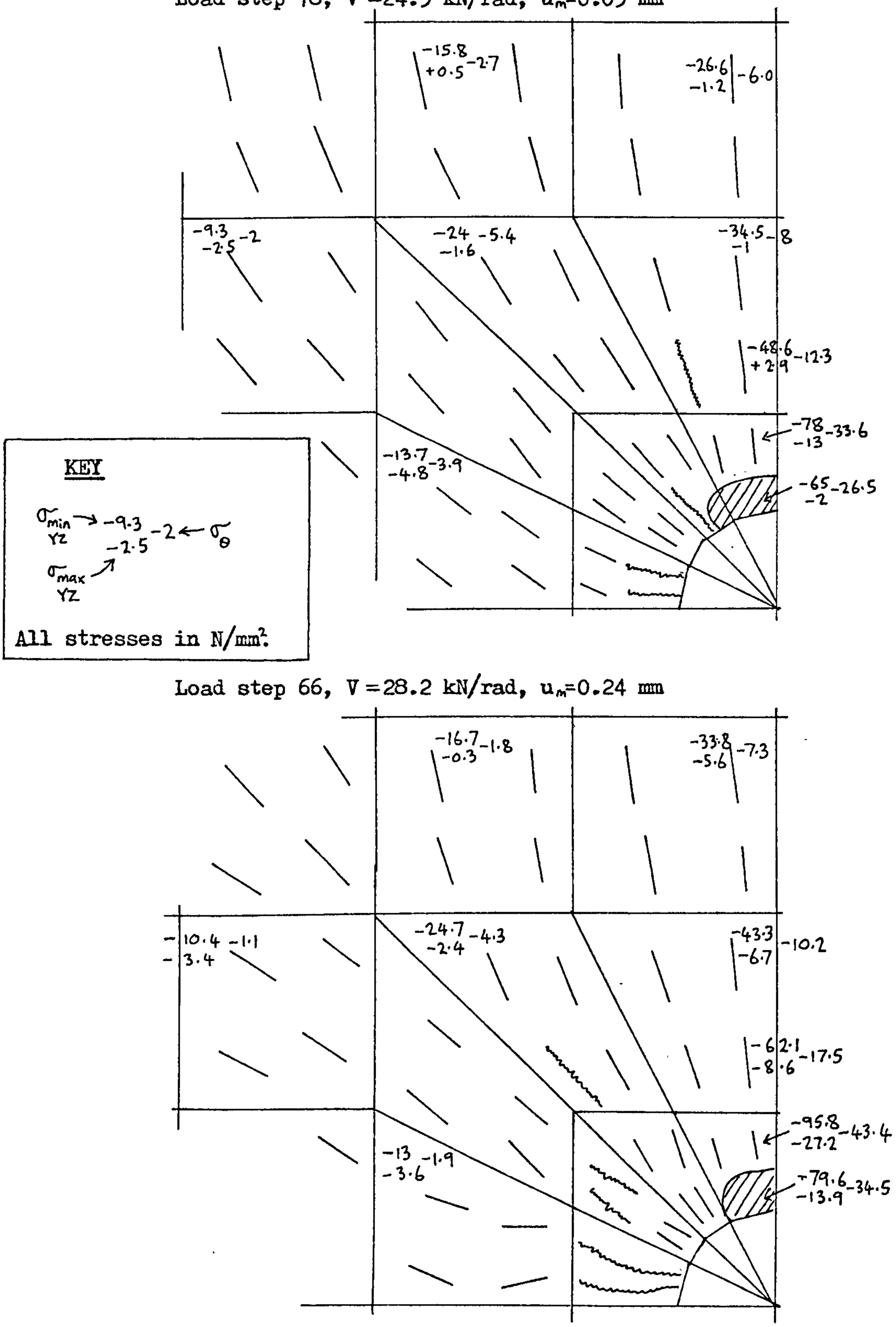

FIGURE 7.6 PRINCIPAL STRESSES AROUND THE SHEAR KEY AT ULTIMATE LOAD.

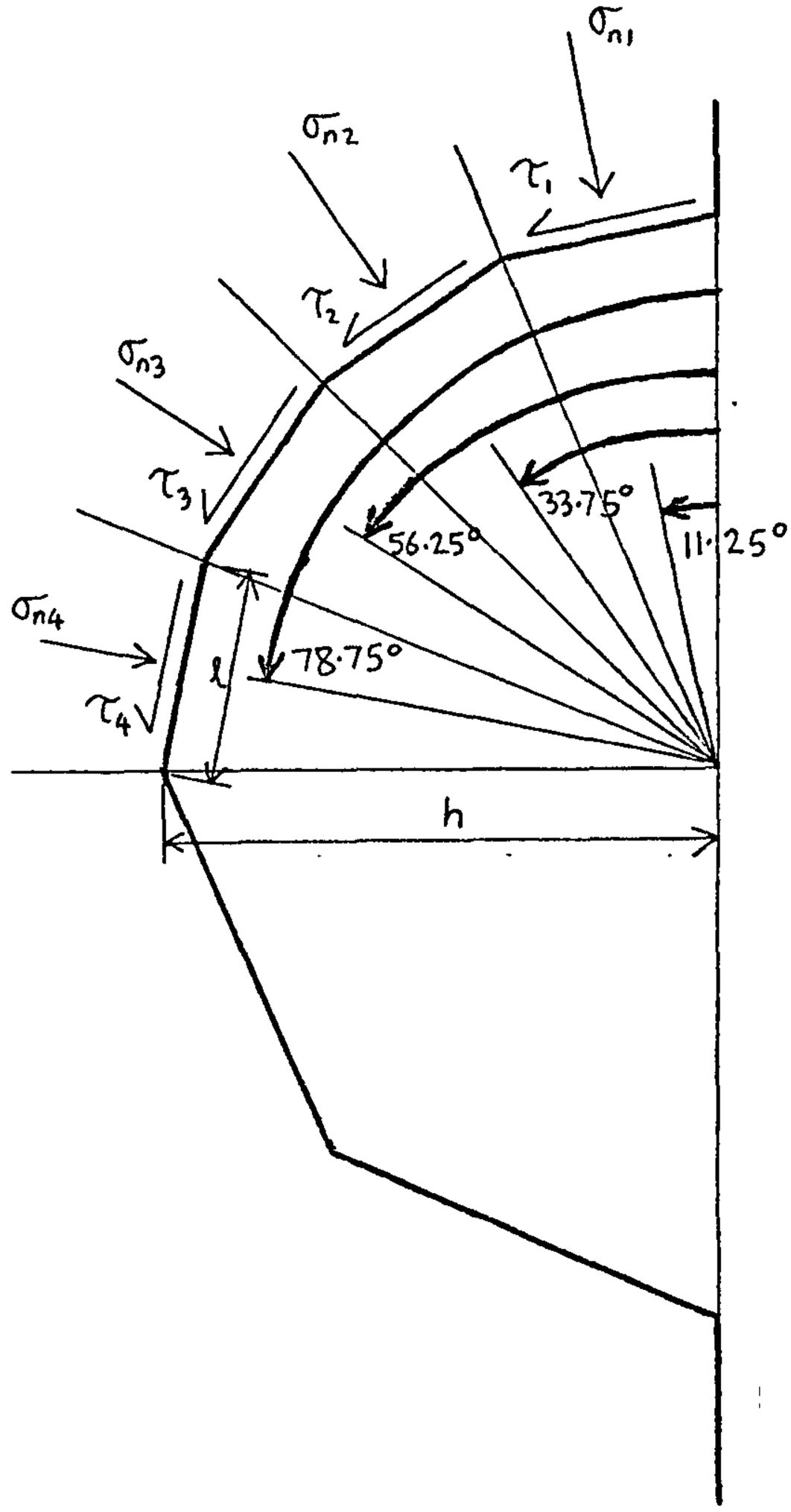

σ_{ni}, τ_i, i = 1 to 4, give the mean bond stresses for each of the four friction-gap elements.

FIGURE 7.7 STRESSES APPLIED TO THE SHEAR KEY.

$$V/\text{rad} = \left\{\sigma_{n1}\cos 11.25^\circ + \sigma_{n2}\cos 33.75^\circ + \sigma_{n3}\cos 56.25^\circ + \sigma_{n4}\cos 78.75^\circ + \tau_1\sin 11.25^\circ + \tau_2\sin 33.75^\circ + \tau_3\sin 56.25^\circ + \tau_4\sin 78.75^\circ\right\} \ell R$$

where $\ell = 2.h.\sin 11.25^\circ$, (7.1)

h = key upstand and

R = mean radius, i.e. inner sleeve radius less h/2, or outer pile radius plus h/2.

The radial force on the shear key V_R, is given by

$$V_R/\text{rad} = \left\{\sigma_{n1}\sin 11.25^\circ + \sigma_{n2}\sin 33.75^\circ + \sigma_{n3}\sin 56.25^\circ + \sigma_{n4}\sin 78.75^\circ - \tau_1\cos 11.25^\circ - \tau_2\cos 33.75^\circ - \tau_3\cos 56.25^\circ - \tau_4\cos 78.75^\circ\right\} \ell R \quad (7.2)$$

The ratio of radial key force to axial key force β, used in the friction-gap element data, is then given by

$$\beta = V_R/V \quad (7.3)$$

Values of V, V_R and β have been calculated for cases with and without the sleeve radially restrained, with various values of u_m and at different load levels. All the results give $\beta = 0.5$, so this is the value used for the friction-gap element shear key data.

A plot of V against bond slip is shown in Figure 7.8, from which it can be seen that the shear key stiffness k_{sc}, represented by the gradient of the line, remains constant over the given load range for any particular key shape. The shear key stiffness can therefore be calculated as follows:

$$k_{sc} = \frac{V/\text{rad}}{R.h.\Delta t} \quad (7.4)$$

Typical results for the pile key give

$$k_{sc} = \frac{28.2 \times 10^3}{255 \times 2.03 \times 1.4} = 38.9 \text{ N/mm}^3$$

All the results approximate to this value, justifying the initial value of $k_{sc} = 37$ N/mm^3 used in the friction-gap element shear key data.

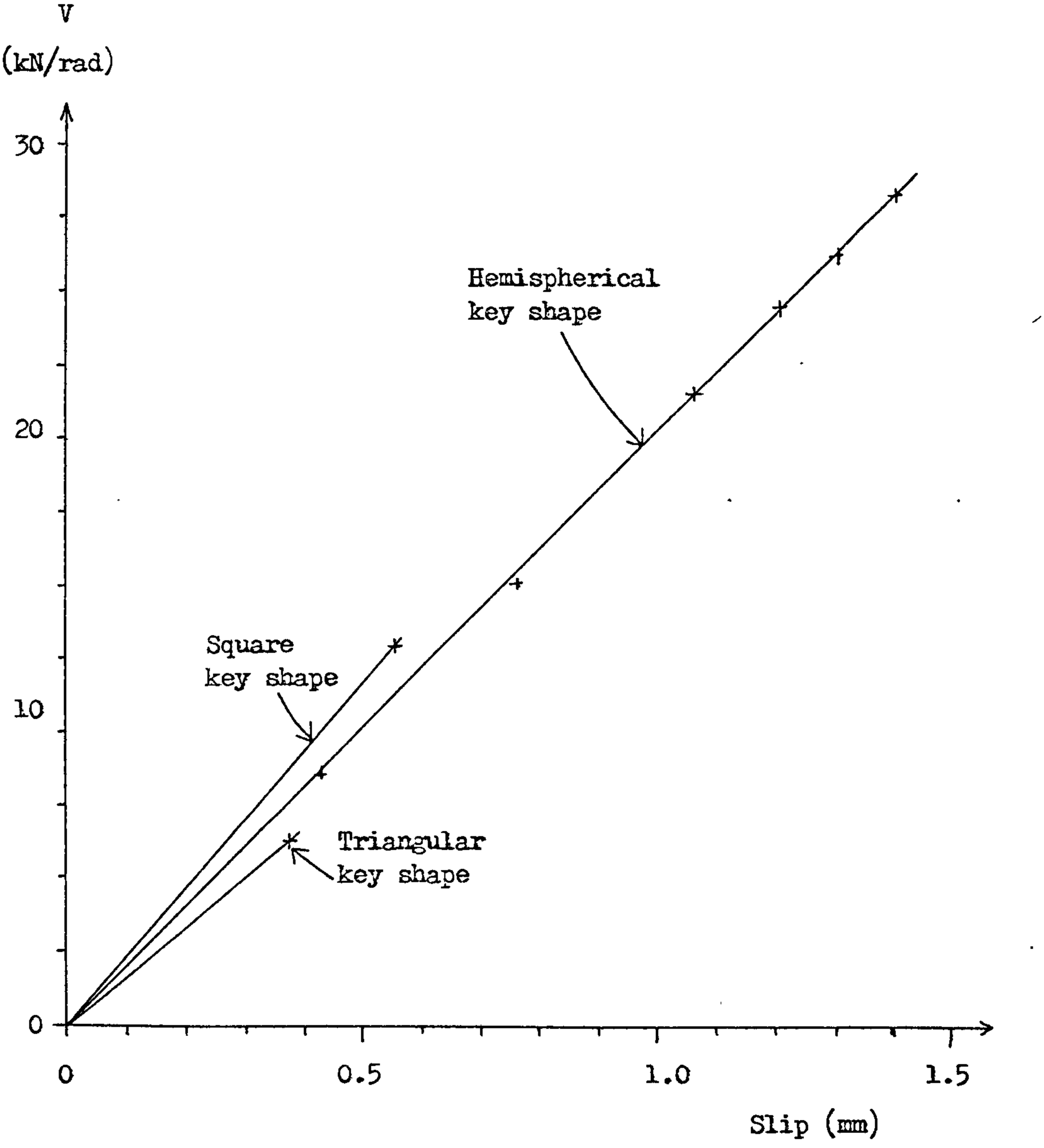

FIGURE 7.8 AXIAL KEY LOAD AGAINST BOND SLIP FROM THE FINITE ELEMENT ANALYSIS RESULTS.

For square or triangular shape shear keys, the stiffness is slightly larger or slightly smaller, respectively.

Figure 7.9 plots the bond stresses around the pile key for various analyses and load levels. From this, it can be seen that the stress distribution remains about constant, justifying the constant ratio between axial and radial shear key forces.

The normal bond stress, although falling off rapidly away from the pile, is still sufficient to make the radial key force large. This must have a substantial weakening effect since it tends to open the bond and reduce the grout confinement. A square shape shear key may be beneficial as this would eliminate the radial component of normal bond stress. Other key shapes are examined in detail in Section 7.1.4.

7.1.3 Bending Effects in the Grout

It is interesting to study the radial displacements in the connection as a whole since these govern the normal bond stresses and follow a distinctive pattern shown schematically in Figure 7.10a. The large radial movements at the ends of the grout can be explained by considering the forces on the grout, which are given in Figure 7.10b. The key forces (V) and bond stresses (τ) exert an anticlockwise bending moment on the grout with a moment arm equal to the grout annulus thickness (t_g). Apart from the radial key forces (V_R), the only other forces able to counter this bending moment are due to the normal bond stresses (σ_n) above the sleeve key and below the pile key. The radial displacements in Figure 7.10a are necessary in order to make σ_n large enough to balance the anticlockwise bending moment. As the moment arm associated with V_R is only equal to t_g in this particular orientation of shear keys and as V_R

KEY

——— u_m=0.24 mm

– – – – – u_m=0.05 mm

—— · —— u_m=0.10 mm

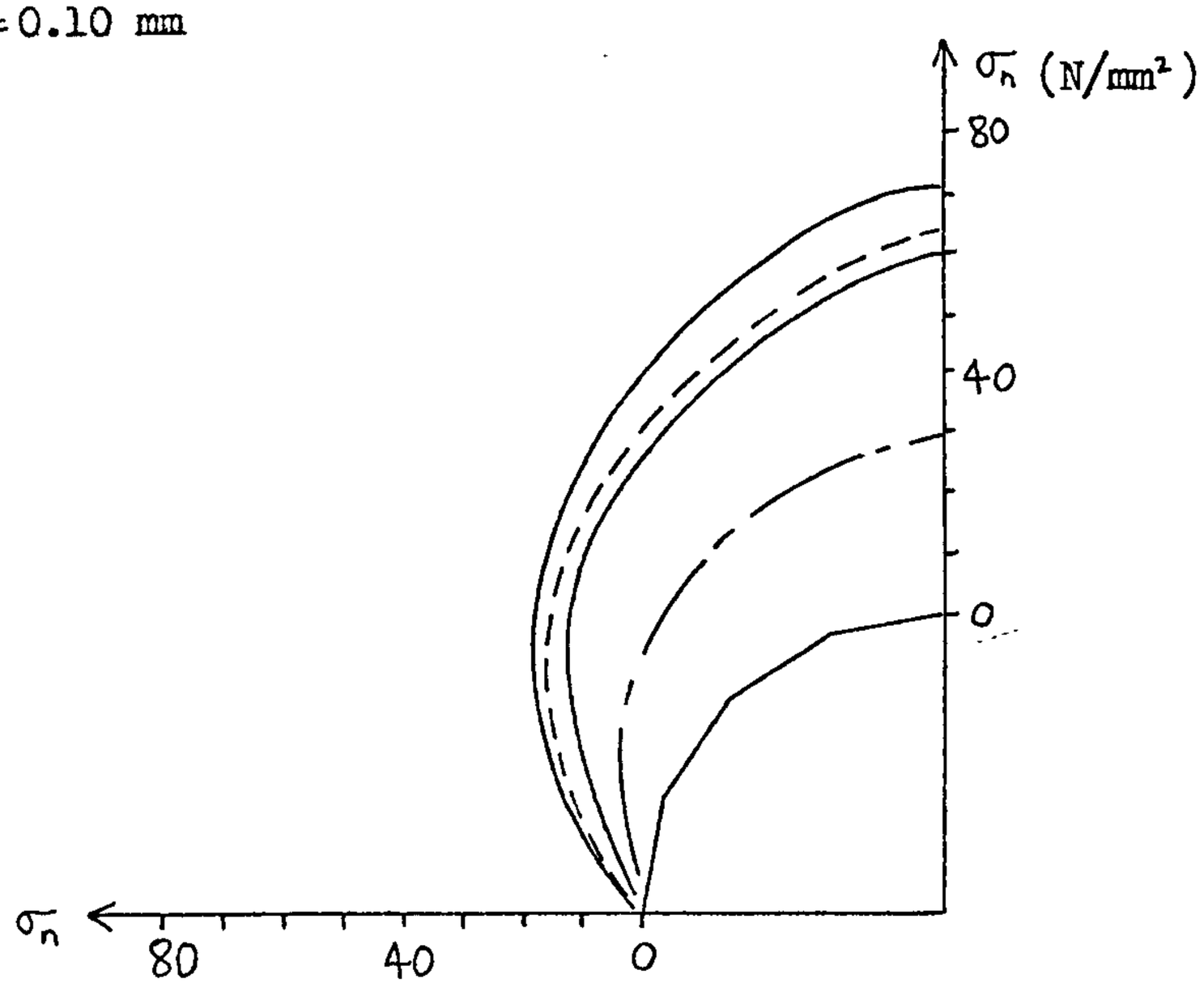

FIGURE 7.9 BOND STRESSES AROUND THE PILE SHEAR KEY.

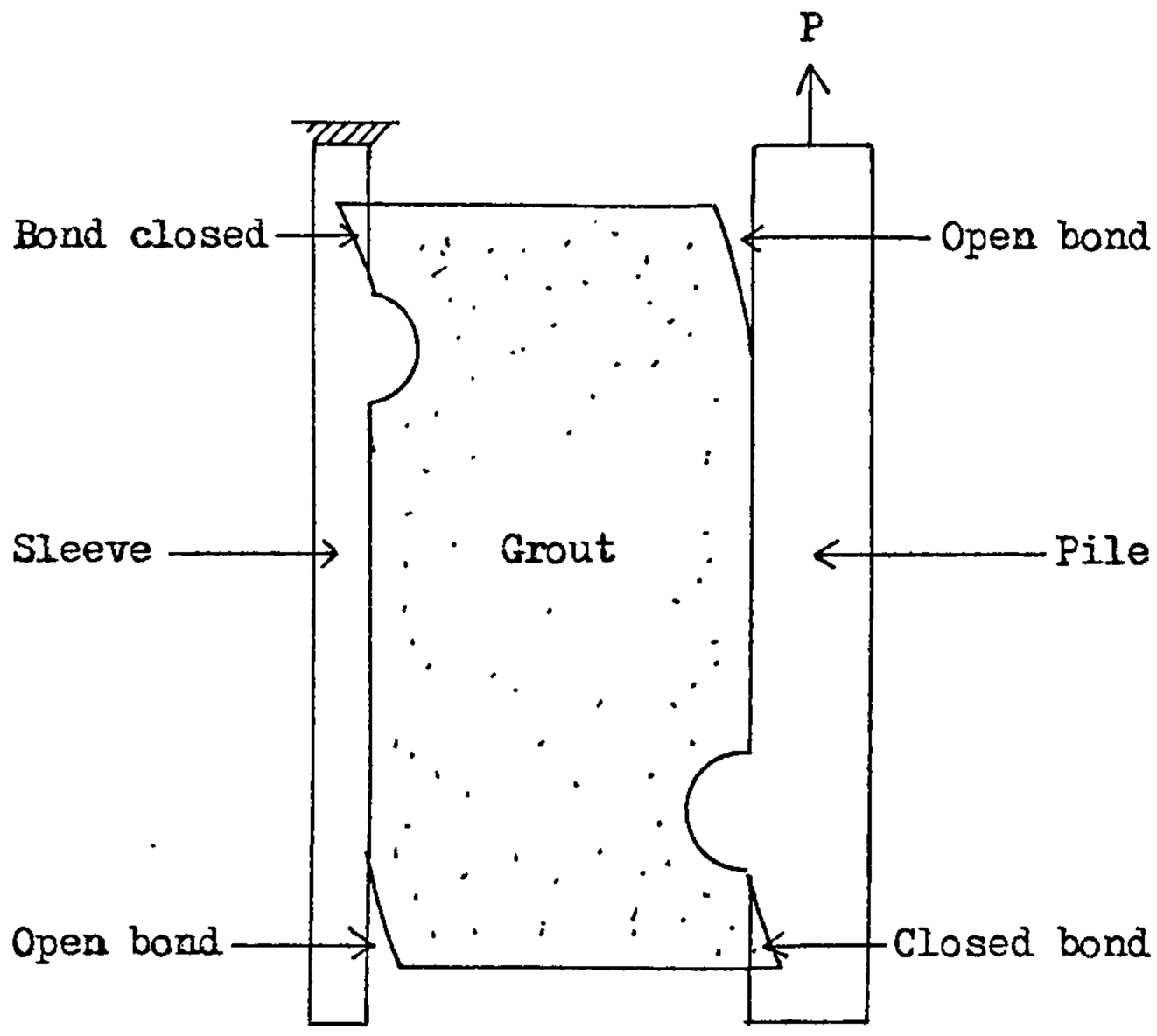

(a)Radial displacements (shown exaggerated) and the bond status.

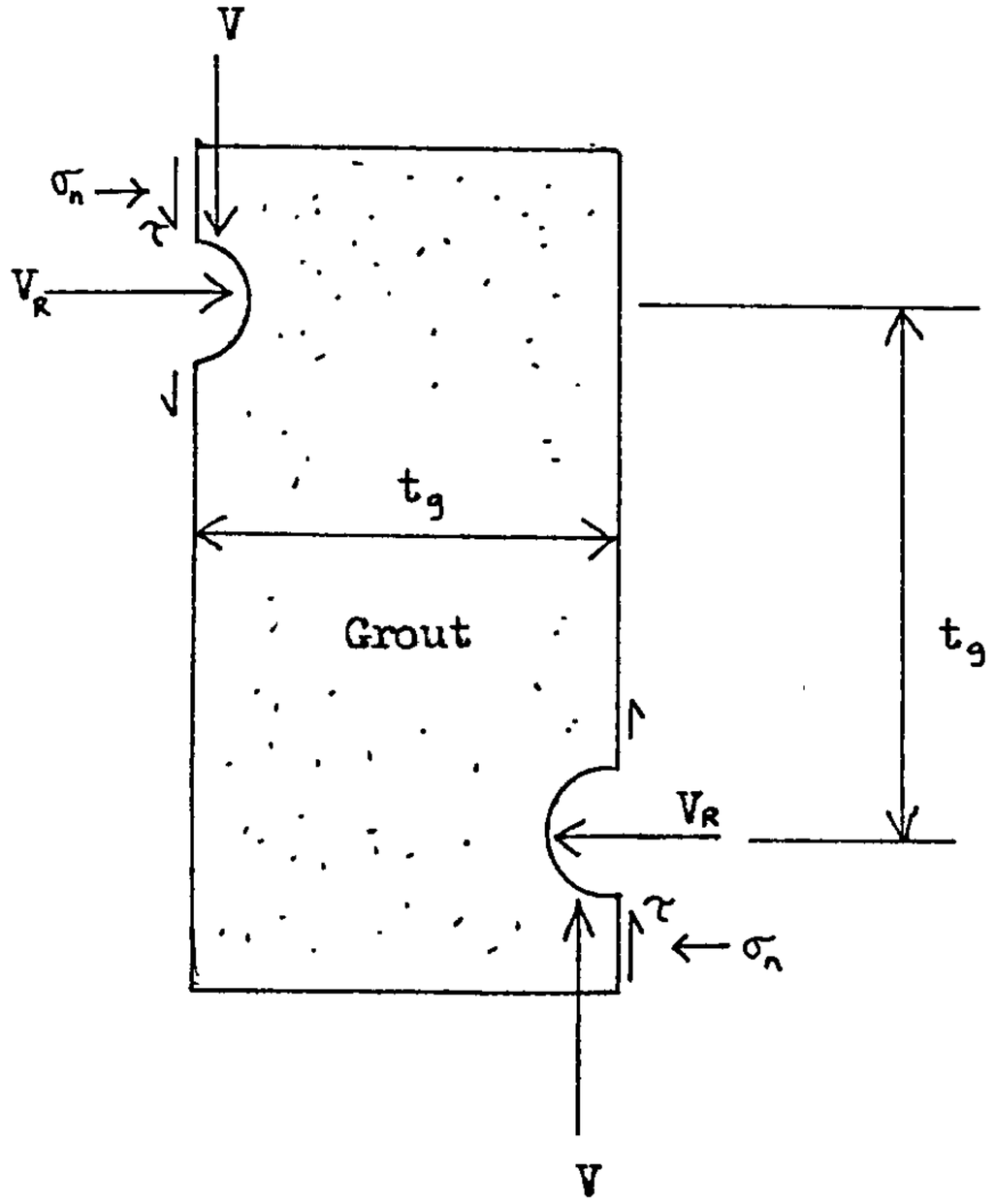

(b)Forces and stresses on the grout.

FIGURE 7.10 BENDING EFFECTS IN THE GROUT.

is only half the magnitude of V, the size of the normal bond stress must become very large as the key force grows. This is especially so with such a short connection because the moment arm for σ_n is very small and there must be a limit to how large σ_n can be before the grout crushes. This explains why such short connections are so weak.

One factor that will limit the ultimate size of the radial load created by the normal bond stress is the void which forms behind the shear key when slipping and crushing occurs. This void is on the same side of the shear key as the normal bond stress and so the length over which σ_n can act will be reduced by the growing length of the void.

7.1.4 Square and Triangular Section Shear Keys

The analysis is easily extended to include square and triangular shape shear keys by adjusting the coordinates of the nodes on the shear key surface. Only the pile key shape is changed because the sleeve and grout top are restrained. The bond surface roughness is set at 0.05 mm for comparison with previous analyses.

For a triangular key shape, the analysis did not proceed very far before becoming unstable. This may be due to an unstable situation arising around the sharp corner of the shear key as the slip increases. Figure 7.11 shows the effective stress contours around the key when V = 6.23 kN/radian. At this load level the grout is still acting linearly. The bond stresses on the shear key surface are virtually constant over the whole width of the key and the values of β and k_{sc} have been calculated as

$$\beta = 0.83 \qquad k_{sc} = 33 \text{ N/mm}^3$$

The radial key force is therefore quite large and would be expected for

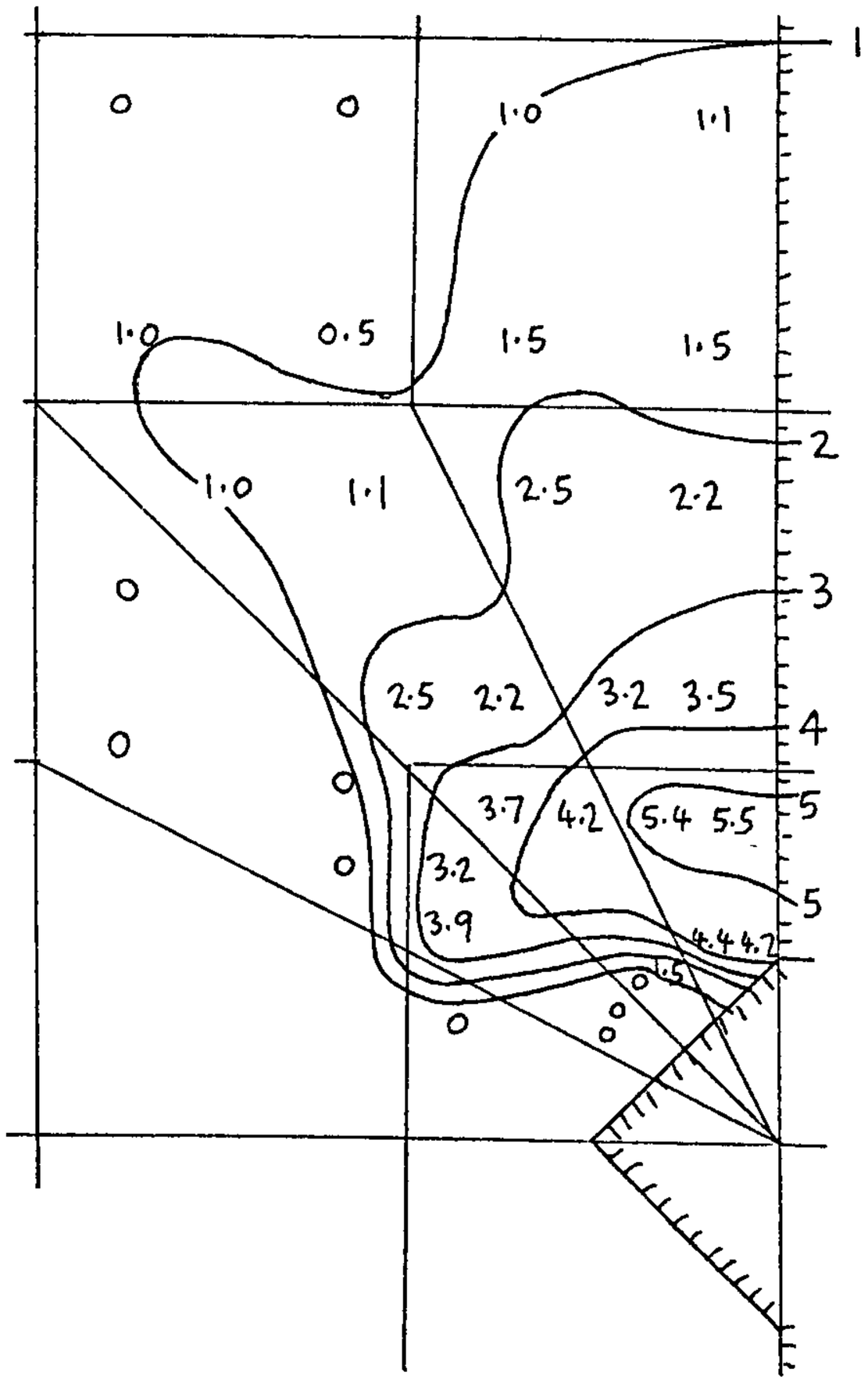

$V = 6.23$ kN/rad

$V_R = 5.14$ kN/rad

FIGURE 7.11 THE EFFECTIVE STRESS (σ_e) DISTRIBUTION AND CONTOURS AROUND A TRIANGULAR SHAPE PILE SHEAR KEY.

this shape of key. This will result in a greater bond opening action than for the normal hemispherical key shape, leading to lower grout confinement and hence to a lower crushing load on the shear keys.

The results of the analysis on a square shape pile key are shown in Figure 7.12. A maximum key load of 12.94 kN/radian is reached before the analysis becomes unstable, but as the grout has not yet crushed at this load level, it is possible that substantially greater loads could be achieved in reality. The instability in the analysis at higher loads is probably due to the high stresses and crack propagation around the sharp corner of the key. The results show a second plane of cracks close to the corner of the key, which is caused by the grout trying to slip past the key. In the final load step, a second crack in this second plane occurs, which results in some earlier cracks in the main crack plane closing. This second plane of cracks will leave a wedge shape of grout above the pile key as cracking propagates with the wedge boundary formed by the crack plane. The main body of grout will then be able to slide over this wedge, easing its passage past the shear key. Tests with hemispherical shape keys have been cut open after failing, revealing these wedges of grout still attached to the shear keys after removal of the grout annulus. The computer did not show these effects when hemispherical keys were used since the loads reached were not great enough to cause this phenomena to occur.

The bond stresses for square keys are dominated by a large normal bond stress distributed evenly across the flat key surface. Calculations of the key parameters give the following:

$$\beta = 0.006 \text{ to } 0.04 \qquad k_{sc} = 44 \text{ N/mm}^3$$

The bond opening should be low, as the radial key force is insignificant

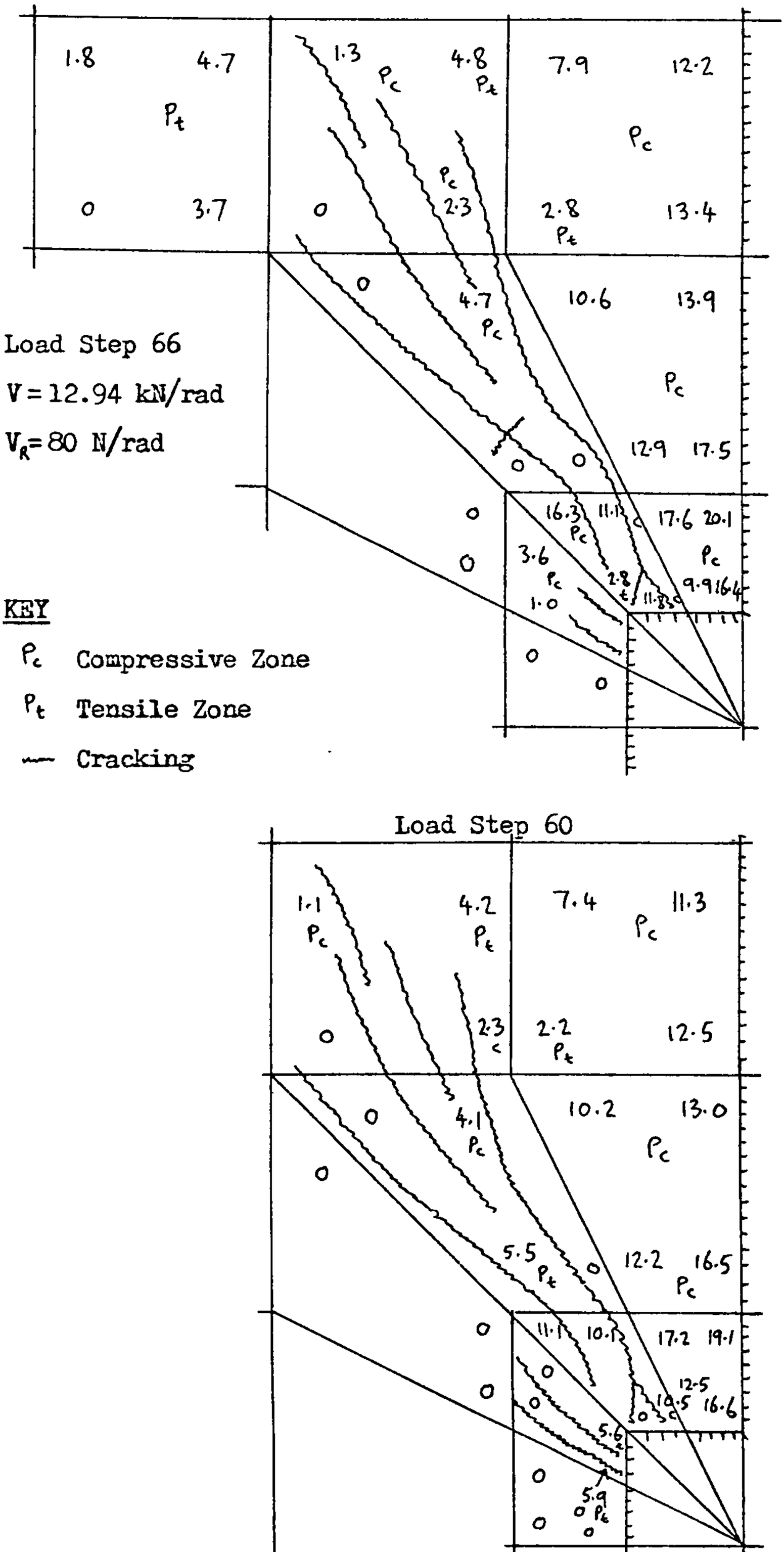

FIGURE 7.12 THE EFFECTIVE STRESS (σ_e) DISTRIBUTION AROUND A SQUARE SHAPE PILE SHEAR KEY. NOTE THAT SOME CRACKS CLOSE IN THE FINAL LOAD STEP, BUT A SECOND CRACK PLANE IS INITIATED.

leading to high grout confinement and a high shear key crushing load. It may therefore be possible to produce stronger grouted connections by using square shape shear keys. This agrees with the findings of the square punch tests reported by Paslay, where high key loads were achieved. This has been reported in Chapter 3.

The radial shear key force has been shown in Section 7.1.3 to play a part in balancing the bending moments in the grout. As this force varies with key shape, the distribution of normal bond stresses must also differ in order to maintain equilibrium. Figure 7.13 shows the normal bond stress distribution along the pile/grout bond for all three key shapes. It can be seen that for a square shape key, the value of σ_n rises dramatically on the compressive side of the key, compensating for the lack of a radial key force. This will result in a high radial compression of the grout above the shear key, which in turn will raise the threshold for crushing. This again indicates that square shear keys should produce the highest bond strengths. In Section 7.3 the effects of key shape on a whole length grouted connection are investigated.

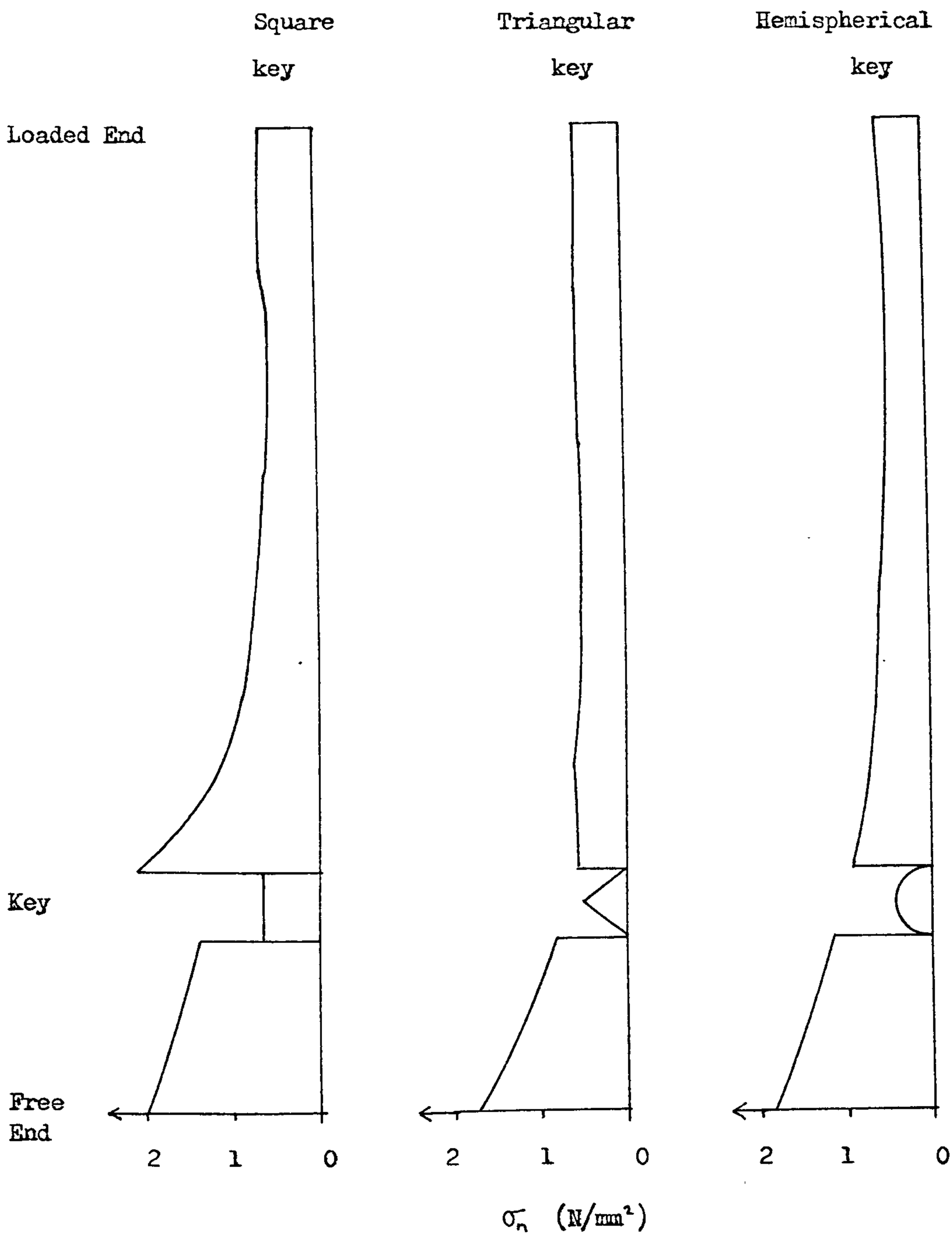

FIGURE 7.13 NORMAL BOND STRESS DISTRIBUTION ALONG THE PILE/GROUT BOND FOR DIFFERENT SHEAR KEY SHAPES.

7.2 Plain Pipe Grouted Connections

Laboratory tested plain pipe grouted connections can be simulated by finite elements using a mesh similar to that shown in Figure 4.4, but without the shear keys or stiffeners.

7.2.1 The Basic Test Case

It was found in early analyses that it is unnecessary to use a nonlinear grout model as the stress concentrations in the grout are too low to cause nonlinear behaviour with the Chen model. The following linear-elastic grout properties are used: $E_g = 1.2 \times 10^4$ N/mm^2 and $\nu_g = 0.25$, which are appropriate for a cube strength of about 50 N/mm^2. Other values, such as $E_g = 0.41 \times 10^4$ N/mm^2 and $\nu_g = 0.12$, corresponding to a cube strength of 15 N/mm^2, have been tried. However, changing the values of the grout material parameters had virtually no effect on the results of the analysis, which seems surprising as the bond strength should be proportional to the square root of cube strength. It would seem that the slip behaviour of the friction-gap elements govern the overall performance of the connection, and so it may be necessary to alter the bond properties of these elements when a lower cube strength is required. For example, the value of u_m could be reduced as the weaker grout would not be able to produce such a large dilation effect.

The bond properties used by the friction-gap elements in this analysis are

$\mu = 3.0$	$k_n = 50$ N/mm^3
$u_m = 0.04$ mm	$k_t = 5$ N/mm^3
$n = 1.0$	$c = 0$

FAC1 = FAC2 = 2.0

The M/N series of tests in the Department of Energy Programme (8) gave the only plain pipe geometry for which there are a large number of results and so this has been chosen for the analysis. Two other geometries with increased and reduced tubular thicknesses are also investigated and the dimensions are given in Table 7.1.

Figure 7.14 shows a plot of the normalised bond stress against total slip for the standard M test obtained from finite element analysis results. Superimposed on this graph are the experimental results from several tests with the same geometry. It can be seen that there is a certain amount of scatter in the experimental results, but this can be largely attributed to the variation in age of the grout. The computer results predict the strength for 31-day grout and it can be seen that this is in reasonable agreement with the experimental results when corrected for age using the factors of Table 2.3.

7.2.2 Effect of Varying the Tubular Thicknesses

Computer results for the extra-thick and extra-thin tubular specimens are plotted in Figure 7.15 with the standard M case for comparison. The ultimate load is considered to be reached when the slip on one surface exceeds 5 mm , and has been previously described in Chapter 4. The finite element ultimate loads are compared against the experimental results and bond formulae in Table 7.2, where the good agreement between these various predictions is evident.

Figure 7.15 also shows this close agreement with the bond formulae and in addition, it is shown that the bond strength is approximately proportional to the sum of the sleeve and pile thicknesses. This effect can only be shown when the sleeve and pile radii are approximately constant since these also influence the bond strength and this is described in

TEST	Sleeve		Pile	
	r	t	r	t
Standard M	254	6	228.6	19.05
Extra thick	268	20	228.6	36.00
Extra thin	252	4	228.6	12.70

TABLE 7.1. DIMENSIONS OF PLAIN-PIPE SPECIMENS, IN MILLIMETRES. l/d_p = 2.0 FOR ALL TESTS, AND NO STIFFENERS ARE USED.

TEST	BOND STRENGTH, F_{BU}			
	Experimental	Finite element	Bond formula	New Bond formula *
Standard M	1.10	0.98	0.87	1.09
Extra thick	-	2.08	2.18	1.95
Extra thin	-	0.72	0.63	0.82

* See Chapter 8.

TABLE 7.2 COMPARISONS BETWEEN VARIOUS BOND STRENGTH PREDICTIONS FOR PLAIN PIPE CONNECTIONS.

Type	Loading arrangement	Max load/ radian	Failure bond	$\frac{F_{BU}}{F_{BU}\ \text{ten/comp}}$
Standard M	ten/comp	22.5 t	Sleeve & Pile	1.0
"	ten/ten	50.5 t	Pile	2.24
"	comp/comp	24.0 t	Sleeve	1.07
Extra thick	ten/comp	48.0 t	Pile	1.0
" "	ten/ten	74.0 t	Pile	1.54

TABLE 7.3. RESULTS OF THE FINITE ELEMENT ANALYSES WITH DIFFERENT LOADING ARRANGEMENTS.

KEY

▣ M3 (365 days old)
□ N9 (31 days old)
△ N5 (9 days old)
○ N3 (31 days old)
\+ Finite Element Result

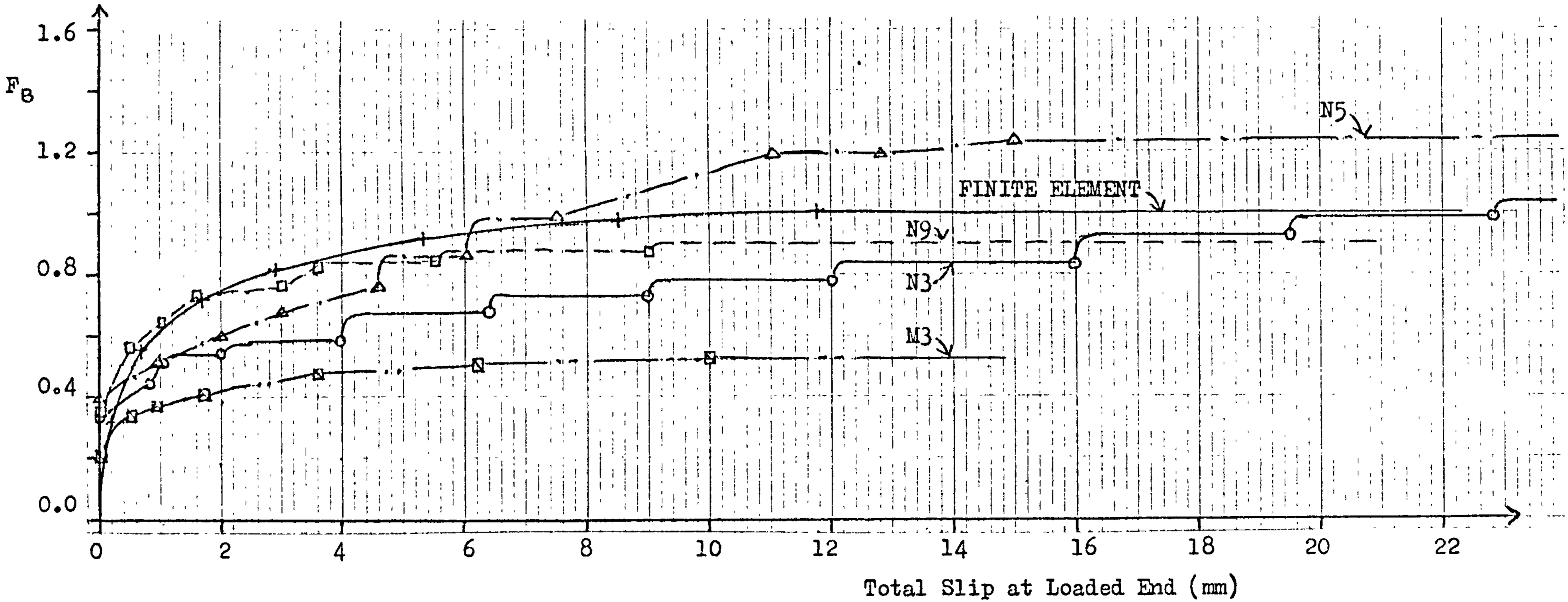

FIGURE 7.14 NORMALISED BOND STRESS AGAINST TOTAL SLIP FOR THE STANDARD M-SERIES PLAIN-PIPE TEST. SLEEVE LOADED IN COMPRESSION AND PILE IN TENSION.

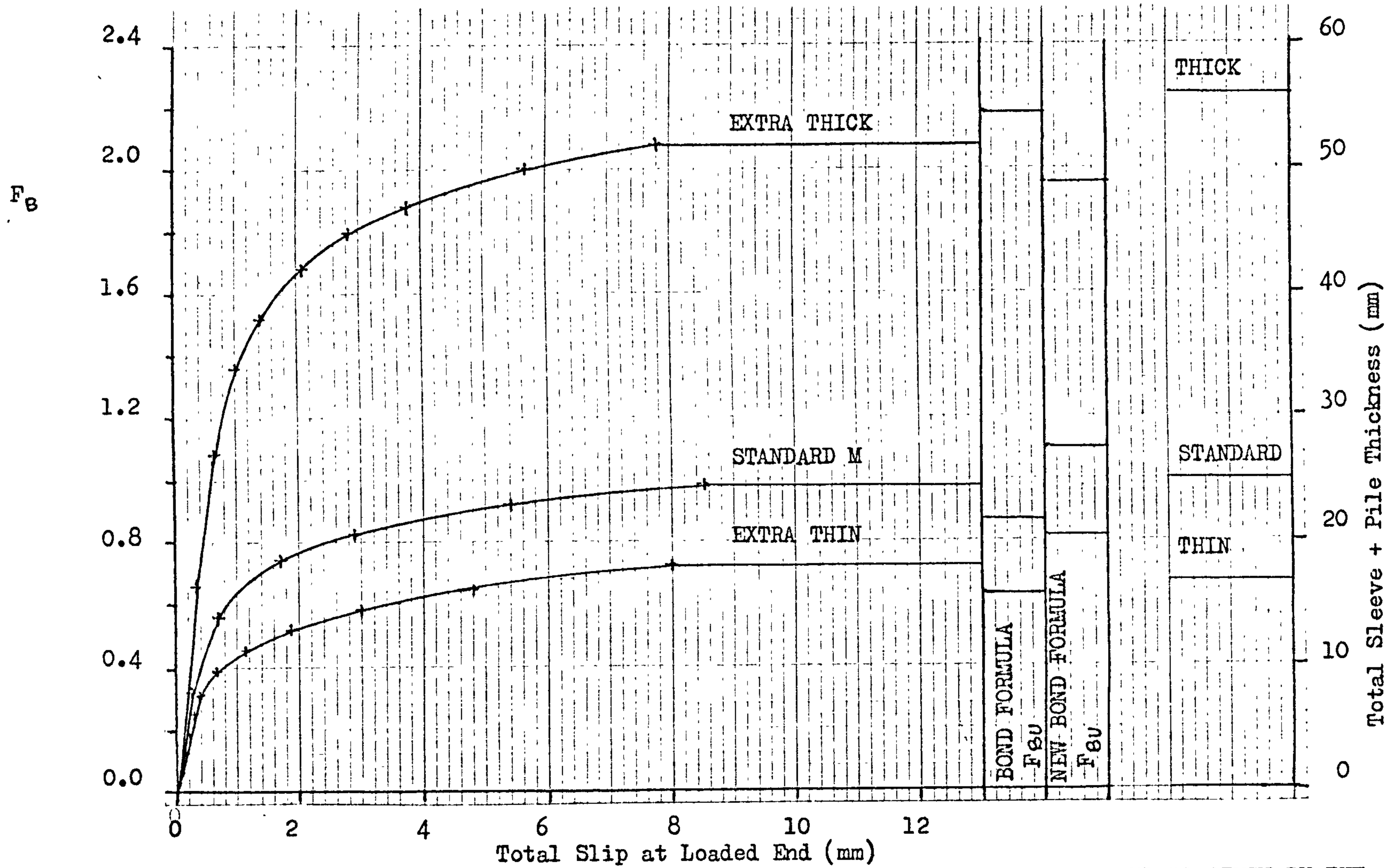

FIGURE 7.15 BOND STRESS AGAINST TOTAL SLIP FOR THE EXTRA THICK, STANDARD AND EXTRA THIN TUBULARS, GIVEN BY THE FINITE ELEMENT ANALYSIS.

It is interesting to note the variations in mode of failure predicted for the three geometries. For the specimen with extra-thick tubulars, failure is by slip on the pile bond. This is logical since the contact area is smaller on this bond and hence the bond stresses will be larger. The specimen with extra-thin tubulars on the other hand, fails on the sleeve bond. This is because the sleeve is thin enough to cause a relatively large radial expansion, which reduces the normal bond stress on the sleeve bond and results in a lower bond strength. The sleeve and pile need to be thick enough to enable large normal bond stresses to exist when dilation occurs on the interface for large bond shear stresses to be achieved. The standard M case is intermediate between the two extremes of geometry and shows slip to occur simultaneously on both bonds. As a result, ultimate load is achieved at a slightly greater slip in this case.

7.2.3 Bond Stresses

The development of the shear bond stresses (τ), under increasing axial load are shown in Figure 7.16. It can be seen that the bond stress distribution begins to change at approximately half the ultimate load, as maximum friction is attained at the loaded end of the connection and gradually spreads to the other end. The frictional limit reduces towards the loaded end as Poisson effects are larger here and by expanding radially, the value of σ_n is reduced, which in turn limits τ.

At either end of the connection, the bond stress pattern is distorted by end effects (as previously described in Section 7.1.2). In order to balance the bending moments in the grout, it is necessary to generate large normal bond stresses on opposite ends of the sleeve and pile,

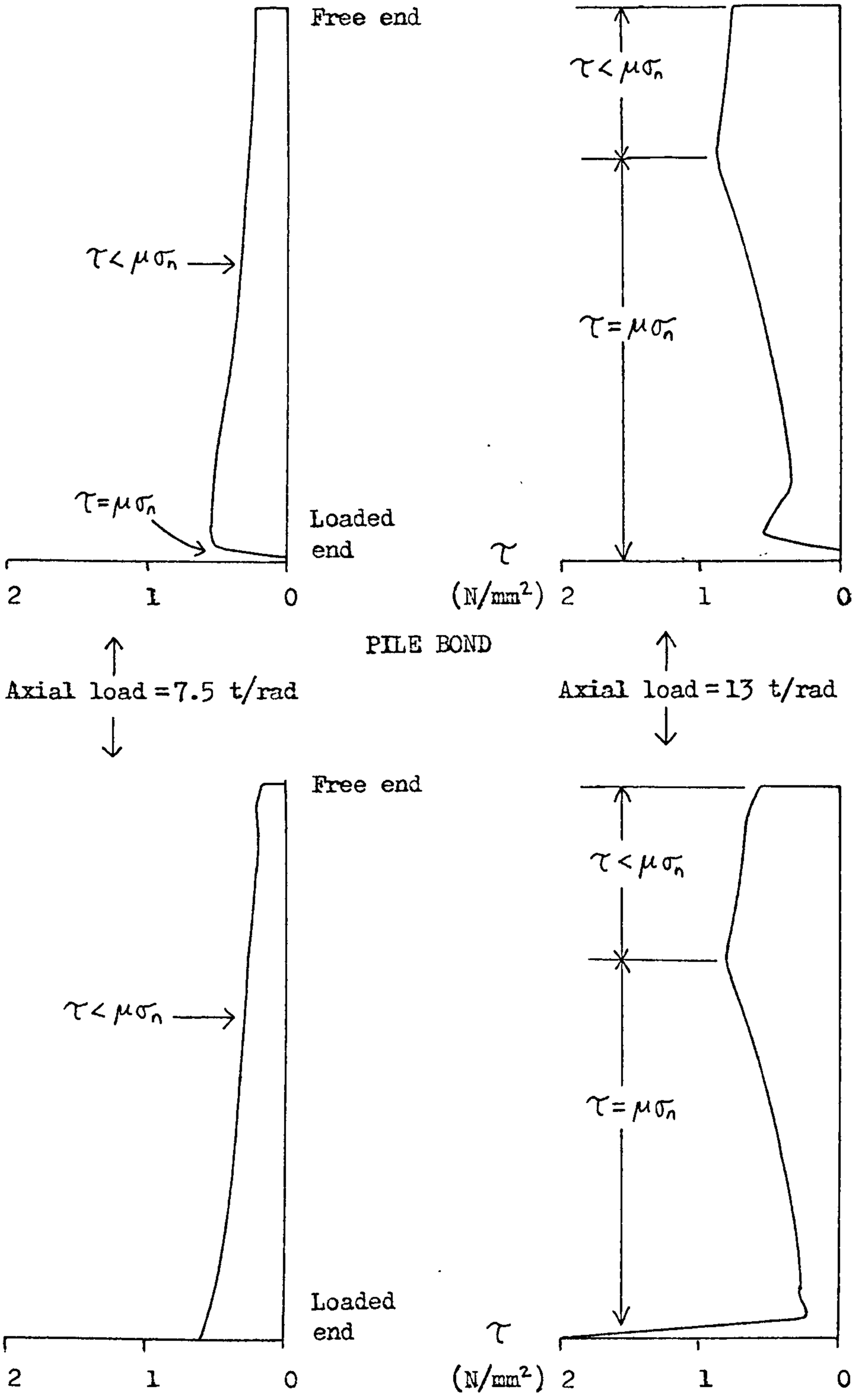

FIGURE 7.16 THE DEVELOPMENT OF THE SHEAR BOND STRESS (τ) UNDER INCREASING AXIAL LOAD, GIVEN BY THE FINITE ELEMENT ANALYSIS. A STANDARD M-SERIES GEOMETRY IS USED, LOADED FROM ONE END WITH THE SLEEVE IN COMPRESSION AND PILE IN TENSION.

Continued

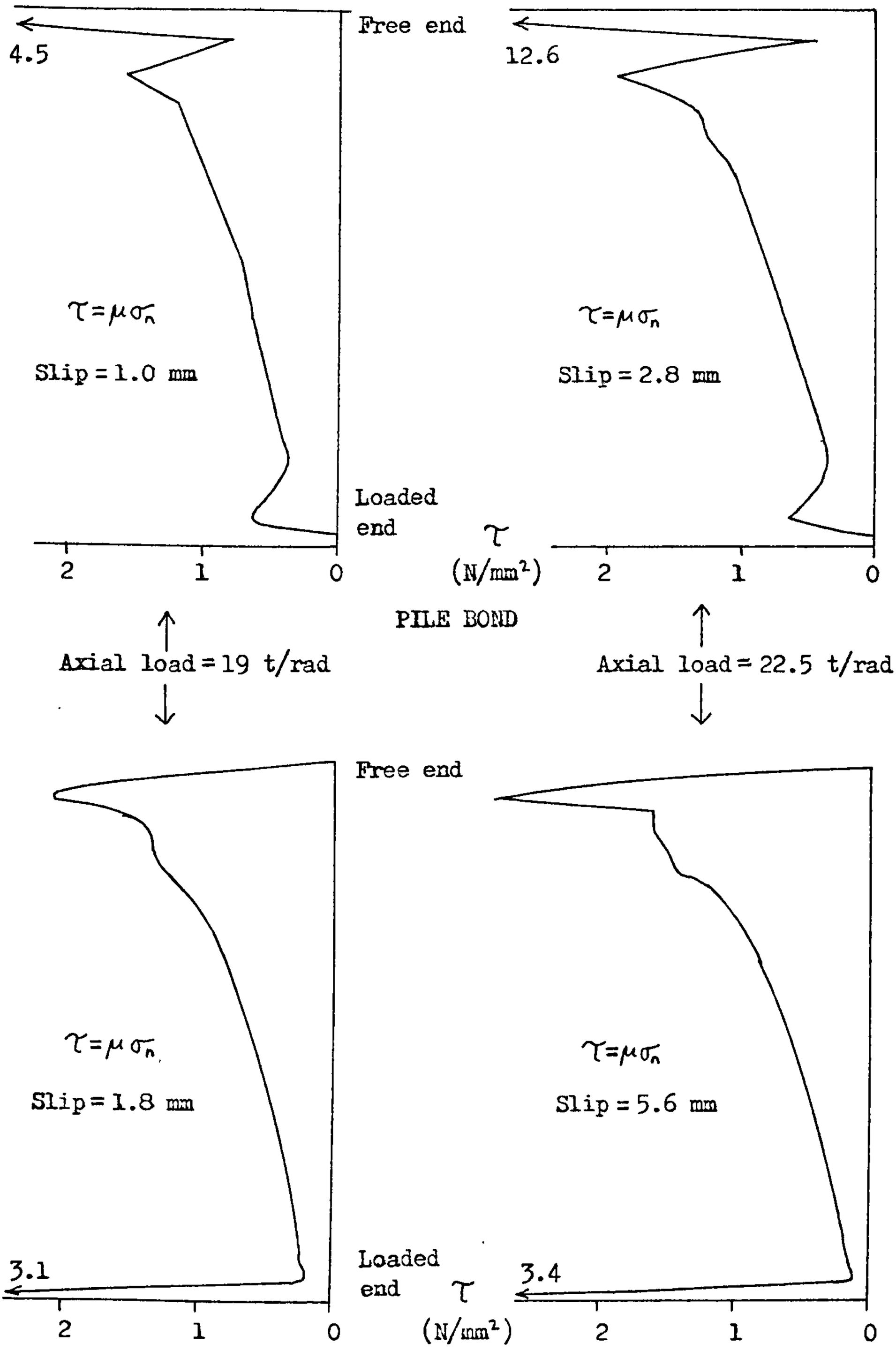

FIGURE 7.16 Continued

which is the reason for the irregularities in the bond stress patterns at the ends of the connection. The size of these bending moments will increase proportionately with length of connection, due to increased load, but the distortions to the σ_n distribution will not increase, as the moment arm used by σ_n is also proportional to the length of the connection. End restraints will induce small bending moments in the ends of the tubulars, which will also influence the bond stress distributions at the connection ends to some extent.

Figure 7.17 shows the shear bond stresses at ultimate load for the grouted connections with extra-thick and extra-thin tubulars. This shows how the frictional limit increases for connections with thicker tubulars, due to greater confinement.

7.2.4 Effect of ℓ/d_p

The length of the grouted connection can be increased by the addition of more elements and analysed to find the effect of ℓ/d_p on ultimate bond strength. Figure 7.18 shows the computed results. There is no reduction in F_{BU} for $\ell/d_p < 2$, but the reduction when $\ell/d_p > 2$ appears realistic. This reduction is less rapid for more radially stiff connections and can be explained by inspecting the bond stresses at ultimate load, given in Figure 7.19. For the standard M geometry, with $\ell/d_p = 2$, the normal bond stress (σ_n) is reduced to nearly zero at the loaded end by the Poisson effects. Therefore, when ℓ/d_p is increased to 3 or 4, the extra length of connection will carry very little bond stress due to σ_n being so low. Hence, the mean bond stress is reduced as ℓ/d_p increases.

For the more radially stiff connection, also shown in Figure 7.19 for $\ell/d_p = 4$, the axial load needed to make the Poisson effects large

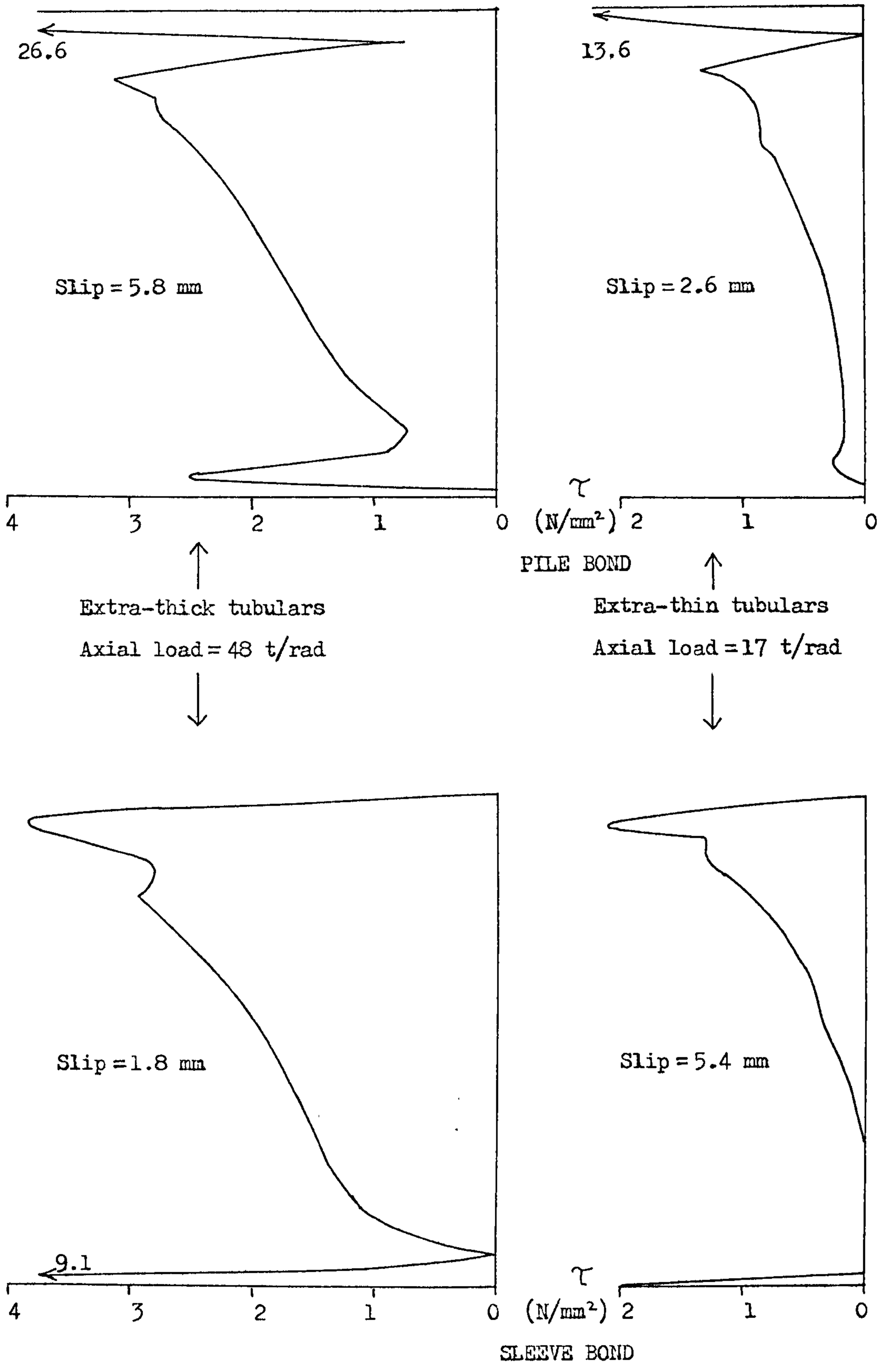

FIGURE 7.17 SHEAR BOND STRESSES AT ULTIMATE LOAD FOR EXTRA-THICK AND EXTRA-THIN TUBULARS. COMPARE WITH FIGURE 7.16 FOR STANDARD THICKNESSES.

$$C_L = \frac{F_{BU}}{F_{BU}(\ell/d_p=2)}$$

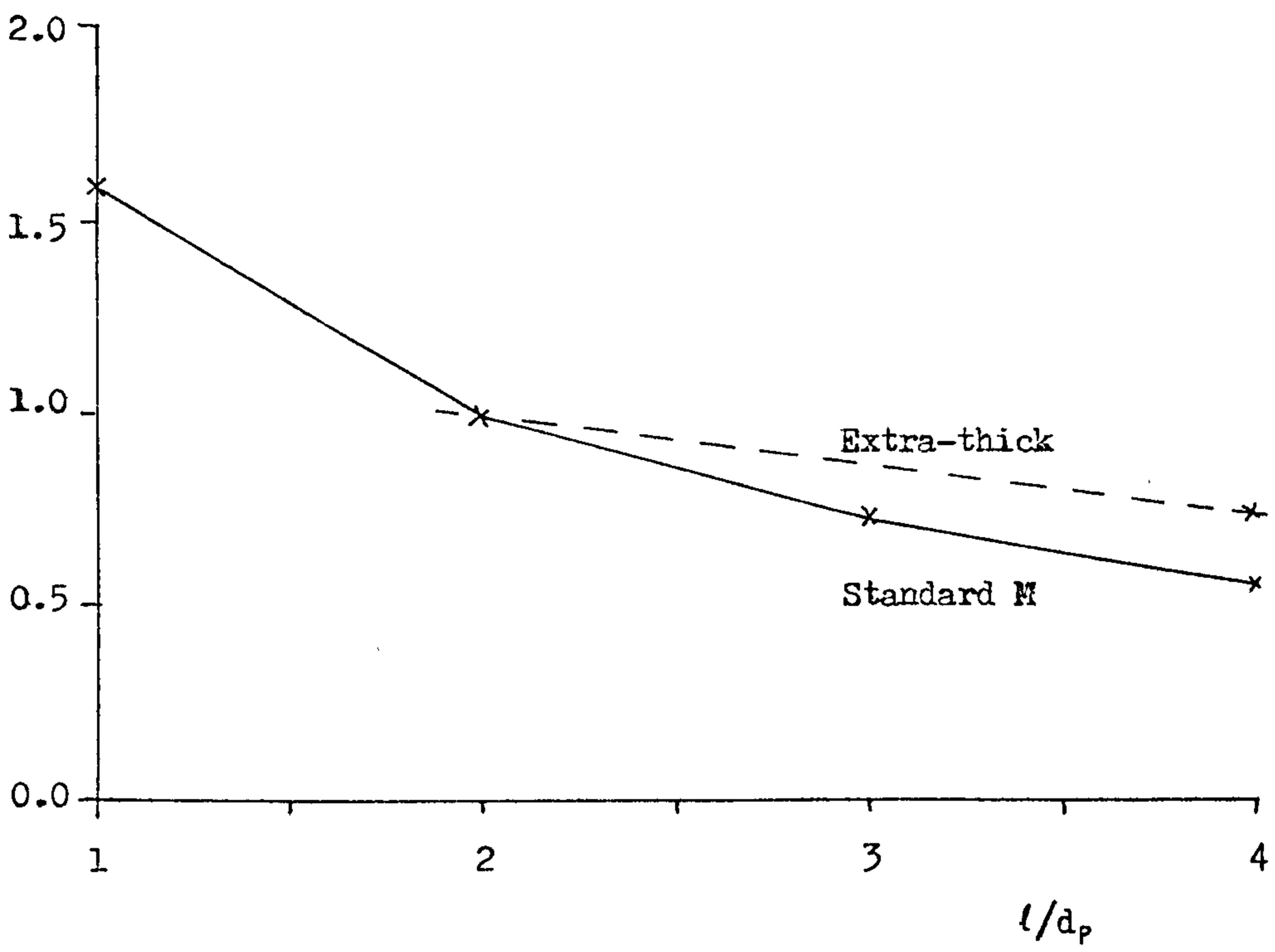

FIGURE 7.18 EFFECT OF ℓ/d_p ON BOND STRENGTH FOR PLAIN PIPE CONNECTIONS, PREDICTED BY THE FINITE ELEMENT ANALYSIS.

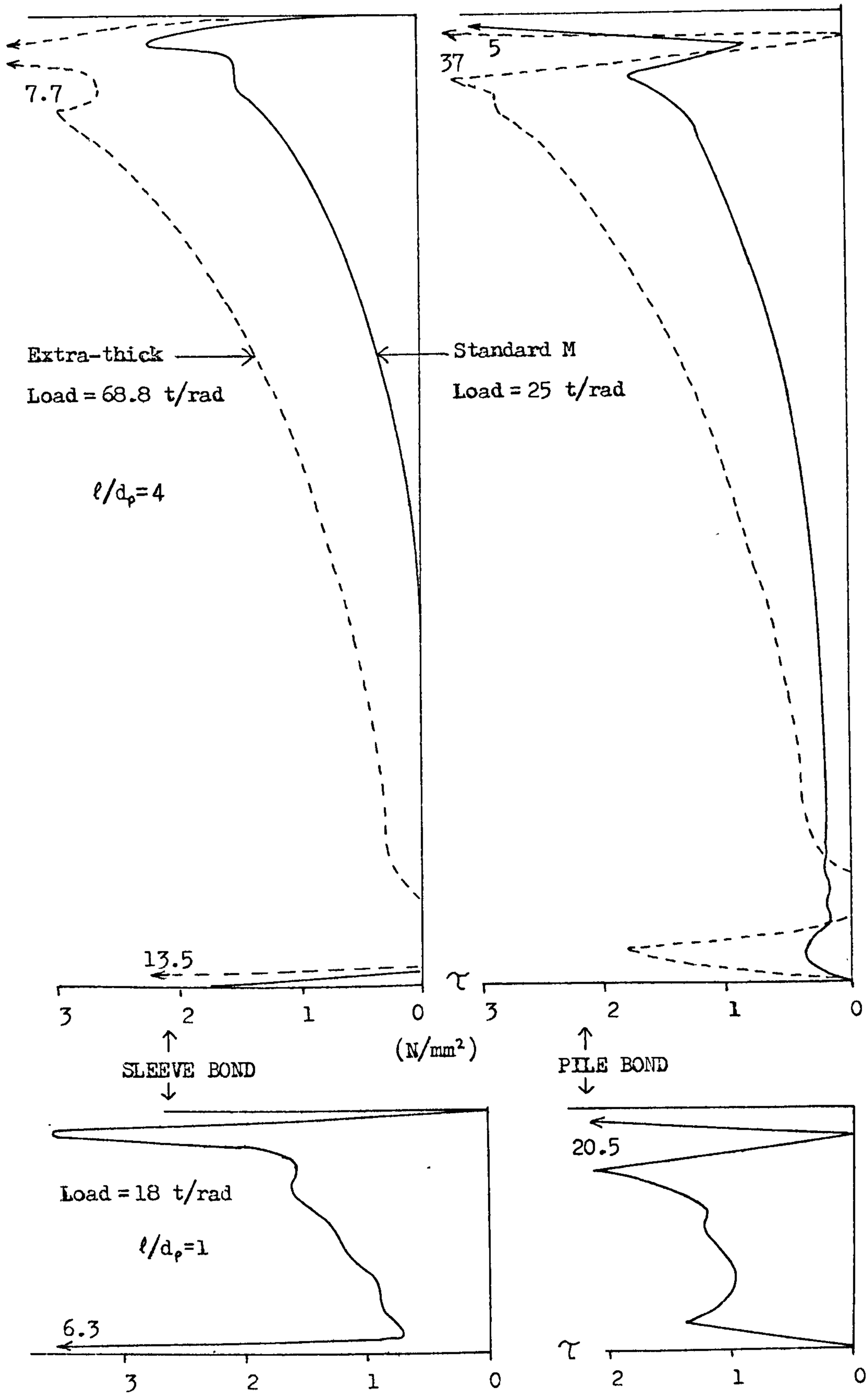

FIGURE 7.19 BOND STRESSES AT ULTIMATE LOAD FOR VARIOUS ℓ/d_p VALUES.

Continued

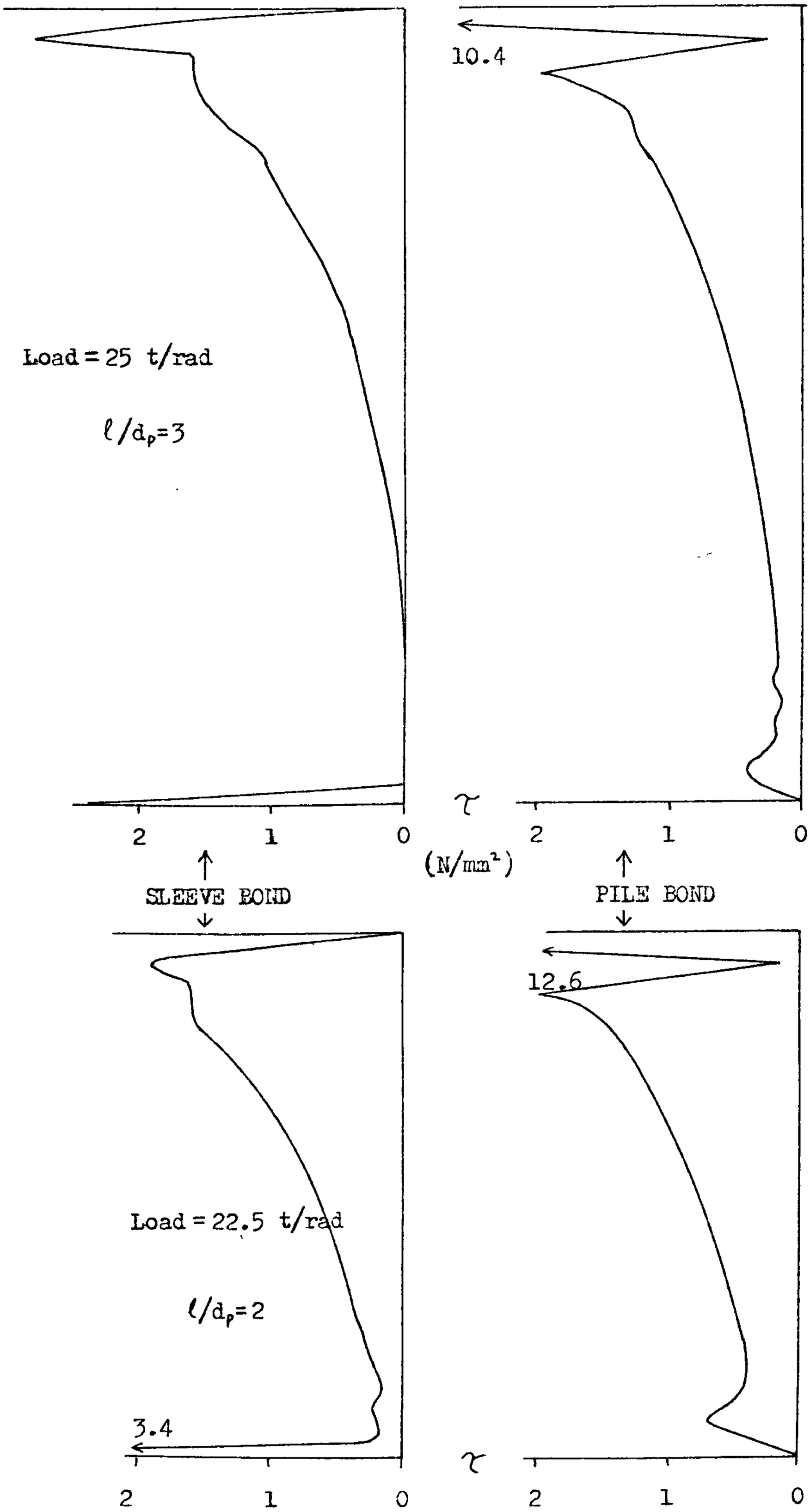

FIGURE 7.19 Continued

enough to reduce σ_n to zero becomes much larger. Only when $\ell/d_p = 4$, will maximum load reduce σ_n to zero at the loaded end. Therefore, the rate of reduction in F_{BU} with ℓ/d_p will be less than for a connection with more flexible tubulars.

7.2.5 Alternative Loading Conditions

Up to now, the sleeve has been loaded in compression and the pile in tension, as this arrangement is considered to give the weakest bond strength (due to Poisson effects). Further analyses have been made with the pile and sleeve both loaded in compression or both in tension in order to verify this assumption. The results are summarised in Table 7.3. It can be seen from these results that compression loading gives a slight strength increase, and tension loading a very considerable strength increase. This is because the sleeve is substantially thinner than the pile and when the sleeve is in tension the Poisson effects cause it to shrink enough to significantly increase the normal bond stress. Figure 7.20 shows the bond stresses under these alternative loading conditions at maximum load.

With thicker tubulars the variation of bond strength with loading arrangement is less since Poisson effects are less for the thicker tubulars. For other geometries it is possible for the compression loading arrangement to be strongest. This was found to be the case with the S-series tests carried out by Wimpey Laboratories (10). In this case, the pile was almost as thin as the sleeve and the overall diameter was quite small, making the radial stiffness of the sleeve almost as great as that of the pile. The sleeve has the greater radial stiffness when the sleeve stiffeners are taken into consideration. As a result, the pile

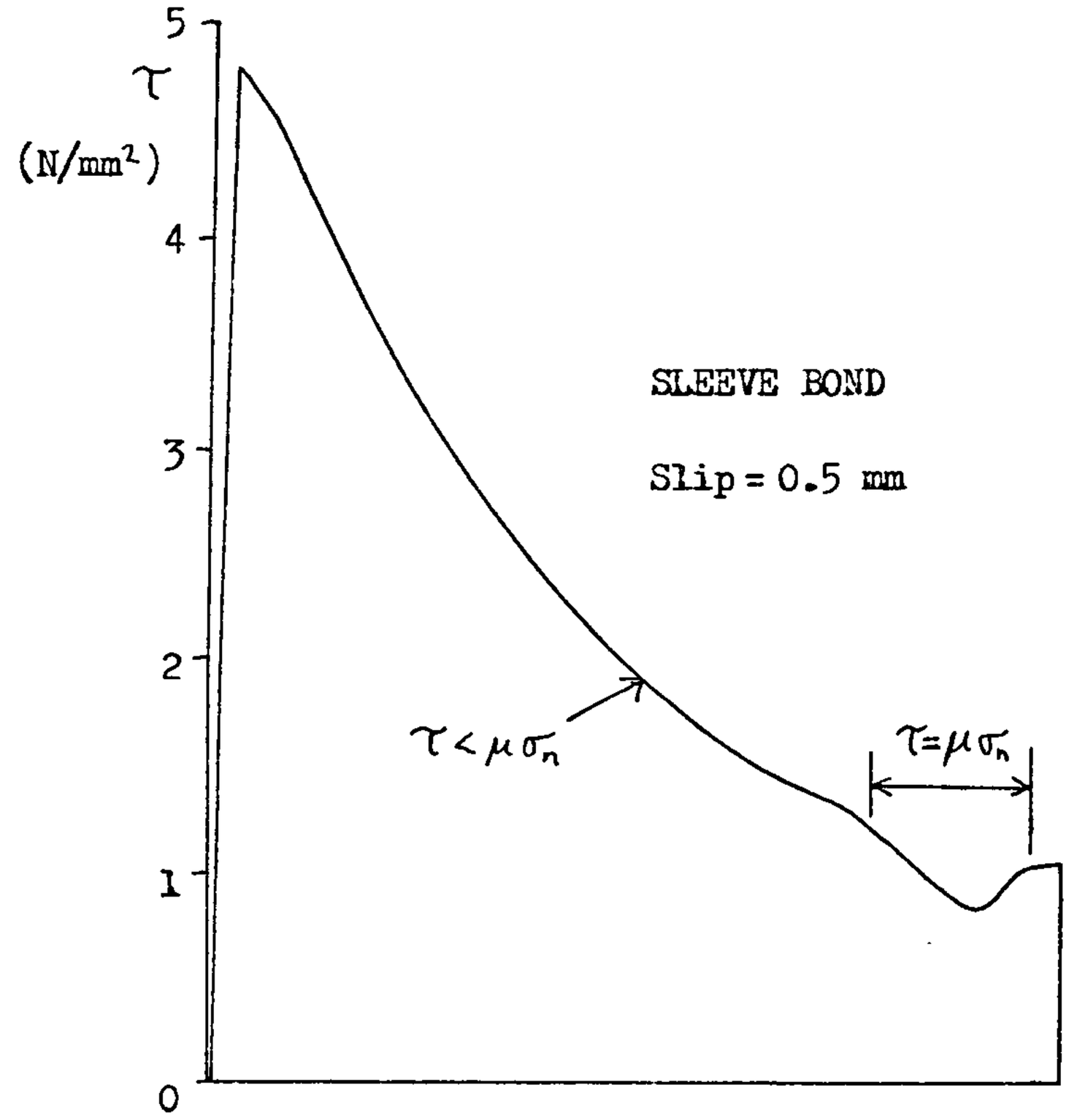

Load = 50.5 t/rad

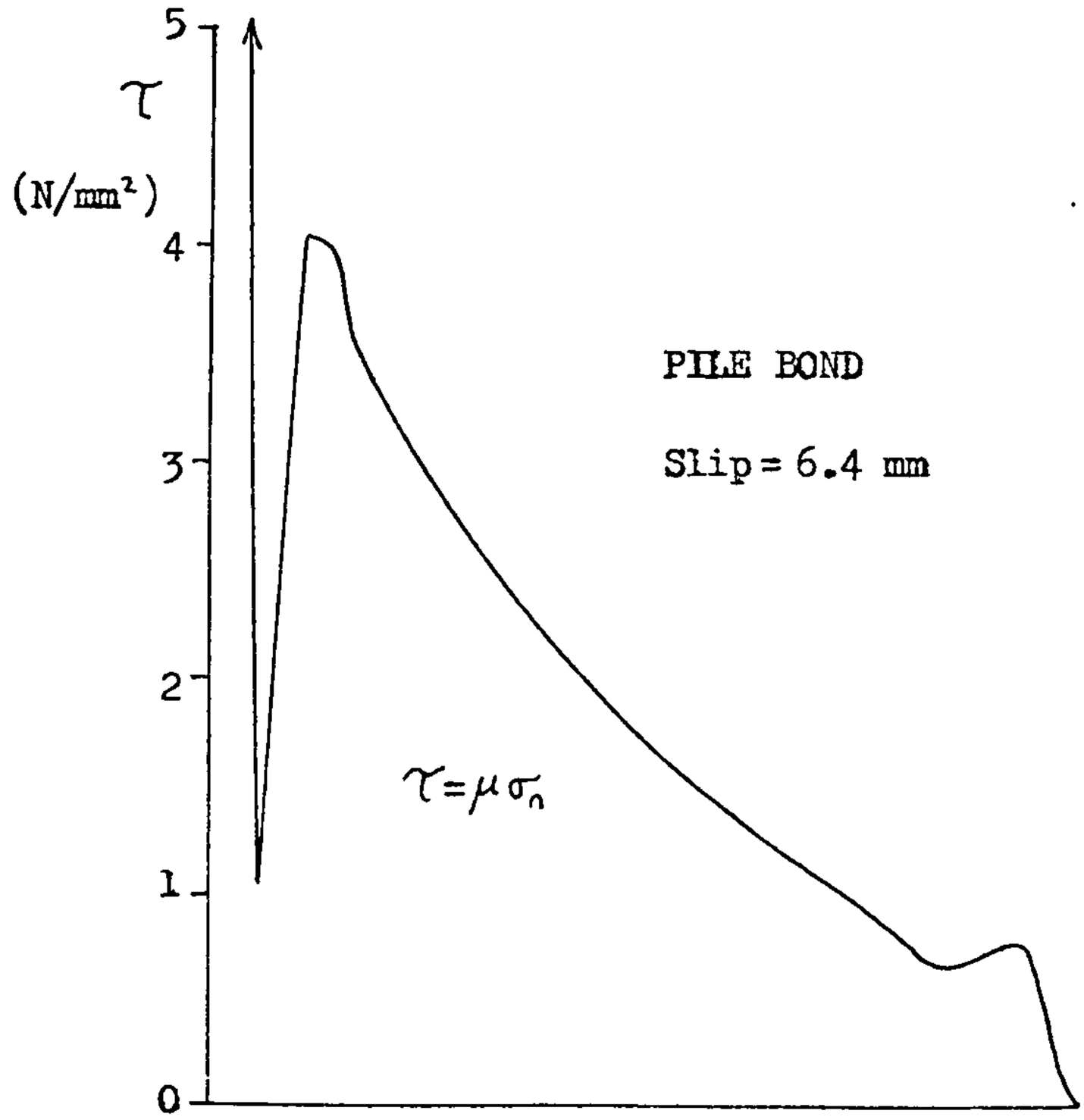

(a)Tension loading

FIGURE 7.20 BOND STRESSES AT ULTIMATE LOAD UNDER ALTERNATIVE LOADING CONDITIONS.

Continued

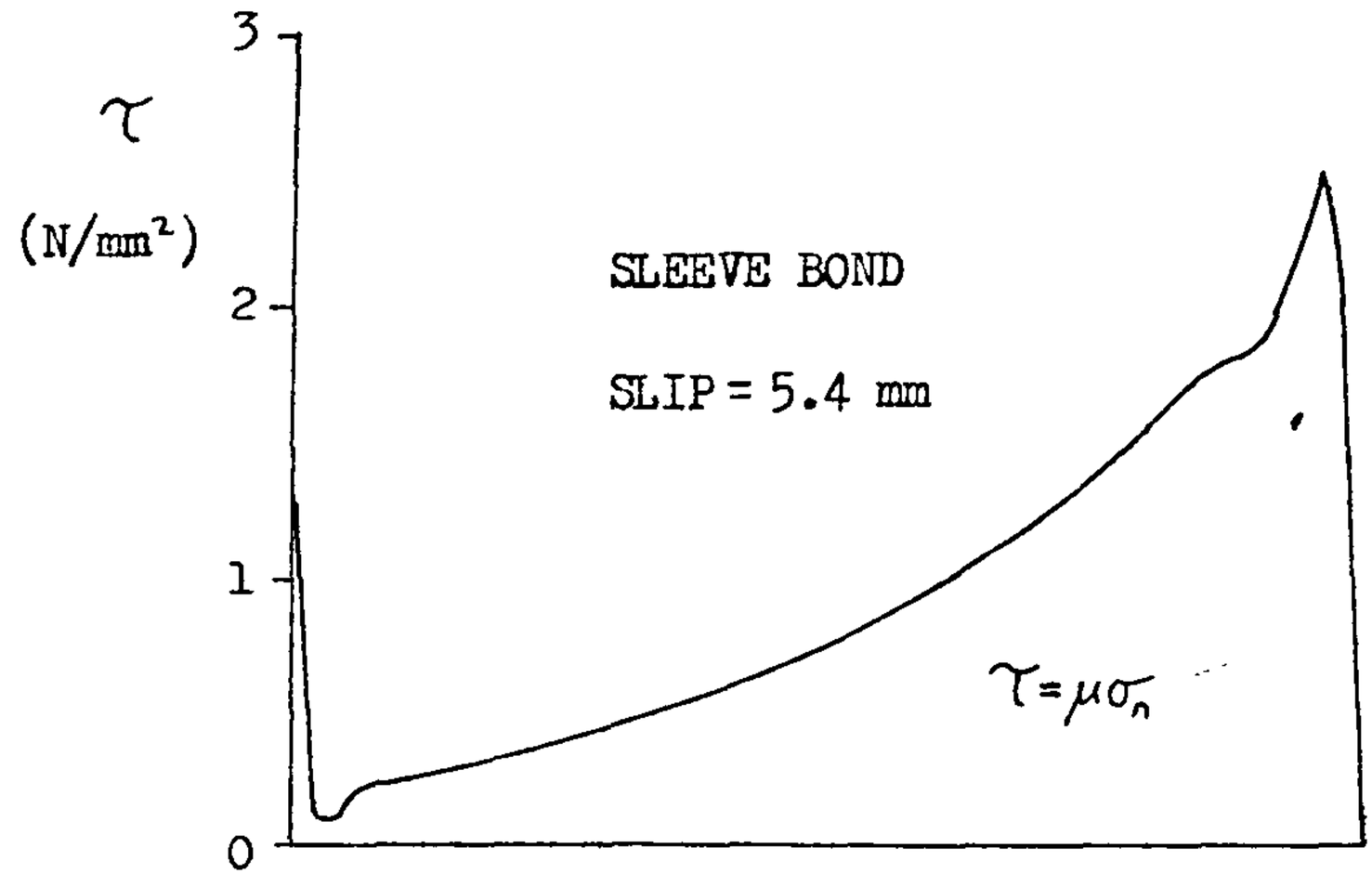

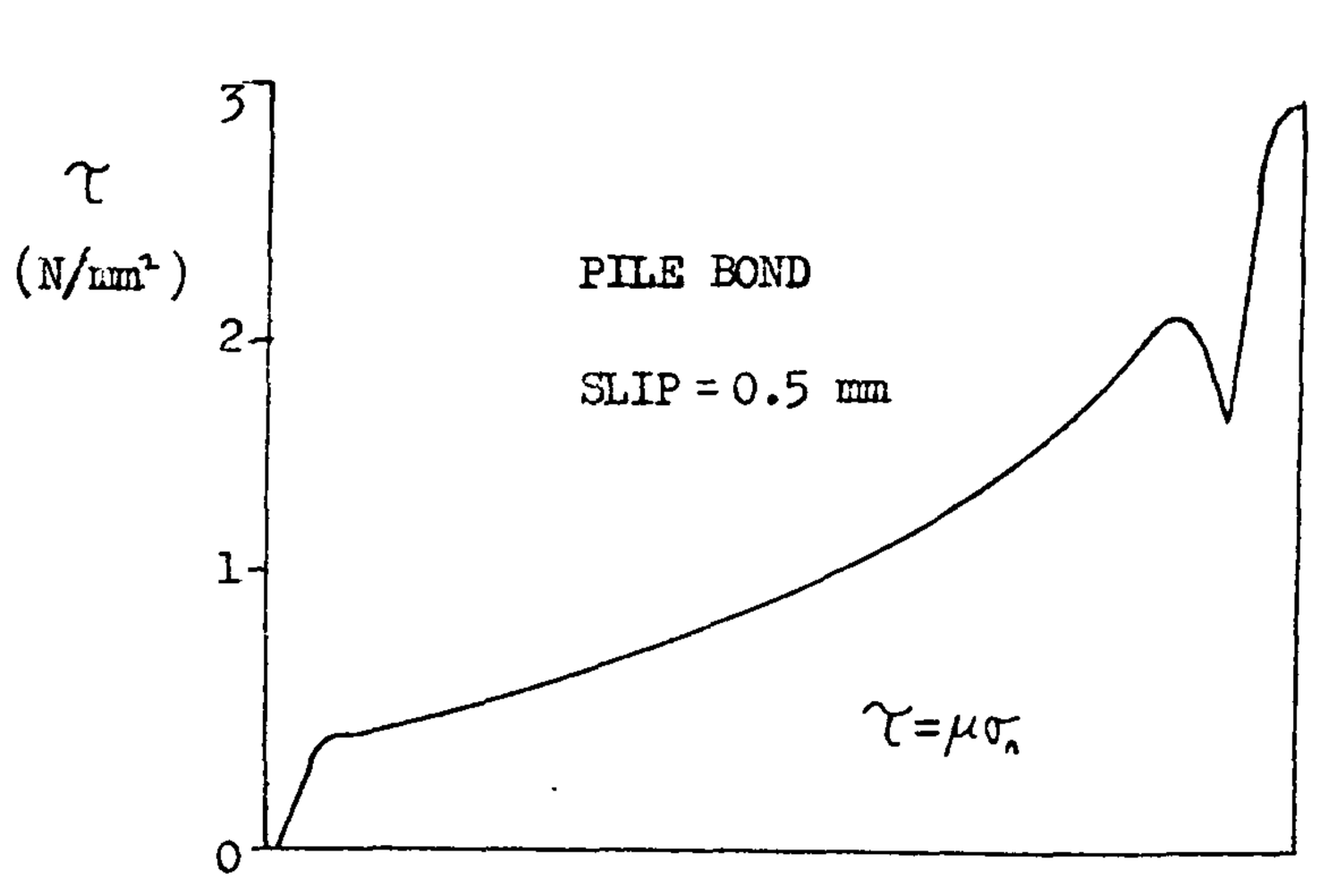

(b)Compression loading

FIGURE 7.20 Continued

radial expansion under compression loading was enough to make the bond strength 50% greater than under tension loading. So the effect of alternative loading arrangements depends greatly on the geometry of the connection.

7.3 Grouted Connections with Shear Keys

7.3.1 Shear Key Properties

The finite element mesh is again based on that shown in Figure 4.4. The shear keys are evenly spaced so that all elements can be the same thickness thus allowing data generation to be used. This results in a slightly smaller value for the key spacing (s) since the end shear keys are further from the end of the connection. Errors caused by this slight shift in the positions of the shear keys appear to be negligible. One particular connection geometry was analysed using the correct spacing and produced the same results as the approximate spacing.

Bond properties are the same as those used for the plain pipe connections, but with the addition of shear keys, some extra parameters have to be specified using the values calculated in the detailed shear key analysis (Section 7.1). The value of the shear key force ratio (β) is 0.5 and the data for the shear key stiffness curve are given in Figure 5.7.

7.3.2 Effect of Tubular Stiffness Variation

Three experimentally tested geometries from the Department of Energy Programme (8) have been chosen for analysis. From the dimensions of these given in Table 7.4, it can be seen that a wide range of tubular thicknesses has been selected. The hoop stiffness is low for tests P17/18, high for tests P1/2, and mid-range for tests P9/10.

Figures 7.21a,b,c show the bond stress plotted against slip for the three geometries and compare the finite element results with the test results. The experimental specimens were cured for 22 days before testing and so the results should be divided by 1.04 to give F_{BU31} (see Table 2.3) for a true comparison with the numerical analysis.

TEST	SLEEVE		PILE	
	d_s	t_s	d_p	t_p
P1/2	574.75	8.0	508.0	25.4
P9/10	569.0	5.0	508.0	16.0
P17/18	566.93	4.0	508.0	12.7

TABLE 7.4. SPECIMEN DIMENSIONS, IN MILLIMETRES.
For all cases, l/d = 2 , h = 2.03 mm, s = 152.4 mm
(s = 169 mm in the experiment).

TEST	BOND STRENGTH, F_{BU3}			
	Experimental	Finite Element	Bond Formula	New Bond Formula *
P1/2	2.56	2.40	2.77	2.03
P9/10	1.80	1.93	1.90	1.70
P17/18	1.63	1.75	1.61	1.56
* See Chapter 8.				

TABLE 7.5. COMPARISONS BETWEEN VARIOUS BOND STRENGTH PREDICTIONS FOR KEYED CONNECTIONS.

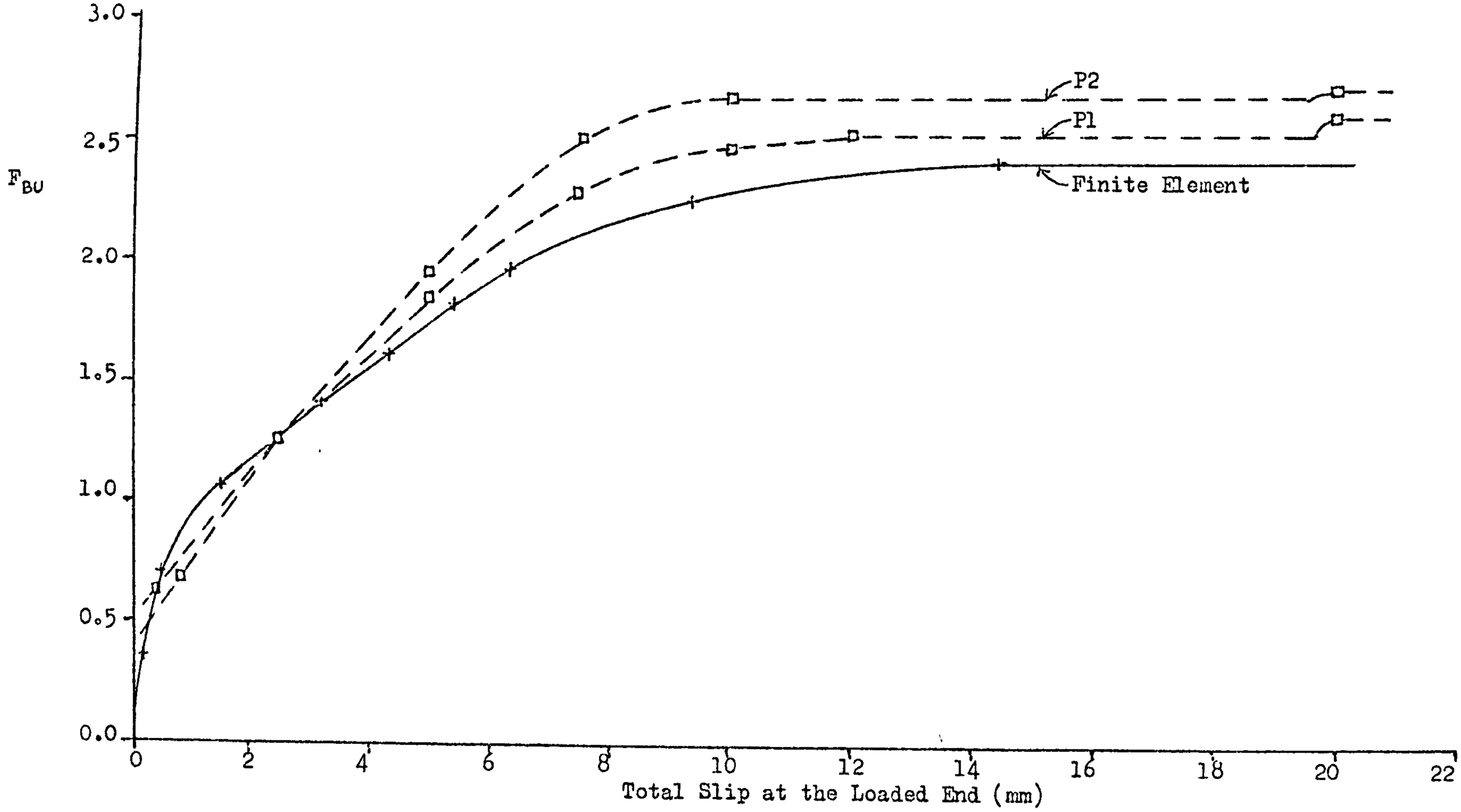

FIGURE 7.21a COMPARISON BETWEEN THE EXPERIMENTAL AND FINITE ELEMENT RESULTS FOR THE P1/2 TESTS.

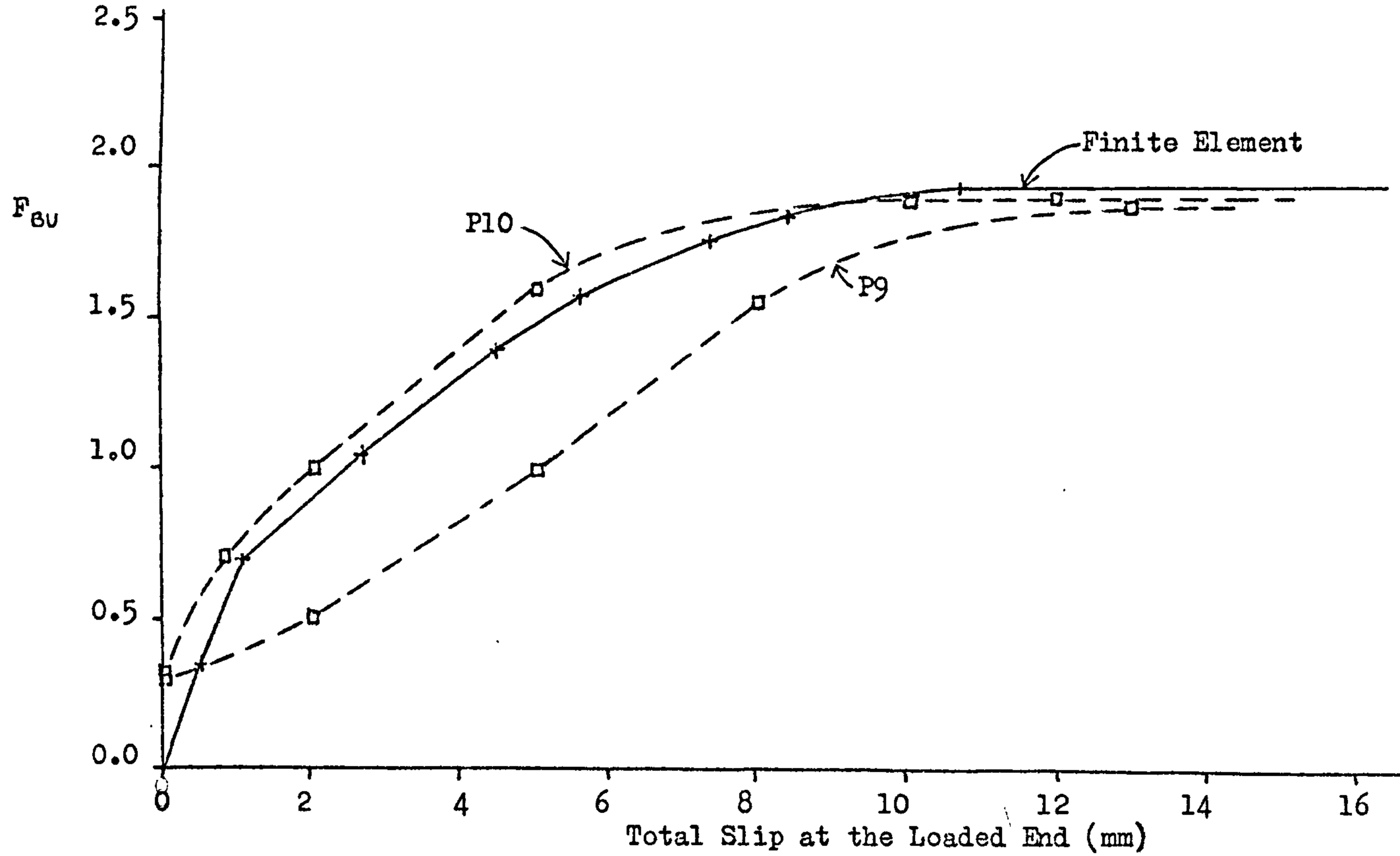

FIGURE 7.21b COMPARISON BETWEEN THE EXPERIMENTAL AND FINITE ELEMENT RESULTS FOR THE P9/10 TESTS.

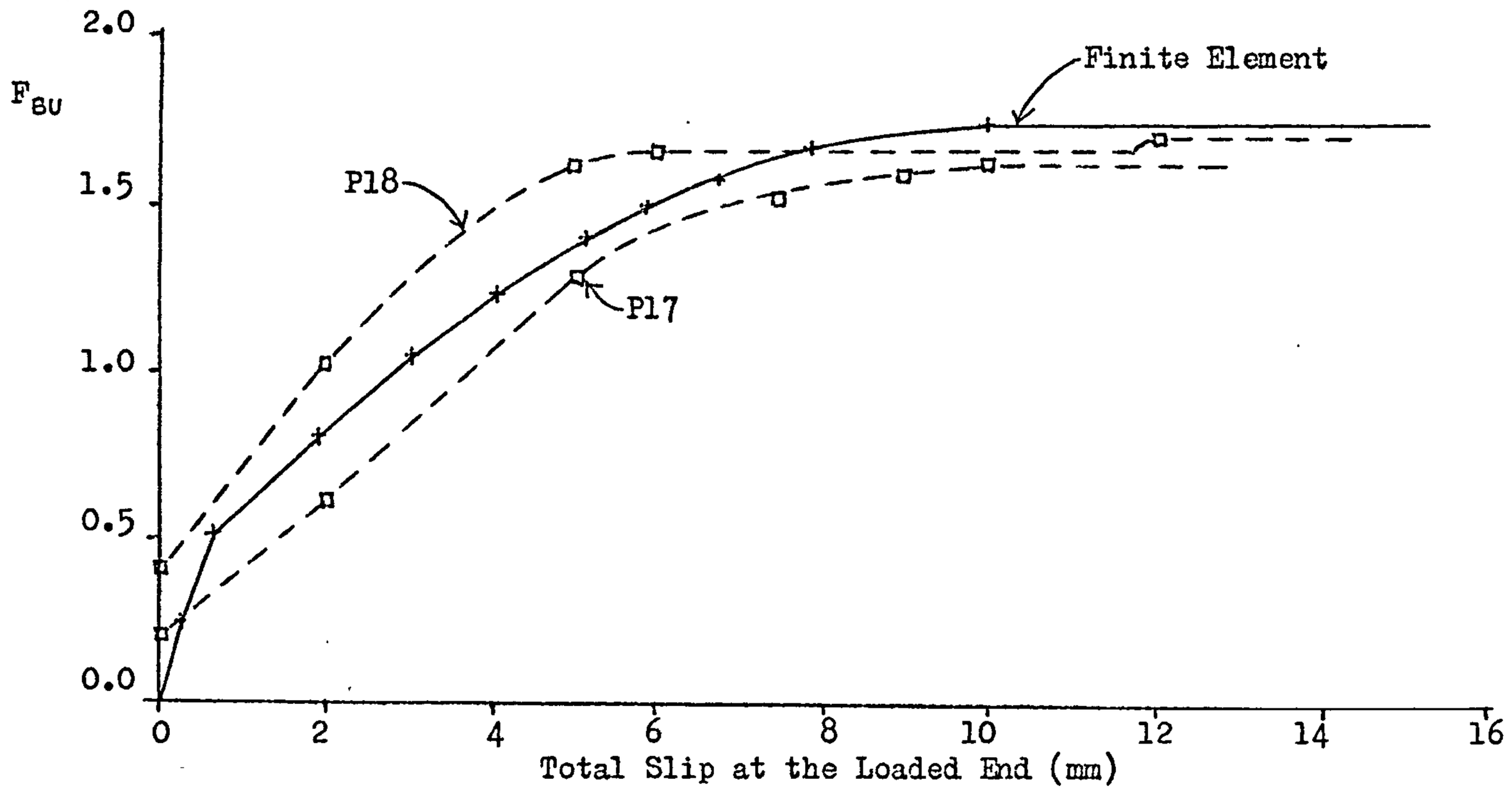

FIGURE 7.21c COMPARISON BETWEEN THE EXPERIMENTAL AND FINITE ELEMENT RESULTS FOR THE P17/18 TESTS.

It can be seen that for all three geometries, reasonably close agreement is achieved between theory and experiment.

Table 7.5 compares the finite element and experimental ultimate bond strengths with the bond formulae predictions. Even more extreme variations in the cylinder thicknesses without stiffeners have been analysed. These results were reported in Chapter 3, where they are compared with Paslay's results.

7.3.3 Bond Stresses and Failure Mode

For the P-series tests mentioned above, final failure is caused by crushing of the grout around the pile shear keys. This is normally the case as the shorter circumference on the pile results in higher shear key stresses. The actual loads per unit circumference reached on the shear keys at ultimate load vary according to position along the length of the connection and with sleeve/pile thickness. This is because variations in radial displacements result in different effective shear key heights and grout confinement levels. Values reached in the finite element analyses were as follows. For P17/18, $V = 222$ to 253 N/mm, for P9/10, $V = 234$ to 274 N/mm, and for P1/2, $V = 272$ to 315 N/mm.

Figure 7.22 shows the bond stresses and shear key loads per unit circumference at various stages in the loading process for the P9/10 test. At low loads, the key forces, including the radial components are low and so a smooth distribution of frictional bond stresses exists as the frictional limit has not yet been reached. The key forces build up more and more rapidly as the loads increase. The radial key forces open the bond thus reducing the frictional bond stresses in the vicinity of the shear keys. Initially, the pile key stresses are larger than those on the sleeve and this is due to the shorter circumference.

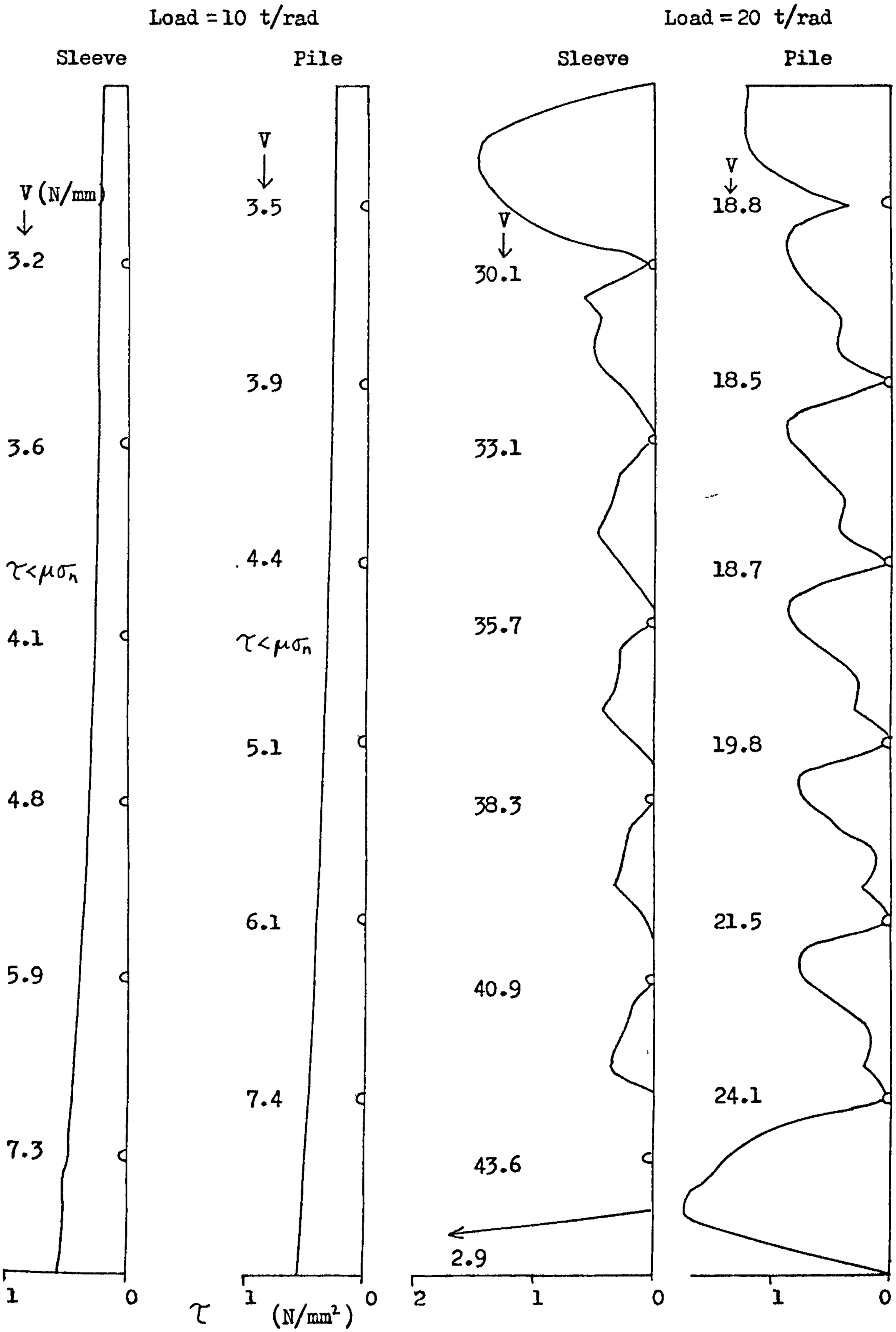

FIGURE 7.22 BOND STRESS DISTRIBUTIONS AND SHEAR KEY LOADS FOR THE P9/10 GEOMETRY UNDER INCREASING APPLIED LOAD.

Continued

Load = 40 t/rad

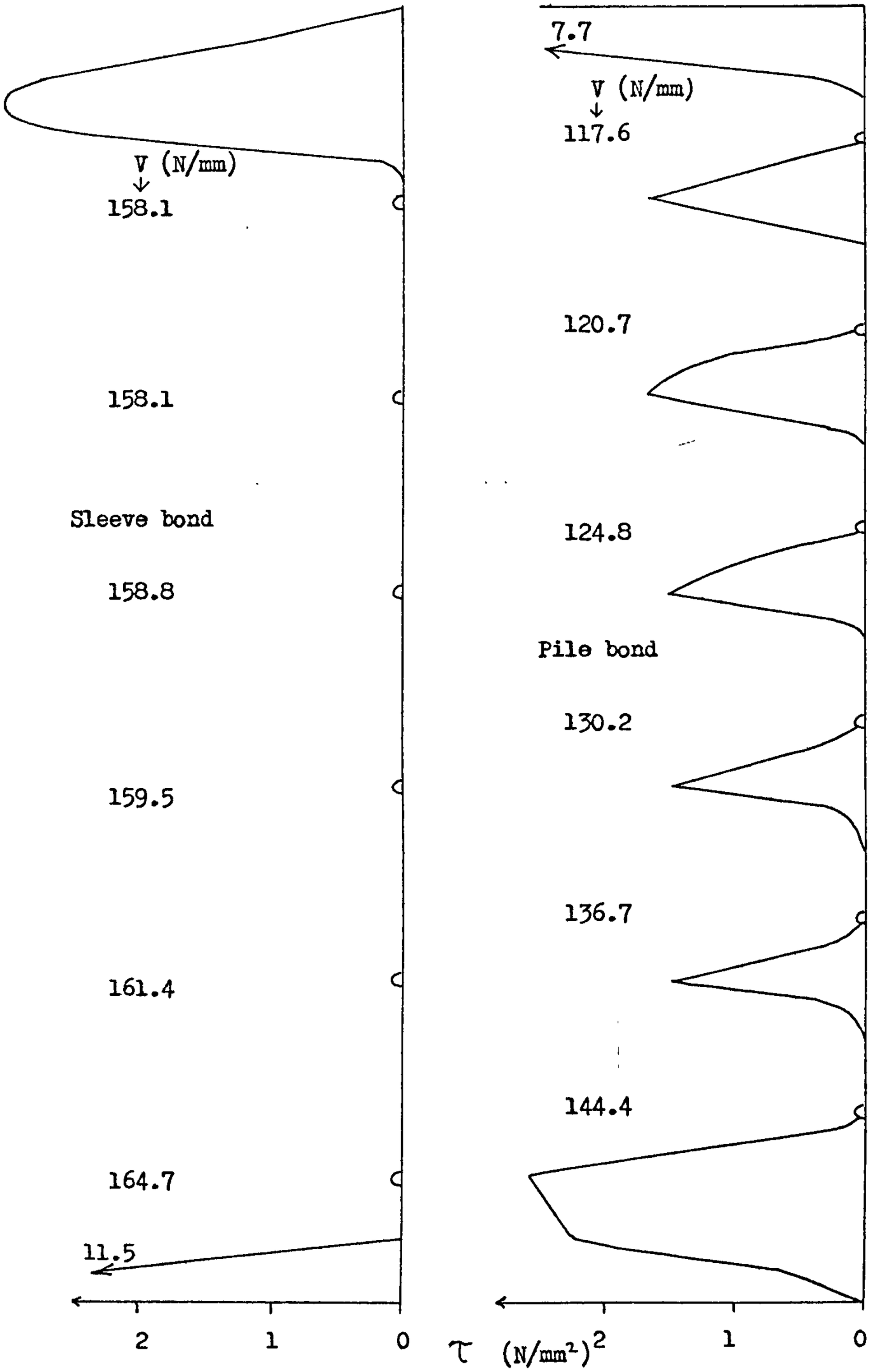

FIGURE 7.22 Continued

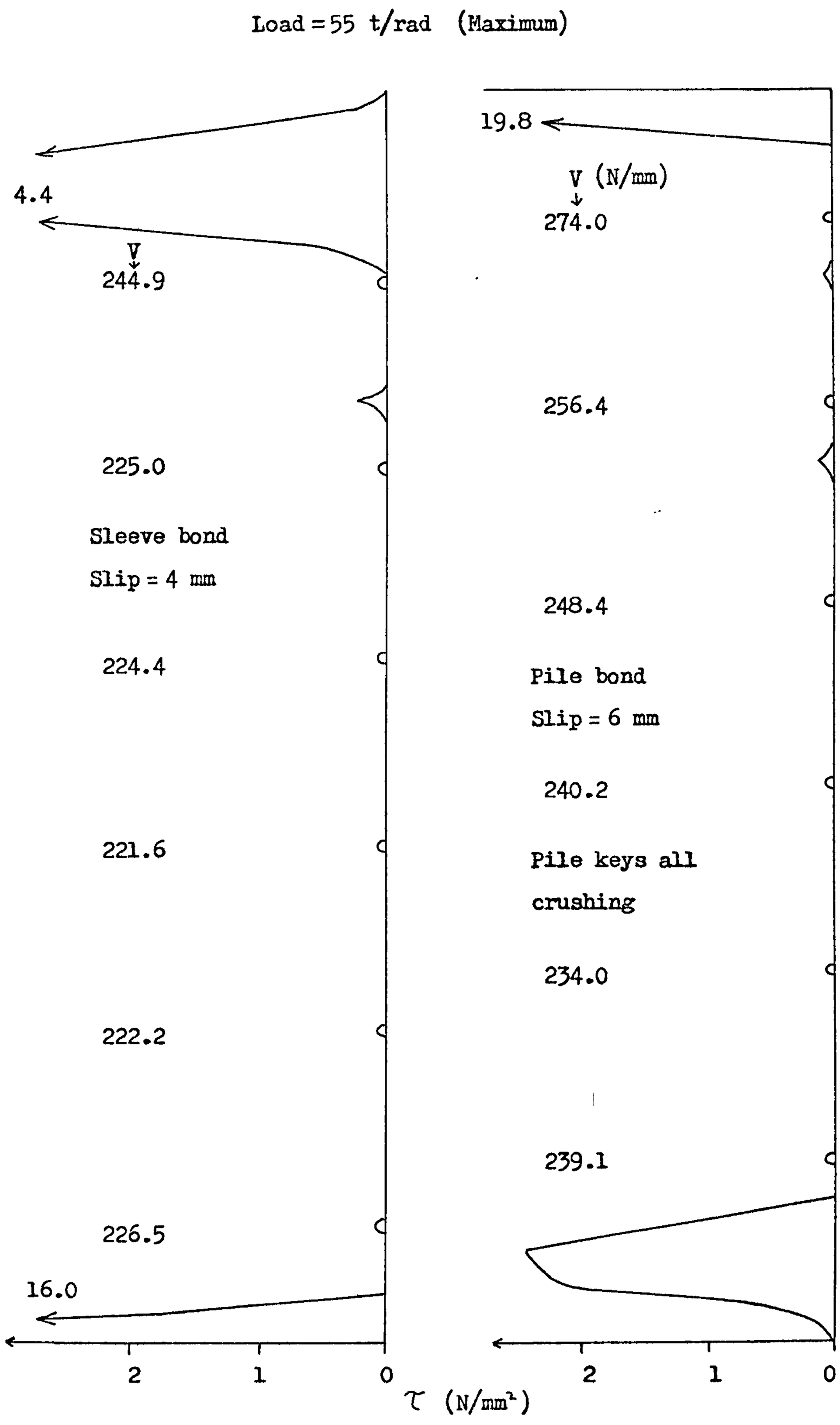

FIGURE 7.22 Continued

The sleeve key stresses then become greater because for these geometries where the sleeve is thinner than the pile, the sleeve bond reaches limiting friction sooner than the pile and the sleeve keys have to take additional loads.

Eventually the loads become large enough for Poisson effects to reduce the pile bond stresses to zero, (except at the ends) and then the pile key stresses again become greatest. Finally, the stresses exerted by the pile keys on the grout cause the grout to crush, making it impossible to sustain higher loads.

Results for the P1/2 and P17/18 analyses were very similar, although at ultimate load there were still some frictional bond stresses between the keys on the stiffer P1/2 geometry.

7.3.4 Effect of l/d_p

The effect on bond strength of varying l/d_p was analysed with the sleeve in compression and pile in tension. The results, which are plotted in Figure 7.23, show that l/d_p has less effect on bond strength when shear keys are used, (the plain pipe results, plotted in Figure 7.18, showed a greater effect). This is because shear key loads are less sensitive to radial movements of the tubulars than the frictional bond stresses. The maximum key loads achieved per unit circumference on the pile were as follows. For $l/d_p = 1$, V = 266 to 308 N/mm, for $l/d_p = 2$, V = 239 to 274 N/mm and for $l/d_p = 3$, V = 222 to 365 N/mm. The The exceptionally high load of 365 N/mm for $l/d_p = 3$ is due to a tenth key being placed on the extreme unloaded end of the pile. Had only nine keys been used, then the bond strength for $l/d_p = 3$ would have been slightly less. By the time all ten pile keys are crushing, four sleeve

$$C_L = \frac{F_{BU}}{F_{BU}(\ell/d_p = 2)}$$

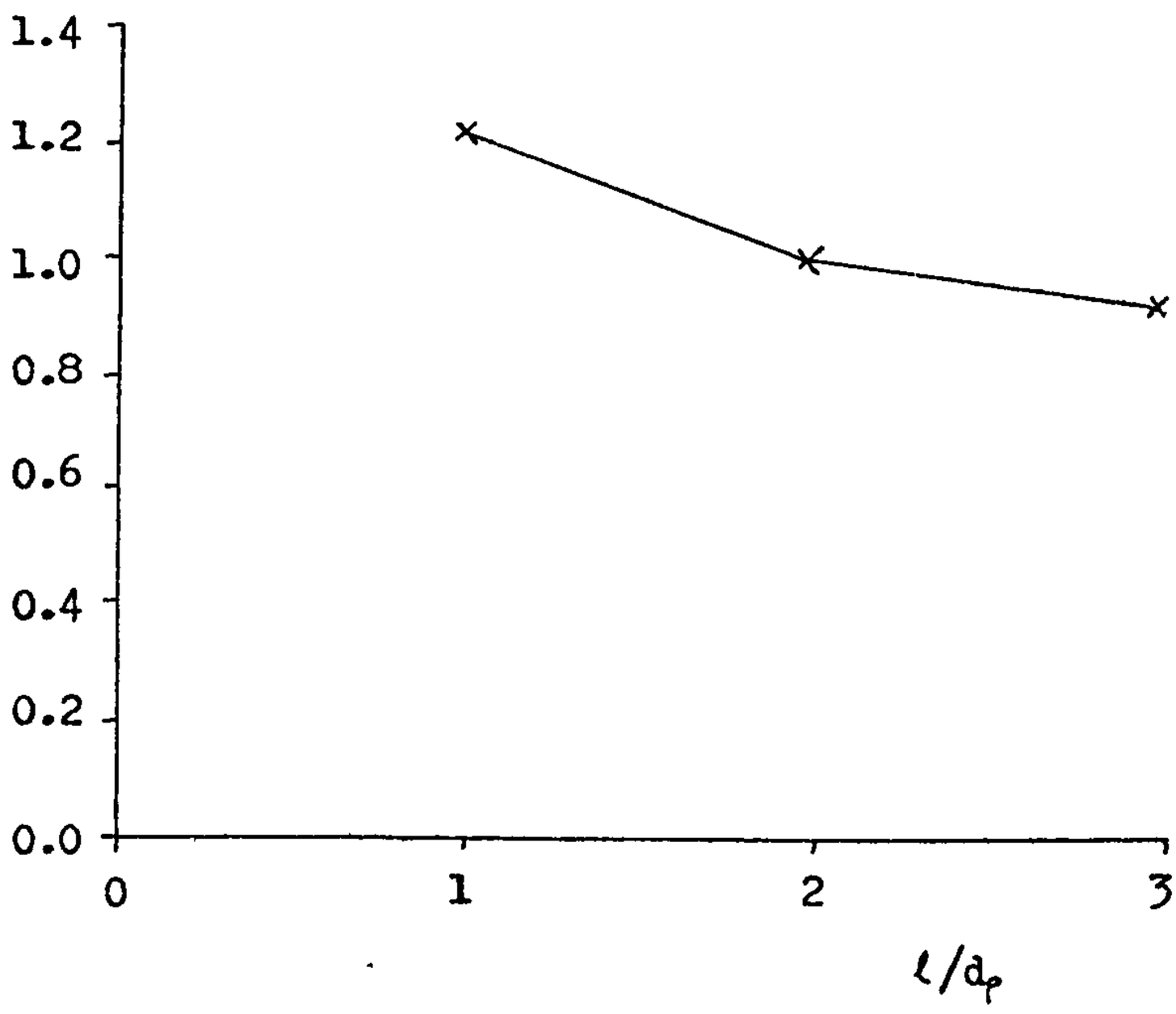

FIGURE 7.23 EFFECT OF ℓ/d_p ON BOND STRENGTH FOR CONNECTIONS WITH SHEAR KEYS, PREDICTED BY THE FINITE ELEMENT ANALYSIS.

keys are also crushing at the loaded end where Poisson effects are greatest. The loads on these sleeve keys vary from V = 199 to 203 N/mm. Although not all the sleeve keys are crushing, the load they can sustain is less than for the pile keys, due to the greater radial movement on the sleeve bond.

7.3.5 Varying h and s

In order to study the effects of varying h and s, the P9/10 geometry was again chosen. Also, a number of experimental results (8) are based on this case. Any magnitude of shear key height (h) can be chosen for the analysis and the spacing (s) can be 1/3 or 2/3 of the spacing used in the P9/10 analysis.

Table 7.6 gives the results of these analyses, as well as the corresponding bond formulae predictions for comparison. Unfortunately it is not possible to make direct comparisons with the experimental results as the values of h and s differ. However, by plotting bond strength against h/s (Figure 7.24), it is possible to see the trends of the various predictive methods and to compare against the experimental results which are also plotted. It can be seen that the current bond formula tends to over-estimate the bond strength at high h/s and both bond formulae continue to show a linear increase in bond strength with h/s. The finite element results are interesting as the bond strength appears to level off for high h, whilst a low spacing s, continues to show strength increases. The experimental results would appear to agree with this trend as the R-series results, for which h is varied, fall slightly below the Q-series results, where s is varied.

h	s	h/s	F_{BU3I}			
			Exptl.	Finite Element	Bond Formula	New Bond Formula
2.03	152.4	0.012	1.80	1.93	1.90	1.70
10.15	152.4	0.060	-	3.51	6.44	4.52
5.075	152.4	0.030	-	2.70	3.60	2.75
2.03	101.6	0.018	-	2.32	2.46	2.05
2.03	50.8	0.036	-	3.58	4.17	3.11

TABLE 7.6. BOND STRENGTH PREDICTIONS MADE BY FINITE ELEMENT ANALYSIS AND BOND FORMULAE FOR VARIOUS VALUES OF h AND s .

V_{max} N/mm	s mm
274	152
247	105
210	51

TABLE 7.7. EFFECT OF KEY SPACING,s, ON MAXIMUM KEY LOAD.

$\frac{\sigma_{key}}{CONF}$ (N/mm^2)	Slip/CONF (mm)		
	Square Key	Hemisphere Key	Triangle Key
296	6.7	8.0	9.0
420	12.6	15.0	16.8
450	15.1	18.0	20.2

TABLE 7.8. SHEAR KEY STRESS-SLIP DATA FOR VARIOUS KEY SHAPES.

KEY

——— o = Vary h } Finite Element Analysis,
——— + = Vary s } P9/10 type , 1/d=2 , Stiffened.
– – – – – □ = New Bond Formula
———– – – Δ = Current Bond Formula
× = Experimental Results :-

R-Series:

Have double no. of stiffeners,

s=169.32 , and h is varied.

Q-Series:

Results multiplied by 0.8 for

1/d=2 (actual 1/d=1) ,

h=2.03 , and s is varied.

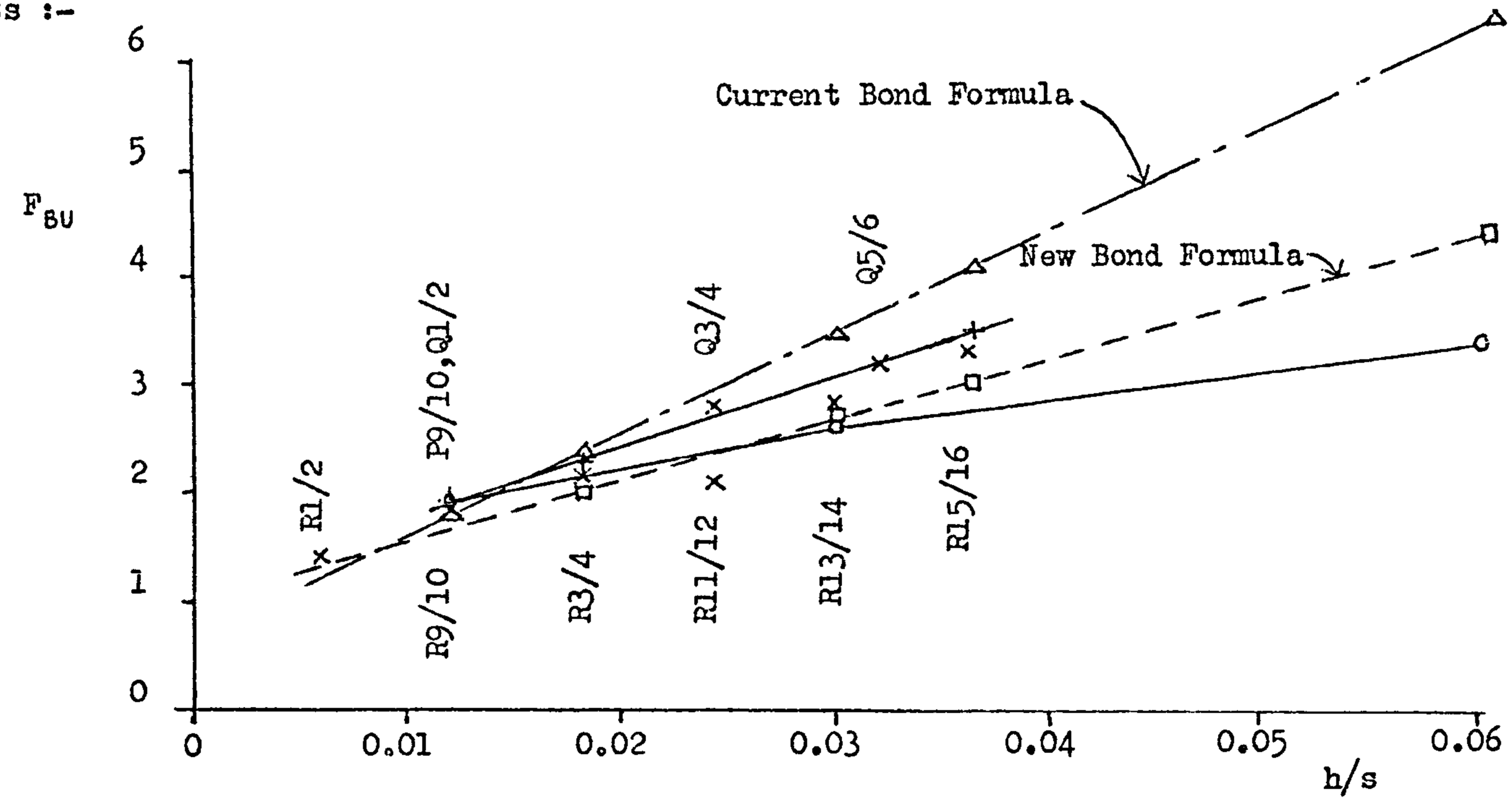

FIGURE 7.24 EXPERIMENTAL AND PREDICTED EFFECTS OF h/s ON ULTIMATE BOND STRENGTH.

When a higher shear key upstand is used, the shear key load V, is also increased due to the larger contact area between key and grout, giving an increased bond strength. However, the radial key force V_R, will also increase, further opening the steel/grout bond. This tends to cause particular problems at the ends of the connection where, as previously described in Section 7.1.3, it is necessary to generate a large σ_n to balance the bending moments in the grout. If the radial key force is large and the shear key close to the end of the connection, it may not be possible to generate the normal bond stress and the grout cracks, (Figure 7.25). In order to maintain equilibrium without σ_n, the shear key loads redistribute between keys, concentrating loads at the ends where σ_n should be generated. This results in increased values of V_R at the ends to compensate for zero σ_n. However, as the shear key loads are no longer so evenly distributed, the keys carrying the peak loads will soon reach the point of crushing, which will then rapidly spread to the other keys. This is possibly the main reason why there is a limit to the maximum bond strength with increasing h. Figure 7.26 shows how the distribution of key loads change under increasing applied load, for h = 10.15 mm, given by the finite element analysis. The stress under the shear key at which crushing commences also falls with increasing h because the correspondingly increased radial key forces result in a larger bond opening and hence, reduced confinement of the grout.

It has been previously mentioned that increasing the shear key height above a certain size results in no additional bond strength. It may be possible to overcome this limitation by restricting the use of shear keys with increased upstand to the centre portion of the grouted connection. The smaller shear keys (or plain sections) at the ends of the connection

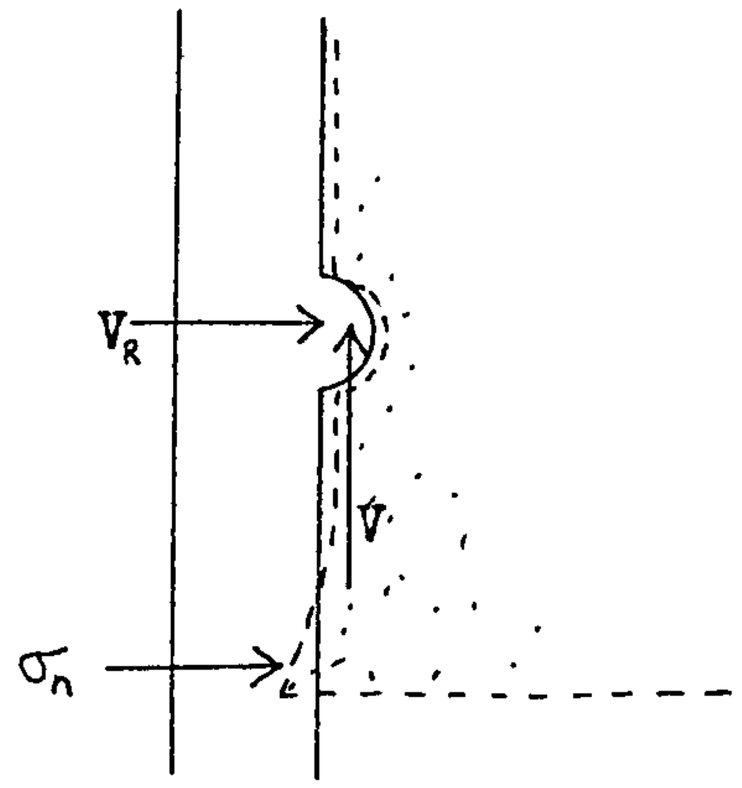

(a)Small shear key,low V_R,and σ_n is generated.

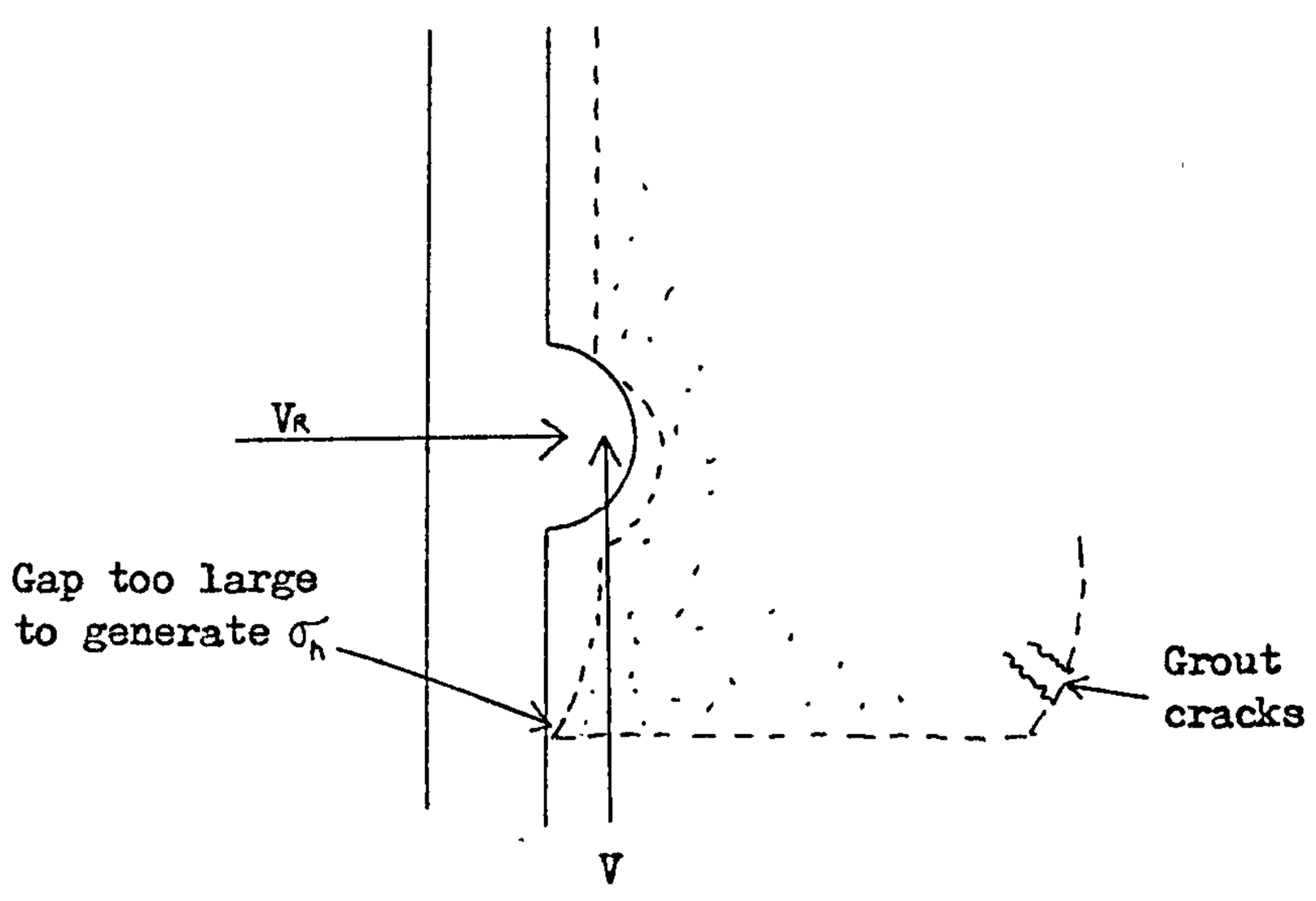

(b)Large shear key,high V_R,and large bond opening.

FIGURE 7.25 EFFECT OF A LARGE SHEAR KEY AT THE END OF A GROUTED CONNECTION ON THE NORMAL BOND STRESS.

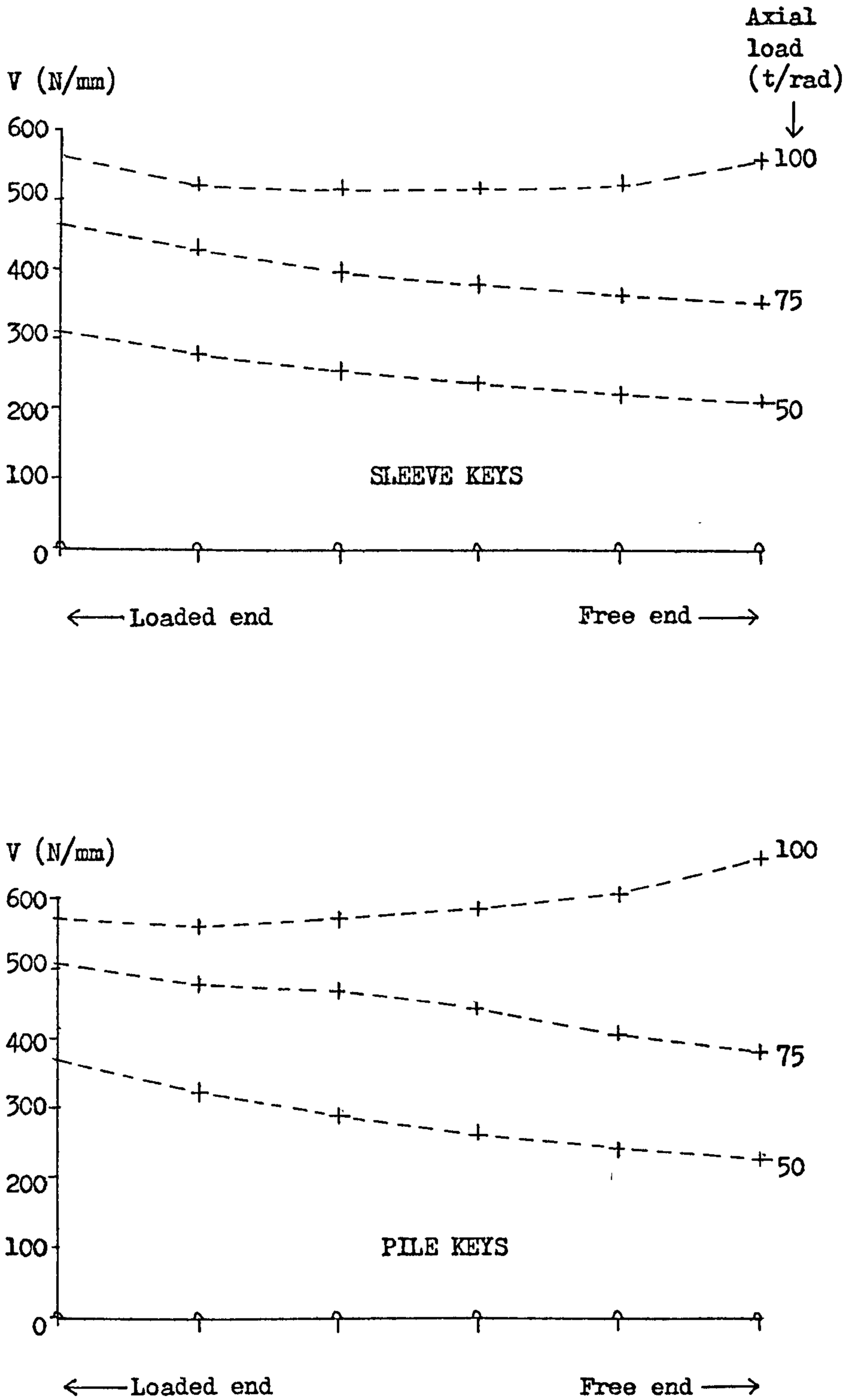

FIGURE 7.26 SHEAR KEY LOADS PER UNIT CIRCUMFERENCE (V) UNDER INCREASING APPLIED LOAD, FOR SHEAR KEYS WITH AN UPSTAND OF $h = 10.15$ mm. $(h/s = 0.06)$

will then produce lower radial key forces and so the normal bond stresses will still be generated to balance the bending moments in the grout. Another possibility would be to have wedge-shape ends on the sleeve and pile such as those shown in Figure 7.27. These would act like triangular shape shear keys, which have a high β ratio, so that V_R would be large, making σ_n unnecessary. This technique would not be practical on pile-sleeve connections since the section of pile coinciding with the grout annulus cannot be predetermined. However, for grouted repair work, such techniques may be useful.

For shear keys of fixed upstand but reduced spacing, the ultimate bond strength is greater than for keys of high h, but the same h/s ratio, because the value of V_R does not increase. However, as the keys become closer, the next key along tends to influence the bond opening and grout confinement. Therefore, the key crushing load will slowly reduce with reduced spacing and there will eventually be an upper limit on bond strength with increasing h/s. Table 7.7 shows the reduction in maximum key load with falling s at a distance of 100 to 150 mm from the unloaded end of the connection (where Poisson effects are small), given by the finite element analysis.

7.3.6 Alternative Loading Conditions

The analysis of the P9/10 geometry was repeated with the pile and sleeve both loaded in tension or compression. Results indicated that the compression loading was strongest with $F_{BU} = 2.28$ and for tension loading $F_{BU} = 2.22$. (The standard tension-compression case gave $F_{BU} = 1.93$).

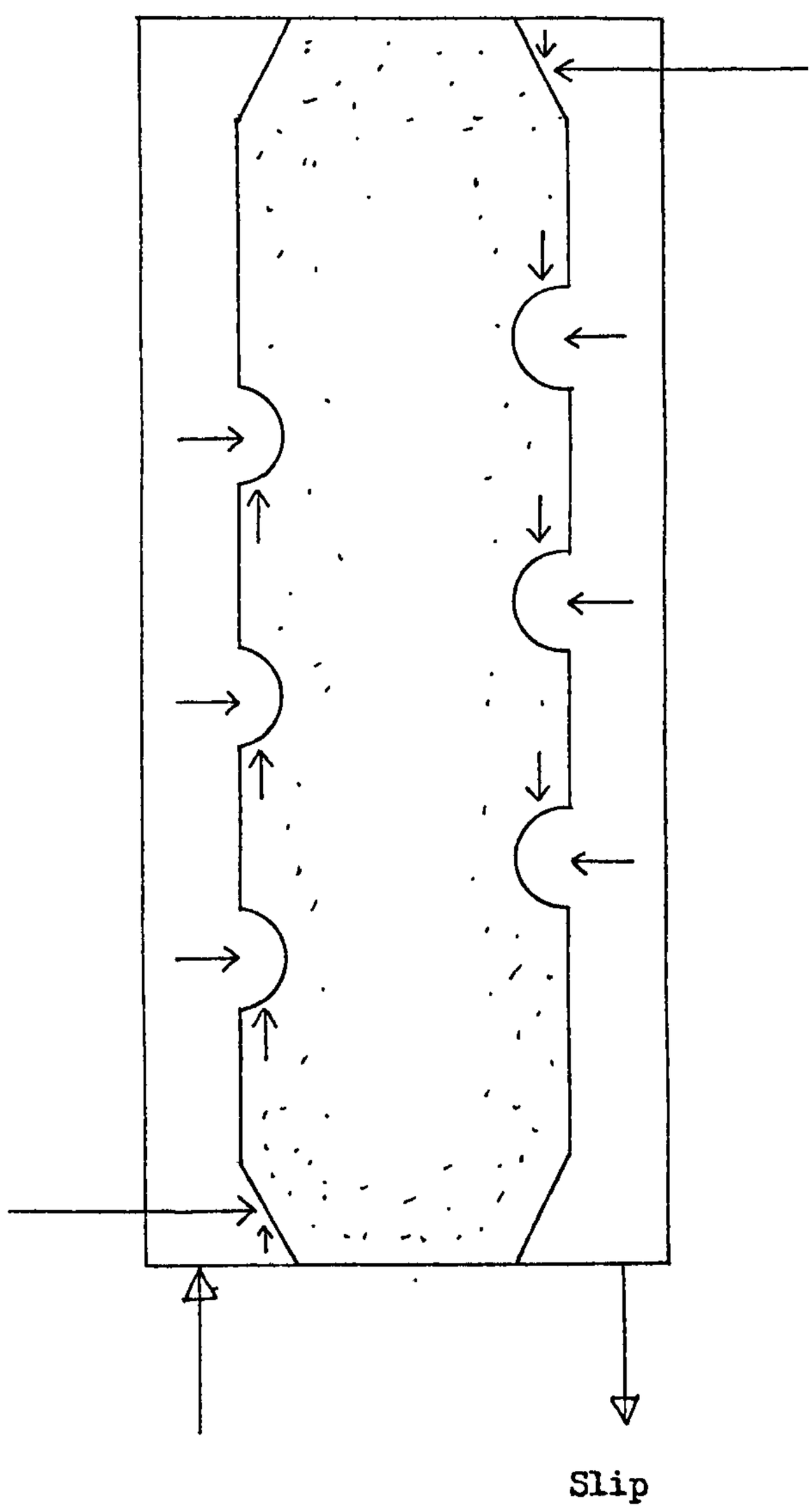

FIGURE 7.27 WEDGE-SHAPED ENDS MAY ENHANCE THE STRENGTH OF CONNECTIONS WITH LARGE SHEAR KEYS. LOADS ON THE GROUT ARE INDICATED.

For compression loading, the sleeve keys crush with V = 236 to 311 N/mm. On the pile, V = 61 to 69 N/mm, which is very small because the bond stresses remain high on the pile bond. The sleeve bond on the other hand opens completely, which is why the sleeve key loads are so high.

For the tension loading, the reverse situation arises, with the pile keys crushing. V = 236 to 324 N/mm on the pile and V = 44 to 84 N/mm on the sleeve. Figures 7.28 and 7.29 give plots of the bond stresses at ultimate load for these two loading arrangements.

These alternative loading conditions have less effect on ultimate load when shear keys are used. For these conditions the shear key ultimate crushing loads are less sensitive to Poisson effects than plain pipe frictional bond stresses. (For comparison, see the plain pipe results in Section 7.2.5).

The tests reported by Wimpey Laboratories (10) for connections with split sleeves show tension loading to be stronger than compression loading, which contradicts the above findings. In fact, the differences can be easily accounted for by the split-sleeves. The circumferential stiffness of the sleeve will be less in tension than in compression because the joint will open under tension. When the sleeve is axially loaded in compression, Poisson effects cause a tensile hoop stress and the radial bond opening will be increased by the relatively low tensile stiffness of the joint. The compression loading strength will therefore be lower with split-sleeves.

Another situation which has been studied involves the transfer of load onto the sleeve at a number of points along the sleeve's axis, rather than end loading. This would more accurately represent the method

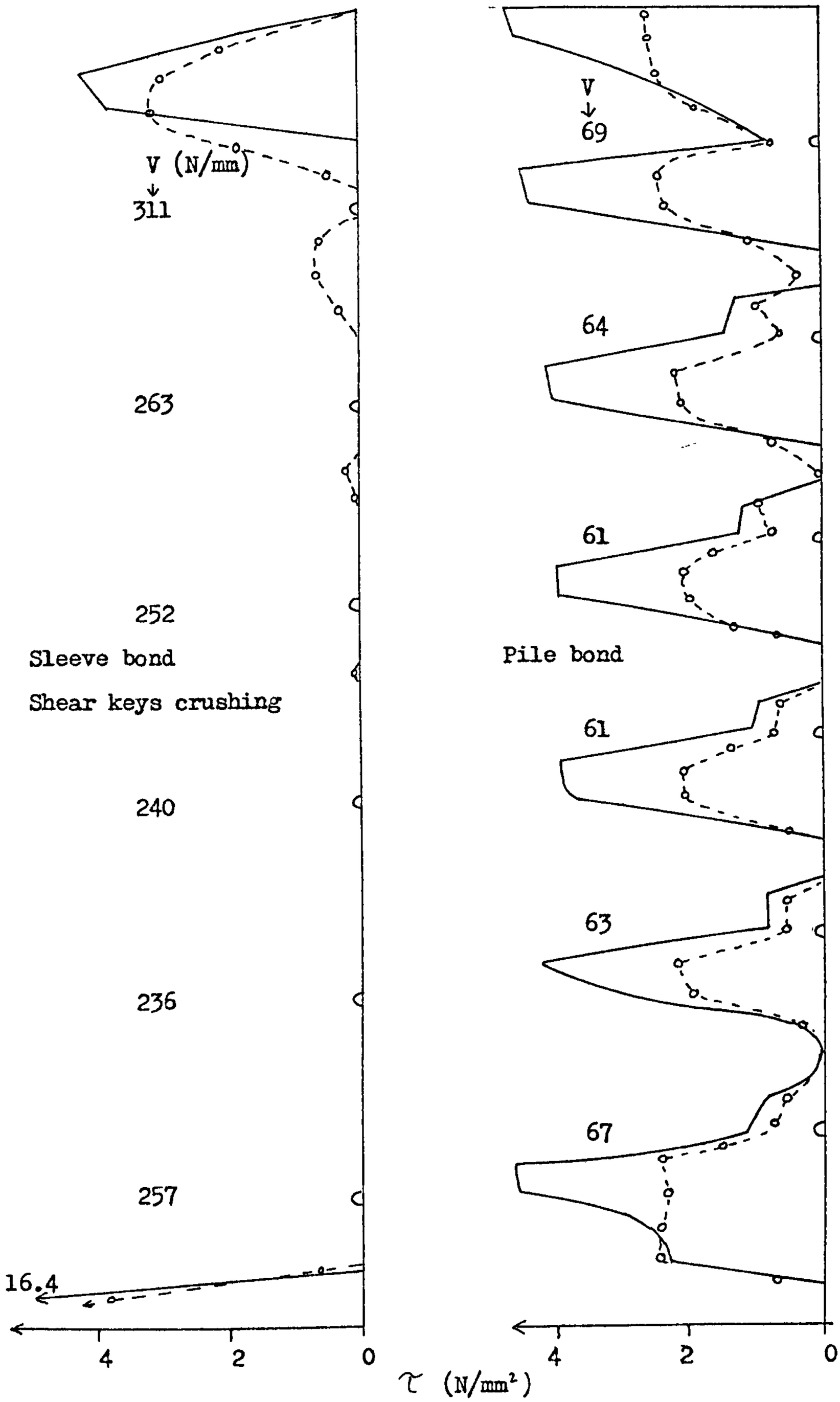

FIGURE 7.28 BOND STRESSES AND SHEAR KEY LOADS AT ULTIMATE LOAD UNDER COMPRESSION LOADING FOR THE P9/10 GEOMETRY.

Load = 63.3 t/rad (maximum)

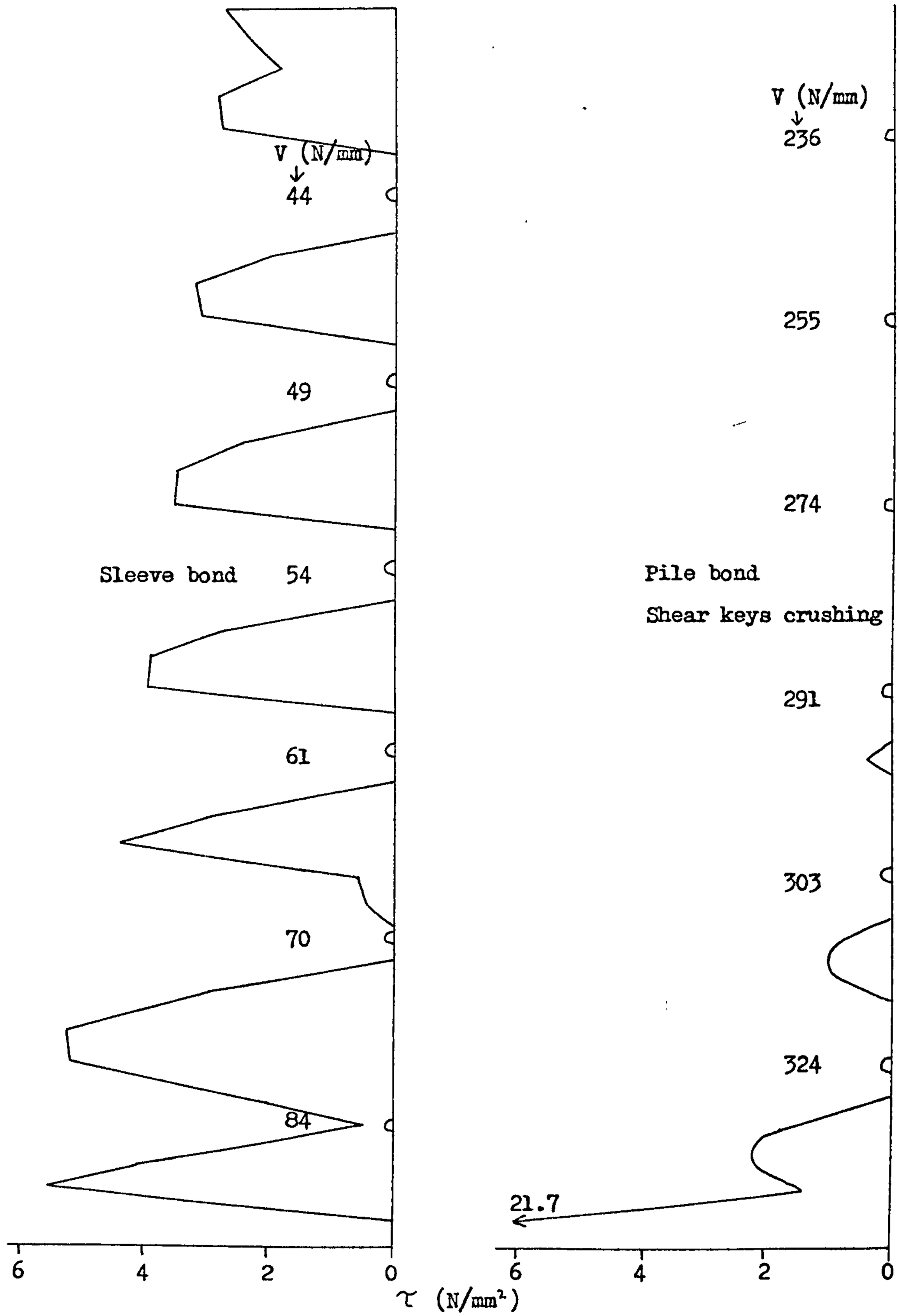

FIGURE 7.29 BOND STRESSES AND SHEAR KEY LOADS AT ULTIMATE LOAD UNDER TENSION LOADING FOR THE P9/10 GEOMETRY.

of transferring load from a jacket leg to the sleeve.

To analyse this situation, the sleeve nodes were restrained axially at every second shear key location (that is, at three locations for the P9/10 geometry). The analysis was repeated with axial and radial restraints at these three points in order to represent the high radial stiffness adjacent to the structure which transfers the load to the sleeve. Compression loading was used for both of these cases.

The bond stresses and shear key loads at ultimate load are plotted in Figures 7.30 and 7.31 and can be compared with the results for compression end-loading given in Figure 7.28. It can be seen that with the three axial restraints, the bond stresses on the sleeve remain fairly high over the whole length of the connection. This is because one third of the axial load is removed at each of the three fixed points and so the Poisson effects are limited and do not become larger towards one end.

The analysis did not reach ultimate load. When the load was increased to 41 t/radian, convergence was not achieved in 35 iterations and so the analysis was terminated. At this load, the sleeve bond suddenly opens over the whole length of the connection, creating too many state changes for the analysis to deal with, and thus convergence is not achieved. The problem arises because the bond stresses are of almost constant magnitude over the whole length of the sleeve bond and so the whole bond will simultaneously reach the point of slipping and opening.

When the sleeve is restrained radially as well as axially at the three levels, then the bond stresses become significantly higher due to the radial restraints. The ultimate load was 125 t/radian, which is nearly double the strength of an end-loaded connection. Failure was by crushing around the pile shear keys.

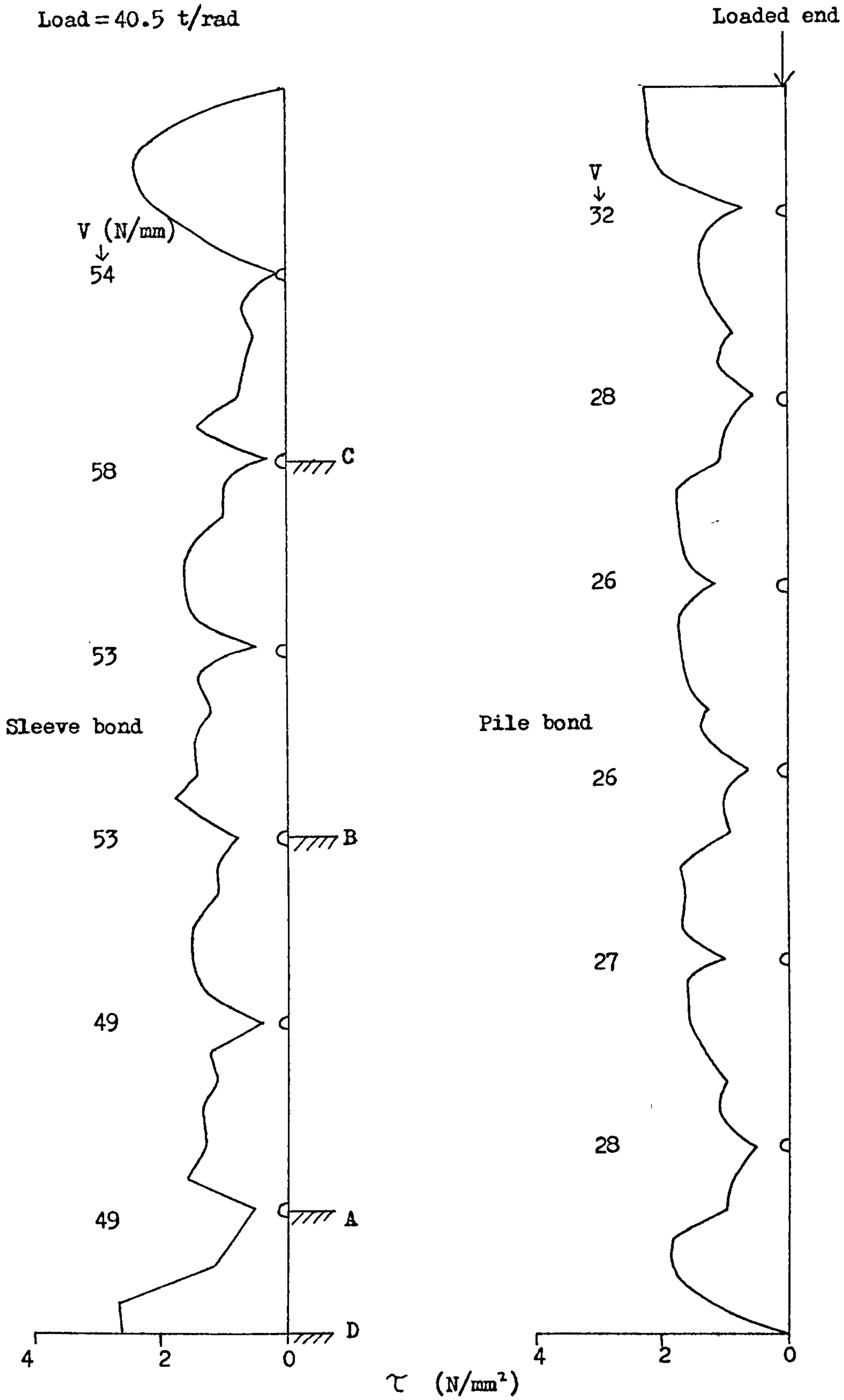

FIGURE 7.30 BOND STRESSES AND SHEAR KEY LOADS FOR P9/10 UNDER COMPRESSION LOADING AND RESTRAINED AXIALLY AT POINTS A,B,C AND D.

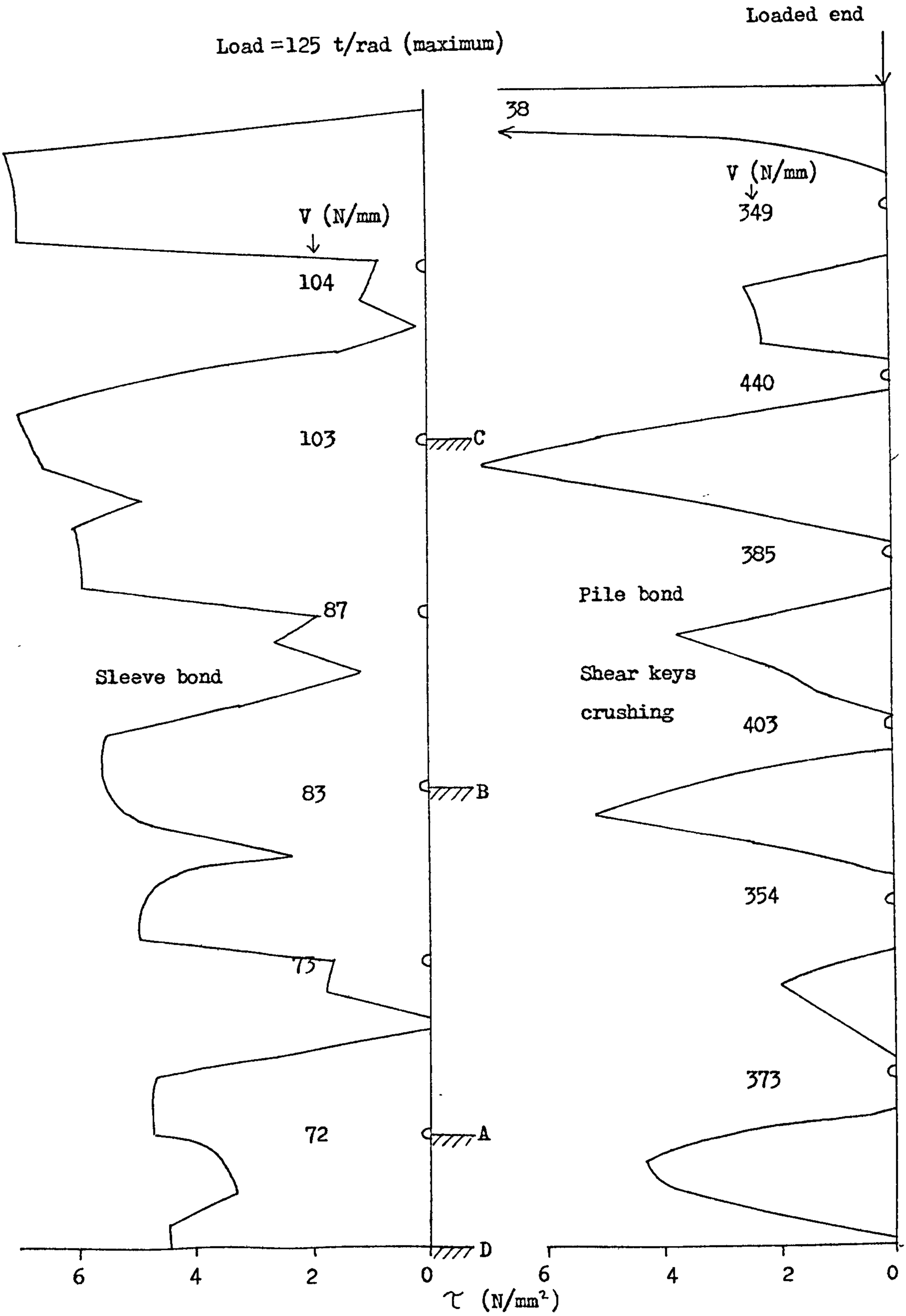

FIGURE 7.31 BOND STRESSES AND SHEAR KEY LOADS FOR P9/10 UNDER COMPRESSION LOADING AND RESTRAINED AXIALLY AND RADIALLY AT POINTS A,B,C AND D.

This analysis shows that bond strengths can be greatly increased when a thin sleeve is used by the addition of hoop stiffeners around the sleeve to resist radial displacements. These stiffeners should be arranged to coincide with the shear keys in order to provide maximum resistance against the radial key forces.

7.3.7 Effect of Removing the Stiffeners

In reality, the sleeve would buckle or yield without some stiffening at ultimate load, but as the steel is treated as linear-elastic in the analysis, it is possible to remove the longitudinal stiffeners to see what effect they have on the bond strength. This is of interest since connections are not generally stiffened.

The effect of removing the stiffeners is achieved in the analysis by reducing the thickness of the plane stress elements which represent the stiffeners from 12.414 mm to 0.1 mm, which is considered to be insignificant.

Using the P9/10 geometry and tension-compression loading, a bond strength of $F_{bu} = 1.30$ was produced, which is only 67% of the strength of a stiffened connection. Failure was by crushing around the sleeve shear keys, whereas for the stiffened connection crushing occurs around the pile shear keys. This is because the axial stresses in the sleeve are approximately doubled by removing the stiffeners, which results in a doubling of the Poisson effects. This causes reduced confinement of the grout under the sleeve shear keys and leads to crushing at a relatively low shear key load. The ultimate shear key loads on the sleeve were $V = 144$ to 189 N/mm, whilst the loads on the pile keys, which did not crush were $V = 164$ to 186 N/mm.

Figure 7.32 shows the unstiffened bond stresses and key loads which can be compared with the corresponding stiffened values in Figure 7.22. Note that at this load level, bond stresses are not completely reduced to zero. Bond stresses remain on the sleeve opposite the pile keys due to the effects of V_R on the pile key radially expanding the grout. Similarly, pile bond stresses are influenced by the sleeve shear keys.

The effect of stiffeners on ultimate bond strength can therefore be quite significant and adequate allowance for this effect should be made when using laboratory test results from stiffened connections.

The bond formulae also predict a bond strength reduction when stiffeners are removed, but not to the same extent as the finite element analysis. The new bond formula (Chapter 8), gives a bond strength of $F_{BU} = 1.41$ without stiffeners, which is 83% of the stiffened strength and the standard bond strength formula gives a strength 93% of the stiffened value.

7.3.8 Scale Effects

In order to investigate the effects of a change in scale on the bond strength, the P9/10 analysis was repeated with all the coordinate dimensions doubled. The shear key height was also doubled to 4.06 mm, and the plane stress stiffener elements doubled in thickness to 24.828 mm. The surface roughness of the steel is not affected by scale and so $u_m = 0.04$ mm as before.

For the same bond strength, the double size specimen should have a quadrupled load capacity. The load capacity predicted by the finite element analysis was 160 tonnes/radian, which gives $F_{BU} = 1.40$.

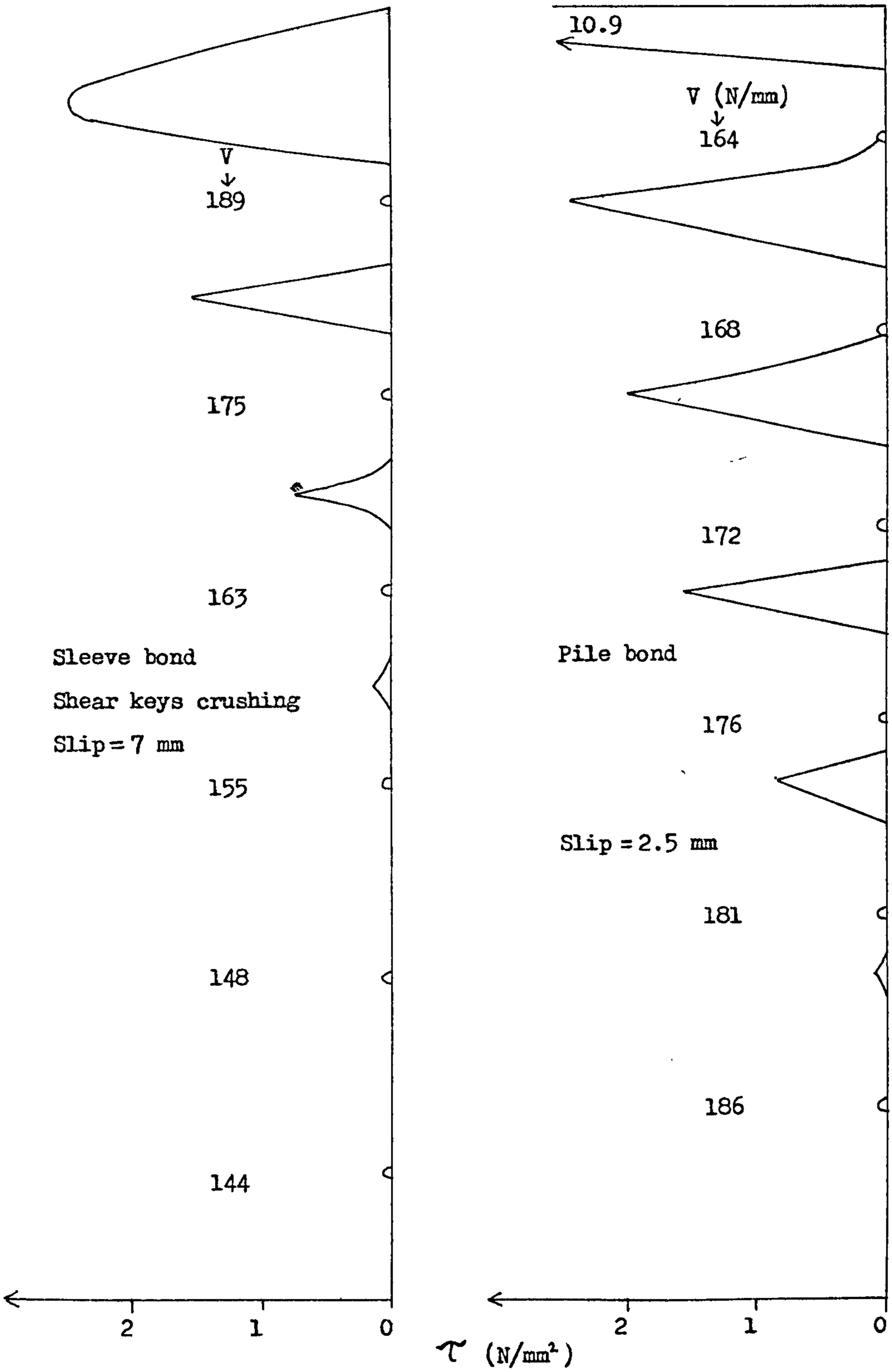

FIGURE 7.32 BOND STRESSES AND SHEAR KEY LOADS AT ULTIMATE LOAD FOR THE UNSTIFFENED P9/10 CASE.

This is 73% of the bond strength at the standard scale. Failure was by crushing around the pile shear keys, although the sleeve shear keys were also close to failing. Maximum pile shear key loads were V = 339 to 403 N/mm and sleeve key loads were V = 326 to 387 N/mm. Bond stresses were reduced to zero except at the extreme ends of the connection. Figure 8.2 gives a plot of bond strength against scale, where it is seen that the bond formula of Chapter 8 also predicts a reduction in bond strength of the same order of magnitude.

Slip at maximum load was about twelve millimetres and was identical to the previous smaller scale P9/10 analysis. This suggests that slip at ultimate load is unaffected by scale and this agrees with the conclusions of Section 2.15.

Many laboratory tests are made at a reduced scale and so an allowance should be made for a lower bond strength in the full size case. Figure 8.2 suggests that the error will be greater for smaller scale models.

7.3.9 Other Key Shapes

In Section 7.1.4 a detailed analysis of square and triangular shape shear keys was carried out. From this analysis, parameters were derived which can be used in the present study to represent square or triangular shaped shear keys on the P9/10 geometry. The values of β used are 0.04 and 0.83 for square and triangular shapes respectively. Values of slip for the shear key stress-slip curve are increased or reduced in accordance with the larger or smaller value of k_{sc} derived in Section 7.1.4, so that the initial value of k_{sc} given by the curve will be correct. The values used are given in Table 7.8.

Results for the triangular shear keys give an ultimate bond strength of $F_{BU} = 1.51$, which is 78% of the strength for hemispherical weld bead shear keys. Failure was by crushing around the sleeve shear keys, with $V = 166$ to 197 N/mm, whilst the pile shear key loads were only 32 to 48 N/mm, as bond friction remained high on the pile bond. With hemispherical shear keys, failure is on the pile bond, but with such high radial key forces, the triangular keys cause the sleeve bond to open sufficiently for the grout to crush around the sleeve shear keys in the first instance.

For square shape shear keys, the analysis gives an ultimate bond strength of $F_{BU} = 3.37$, which is 75% stronger than for the standard weld bead keys. Failure was by crushing around the pile shear keys, with ultimate key loads of $V = 304$ to 917 N/mm. The 917 N/mm only occurred on the top key, away from the loaded end, where radial confinement is high due to end effects. Although the sleeve keys did not crush, they ultimately carried higher loads than the pile keys at the loaded end. This would not have been possible without stiffeners on the sleeve, which reduce the Poisson effects.

Figures 7.33 and 7.34 show the bond stress distributions and shear key loads at ultimate load, which differ considerably from the results for hemispherical shape shear keys shown in Figure 7.22.

It can be concluded that square shape shear keys should be the most effective at producing high bond strengths. Unfortunately, it seems unlikely that square keys could be produced conveniently and economically and so the standard hemispherical weld bead is likely to remain as the form of shear key used in most applications.

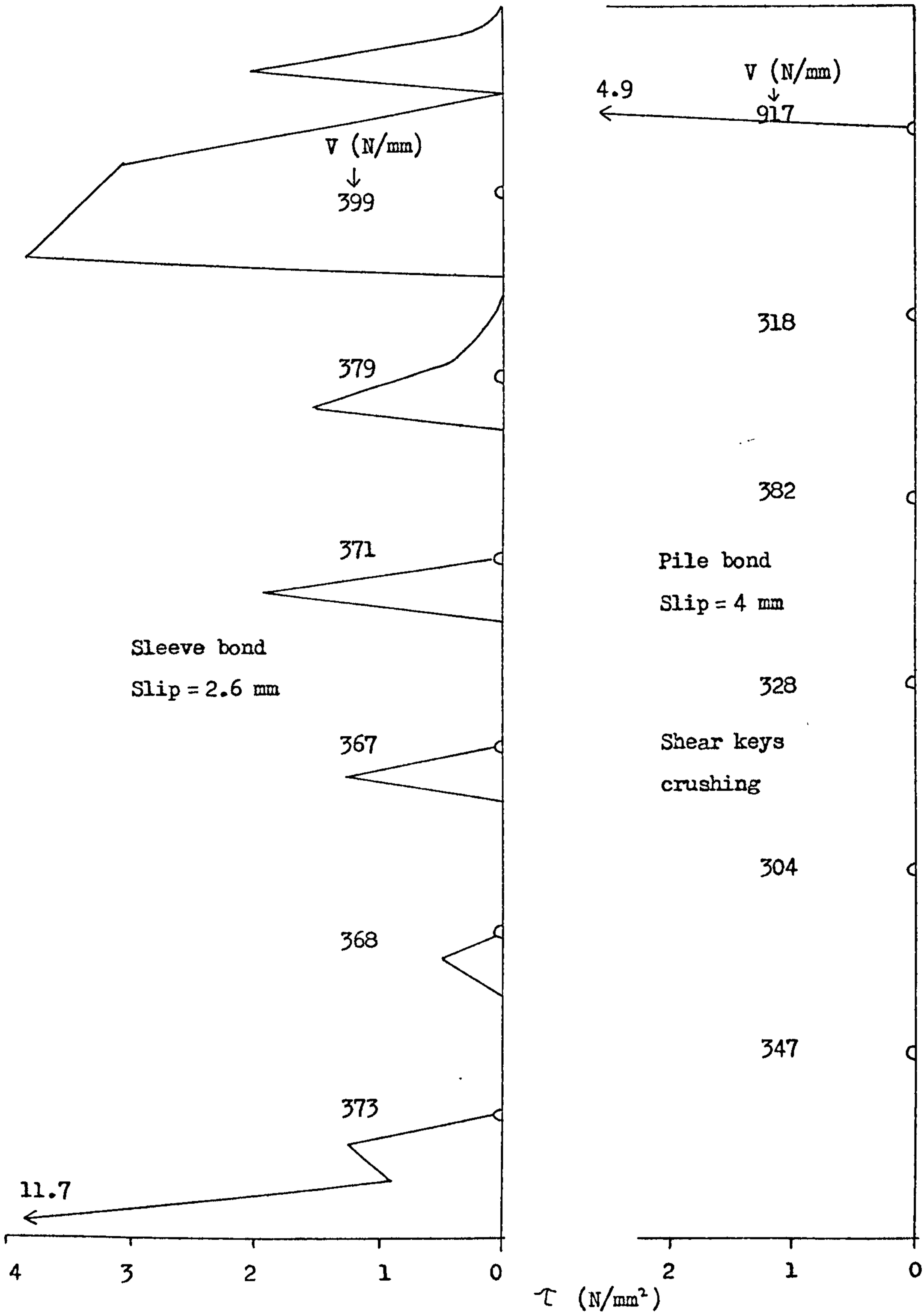

FIGURE 7.33 BOND STRESS DISTRIBUTION AND SHEAR KEY LOADS AT ULTIMATE LOAD USING SQUARE SHAPE SHEAR KEYS.

Load = 43.3 t/rad (maximum)

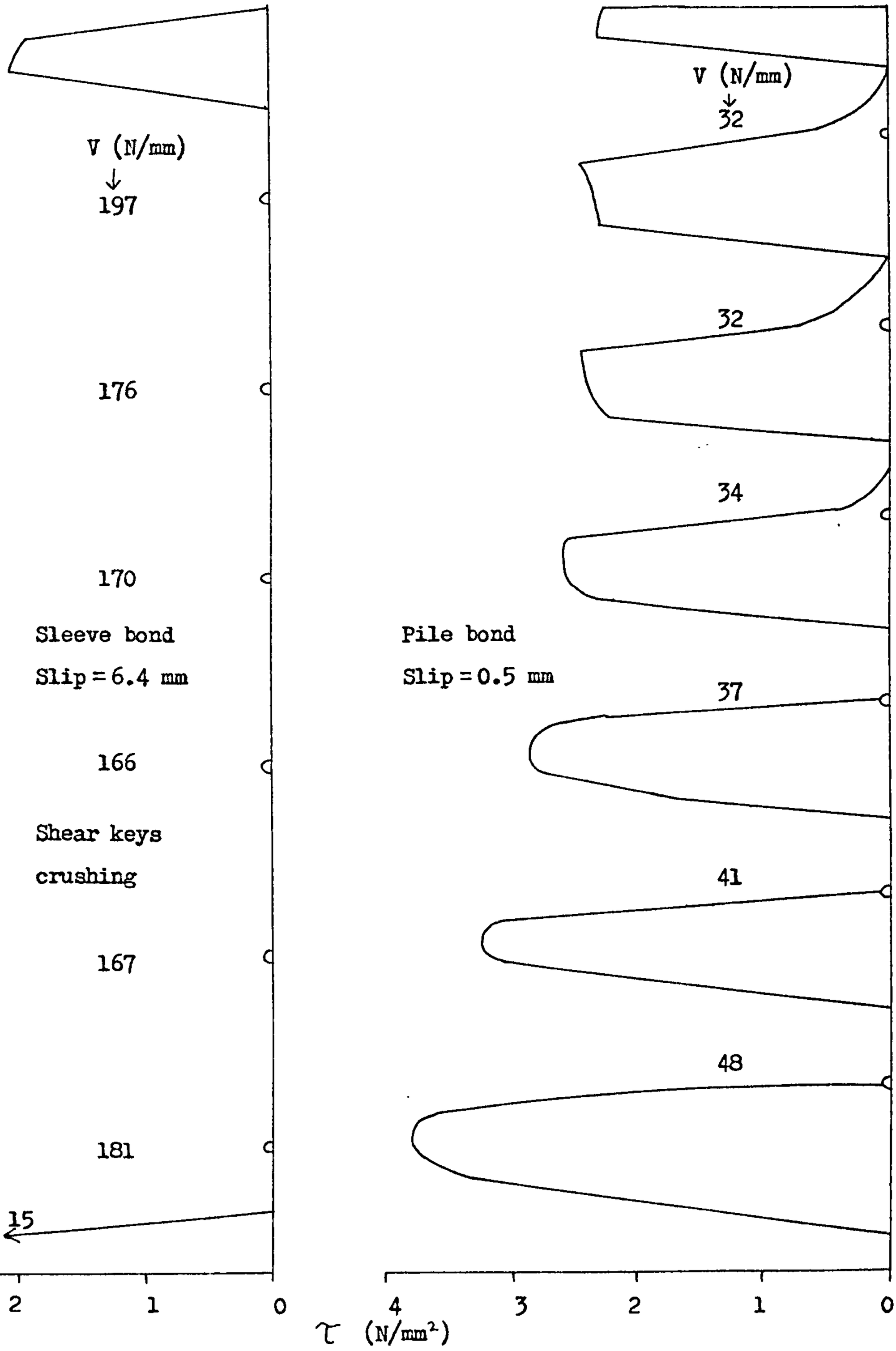

FIGURE 7.34 BOND STRESS DISTRIBUTION AND SHEAR KEY LOADS AT ULTIMATE LOAD USING TRIANGULAR SHAPE SHEAR KEYS.

CHAPTER 8

A NEW STRENGTH FORMULA FOR GROUTED CONNECTIONS

8.1 Introduction

The existing bond strength formula has been described in Chapters 1 and 2 and whilst being applicable, it does lack a sound theoretical basis. Also, the formula has been developed for a limited range of geometries and for extreme geometries it is less convincing. For a hypothetical grouted connection with hoop stiffness K, approaching infinity, the formula predicts a strength approaching infinity. This is not possible since the sleeve and pile could be held rigid radially but there would still be an upper limit on the strength. This strength is determined by the surface bond friction strength and grout crushing strength around the shear keys.

The proposed formula is based on the ideas of friction and roughness which have been used in the finite element analysis. Also, the formula accounts for the effects of ℓ/d_p and sleeve stiffeners. Shear keys are treated similarly in the finite element analysis, but for simplicity the effects of confinement are excluded. The following derivation of this formula is based on the sleeve being loaded in compression and the pile in tension, so that Poisson effects will cause separation on both bonds.

8.2 Derivation of the Strength Formula

A mean value for normal bond stress $\overline{\sigma}_n$, over the whole length of the grouted connection at ultimate loading is given as follows

$$\overline{\sigma}_n = k_n(u_m - \delta') \geq 0 \qquad (8.1)$$

where k_n = normal bond stiffness in N/mm^3,

u_m = maximum surface roughness in mm and

δ' = mean radial bond opening in mm.

$\bar{\sigma}_n$ is a general term, not accounting for the difference in σ_n on the sleeve and pile bonds.

The hoop stress, $\bar{\sigma}_\theta$, is then given by

$$\bar{\sigma}_\theta = \frac{\bar{\sigma}_n 2r}{2t} = \bar{\sigma}_n \frac{r}{t} \qquad (8.2)$$

where Figure 8.1 describes the geometric terms.

The maximum bond stress due to the shear keys τ_{sk}, is given by

$$\tau_{sk} = \sigma_m h/s \qquad (8.3a)$$

where σ_m is a constant. A radial component of shear key stress may exist σ_{sk}, and is given as a constant function of τ_{sk}.

$$\sigma_{sk} = \beta \tau_{sk} = \beta \sigma_m h/s \qquad (8.3b)$$

where β = constant, $0 \leq \beta \leq 1$, the value being dependent on the shear key shape.

The total hoop stress then becomes

$$\bar{\sigma}_\theta = (\bar{\sigma}_n + \sigma_{sk})r/t$$

Therefore
$$\bar{\sigma}_\theta = k_n \frac{r}{t}(u_m - \delta') + \beta \sigma_m \frac{h}{s} \frac{r}{t} \qquad (8.4)$$

Mean hoop strain $\bar{\epsilon}_\theta$, is given by

$$\bar{\epsilon}_\theta = \frac{\bar{\delta}}{r} = \frac{1}{E}(\bar{\sigma}_\theta - \nu \bar{\sigma}_z) \qquad (8.5)$$

where $\bar{\sigma}_z$ = mean axial stress. (Radial stress $\simeq 0$).

E, ν are Young's Modulus and Poisson's Ratio for steel.

$$\bar{\sigma}_z = \frac{P/2}{2\pi rt + A_{stiff}} \qquad (8.6)$$

where $P = -f_{bu} . 2\pi r_p \ell$ = axial load (8.7)

A_{stiff} = total cross-sectional area of all stiffeners on the sleeve

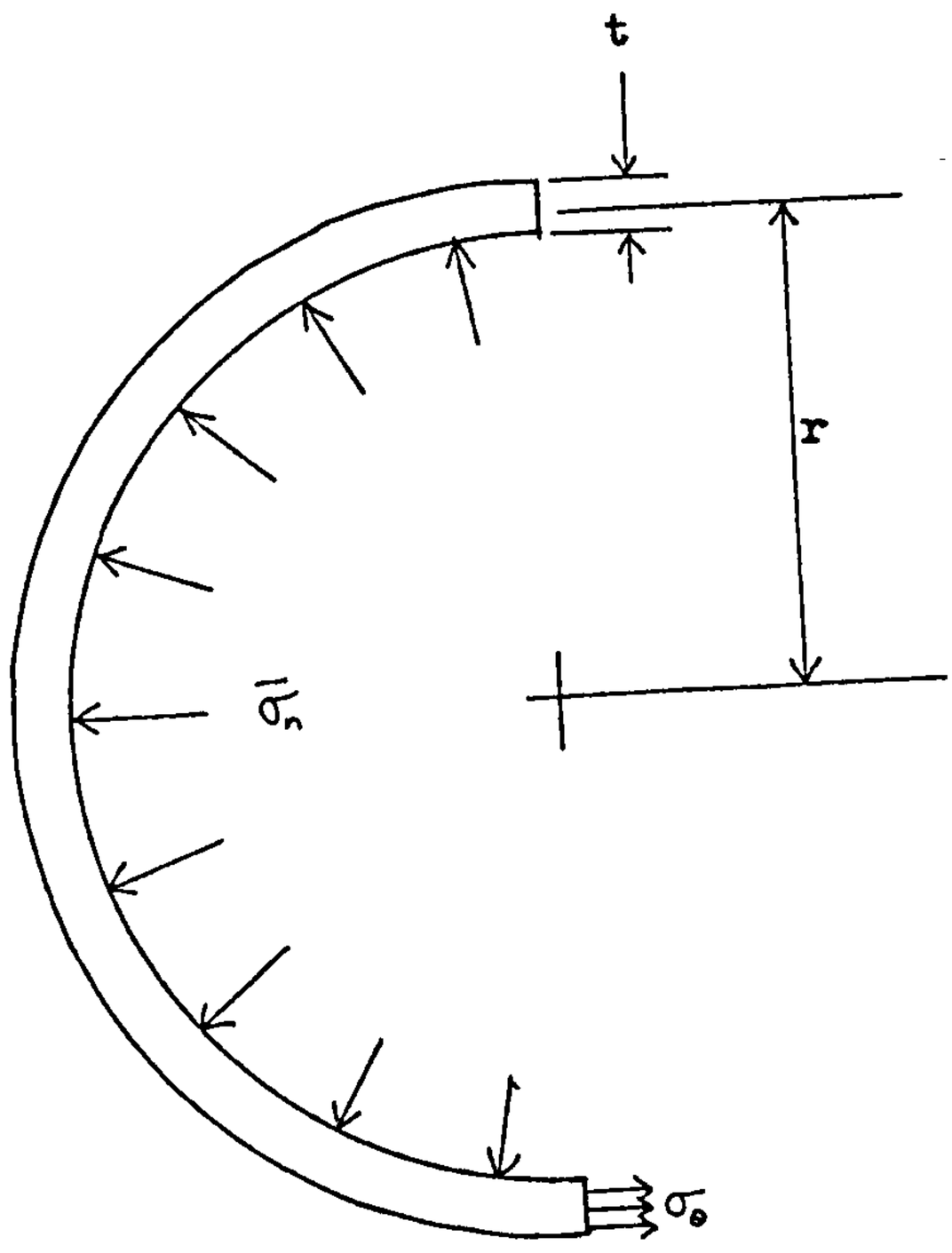

FIGURE 8.1 GEOMETRIC TERMS.

l = grouted length, and

f_{bu} = ultimate bond strength.

Therefore $\quad \bar{\sigma}_z = \dfrac{-\pi r_p l f_{bu}}{2\pi r_s t_s + A_{stiff}}$ for the sleeve. (8.8)

Equations (8.8), (8.4) and (8.5) combine to give radial sleeve and pile openings, $\bar{\delta}_s$ and $\bar{\delta}_p$ respectively.

$$\bar{\delta}_s = \frac{r_s}{t_s E}\left(k_n r_s(u_m - \delta') + \beta\sigma_m\frac{h}{s}r_s + \frac{\nu\pi r_p l f_{bu}}{2\pi r_s + A_{stiff}/t_s}\right) \tag{8.9a}$$

and

$$\bar{\delta}_p = \frac{r_p}{t_p E}\left(k_n r_p(u_m - \delta') + \beta\sigma_m\frac{h}{s}r_p + \frac{\nu f_{bu} l}{2}\right) \tag{8.9b}$$

The mean bond opening is then given by

$$\delta' = \frac{\bar{\delta}_s + \bar{\delta}_p}{2} \tag{8.10}$$

Substituting equation (8.9) into equation (8.10) gives

$$\delta' = \frac{1}{2E}\left\{ k_n(u_m - \delta')\left(\frac{r_s^2}{t_s} + \frac{r_p^2}{t_p}\right) + \beta\sigma_m\frac{h}{s}\left(\frac{r_s^2}{t_s} + \frac{r_p^2}{t_p}\right) + \frac{\nu f_{bu} l r_p}{2}\left(\frac{\pi r_s}{\pi t_s r_s + A_{stiff}/2} + \frac{1}{t_p}\right)\right\} \tag{8.11}$$

Let

$$\gamma = \left(\frac{r_s^2}{t_s} + \frac{r_p^2}{t_p}\right) \tag{8.12a}$$

$$\theta = \left(\frac{\pi r_s}{\pi t_s r_s + A_{stiff}/2} + \frac{1}{t_p}\right) \tag{8.12b}$$

This assumes no stiffeners on the pile, otherwise the pile term will be similar to the sleeve term.

Then $\quad \delta' = \dfrac{1}{2E}\left\{ k_n(u_m - \delta')\gamma + \beta\sigma_m\dfrac{h}{s}\gamma + \dfrac{\nu f_{bu} l r_p \theta}{2}\right\}$.

Therefore $\quad \delta'\left\{1 + \dfrac{k_n\gamma}{2E}\right\} = \dfrac{1}{2E}\left\{ k_n u_m\gamma + \beta\sigma_m\dfrac{h}{s}\gamma + \dfrac{\nu f_{bu} l r_p\theta}{2}\right\}$,

giving $\quad \delta' = \dfrac{k_n u_m\gamma + \beta\sigma_m\gamma h/s + \nu f_{bu} l r_p\theta/2}{2E + k_n\gamma}$ (8.13)

The basic formula for bond and shear key strength is given as

$$f_{bu} = c + \mu\bar{\sigma}_n + \sigma_m h/s \qquad (8.14)$$

where c = constant for adhesion. This term is probably small and may be zero.

Substituting from equations (8.1) and (8.13) gives

$$f_{bu} = c + \mu k_n(u_m - \delta') + \sigma_m h/s \quad ,$$

$$\text{then} \quad f_{bu} = c + \mu k_n u_m - \left\{ \frac{\mu k_n^2 u_m \gamma + \mu k_n \beta \sigma_m \gamma h/s + \mu k_n \nu f_{bu} \ell r_p \theta/2}{2E + k_n \gamma} \right\} + \sigma_m h/s \qquad (8.15)$$

$$\text{Therefore} \quad f_{bu} \left\{ 1 + \frac{\mu k_n \nu \ell r_p \theta/2}{2E + k_n \gamma} \right\} = c + \mu k_n u_m - \frac{(\mu k_n^2 u_m \gamma + \mu k_n \beta \sigma_m \gamma h/s)}{2E + k_n \gamma} + \sigma_m h/s \quad ,$$

$$\text{giving} \quad f_{bu} = \frac{(c + \mu k_n u_m + \sigma_m h/s)(2E + k_n \gamma) - \mu k_n^2 u_m \gamma - \mu k_n \beta \sigma_m \gamma h/s}{2E + k_n \gamma + \mu k_n \nu \ell r_p \theta/2}$$

$$f_{bu} = \frac{2E \{ c + \mu k_n u_m + \sigma_m h/s \} + \{ c + (1 - \mu\beta) \sigma_m h/s \} k_n \gamma}{2E + k_n \gamma + \mu k_n \nu \ell r_p \theta/2} \qquad (8.16)$$

By gathering constants, equation (8.16) gives the final bond strength formula.

$$f_{bu} = \frac{A + Bh/s + (C + Dh/s)\gamma}{E + F\gamma + G\ell r_p \theta} \qquad (8.17)$$

where A, B, C, D, E, F and G are constants.

8.3 Numerical Values for the New Formula

In order to validate and use equation (8.17) it is necessary to put values to the constants, expressed below in terms of material/joint parameters obtained from equation (8.16).

$$A = 2Ec + 2E\mu k_n u_m \qquad B = 2E\sigma_m$$

$$C = ck_n \qquad D = (1 - \mu\beta)\sigma_m k_n \qquad (8.18)$$

$$E = 2E \qquad F = k_n \qquad G = \mu k_n \nu/2$$

Typical parameter values obtained from experimental joint tests (Chapter 9) and values used in the finite element analysis are

$k_n = 25$ N/mm^3 $\quad \sigma_m = 100$ N/mm^2 $\quad$ for $f_{cu} = 50$ N/mm^2

$u_m = 0.05$ mm $\quad \beta = 0.0$

$\mu = 3.0$ $\quad E = 2 \times 10^5$ N/mm^2

$c = 0.0$ $\quad \nu = 0.3$

These give

$A = 1.5 \times 10^6$ $\quad B = 4 \times 10^7$ $\quad C = 0.0$

$D = 2500$ $\quad E = 4 \times 10^5$ $\quad F = 25$

$G = 11.25$

The parameter β is not the same as that used in the finite element analysis. It is used here to produce an equivalent mean bond stress rather than a concentrated load. Such an approximation is unsatisfactory and so this parameter is set equal to zero.

In some cases final values used in the finite element analysis are a little different from the bond formula. This can be attributed to the fact that the bond formula uses mean values rather than the specific values needed for the finite element analysis.

In order to allow for the effects of different grout cube strengths it is common practice to express the bond strength in terms of the normalised bond strength F_{BU}, (Chapter 2). Since the above constants are expressed for a cube strength of 50 N/mm^2, the normalised bond strength is given by $\quad F_{BU} = f_{bu}/1.105$. $\quad$ (8.19)

Hence, terms A, B, C and D on the numerator of equation (8.17) should be divided by 1.105. The resulting equation is then given by

$$F_{BU} = \frac{1.36 \times 10^6 + 3.62 \times 10^7 h/s + 2260 h/s\,\gamma}{4 \times 10^5 + 25\gamma + 11.25 l r_p \theta}$$

This simplifies to

$$F_{Bu} = \frac{13.6 + [362 + 226\gamma/10^4]\ h/s}{4 + 10^{-4}\,[2.5\gamma + 2.25(\ell/d_p)r_p^2\theta]} \quad . \qquad (8.20)$$

8.4 Characteristics of the New Formula

The design variables of the new formula are: γ, θ, $h/s, \ell$, r_p and constant A which is dependent on surface roughness u_m. γ and θ are as defined in equation (8.12).

$\gamma = \frac{r_s^2}{t_s} + \frac{r_p^2}{t_p}$, is the most important geometric parameter and it is interesting to compare it with the existing formula of Billington and Tebbett where K is the important parameter.

$$K = \frac{E_g}{E_s}\left(\frac{d_g}{t_g}\right)^{-1} + \left(\frac{d_p}{t_p} + \frac{d_s}{t_s}\right)^{-1} \qquad (8.21)$$

In K, r/t is important, but in γ, r^2/t is used. This is particularly important as r/t is dimensionless, making the existing formula independent of grouted connection size (or scale). The proposed formula would suggest a degree of weakening with increasing scale, but this effect would become less significant with more flexible tubulars, that is higher γ or radius. Figure 8.2 shows this effect for the P9/10 geometry and the finite element results are also plotted, showing an identical trend to the bond formula. Some evidence for scale weakening can be seen in the results of grout bond tests for the BP Magnus Field (7). Test D is 5.7 times the scale of test C and its bond strength is only 60% of test C. Similarly, on the Department of Energy Grouted Repairs Programme (10), test S/D is twice the scale of test S/A, but has only 73% of the strength of test S/A. These strength reductions agree well with Figure 8.2 when the appropriate radii are used. More evidence was given in

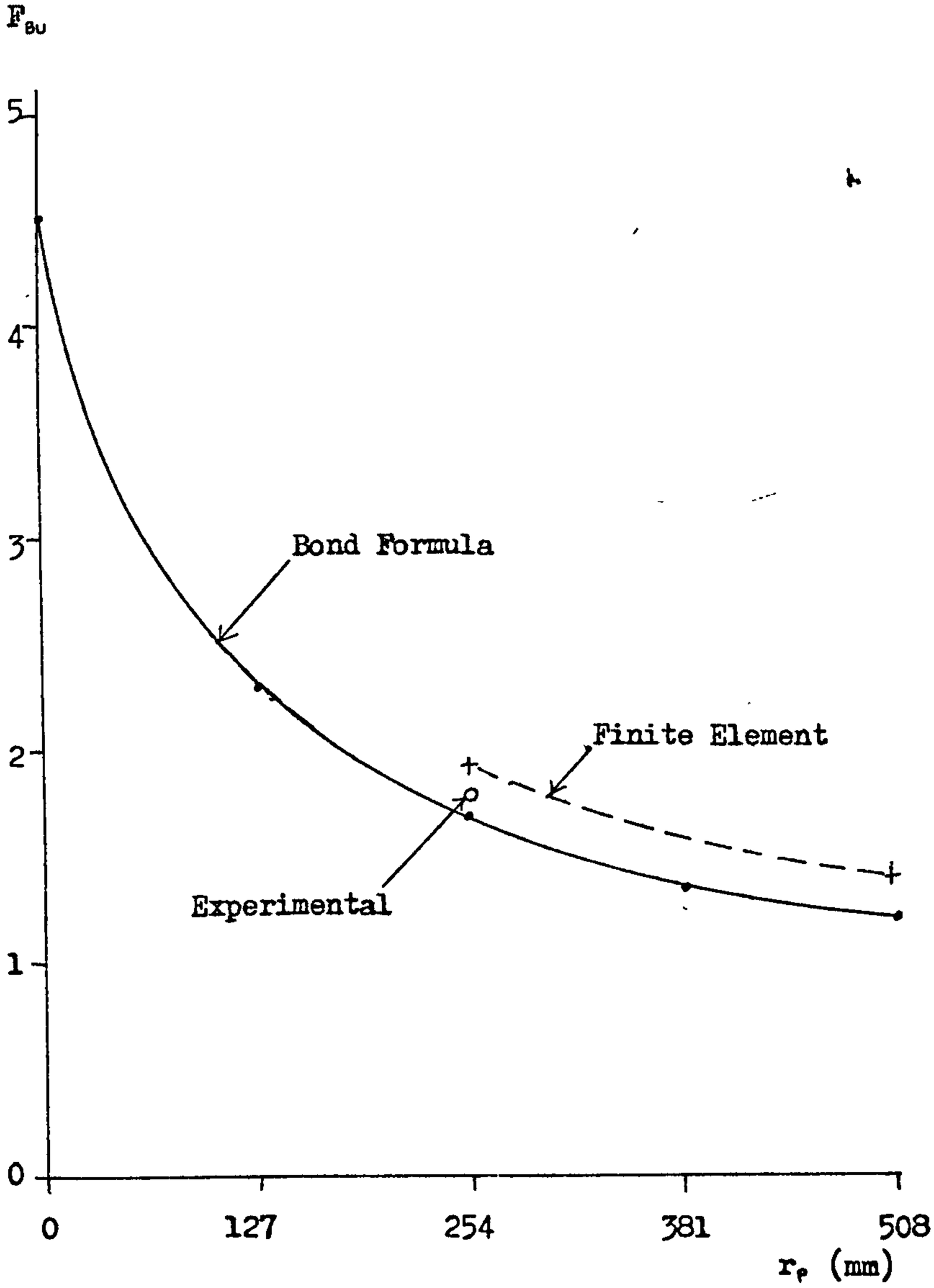

FIGURE 8.2 EFFECT OF SCALE ON BOND STRENGTH FOR THE P9/10 GEOMETRY AS PREDICTED BY THE NEW BOND STRENGTH FORMULA AND THE FINITE ELEMENT ANALYSIS. (THE CURRENT FORMULA GIVES $F_{BU} = 1.90$ FOR ALL SCALES).

Section 2.4 and all the results are tabulated in Appendix B.

It is possible to investigate the properties of the new formula more generally as follows. Consider a plain pipe connection, so that $h/s = 0$ and for simplicity let the adhesion c, be zero. The formula then reduces to

$$F_{BU} = \frac{K}{1 + K'\gamma + K''\ell r_p\theta} \qquad (8.22)$$

where K, K', and K'' are constants.

Let $\ell/d_p = 2 =$ constant, so that $\ell = 4r_p$, then $K''\ell r_p\theta = K'''r_p^2\theta$.

As $\theta \simeq 1/t$, $r_p^2\theta \simeq \gamma$.

Therefore
$$F_{BU} \simeq \frac{K}{1 + K^{IV}\gamma} \qquad (8.23)$$

and
$$\frac{1}{F_{BU}} \simeq C + C'\gamma \qquad (8.24)$$

where C and C' are constants giving the equation of a straight line. If adhesion c, had not been zero, $1/F_{BU}$ would have reduced slightly with γ as shown in Figure 8.3a. The relationships in Figures 8.3b and 8.3c are deduced from Figure 8.3a and then from the definition of γ given by equation (8.12a), the effects of radius and thickness can be deduced and plotted, (Figures 8.4 and 8.5).

It can be seen that the main difference between the new formula and the current one is the establishment of an upper limit on the bond strength. For shear keyed connections the graphs will be essentially the same shape, as the numerator in the formula is simply increased by a constant proportional to h/s.

The new formula also takes into account the length of the connection and produces the trend shown in Figure 8.6. The rate of reduction of bond strength with ℓ/d_p continues to fall with increasing length, but never quite reaches zero. This rate of reduction in F_{BU} with ℓ/d_p can be

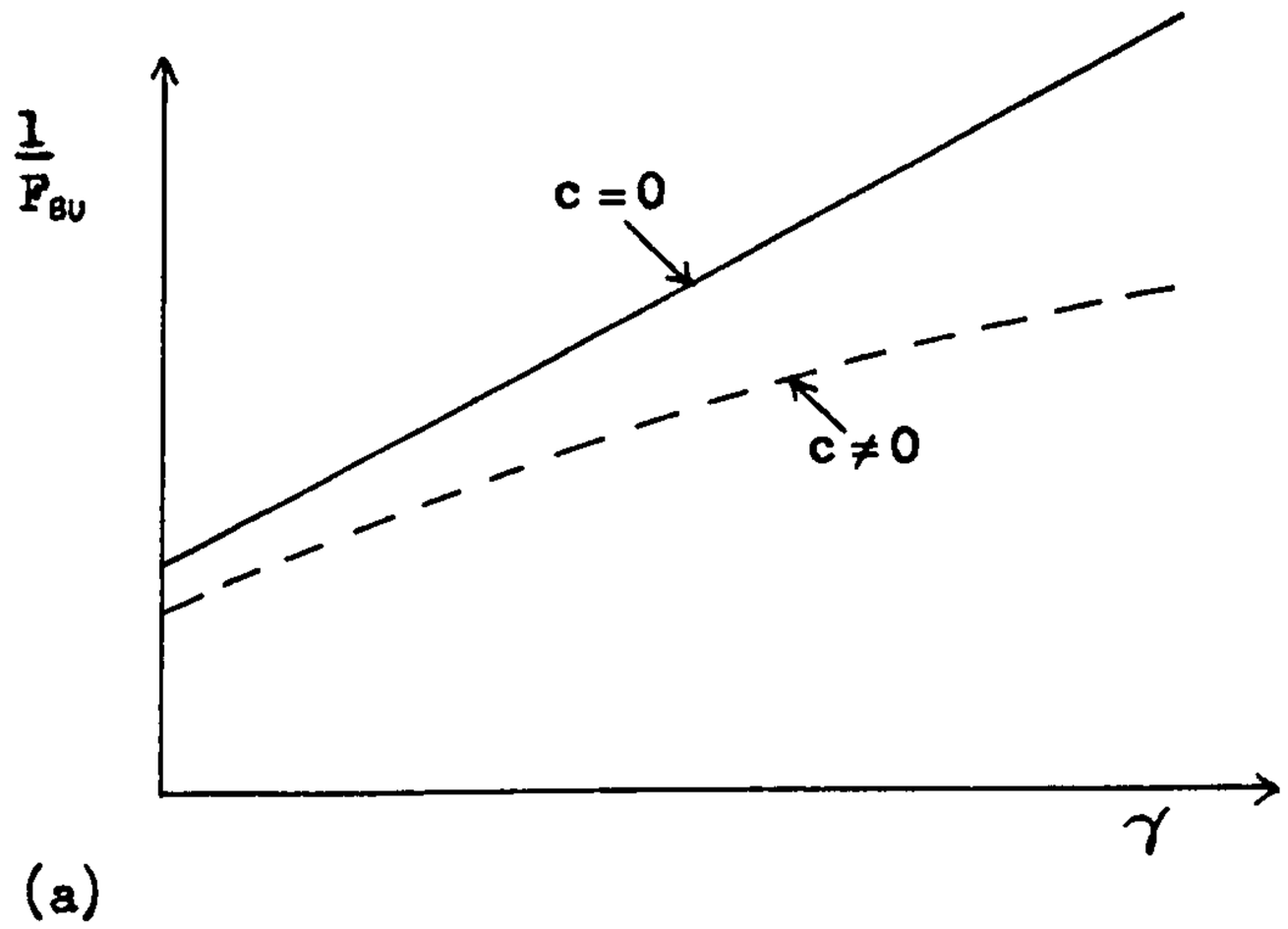

(a)

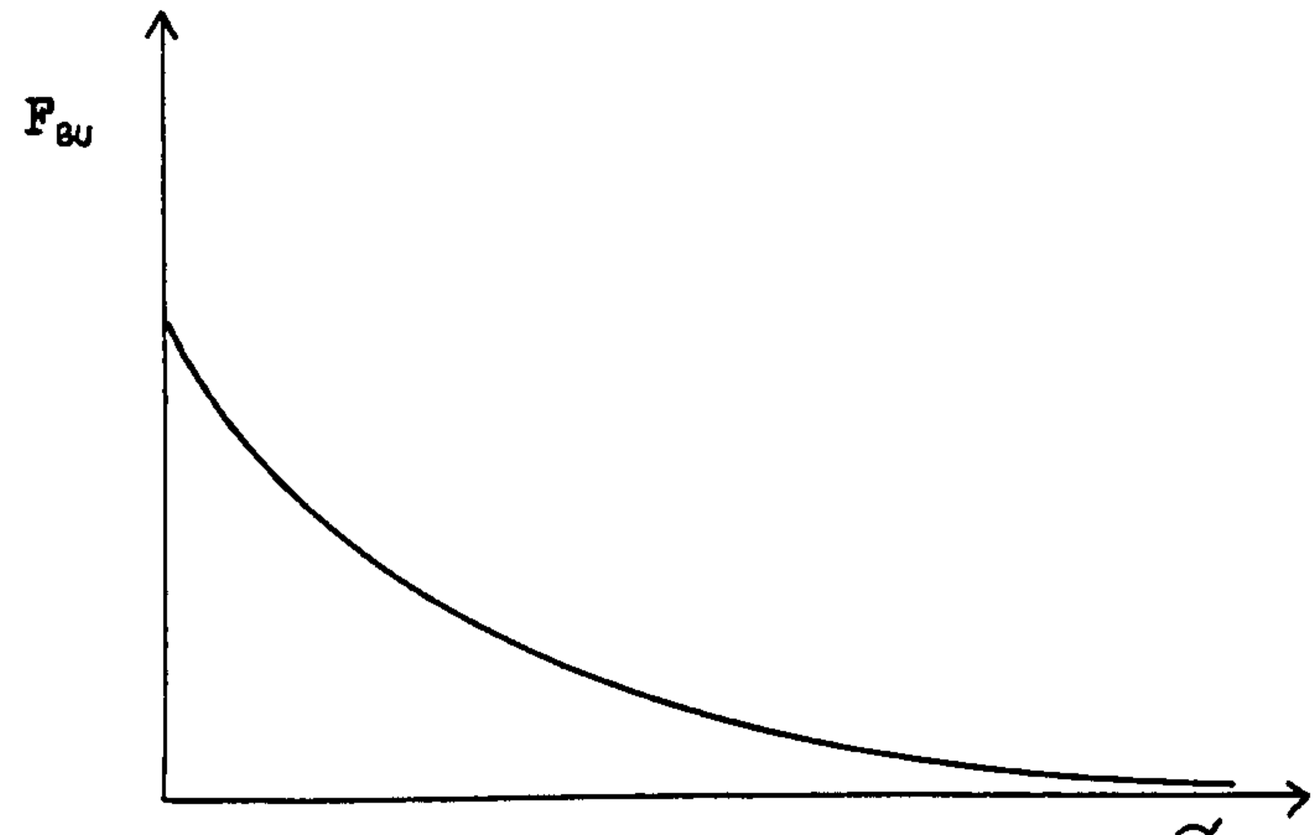

(b)

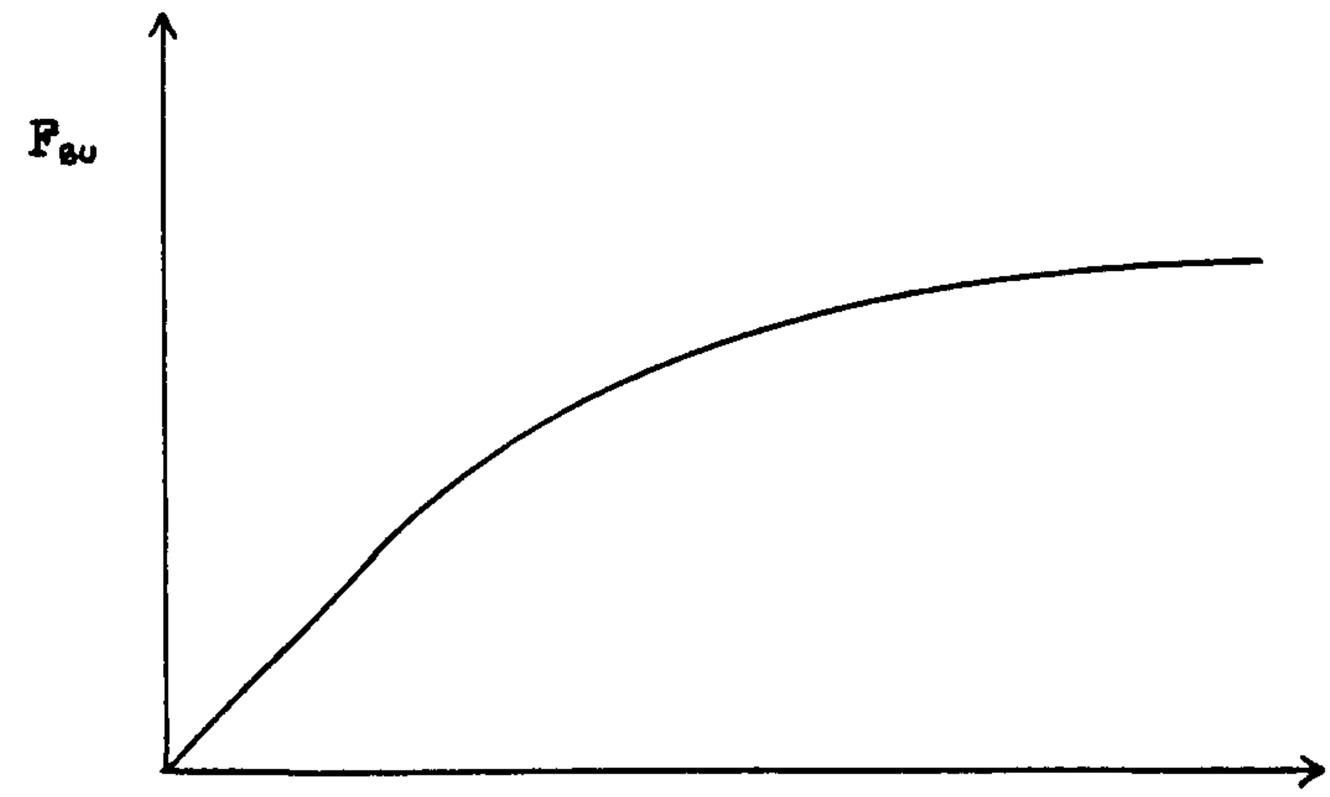

(c)

FIGURE 8.3 RELATIONSHIP BETWEEN F_{BU} AND γ IN THE NEW BOND STRENGTH FORMULA.

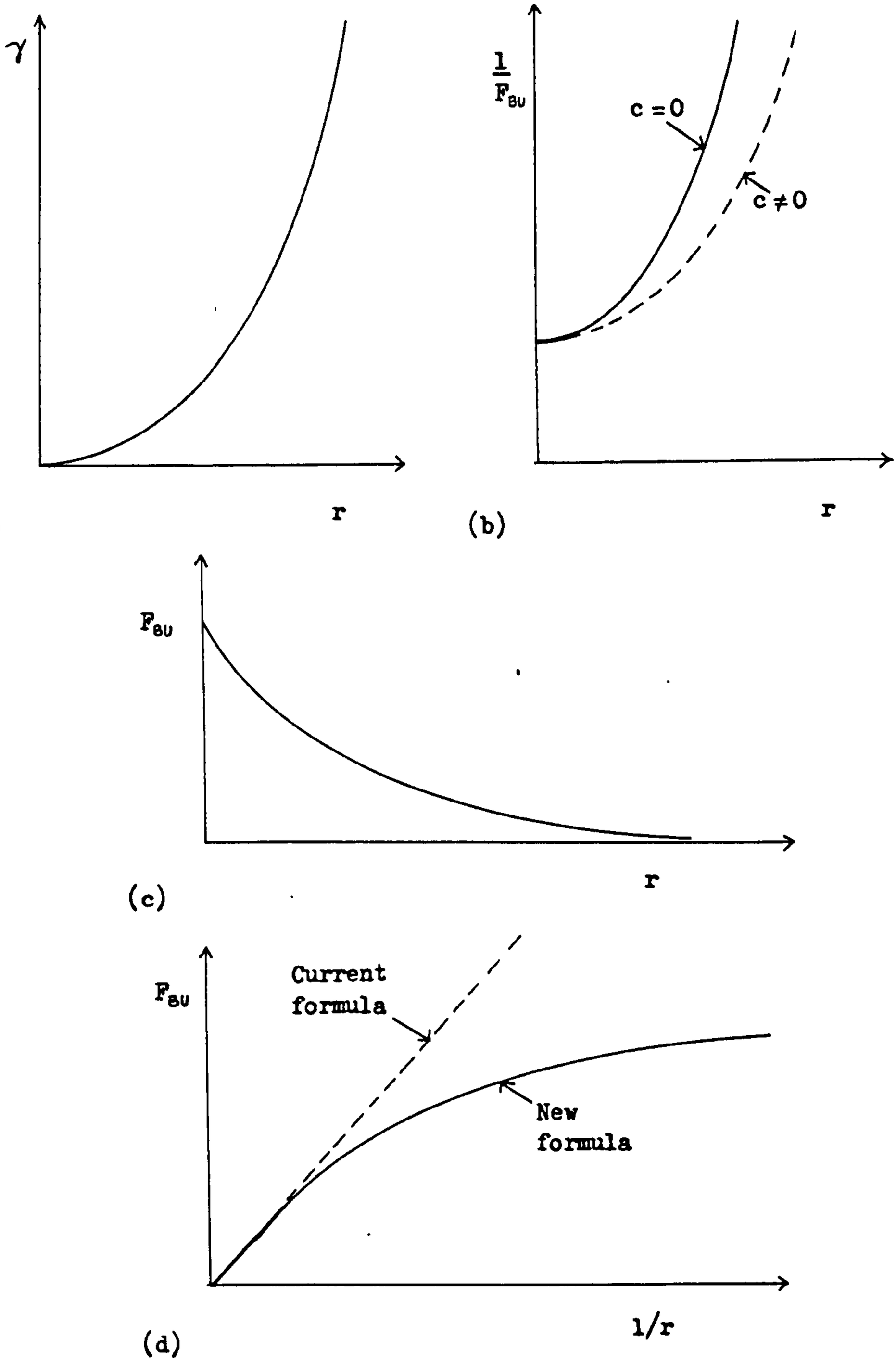

FIGURE 8.4 EFFECTS OF PILE OR SLEEVE RADIUS ON THE BOND STRENGTH PREDICTED BY THE NEW FORMULA.

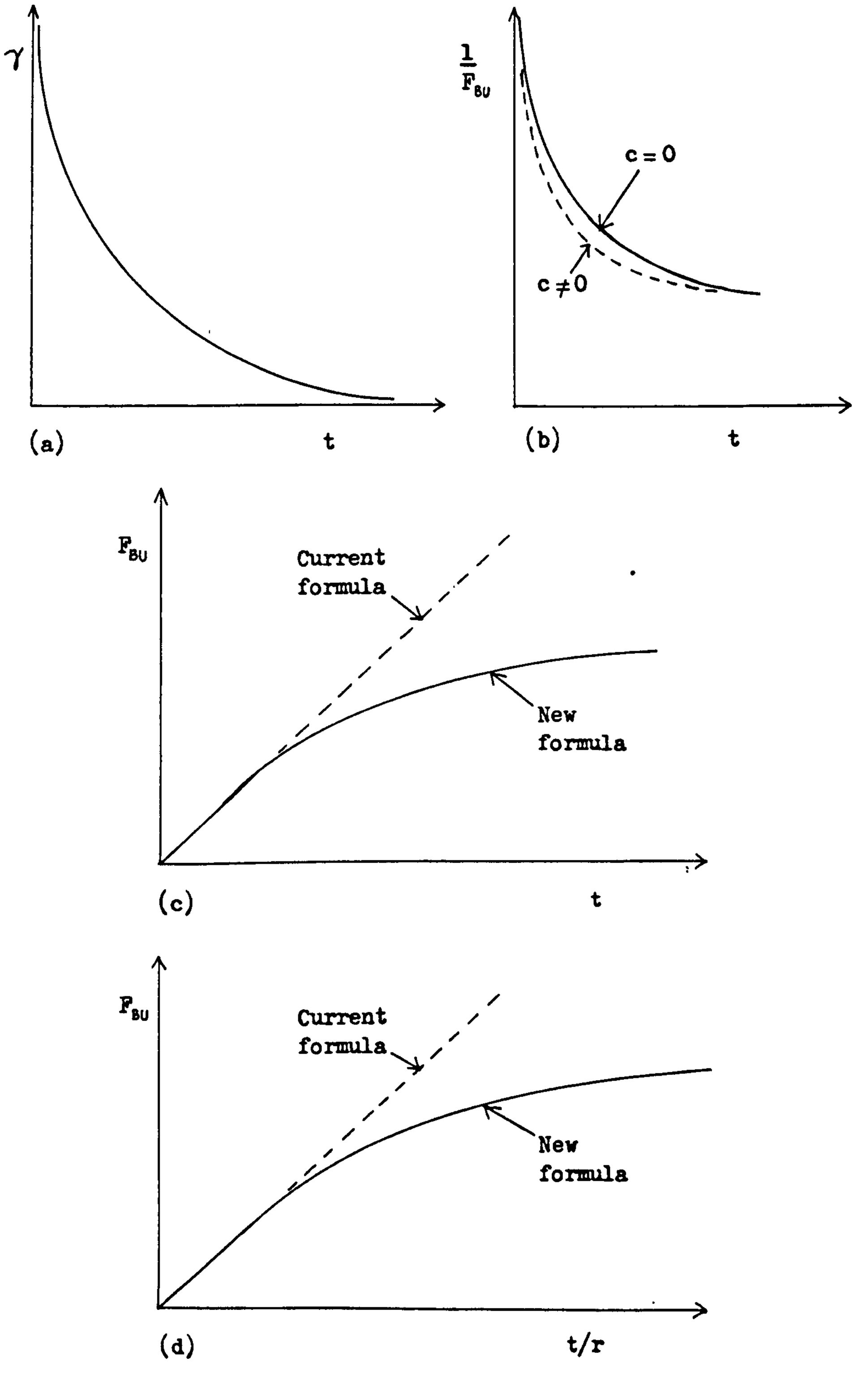

FIGURE 8.5 EFFECTS OF PILE OR SLEEVE THICKNESS AND RADIUS ON THE BOND STRENGTH PREDICTED BY THE NEW FORMULA.

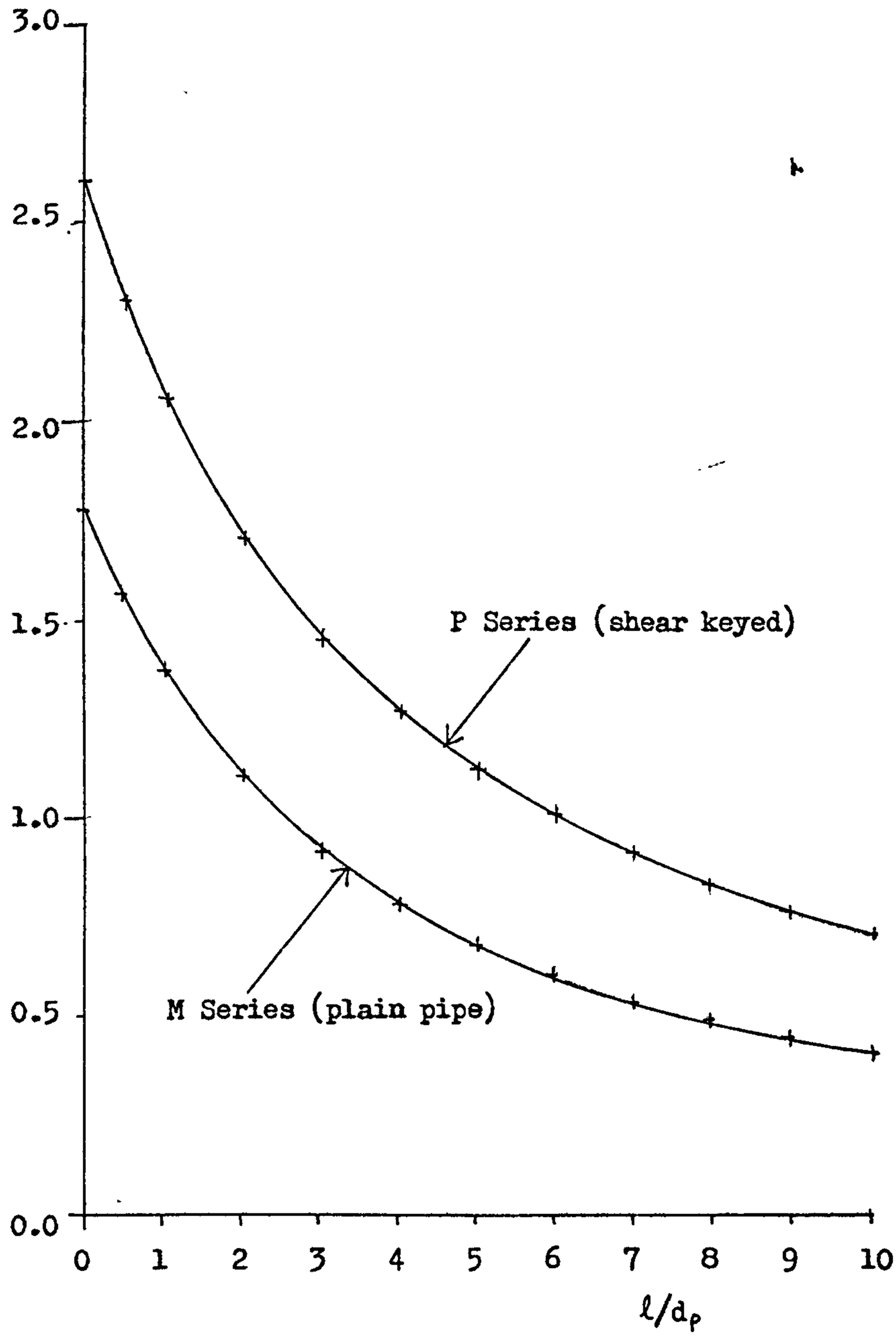

FIGURE 8.6 THE EFFECT OF ℓ/d_p ON BOND STRENGTH PREDICTED BY THE NEW BOND STRENGTH FORMULA.

calculated from the bond formula as follows:

$$F_{BU} = \frac{a}{b + c\ell/d_p} \qquad (8.25)$$

where a, b and c are constants for any given geometry. Differentiating equation (8.25) with respect to ℓ/d_p gives

$$\frac{\partial F_{BU}}{\partial(\ell/d_p)} = \frac{-ac}{[b + c\ell/d_p]^2} \qquad (8.26)$$

Let the rate of reduction in F_{BU} be considered small when

$$\frac{\partial F_{BU}}{\partial(\ell/d_p)} > -0.1 \times F_{BU} \qquad (8.27)$$

that is, when F_{BU} falls by less than 10% when ℓ/d_p is increased by unity. On substituting equations (8.25) and (8.26) into (8.27), the following is obtained

$$\frac{-ac}{[b + c\ell/d_p]^2} = \frac{\partial F_{BU}}{\partial(\ell/d_p)} > -\frac{0.1\,a}{b + c\ell/d_p}$$

Simplifying gives

$$-c > -0.1(b + c\ell/d_p)$$

Therefore $$\ell/d_p > 10 - b/c \qquad (8.28)$$

Equation (8.28) shows how large ℓ/d_p must be for only a 10% bond strength reduction when ℓ/d_p is increased by unity.

Typical values for a plain pipe (M-series) test are

$b = 7.37$, $c = 2.58$ $(r_p = 228.6$ mm).

Then equation (8.28) gives

$$\ell/d_p > 10 - 7.37 / 2.58 = 7.14$$

For a typical connection with shear keys (P9/10),

$b = 8.93$, $c = 2.4$ $(r_p = 254$ mm).

Therefore $$\ell/d_p > 10 - 8.93 / 2.4 = 6.28$$

For test T49/50, which had a high hoop stiffness due to a small diameter, $(r_p = 114.5$ mm), $b = 5.27$, and $c = 0.76$.

Therefore $\ell/d_p > 10 - 5.27 / 0.76 = 3.07.$

It can be seen that the stiffer connections have a smaller rate of change of bond strength with ℓ/d_p, as < 10% reduction in F_{BU} is reached at lower ℓ/d_p. Also, the shear keyed examples have a lower rate of change of F_{BU} than the plain pipe test. Both of these effects agree with the findings of the finite element analysis given in Chapter 7.

Unfortunately, the formula cannot show the strength reduction typical for $\ell/d_p < 2$, since this is considered to be due to end effects which are not considered in the equation. For this reason, $\ell/d_p < 2$ should not be used in the formula. To calculate F_{BU} for $\ell/d_p = 1$, find F_{BU} for $\ell/d_p = 2$ and then multiply by 0.8, (that is the same as the current formula, where $C_L = 0.8$).

The strength reduction in the new bond formula will be greater for larger radius, smaller thickness tubulars, or smaller stiffeners.

Maximum possible bond strength given by equation (8.17) is $F_{BU} = A/E = 13.6/4 = 3.4$, (for plain pipe connections), when $r_p = r_s = 0$ and $t_s = t_p =$ infinity.

Minimum strength is zero, when γ approaches infinity.

8.5 Performance of the New Equation

Results of the experimental bond strengths, adjusted to 31-days old (F_{BU31}), are compared to predictions from the new bond formula and the existing formula in Figures 8.7 and 8.8. Tabulated results are given in Appendix B. The closer the plotted points are to the diagonal line, the more accurate the prediction. It can be seen that there is a fairly close correlation between both formulae and the experimental results, especially

KEY

o =P,Q,R,O Keyed
□ =A _____ Plain
● =U,T Keyed } Split-sleeve (weaker)
■ =S __ Plain }
θ =Magnus Field
△ =Heather Field
⊠ =Thistle Field
◇ =Ninian Field
× =City Tests
▽ =C.B.I. Tests
Ⓛ=Use h/s=0.06 when
actual h/s>0.06

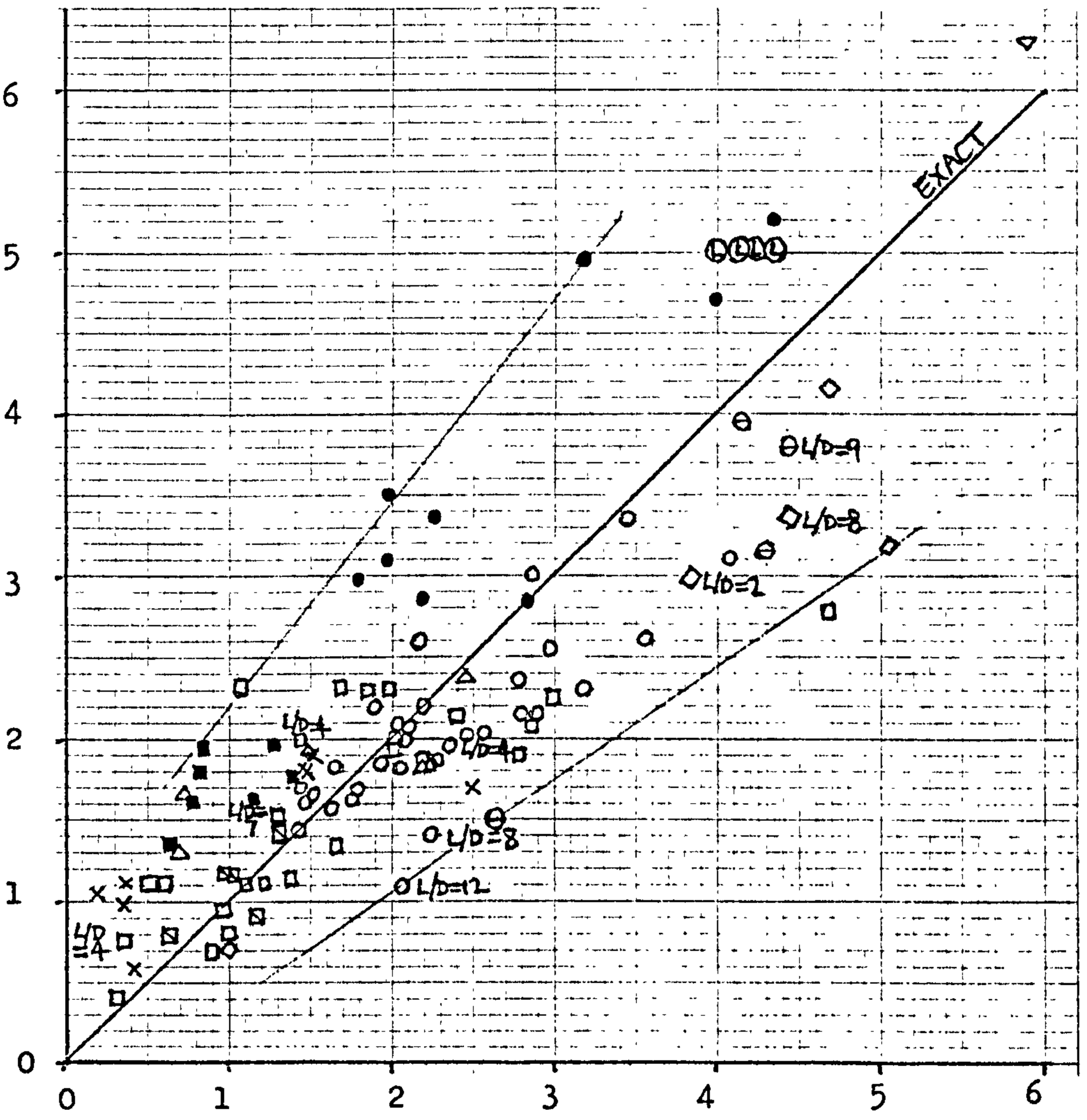

FIGURE 8.7 PERFORMANCE OF THE NEW BOND STRENGTH FORMULA.

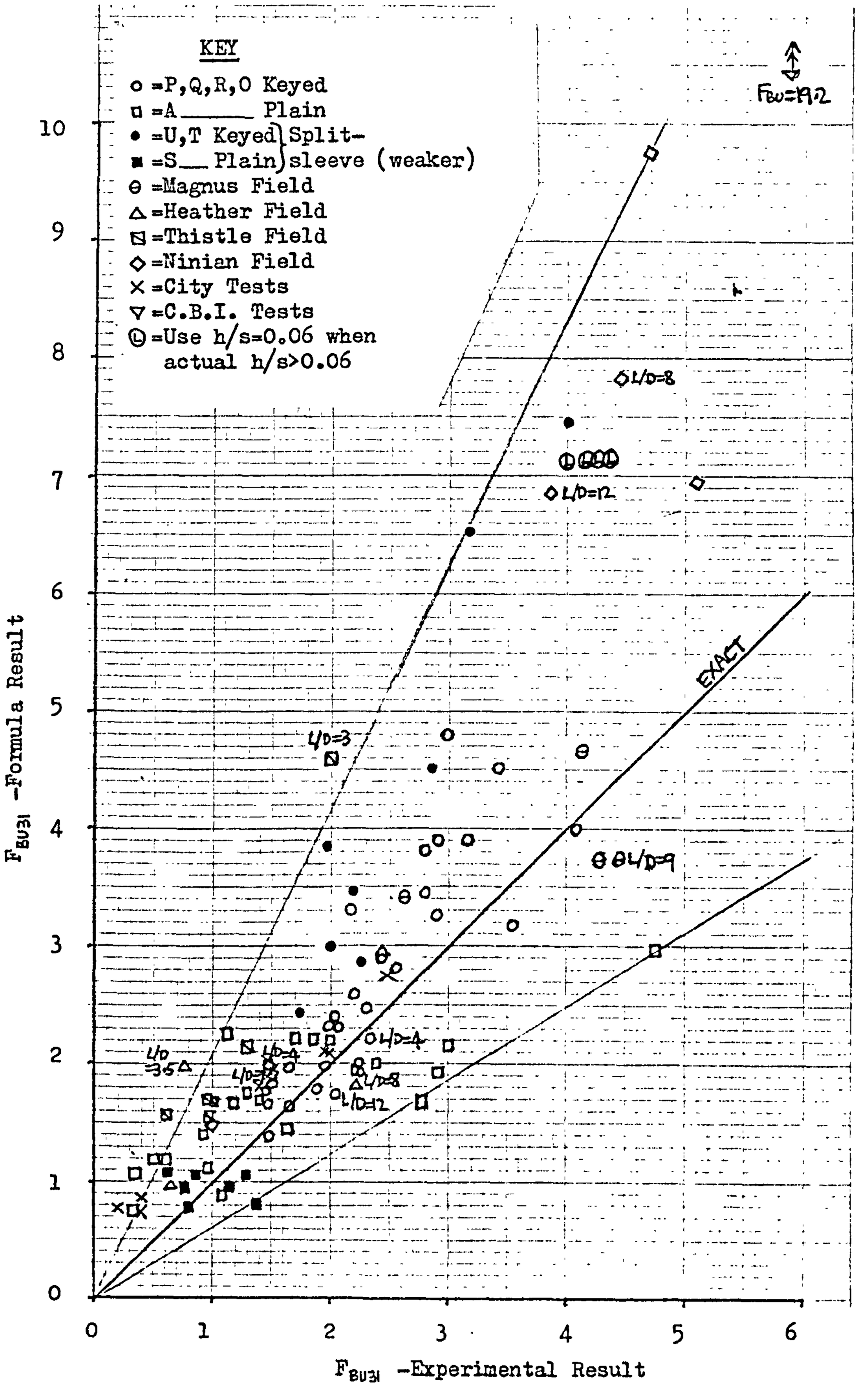

FIGURE 8.8 PERFORMANCE OF THE EXISTING BOND STRENGTH FORMULA.

for shear keyed connections. There is some scatter in the results, especially for plain pipes where variations due to surface roughness and irregularities in the cylinder geometry may affect the strength.

Figure 8.9 shows a plot of F_{BU31} from both formulae, and experiment, against ℓ/d_p for the O-series tests. This figure shows that whilst underestimating F_{BU}, the new formula does at least show the correct rate of reduction in bond strength with increasing ℓ/d_p.

8.6 Split Sleeve Weakening

Results for specimens with split sleeves seem to consistently overestimate the strength of the connection by 30 to 50%. It appears that the hoop stiffness of the sleeve may be significantly reduced by this arrangement, hence causing the lower bond strength. This can be explained by examining the method of clamping the split sleeves, shown in Figure 8.10. The split sleeves are joined together by means of bolted flanges shown in Figure 8.10a, and these flanges carry forces T, resisting the hoop stress, and a bending moment, M = xT, shown in Figure 8.10b. This bending moment causes an additional circumferential deflection δ, shown in Figure 8.10c, hence reducing the effective hoop stiffness. The effect could be reduced by stiffening the flanges between the bolts as shown in Figure 8.10d. Figure 8.11, which has been obtained from a report on grouted repairs (50), shows how the sleeves with no split of the R-series tests are distinctly stronger than those with split sleeves.

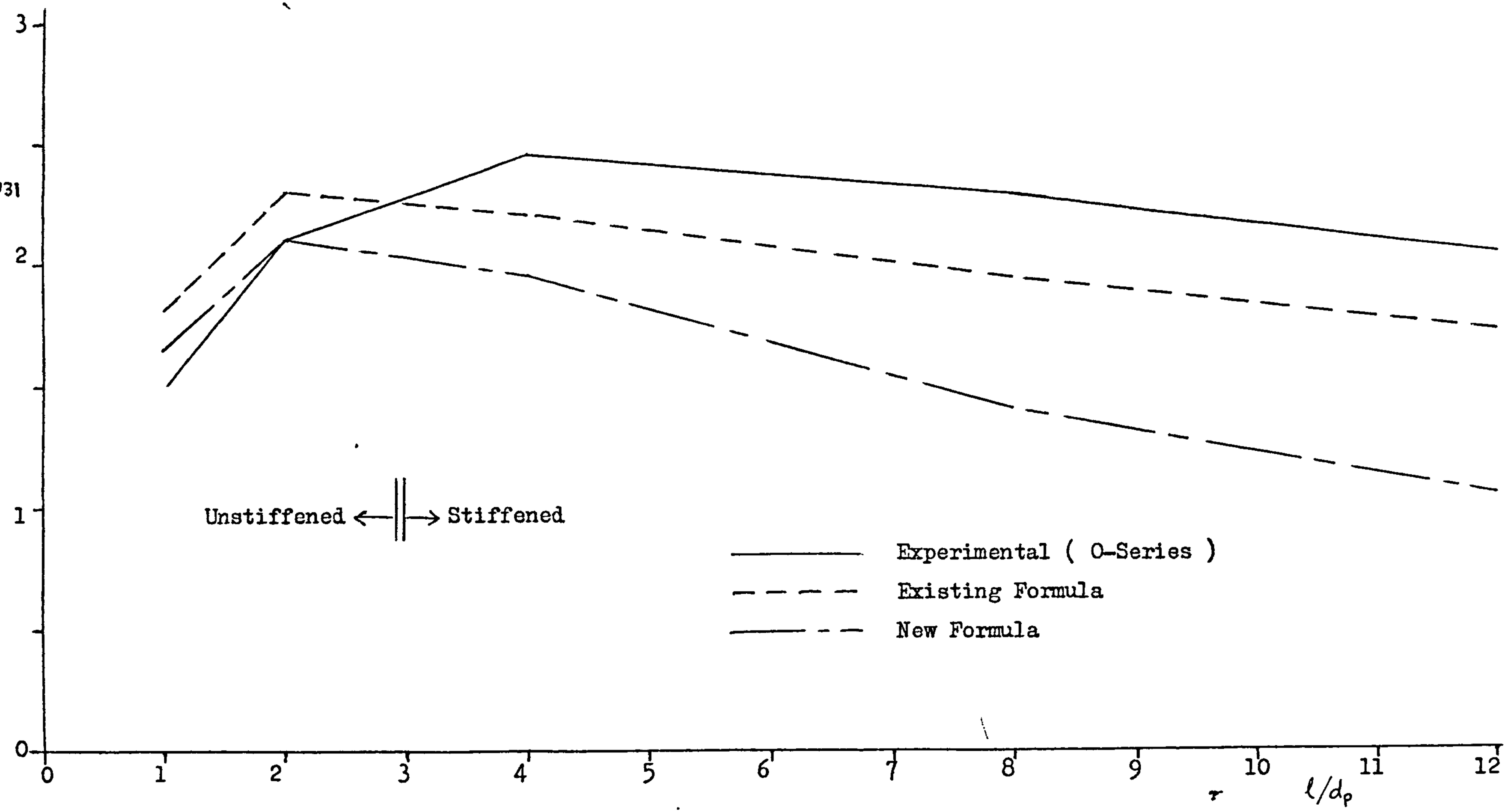

FIGURE 8.9 EXPERIMENTAL AND PREDICTED EFFECT OF $1/d_p$ ON BOND STRENGTH.

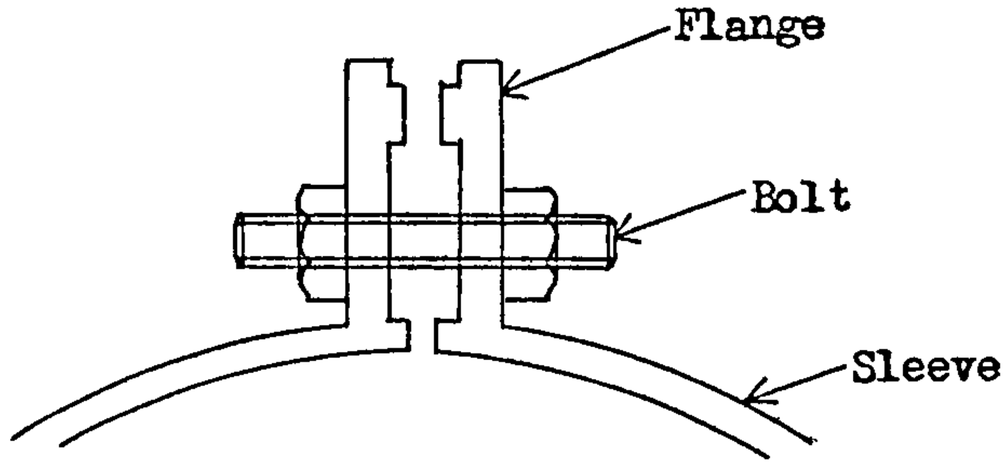

(a)Fixing arrangement

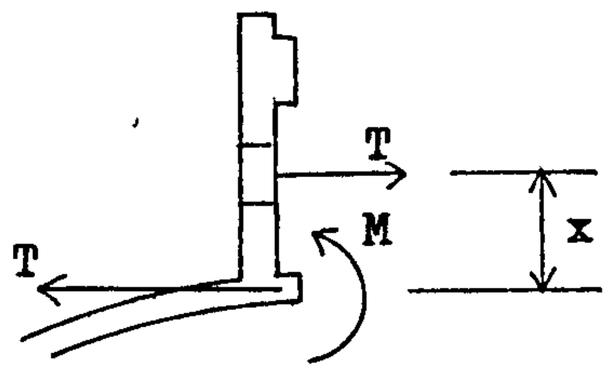

(b)Forces and moments on the fixing bracket

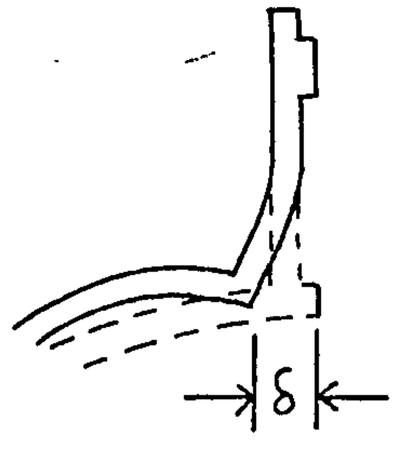

(c)Deflection due to the bending moment

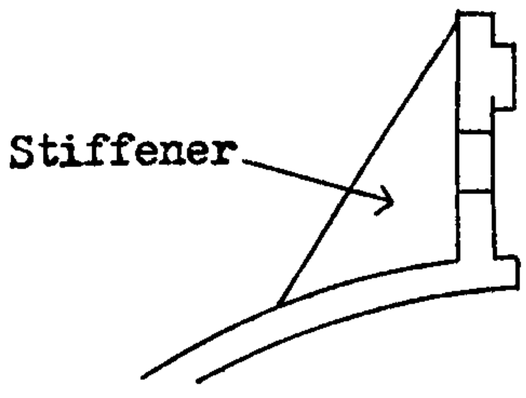

(d)Stiffened flange

FIGURE 8.10 SPLIT-SLEEVE FIXING.

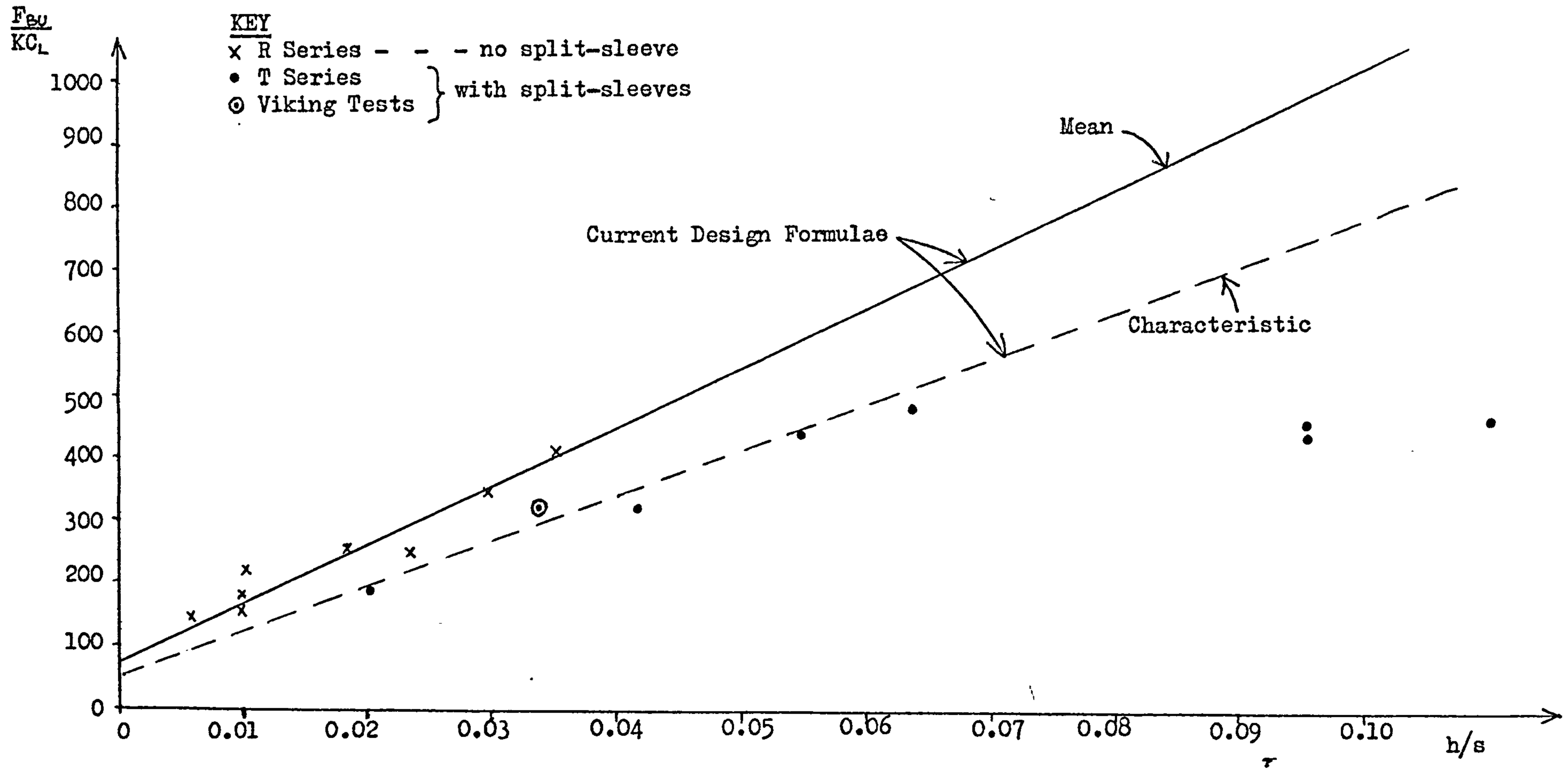

FIGURE 8.11 COMPARED AGAINST THE CURRENT DESIGN FORMULAE, THE SPLIT-SLEEVE SPECIMENS SHOW A DISTINCTLY WEAKER TREND.

8.7 Limiting Value for h/s

Experiments on split sleeve specimens with various values of h/s show that F_{su} increases linearly with h/s for increasing either h or s up to a limit. Above h/s = 0.06 no further strength is gained. This is shown by the T-series results in Figure 8.12. A restriction has been placed on the existing bond strength formula, therefore, and this should also apply to the new bond strength formula, as follows:

For h/s > 0.06, the ratio h/s = 0.06 is used in the formula.

This limiting value of h/s should also apply when the sleeve is not split. Some possible reasons for this limitation on bond strength have been given in Section 7.3. Figure 8.12 also shows how both formulae overestimate the strength when h/s < 0.06 and this is due to the split sleeve. Much closer correlation is achieved with unsplit sleeves.

8.8 Extra Stiff Pile and Sleeve

Testing of grouted pile/sleeve connections with high pile and sleeve hoop stiffness at Wimpey Laboratories (51) showed that the existing formula would overestimate the bond strength and that an upper limit should be placed on the strength. However, when the strength is predicted with the proposed new formula, no cut-off is necessary. This is not surprising as the new formula tends towards a maximum value of bond strength for any given geometry, unlike the current formula which has no upper strength limit. The results plotted in Figures 8.13a and 8.13b (and obtained from the Wimpey Laboratory results,) demonstrate this fact.

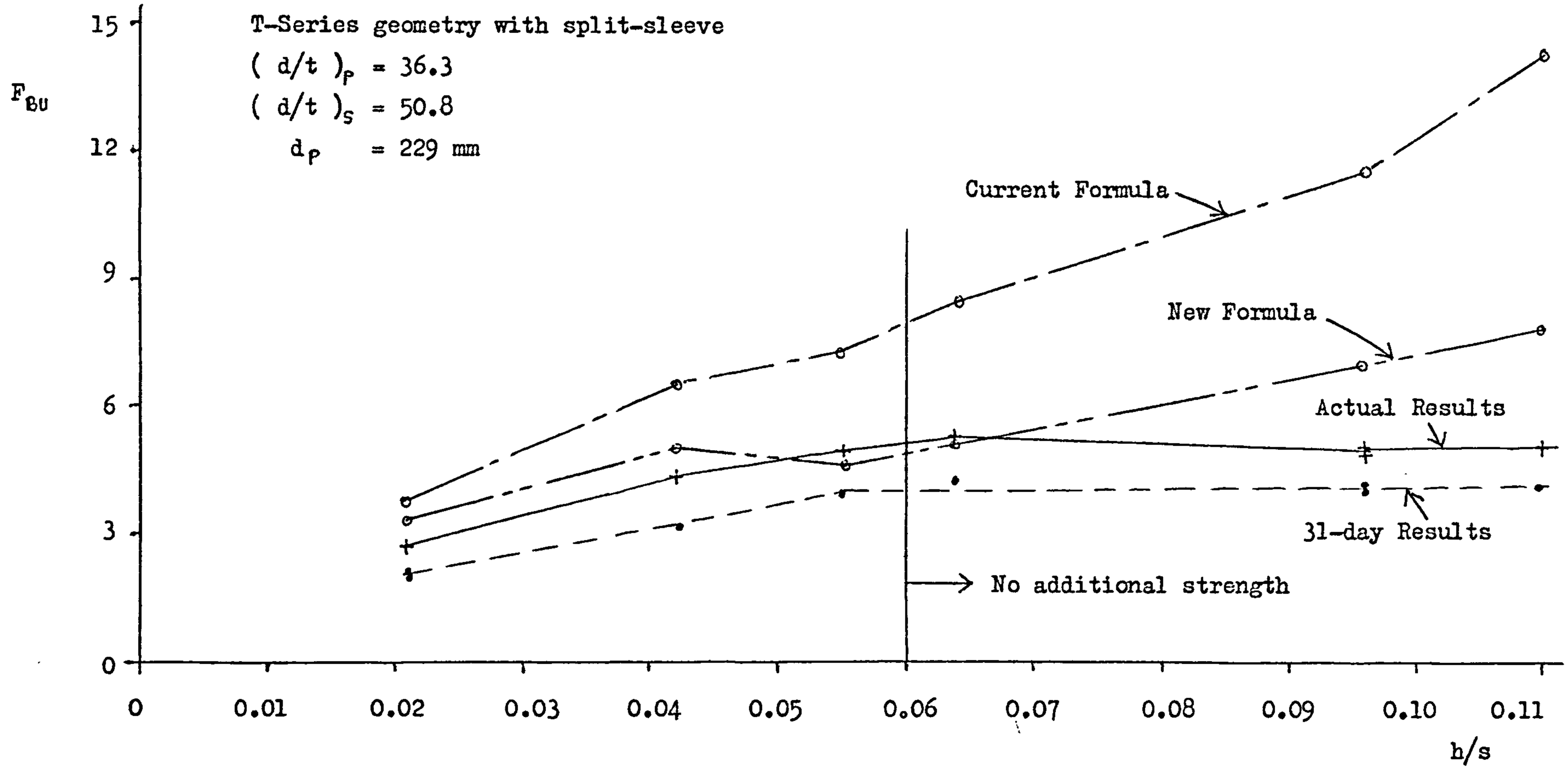

FIGURE 8.12 SHOWS HOW THE STRENGTH WILL NOT INCREASE FOR h/s > 0.06 .

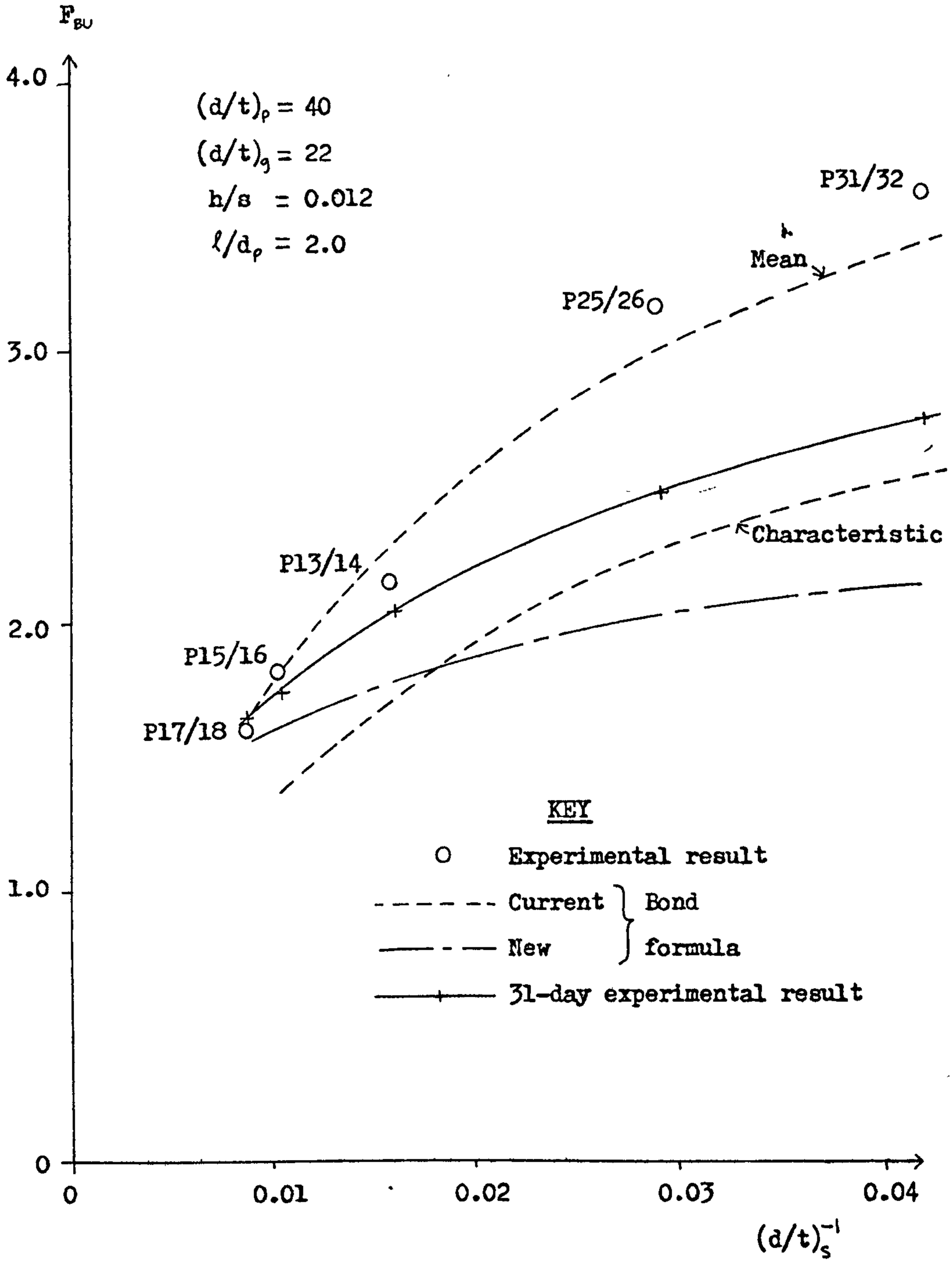

FIGURE 8.13a EFFECT OF SLEEVE STIFFNESS ON BOND STRENGTH.

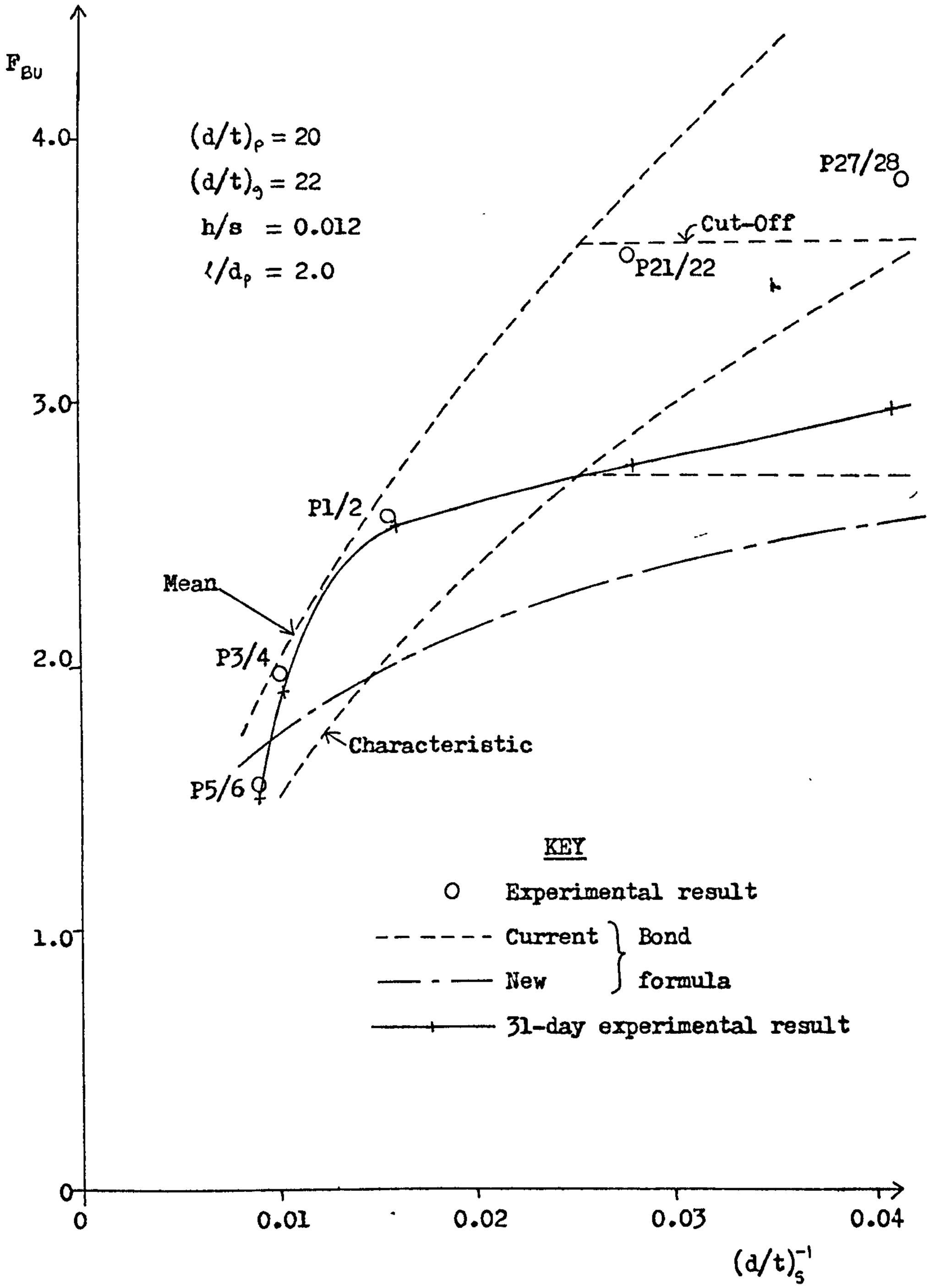

FIGURE 8.13b EFFECT OF SLEEVE STIFFNESS ON BOND STRENGTH.

NOTE CUT-OFF NEEDED FOR THE CURRENT FORMULA.

8.9 Possible Improvements to the New Bond Formula

Other values can be assigned to the constants in the formula which may result in some further improvement in the formula's performance. Using values other than zero for c or β does not appear to be of any great benefit. Using $\tau = c + \mu\sigma_n$ in the formula does not reflect the fact that $\tau = 0$ when the bond is open and so it is conservative to use $c = 0$. Lateral key forces only represent a small part of the normal bond stress when distributed over the whole bond surface and so changing β has little effect. If typical h/s values were much higher, then β would be more important.

8.10 Summary of Rules Governing the New Strength Formula

a) The basic formula used is

$$F_{BU} = \frac{13.6 + (362 + 226 \times 10^{-4}\gamma)h/s}{4 + 10^{-4}(2.5\gamma + 2.25r_p^2\theta l/d_p)}$$

where

$$\gamma = \frac{r_s^2}{t_s} + \frac{r_p^2}{t_p}$$

$$\theta = \frac{\pi r_s}{\pi t_s r_s + A_{stiff}/2} + \frac{1}{t_p}$$

b) If $h/s > 0.06$, then use $h/s = 0.06$ in the formula.

c) For split sleeves, the value of F_{BU} may need to be reduced by up to 30%.

d) For $l/d_p < 2$, use $l/d_p = 2$ in the formula and multiply the result by 0.8. This is an approximate allowance for end effects.

e) The result gives the value of F_{BU} when the grout is 31-days old, assuming oilwell B grout is used and cured at 8°C under water. For plain pipe connections, long-term strength may be further reduced if shrinkage occurs as a result of drying out or higher temperatures.

f) The constant 13.6 in the equation, is proportional to the surface roughness and so may need reducing if the surfaces are not shot-blasted.

CHAPTER 9

EXPERIMENTAL TEST RESULTS

9.1 Steel/Grout Frictional Bond Tests

In order to determine the coefficient of friction required for the analysis, a series of bond tests were devised.

9.1.1 Test Rig and Experimental Procedures

The test piece basically consisted of a 10mm thick layer of grout cast between two shot-blasted steel plates. This gave two steel/grout bonds which measured 75 x 100mm in area. For the purposes of casting the grout, end plates were screwed into three sides of the steel plates, which were set 10mm apart and stood vertically to form a mould into which the grout could be poured.

The grout mix was similar to those used in the North Sea, but using tap water rather than seawater, as specified in Table 9.1.

Ingredient	Weight ratio
Oilwell 'B' cement	1.0
Tap water	0.34
Cormix SP1G	0.02

TABLE 9.1 GROUT MIX USED FOR THE BOND TESTS.

Only a small volume of grout was required to fill the test piece and two 76mm cube moulds. The mixing was done by hand. In order to represent

the North Sea conditions, the grout was cured at 8°C and 100% humidity for two weeks before testing using a Weyco Climatic Cabinet. Two weeks are considered to be the minimum time needed for the grout to gain most of its strength and stiffness under these conditions. Figure 9.1 shows a photograph of a specimen after two weeks curing with the end plates of the mould still in place.

The shot-blasting used by Wimpey Laboratories is to the second quality standard of BS 4232. This standard was used for the first joint test, but all succeeding tests were of first quality, where the shot-blasting is of even quality over the whole surface. The quality standard did not appear to affect the results and both qualities gave a surface roughness, peak to trough, of about 0.04mm. The surface was measured using a roughness meter and the value agrees with the u_m used in the analysis. Figure 9.2 shows a close-up photograph of the texture of the freshly shot-blasted plate.

After curing, the test piece is inserted into the loading rig ready for testing and the grout cubes are tested to check the strength of the grout. Figure 9.3 shows the basic arrangement of the loading rig, indicating the loads and deflections to be measured. Figures 9.4 and 9.5 show photographs of the test rig with a specimen about to be tested.

A total of six tests were made with a constant value of vertical load P, chosen for each test, varying between 2.4 and 7.5 kN. The test procedure was as follows:-

(1) Apply a small vertical load (P) to remove slack in the plates and measure γ_4.

(2) Apply full vertical load and measure γ_4 again. The pre-slip effects of the vertical load are given by the change in γ_4.

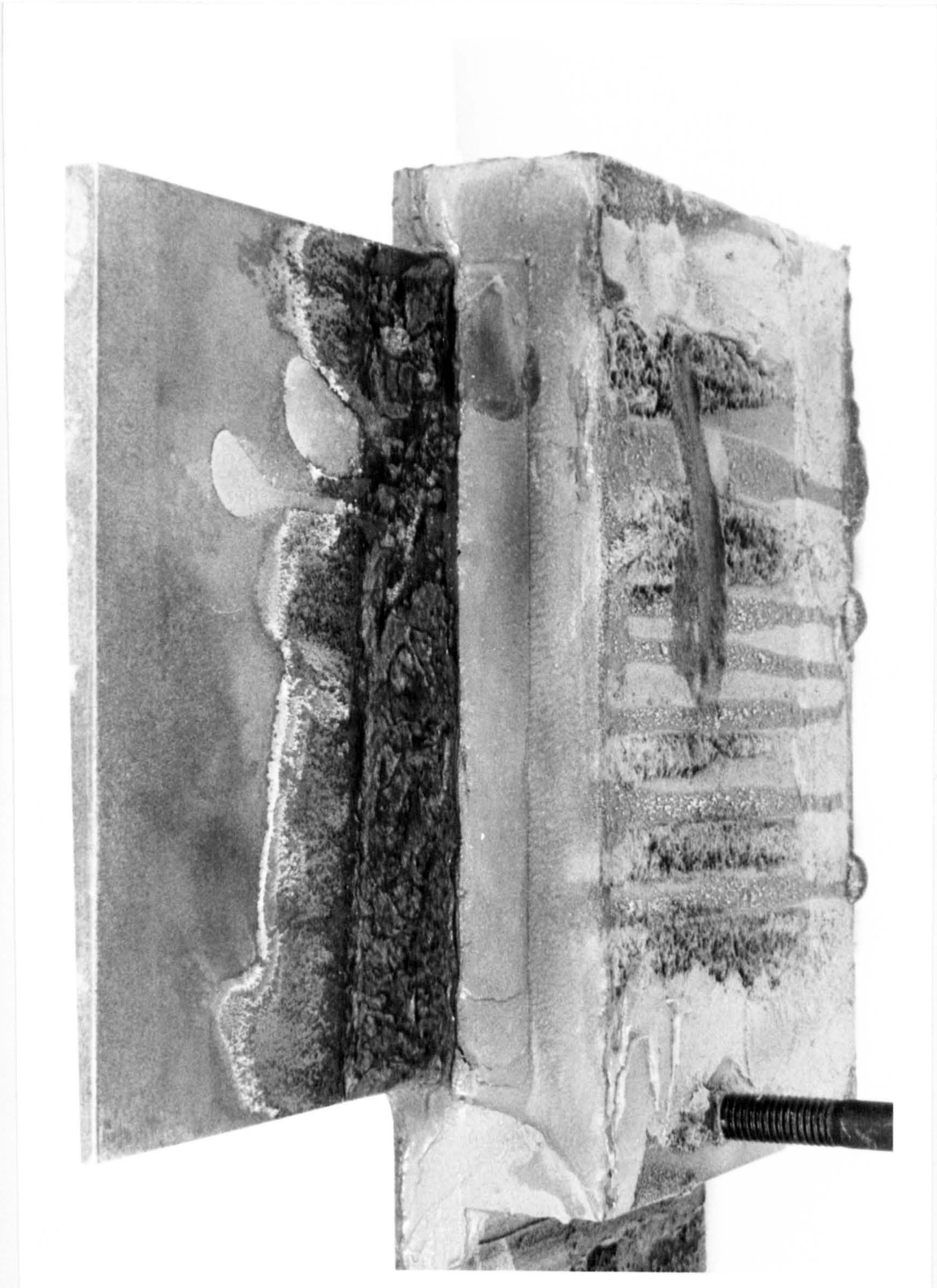

FIGURE 9.1. SPECIMEN STILL IN ITS MOULD AFTER TWO WEEKS CURING UNDER NORTH SEA CONDITIONS.

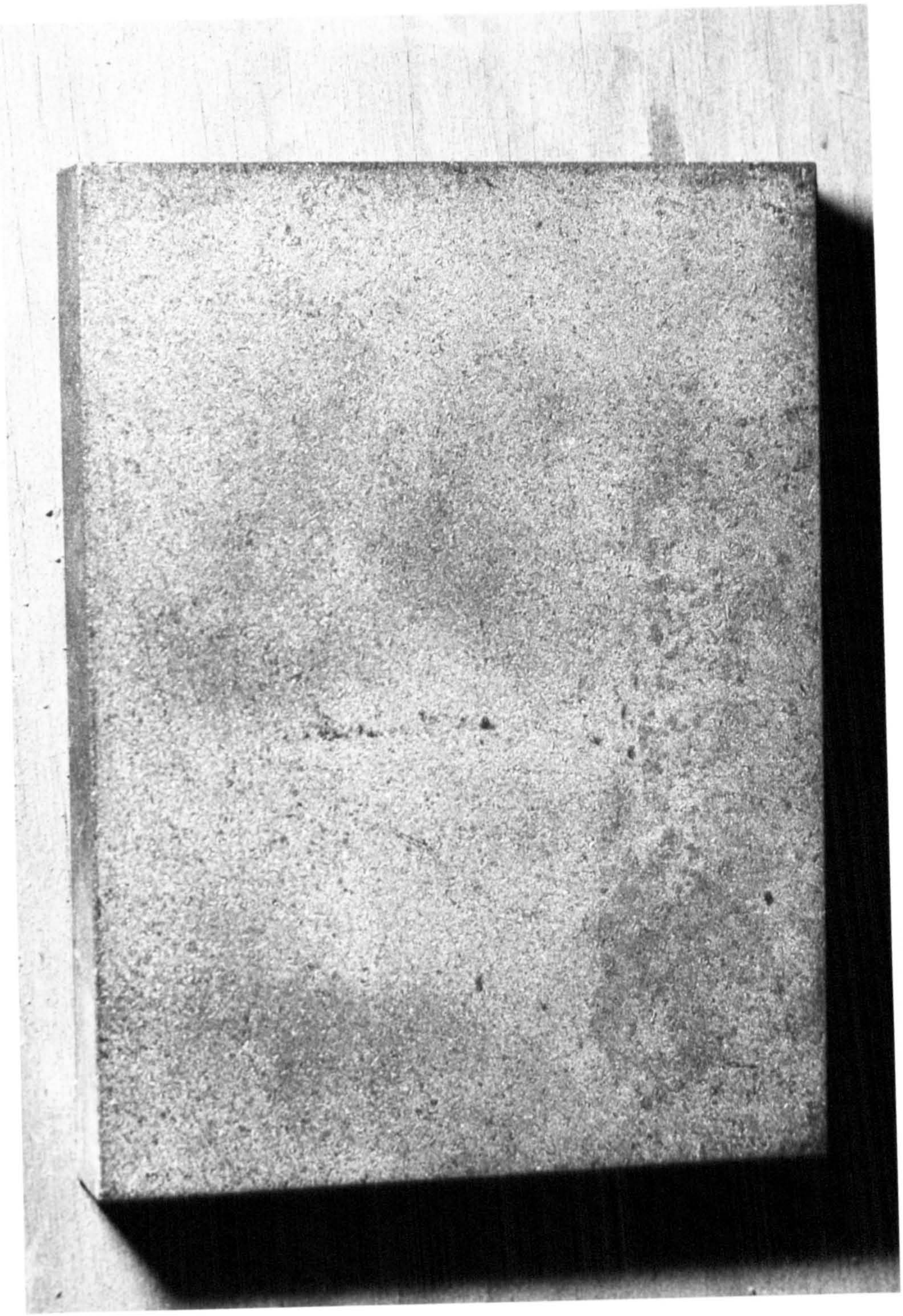

FIGURE 9.2. CLOSE-UP VIEW OF THE SHOT-BLASTED PLATE BEFORE GROUTING.

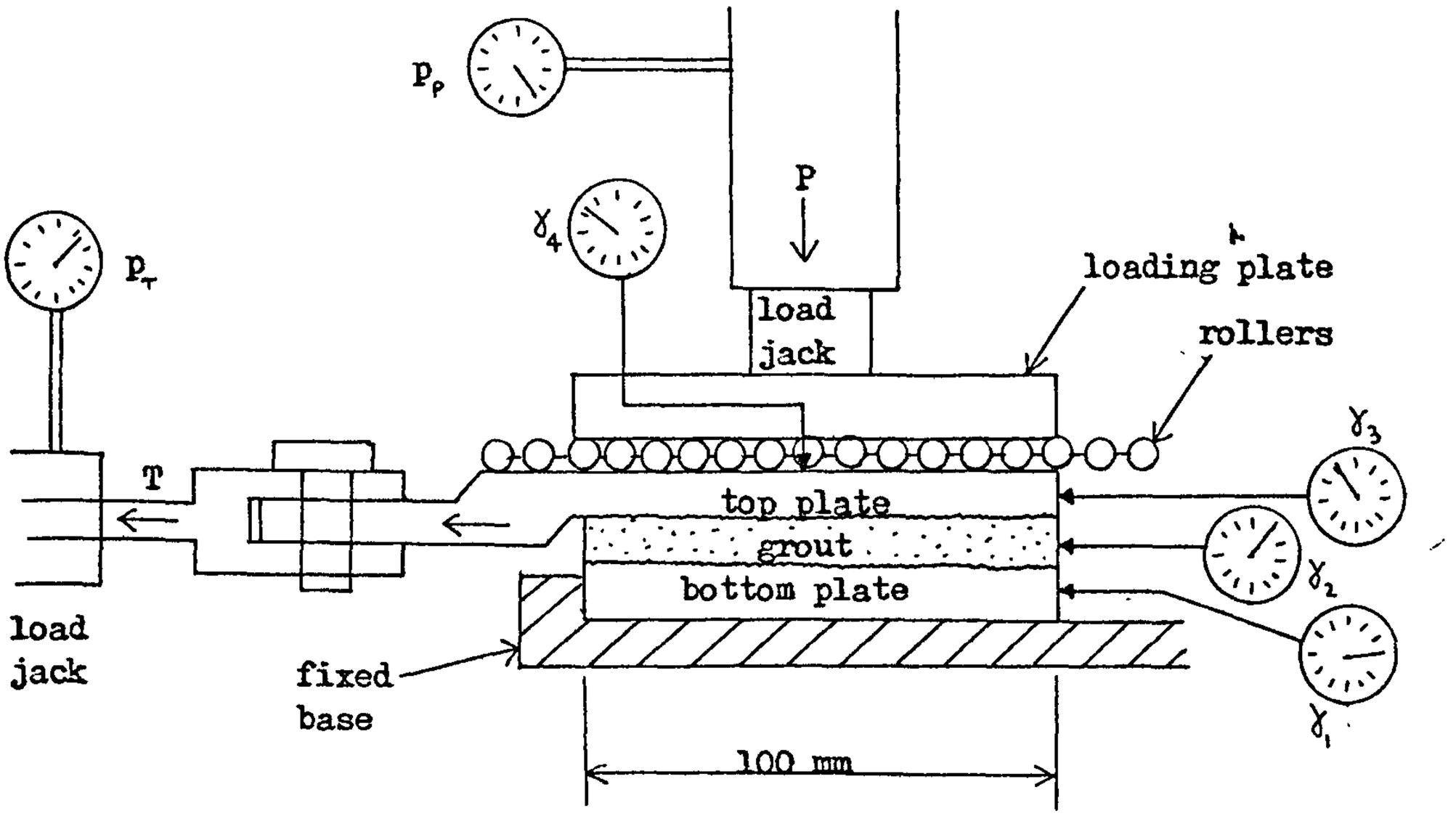

Measurement	Quantity
γ_1	Horizontal rig movement
γ_2	" grout movement
γ_3	" top plate movement
γ_4	Vertical movement between top and bottom plates
p_ρ	Pressure generating load P
p_T	" " " T

FIGURE 9.3 LAYOUT OF THE TEST RIG. THE BOND SURFACE IS 100 mm LONG (AS INDICATED), AND 75 mm WIDE. THE TOP PLATE IS WIDER IN ORDER TO GIVE A BEARING TO MEASURE THE VERTICAL MOVEMENT (γ_4) ON ONE SIDE.

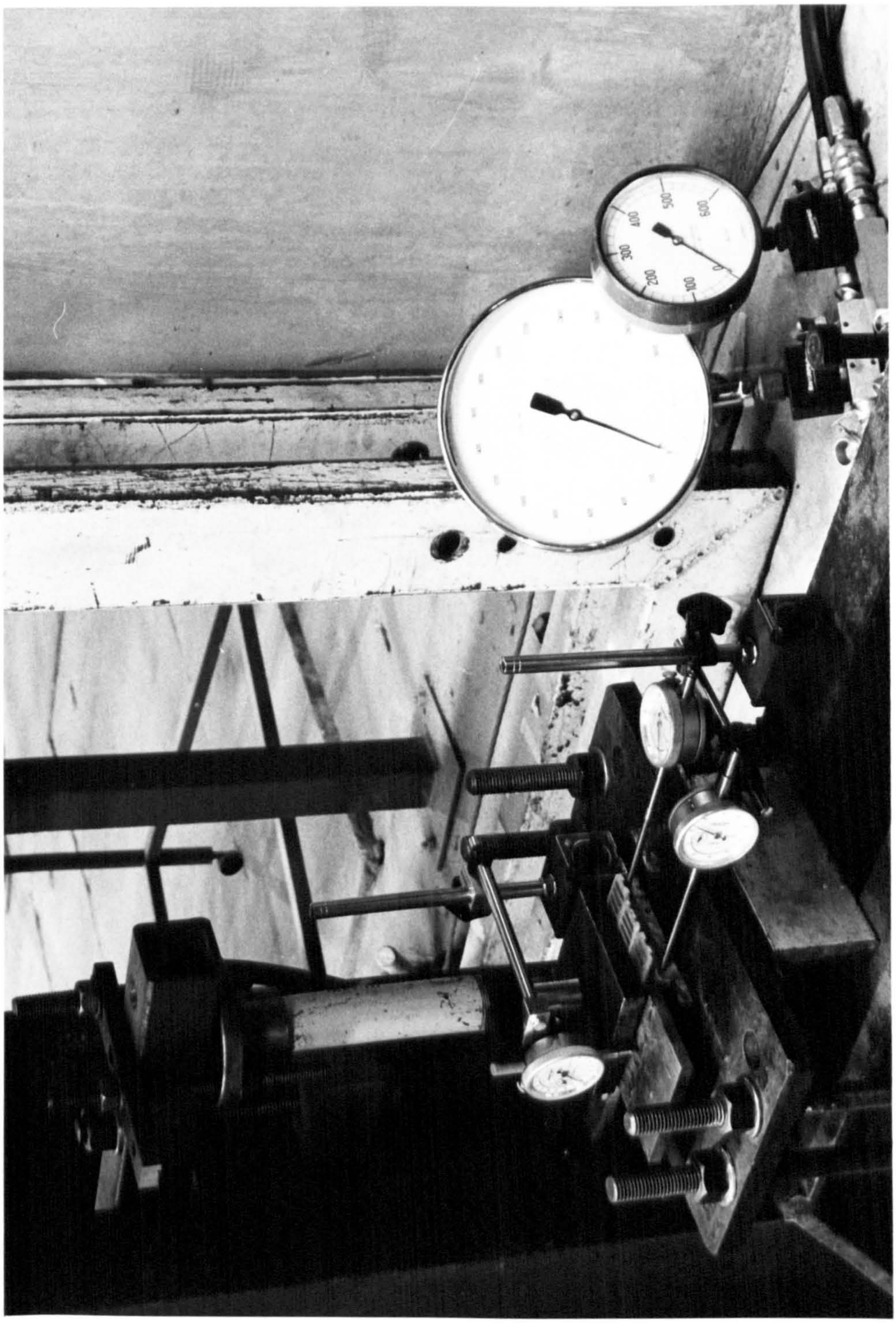

FIGURE 9.4 GENERAL VIEW OF THE TEST-RIG. THE VERTICAL LOAD JACK CAN BE SEEN TO THE LEFT OF THE PICTURE, BUT THE HORIZONTAL LOAD JACK, WHICH PULLS THE TOP PLATE TO THE LEFT, IS OUT OF VIEW.

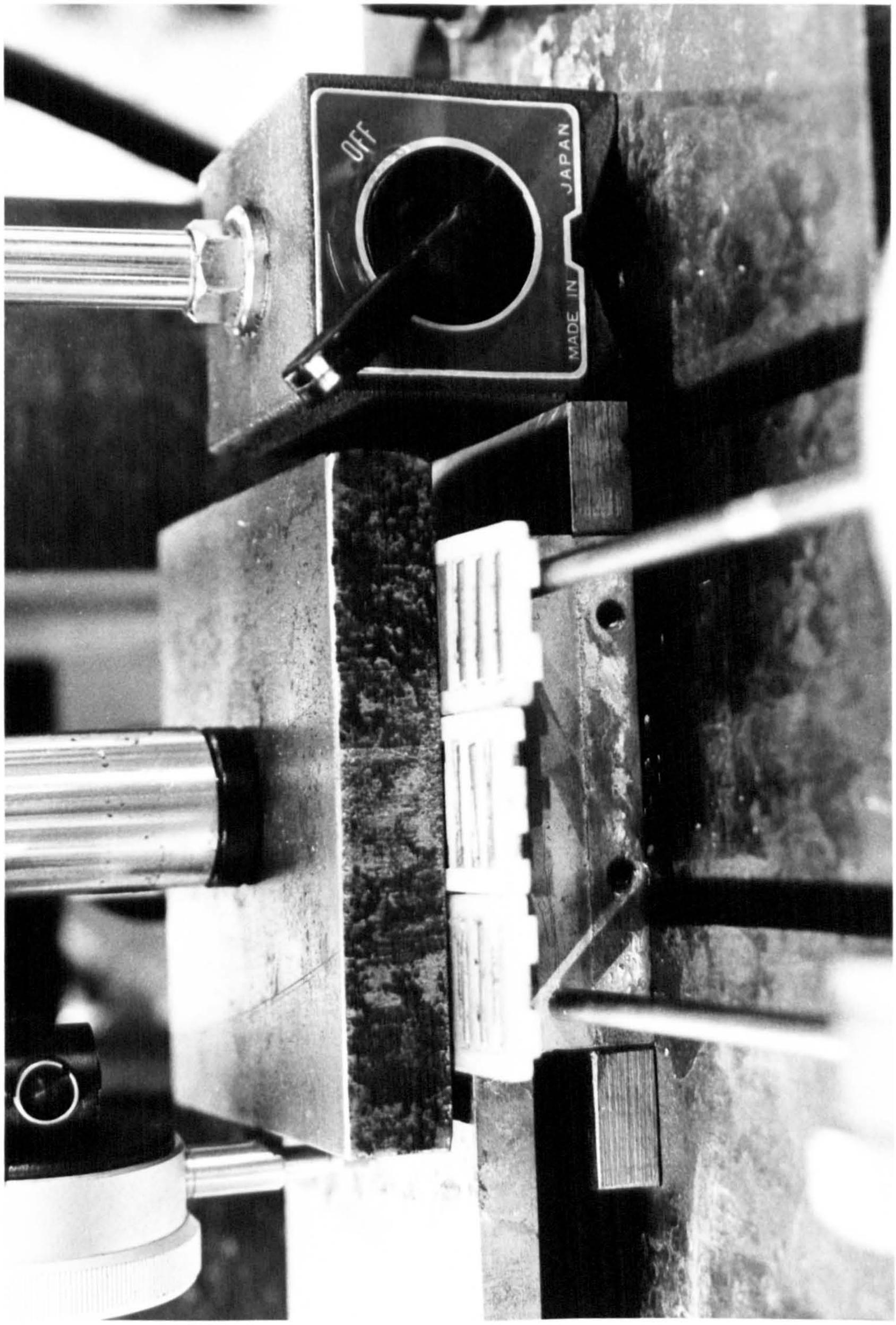

FIGURE 9.5. CLOSE-UP VIEW OF THE TEST SPECIMEN BEFORE LOADING. THE LAYER OF GROUT IS CLEARLY VISIBLE BENEATH THE ROLLERS.

(3) Apply increments to the horizontal load (T), monitoring the deflections at the end of each increment.

Top bond slip = $\gamma_3 - \gamma_2$, bottom bond slip = $\gamma_2 - \gamma_1$ and the tangential bond stiffness (k_t) is calculated for each bond, where $k_t = \tau/(\text{bond slip})$.

(4) After the slip has increased by about 0.1mm, remove T and then P. Record all the deflection changes after unloading, from which u_a and k_n can be calculated.

(5) Restore load P and return to step (3), repeating until T is large enough to cause the bond to break.

Failure always occurred on the top bond, with no slip on the bottom bond. In order to take advantage of this fact, a second stage test was subsequently devised to enable the remaining bond to be tested. This involved reversing the bottom plate and grout and is shown in Figure 9.6. The second bond test was always carried out with a low vertical load in order to evaluate the adhesive, rather than the frictional bond.

The test could not be carried out with zero vertical load as the vertical load jack also resisted a small bending moment which caused the right hand end of the top plate and grout (as depicted in Figure 9.6) to raise. These bending effects could not be eliminated and their cause is explained by the force diagrams of Figure 9.7. The small vertical arrows represent forces generated by an anticlockwise rotation of the plates, which results in the applied stress under the vertical load jack being greater on the right hand side. This anticlockwise rotation exists because of the bending moment generated by the frictional stresses acting on the two surfaces of the grout and cannot be avoided.

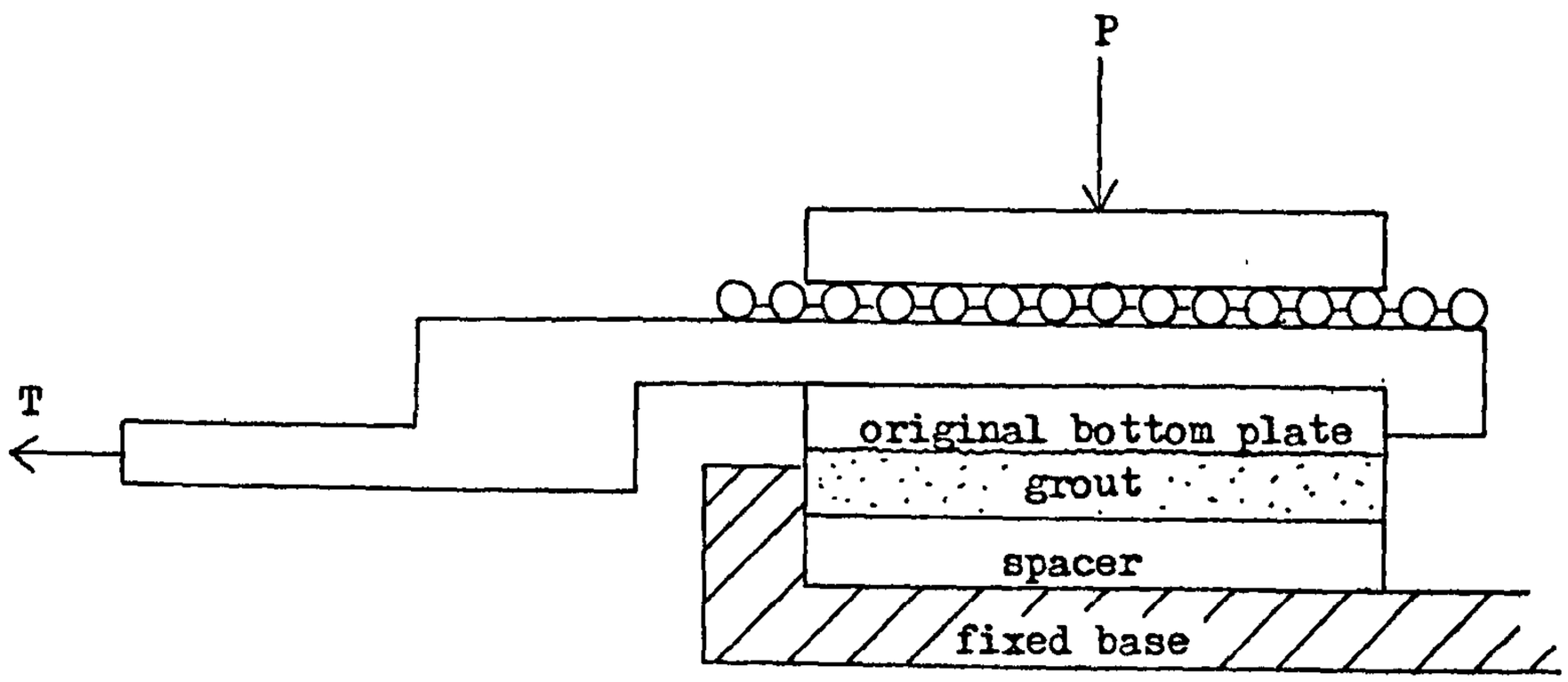

FIGURE 9.6 TEST RIG REARRANGED TO TEST THE LOWER BOND.

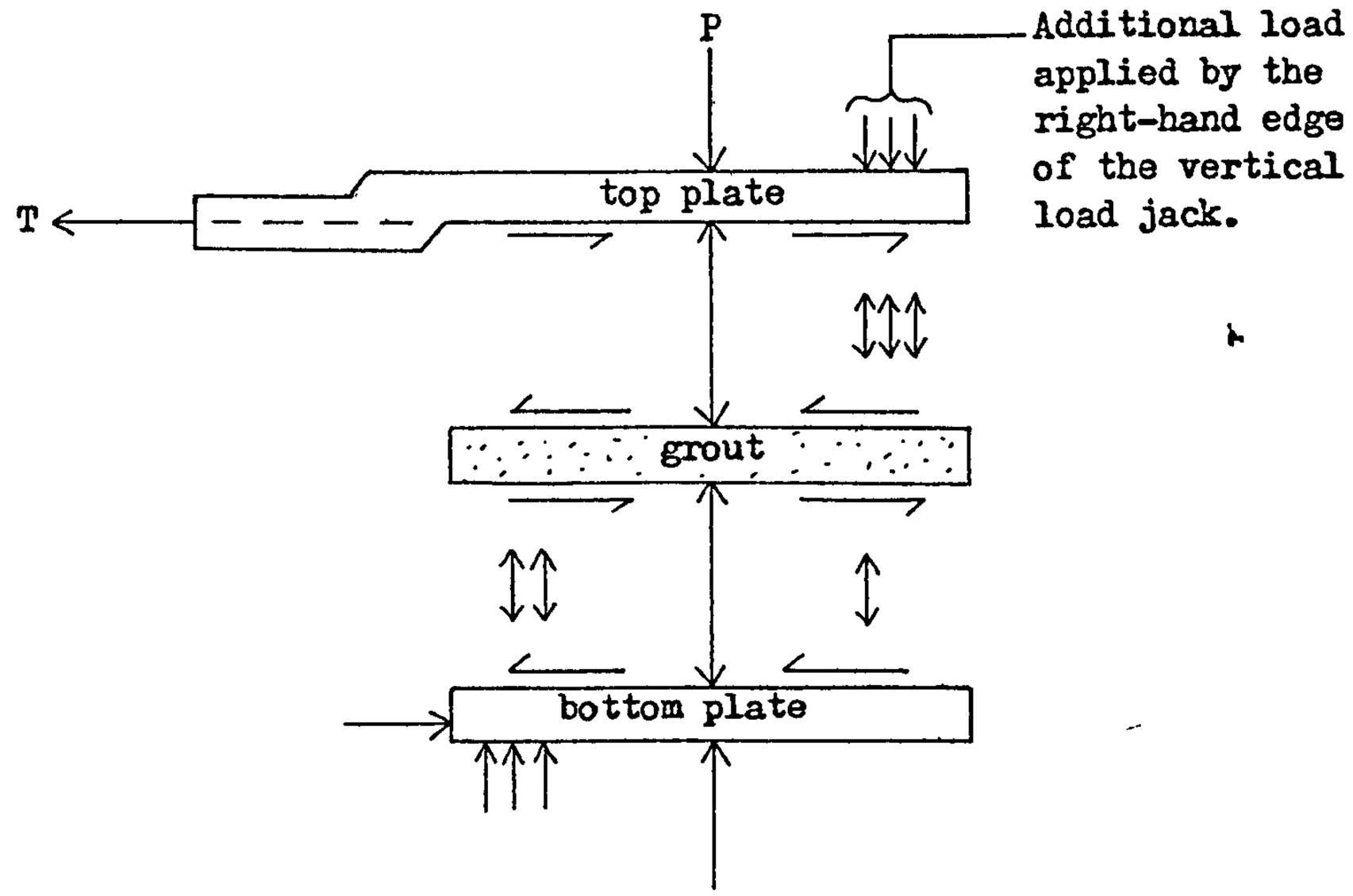

(a)First bond test,as Figure 9.3

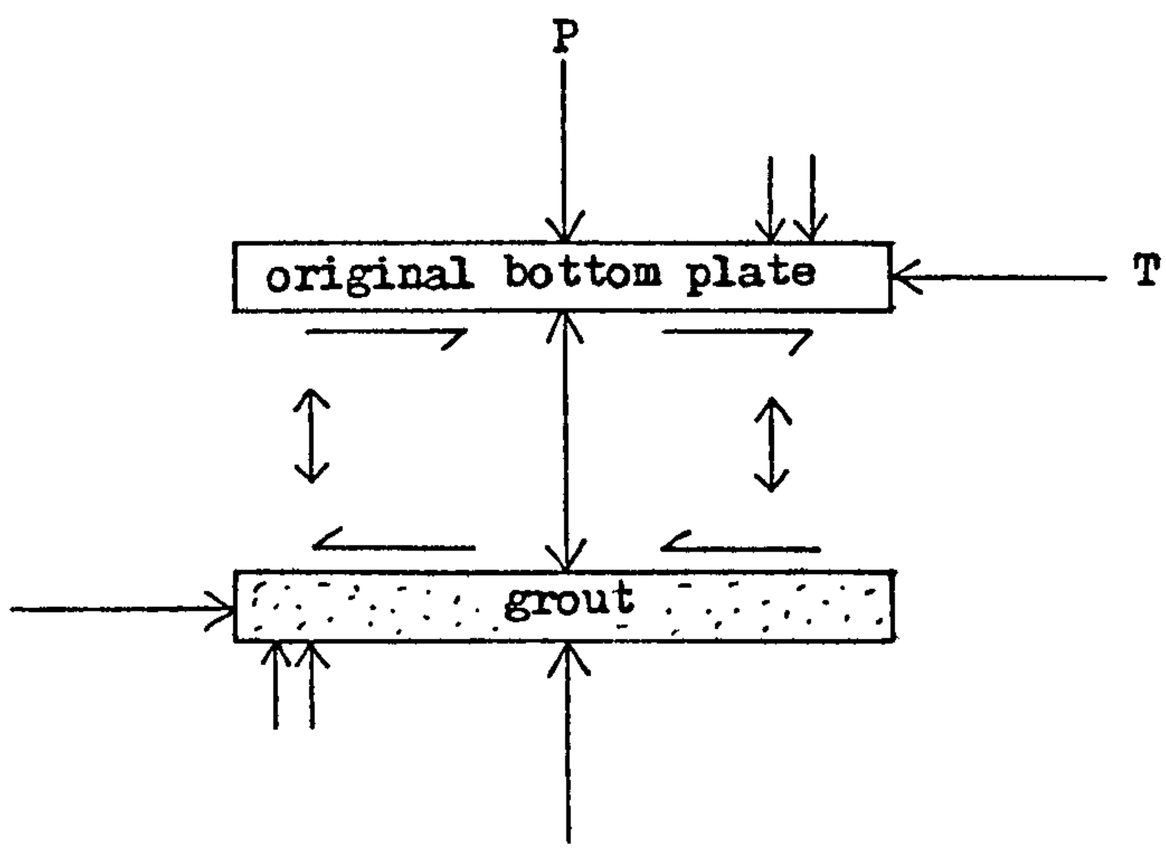

(b)Second bond test,as Figure 9.6

FIGURE 9.7 FORCES APPLIED TO THE INDIVIDUAL PLATES,INDICATING AN UNEVEN NORMAL BOND STRESS DISTRIBUTION.

This is the same effect as occurs in the grout annulus of the grouted connection analysed in Chapter 7, where high values of σ_n occur at the connection ends to resist bending in the grout. For the bond tests, this means that the normal bond stress (σ_n) will not be quite evenly spread over the plate and so the results may be marginally affected. This may explain why the top bond always fails first, as σ_n will be lower on the left hand side of the top bond than on any part of the lower bond. This is indicated by the number of vertical load arrows on each bond surface in Figure 9.7a.

9.1.2 Results and Findings

The results of the six tests are summarised in Table 9.2. Of most significance is the determination of the coefficient of friction, which is calculated as follows:

$$\mu = P/T_{max} \qquad (9.1)$$

Figure 9.8 gives a plot of ultimate mean shear bond stress against mean normal bond stress suggesting a straight line relationship with gradient of 3.0. The coefficient of friction can therefore be taken to have a value of 3.0 and is used for the finite element analysis.

On testing the second bond, the initial vertical load was about 0.025 N/mm^2 and rose to about 0.05 N/mm^2 before failure. This was because the shear load (T) creates an anticlockwise bending moment which rotates the plates bearing on the vertical load jack. However, the normal bond stress was low enough to demonstrate that there is significant adhesion c. The actual values of the adhesion obtained vary considerably. This was because some specimens were left to dry and warm for several days before testing so that shrinkage of the grout or

Test	Date	Age (days)	f_{cu} N/mm²	P kN	μ	c N/mm²
1	12/4/83	15	46.0	2.40	3.0	0.0 a
2	7/6/83	14	39.3	4.85	3.9	0.27
3	28/6/83	14	38.6	2.40	3.5	0.36
4	13/7/83	14	38.3	3.60	2.7	0.80
5	29/7/83	15	20.4	6.00	2.4	0.36 a
6	6/9/83	14	30.4	7.50	2.2	0.83
Mean					2.95	

a = After drying out at room temperature for an additional seven days.

TABLE 9.2 RESULTS OF THE STEEL/GROUT BOND TESTS.

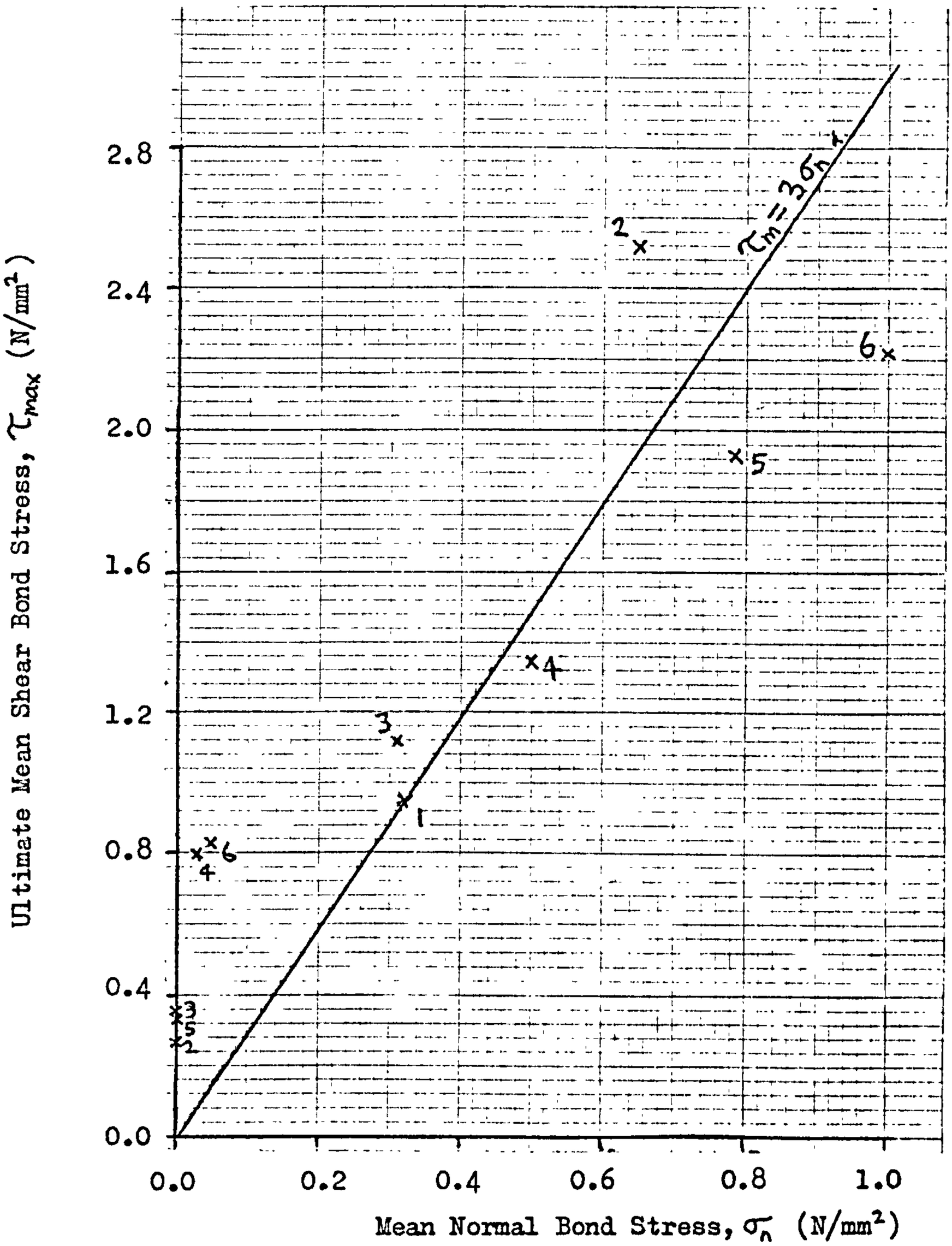

FIGURE 9.8 THE RELATIONSHIP BETWEEN ULTIMATE MEAN SHEAR BOND STRESS, AND MEAN NORMAL BOND STRESS.

differential thermal expansion between the steel and grout may weaken the adhesive bond.

This adhesion does not appear to add to the ultimate frictional shear stress, except when the normal bond stress is low and once slip commences the adhesion is zero. Therefore, the relationship $\tau_{max} = 3.\sigma_n$ appears to be satisfactory for the analysis.

During the tests, no slip was recorded on the bottom bond and so it is assumed that prior to ultimate load the same must be true for the top bond. As a small slip is recorded for the top bond, which increases linearly with T, it is considered that this must be due to shear strains across the thickness of the grout. Since the bond slip is negligible, it can be concluded that the tangential bond stiffness (k_t) is very large in reality.

The vertical displacement (δ_4) was very difficult to measure accurately. This was because the top plate was found to tilt in response to increasing load T. When the component of δ_4 relating to T was removed, it was found that there is negligible vertical movement prior to the ultimate slip. It can therefore be deduced that no dilation of the bond took place. This was not surprising since no slip occurred either until the ultimate shear bond stress was reached.

At ultimate load, the top plate would suddenly slip free and be accompanied by a loud crack. Little residual strength remained after this slip. In a complete grouted connection, as the shear bond stress reached the ultimate condition, slip would commence and cause surface dilation effects, (that is, u_a would increase). Since the grout is confined by the sleeve and pile, an increase in normal bond stress

results and the shear bond stress would no longer be at the ultimate state. In the joint tests carried out here, there is no confinement to the grout and so the initial slip leads to ultimate failure. No increase in σ_n is possible. This explains why the bond dilation effect could not be measured by this test. The normal bond stiffness (k_n) also could not be determined. At zero slip and dilation the bond thickness is zero making k_n equal infinity.

Figure 9.9 shows a photograph of the steel and grout bond surfaces after slip failure. Scratch lines in the direction of slip are apparent on the grout surface, which is much smoother than the pre-slip surface. The steel surface is also smoother due to the presence of powdered grout filling the hollows of the shot-blasted surface. The photograph also shows small areas of grout which have adhered to the steel, leaving hollows in the grout surface. This effect, which only occurred in tests 1 and 6, would locally increase σ_n in a grouted connection and would be a random factor affecting the characteristics of the bond stresses near to ultimate load.

9.2 Grouted Connection Tests at The City University

This is a separate programme funded by the Science and Engineering Research Council to test connections with extreme geometries and later to include specimens with split sleeves and alternative shear key shapes.

9.2.1 The Test Programme

The specimens in the tests were strain-gauged on the outside surface of the sleeve and inside surface of the pile. Three rows of strain-

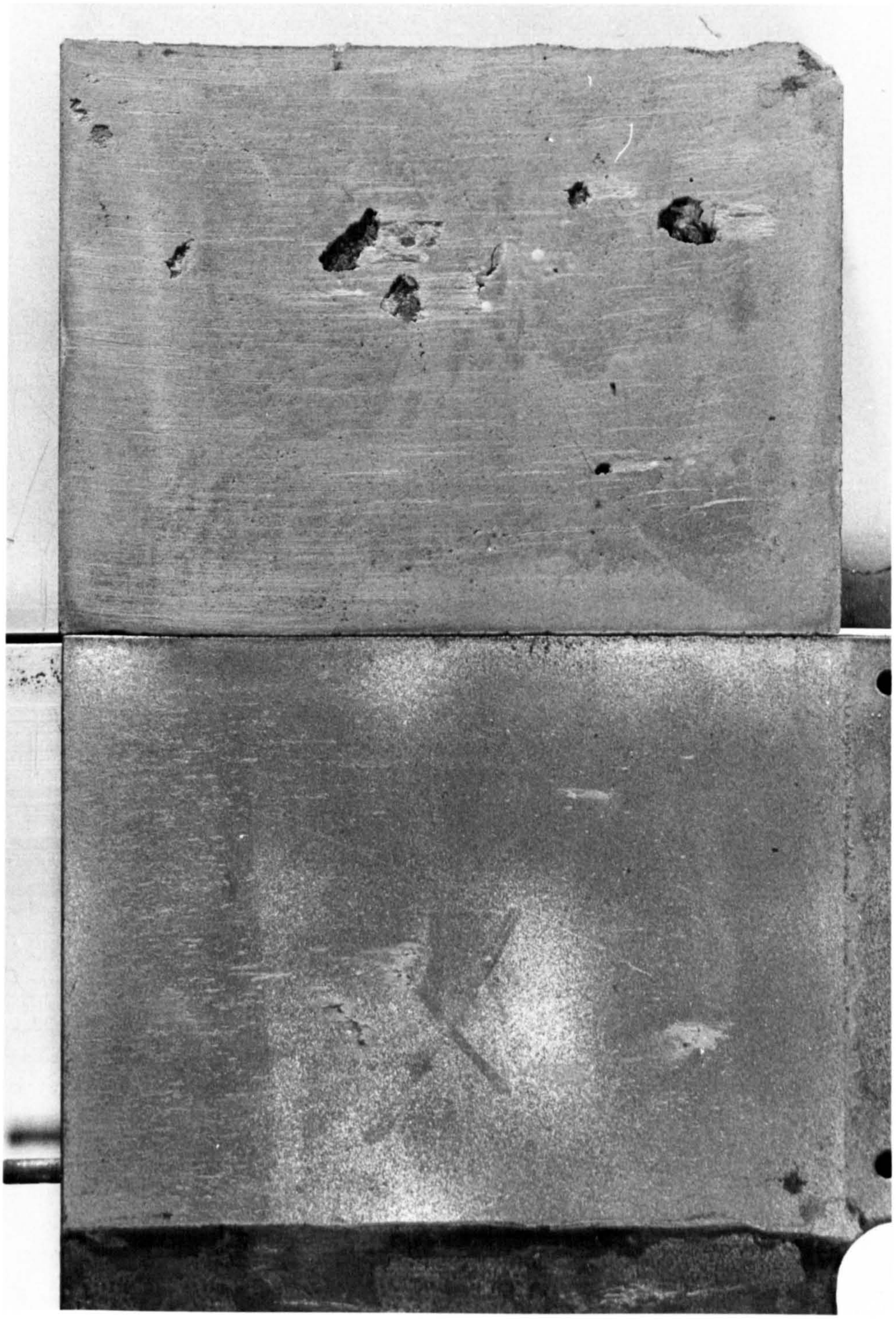

FIGURE 9.9. CLOSE-UP VIEW OF THE STEEL AND GROUT SURFACES AFTER SLIP FAILURE.

gauges, equi-spaced around the circumference, measure the axial and circumferential strains at intervals along the length of the connection, including either side of every second shear key. The strain readings are very useful not only to investigate the behaviour of the connection, but also to compare with the results of the finite element analysis.

Table 9.3 gives details of the tests carried out to date, and Figures 9.10 and 9.11 show photographs of the test rig set up ready for testing. Six 90 tonne load jacks are used, giving a maximum load capacity of 540 tonnes. All the connections tested so far have twelve equally spaced longitudinal stiffeners on the sleeve, measuring 90 x 12 mm in section and so far no tests have been carried upon split sleeve specimens.

9.2.2 Results and Findings

The results of the above tests are given in Table 9.4, where the ultimate bond strengths are compared to the bond formulae and finite element predictions. The A and B series tests were loaded with both pile and sleeve in tension and so the actual results should be stronger than the bond formulae predictions which only consider tension-compression loading. The finite element analyses were for tension loading and so give higher bond strength predictions as would be expected.

Actual bond strengths achieved were substantially below expectations, especially for the plain-pipe specimens. Figure 9.12 shows the load-slip curve for test B3 with the finite element results also plotted for comparison. Results for tests B1 and B2 were very similar, although B2 proved to be noticeably weaker than B1 and B3.

Test Specimen	Loading Arrangement	l/d_p	Pile		Sleeve		Grout		Shear Connectors		
			d_p	t_p	d_s	t_s	d_g	t_g	h	s	h/s
A1	Ten/Ten	2	508	25	569	5	559	25.5	2.03	169	0.012
A2	"	2	508	16	569	5	559	25.5	2.03	169	0.012
A3	"	2	508	12.5	569	5	559	25.5	2.03	169	0.012
B1	"	2	508	25	569	5	559	25.5	0		0
B2	"	2	508	16	569	5	559	25.5	0		0
B3	"	2	508	12.5	569	5	559	25.5	0		0
C1	Ten/Comp	2	508	16	689.4	6	677	84.7	2.03	169	0.012
D1	"	2	508	16	569	5	559	25.5	7.11	169	0.042
E1	"	2	508	30	599	20	559	25.5	2.03	169	0.012
F1	"	2	508	9.5	599	20	559	25.5	2.03	169	0.012

TABLE 9.3. GEOMETRIC DETAILS OF THE FIRST TEN CITY UNIVERSITY TESTS. DIMENSIONS IN MILLIMETRES.

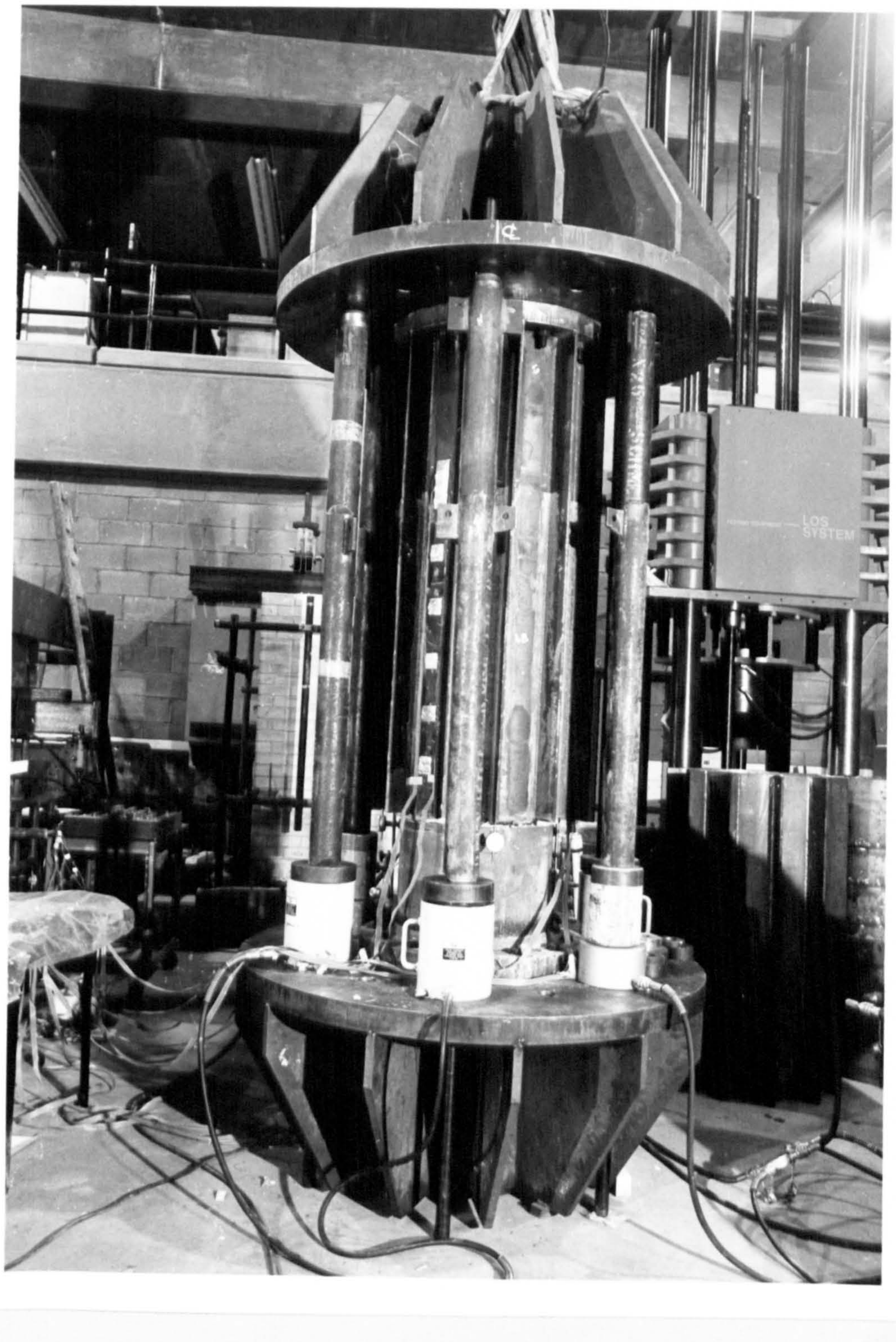

FIGURE 9.10. THE TEST RIG SET UP FOR TENSION LOADING. SIX JACKS ARE CONNECTED TO STRUTS WHICH FORCE APART THE STIFFENED END PLATES, ONE OF WHICH IS BOLTED TO THE PILE, AND THE OTHER TO THE SLEEVE.

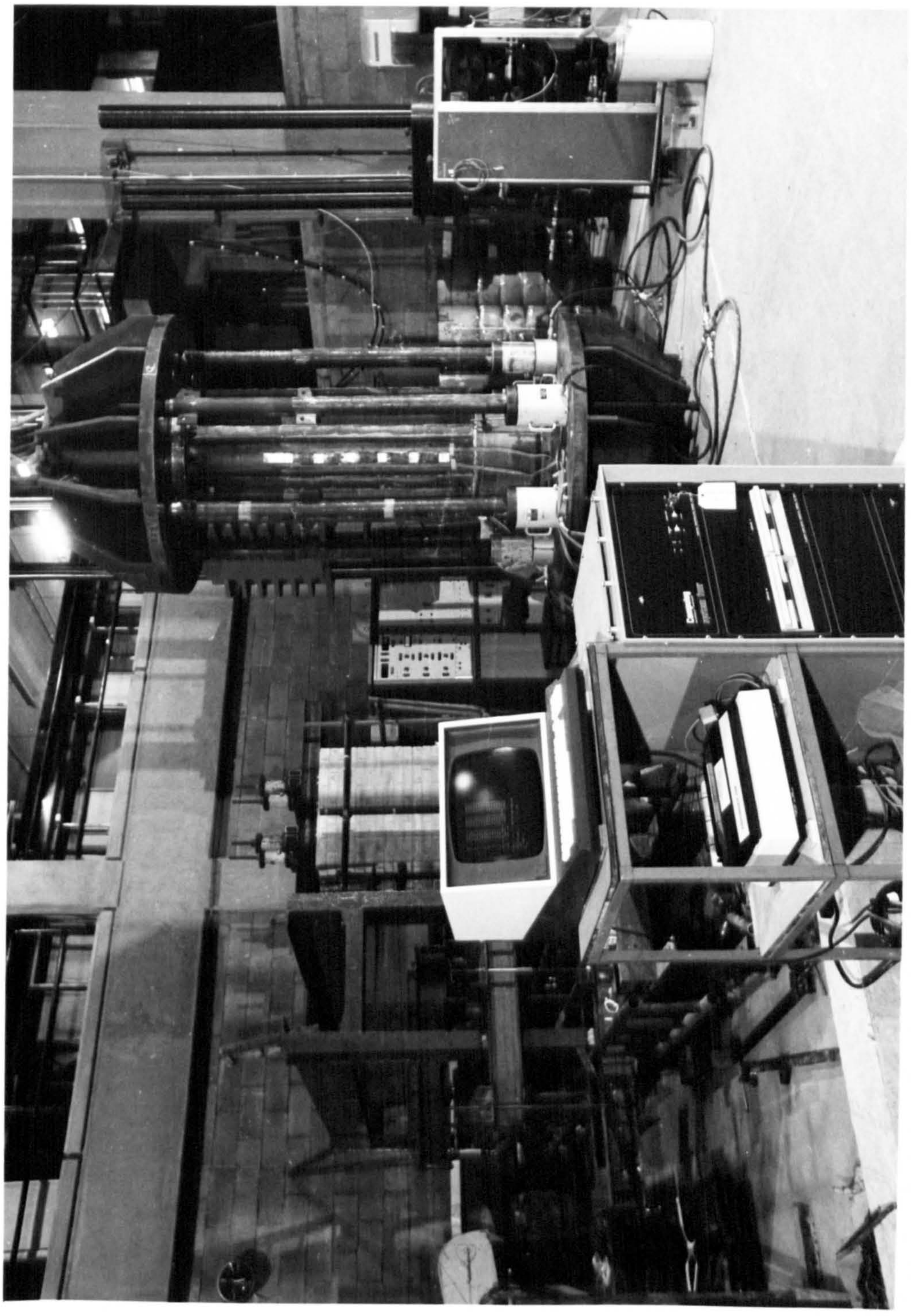

FIGURE 9.11. PHOTOGRAPH OF ALL THE TEST EQUIPMENT, INCLUDING THE COMPULOG SYSTEM IN THE FOREGROUND, WHICH RECORDS ALL THE STRAIN GAUGE READINGS.

TEST	f_{cu} N/mm²	Age (days)	Test Results		F_{BU31}		
			F_{BU}	F_{BU31}	Bond Formula	New Bond Formula	Finite Elements
A1	71	9	1.80	1.52	2.10	1.90	2.49 t
A2	66	12	1.71	1.50	1.95	1.78	2.11 t
A3	71	9	1.66	1.41	1.85	1.70	1.93 t
B1	65	11	0.43	0.37	0.84	1.13	1.59 t
B2	62	9	0.23	0.20	0.79	1.04	1.38 t
B3	67	9	0.40	0.33	0.75	0.97	1.17 t
C1	43	4	>3.14 *	>2.47	2.75	1.71	2.42
D1					4.87	3.63	3.11
E					5.11	2.59	2.42
F1	54	7	2.59	2.12	2.99	1.96	1.66

t = tension loading

* C1 reached the capacity of the rig (540tonnes) without failing.

TABLE 9.4. EXPERIMENTAL AND PREDICTED BOND STRENGTHS FOR THE CITY UNIVERSITY TESTS.

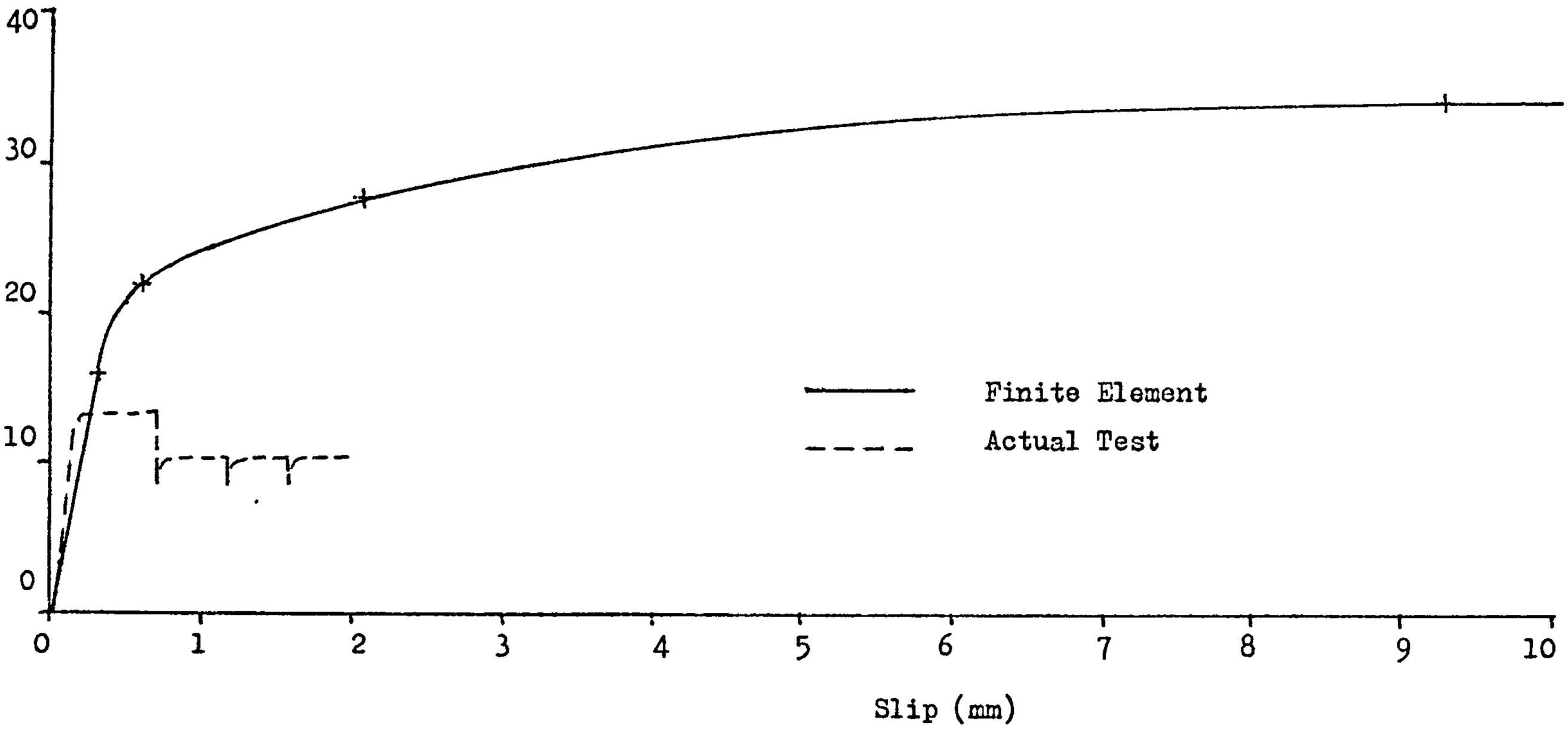

FIGURE 9.12 LOAD-SLIP CURVE FOR THE B3, PLAIN-PIPE, TENSION LOADED TEST.

Such a scatter in the results has been found to be typical for plain pipe tests which may be influenced by geometrical imperfections in the tubulars.

Figures 9.13a-d show the strain distributions recorded on the sleeve and pile of specimen B3, which again were similar for the B1 and B2 tests. Maximum load of 13.2 t/radian is achieved on load-scan 6, just prior to the first major slip. After this slip, load-scan 7 shows the sleeve hoop strain to have suddenly increased (: Figure 9.13b). This can be attributed to the bond dilation effect.

The reason for the low bond strengths is thought to be due to shrinkage of the grout. The test specimens were transported to the laboratory by lorry after grouting and then kept at room temperature until the test date. This enabled the grout to dry out and shrink, especially as room temperature is considerably higher than the North Sea temperature at which the specimens were cast. Grout shrinkage has been found to be very sensitive to temperature, Billington (11). Shrinkage would result in failure occurring on the sleeve bond as the grout annulus contracts circumferentially on to the pile and away from the sleeve. The B series tests did fail on the sleeve bond unlike the finite element results, which did not include the effects of shrinkage. The sleeve was cut open after the test and the grout was observed to have a random pattern of cracks which again suggests shrinkage to have occurred. The photograph in Figure 9.14 clearly shows these cracks.

The maximum load was achieved after only about 0.3 mm slip (see Figure 9.12), whereas normally about 10 mm slip would be needed to reach ultimate load. This can be interpreted again as the result of grout shrinkage.

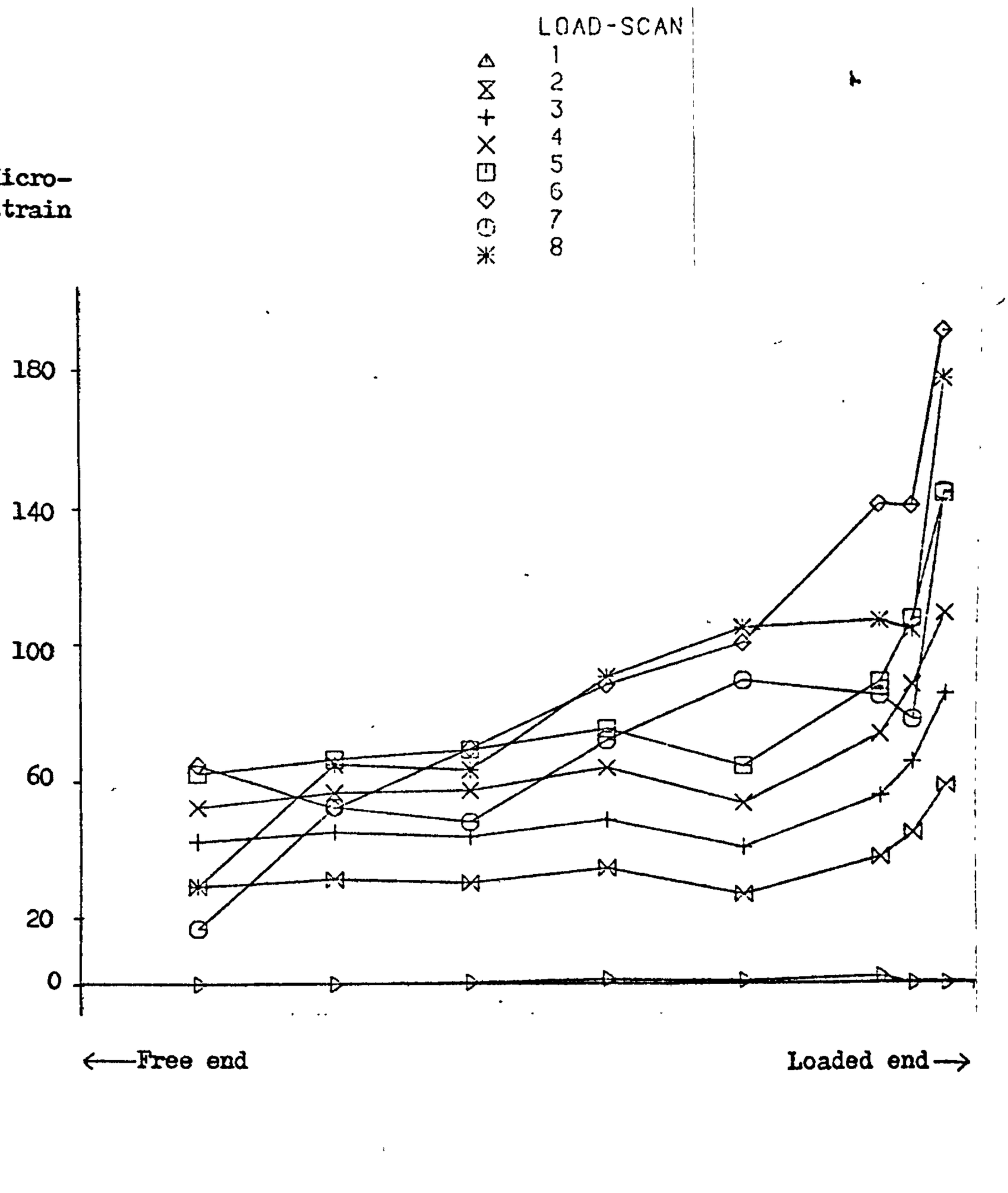

FIGURE 9.13a LONGITUDINAL SLEEVE STRAINS FOR PLAIN-PIPE SPECIMEN B3.

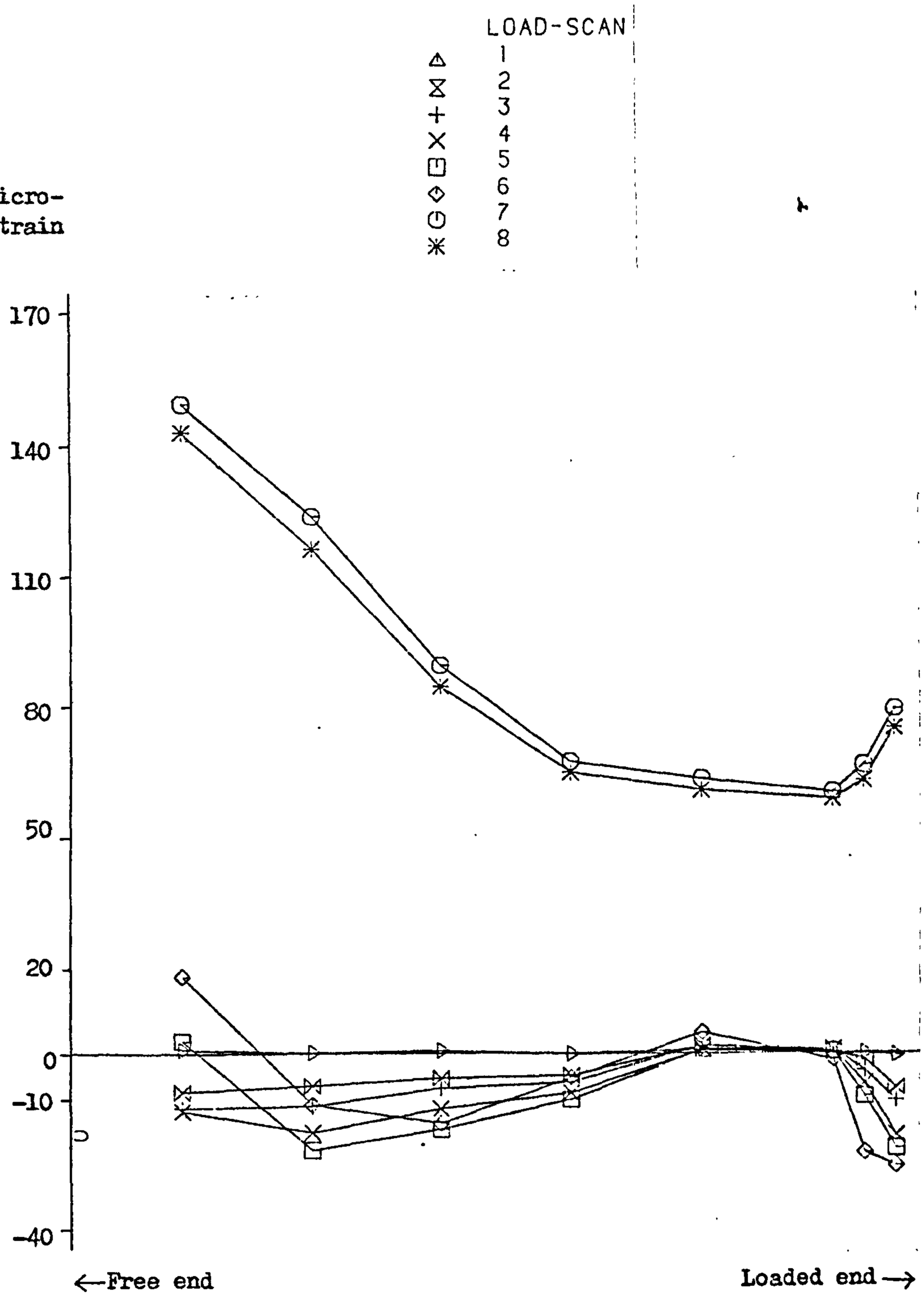

FIGURE 9.13b HOOP SLEEVE STRAINS FOR PLAIN-PIPE TEST B3.

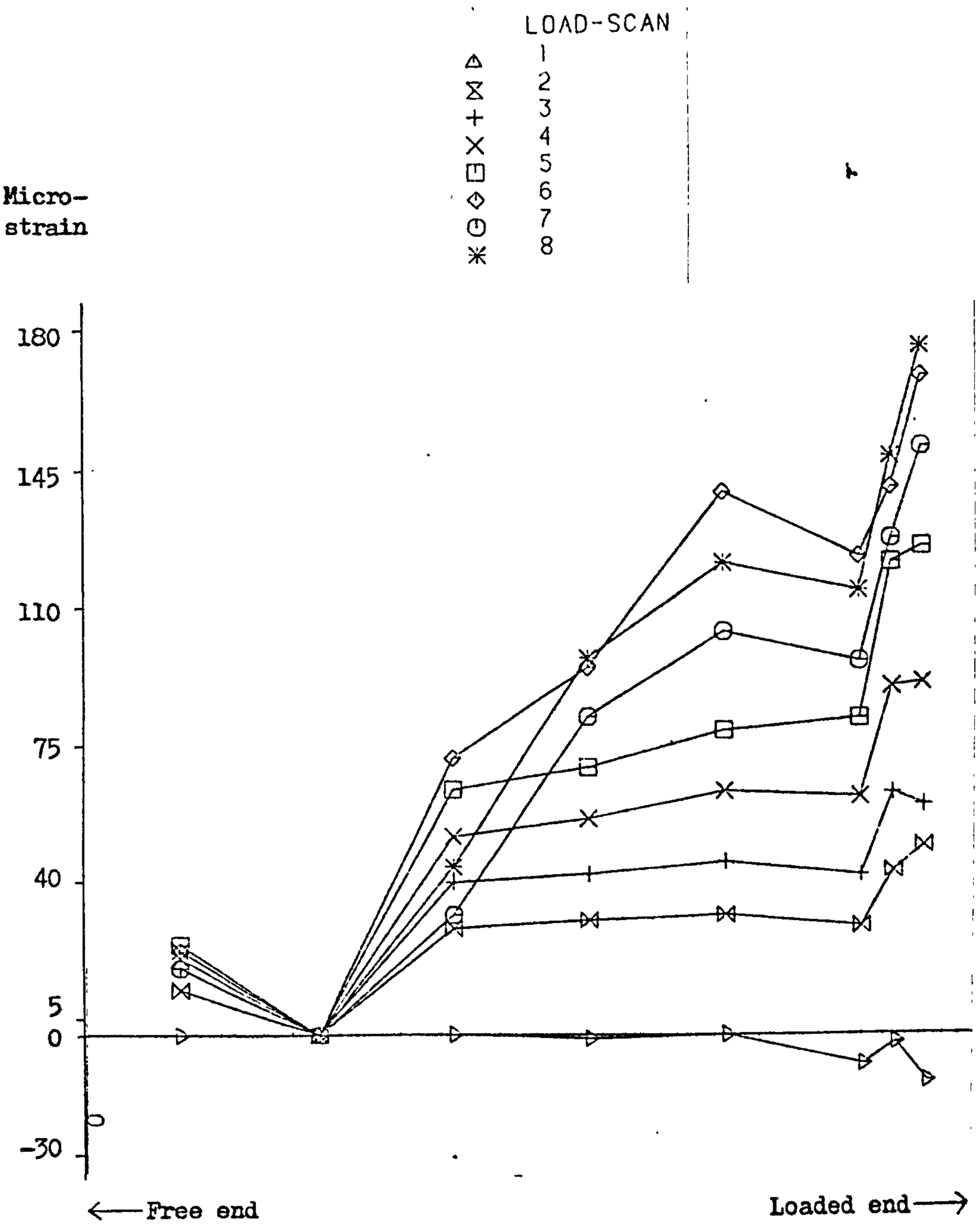

FIGURE 9.13c LONGITUDINAL PILE STRAINS FOR PLAIN-PIPE TEST B3.

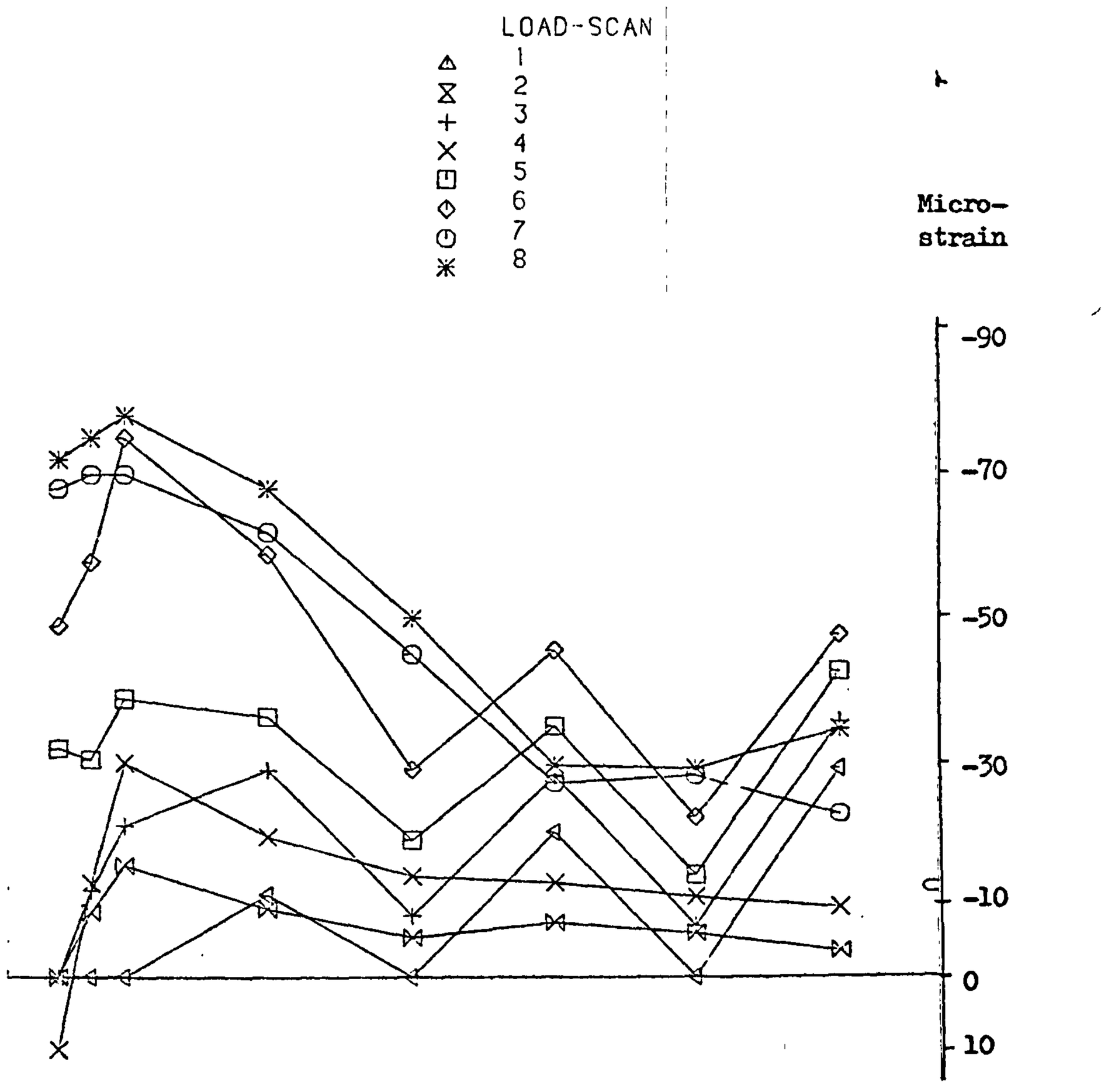

FIGURE 9.13d HOOP PILE STRAINS FOR PLAIN-PIPE TEST B3.

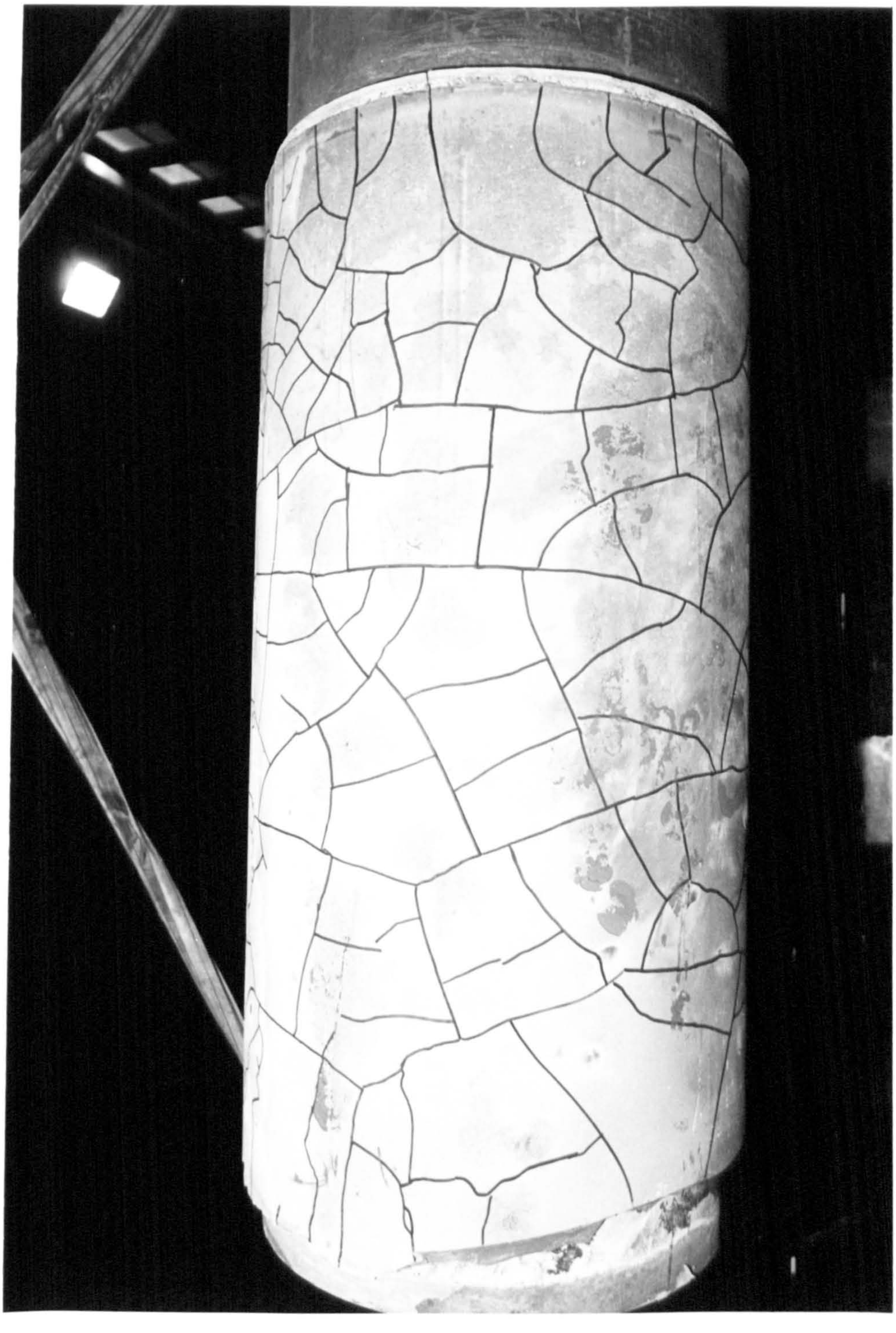

FIGURE 9.14. CRACK PATTERNS (TRACED WITH BLACK PEN), AFTER TESTING AND REMOVAL OF THE SLEEVE, TYPICAL OF THE PLAIN-PIPE TESTS.

The potential for bond dilation is reduced by the amount of radial shrinkage and so the amount of slip needed to reach this reduced u_m must also be proportionally less.

After testing, the sleeve was cut off when it was noticed that the grout on the slip surface had become completely smooth, as if polished, whereas the unslipped pile surface was still partially rough. These observations agree with the mechanism for bond dilation described in Chapter 5.

The shear-keyed tension tests were also weaker than predicted and this is shown by the load-slip curve for test A3 in Figure 9.15. (In fact, if no adjustment is made for cube strength and age of grout, then the results agree well with those obtained from the finite element analysis). Again, it is likely that shrinkage is the cause of the reduced bond strength. The shrinkage would reduce the confinement of the grout and so the grout under the shear keys would crush at a lower level of compression.

Figures 9.16a-d show the sleeve and pile strains recorded by test A3, which were similar for tests A1 and A2. Large peaks of strain in the vicinity of the shear keys were recorded, especially on the sleeve. These can be explained in terms of the radial shear key force (V_R). The radial shear key force expands the sleeve radius in the vicinity of the shear key, which in turn must increase the hoop strain. This also results in bending in the axial direction, which locally increases the axial tensile strain and is shown in Figure 9.17. Similar effects on the pile (but with hoop compression rather than tension), are less significant due to the greater thickness of the pile.

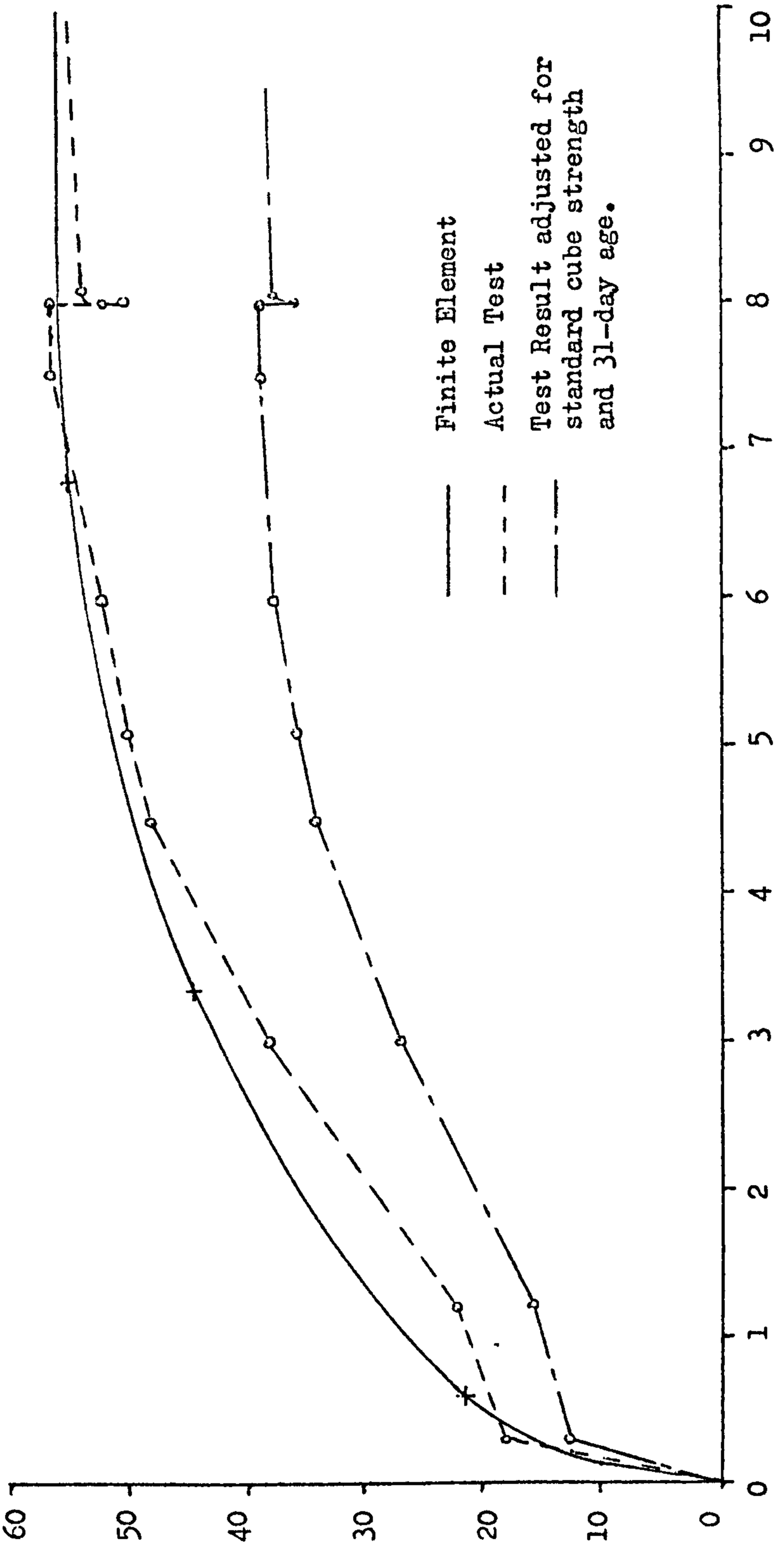

FIGURE 9.15 LOAD-SLIP CURVE FOR THE A3, SHEAR-KEYED, TENSION LOADED TEST.

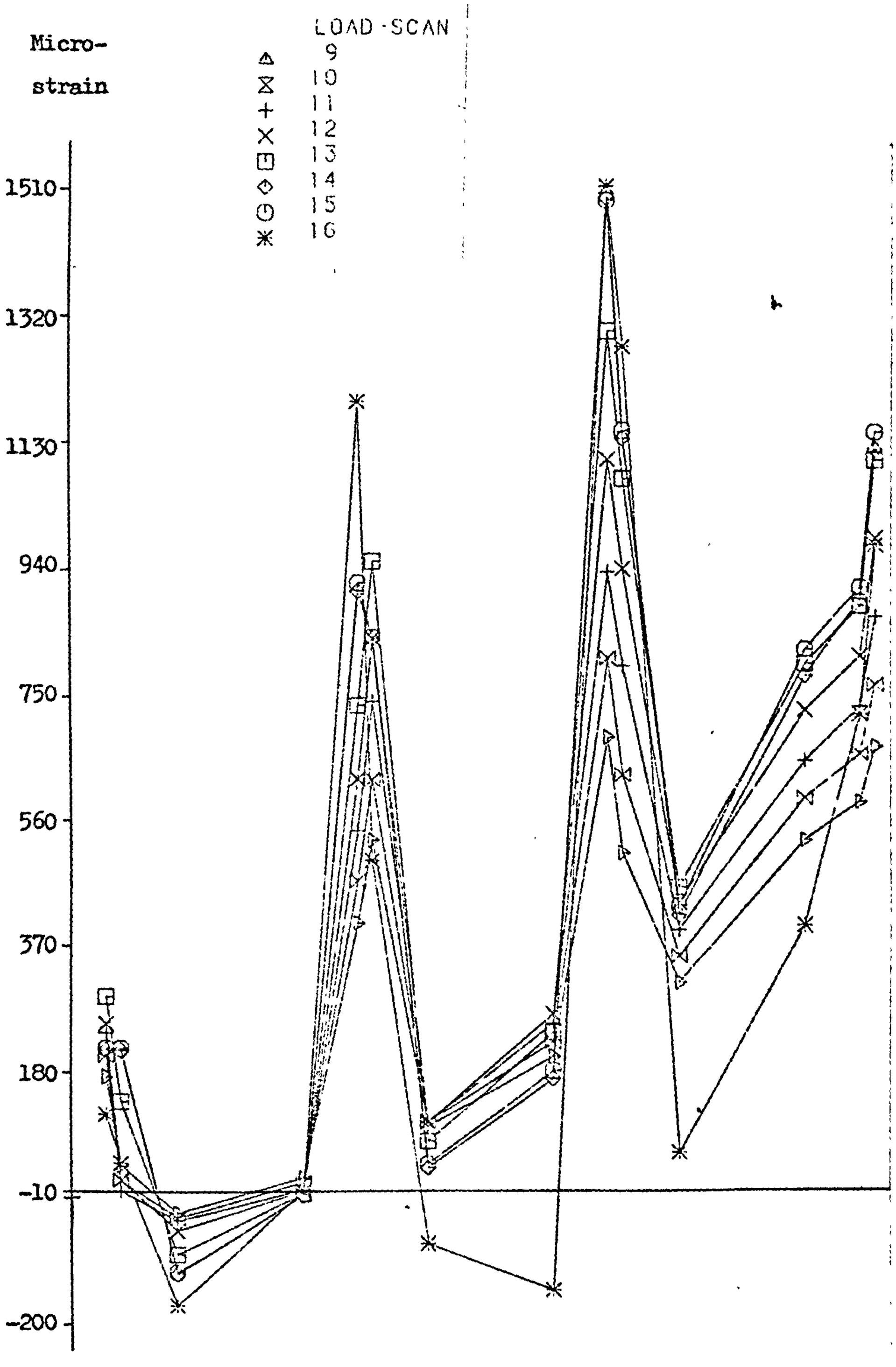

FIGURE 9.16a AXIAL SLEEVE STRAINS FOR SHEAR-KEYED TEST A3.

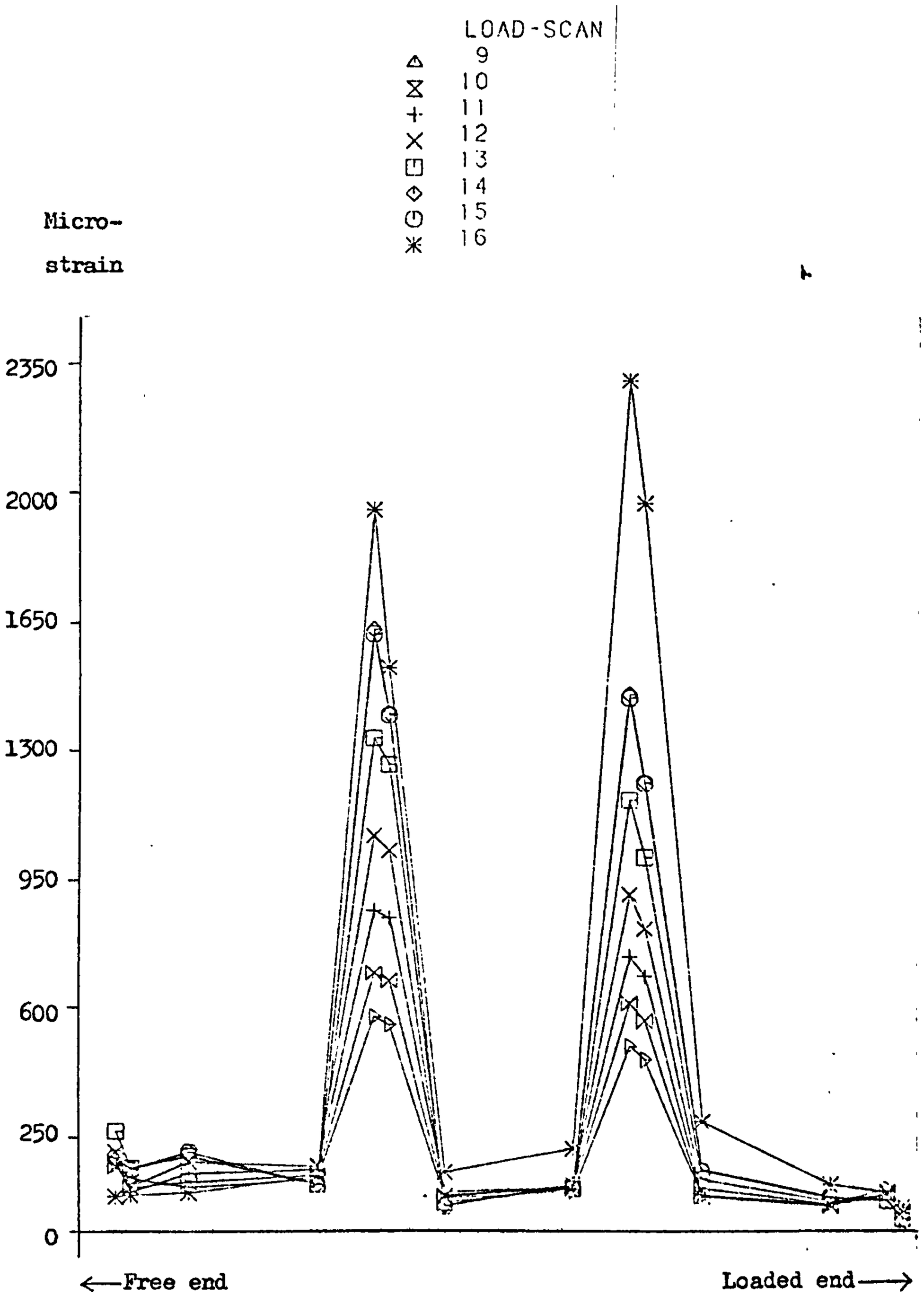

FIGURE 9.16b HOOP SLEEVE STRAINS FOR SHEAR-KEYED TEST A3.

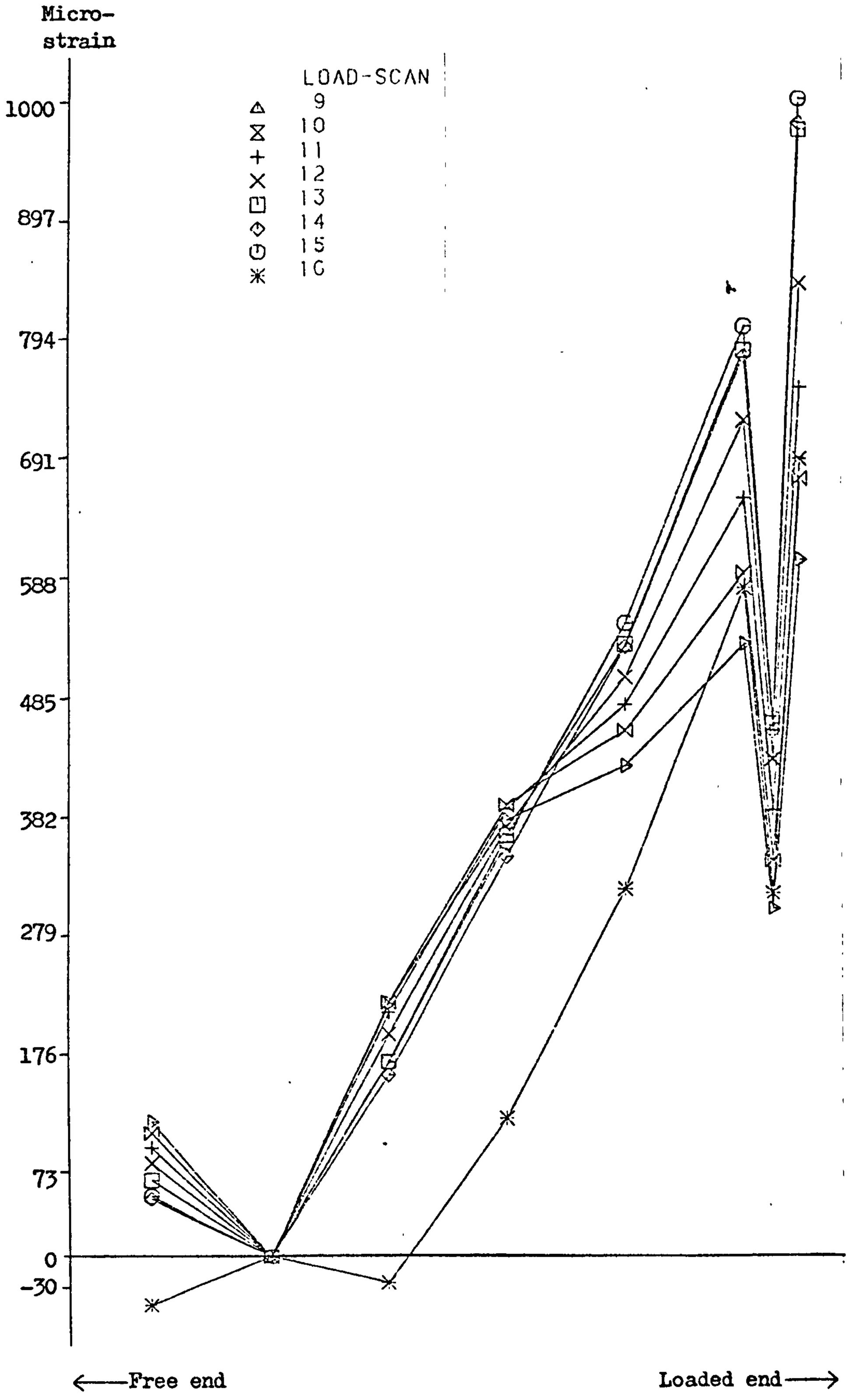

FIGURE 9.16c LONGITUDINAL PILE STRAINS FOR SHEAR-KEYED TEST A3.

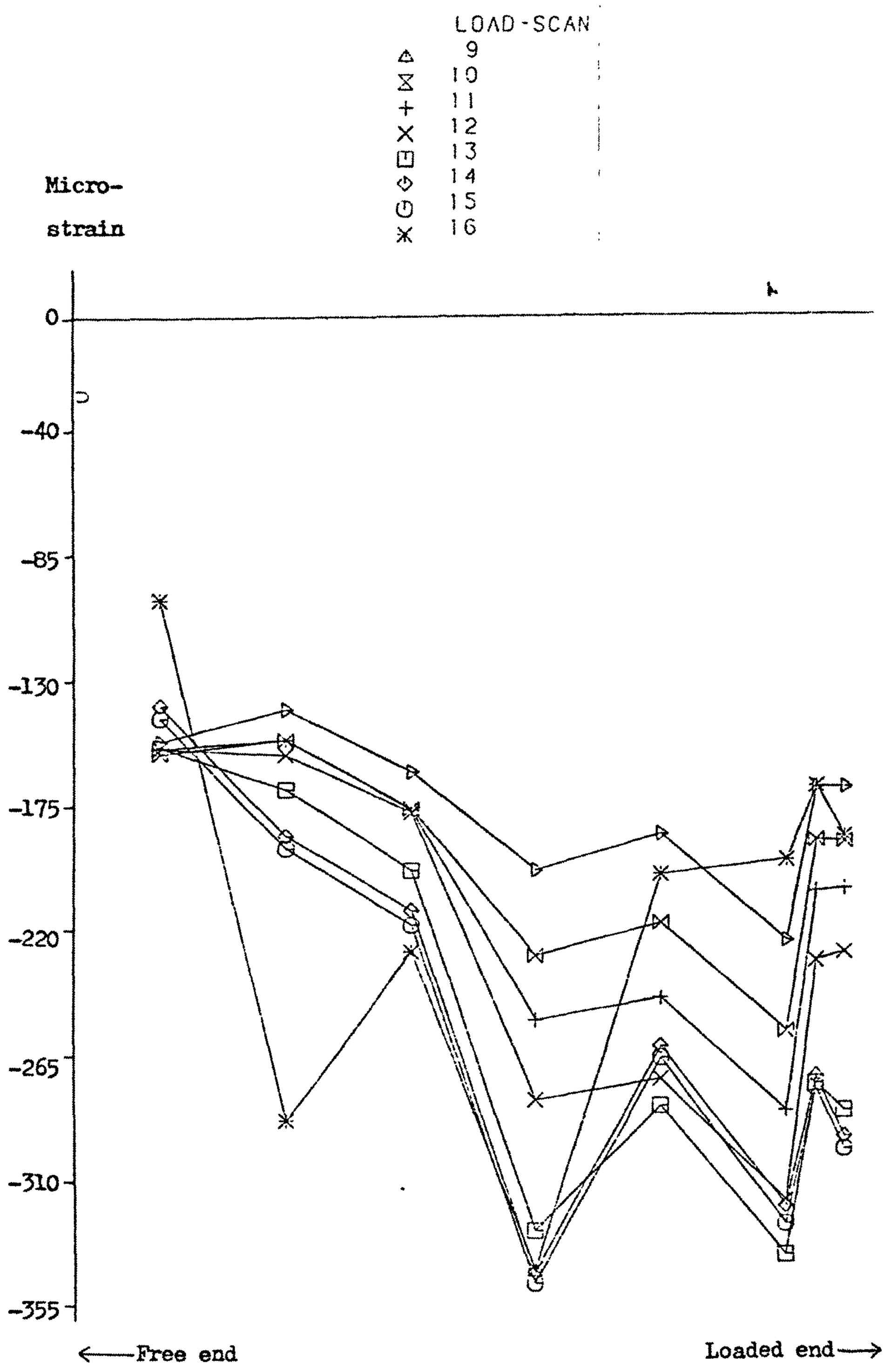

FIGURE 9.16d HOOP PILE STRAINS FOR SHEAR-KEYED TEST A3.

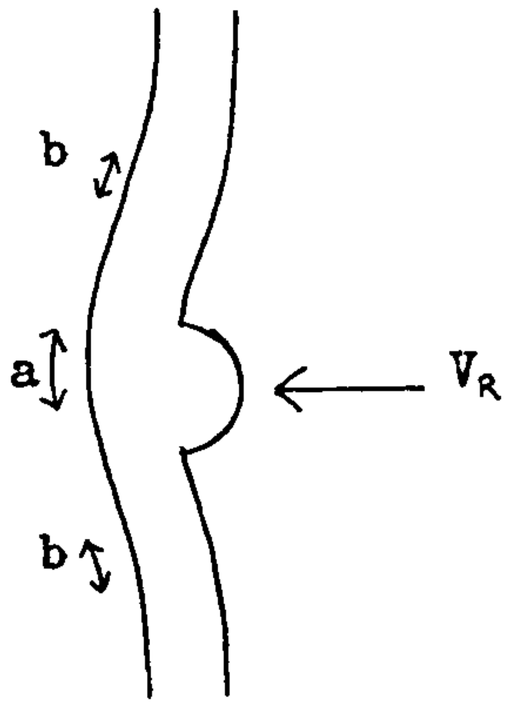

KEY

a = increased } axial strain due to
b = reduced } local bending

FIGURE 9.17 LOCAL VARIATIONS IN AXIAL STRAIN AROUND THE SHEAR KEYS CAUSED BY THE RADIAL SHEAR KEY LOAD.

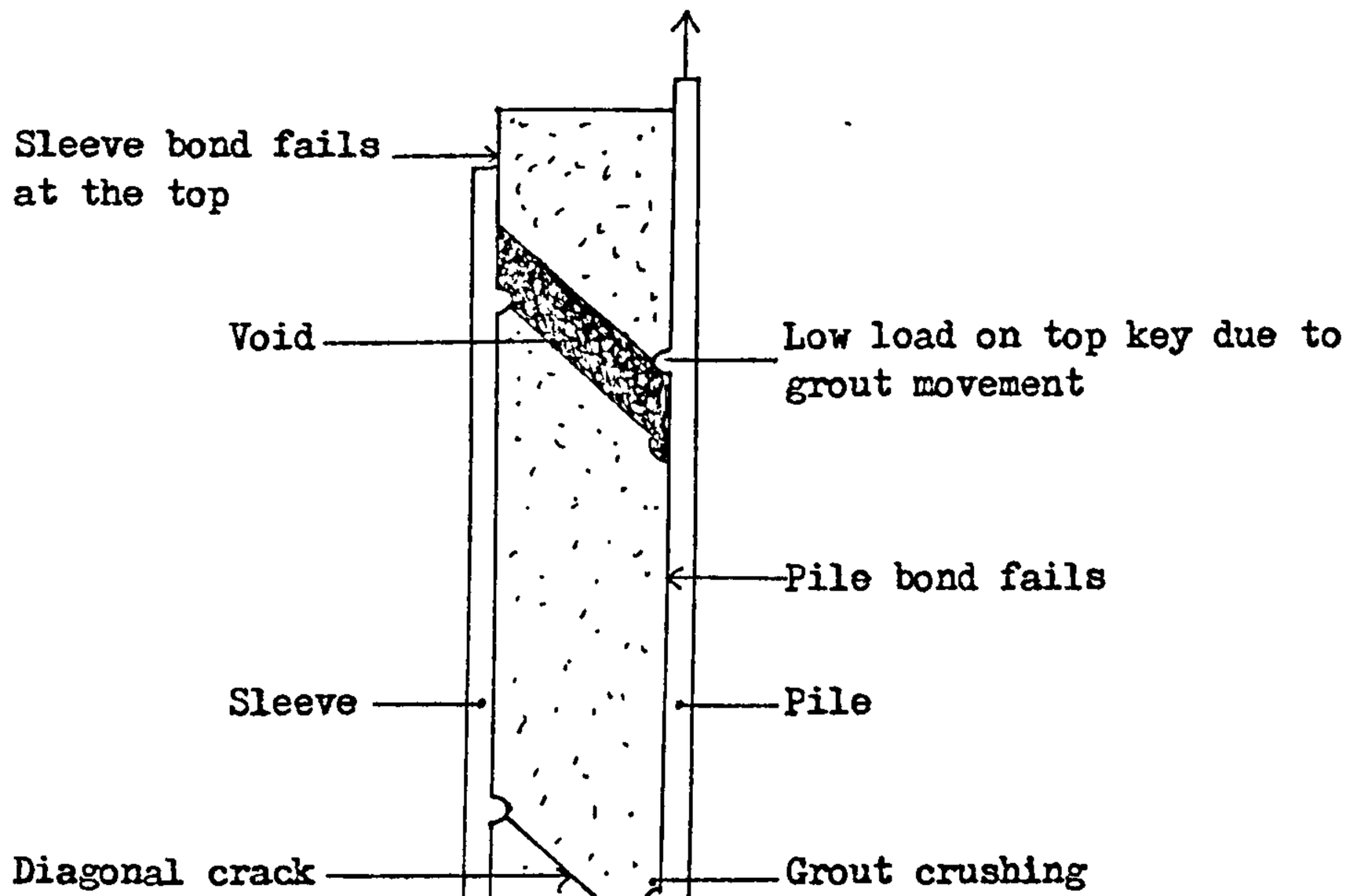

FIGURE 9.18 TYPICAL A-SERIES FAILURE MECHANISM.

Ultimate failure at first appeared to be on the sleeve bond as the top of the grout had slipped substantially on this bond. However, on cutting open the sleeve, it was found that failure was in fact on the pile bond, with substantial voids behind each pile key. The top pile key did not crush the grout, but moved it along, making the failure appear to be on the sleeve bond, as shown by Figure 9.18. The end pile key was therefore virtually redundant because the grout resisting its movement was too near the end of the connection to be able to support large loads. Figure 9.19 shows a photograph of the failed A2 specimen after removal of the sleeve. The voids behind some of the pile keys are visible as well as the diagonal cracks.

Another interesting feature which was observed after removing the sleeve was a layer of pulverised grout filling the open bond on the compressive side of the shear keys. This effect, which is depicted in Figure 9.20, was described in Chapter 7 for its importance in increasing the confinement of the grout under the shear key.

Test C1 was loaded with the sleeve in compression and pile in tension, but was unusual because the grout annulus was 85 mm thick, rather than the normal 25 mm. On testing, the maximum load capacity of 540 tonnes was applied without reaching ultimate load. The new bond formula underestimated this strength as no account is made of the effect of variations in the thickness of the grout annulus, but the existing formula and the finite element analysis did predict relatively high bond strengths, given in Table 9.4. This increased bond strength may be attributed to the fact that the greater thickness of grout will be able to compress more under the radial key forces and so the radial movements in the sleeve and pile will be correspondingly less.

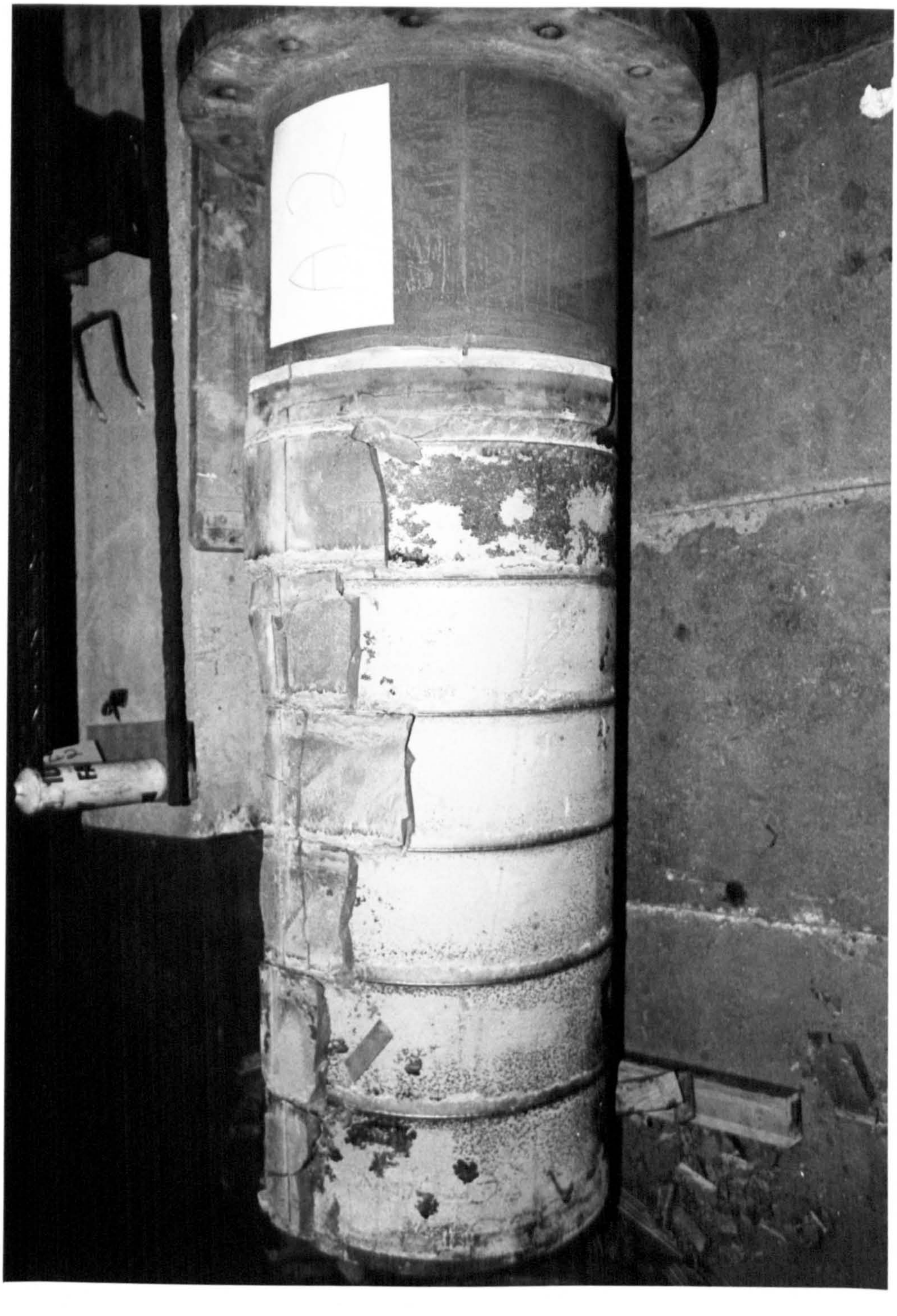

FIGURE 9.19. THE FAILED A2 SPECIMEN AFTER REMOVAL OF THE SLEEVE, SHOWING THE VOIDS BEHIND THE PILE KEYS AND THE DIAGONAL CRACKS.

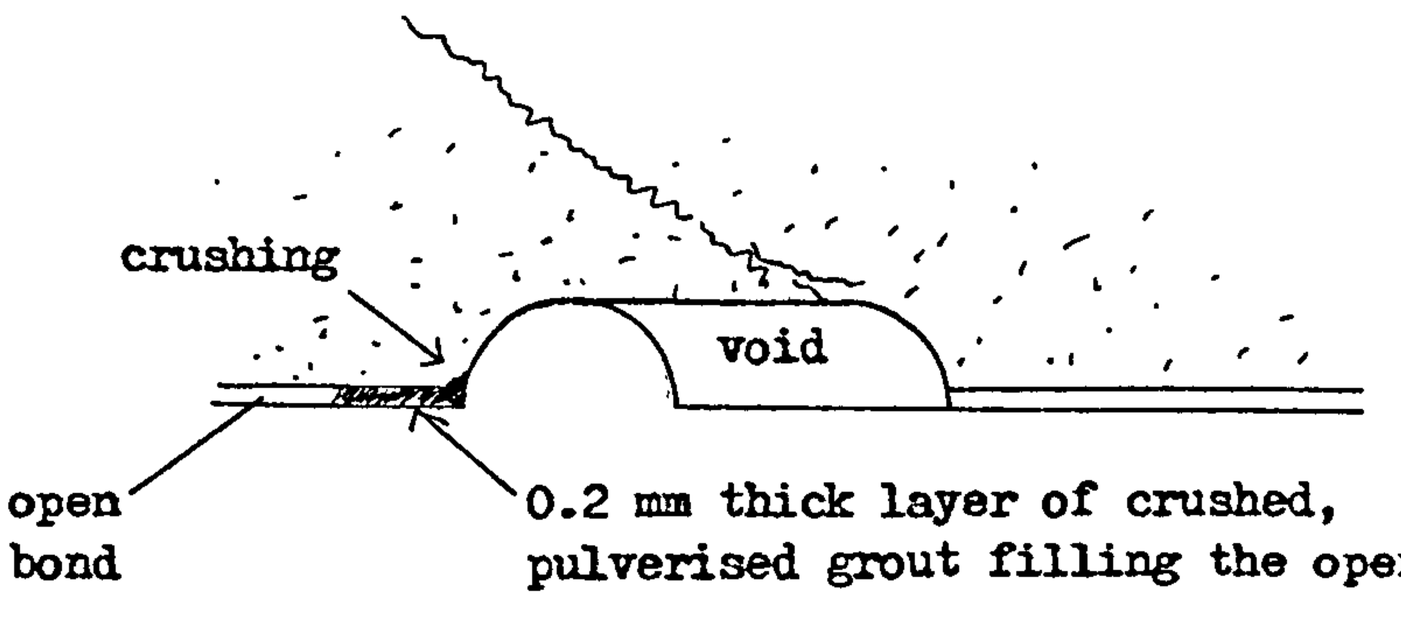

FIGURE 9.20 DEPOSITS OF PULVERISED GROUT FOUND TO BE FILLING THE OPEN BOND AFTER REMOVAL OF THE SLEEVE.

It was also noticed that the tubulars for the C1 test were very well shot-blasted before grouting. This could explain the slightly higher than expected bond strength being due to greater frictional effects.

The next test to be made was F1, also under tension-compression loading. This specimen was unusual in that the sleeve was twice as thick as the pile. The bond strength achieved was only slightly greater than predicted by the new bond strength formula, although the finite element prediction was slightly less. The finite element analysis also showed failure to be on the pile bond which was the case for all the shear-keyed specimens. The loads on the sleeve shear keys were very low as the thick sleeve enabled the sleeve bonds to remain closed with much of the load being taken by the bond friction.

Grout shrinkage did not appear to be a problem with the C1 and F1 tests, which were tested at a low age and not exposed to room temperature for long periods.

9.2.3 Comparison with the Finite Element Results

Figures 9.21a and b give the sleeve and pile strains produced by the finite element analysis for the B3 test at the maximum load of 34 tonnes/radian. The strains are given for the Gauss Points closest to the sleeve/pile surface. These approximately equal the experimentally measured strains as there is little variation in strain through the thickness of the sleeve or pile except at the extreme ends of the connection where there are bending effects.

Comparisons can be made with the experimental strain readings plotted in Figure 9.13, and although the ultimate load is approximately 2.5 times larger for the finite element analysis, similarities in the axial strain

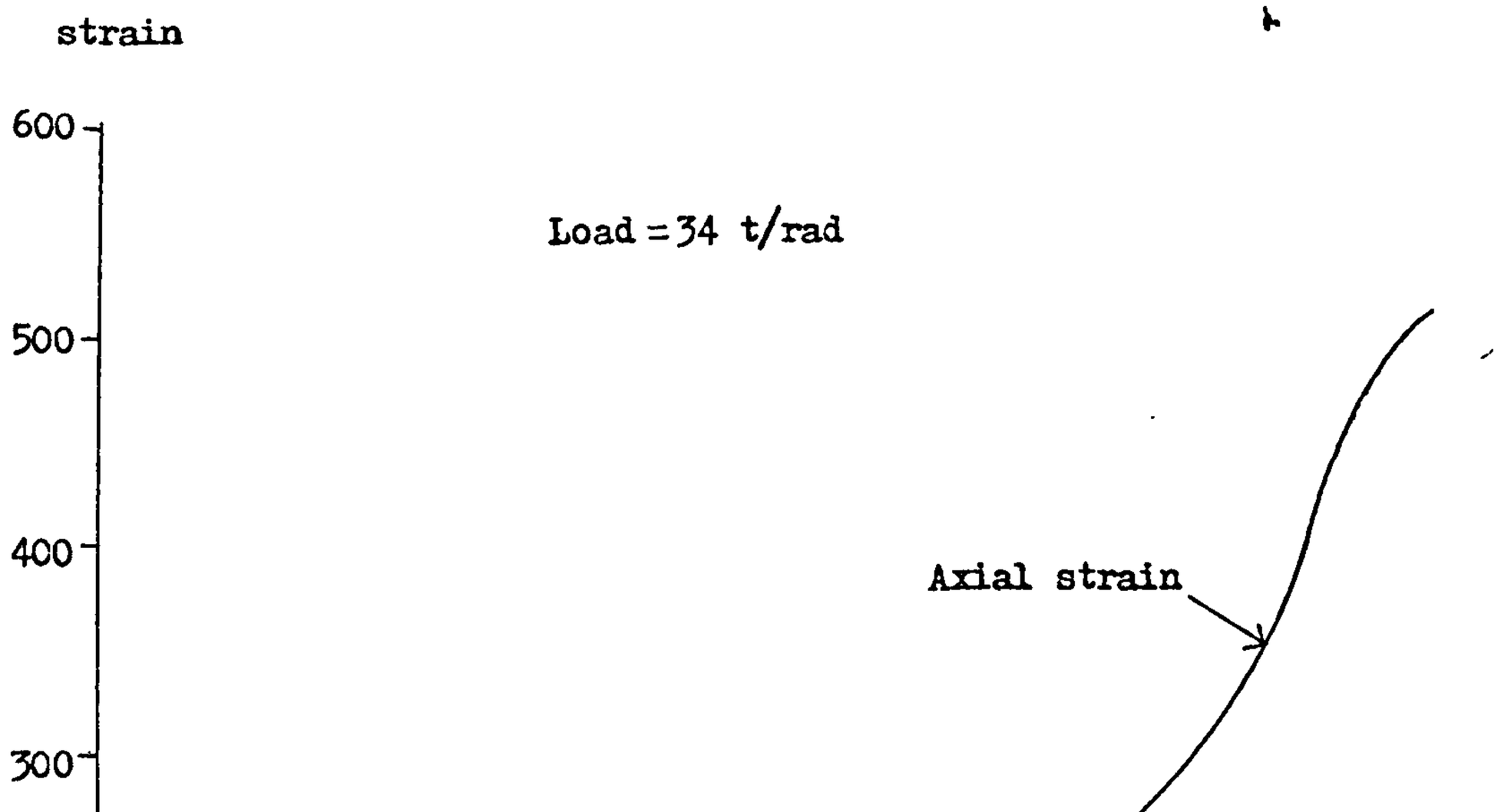

FIGURE 9.21a STRAIN DISTRIBUTIONS IN THE SLEEVE FOR PLAIN-PIPE SPECIMEN B3 AT MAXIMUM LOAD GIVEN BY THE FINITE ELEMENT ANALYSIS.

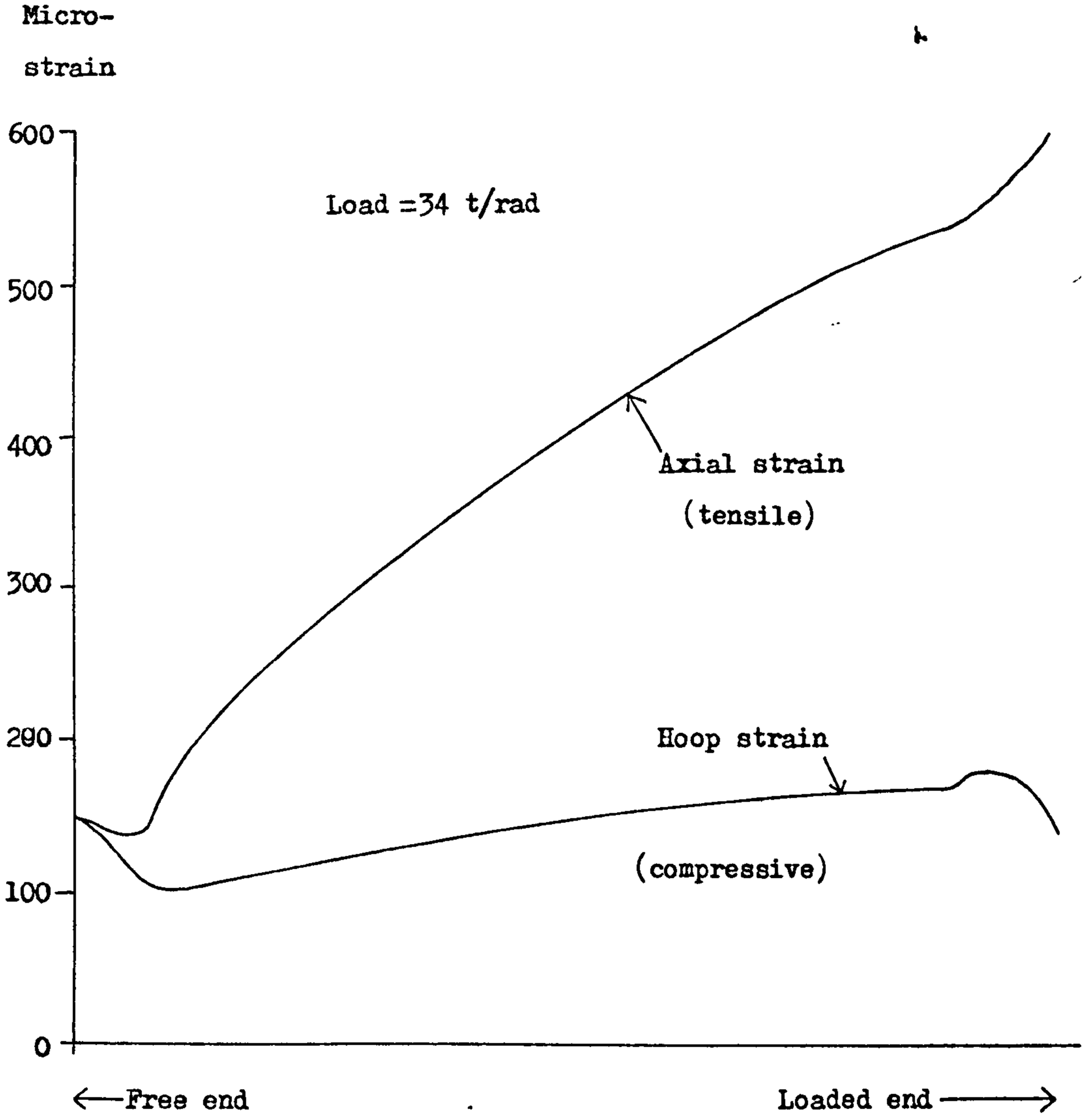

FIGURE 9.21b STRAIN DISTRIBUTIONS IN THE PILE FOR PLAIN-PIPE SPECIMEN B3 AT MAXIMUM LOAD GIVEN BY THE FINITE ELEMENT ANALYSIS.

distributions can be seen. Experimentally, the sleeve hoop strains were greater than the pile hoop strains because ultimate slip and failure was on the sleeve bond, but in the finite element analysis, the pile hoop strain was greatest since failure was on the pile bond. The orders of magnitude of the hoop strains produced by the finite element analysis and the bond dilation effects for the slipped and unslipped bonds compare well with the experimental results and justify the methods and values used in the analysis.

Figures 9.22a, b and c give the sleeve and pile strains produced by the finite element analysis at ultimate load for the shear-keyed A3 test. These results can be compared to the experimental results given in Figure 9.16. Figure 9.22a shows the sleeve axial strains, where the outer Gauss Points give the strains closest to the outside of the sleeve and so should be similar to the experimental results. The inner Gauss Points show there to be some variation in strain through the thickness of the sleeve in the vicinity of the shear keys. This is due to bending moments in the sleeve created by the radial shear key forces.

A comparison of the analytically obtained strains with the experimental axial sleeve strains shows a similar trend apart from the very large strains measured at the shear key locations. In the analysis, these variations at the key locations were not apparent for two reasons: (a) The stiffeners are distributed evenly around the circumference in the analysis, creating a larger bending stiffness than exists in reality midway between the real stiffeners, and (b) The nearest Gauss Points to the shear keys are about 12 mm away and the strains indicated at these points will be far less than the peaks at the shear keys.

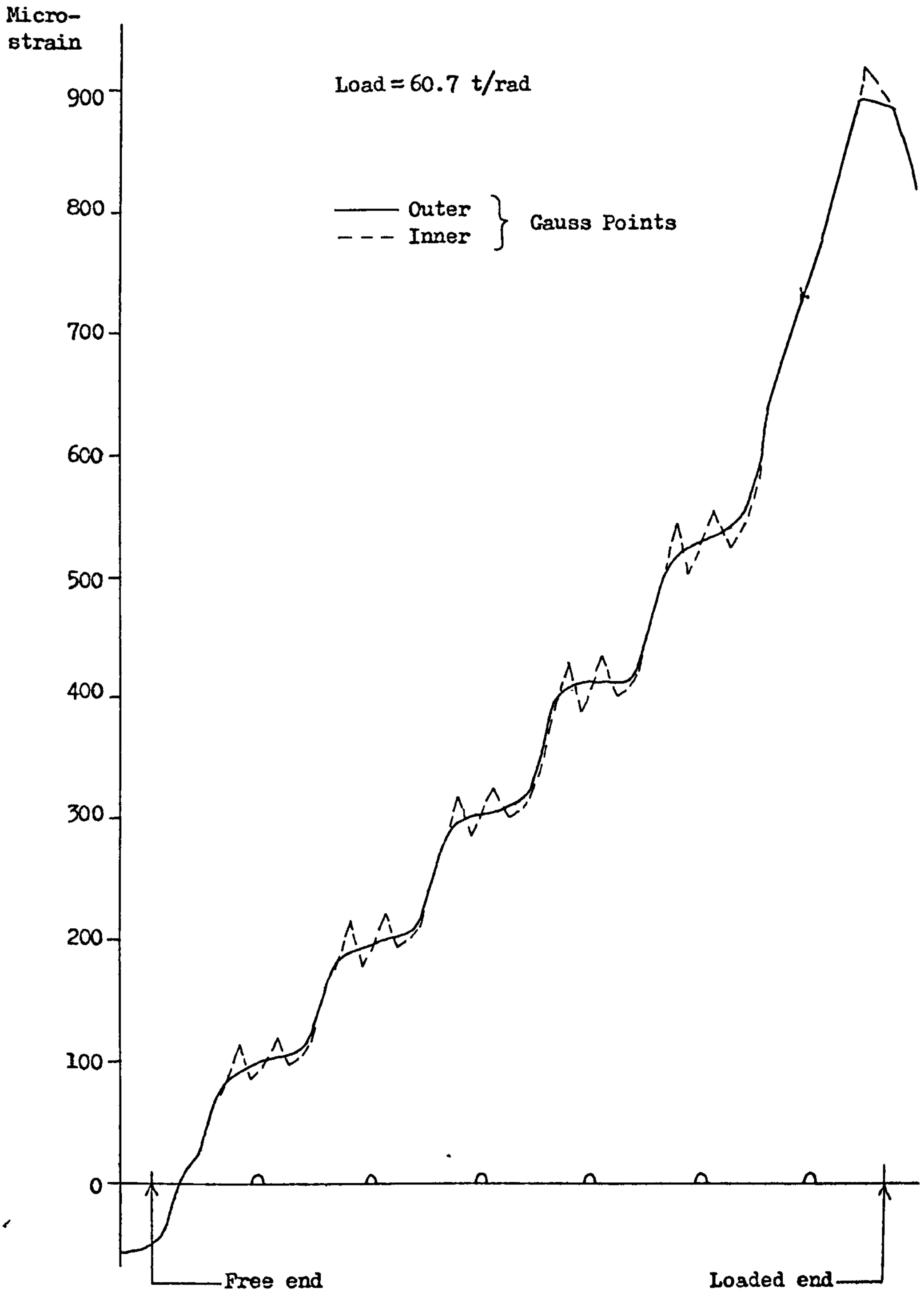

FIGURE 9.22a SLEEVE AXIAL STRAINS AT ULTIMATE LOAD FOR TEST A3 GIVEN BY THE FINITE ELEMENT ANALYSIS.

FIGURE 9.22b PILE AXIAL STRAINS AT ULTIMATE LOAD FOR TEST A3 GIVEN BY THE FINITE ELEMENT ANALYSIS.

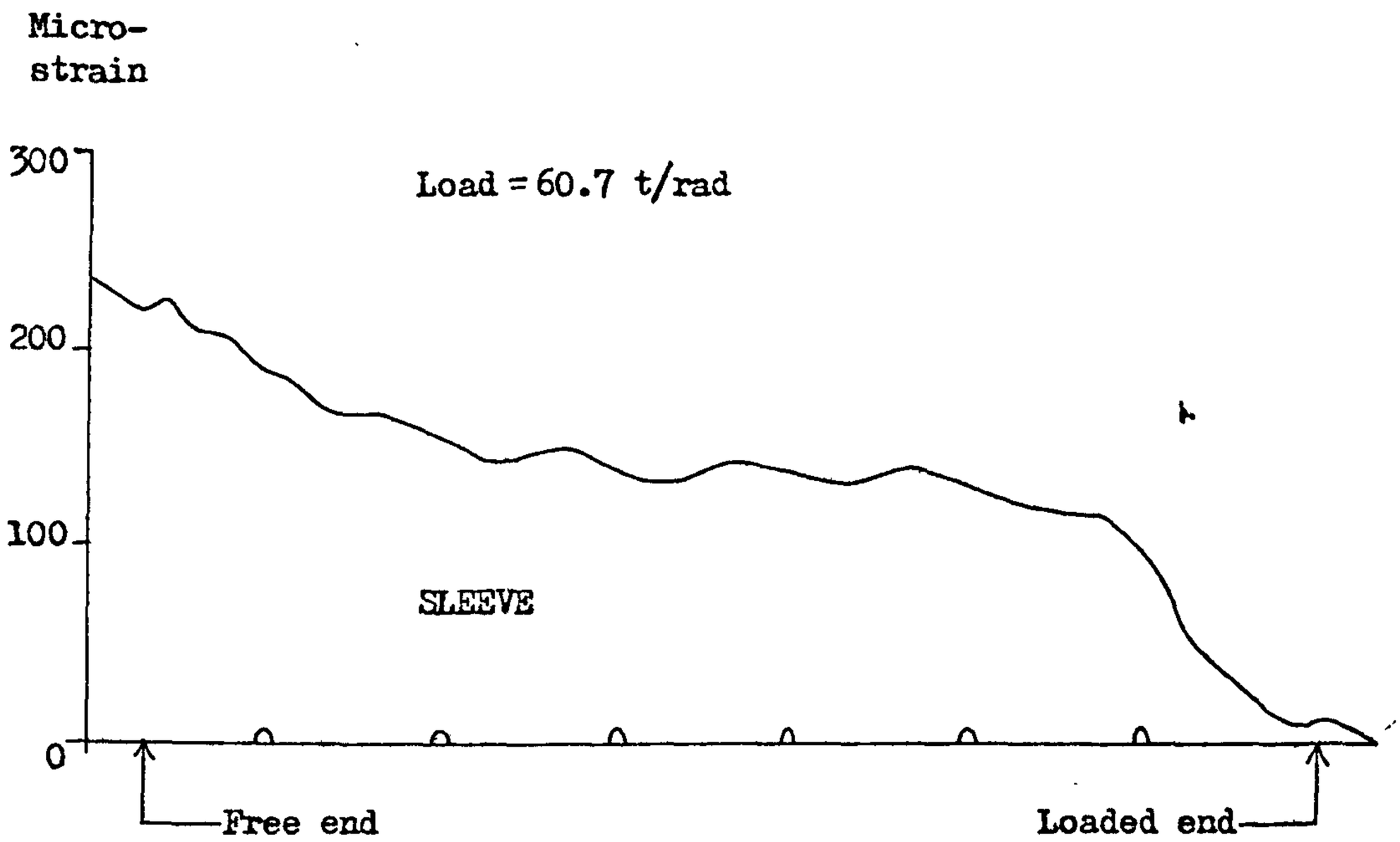

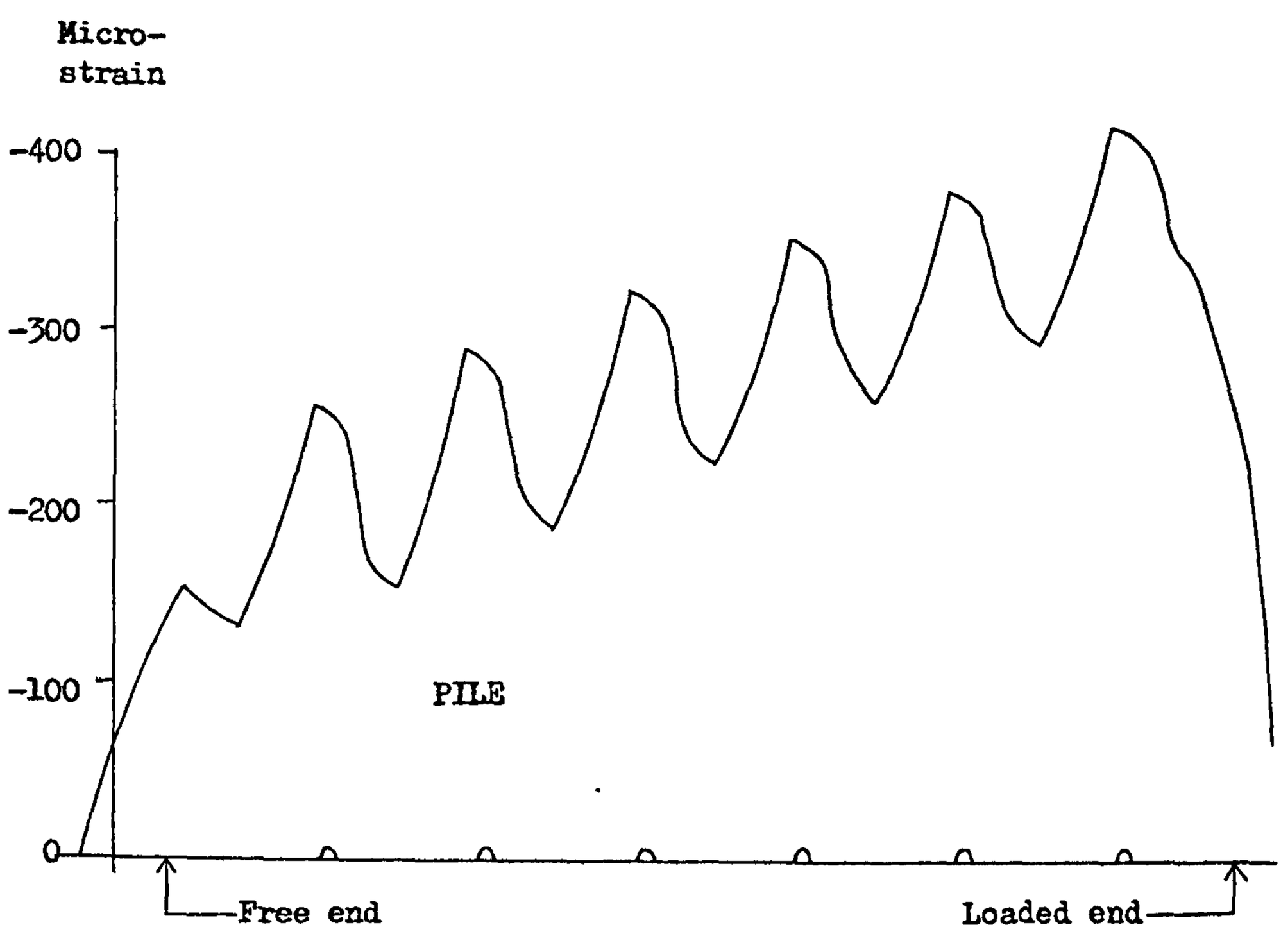

FIGURE 9.22c SLEEVE AND PILE HOOP STRAINS AT ULTIMATE LOAD FOR TEST A3 GIVEN BY THE FINITE ELEMENT ANALYSIS.

Smaller elements would be needed to show the strain peaks at the shear key locations.

Figure 9.22b shows the pile axial strains, where the inner Gauss Points give the strains closest to the inside of the pile, which should be similar to the experimental results. The strains at the outer Gauss Points vary substantially from the inner Gauss Point strains at the shear key locations, indicating large bending strains at the shear keys. These bending effects are much greater than on the sleeve, even though the pile is thicker than the sleeve, for two reasons. Firstly, at ultimate load the sleeve bond remains closed, whereas the pile bond is open. Friction on the sleeve bond results in much smaller key forces on the sleeve keys than on the pile keys, as there is little bond friction on the pile bond. The radial sleeve key force is much smaller as a result than the pile radial key force, leading to much smaller bending effects. The second reason is the high bending stiffness of the stiffeners, which reduce bending strains on the sleeve. Experimentally, the pile axial strains appear to show the same trend as the finite element analysis, although only one strain gauge is suitably sited to detect the local variations at the shear key locations. The local strain variations recorded in the analysis would have been even greater close to the shear keys, if smaller elements had been used.

Figure 9.22c shows the hoop strains for pile and sleeve. In these cases the inner and outer Gauss Points gave little variation in strain. Comparing the sleeve hoop strains with the experimental results, the magnitudes are seen to be much the same, apart from the extreme variations in strain recorded experimentally at the shear key locations.

Again the finite element analysis fails to show this effect due to the large elements used.

The pile hoop strains compare very favourably with the experimental results. These strains are larger than on the sleeve as the Poisson effects, dilation and radial key forces all tend to create a compressive pile hoop strain. On the sleeve, for tension loading, the Poisson effects have a compressive effect, but this opposes the dilation and radial key force effects which are tensile, hence creating a lower overall hoop strain than on the pile. The analysis shows larger local variations in hoop strain on the pile than on the sleeve and this can be attributed to the much larger radial key forces on the pile. In the experimental results, these variations are not very clear as the strain gauges are too widely spaced to detect such rapid variations in strain.

For the A1 and A2 tests, which have thicker piles, the results were very similar. The sleeve hoop strain was marginally greater, and the pile hoop strain was smaller due to the greater thickness. Local variations in the pile strains were also less, but the axial sleeve strain did not differ. The smaller radial movements of the thicker piles resulted in higher grout confinement and higher ultimate key loads.

The analyses of tests C1 to F1 yielded the following results. Test C1, which had a large grout annulus, appeared to be stronger because the stiffer grout ring expanded less and so the confinement around the pile keys was greater, leading to higher crush loads on the pile keys.

For test E1, the higher key loads on the pile bond result in the pile bond opening, whilst the sleeve bond remains intact opposite the pile keys. This is because the radial forces from the pile keys force the pile bond to open and the sleeve bond to close.

Similar results occur for test F1, but the sleeve bond stresses and pile key loads are lower due to the thinner pile.

For test D1, with a large shear key upstand, the key loads and Poisson effects are large enough to open both bonds and failure is by crushing around the pile shear keys.

9.2.4 Conclusions

The finite element analysis has been shown to be of great value when analysing grouted connections with extreme geometries. It can show in detail the different forms of failure associated with a variety of geometries. The weakest dimension of a particular grouted connection design can therefore be determined and used to improve the efficiency of that design. Influencing factors such as tubular dimensions, shear key geometry, stiffeners, alternative loading conditions, scale and length of connection can easily be considered. Experimental testing, whilst important for verifying the final design, cannot be economically used to explore all the design possibilities investigated by the finite element method.

CHAPTER 10

CONCLUSIONS

10.1 The Main Findings

The main findings of this research project are summarised in the following.

1. On inspection of the existing experimental results it was found that bond strength is not only a function of grout compressive strength, but also of grout age. Age factors are created to normalise the bond strength to one month old, but these factors are also sensitive to grout type and curing conditions.
2. Comparing the fully normalised bond strengths for specimens of different scales, it was found that larger scale tests always gave lower bond strengths. Previously it was thought that scale did not affect bond strength and no allowance was made for scale on the reduced scale laboratory tests. The finite element results also show this effect.
3. The stiffness factor, $K \alpha (t/d)$, should be $\alpha (t/d^2)$, which will also make it sensitive to scale effects.
4. Laboratory tests are usually end-loaded, but real pile/sleeve/leg structures transfer the load at various points along the sleeve. Tests have shown that this can substantially increase the bond strength.

5. Slip at ultimate load was previously considered to be proportional to scale, but close examination of the results suggests this slip to be constant for all scales. This is because the bond is physically the same at all scales. The results of the finite element analysis agree with this effect.

6. The current bond strength formula does not account for scale effects and is not applicable in case of very high hoop stiffnesses. Also, the effects of ℓ/d_p, surface roughness and sleeve stiffeners are approximated by simple empirical methods. The formula therefore has to be highly conservative in estimating bond strengths for realistic ℓ/d_p values, which are generally much greater than those used in experiments.

7. A new bond strength formula is suggested, which attempts to overcome the limitations of the existing formula.

8. The concept of dilation on the steel/grout bond under slip, resulting from the roughness of the shot-blasted steel surface was developed. This proved to be a useful way to explain the behaviour of grouted connections and is an integral part of the finite element analysis.

9. Steel/grout bond tests showed the coefficient of friction between shot-blasted steel and grout to be 3.0.

10. Experimental and finite element results show the shear keys to have constant tangential load-slip bond stiffness until close to ultimate load. Also, a radial shear key load is found to exist, which is a constant factor of the axial shear key load. This factor depends on the shape of the shear key and equals 0.5 for standard weld bead keys.

11. The ultimate stress at which the grout crushes under the shear key is greater for stiffer tubulars and is due to the increased confinement of the grout. This effect was noted in the detailed finite element analysis, and included in the simplified whole connection analysis by means of a confinement factor, CONF.

12. On crushing, the pulverised grout fills the open bond, which increases the grout confinement enabling substantially higher loads to be achieved than at the initial crush. Experimental work at City University has shown this effect.

13. The grout tends to slide around the shear key, which reduces the radial confinement of the grout. Possibly, the areas around and on the shear keys could be made extra rough, limiting slip and increasing the confinement and ultimate load.

14. Bending effects in the grout are caused by the bond shear stresses and key forces acting across the thickness of the grout annulus. These result in a high σ_n at one end of the sleeve and the other end of the pile to balance the bending moments. The maximum value of σ_n possible before crushing or cracking of the grout is therefore an ultimate limiting factor, especially for very short connections where the moment arm is equally short.

15. For plain-pipe connections, failure is normally on the pile bond, as the surface area is less than on the sleeve bond, but with very thin sleeves, failure can be on the sleeve bond.

16. With thicker tubulars, the increased confinement results in higher σ_n when bond dilation occurs. Therefore, frictional bond strengths are enhanced until Poisson effects become the limiting factor at higher loads.

17. For increasing ℓ/d_p, the load at the loaded end becomes greater, which in turn increases the Poisson effects, resulting in lower bond strengths. A stiffer sleeve or pile reduces the influence of Poisson effects and so the rate of reduction of bond strength with ℓ/d_p becomes less.

18. The difference between loading the sleeve and pile in compression or tension can have a very significant effect on bond strength. This is because reversing the axial load reverses the Poisson effects on the radial expansion or contraction and is particularly significant for a less stiff thin sleeve or pile. Experimental and finite element results show these effects.

19. The results of finite element analysis of connections with shear keys shows that the sleeve keys soon resist the highest stress concentration as the sleeve bond opens first when typically, $t_s \ll t_p$. With increasing load, however, the pile bond also opens and the stresses around the pile keys become greater, ultimately leading to crushing around the pile keys.

20. Only if the sleeve is very thin will sleeve keys have a chance of crushing first according to the finite element and Paslay analyses. These analyses also agree that for a given diameter, increasing the sleeve or pile thickness can only produce a limited bond strength increase.

21. The finite element analysis shows the effect of increasing ℓ/d_p when shear keys are used to be less than for plain-pipes because shear keys are less sensitive to Poisson effects.

22. Increasing the shear key height (h) increases the radial key force (V_R) which reduces the grout confinement and limits σ_n at the ends of the connection. As a result, the shear key loads (V and V_R) become more concentrated where σ_n should be high. This leads to crushing around these shear keys and a limited ultimate bond strength. Higher bond strengths may be possible if shear keys with smaller height are used at the connection ends, enabling larger σ_n. Alternatively, wedge-shaped ends to the tubulars could be used, acting like triangular-shape shear keys with a larger V_R.

23. Reducing the shear key spacing (s) may be more effective than increasing h on raising the bond strength, according to the analytical results. However, there is still an upper limit on bond strength and this occurs when the keys are too close, thus influencing each other's degree of confinement.

24. Analysis showed square-shape shear keys to be stronger than hemispherical weld beads since the radial key force is negligible and the grout confinement greater. Unfortunately, it would not be practical to manufacture square keys. Triangular keys gave a high V_R and low bond strength.

25. Shear keys at the end of the connection appear to have little effect as the grout they bear against cannot resist slipping. Experimental evidence of this was found in the City University tests.

26. Varying the axial load from tensile to compressive appears to have less effect than on the plain-pipe tests because shear keys are less sensitive to Poisson effects. The finite element analysis shows that for compression loading, the sleeve keys may crush first since the pile bond remains intact.

27. Split sleeve tests appear to be weaker as the tensile hoop strains which occur in the sleeve cause the joint in the split-sleeve to open up. Extra stiffening of the sleeve joint could reduce this weakening effect, which otherwise reduces the level of confinement of the whole connection.

28. When a connection without longitudinal sleeve stiffeners was analysed using the finite element method, it was found to be substantially weaker than the stiffened connection (ignoring plasticity in the sleeve steel which would make it weaker still). This was due to doubling of the axial stresses and hence of the Poisson effects in the sleeve, which resulted in crushing around the sleeve shear keys rather than the pile keys. The stiffened laboratory test results should therefore be reduced to allow for the effects of stiffeners.

10.2 Suggestions for Future Research

1. It may be considered worthwhile making improvements to the Paslay programme as an alternative to the finite element analysis. The fact that normal bond stress variations between shear keys are not accounted for is not normally a problem as at ultimate load σ_n is normally very low or zero anyway.

   The shear key load function needs improving, with a smaller shear key stress per unit slip for standard hemispherical weld bead shear keys. The shear key stress should also be made a function of σ_n, to allow for the effects of grout confinement on ultimate shear key stress.

   Another improvement would be to adjust the sleeve axial stress to

allow for the effects of longitudinal stiffeners on reducing this stress.

Bond dilation is not accounted for and so plain pipe connections could not be considered without making major changes to the programme.

2. Other work could include more improvements to the new bond strength formula. For example, the effects of varying the thickness of the grout annulus (t_g) could possibly be included in the stiffness parameter (γ) in the following way

$$\gamma = \left(\frac{r_s^2}{t_s} + \frac{r_p^2}{t_p} \right) \frac{1}{t_g}$$

This would make the connection stronger as t_g is increased, an effect which was found to occur in the City University tests. The term then becomes non-dimensional and unaffected by scale. However, in the complete bond formula, the $r_p^2\theta$ term will still create a scale effect much as before.

Another feature not accounted for in the bond formula is the effect of confinement of the grout on the shear key crushing load, It would appear that to include this effect, the bond formula would become quadratic as confinement is a function of the radial displacement. Solving the bond formula could therefore become rather more complicated. Since the existing form of the new bond strength formula gives good results, it may be hard to justify creating a quadratic formula for only slight gains in accuracy.

3. Further research work could be directed towards extending the friction-gap element into a three-dimensional finite element analysis. This would enable many loading conditions to be investigated which are impossible with the axisymmetric analysis.

The stresses between sleeve stiffeners could then be studied and the structure transferring load from leg to sleeve to pile could be analysed. Other problems, such as grouted nodes, could also be studied.

APPENDIX A

THIN SHELL ANALYSIS OF THE BOND DILATION EFFECTS

A.1 Deriving the Equations

This analysis is concerned with the radial displacements and normal bond stresses, but does not include the Poisson effects of the axial load, as these effects would vary with position along the axis and complicate the analysis. However, the results are useful for assessing the effects of slip and dilation on the residual displacements after the connection has been unloaded, when the Poisson effects are zero and to assess the significance of the sleeve and pile hoop stiffnesses, k_n and u_m.

For the purpose of the analysis, all radial forces are considered acting on one half of the cylinder, (Figure A.1.). The following definitions can be stated:

$$F = 2r\sigma_n \tag{A.1}$$

$$\sigma_n = u_m k_n \tag{A.2}$$

$$\sigma_\theta = \frac{r}{t}\,\sigma_n \tag{A.3}$$

for unit length (in the axial direction).

Hoop strain, $$\epsilon_\theta = \frac{1}{E}\,\sigma_\theta = \frac{r\sigma_n}{Et} \tag{A.4}$$

but $$\epsilon_\theta = \frac{u}{r} \qquad \text{where u = radial displacement.}$$

Therefore $$u = \frac{r^2\sigma_n}{Et} = \frac{rF}{2Et} \tag{A.5}$$

giving $$F = \frac{2Et}{r}.u \qquad \text{and} \qquad \sigma_n = \frac{Et}{r^2}.u \tag{A.6}$$

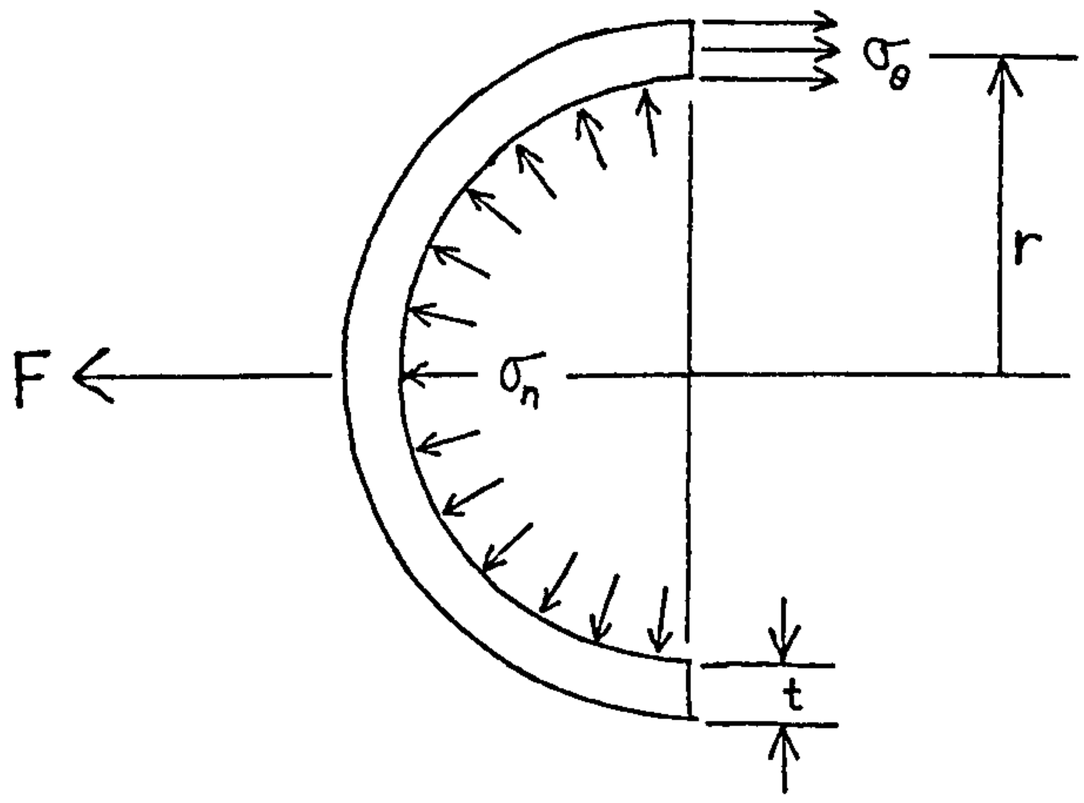

FIGURE A.1 DEFINITIONS.

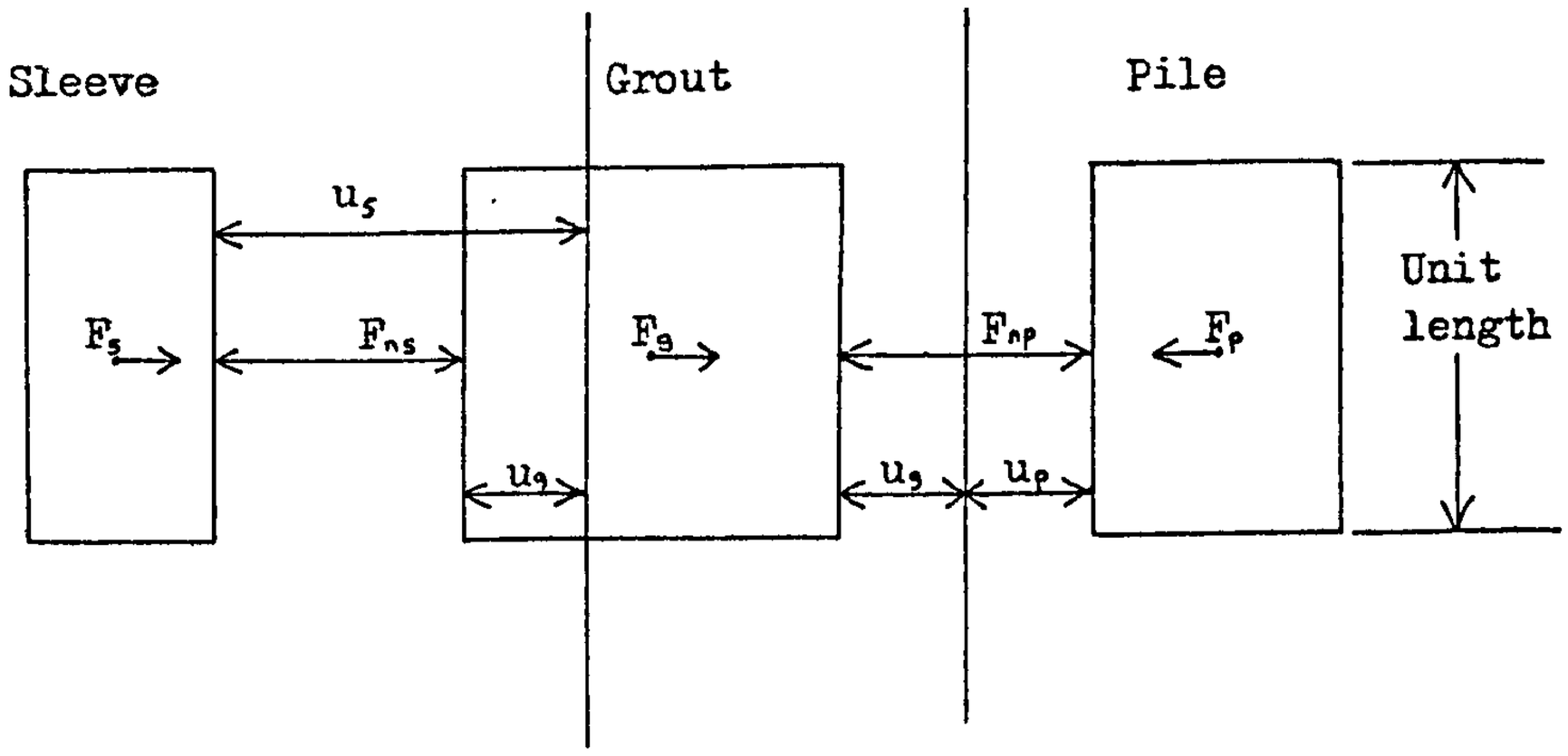

FIGURE A.2 FORCES AND DISPLACEMENTS USED IN THE ANALYSIS.

The hoop stiffness of sleeve or pile is then given by

$$F = K.u \qquad \text{or} \qquad \sigma_n = k.u \tag{A.7}$$

where $$K = \frac{2Et}{r} \ N/mm^2 \qquad \text{and} \qquad k = \frac{Et}{r} \ N/mm^3 \tag{A.8}$$

Figure A.2 defines the forces per unit length and the displacements acting on a complete section of grouted connection. Considering equilibrium, stiffnesses and compatibilities, the following equations can be written; where dilation = u_m, $A_s = 2r_s$, $A_p = 2r_p$,

k_n = normal bond stiffness.

<u>Sleeve</u>

$$F_s = F_{ns} \tag{A.9}$$

$$F_s = K_s u_s \tag{A.10}$$

$$F_{ns} = k_n A_s (u_m + u_g - u_s) \tag{A.11}$$

<u>Pile</u>

$$F_{np} = F_p \tag{A.12}$$

$$F_p = K_p u_p \tag{A.13}$$

$$F_{np} = k_n A_p (u_m - u_g - u_p) \tag{A.14}$$

<u>Grout</u>

$$F_{ns} + F_g = F_{np} \tag{A.15}$$

$$F_g = K_g u_g \tag{A.16}$$

Equations (A.9) and (A.10) give

$$F_{ns} = K_s u_s \tag{A.17}$$

and substituting equation (A.17) into equation (A.11) gives

$$K_s u_s = k_n A_s (u_m + u_g - u_s) \quad .$$

Therefore

$$u_s = \frac{k_n A_s}{K_s + k_n A_s} (u_m + u_g) \tag{A.18}$$

Equations (A.12) and (A.13) give

$$F_{np} = K_p u_p \tag{A.19}$$

and substituting into equation (A.14) gives

$$K_p u_p = k_n A_p (u_m - u_g - u_p)$$

Therefore

$$u_p = \frac{k_n A_p}{K_p + k_n A_p} (u_m - u_g) \tag{A.20}$$

Equations (A.15) and (A.16) give

$$F_{ns} + K_g u_g = F_{np} \tag{A.21}$$

Combining equations (A.17), (A.19) and (A.21)

$$K_s u_s + K_g u_g = K_p u_p \tag{A.22}$$

and substituting from equations (A.18) and (A.20), equation (A.22)

then becomes

$$\frac{K_s k_n A_s}{K_s + k_n A_s} (u_m - u_g) + K_g u_g = \frac{K_p k_n A_p}{K_p + k_n A_p} (u_m - u_g)$$

Let

$$\psi = \frac{k_n A_s}{K_s + k_n A_s} \tag{A.23}$$

$$\omega = \frac{k_n A_p}{K_p + k_n A_p} \tag{A.24}$$

Then

$$K_s \psi (u_m + u_g) + K_g u_g = K_p \omega (u_m - u_g)$$

which gives

$$u_g = \frac{u_m (K_p \omega - K_s \psi)}{K_s \psi + K_g + K_p \omega} \tag{A.25}$$

Equations (A.18) and (A.23) give

$$u_s = \psi (u_m + u_g) \tag{A.26}$$

and equations (A.20) and (A.24) give

$$u_p = \omega (u_m - u_g) \tag{A.27}$$

Equations (A.25), (A.26) and (A.27) enable the radial displacements to be found for any given geometry, u_m and k_n. The normal bond stresses, which are a limiting factor to the ultimate bond strength, are given by

$$\sigma_{ns} = k_n(u_m - u_s + u_g) \qquad (A.28)$$

$$\sigma_{np} = k_n(u_m - u_g - u_p) \qquad (A.29)$$

A.2 Example Calculations

This example is based on the strain-gauged Forties field specimen, which has been discussed in Chapter 5.

Data: $E_p = E_s = 2 \times 10^5$ N/mm^2 $\quad E_g = 1.2 \times 10^4$ N/mm^2

$r_s = 330$ mm $\quad r_p = 305$ mm $\quad t_s = 12.7$ mm

$t_p = 25.4$ mm $\quad k_n = 50$ N/mm^3

Calculating the stiffness factors gives

$$K_s = 1.539 \times 10^4 \text{ N/mm}^2$$

$$K_p = 3.331 \times 10^4 \text{ N/mm}^2$$

$$K_g = 1.920 \times 10^3 \text{ N/mm}^2$$

$$\psi = 0.68197 \quad , \quad \omega = 0.4779$$

Therefore

$$u_g = u_m \times 0.19136$$

$$u_s = (u_m + u_g) \times 0.68197$$

$$u_p = (u_m - u_g) \times 0.4779$$

Various values of dilation can be tried in the above equations and then the bond stresses calculated using equations (A.28) and (A.29). Results are given in Table 5.2.

A.3 Dilation on Pile Bond Only

It was considered that dilation may only occur on one bond surface, as slip and ultimate failure are generally limited to one bond, (but it is in fact more probable that there will be some dilation on the

unfailed bond too). This possibility is analysed by modifying certain equations as follows.

Equation (A.11) becomes $F_{ns} = k_n A_s (u_g - u_s)$ as $u_m = 0$

which in turn affects equations (A.25) and (A.26).

$$u_g = \frac{u_m K_p \omega}{K_s \psi + K_g + K_p \omega} \qquad \text{Equation (A.25)}$$

$$u_s = u_g \psi \qquad \text{" (A.26)}$$

Also, equation (A.28) becomes $\sigma_{ns} = k_n (u_g - u_s)$.

Table 5.2 gives results for this analysis on the example problem.

A.4 Effect of u_m and k_n on σ_n

The effects of u_m and k_n upon σ_n and hence on overall bond strength, have been investigated using the above equations for dilation on both bonds. Figure A.3 plots the findings, which indicate a linear increase in σ_n with u_m, but a falling rate of increase of σ_n with k_n.

There is obviously an upper limit on σ_n governed by the hoop stiffnesses of the sleeve and pile and so there is little point in using $k_n > 50$ N/mm^3.

A.5 Effect of Sleeve and Pile Hoop Stiffness on σ_n

It is also possible to vary K_s or K_p while all other factors are held constant and the results of such an exercise are plotted in Figure A.4. It can be seen that σ_n is more sensitive to the sleeve stiffness than to the pile stiffness. This can be attributed to the fact that K_s is smaller than K_p and so its radial displacement components will be larger and have more influence on σ_n. As K_p (or K_s)

is increased, the rate of increase in σ_n gradually reduces. This is because the stiffness of the other tubular is held constant and so cannot take a greater σ_n without increased radial displacement. Also, there is an upper limit on σ_n ; in this case $\sigma_n \leq u_m k_n = 2.5\ N/mm^2$.

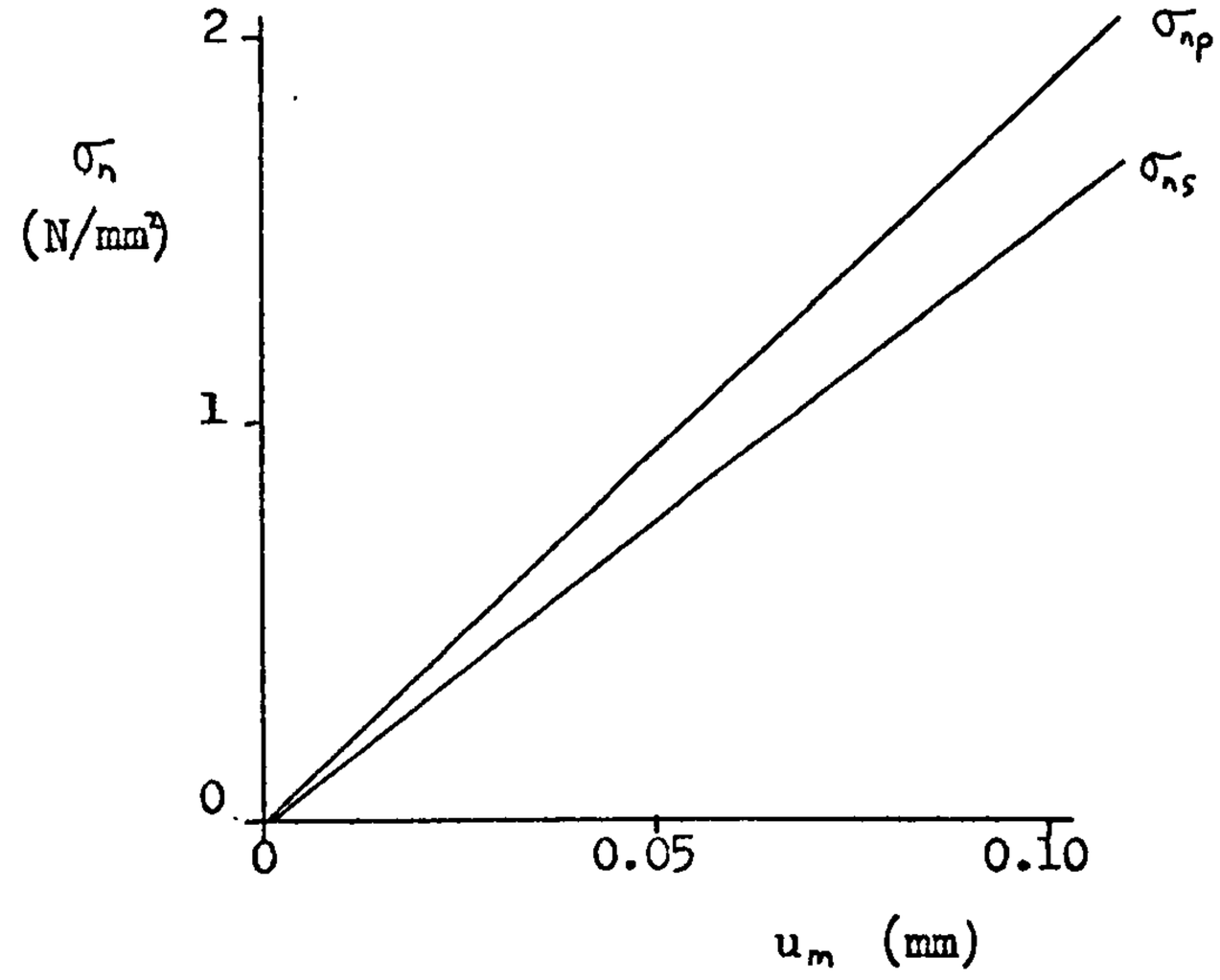

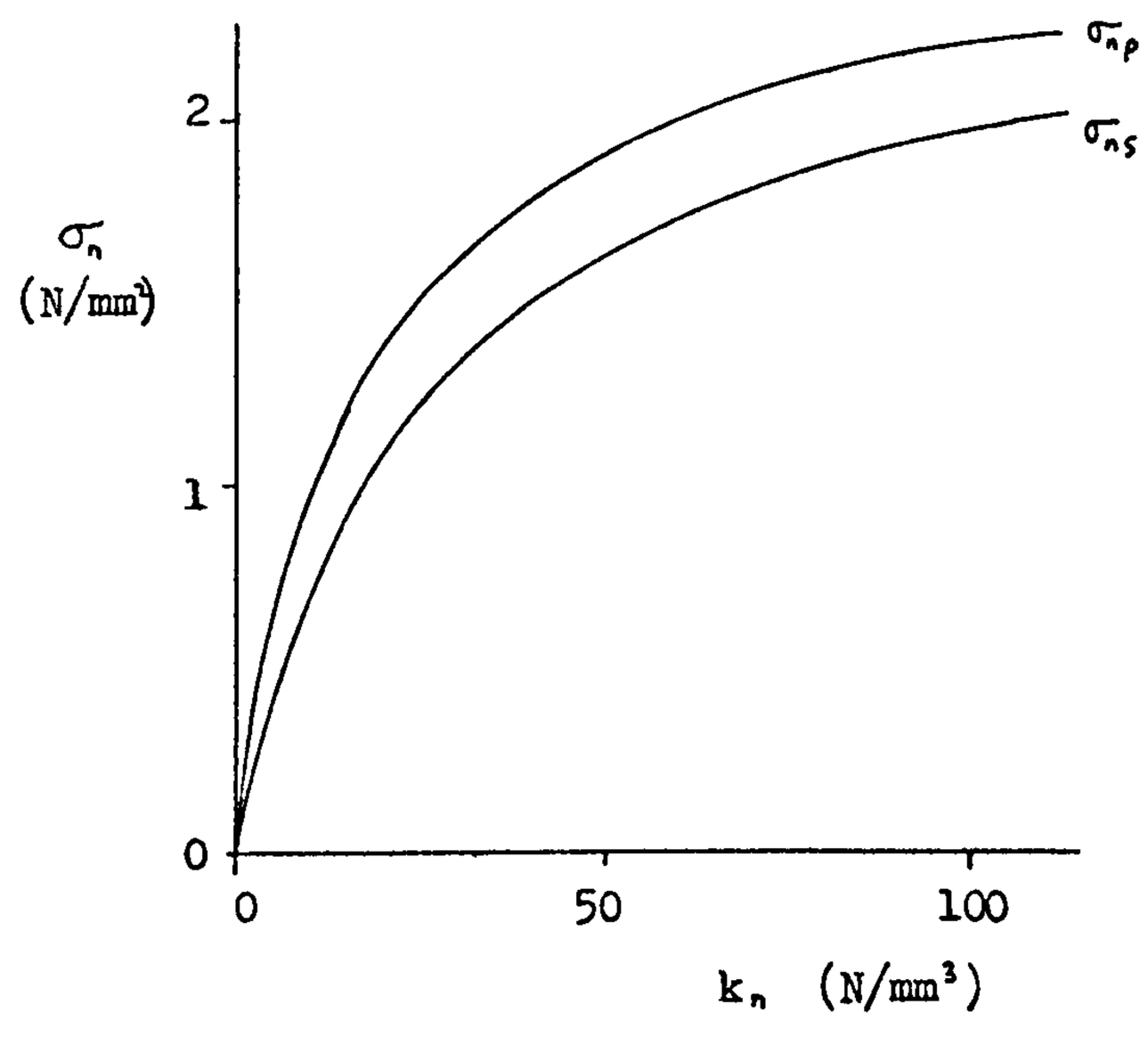

FIGURE A.3 EFFECTS OF u_m AND k_n ON σ_n.

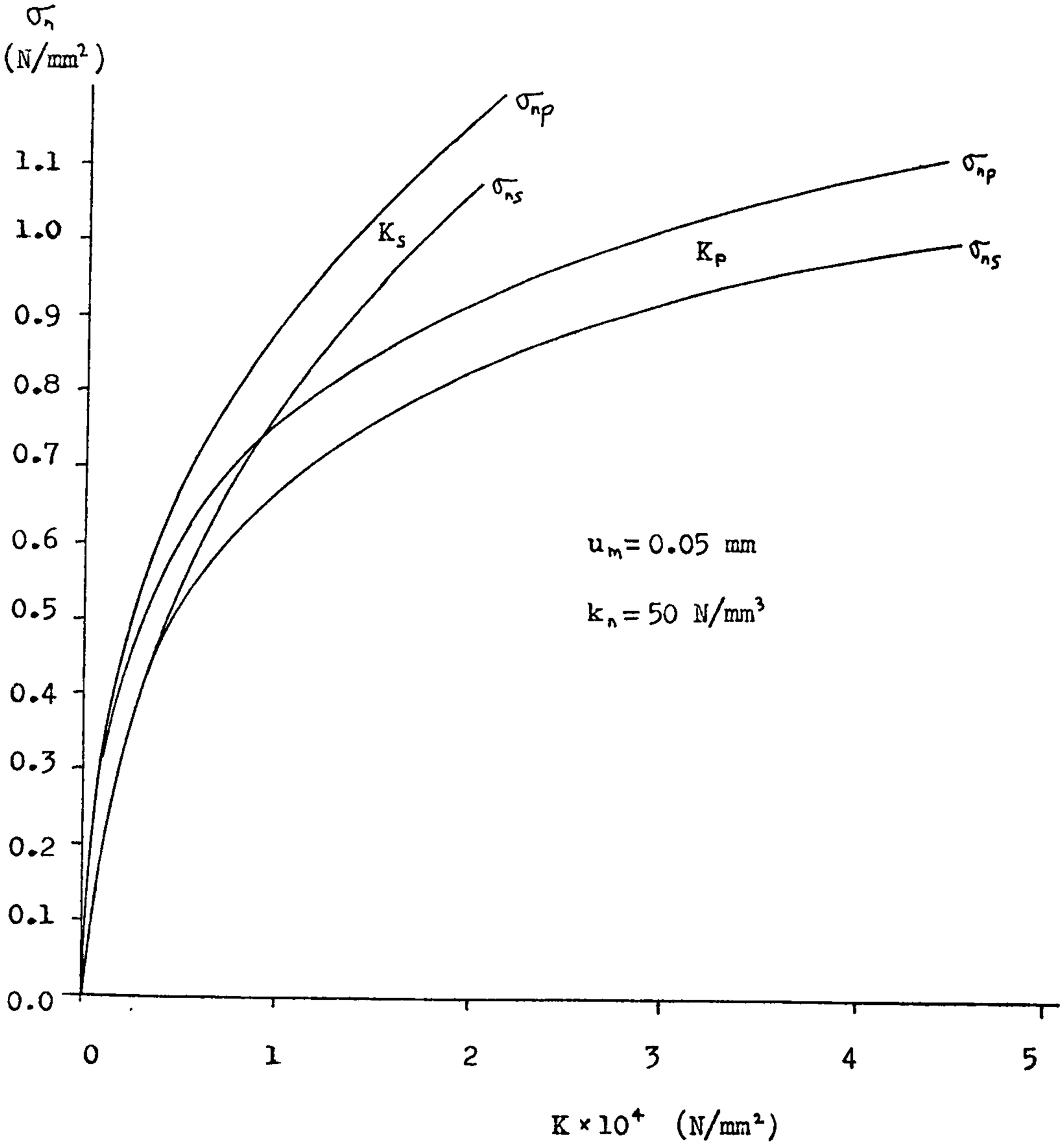

FIGURE A.4 EFFECT OF SLEEVE OR PILE CIRCUMFERENTIAL STIFFNESS ON THE NORMAL BOND STRESS.

APPENDIX B

Table of Results Comparing Experimental Bond Strengths with the Existing and New Bond Strength Formulae.

Existing Formula:-

(Chapter 2)

$$F_{BU} = K_m(76+9468\ h/s)\ C_L$$

New Formula:-

(Chapter 8)

$$F_{BU} = \frac{13.6+\ (362+226\times10^{-4}\gamma)\ h/s}{4 + 10^{-4}\left[2.5\gamma + 2.25\ r_p^2(l/d_p)\theta\right]}$$

TEST	$1/d_p$	h/s	r_p mm	K_m	$\gamma \times 10^4$ mm	θ mm^{-1}	F_{BU}		
							Exptl.- adjusted to 31-day	Formula	
								Existing	New
Forties Field Tests (1)									
A1	0.9	0	50.8	0.0388	0.2259	0.328	3.95	2.36	2.20
A2	0.9	0	110.5	0.02185	0.5816	0.317	2.33	1.33	2.18
A2a	2.3	0	109.2	0.02543	0.4275	0.266	2.88	1.93	2.03
A2b	4.2	0	109.2	0.02838	0.3637	0.218	2.22	1.94	1.84
A4	0.93	0	179.1	0.01851	1.1207	0.236	1.36	1.13	1.06
A5	0.91	0	252.7	0.01443	1.7608	0.219	0.81	0.85	0.74
$A6_{1-3}$	1.10	0	419.1	0.02158	1.3446	0.066	1.03	1.31	0.90
$A6_{4-6}$	1.07	0	419.1	0.02206	1.3004	0.064	1.16	1.34	0.90
A7	0.91	0	683.3	0.00976	5.0877	0.094	0.17	0.59	0.30
A8	1.03	0	123.2	0.02881	0.3289	0.161	1.40	1.75	1.83
A8a	1.99	0	123.2	0.02893	0.3324	0.161	1.08	2.20	2.29
A8b	3.71	0	123.2	0.02881	0.3289	0.161	1.46	1.97	1.98
A8c	7.57	0	123.2	0.02881	0.3289	0.161	1.29	1.75	1.51
A9	0.93	0	304.8	0.01538	1.2262	0.118	0.50	0.94	0.90
A9a	1.89	0	304.8	0.01538	1.2343	0.119	0.58	1.16	1.00
A9b	4.38	0	304.8	0.01538	1.2262	0.118	0.34	1.05	0.76
A10	1.0	0	680.7	0.01832	2.2682	0.044	0.73	1.11	0.58

TEST	$1/d_p$	h/s	r_p mm	K_m	$\gamma \times 10^4$ mm	θ mm^{-1}	F_{BU} Exptl.-adjusted to 31-day	F_{BU} Formula: Existing	F_{BU} Formula: New
* B-series HT. grout	2.0	0	109.5	0.02606	0.4211	0.2475	2.38	1.98	2.13
A11a	0.5	0.0208	685.8	0.00888	5.2048	0.09843	1.05	1.94	1.33
Department of Energy Tests (8,10,51)									
P1,2	2.0	0.012	254.0	0.0146	1.2330	0.1179	2.56	2.77	2.03
P3,4	2.0	0.012	254.0	0.0106	1.8184	0.1419	1.92	2.01	1.81
P5,6	2.0	0.012	254.0	0.0093	2.2098	0.1535	1.46	1.76	1.71
P7,8	2.0	0.012	254.0	0.0131	1.3850	0.1415	2.27	2.48	1.88
P9,10	2.0	0.012	254.0	0.0100	1.9704	0.1655	1.80	1.90	1.70
P11,12	2.0	0.012	254.0	0.0088	2.3618	0.1771	1.48	1.67	1.62
P13,14	2.0	0.012	254.0	0.0120	1.4867	0.1573	2.06	2.28	1.79
P15,16	2.0	0.012	254.0	0.0095	2.0720	0.1812	1.75	1.80	1.63
P17,18	2.0	0.012	254.0	0.0085	2.4635	0.1929	1.63	1.61	1.56
P19,20	2.0	0.012	228.6	0.0121	1.3020	0.1407	2.03	2.29	2.03
Q1,2	1.0	0.012	254.0	0.0105	1.9704	0.1319	2.26	1.99	1.83
Q3,4	1.0	0.024	254.00	0.0105	1.9704	0.1319	3.58	3.18	2.59
Q5,6	1.0	0.032	254.0	0.0105	1.9704	0.1319	4.08	3.98	3.09

* HT. = Halliburton Tuf Grout

TEST	$1/d_p$	h/s	r_p mm	K_m	$\gamma \times 10^4$ mm	θ mm^{-1}	F_{su}		
							Exptl.- adjusted to 31-day	Formula	
								Existing	New
R1,2	2.0	0.006	254.0	0.0105	1.9704	0.1319	1.45	1.39	1.45
R3,4	2.0	0.018	254.0	0.0105	1.9704	0.1319	2.20	2.59	2.21
R5,6	2.0	0.012	254.0	0.0095	1.8304	0.0668	1.90	1.80	2.18
R7,8	2.0	0.012	254.0	0.0125	2.2697	0.0729	2.08	2.37	2.04
R9,10	2.0	0.012	254.0	0.0105	1.9704	0.1319	1.67	1.99	1.83
01,2	1.0	0.012	161.9	0.0120	0.9065	0.3019	1.51	1.82	1.66
03,4	2.0	0.012	161.9	0.0120	0.9065	0.3019	2.05	2.28	2.08
05,6	4.0	0.012	161.9	0.0129	0.9065	0.1783	2.32	2.21	1.95
07,8	8.0	0.012	161.9	0.0129	0.9065	0.1783	2.23	1.96	1.39
09,10	12.0	0.012	161.9	0.0129	0.9065	0.1783	2.05	1.72	1.08
P21,22	2.0	0.012	254.0	0.0201	0.8820	0.0836	2.77	3.81	2.36
P23,24	2.0	0.012	254.0	0.0170	1.0340	0.1072	2.89	3.22	2.14
P25,26	2.0	0.012	254.0	0.0155	1.1357	0.1230	2.46	2.94	2.02
P27,28	2.0	0.012	254.0	0.0253	0.6480	0.0727	2.98	4.80	2.55
P29,30	2.0	0.012	254.0	0.0204	0.8000	0.0963	3.18	3.87	2.29
P31,32	2.0	0.012	254.0	0.0182	0.9017	0.1121	2.79	3.45	2.14
R11,12	2.0	0.024	254.0	0.0108	1.9704	0.1286	2.17	3.27	2.60
R13,14	2.0	0.030	254.0	0.0108	1.9704	0.1286	2.92	3.89	2.99
R15,16	2.0	0.036	254.0	0.0108	1.9704	0.1286	3.45	4.50	3.37

TEST	$1/d_f$	h/s	r_f mm	K_m	$\gamma \times 10^4$ mm	θ mm^{-1}	F_{BU}			
							Exptl.- adjusted to 31-day		Formula	
									Existing	New
M/N series	2.0	0	228.6	0.0114	1.3496	0.21916	1.10		0.87	1.09
Split-Sleeve Tests (10,50)							Ten	Comp		
SA	2.0	0	114.5	0.01427	0.50681	0.25938	0.86	1.27	1.05	1.94
SB	2.0	0	114.5	0.01087	0.70522	0.28341	0.80	1.37	0.81	1.77
SC	4.0	0	114.5	0.01427	0.50681	0.25938	0.74	1.16	0.94	1.60
SD	2.0	0	229.0	0.01427	1.01518	0.12969	0.63	-	1.05	1.36
U Series	3.38	0.02	97.0	0.01671	0.3366	0.3175	2.84		4.48	3.14
T 1-4	2.0	0.0212	114.5	0.01319	0.5068	0.259	1.97		3.82	3.49
T 15-18	2.0	0.0212	114.5	0.01007	0.7052	0.283	2.25		2.93	3.32
T 23-26	4.0	0.0212	114.5	0.01319	0.5068	0.259	2.19		3.44	2.85
T 31-34	2.0	0.0424	114.5	0.01319	0.5068	0.259	3.14		6.59	4.98
T 41-42a	1.0	0.064	114.5	0.01319	0.5068	0.259	4.34		* 7.11	* 4.97
T 43-44	1.0	0.096	114.5	0.01319	0.5068	0.259	4.16		* 7.11	* 4.97
T 45-46	1.0	0.096	114.5	0.01319	0.5068	0.259	4.01		* 7.91	* 4.97
T 47-48	1.0	0.0552	114.5	0.01319	0.5068	0.259	4.00		7.44	4.70
T 49-50	1.0	0.1104	114.5	0.01319	0.5068	0.259	4.20		* 7.11	* 4.97
T51-52a	2.0	0.0212	120.0	0.0088	0.9028	0.3768	1.78		2.44	2.94
T53-54	2.0	0.0212	120.0	0.0108	0.6861	0.3515	1.98		2.99	3.07

* Use h/s = 0.06 (ie Maximum Permitted value).

TEST	$1/d_p$	h/s	r_p mm	K_m	$\gamma \times 10^4$ mm	θ mm^{-1}	F_{sv}		
							Exptl.- adjusted to 31-day	Formula	
								Existing	New
Burmah Oil Tests for Thistle Field (2,3)									
1.1-2	0.67	0.01389	685.8	0.00933	5.8153	0.1050	0.63	1.55	0.72
5.1-2	0.67	0.01389	685.8	0.00933	5.8153	0.105	2.30	1.55	0.72
8.1-2	2.24 2.52	0.01389	269.9	0.01031	1.9517	0.2298	1.29	2.14	1.43 1.35
11.1-2 13.1-2 15.1-2	0.67	0.01389	685.8	0.00933	5.8153	0.1050	0.98	1.55	0.72
12.1-2	0.80	0.01389	685.8	0.01154	4.2915	0.07874	0.76	1.92	0.82
14.1-2	0.67	0.01389	685.8	0.01154	4.2915	0.07874	1.58		
16.1-2	1.0	0.01389	269.9	0.01031	1.9517	0.2298	0.97	1.71	1.21
18.1-2	1.0	0.01389	269.9	0.01031	1.9517	0.2298			
17.1-2	0.83	0.01389	269.9	0.01031	1.9517	0.2298	1.00	1.71	1.21
22-24	3.0	0.01389	685.8	L.02474	1.0381	0.1050	2.00	4.62	1.96
C.B.I. Test, quoted by Paslay (18)									
	2.27	0.075	161.9	0.02981	0.38644	0.1098	5.90	*19.20	*6.30
C.B.I.Test, quoted by Van Lee (20)									
Assume $f_{cu}=50N/mm^2$	2.26	0	109.5	0.02424	0.44845	0.25197	2.50	1.84	2.04
* Use h/s=0.06									

TEST	$1/d_p$	h/s	r_p mm	K_m	$\gamma \times 10^4$ mm	θ mm^{-1}	F_{BU} Exptl.-adjusted to 31-day	F_{BU} Formula Existing	F_{BU} Formula New
Chevron Ninian Field Tests (4)									
A1	1.0	0.016	109.5	0.03885	0.15264	0.11032	5.09	6.95	3.18
A2	2.0	0.016	109.5	0.03885	0.15264	0.11032	6.21	8.69	3.98
A3	4.0	Q.016	109.5	0.03885	0.15264	0.11032	5.41	7.82	3.55
A7	2.0	0.016	109.5	0.04361	0.15264	0.06971	4.69	9.76	4.16
A8	8.0	0.016	109.5	0.04361	0.15264	0.06971	4.42	7.81	3.36
A9	12.0	0.016	109.5	0.04361	0.15264	0.06971	3.84	6.83	2.98
B	2.0	0.016	228.5	0.00836	1.9984	0.20897	1.50	1.90	1.91
F	1.0	0.016	914.5	0.00821	7.7632	0.08132	0.98	1.49	0.70
BP Magnus Field Tests (7)									
A	1.93	0.03636	162.0	0.01107	1.0257	0.200	4.15	4.65	3.94
B+leg	9.0	0.03636	162.0	0.01108	1.0257	0.0510	4.44 c	3.72	3.79
C	0.9	0.03636	162.0	0.01107	1.0257	0.200	4.32	3.72	3.15
D	0.9	0.03636	931.5	0.01005	6.08601	0.060	2.62 c	3.38	1.44
G+leg	1.93	0.03636	162.0	0.01108	1.0257	0.0510	5.64 c	4.65	4.91

c Compression-Compression loading

TEST	$1/d_p$	h/s	r_p mm	K_m	$\gamma \times 10^4$ mm	θ mm^{-1}	F_{BU}		
							Exptl.-adjusted to 31-day	Formula	
								Existing	New
Union Oil, Heather Field Tests (5)									
E	2.0	0	228.6	0.01266	1.3026	0.14728	0.65	0.96	1.27
F	2.0	0.0083	228.6	0.01266	1.3026	0.14728	2.23	1.96	1.82
H	2.0	0.0167	228.6	0.01266	1.3026	0.14728	2.44	2.96	2.38
J	3.5	0	190.5	0.02293	0.47207	0.10169	0.73	1.97	1.68
City University Tests									
A1	2.03	0.012	254.0	0.01106	1.8238	0.12121	1.52 t	2.10	1.90
A2	2.03	0.012	254.0	0.01028	1.9687	0.14371	1.50 t	1.95	1.79
A3	2.03	0.012	254.0	0.00976	2.0815	0.16121	1.41 t	1.85	1.72
B1	2.03	0	254.0	0.01106	1.8238	0.12121	0.37 t	0.84	1.12
B2	2.03	0	254.0	0.01028	1.9687	0.14371	0.20 t	0.78	1.03
B3	2.03	0	254.0	0.00976	2.0815	0.16121	0.33 t	0.74	0.97
C	2.03	0.012	254.0	0.01451	2.3737	0.14574	>2.47	2.75	1.71
D	2.03	0.042	254.0	0.01028	1.9687	0.14371		4.87	3.63
E	2.03	0.012	254.0	0.02696	0.6080	0.07018		5.11	2.59
F	2.03	0.012	254.0	0.01577	1.0376	0.13685	2.12	2.99	1.96

t Tension-Tension loading

APPENDIX C

THE FRICTION-GAP ELEMENT SUBROUTINE

This subroutine is designed for use with the program NONSAP.

C.1 Key to Variables

(a) Integers

ID (I,J) : I = 1 for Y-dirn., = 2 for Z-dirn. ID gives the equation number for node J.

ICOUNT : = 1 initially, = 2 start of load step, = 3 during iterations.

IFAIL (I) : Gives the no. of bond pairs in bond state I (I = 1 to 6 for six physical bond states - see IFGAP).

IFGAP : = 1, bond closed, = 2, closed, slipping, = 3, opening, = 4, opening and slipping, = 5, bond open, = 6, shear key crushing.

IND : = 0 at input stage, = 1 at assembly stage, = 4 during solution stages.

IREF : = 0 when stiffness matrix is to be recalculated, else = 1.

IS=IPS=IPST : Print flag. Also, if IS$\geq$10, then the element has a shear key.

ISC : = 0 for no shear key, = 1 with a shear key.

KG = KKK : node increment for element data generation.

KPRI : = 0 for output printing, = 1 for no output.

LM(12,I) : Gives the eqn, nos. for the twelve displacements of element no. I.

LMM (4) : Local LM vector for just one node-pair.

M = N : Element number

MATP (N) : Material property set no. for element N.

MTYPE=MTYP : Material property set no. for element M.

N=M : Element number

NB : No. of node pairs (=2 or 3)

NCON : = 0 for no shear keys, or = 2 x (no. of key stress-slip points in the data) with shear keys.

NOF(I)=NOFM(I) : For I=1 to 6, gives the global node nos. for the six local element nodes.

NS : = 1 to 3, indicates which node-pair is being considered.

NUME : Number of elements in the element group.

NUMMAT : Number of sets of material properties in the element group.

(b) Floating -Point Numbers

AREA : Gives a fraction of the bond surface area per radian, (the fraction = $\frac{1}{2}$ for NB = 2, or $\frac{1}{30}$ for NB = 3).

BL (I) : = n for property set I.

CN : = $\cos\Theta$

CONF : = Confinement factor, = $u_a / \Delta n$

ESN : = $2e^{\Delta t/n}$, part of surface dilation function.

E(I) = EC : = k_n, normal bond stiffness

FAC1 (I) : = k_t reduction factor, when slipping

FAC2 (I) : = k_n, k_t reduction factor when bond opens

FAC3 (I) : = β ratio for shear key force

G(I) = GT : = k_t , shear bond stiffness

H(I) : = Shear key height, h

} for property set No. I

HT : Gives the stiffness matrix bandwidth vector in the initial phase, and later represents the nodal load vector.

HEFF : The effective shear key height, = h-Δn

PP(I) : Global force in the Y-dirn. resulting from the bond stresses for node-pair I.

PROP : Shear key stress-slip data.

S(10) : Vector of element stiffness coefficients (upper triangle only)

SCK(I) : = c

SMU(I) : = μ

} for property set I

SKE : = $k_{sc} \times h_{eff}$, shear key stiffness

SIG : = σ_n, normal bond stress

SIGU : = σ_{no}, normal bond stress due to u_a

SLIP : = Total slip from the pile/grout and grout/sleeve bonds.

SN : = $\sin\Theta$

TAU : = τ, shear bond stress

TAUB : = V, the shear key load/unit circumference

TAUO : = $c + \mu\sigma_n$, the limiting frictional shear stress.

U(I) : = u_m for property set no.I

UA : = u_a

VV(I) : Global force in the Z-dirn. resulting from the bond stresses for node-pair I.

XL : Bond opening, Δn.

XYZ (6,NUME) : The initial element coordinates

Y(I) : } Global coordinates of node I, updated at

Z(I) : } each load-step end.

ZA : Absolute bond slip, $|\Delta t|$

ZL : Bond slip, Δt

ZLONG : Element length

C.2 Subroutines

COLHT (HT,ND,LMM) :-

Updates the global stiffness matrix bandwidth.

ADDBAN (A(N4), A(N1),S,LMM,ND) :-

Adds the element stiffness coefficients, S, into the global stiffness matrix, part of A.

C.3 Input Data Instructions

Card 1 (20I4)

Element Control Data

Cols.	Variable	Entry	Comment
1 - 4	NPAR (1)	= 1 = NPAR1	Identifies with one-dimensional elements
5 - 8	NPAR (2)	= NUME	Number of elements in the group (GE.1)
9 -12	NPAR (3)	= 2=INDNL	
21 -24	NPAR (6)	= 1	(Equals 1 for friction-gap element or 2 for Truss element).
25 -28	NPAR (7)	= NB	Equals 2 for 2 node-pairs or 3 for 3 node-pairs. (Default = 3).
56 -60	NPAR(15)	= 1	
61 -64	NPAR(16)	= NUMMAT	Number of sets of material properties, (GE.1).
65 -68	NPAR(17)	= NCON	Equals zero for no shear keys, or 2 x (no. of shear key stress-slip data points) with shear keys. (Default = 0).

Bond Property Cards

Read NPAR (16) sets of cards 2a,2b and 3.

Card 2a. (I5)

Cols.	Variable	Entry	Comment
1 - 5	N	Property No.	GE.1 and LE.NPAR (16)

Card 2b. (8F10.0)

1 -10	E(N)	k_n (N/mm^3)	Bond stiffnesses
11 -20	G(N)	k_t (N/mm^3)	
21 -30	SMU(N)	μ	Coefficient of Friction
31 -40	SCK(N)	c (N/mm^2)	Bond adhesion
41 -50	U(N)	u_m (mm)	= ½(Steel surface roughness) ie. max. dilation.
51 -60	BL(N)	n	=1 for $u_\alpha \simeq u_m$ @ 5mm slip =2 " " " "10mm " etc.
61 -70	FAC1(N)	On slipping, $k_t \rightarrow k_t$/FAC1	
71 -80	FAC2(N)	For Open bond, $k_n \rightarrow k_n$/FAC2 $k_t \rightarrow k_t$/FAC2	

Shear Key Data

Card 3 (8F10.0)

Only provide card 3 if NPAR (17)>0. (NCON = NPAR (17))

Cols.	Variable	Entry		Comment
1 -10	PROP (1,N)	$\frac{V(1)}{CONF.R.h}$	= 0.0	Stress on Shear Key in N/mm^2 (Zero for pt.(1))
11-20	PROP (2,N)	$\frac{V(2)}{CONF.R.h}$		
:	:	:		
↓	↓	↓		
:	PROP ($\frac{NCON}{2}$ -1,N)	$\frac{V_{cr}}{CONF.R.h}$		Stress to just cause crushing
:	PROP ($\frac{NCON}{2}$,N)	"		" "
:	PROP ($\frac{NCON}{2}$+1,N)	$\frac{ZL(1)}{CONF.}$	= 0.0	Slip in mm for pt.(1)
↓	↓	↓		
:	PROP (NCON-1,N)	$\frac{ZL(NCON-1)}{CONF.2}$		Slip to start crushing
:	PROP (NCON,N)	$\frac{ZL(\frac{NCON}{2})}{CONF.\ 2}$		
:	H (N)	h		Height of Shear Key in mm.
:	FAC3(N)	β		Fraction of axial shear key force in radial direction.

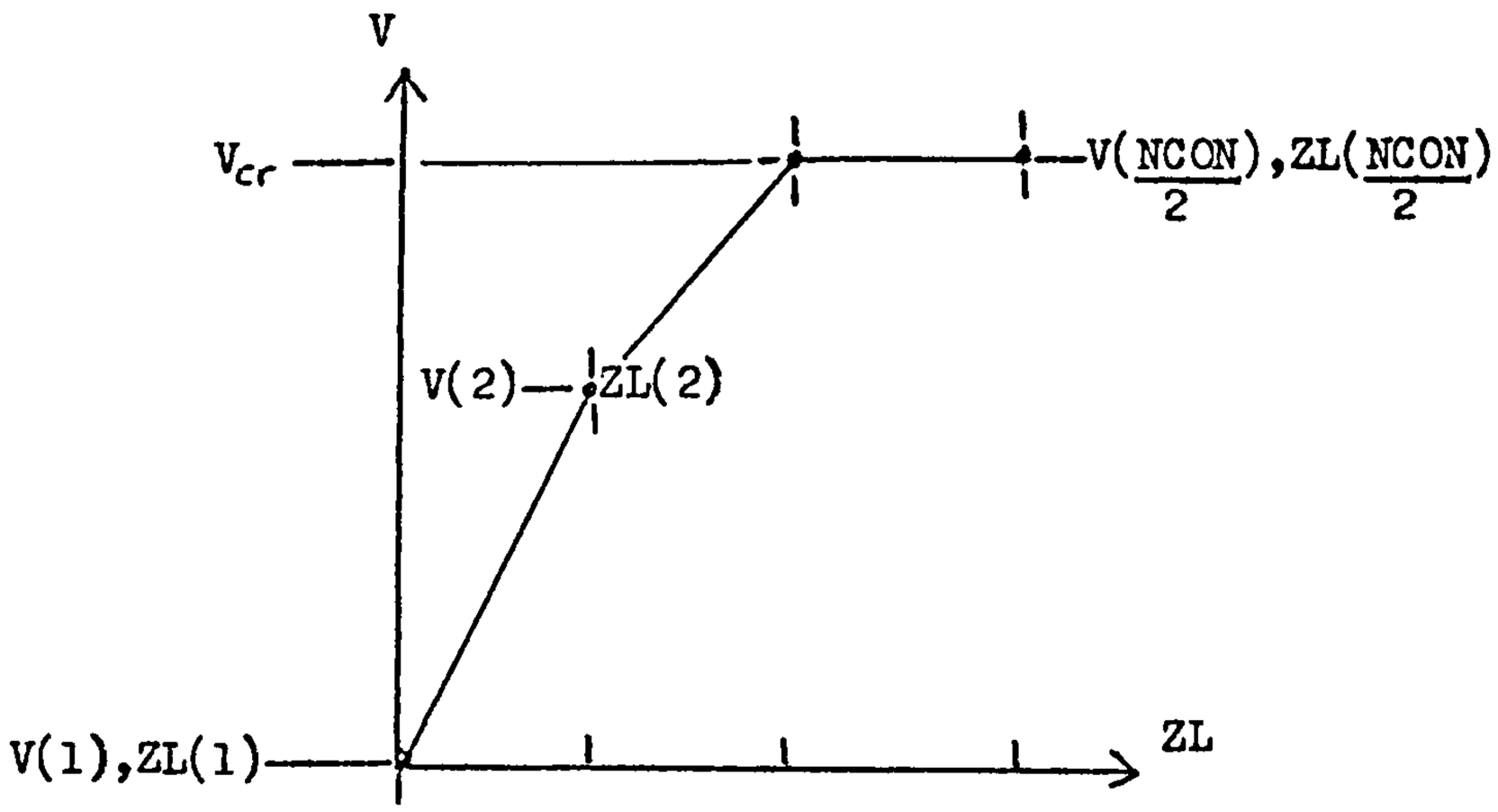

Element Data Cards

Card 4 (10I5)

NPAR (2) elements must be input and/or generated in this section in ascending sequence beginning with "1".

Cols.	Variable	Entry	Comment
1- 5	M	(Element number)	GE.1 and LE.NPAR(2)
6-10	MTYP =MTYPE	(Material property set no.)	GE.1 and LE.NPAR(16)
11-15	IPS	= 0 , No printing of bond stresses = 1 , Print stresses at pts. 1 and 2 = 2 , " " " " 1, 2 and 3 = 3 , As = 1, plus print total slip, (for M.LE.$\frac{NUME}{2}$). = 4 , As = 2, plus print total slip, (for M.LE.$\frac{NUME}{2}$). For Shear Connectors, add 10 to the IPS value chosen above (ie.IPS=10 to 14)	
16-20	KG	Node generation increment used to compute node nos. for missing elements. EQ.0, default sets to "1".	
21-25	NOF(1)	Local element node nos. Must be correctly orientated within the global axes.	
26-30	NOF(2)		
31-35	NOF(3)		
36-40	NOF(4)		
41-45	NOF(5) *		
46-50	NOF(6) *		

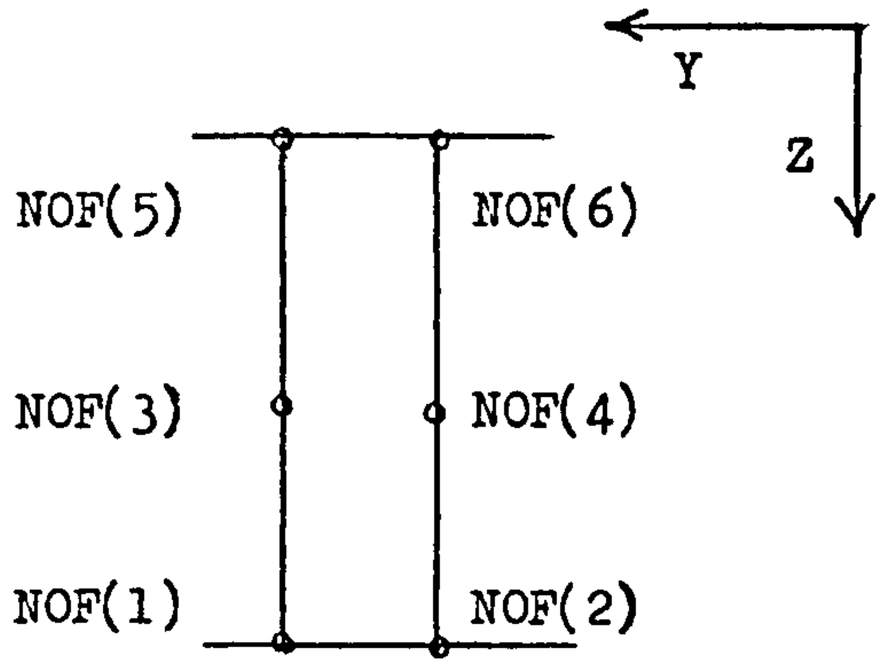

* NOF(5)=NOF(6)=0 when only two node-pairs are used.

```
C
      SUBROUTINE FGAP(ID,X,Y,Z,HT,E,G,SMU,U,BL,LM,XYZ,MATP,IPS,SCK,
     1     FAC1,FAC2,FAC3,H,PROP,NCON)
C
      COMMON /EL/ IND,ICOUNT,NPAR(20),NUMEG,NEGL,NEGNL,IMASS,IDAMP,ISTAT
     1     ,NDOF,KLIN,IEIG,IMASSN,IDAMPN
      COMMON /DIM/ N1,N2,N3,N4,N5,N6,N7,N8,N9,N10,N11,N12,N13,N14,N15
      COMMON /VAR/ NG,KPRI,MODEX,KSTEP,ITF,ITEMAX,IREF,IEQREF,INOCMD
      COMMON /EM/ S(21),NOF(6),NOFM(6),LMM(4),IFAIL(6),PP(3),VV(3),
     1  AEM(451)
      COMMON A(1)
      DIMENSION X(1),Y(1),Z(1),ID(2,1),E(1),G(1),U(1),SMU(1),
     1    BL(1),LM(12,1),XYZ(6,1),MATP(1),HT(1),IPS(1),SCK(1)
     2     ,H(1),PROP(NCON,1),FAC1(1),FAC2(1),FAC3(1)
      EQUIVALENCE (NPAR(1),NPAR1),(NPAR(2),NUME),(NPAR(16),NUMMAT),
     1           (NPAR(3),INDNL),(NPAR(7),NB)
C
      ND=4
      NC=2*NB
      IF(KPRI.EQ.0)GOTO 800
      IF(IND.GT.0)GOTO 700
C
C     READ AND GENERATE ELEMENT INFORMATION
      IF(INDNL.EQ.0)INDNL=1
      WRITE(6,2030)NUME
      IF(NUMMAT.EQ.0)NUMMAT=1
      WRITE(6,2000)NUMMAT
      DO 10 I=1,NUMMAT
      READ(5,1000)N
      WRITE(6,2006)N
      READ(5,1001)L(N),G(N),SMU(N),SCK(N),U(N),BL(N),FAC1(N),FAC2(N)
      WRITE(6,2002)  E(N),G(N),SMU(N),SCK(N),U(N),BL(N),FAC1(N),FAC2(N)
      IF(NCON.EQ.0) GOTO 10
      IP=NCON/2
```

```
      READ(5,1001)(PROP(J,N),J=1,NCON),H(N),FAC3(N)
      WRITE(6,2001)
      DO 5 J=1,IP
    5 WRITE(6,2007)J,PROP(J,N),PROP(J+IP,N)
      WRITE(6,2008) H(N),FAC3(N)
   10 CONTINUE
C
C     ELEMENT INFORMATION
      ANODE=4HNODE
      IF(NB.NE.2) NB=3
      NC=2*NB
      WRITE(6,2005)(ANODE,I,I=1,6)
      N=1
  100 READ(5,1004)M,MTYP,IS,KG,(NOF(I),I=1,6)
      IF(KG.EQ.0)KG=1
  120 IF(M.NE.N)GOTO 200
      MTYPE=MTYP
      KKK=KG
      IPST=IS
      DO 130 I=1,6
  130 NOFM(I)=NOF(I)
C
C     SAVE ELEMENT INFORMATION
  200 DO 210 I=1,NB
      J=2*I-1
      K=2*I
      XYZ(J,N)=Y(NOFM(J))
  210 XYZ(K,N)=Z(NOFM(J))
      MATP(N)=MTYPE
      IPS(N)=IPST
      DO 250 K=1,NC
      KK=2*K
      KL=KK-1
```

```
                  LM(KK,N)=ID(2,NOFM(K))
              250 LM(KL,N)=ID(1,NOFM(K))
                C
                C     UPDATE COLUMN HEIGHTS AND BANDWIDTH
                      DO 255 I=1,NB
                      K=I-1
                      DO 254 J=1,4
              254 LMM(J)=LM(J+K*4,N)
                      CALL COLHT(HT,ND,LMM)
              255 CONTINUE
                      WRITE(6,2004)N,MTYPE,IPST,KKK,(NOFM(I),I=1,6)
                      IF(N.EQ.NUME)RETURN
                      N=N+1
                      DO 270 I=1,6
                      IF(NOFM(I).EQ.0) GOTO 270
                      NOFM(I)=NOFM(I)+KKK
              270 CONTINUE
                      IF(N.GT.M)GOTO 100
                      GOTO 120
                C
                C     ASSEMBLE NONLINEAR FINAL STRUCTURE STIFFNESS
                C     AND EFFECTIVE LOADS
              700 ISTR=0
                      DO 717 I=1,6
              717 IFAIL(I)=0
                      N=0
              702 N=N+1
                      NS=0
                C
              701 MTYPE=MATP(N)
                      DY=XYZ(NC-1,N)-XYZ(1,N)
                      DZ=XYZ(NC,N)-XYZ(2,N)
              635 ZLONG=SQRT(DY*DY+DZ*DZ)
                      CS=DZ/ZLONG
                      SN=DY/ZLONG
```

```
C
C     FIND RELATIVE DISPLACEMENTS
  703 NS=NS+1
      EC=E(MTYPE)
      GT=G(MTYPE)
C     ISC=1 FOR SHEAR CONNECTORS
      ISC=0
      IF(IPS(N).GE.10.AND.NS.EQ.1) ISC=1
      IF(ICOUNT.GE.2) GO10 704
      SIG=0.
      TAU=0.
      SIGU=-U(MTYPE)*EC/2.
      IFCAP=1
      ZA=0.0
      ZL=0.0
      XL=0.0
      GOTO 723
  704 I=LM(4*NS-1,N)
      XL=0.
      IF(I)705,705,706
  706 XL=XL-X(I)
  705 J=LM(4*NS-3,N)
      IF(J)720,720,719
  719 XL=XL+X(J)
  720 I=LM(4*NS,N)
      ZL=0.
      IF(I)707,707,708
  708 ZL=-X(I)
  707 J=LM(4*NS-2,N)
      IF(J) 790,790,711
  711 ZL=ZL+X(J)
      ZLA=ZL
      XLA=XL
      ZL=-ZLA*CS-XLA*SN
      XL=ZLA*SN-XLA*CS
```

```
C
C     DETERMINE SURFACE ROUGHNESS
C
  790 ZA=ABS(ZL)
      ESN=ZA/BL(MTYPE)
      ESN=2.*EXP(ESN)
      UA=U(MTYPE)*(1.-1./ESN)
C
C     CALCULATE BOND STRESSES
C
      SIGU=-UA*EC
      IF(XL.GT.UA) GOTO 725
C
C     GAP CLOSED OR OPENING
      IFGAP=1
      SIG=XL*EC
      TAU=ZL*GT
      IF(XL.GT.0.0) IFGAP=3
C     CHECK IF SHEAR STRESS HAS REACHED FRICTIONAL LIMIT
C
      TAUO=-SMU(MTYPE)*(SIG+SIGU)+SCK(MTYPE)
      IF(ABS(TAU).LE.TAUO) GOTO 723
C
C     STATE OF SLIP
      IF(TAU.GE.TAUO)TAU=TAUO
      IF(TAU.LE.(-TAUO))TAU=-TAUO
      IFGAP=IFGAP+1
      GT=GT/FAC1(MTYPE)
      GOTO 723
C     OPEN GAP
  725 SIG=-SIGU
      TAU=0.
```

```
                EC=EC/FAC2(MTYPE)
                GT=GT/FAC2(MTYPE)
                IFGAP=5
175           723 IF(ISC.EQ.0) GOTO 400
              C
              C     FIND SHEAR KEY FORCE AND STIFFNESS
              C
                HEFF=H(MTYPE)-XL
180             IF(HEFF.LT.0.0) HEFF=0.0
                IF(HEFF.GT.H(MTYPE)) HEFF=H(MTYPE)
                IF(ICOUNT.GE.2) GOTO 15
                CONF=1.5
                GOTO 20
185           15 CONF=UA/XL
                IF(CONF.GT.1.5) CONF=1.5
              20 ZC=ZA/CONF
                IP=NCON/2
                DO 25 I=2,IP
190             L=I
                IF(ZC.LE.PROP(I+IP,MTYPE)) GOTO 30
              25 CONTINUE
              30 DS=PROP(L,MTYPE)-PROP(L-1,MTYPE)
                DE=PROP(L+IP,MTYPE)-PROP(L+IP-1,MTYPE)
195             SKE=DS*HEFF/DE
                TAUB=PROP(L-1,MTYPE)*HEFF+(ZC-PROP(L+IP-1,MTYPE))*SKE
              40 TAUB=TAUB*CONF
                IF(ZL.LT.0.0) TAUB=-TAUB
                IF(L.EQ.IP) IFGAP=6
200           C
              C     CALCULATE FORCES
            400 IF(ISTR.EQ.1) GOTO 804
                IFAIL(IFGAP)=IFAIL(IFGAP)+1
                IF(NB.EQ.3) GOTO 744
205             AREA=(XYZ(1,N)+XYZ(3,N))*ZLONG/4.
```

```
                VA=TAU*AREA
                PA=(SIG+SIGU)*AREA
                PP(1)=-PA*CS-VA*SN
                PP(2)=PP(1)
210             VV(1)=PA*SN-VA*CS
                VV(2)=VV(1)
                GOTO 770
            744 AREA=XYZ(3,N)*ZLONG/30.
                VA=TAU*AREA
215             PA=(SIG+SIGU)*AREA
                V=PA*SN-VA*CS
                P=-PA*CS-VA*SN
                IF(ISC.EQ.0) GOTO 766
                I=LM(1,N)
220             HT(I)=HT(I)+TAUB*XYZ(1,N)*SN
                HT(I+1)=HT(I+1)+TAUB*XYZ(1,N)*CS
                HT(I+2)=HT(I+2)-TAUB*XYZ(1,N)*SN
                HT(I+3)=HT(I+3)-TAUB*XYZ(1,N)*CS
                TAUB=ABS(TAUB)*H(MTYPE)/HEFF
225             HT(I)=HT(I)-TAUB*XYZ(1,N)*FAC3(MTYPE)*CS
                HT(I+1)=HT(I+1)+TAUB*XYZ(1,N)*FAC3(MTYPE)*SN
                HT(I+2)=HT(I+2)+TAUB*XYZ(1,N)*FAC3(MTYPE)*CS
                HT(I+3)=HT(I+3)-TAUB*XYZ(1,N)*FAC3(MTYPE)*SN
              C
230           C     UPDATE LOAD VECTOR
            766 IF(NS-2) 767,768,769
            767 PP(1)=4.*P
                VV(1)=4.*V
                PP(2)=2.*P
235             VV(2)=2.*V
                PP(3)=-P
                VV(3)=-V
                GOTO 770
```

```
      768 PP(1)=2.*P
240       VV(1)=2.*V
          PP(2)=16.*P
          VV(2)=16.*V
          PP(3)=2.*P
          VV(3)=2.*V
245       GOTO 770
      769 PP(1)=-P
          VV(1)=-V
          PP(2)=2.*P
          VV(2)=2.*V
250       PP(3)=4.*P
          VV(3)=4.*V
      770 DO 773 L=1,NB
          J=(L-1)*4
          DO 773 K=1,4
255       GOTO(774,775,776,777) K
      774 RLOAD=-PP(L)
          GOTO 771
      775 RLOAD=-VV(L)
          GOTO 771
260   776 RLOAD=PP(L)
          GOTO 771
      777 RLOAD=VV(L)
      771 I=LM(J+K,N)
          IF(I)773,773,772
265   772 HT(I)=HT(I)+RLOAD
      773 CONTINUE
          IF(ICOUNT-2)745,745,710
C
C     ADD ELEMENT STIFFNESS
270   745 IF(IREF)710,750,710
      750 DO 751 I=1,9
      751 S(I)=0.
```

```
      IF(NB.EQ.2) GOTO 752
      AREA=AREA*5.
      IF(NS.EQ.2) AREA=AREA*4.
  752 SA=AREA*EC
      SB=AREA*GT
      IF(ISC.EQ.1) SB=SB+SKE*XYZ(1,N)
      S(1)=SA*CS*CS+SB*SN*SN
      S(3)=-S(1)
      S(5)=SB*CS*CS+SA*SN*SN
      S(7)=-S(5)
      S(8)=S(1)
      S(10)=S(5)
      K=NS-1
      DO 754 I=1,4
  754 LMM(I)=LM(I+K*4,N)
      CALL ADDBAN (A(N4),A(N1),S,LMM,ND)
  710 IF(NS.LT.NB) GOTO 703
      IF(N.LT.NUME) GOTO 702
      WRITE(6,2015) (IFAIL(I),I=1,6)
      RETURN
C
C     STRESS CALCULATIONS
  800 DO 810 N=1,NUME
      IPST=IPS(N)
      IF(IPST.GE.10) IPST=IPST-10
      IF(IPST.EQ.0)GOTO 810
      IF(N.NE.1) GOTO 803
      WRITE(6,2010)NG
  803 ISTR=1
      IF(IPST.LT.3) GOTO 801
      IPST=IPST-2
      SLIP=X(LM(6,N))
      NA=NUME/2+N
```

```
                SLIP=SLIP-X(LM(8,NA))
                WRITE(6,2012) N,SLIP
                GOTO 802
            801 WRITE(6,2011) N
310         802 IPA=IPST+1
                IF(NB.EQ.2) IPA=2
                DO 809 NSS=1,IPA
                NS=NSS-1
                IF(NS.EQ.0) GOTO 701
315             GOTO 703
            804 SIG=SIG+SIGU
                IF(ISC.EQ.1) TAU=TAUB
                GOTO(805,806,807,808,812,811) IFGAP
            805 WRITE(6,2020)ISC,NS,SIG,TAU,UA,ZL
320             GOTO 809
            806 WRITE(6,2021)ISC,NS,SIG,TAU,UA,ZL
                GOTO 809
            807 WRITE(6,2022)ISC,NS,SIG,TAU,UA,ZL
                GOTO 809
325         808 WRITE(6,2023)ISC,NS,SIG,TAU,UA,ZL
                GOTO 809
            812 WRITE(6,2025)ISC,NS,SIG,TAU,UA,ZL
                GOTO 809
            811 WRITE(6,2024)ISC,NS,SIG,TAU,UA,ZL
330         809 CONTINUE
                ISTR=0
            810 CONTINUE
                RETURN
C
```

```
      2030 FORMAT(36H E L E M E N T   D E F I N I T I O N ///,
     1       22H FRICTION-GAP ELEMENTS //,
     2       20H NUMBER OF ELEMENTS.,10(2H .),16H( NPAR(2) ). . =,
     3      I5//)
      2000 FORMAT(42H M A T E R I A L   D E F I N I T I O N    ///,
     1       37H NUMBER OF DIFFERENT SETS OF MATERIAL/,
     2       14H     CONSTANTS,13(2H .),16H( NPAR(16)). . =,I5//)
      2001 FORMAT(/5X,19HSHEAR KEY LOAD DATA,//
     1    10H     POINT,15H     KEY-STRESS,15H           SLIP)
      2002 FORMAT(/5X,8F13.5)
      2004 FORMAT(4I7,5X,6I9)
      2005 FORMAT(///40H E L E M E N T   I N F O R M A T I O N ///,
     1  6X,1HN,4X,4HTYPE,4X,3HIPS,5X,2HKG,
     2   10X,6(A4,I1,3X))
      2006 FORMAT(///28H MATERIAL CONSTANTS SET NO. ,I5//
     1      10X,2HKN,10X,2HKS,14X,2HMU,9X,3HSCK,
     2      11X,1HU,11X,2HBL,10X,4HFAC1,10X,4HFAC2)
      2007 FORMAT(I10,2E15.4)
      2008 FORMAT(/5X,18HSHEAR KEY UPSTAND=,F10.5,10H     FAC3=,F10.5)
      1000 FORMAT(I5)
      1001 FORMAT(8F10.0)
      1004 FORMAT(10I5)
      2010 FORMAT(///,75H S T R E S S   C A L C U L A T I O N S   F O R   E
     1L E M E N T   G R O U P ,I5,17H ( FRICTION-GAP )//,2X,
     2 19HELEMENT SC LOCATION,6X,8HN-STRESS,6X,8HS-STRESS,14X,
     3 10HBOND STATE,14X,2HUA,15X,4HSLIP,10X,10HTOTAL SLIP/)
      2011 FORMAT(4X,I5)
      2012 FORMAT(4X,I5,106X,E13.6)
      2020 FORMAT(7X,2I5,6X,E13.6,4X,E13.6,6X,10HGAP CLOSED,14X,
     1 E13.6,3X,E13.6)
      2021 FORMAT(7X,2I5,6X,E13.6,4X,E13.6,6X,19HCLOSED,MAX FRICTION,5X,
     1 E13.6,3X,E13.6)
```

```
      2022 FORMAT(7X,2I5,6X,E13.6,4X,E13.6,6X,11HGAP OPENING,13X,
     1 E13.6,3X,E13.6)
      2023 FORMAT(7X,2I5,6X,E13.6,4X,E13.6,6X,20HOPENING,MAX FRICTION,4X,
     1 E13.6,3X,E13.6)
      2024 FORMAT(7X,2I5,6X,E13.6,4X,E13.6,6X,18HSHEAR-KEY-CRUSHING,6X,
     1 E13.6,3X,E13.6)
      2025 FORMAT(7X,2I5,6X,E13.6,4X,E13.6,6X,14HFULLY OPEN GAP,10X,
     1 E13.6,3X,E13.6)
      2015 FORMAT(3X,6H1FAIL=,6I8)
           END
```

-349-

APPENDIX D

SUBROUTINES FOR THE CONSTITUTIVE BEHAVIOUR OF THE GROUT MATERIAL

These subroutines are designed for use with the program NONSAP.

D.1 Key to Variables

(a) Integers

Important integers not listed are given in Section C.1.

IDW : = 12, gives the dimension of the storage array required for data stored from the previous load step.

IHOOP : = 0 for no circumferential crack, else = 1.

IM= M : Subincrement counter for the cracked or plastic states.

IPEL : = 1 for elastic, = 2 for plastic, = 3 for cracked, = 4 for crushed state.

ITYP2D : = 0 for axisymmetric, = 1 for plane strain, = 2 for plane stress.

M = IM : Subincrement counter

NEL : Element number

NINT : = 2, Gives the numerical integration order to be used in the Gauss Quadrature Formulae.

NUMCR : Crack Status

NUMCRK : New Crack Status

(b) Floating-Point Numbers

AG : Angle of the principal stresses to the global axes.

ANGLE : Crack angle (in degrees), = 1000.0 for uncracked state, = 360.5 for a hoop crack only.

AO : = A_o

AU : = A_u

C : =[D] - matrix

CG : = cos (GAM)

DELSIG : = Elastic stress increment vector

DELEPS : = Strain increment vector

DEPS : = Subincremental strain vector

DFAC = STIFAC

DP = C : Elastic-plastic [D] matrix

EPS : Strain vector at end of last load increment

EFSG : = σ_e , effective stress

EST = HP

FCU : = f'_{cu}

FCO : = f_{co}

FTU : = f'_{tu}

FTO : = f_{to}

FBCU : = f'_{bc}

FBCO : = f_{bc}

F1 : = σ_e^2, value of loading function

FT : = $\sigma_e^2 - YLD^2$, FT > 0 = plastic, FT ⩽ 0 = elastic

GAM= GAMMA : = - (Crack angle) in radians

H : Work-hardening modulus

HP : = H' , tangent to the effective stress-plastic strain curve

P1,P2 : = Principal Stresses

PROP : = Material property vector

PV = PROP (2) : = Initial Poisson's Ratio

RATIO : = Fraction of elastic stress increment to reach yield surface

RTC : = 1.0 for compression/compression region,
= -1.0 for tension/compression region

STIFAC = SHEFAC = PROP (26) : Stiffness reduction factor on cracking or crushing

SIG : = Stress vector at end of last load increment

STRESS : = Updated stress vector

STRAIN : = Updated strain vector

SG : = Sin (GAM)

STR : = Parameter defining extent of yield, (= YLD for compression region)

S11, S22 : = Stresses in the crack planes

SM : = $\sigma_{xx} + \sigma_{yy} + \sigma_{zz}$

SX : = σ_{xx}

SY : = σ_{yy}

SS : = τ_{yz}

SZ : = σ_{zz}

} for SIG or STRESS vector

TAU : = Working stress vector

TO : = τ_o, initial effective yield stress

TU : = τ_u, ultimate effective stress

T : = Transformation matrix used to rotate the $[D]$ - matrix from the crack plane orientation to the global orientation

WA (12,I) : = Working storage array - see IMODIO sub-routine

XA : = α

XB : = β

XJ2 : = Second invariant of deviatoric stress

YLD = YIELD : = Effective stress at which yielding commences

YLDC : = τ_o, compression region

YLDT : = τ_o, tension/compression region

YM = PROP(1) : = Initial Young's Modulus

D.2 Subroutines

CONC2D (PROP, SIG, EPS, YIELD, IPEL, NUMCR, ANGLE):-

This is the main program subroutine.

IMODIO (WA, IWA, NPT, PROP):-

This subroutine initializes the variables in the working array, WA (12,I) for each Gauss point, where I=1 to (NUME*NINT*NINT).

WA (J,I) = 0.0 for J=1 to 8, representing the initial stresses and strains.

WA (9,I) = -1.0 = YIELD = the yield point (negative, therefore still elastic)

IWA (10,I) = 1 = IPEL, = 1 for elastic state

IWA (11,I) = 0 = NUMCR = No. of cracks

WA (12,I) = 1000.0 = Crack angle (> 360.5, therefore uncracked).

The material property vector, PROP (I), I = 1 to 26, is also generated, using the cube strength, FCU, as basic data.

MIDEP2 (TAU, DEPS, DP, PROP):-

Calculates the elastic-plastic stress-strain D matrix.

EPSLOP (STR, EST, PROP):-

Calculates the tangent to the effective stress-plastic strain curve from the supplied data points.

DCRACK (C, ANGLE, NUMCRK):-

Modifies the [D] matrix for the cracked state.

MAXMIN (TAU, S11, S22, AG):-

Calculates the principal stresses, S11 and S22, in the Y-Z plane, and their angle of rotation, AG.

CAUCHY:-

Converts stresses defined in the Total Lagrangian formulation to true Cauchy stresses.

D.3 Input Data Instructions

For the Element Group Control Card:-

NPAR(17) = 26 = No. of constants per property set.

NPAR(18) = 12 = No. of items per Gauss Point to be stored from the last loadstep.

For the Material Property Data Cards:-

NUMMAT (=NPAR(16)) sets of 4 cards, ie one set for each material property set, are supplied. The data for each set of 4 cards for property set No. N, are as follows:-

Cols.	Variable	Entry (a)Generated OR (b)Specified		
CARD 1				
1-10	PROP(1,N)	E (N/mm^2)	E (N/mm^2)	
11-20	PROP(2,N)	ν	ν	
21-30	PROP(3,N)	-	A_o	Comp. Region
31-40	PROP(4,N)	0.0	τ_o	
41-50	PROP(5,N)	-	A_u	
51-60	PROP(6,N)	-	τ_u	
61-70	PROP(7,N)	-	A_o	Ten./ Comp. Region
71-80	PROP(8,N)	-	τ_o	
CARD 2				
1-10	PROP(9,N)	-	A_u	
11-20	PROP(10,N)	-	τ_u	
21-30	PROP(11,N)	σ_e/f'_{cu} (1)	σ_e/f'_{cu} (1)	Non-dimensional stress-plastic strain curve.
31-40	:	" (2)	" (2)	
41-50	:	" :	" :	
51-60	:	" :	" :	
61-70	:	" :	" :	
71-80	PROP(16,N)	" :	" :	

Cols.	Variable	Entry (a)Generated OR (b)Specified		
CARD 3				
1-10	PROP(17,N)	σ_e/f'_{cu} (7)	σ_e/f'_{cu} (7)	Non-
11-20	:	ϵ_p (1)	ϵ_p (1)	dimensional
21-30	:	" (2)	" (2)	stress-
31-40	:	" :	" :	plastic
41-50	:	" :	" :	strain
51-60	:	" :	" :	curve.
61-70	:	" :	" :	
71-80	PROP(24,N)	ϵ_p (7)	ϵ_p (7)	
CARD 4				
1-10	PROP(25,N)	f'_{cu} (N/mm^2)	f'_{cu} (N/mm^2)	
11-20	PROP(26,N)	STIFAC	STIFAC	
		(eg. , STIFAC = 10^5)		

```
      OVERLAY (NSAP,3,7)
      PROGRAM EL2D10
C
C     M O D E L     =     10
CC        G R O U T    M O D E L      (CHEN)
C
      COMMON /EL/ IND,ICOUNT,NPAR(20),NUMEG,NECL,NEGNL,IMASS,IDAMP,ISTAT
     1           ,NDOF,KLIN,IEIG,IMASSN,IDAMPN
      COMMON  /DIMEL/ N101,N102,N103,N104,N105,N106,N107,N108,N109,N110,
     1                N111,N112,N113,N114,N120,N121,N122,N123,N124,N125
      COMMON  /MATMOD/ STRESS(4),STRAIN(4),D(4,4),IPT,NEL
      COMMON  A(1)
      DIMENSION  IA(1)
      EQUIVALENCE (NPAR(10),NINT),(A,IA),(NPAR(18),IDW)
      NPT=NINT*NINT
      MATP=IA(N107+NEL-1)
      NM=N109+(MATP-1)*NPAR(17)
C
      IF(IND.NE.0) GOTO 100
C
C     INITIALIZE WORKING ARRAY WA
      NN=N110+(NEL-1)*NPT*IDW
      CALL IMOD10 (A(NN),A(NN),NPT,A(NM))
      RETURN
C
C     FIND STRESS-STRAIN LAW AND STRESS
  100 NN=N110+(NEL-1)*NPT*IDW+ (IPT-1)*IDW
      CALL CONC2D(A(NM),A(NN),A(NN+4),A(NN+8),A(NN+9),A(NN+10),A(NN+11))
C
      RETURN
      END
```

```
      SUBROUTINE IMOD10 (WA,IWA,NPT,PROP)
      COMMON /MATMOD/ STRESS(4),STRAIN(4),C(4,4),IPT,N
      COMMON /CRACK/ GAMMA,STIFAC,SHEFAC
      DIMENSION PROP(1)
      DIMENSION WA(12,1),IWA(12,1)
C
C     INITIALIZE WORKING ARRAY WA
      DO 10 J=1,NPT
      DO 15 I=1,8
   15 WA(I,J)=0.0
      WA(9,J)=-1.0
      IWA(10,J)=1
      IWA(11,J)=0
   10 WA(12,J)=1000.
C
      STIFAC=PROP(26)
      SHEFAC=PROP(26)
      IF(N.GT.1) RETURN
      FCU=PROP(25)
      IT=0
      IF(PROP(4).GT.0.01) IT=1
      IF(IT.EQ.1) GOTO 16
      FCO=0.6*FCU
      FTU=0.09*FCU
      FTO=0.054*FCU
      FBCU=1.16*FCU
      FBCO=0.6*FBCU
      PROP(3)=(FBCO**2.-FCO**2.)/(2.*FBCO-FCO)
```

```
      A=FCO*FBCO*(2.*FCO-FBCO)
      B=3.*(2.*FBCO-FCO)
      PROP(4)=SQRT(A/B)
      PROP(5)=(FBCU**2.-FCU**2.)/(2.*FBCU-FCU)
      A=FCU*FBCU*(2.*FCU-FBCU)
      B=3.*(2.*FBCU-FCU)
      PROP(6)=SQRT(A/B)
      PROP(7)=(FCO-FTO)/2.
      PROP(8)=SQRT(FCO*FTO/6.)
      PROP(9)=(FCU-FTU)/2.
      PROP(10)=SQRT(FCU*FTU/6.)
   16 DO 17 I=1,7
      J=I+10
   17 PROP(J)=PROP(J)*FCU
      IF(IT.EQ.1) RETURN
      WRITE(6,18)
   18 FORMAT(//29H      .....GENERATED DATA.....)
      WRITE(6,20)
   20 FORMAT(//59H      FCU        FCO        FTU        FTO        FBCU
     1 FBCO)
      WRITE(6,25)FCU,FCO,FTU,FTO,FBCU,FBCO
   25 FORMAT(2X,6(F10.5),/)
      WRITE(6,30)(I,PROP(I),I=1,17)
   30 FORMAT(5X,5HPROP(,I2,10H) ..... =,E14.6)
      WRITE(6,35)
   35 FORMAT(/15H      ...........//)
      RETURN
      END
```

```
      SUBROUTINE CONC2D(PROP,SIG,EPS,YIELD,IPEL,NUMCR,ANGLE)
C
C     CONSTITUTIVE RELATIONS OF CONCRETE UNDER 2-D STRESSES
C     PLANE STRESS, PLANE STRAIN, OR AXISYMMETRIC DEFORMATION STATE
C
C
      COMMON /EL/IND,ICOUNT,NPAR(20),NUMEG,NEGL,NEGNL,IMASS,IDAMP,ISTAT
     1          ,NDOF,KLIN,IEIG,IMASSN,IDAMPN
      COMMON /VAR   / NG,KPRI,MODEX,KSTEP,ITE,ITEMAX,IREF,IEQREF,INOCMD
      COMMON /ELPMID/ YM,PV,YLD,XN,XA,XB,XK,RTC
     1              , A1,A2,B1,B2,C1,C2,D1,BM,YLDC,YLDT,ISR,IST
      COMMON /MATMOD/ STRESS(4),STRAIN(4),C(4,4),IPT,NEL
      COMMON /DISDER/ DISD(5)
      COMMON /CRACK/ GAMMA,STIFAC,SHEFAC
C
      DIMENSION PROP(1),SIG(1),EPS(1)
      DIMENSION TAU(4),DELSIG(4),DELEPS(4),DEPS(4),STATE(4)
      DIMENSION LPR(4),LPC(4)
C
      EQUIVALENCE (NPAR(3),INDNL),(NPAR(5),ITYP2D),(DELEPS(1),DEPS(1))
C
      DATA NGLAST/1000/,STATE/7HELASTIC,7HPLASTIC,7HCRACKED,7HCRUSHED/
C
C
      IST=4
      IF (ITYP2D.EQ.2) IST=3
      ISR=3
      IF (ITYP2D.EQ.0) ISR=4
      YM=PROP(1)
      PV=PROP(2)
C     CRUSHED
      IF(IPEL.NE.4) GOTO 103
```

```
      DO 111 I=1,4
  111 TAU(I)=SIG(I)
  112 RTC=100
      YM=YM/PROP(26)
C
  103 XK=1.732
      D1=PV/(PV-1.)
      A2=YM/(1.+PV)
      B2=(1.-PV)/(1.-2.*PV)
      C2=PV/(1.-2.*PV)
      C1=A2/2.
      BM=YM/(1.-2.*PV)/3.
      YLDC=PROP(4)
      YLDT=PROP(8)
C
      IF(ITYP2D.EQ.2) GOTO 105
C
C     PLANE STRAIN / AXISYMMETRIC
      B1=A2*C2
      A1=B1+A2
      GO TO 110
C
C     PLANE STRESS
  105 A1=YM/(1.-PV*PV)
      B1=A1*PV
C
  110 YLD=YIELD
C
C
C        1. CALCULATE INCREMENTAL STRAINS
C
      IF(IPELOC.EQ.4) GOTO 163
  119 DO 120 I=1,ISR
  120 DELEPS(I)=STRAIN(I)-EPS(I)
C
```

```
C       CRACKED
        IF(IPEL.NE.3) GOTO 130
70      M=10
        IM=0
        DEPS(4)=0.0
        DO 195 I=1,ISR
195     DEPS(I)=DELEPS(I)/M
75      200 TAU(4)=0.0
        DO 202 I=1,IST
202     TAU(I)=SIG(I)
        IF(IM.EQ.M) GOTO 600
205     IM=IM+1
80      IF(NUMCR.EQ.0.OR.NUMCR.EQ.7) GOTO 225
        IF(NUMCR.EQ.4.OR.NUMCR.LE.2) GOTO 220
        A1=YM
        B1=PV
        GOTO 225
85      220 A1=YM/(1.-PV*PV)
        B1=A1*PV
225     DO 206 I=1,4
        DO 206 J=1,4
206     C(I,J)=0.
90      C(1,1)=A1
        C(2,1)=B1
        C(1,2)=B1
        C(2,2)=A1
        C(3,3)=C1
95      IF(ITYP2D.EQ.2) GOTO 207
        C(1,4)=B1
        C(2,4)=B1
        C(4,1)=B1
        C(4,2)=B1
100     C(4,4)=A1
207     IRTC=5
        GOTO 165
```

```
  209 IRTC=0
      IF(FTOLE.0.0) GOTO 208
      IF(F1.GT.YLD*YLD)YLD=SQRT(F1)
      IF(YLD.GT.TU)YLD=TU
      CALL MIDEP2(TAU,DEPS,C,PROP)
  208 CALL DCRACK (C,ANGLE,NUMCR)
      DO 210 I=1,IST
      DO 210 J=1,ISR
  210 TAU(I)=TAU(I)+C(I,J)*DEPS(J)
C
C     FIND STRESSES IN PLANES OF CRACKS
C
      IF(ANGLE.GT.360.1) GOTO 240
      GAM=-ATAN(1.0)*ANGLE/45.
      SG=SIN(GAM)
      CG=COS(GAM)
      R11=CG*TAU(1)-SG*TAU(3)
      R12=CG*TAU(3)-SG*TAU(2)
      R21=SG*TAU(1)+CG*TAU(3)
      R22=SG*TAU(3)+CG*TAU(2)
      S11=R11*CG-R12*SG
      S22=R21*SG+R22*CG
      GOTO 165
  240 CALL MAXMIN(TAU,S11,S22,AG)
      GOTO 165
  243 CONTINUE
      IF(NUMCR.NE.1.OR.NUMCR.NE.5) GOTO 245
      IF(S11.LE.0.0) GOTO 245
      S22=S11
      S11=0.0
  245 IHOOP=0
      IF(NUMCR.LT.4) GOTO 250
      NUMCR=NUMCR-4
      IHOOP=1
```

```
      250 NUMCRK=0
          IF(RTC.GT.0.0) GOTO 255
          IF(F1.LT.TU*TU) GOTO 255
          IF(FT)255,255,260
      255 IF(NUMCR.EQ.0) GOTO 256
          IF(NUMCR.NE.2.AND.S11.GE.0.0) NUMCRK=1
      256 IF(NUMCRK.LT.1.AND.S11.GE.TU) NUMCRK=1
          IF(NUMCR.GE.2.AND.S22.GE.0.0) NUMCRK=NUMCRK+2
          IF(NUMCRK.LT.2.AND.S22.GE.TU) NUMCRK=NUMCRK+2
          IF(IHOOP.EQ.1.AND.TAU(4).GE.0.0) NUMCRK=NUMCRK+4
          IF(NUMCRK.LT.4.AND.TAU(4).GE.TU) NUMCRK=NUMCRK+4
          IF(NUMCRK.GT.NUMCR+4*IHOOP) YLD=TO
          GOTO 280
      260 YLD=TO
          IF(NUMCR.EQ.0) GOTO 268
          IF(NUMCR-2)262,264,266
      262 IF(ABS(S11).GT.1.E-6) GOTO 265
      263 NUMCRK=3
          IF(S22.LT.TAU(4)) NUMCRK=NUMCRK+2
          GOTO 270
      264 IF(ABS(S22).GT.1.E-6) GOTO 263
      265 NUMCRK=3
          IF(S11.LT.TAU(4)) NUMCRK=NUMCRK+3
          GOTO 270
      266 NUMCRK=7
          GOTO 280
      268 NUMCRK=5
          GOTO 280
      270 IF(IHOOP.EQ.1.AND.NUMCRK.EQ.3) NUMCRK=7
      280 NUMCR=NUMCRK
C
C     CHECK FOR CRUSHING
C
          TUS=PROP(6)*PROP(6)
          IF(F1.GE.TUS.AND.RTC.GT.0.0) GOTO 288
```

```
      IF(NUMCRK.NE.0) GOTO 285
      ANGLE=1000.
      GOTO 295
  288 IPEL=4
      GOTO 112
  285 IF(ANGLE.LT.360.1) GOTO 290
      ANGLE=AG
  290 IF(NUMCRK.EQ.4) ANGLE=360.5
      NK=NUMCRK
      IF(NK.LT.4) GOTO 292
      NK=NUMCRK-4
      TAU(4)=0.0
      IF(NK.EQ.0) GOTO 295
  292 IF(NK.EQ.1.OR.NK.EQ.3) S11=0.0
      IF(NK.GE.2) S22=0.0
      GAMMA=-ATAN(1.0)*ANGLE/45.
      SG=SIN(GAMMA)
      CG=COS(GAMMA)
      TAU(1)=CG*CG*S11+SG*SG*S22
      TAU(2)=SG*SG*S11+CG*CG*S22
      TAU(3)=SG*CG*(S22-S11)
  295 IF(IM.LT.M) GOTO 205
      STRESS(4)=0.0
      DO 296 I=1,IST
  296 STRESS(I)=TAU(I)
C
      IF(ITYP2D.NE.2) GOTO 402
      DELEPS(1)=STRAIN(1)-EPS(1)
      DELEPS(2)=STRAIN(2)-EPS(2)
      IF(IK.EQ.0) GOTO 299
      IF(IK.LT.3) GOTO 297
      STRAIN(4)=EPS(4)
      GOTO 402
  297 GAM=ATAN(1.0)*ANGLE/45.
```

```
      SG=SIN(GAM)
      CG=COS(GAM)
      IF(IK.EQ.2) GOTO 298
      DELEPS(1)=DELEPS(1)*CG*CG+DELEPS(2)*SG*SG
210   DELEPS(2)=0.0
      GOTO 299
  298 DELEPS(1)=DELEPS(1)*SG*SG+DELEPS(2)*CG*CG
      DELEPS(2)=0.0
  299 STRAIN(4)=EPS(4)+D1*(DELEPS(1)+DELEPS(2))
215   GOTO 402
C
C        2. CALCULATE THE STRESS INCREMENT,
C           ASSUMING ELASTIC BEHAVIOUR
C
220   130 DELSIG(1)=A1*DELEPS(1)+B1*DELEPS(2)
      DELSIG(2)=B1*DELEPS(1) + A1*DELEPS(2)
      DELSIG(3)=C1*DELEPS(3)
      DELSIG(4)=0.
      IF(ITYP2D.EQ.2) GOTO 150
225   DELSIG(4)=B1* (DELEPS(1)+DELEPS(2))
      IF(ITYP2D.EQ.1) GO TO 150
      DELSIG(1)=DELSIG(1) + B1*DELEPS(4)
      DELSIG(2)=DELSIG(2) + B1*DELEPS(4)
      DELSIG(4)=DELSIG(4) + A1*DELEPS(4)
230
C
C        3. CALCULATE TOTAL STRESSES,
C           ASSUMING ELASTIC BEHAVIOUR
C
  150 TAU(4)=0.
235   DO 160 I=1,IST
  160 TAU(I)=SIG(I)+DELSIG(I)
C
  164 IRTC=0
C
```

```
      165 SM=TAU(1)+TAU(2)+TAU(4)
          SX = TAU(1)
          SY = TAU(2)
          SS = TAU(3)
          SZ = TAU(4)
          XJ2 = 0.5*(SX*SX+SY*SY+SZ*SZ+2.*SS*SS)-SM*SM/6.0
          RTC=1.0
          IF (SM.GT.0.0) RTC=-1.0
          XX=SQRT(XJ2)+SM/1.732
          IF (XX.GT.0.0) RTC=-1.0
          IF (RTC.LT.0.) GO TO 166
C
C     CONSTANTS FOR COMPRESSION REGION
C
      163 AO=PROP(3)
          TO=PROP(4)
          AU=PROP(5)
          TU=PROP(6)
          GO TO 167
      166 CONTINUE
C
C     CONSTANTS FOR TENSION-COMPRESSION REGION
C
          AO=PROP(7)
          TO=PROP(8)
          AU=PROP(9)
          TU=PROP(10)
      167 CONTINUE
          XA = (AU-AO)/(TU*TU-TO*TO)
          XB = (AO*TU*TU-AU*TO*TO)/(TU*TU-TO*TO)
          XN = (3.*RTC-XK*XK)/36.
          IF(IPEL.EQ.4) GOTO 175
          IF(YLD.LT.TO) YLD=TO
C
```

```
C       ADJUST YLD FOR CHANGE FROM COMP TO TENSION REGION
275     IF(YLD.GT.TU+1.E-4) YLD=TO
        IF(IRTC.EQ.2) GOTO 304
C
C          4. CHECK WHETHER *TAU* STATE OF STRESS FALLS
C             OUTSIDE THE LOADING SURFACE
C
280   C
        DEN=16.*XA*SM/3.
        IF(DEN.LT.1.E-3) DEN=1.E-3
        F1=((XK*XK/3.)*(0.5*(SX*SX+SY*SY+SZ*SZ+2.*SS*SS)-SM*SM/6.0)
       1      +XN*SM*SM+XB*SM/3.)/DEN
285     FT=F1-YLD*YLD
        IF(IRTC) 482,169,209
  169   IF(IPEL.EQ.3) GOTO 243
C
        IF(FT) 170,170,300
290   C
C       STATE OF STRESS WITHIN LOADING SURFACE-ELASTIC BEHAVIOUR
C
  170   IPEL=1
  175   STRESS(4)=0.0
295     DO 180 I=1,IST
  180   STRESS(I)=TAU(I)
        IF(ITYP2D.EQ.2) STRAIN(4)=EPS(4)+D1*(DELEPS(1)+DELEPS(2))
        GO TO 400
C
300   C       STATE OF STRESS OUTSIDE LOADING SURFACE - PLASTIC BEHAVIOUR
C
C       DETERMINE PART OF STRAIN TAKEN ELASTICALLY
C
  300   IF(IPEL.EQ.1) GOTO 305
305     RATIO=0.0
        TAU(4)=0.0
```

```
                DO 302 I=1,IST
              302 TAU(I)=SIG(I)
                IRTC=2
310             GOTO 165
              304 IRTC=0
                GOTO 370
              305 IPEL=2
            C
315             SM=SIG(1)+SIG(2)+SIG(4)
                SX=SIG(1)
                SY=SIG(2)
                SS=SIG(3)
                SZ=SIG(4)
320         C
                DM=DELSIG(1)+DELSIG(2)+DELSIG(4)
                DX=DELSIG(1)
                DY=DELSIG(2)
                DS=DELSIG(3)
325             DZ=DELSIG(4)
            C
                X1=XB+XA*YLD*YLD
                A=(XK*XK/3.)*(0.5*(DX*DX+DY*DY+DZ*DZ+2.*DS*DS)-DM*DM/6.)
               1  +XN*DM*DM
330             B=(XK*XK/3.)*(0.5*(SX*DX+SY*DY+SZ*DZ+2.*SS*DS)-SM*DM/6.)
               1    +XN*SM*DM+X1*DM/6.
                E=(XK*XK/3.)*(0.5*(SX*SX+SY*SY+SZ*SZ+2.*SS*SS)-SM*SM/6.)
               1    +XN*SM*SM+X1*SM/3.-YLD*YLD
            C
335             IF(E.LT.1.E-2) GOTO 330
                WRITE(6,325)E,NEL
              325 FORMAT(4H  E=,F12.8,4X,I4)
              330 RR=B*B-A*E
                IF(RR.GT.0.0) GOTO 340
340             WRITE(6,335)RR,NEL
```

```
      335 FORMAT(5H  RR=,F12.8,4X,I4)
          RR=0.0
      340 RATIO=(-B+SQRT(RR))/A
          IF(RATIO.GE.0.0) GOTO 349
345       IF(RATIO.GT.-1.E-2) GOTO 348
          WRITE(6,346)RATIO,NEL
      346 FORMAT(8H  RATIO=,F12.8,4X,I4)
      348 RATIO=0.0
C
      349 DO 350 I=1,IST
350   350 TAU(I)=SIG(I)+RATIO*DELSIG(I)
          IF(ITYP2D.EQ.2) STRAIN(4)=EPS(4)+RATIO*D1*(DELEPS(1)
         1          +DLLEPS(2))
C
355   C     *TAU* NOW CONTAINS (PREVIOUS STRESSES +
      C     STRESSES DUE TO ELASTIC STRAIN INCREMENTS)
      C
      C        5. CALCULATE PLASTIC STRESSES
      C
360   C     DETERMINE INCREMENT INTERVAL
      C
      370 M=10.*SQRT(FT)/YLD+1
          IF(M.GT.30) M=30
          XM=(1.-RATIO)/M
365   C
      375 DEPS(4)=0.0
          DO 380 I=1,ISR
      C
      C     ELASTIC-PLASTIC MATERIAL MATRIX
370   C
      380 DEPS(I)=XM*DELEPS(I)
      C
      C     ...C. CALCULATION OF ELASTOPLASTIC STRESSES ..... (START)
```

```
C
      IM=0
500   IM=IM+1
      IMI=IM
C
      CALL MIDEP2(TAU,DEPS,C,PROP)
C
      DO 560 I=1,IST
      DO 560 J=1,ISR
560   TAU(I)=TAU(I)+C(I,J)*DEPS(J)
C
C     UPDATE YLD
C
      SM=TAU(1)+TAU(2)+TAU(4)
      SX=TAU(1)
      SY=TAU(2)
      SS=TAU(3)
      SZ=TAU(4)
      DEN=1.-XA*SM/3.
      IF(DEN.LT.1.E-3) DEN=1.E-3
      F1=((XK*XK/3.)*(0.5*(SX*SX+SY*SY+SZ*SZ+2.*SS*SS)-SM*SM/6.)
     1   +XN*SM*SM+XB*SM/3.)/DEN
      IF(F1.GT.0.0) GOTO 590
      WRITE(6,575)F1,NEL
575   FORMAT(5H  F1=,F12.8,4X,I4)
      GOTO 595
C
590   YLD=SQRT(F1)
      IF(YLD.LT.TU) GOTO 600
595   YLD=TU
C
      IF(RTC.LT.0.0) GOTO 610
C
      IPEL=4
      GOTO 112
```

```
      610 IPEL=3
410       YLD=TO
          DO 604 I=1,IST
      604 SIG(I)=TAU(I)
          CALL MAXMIN(TAU,S11,S22,ANGLE)
          IF(TAU(4).GT.S11) GOTO 630
415       NUMCR=1
          S11=0.0
          GAMMA=.5*ATAN(1.0)*ANGLE/45.
          SG=SIN(GAMMA)
          CG=COS(GAMMA)
420       SIG(1)=SG*SG*S22
          SIG(2)=CG*CG*S22
          SIG(3)=SG*CG*S22
          GOTO 200
      630 NUMCR=4
425       ANGLE=360.5
          SIG(4)=0.0
          GOTO 200
      C
        600 IF(IM.LT.M) GOTO 500
430   C
      C     ..... CALCULATION OF ELASTOPLASTIC STRESSES .....(END)
      C
          STRESS(4)=0.
          DO 390 I=1,IST
435     390 STRESS(I)=TAU(I)
      C
      C     CHECK FOR ULTIMATE TENSILE STRESS
      C
        400 IF(RTC.GE.0) GOTO 402
440       IF(IPEL.GT.2) GOTO 402
          CALL MAXMIN(TAU,S11,S22,ANG)
          M=1
```

```
            IM=1
            IF(TAU(4).GE.TU) GOTO 610
445         IF(S11.GE.TU) GOTO 610
C
C           6. UPDATING STRESSES, STRAINS, YIELD, NS
C
  402 DO 410 I=1,IST
450 410 SIG(I)=STRESS(I)
            DO 420 I=1,ISR
  420 EPS(I)=STRAIN(I)
            YIELD=YLD
            IF(ITYP2D.EQ.2) EPS(4)=STRAIN(4)
455         IF(KPRI.EQ.0) GOTO 700
C
            IF(ICOUNT.EQ.3) RETURN
C
C           7. FORM THE MATERIAL LAW
460         C
            IF(IPEL.NE.2) GOTO 450
C
C           ELASTIC-PLASTIC MATERIAL MATRIX
C
465         CALL MIDEP2(TAU,DEPS,C,PROP)
            RETURN
C
C           ELASTIC
  450 DO 460 I=1,4
470         DO 460 J=1,4
  460 C(I,J)=0.
            C(1,1)=A1
            C(2,1)=B1
            C(1,2)=B1
475         C(2,2)=A1
            C(3,3)=C1
```

```
                IF(ITYP2D.EQ.2) GOTO 480
                C(1,4)=B1
                C(2,4)=B1
480             C(4,1)=B1
                C(4,2)=B1
                C(4,4)=A1
C
  480 IF(IPEL.NE.3) RETURN
485 C
C       CRACKED
        IRTC=-1
        GOTO 165
  482 IRTC=0
490     IF(FTOL.LE.0.0) GOTO 484
        IF(F1.GT.YLD*YLD) YLD=SQRT(F1)
        CALL MIDEP2(TAU,DEPS,C,PROP)
  484 CALL DCRACK(C,ANGLE,NUMCR)
        RETURN
495 C
C       P R I N T I N G   O F   S T R E S S E S
C
  700 CONTINUE
C
500     SM=STRESS(1)+STRESS(2)+STRESS(4)
        SX=STRESS(1)
        SY=STRESS(2)
        SS=STRESS(3)
        SZ=STRESS(4)
505   705 IF(INDNLL.NE.2) GOTO 800
C
C       IN TOTAL LAGRANGIAN FORMULATION,
C       CAUCHY STRESSES ARE CALCULATED AND PRINTED
        CALL CAUCHY
510 C
```

```
      800 IF(NG.NE.NGLAST) GOTO 802
          IF(NEL.GT.NELAST) GOTO 806
          IF(IPT.EQ.1) 810,808,810
C
  802 NGLAST=NG
  808 IF(ITYP2D.EQ.1) 805,805,803
  803 WRITE(6,2002)
          GOTO 806
  805 WRITE(6,2003)
C
  806 NELAST=NEL
          WRITE(6,2004) NEL
  810 CALL MAXMIN(STRESS,P1,P2,AG)
          DEN=1.E-XA*SM/3.
          IF(DEN.LT.1.E-3) DEN=1.E-3
          F1=((XK*XK/3.)*(0.5*(SX*SX+SY*SY+SZ*SZ+2.*SS*SS)-SM*SM/6.)
     1        +XN*SM*SM+XB*SM/3.)/DEN
          EFSG=0.
          IF(F1.GT.0) EFSG=SQRT(F1)
  812 IF(ITYP2D.EQ.1) 815,815,813
C
  813 WRITE(6,2005) IPT,STATE(IPEL),
     1        (STRESS(I),I=1,3),P1,P2,AG,EFSG
          RETURN
C
  815 WRITE(6,2007) IPT,STATE(IPEL),STRESS(4),
     1        (STRESS(I),I=1,3),P1,P2,AG,EFSG,RTC,ANGLE
          RETURN
```

```
C
 2002 FORMAT(101H ELEMENT  STRESS  STRESS-YY  STRESS-ZZ  STRESS-YZ
     1MAX STRESS    MIN STRESS    ANGLE    EFFECTIVE , /
     2        16H NUM/IPT   STATE,79X,6HSTRESS,/)
 2003 FORMAT(120H ELEMENT  STRESS  STRESS-XX  STRESS-YY  STRESS-ZZ  STRE
     1SS-YZ    MAX STRESS    MIN STRESS    ANGLE   EFFECTIVE  CRACKANG,
     2  /,   16H NUM/IPT   STATE,88X,6HSTRESS,/)
 2004 FORMAT (I4/)
 2005 FORMAT(5X,I2,2X,A7,3(2X,F9.3),3(3X,F10.3),4X,F9.3)
 2007 FORMAT(5X,I2,2X,A7,4(2X,F9.3),2X,4(2X,F9.3),2X,F5.1,F9.3)
C
      END
```



```
      SUBROUTINE MIDEP2(TAU,DEPS,DP,PROP)
C
C       FORMS THE ELASTO-PLASTIC MATERIAL MATRIX
C
      COMMON /EL/ IND,ICOUNT,NPAR(20),NUMEG,NEGL,NEGNL,IMASS,IDAMP,ISTAT
     1           ,NDOF,KLIN,IEIG,IMASSN,IDAMPN
      COMMON /MATMOD/ STRESS(4),STRAIN(4),C(4,4),IPT,NEL
      COMMON /ELPMID/ YM,PY,YLD,XN,XA,XB,XK,RIC
     1          ,A1,A2,B1,B2,C1,C2,D1,BM,YLDC,YLDT,ISR,IST
      DIMENSION TAU(1),DEPS(1),DP(1),PROP(1)
C
      EQUIVALENCE (NPAR(5),ITYP2D)
C
```

```
      SM=(TAU(1)+TAU(2)+TAU(4))/3.
      SX=TAU(1)-SM
      SY=TAU(2)-SM
      SS=TAU(3)
      SZ=TAU(4)-SM
C
C     CALCULATE STRAIN-HARDENING FUNCTION 'H'
C
      STR=YLD
      IF(RTC.LT.0.) STR=(1.0+(YLD-YLDT)/YLDT)*YLDC
C
      CALL EPSLOP (STR,HP,PROP)
      H=2.*YLD*HP
      XM=1.-XA*SM
      XJ2=0.5*(SX*SX+SY*SY+SZ*SZ+2.*SS*SS)
      ET=XK*XK/3.
      RO=XN*SM*6.+(XB+XA*YLD*YLD)/3.
      Y1=1+PV
      Y2=1-2.*PV
      Y3=3.*PV*RO
      WINV=Y2*(2.*ET*ET*XJ2+3.*RO*RO)+9.*PV*RO*RO+XM*H*Y1*Y2/YM
     1     *SQRT(2.*ET*ET*XJ2+3.*RO*RO)
      W=1./WINV
C
      F1=Y2*(ET*SX+RO)+Y3
      F11=F1*F1
      F12=F1*(Y2*(ET*SZ+RO)+Y3)
      F13=F1*(Y2*(ET*SY+RO)+Y3)
      F14=F1*(Y2*ET*SS)
      F2 =Y2*(ET*SZ+RO)+Y3
      F22=F2*F2
      F23=F2*(Y2*(ET*SY+RO)+Y3)
      F24=F2*(Y2*ET*SS)
      F3 =Y2*(ET*SY+RO)+Y3
```

```
      F33=F3*F3
      F34=F3*(Y2*ET*SS)
50    F44=(Y2*ET*SS)*(Y2*ET*SS)
C
      A1=YM/(Y1*Y2)
      B1=1.-PV
      C1=PV
55    C
      DP(1)=A1*(B1-W*F11)
      DP(2)=A1*(C1-W*F13)
      DP(3)=A1*(-W*F14)
      DP(4)=A1*(C1-W*F12)
60    DP(5)=DP(2)
      DP(6)=A1*(B1-W*F33)
      DP(7)=A1*( -W*F34)
      DP(8)=A1*(C1-W*F23)
      DP(9)=DP(3)
65    DP(10)=DP(7)
      DP(11)=A1*(.5*Y2-W*F44)
      DP(12)=A1*( -W*F24)
C
      IF(ITYP2D.EQ.1) RETURN
70    C
      DP(13)=DP(4)
      DP(14)=DP(8)
      DP(15)=DP(12)
      DP(16)=A1*(B1-W*F22)
75    C
      IF(ITYP2D.EQ.0) RETURN
C
C     PLANE STRESS / MODIFY DP MATRIX
C
80    DEPS(4)=-(DP(4)*DEPS(1)+DP(8)*DEPS(2)+DP(12)*DEPS(3))/DP(16)
      STRAIN(4)=STRAIN(4)+DEPS(4)
```

```
                      DO 120 I=1,3
                      A=C(I,4)/C(4,4)
                      DO 120 J=I,3
85                    C(I,J)=C(I,J)-C(4,J)*A
                  120 C(J,I)=C(I,J)
                C
                      RETURN
                      END
```



```
 1                    SUBROUTINE EPSLOP (STR,EST,PROP)
                      COMMON /EL/ IND,ICOUNT,NPAR(20),NUMEG,NEGL,NEGNL,IMASS,IDAMP,ISTAT
                     1           ,NDOF,KLIN,IEIG,IMASSN,IDAMPN
                      COMMON /ELPMID/ YM,PV,YLD,XN,XA,XB,XK,RTC
 5                    DIMENSION PROP(1)
                      EQUIVALENCE (NPAR(17),NCON)
                C
                      MAX=7
                      SIGE=STR
10                    IF(SIGE.LE.PROP(11)) GOTO 40
                      DO 10 K=2,MAX
                      N=K
                      IF(SIGE.GE.PROP(K+9).AND.SIGE.LT.PROP(K+10)) GOTO 20
                   10 CONTINUE
15                    IF(SIGE.GE.PROP(10+MAX)) GOTO 30
                      WRITE(6,200)
                      STOP
                C
```

```
      20 CONTINUE
20       RANGE=PROP(10+N)-PROP(9+N)
         RATIO=(PROP(10+N)-SIGE)/RANGE
         IF(RATIO.LE.0.1) N=N+1
         IF(N.GE.MAX) GOTO 30
         EST=(PROP(10+N)-PROP(9+N))/(PROP(10+MAX+N)-PROP(9+MAX+N))
25       GOTO 100
C
      30 CONTINUE
         EST=(PROP(10+MAX)-PROP(9+MAX))/(PROP(10+MAX+MAX)-PROP(9+MAX+MAX))
         GOTO 100
30    40 EST=(PROP(12)-PROP(11))/(PROP(12+MAX)-PROP(11+MAX))
     100 CONTINUE
     200 FORMAT(1H0, 37HERROR - EFFECTIVE STRESS OUT OF RANGE )
C
         RETURN
35       END
```



```
1        SUBROUTINE DCRACK (C,ANGLE,NUMCRK)
C
         DIMENSION C(4,1),D(4,4),T(4,4)
         COMMON /CRACK/ GAMMA,STIFAC,SHEFAC
5        C
         IK=NUMCRK
C
         DFAC=STIFAC
         IF(IK.EQ.0) RETURN
10       IF(IK.EQ.4) GOTO 5
         C(3,3)=C(3,3)/SHEFAC
```

```
      5  IF(IK.LE.3) GOTO 10
         C(4,4)=C(4,4)/DFAC
         IK=IK-4
15       IF(IK.EQ.3) GOTO 10
         IF(IK.EQ.2) C(1,4)=C(1,4)/DFAC
         IF(IK.EQ.1) C(2,4)=C(2,4)/DFAC
         IF(IK.NE.0) GOTO 10
         C(1,4)=C(1,4)/DFAC
20       C(2,4)=C(2,4)/DFAC
         GOTO 13
     10  IF(IK.EQ.1) GOTO 20
         DO 11 I=2,4
     11  C(2,I)=C(2,I)/DFAC
25       C(1,2)=C(1,2)/DFAC
C
         IF(IK.EQ.2) GOTO 13
         C(1,1)=C(1,1)/DFAC
         C(1,3)=C(1,3)/DFAC
30       C(1,4)=C(1,4)/DFAC
C
     13  DO 12 I=1,4
         DO 12 J=1,4
     12  C(J,I)=C(I,J)
35       GOTO 102
C
     20  DO 100 I=1,4
    100  C(1,I)=C(1,I)/DFAC
         DO 101 I=1,4
40       DO 101 J=1,4
    101  C(J,I)=C(I,J)
C
```

```
      102 PI=4.*ATAN(1.0)
          IF(ANGLE.GT.360.4) GOTO 90
45        GAM=(ANGLE/360.)*2.*PI
          IF(ABS(GAM).LT.1.0E-8) GOTO 202
          SG=SIN(GAM)
          CG=COS(GAM)
          T(1,1)=CG**2
50        T(1,2)=SG**2
          T(1,3)=CG*SG
          T(1,4)=0.0
          T(2,1)=T(1,2)
          T(2,2)=T(1,1)
55        T(2,3)=-T(1,3)
          T(2,4)=0.0
          T(3,1)=T(2,3)*2.0
          T(3,2)=-T(3,1)
          T(3,3)=T(1,1)-T(1,2)
60        T(3,4)=0.0
          T(4,1)=0.0
          T(4,2)=0.0
          T(4,3)=0.0
          T(4,4)=1.0
65      202 CONTINUE
        C
          IF(ABS(GAM).LT.1.0E-08) GOTO 90
        C
          DO 60 IR=1,4
70        DO 60 IC=1,4
          D(IR,IC)=0.0
          DO 50 IN=1,4
       50 D(IR,IC)=D(IR,IC)+T(IN,IR)*C(IN,IC)
       60 CONTINUE
75      C
```

```
                DO 80 IR=1,4
                DO 80 IC=IR,4
                C(IR,IC)=0.0
                DO 70 IN=1,4
80          70  C(IR,IC)=C(IR,IC)+D(IR,IN)*T(IN,IC)
            80  C(IC,IR)=C(IR,IC)
          C
            90  RETURN
          C
85              END
```

REFERENCES

1. Wimpey Laboratories Limited. Brown and Root (UK) Limited-BP Forties Field Phase I, Report on grout bond tests for large diameter piles. Report EM/112, December, 1974.
2. Wimpey Laboratories Ltd. Burmah Oil Development Ltd. - Thistle Field grout bond testing, Report on test series 1 to 18. Report ST13/76, July 1976.
3. Wimpey Laboratories Ltd. Burmah Oil Development Ltd. - Thistle Field grout bond testing, Effect of drilling mud on second stage grout bond . Report ST16/76, September 1976.
4. Wimpey Laboratories Ltd. Chevron Petroleum (UK) Limited - Ninian Field - Report on grout bond tests. Report ST11/77, March 1977.
5. Wimpey Laboratories Ltd. Union Oil of Great Britain - Heather Field - Grout bond test results. Report ST7/77, March 1977.
6. Wimpey Laboratories Ltd. Lafarge Aluminous Cement Co. Ltd. Effect of cyclic loading on bond strength. Report ST18/77, May, 1977.
7. Wimpey Laboratories Ltd. CJB Offshore Ltd. BP Magnus Field - Grout bond tests. Report ST58/79, September, 1979.
8. Wimpey Laboratories Ltd. Department of Energy - The Strength of grouted pile/sleeve connections - Phase I Final Report - Static Tests. Report ST22/80, April, 1980.
9. Øystein Løset. Grouted Connections in Steel Platforms - Testing and Design. Joint Institution of Structural Engineers/B.R.E. Seminar, 15th November, 1979.
10. Wimpey Laboratories Ltd. Department of Energy - Grouted repairs to steel offshore structures. Final report on Phase I, Pipe to Pipe tests and Preliminary node tests. Report ST 28/80, March, 1980.
11. C.J. Billington and G.H.G. Lewis. The Strength of Large Diameter Grouted Connections, Offshore Technology Conference, Houston, Texas, 1978, Paper OTC 3083.
12. C.J. Billington and I.E.Tebbett. The basis for new Design Formulae for Grouted Jacket to Pile Connections, Offshore Technology Conference, Texas, 1980. Paper OTC 3788.

13. American Petroleum Institute, Recommended Practice for Planning, Designing and Constructing Fixed Offshore Platforms. Specification API RP2A, Eigth Edition, April, 1977.
14. Department of Energy, Offshore Installations : Guidance on Design and Construction. London, 1977.
15. American Petroleum Institute, Recommended Practice for Planning, Designing and Constructing Fixed Offshore Platforms. Specification API RP2A, Tenth Edition, March 1979.
16. Baker, M.J. Variability in the strength of structural steels - A study in structural safety. Part I, CIRIA Technical Note 44, April 1973.
17. Department of Energy, Offshore Energy Technology Board, OTP11 - Report of the Working Party on the strength of grouted pile/ sleeve connections for offshore structures. Published by CIRIA.
18. Paslay Incorporated. Development of an Analytical Model for the Ultimate Capacity of Axially Loaded Grouted Pile to Jacket Connections, Final Report to the A.P.I., May 1980.
19. Wimpey Laboratories Ltd. The Modulus of Elasticity and Poisson's Ratio of HAC, Oilwell and Halliburton Expansive Grouts. Report No. ST24/77, May 1977.
20. Van Lee, R. Behaviour of Grouted Pile Connections. M.Sc.Thesis, Massachusetts Institute of Technology, 1980.
21. Ostroot, G.W. The Bond Strength of Offshore Platform Grouts. Chemical Research and Development, Report No. C43-A001-78, April 1978.
22. Brown and Root, Inc. Offshore Structures Department. Design of Grouted Pile-to-Jacket Connections. Status Summary. June, 1978.
23. Wimpey Laboratories. Notes on the Analysis of Grouted Connections. Report No. ST94/80, October 1980.
24. Bathe, K.J. Ozdemir, H., Wilson, E.L. Static and Dynamic Geometric and Material Nonlinear Analysis. Report No.UCSESM 74-4, Structural Engineering Laboratory, University of California. February, 1974.

25. Bathe, K.J., Wilson, E.L., Iding, R. NONSAP - A Structural Analysis Program for Static and Dynamic Response of Nonlinear Systems. Report No. UCSESM 74-3, University of California. 1974
26. Zienkiewicz, O.C. (1977). The Finite Element Method. (London: McGraw Hill).
27. Malvern, L.E. (1969). Introduction to the Mechanics of a Continuous Medium. (New Jersey : Prentice-Hall, Inc.).
28. Ghaboussi, J.Wilson, E.L., and Isenberg, J. (1973) Finite Element for Rock Joints and Interfaces. Journal of Soil Mechanics and Foundations Division, ASCE. 99 (SM10): 833-848.
29. Zienkiewicz, O.C., etal. (1970). Analysis of Nonlinear Problems in Rock Mechanics with Particular Reference to Jointed Rock Systems. In: Proceedings of the 2nd Congress of the International Society for Rock Mechanics, Belgrade. pp.501-509.
30. King, G.J.W., and Pandey, P.C.(1978). The Analysis of Infilled Frames using Finite Elements. Proceedings, ICE, Part 2, 65, Dec. 749-760.
31. Goodman, R.E., Taylor, R.L., and Brekke, T.L. (1968). A Model for Mechanics of Jointed Rock. Journal of Soil Mechanics and Foundations Division, ASCE. 94 (SM3) 637-659.
32. Schafer, H. (1975). A Contribution to the Solution of Contact Problems with the Aid of Bond Elements. Computer Methods in Applied Mechanics and Engineering. 6 (3) 335-354.
33. Herrmann, L.R. (1978). Finite Element Analysis of Contact Problems. Journal of Engineering Mechanics Division, ASCE. 104 (EM5) 1043-1057.
34. Arya, S.K. and Hegemier, G.A. (1982). Finite Element Method for Interface Problems. Journal of the Structural Division, ASCE. 108 (ST2) 327-342.
35. Goodman, R.E., and Dubois, J. (1972). Duplication of Dilatency in Analysis of Jointed Rocks. Journal of the Soil Mechanics and Foundations Division, ASCE. 98 (SM4) 399-422.
36. Bazant, Z.P., and Gambarova, P. (1980). Rough Cracks in Reinforced Concrete. Journal of the Structural Division, ASCE. 106 (ST4) 819-842.

37. Bazant, Z.P., and Tsubaki, T.(1980). Slip-Dilatancy Model for Cracked Reinforced Concrete. Journal of the Structural Division, ASCE. 106 (ST9) 1947-1966.

38. Crisfield, M.A. (1979). The automatic non-linear analysis of stiffened plates and shallow shells using finite elements. Proceedings, Part 2, ICE. 69 891-909.

39. Kotsovos, M.D. (1980). A Mathematical model of the deformational behaviour of concrete undergeneralised stress based on fundamental material properties. Matériaux et Constructions 13 (76) 289-298.

40. Chen, C.T. and Chen, W.F. (1975) Constitutive Relations for Concrete. Journal of the Engineering Mechanics Division, ASCE. 101. (EM4) 465-481.

41. Chen, W.F. and Ting, E.C. (1980) Constitutive Models for Concrete Structures. Journal of the Engineering Mechanics Division, ASCE. 106 (EM1) 1-19.

42. Cedolin, L., Crutzen, R.J. and Poli, S.D. (1977) Triaxial Stress-Strain relationship for Concrete. Journal of the Engineering Mechanics Division, ASCE. 103 (EM3) 423-439.

43. Fardis, M.N. and Alibe, B. and Tassoulas, J.L. (1983) Monotonic and Cyclic Constitutive Law for Concrete. Journal of Engineering Mechanics, ASCE. 109 (2)516-536.

44. Lade, P.V. (1982). Three-Parameter Failure Criterion for Concrete. Journal of the Engineering Mechanics Division, ASCE. 108 (EM5) 850-863.

45. Chen, W.F. (1975). Limit Analysis and Soil Plasticity. (Amsterdam : Elsevier Scientific Publishing Co., Inc.)

46. Chang, T.Y. and Chen, W.F. Extended NONSAP Program for OTEC Structural Systems. ERDA Report No. 000-2682-7. Lehigh University, Bethlehem, Pennsylvania, August 1976.

47. Chen, W.F. and Suzuki, H. (1980) Constitutive Models for Concrete. Computers and Structures. 12 23-32.

48. Chen, W.F., Suzuki, H. and Chang, T.Y. (1980) Nonlinear Analysis of Concrete Cylinder Structures under Hydrostatic Loading. Computers and Structures 12 559-570.

49. Peier, W.H. (1983). Model for Pull-Out Strength of Anchors in Concrete. Journal of Structural Engineering, ASCE. 109 (5) 1155-1173.

50. Wimpey Laboratories Ltd. Department of Energy - Grouted repairs to steel offshore structures. Results of further tests. Report No. ST96/81B, October 1981.

51. Wimpey Laboratories Ltd. Department of Energy. The strength of grouted pile/sleeve connections. Results of further static tests. Report No. ST3/81, January 1981.